Large Roughness Effects on the Onshore Tsunami Propagation and Inundation: A Numerical Modelling Study

Von der
Fakultät Architektur, Bauingenieurwesen und Umweltwissenschaften
der Technischen Universität Carolo-Wilhelmina
zu Braunschweig

zur Erlangung des Grades eines
Doktor-Ingenieurs (Dr.-Ing.)
genehmigte

Dissertation

von
Stefan Leschka
geboren am 23.11.1972
aus Magdeburg

2021

Eingereicht am: 14.04.2020
Disputation am: 25.03.2021

Berichterstatter: Prof. Dr.-Ing. Hocine Oumeraci
Prof. Ph.D. Eric Damgaard Christensen
Prof. Dr.-Ing. Nils Goseberg

Acknowledgements

Finalizing this thesis would not have been possible without the support and encouragement of many people, to which I would like to express my gratitude:

First of all, I would like to thank Prof. Hocine Oumeraci for his continuous support and guidance. I had the chance to learn from his experience, not only technically but also on how to look at problems. His uncompromising views and judgements mean a chance for me to gain deep insight into specific topics. I feel privileged to have had the chance having my work discussed with and reviewed by him.

I also highly appreciate the effort of Professor Erik Damgaard Christensen as an external reviewer Professor Nils Goseberg as a further reviewer as well as Professor Jochen Aberle as a Chairman and Professor Martin Geier as an examiner. I would like to thank all of them for their fairness and for providing me with valuable comments.

The next person I want to thank, who exceptionally supported me over the years and who, at the same time, became a close friend, is Ole Larsen. He employed me at DHI, supported me when expressing the wish to work on a specific topic for a longer time than usual professional projects last, and he always searched for ways to make working full time as well as advancing in the thesis possible. He gave me the chance to work in the challenging field of tsunamis, doing my first steps together with my friend and very experienced colleague Widjo Kongko. His incredible goal-orientated and pragmatic view on things is a true inspiration. Over the years, all my colleagues and department heads managed to keep up their supportive attitude, from which I want to mention exemplarily Oliver Stoschek and Elimar Precht, who had been my department heads for many years.

I want to thank Mrs. Fournier, the secretary of Leichtweiss-Institute (LWI) at the University of Braunschweig. She has been always very supportive and warm-hearted. Although I was doing the PhD thesis as an external student, she made me feel welcome at the institute, which was so important to me. I am happy to have had the chance to share my time with the always and uncompromisingly supportive LWI staff, including other PhD students such as Agnieszka Strusinska-Correia, Lisham Bonakdar, David Schürenkamp, Sven Liebisch, Simeidi Husrin and Hisham Elsafti. I want to mention especially Clemens Krautwald, who supported me not only during his work on his master thesis but also afterwards, sacrificing his spare time to work with me on solutions.

While working on this incredibly interesting topic, I have had the chance to meet many knowledgeable colleagues, who were always very supportive, who shared their view with me and gave helpful hints, sharing their data with me and took their precious time to discuss my approaches. Prof. Philip Liu was among the first who I had the chance to share my thoughts with. Prof. Harry Yeh, Prof. Dan Cox and Hyoungsu Park shared their data with me. Xiaoming Wang introduced me to COMCOT. I am grateful for their patience and willingness to answer my questions.

I want to express my gratitude to my friends Selim Karayazici and Susanne Grimski, who always supported me with their time and their hospitality in Braunschweig.

Finally, I am grateful for my parents and my parents in law who have always been very supportive and sharing their views with me. Their patience and considerateness have become increasingly important over the years for finalizing the PhD which had started under different circumstances. Especially, I am grateful for my wife. Although, I had spent my spare time mostly on the PhD thesis while working on a full-time-job as well the past ten years, she has always been encouraging, supportive, never giving up on me, trying to see the positive things while hoping for a sooner end of the PhD thesis. I could not have finalized the work without her. I am looking forward to spending more time with my family.

Kurzfassung

In der Tsunami-Gefahrenbewertung wird das gefährdete Gebiet mit Hilfe von numerischen Modellen bestimmt, die die Tsunami-Ausbreitung im offenen Ozean sowie die Überflutungsfläche berechnen. Meist werden großskalige, tiefengemittelte Modelle verwendet, die z.B. auf der nicht-linearen Flachwassergleichung (NLSW) basieren. Sie stellen gemeinhin den besten Kompromiss zwischen Genauigkeit und benötigter Computer-Leistung dar. In diesen Modellen wird generell das quadratische Reibungsgesetz mit einem Manning-Beiwert angewandt, um die Bodenrauheit in jedem Berechnungselement zu berücksichtigen. Jedoch bestehen küstennahe Gebiete in der Regel auch aus sogenannten Makro-Rauheitselementen (MRE) wie Gebäuden und Vegetation. Allein rein empirische Manning-Beiwerte für die Berücksichtigung so großer Hindernisse zu verwenden ist physikalisch nicht korrekt und hat große Modell-Unsicherheiten zur Folge. Derzeit liegt kein NLSW-Modell vor, das MRE-induzierte Energieverluste bei Tsunami-Überflutungen adäquat berücksichtigt.

In dieser Doktor-Arbeit wurde versucht zu einem besseren Verständnis der Auswirkungen relevanter MRE-Parameter, wie z.B. Form, Größe und Anordnung, auf die Tsunami-Ausbreitung und -Überflutung beizutragen. Zunächst wurde der derzeitige Wissensstand analysiert, um Wissenslücken zu identifizieren und die Ziele und Methoden für diese Arbeit zu präzisieren. In Phase 1 wurde ein drei-dimensionales Reynolds-gemitteltes Navier-Stokes- (RANS)-Modell basierend auf OpenFOAM anhand von verfügbaren gegenständlichen Experimenten systematisch validiert. Die Anwendbarkeit des RANS-Modells wurde erweitert, indem komplexere MRE-Konfigurationen simuliert und die Ergebnisse mit empirischen Formeln und experimentellen Daten evaluiert wurden. In Phase 2 wurde das RANS-Modell in einer Parameterstudie angewandt und eine Datenbasis für Fließparameter in Relation zu MRE-Konfigurationen erstellt, die in Form, Größe, Höhe, Anordnung und Dichte der MRE variierten, um das Verständnis von Energiedissipationen während Tsunami-Überflutungen unter Tsunami-ähnlichen Fließregimen zu verbessern. Hierbei wurde das Augenmerk auf die Effekte der MRE-Konfigurationen auf die Fließtiefe und den Volumenfluss gelegt, da diese Parameter Zustandsgrößen der Impulsgleichung des NLSW-Modells sind. Dadurch konnte die MRE-Formel direkt als neuer Verlustterm der NLSW-Gleichungen ausgedrückt werden. In Phase 3 wurden die maßgebenden MRE-Parameter ermittelt. Die Parameter wurden sorgfältig gebildet, so dass sie für die Tsunami-Modellierung leicht zu ermitteln bzw. verfügbar sind. Die Energieverluste werden in Analogie zur Morison-Gleichung als Trägheits- und Widerstandsverluste formuliert. In Phase 4 wird die MRE-Formel in das NLSW-Modell COMCOT implementiert. Schließlich wird die Leistungsfähigkeit der MRE-Formel durch den Vergleich der Ergebnisse mit gut dokumentieren Laborexperimenten (Park et al., 2013) und mit zwei der herkömmlichen „äquivalenten Rauheitsansätzen“ bewertet.

Die folgenden Erkenntnisse wurden gewonnen: (i) In einer Gruppe von MRE muss zwischen einer Zufluss-seitigen Rand- und einer inneren Zone unterschieden werden. (ii) Die Parameter Form, Anordnungswinkel, relativer Zwischenraum (Verhältnis zwischen blockierter und gesamter Querschnittsfläche einer Einheitsfläche) und der relativen Höhe (Verhältnis zwischen der Höhe (des überfluteten Teils) der MRE und der Fließtiefe) sind maßgebend. (iii) das MRE-

Modell führt im Vergleich zum herkömmlich verwendeten äquivalenten Rauheitsansatz zu verbesserten Ergebnissen auf Rechengittern unterschiedlicher Auflösungen. (iv) Das MRE-Modell benötigt keine Kalibrierung.

Abstract

In tsunami hazard assessment, the vulnerable area is determined using numerical models, which calculate the tsunami propagation and the inundation extent. Large-scale depth-averaged models, e.g. based on non-linear shallow water (NLSW) equations, are commonly applied. They are commonly understood as best compromise between model accuracy and required computational efforts. In such models, the quadratic friction law with a selected Manning's coefficient is generally applied to account for the effect of the bottom surface roughness in each computational cell. However, macro-roughness elements (MRE) such as buildings and tree vegetation generally form also part of coastal areas. Using purely empirical Manning's coefficients to account for such large objects is not physically sound and might result in large uncertainties. To date, there is not generally applicable NLSW model available for adequately considering MRE-induced energy losses during tsunami inundation.

This Ph.D. thesis attempts to contribute to a better understanding of the effects of relevant MRE parameters such as shape, size, and arrangement of the MREs on tsunami bore propagation and inundation. First, the current state of knowledge is reviewed to identify knowledge gaps and to specify the objectives and the methodology for this study. In phase 1 of this study, a three-dimensional Reynolds-averaged Navier-Stokes (RANS) model based on OpenFOAM is systematically validated using available physical model tests. The applicability of the RANS model is further extended by simulating more complex configurations and evaluating the results with empirical formulae and additional physical data. In phase 2, the RANS model is used in a parameter study to create a database for flow parameters associated to MRE configurations, varying shape, size, height, arrangement, and density of MRE to improve the understanding of energy dissipation processes during tsunami inundation under tsunami-like flow regimes. Hereby, the effects of the MRE configurations on the flow parameters flow depth and volume flux are set in the focus because they are state variables of the NLSW momentum equation. Thereby, the MRE formula is formulated directly as a new source term of the NLSW equation. In phase 3, the most relevant MRE parameters and flow regimes are determined. These parameters are carefully formulated so that they are easily obtainable for tsunami modelling. The energy losses are formulated by considering inertia and drag losses in analogy to the Morison equation. In phase 4, the MRE formula is implemented in the NLSW model COMCOT. Finally, the performance of the MRE formula is evaluated by comparing the results with well-documented physical experiments (Park et al., 2013) and with commonly used "equivalent roughness" approaches.

The following findings are obtained: (i) In a group of MRE, an upstream zone and an inner zone can be distinguished; (ii) The shape, arrangement angle, relative spacing (ratio between blocked and total cross-section of a unit area) and relative height (ratio between height of submerged part of MRE and flow depth) are the most relevant parameters; (iii) The MRE model leads to improved results on various model grid resolutions compared to commonly used equivalent roughness models; (iv) The MRE model does not require calibration.

Table of Contents

List of Figures

List of Tables

List of Abbreviations and Symbols

Symbol	Description	unit
a	Lagrangian coordinate	[m]
A	Front face area	[m²]
A_0	Control area, reference area	[m²]
A_B	Fraction of bottom area occupied by MRE	[m²]
A_B^*	Projected tree area fraction, MRE coverage	[-]
$A_{B,i}^*$	MRE coverage in cell i	[-]
A_i	Front face area in the direction of i	[-]
$A_{mod,dx}$	Modelled area with approach mod and grid resolution dx	[m²]
$A_{mod,dx,overest.}$	Overestimated modelled area with approach mod and grid resolution dx	[m²]
$A_{mod,dx,underest.}$	Underestimated modelled area with approach mod and grid resolution dx	[m²]
$A_{ref,dx}$	Reference area for models with grid resolution dx	[m²]
CC	Correlation coefficient	[-]
C_d	Dissipation coefficient	[-]
C_D	Drag coefficient	[-]
C_D^*	Modified drag coefficient	[-]
C_f	Skin friction coefficient	[-]
C_I	Inertia coefficient	[-]
C_L	Lift coefficient	[-]
C_r	Reflection coefficient	[-]
C_t	Transmission coefficient	[-]
d	Still water depth	[m]
d_{design}	Design run-up at site	[m]
dt	Timestep length	[s]
dt_{max}	Maximum averaging period	[s]
D	Diameter, width	[m]
D_B	Width of building, tree diameter, width of macro-roughness element	[m]
$D_{B,num}$	Width of macro-roughness element based on numerical simulation	[m]
$D_{B,obs}$	Width of macro-roughness element based on observation	[m]
$D_{B,trunk}$	Trunk diameter	[m]
D_{grain}	Grain diameter	[m]
D_B^*	Unidirectional relative width	[-]
$D_{B,x}^*$	Relative width, easterly direction	[-]
$D_{B,y}^*$	Relative width, northerly direction	[-]
D_H	Hydraulic diameter	[m]
E_0	Incident wave energy	[kg/s²]

Symbol	Description	unit
E_d	Dissipated wave energy	[kg/s²]
E_r	Reflected wave energy	[kg/s²]
E_t	Transmitted wave energy	[kg/s²]
f	Factor, friction factor	[-]
f_{DW}	Darcy-Weissbach friction factor	[-]
f_{cube}	Cube factor	[-]
$f_{cylinder}$	Cylinder factor	[-]
f_D	Drag factor	[-]
f_f	friction coefficient	[m]
f_I	Inertia factor	[-]
f_{shape}	Shape factor	[-]
f_t	Time correction factor	[-]
$f_{t,dx}$	Time correction factor for models with grid resolution dx	[-]
f_V	Vortex factor	[-]
F	Force	[N]
F_D	Drag force	[N]
F_I	Inertia force	[N]
F_S	Surface tension	[N/m²/m]
Fr	Froude number	[-]
Fr_{num}	Froude number based on numerical data	[-]
Fr_{obs}	Froude number based on observed data	[-]
g	Acceleration due to gravity	[m/s²]
h	Height, flow depth	[m]
h_0	Impoundment height	[m]
h_B	Wall height, tree height, height of filter system, MRE height	[m]
h_{design}	Design height	[m]
h_{eff}	Effective height	[m]
h_{exp}	Height in experiments	[m]
h_{max}	Maximum flow depth	[m]
h_{num}	Height in numerical simulation	[m]
h_{obs}	Observed height	[-]
$h_{BR\ model}$	Flow depth determined by the BR model	[m]
$h_{NF\ model}$	Flow depth determined by the NF model	[m]
$h_{B,1}$	Building height in cell 1	[m]
$h_{B,2}$	Building height in cell 2	[m]
$h_{B,i}$	Building height in cell i	[m]
$h_{B,trunk}$	Trunk height	[m]
h_x	Flow depth at distance x	[m]
$\bar{h}_{i,j}$	Flow depth, averaged over each cross-section i during timestep j	[m]
H	Wave height, solitary wave amplitude	[m]

Symbol	Description	unit
H_0	Incident wave height	[m]
H_d	Damped wave height	[m]
H_r	Reflected wave height	[m]
H_t	Transmitted wave height	[m]
i	Index	[-]
I	Turbulence intensity	[-]
I_1	Bessel function of first order	[-]
I_E	Energy gradient	[m/m]
j	index	[-]
k	Turbulent kinetic energy	[m²/s²]
	Index	[-]
	wave number	[1/m]
	roughness height	
k_{St}	Manning/Strickler roughness value	[$m^{1/3}$/s]
k_S	Nikuradse's effective roughness height, equivalent sand roughness height	[m]
K	Coefficient	[-]
K_1	Bessel function of first order	[-]
K_G	Interference coefficient	[-]
KC	Keulegan-Carpenter number	[-]
l	Length, width, turbulence length scale	[m]
l_0	Characteristic length	[m]
l_B	Length of the blocked flow zone	[m]
$l_{MRE\ zone}$	Length of the MRE zone	[m]
L	Wave length	[m]
L_0	Length of the tsunami source, impoundment length	[m]
M	Moment	[Nm]
n	Manning's roughness coefficient	[$s/m^{1/3}$]
n_0	Manning's roughness coefficient of the bed	[$s/m^{1/3}$]
N	number	[-]
N_T	Total number of trials	[-]
N_V	Number of valid trials	[-]
Q	flow rate, discharge	[m³/s]
P_a	Dispersion parameter	[-]
p_{dyn}	Dynamic pressure	[kg/m/s²]
Per	Performance ratio	[-]
$Per_{mod,dx}$	Performance ratio for a modelling approach mod and grid resolution dx	[-]
$Per_{MRE\ model,5m}$	Performance ratio for the MRE model with grid resolution dx = 5 m	[-]
$Per_{VF\ model,40m}$	Performance ratio for the VF model with grid resolution dx = 40 m	[-]
PR	peak ratio	[-]

Symbol	Description	unit
q	Volume flux	[m³/s/m]
$q(x)_{i,j}$	Volume flux in the direction of x in cross-section i during timestep j	[m³/s/m]
$\overline{q(x)}_{i,j}$	Space-Averaged volume fluxes at each cross-section are calculated	[m³/s/m]
$\overline{q(x,dt)}_{i,j}$	Space- and time-averaged volume fluxes at each cross-section are calculated	[m³/s/m]
r	Radius	[m]
r_H	Hydraulic radius	[m]
Re	Reynolds number	[-]
Re'	Reynolds number based on friction velocity	[-]
Re_{obs}	Reynolds number based on observation	[-]
Re_{num}	Reynolds number based on numerical simulation	[-]
RIE	Relative inundation error	[%]
$RIE_{CF\ model,20m}$	Relative inundation error for the CF model with grid resolution dx = 20 m	[%]
$RIE_{mod,dx}$	Relative inundation error for a modelling approach mod and grid resolution dx	[%]
$RIE_{VF\ model,40m}$	Relative inundation error for the VF model with grid resolution dx = 40 m	[%]
s	Gravity constant	[-]
S	Strain rate tensor	[m²/s]
S_0	Bed surface slope	[-]
$S_{0,i}$	Bed surface slope in the direction of i	[-]
$S_{f,i}$	Bed friction slope in the direction of i	[m²/s²]
S_{ij}	Strain rate	[m²/s]
S_G	Spacing	[m]
SI	Scatter index	[-]
t	Time	[s]
t_1	Time at timestep start	[s]
t_2	Time at timestep end	[s]
t_{A1}	Arrival time at wave gauge A1	[s]
t_{A8}	Arrival time at wave gauge A8	[s]
t_B	Wall thickness	[m]
$t_{Street\ A}$	Arrival time at wave gauge in Street A	[s]
T	Wave period	[s]
u	Velocity, wave front celerity	[m/s]
$u(x)_{obs}$	Observed flow velocity in the direction of x	[m/s]
$u_{1,max}$	Maximum velocity amplitude	[m/s]
$u_{f,num}$	Friction velocity based on numerical simulation	[m/s]
$u_{f,obs}$	Friction velocity based on observations	[m/s]

Symbol	Description	unit
$u(x)_{i,j,k}$	Flow velocity in the direction of x in element k of cross-section i at timestep j	[m/s]
$u(x)_{max}$	Maximum flow velocity in the direction of x	[m/s]
u'_{fc}	Critical friction velocity	[m/s]
u^*_{max}	Maximum normalized flow velocity	[-]
$\bar{u}_i$	Mean velocity component in the direction of i	[m/s]
$\bar{u}_j$	Mean velocity component in the direction of j	[m/s]
$\overline{u'_i}$	Time-averaged turbulent velocity component in the direction of j	[m/s]
$\overline{u'_j}$	time-averaged turbulent velocity component in the direction of j	[m/s]
$\overline{u(x)}_{i,j}$	averaged flow velocity of the water perpendicular to the cross-section i during timestep j	[m/s]
$\overline{u(x)}_{i,j,max}$	Maximum averaged flow velocity of the water perpendicular to the cross-section i during timestep j	[m/s]
u^+	Dimensionless velocity	[-]
V	Volume	[m³]
V_0	Control volume	[m³]
V_B	Occupied volume	[m³]
V_i	Narrow volume of cross-section i	[m³]
$V_{i,k}$	Volume of numerical element k in cross-section i	[m³]
$V_{B,foliage}$	Net volume of foliage	[m³]
V^*_B	Volumetric occupation	[-]
$V^*_{B,foliage}$	Void ratio of foliage	[-]
x	longitudinal horizontal dimension, direction, distance	[m]
x_i	Distance in the direction of i	[m]
x_j	Distance in the direction of j	[m]
X_i	maximum length of a cell in x direction	[m]
y	Transversal horizontal dimension, direction, distance	[m]
y^+	dimensionless distance from a wall in the boundary layer	[-]
Y	Width	[m]
Y_i	Width of cross-section i	[m]
z	vertical dimension, distance from the bottom	[m]
z_1	Minimum height of the pressure-exposed surface	[m]
z_2	Maximum height of the pressure-exposed surface	[m]
Z	Height	[m]
Z_i	Height of cross-section i	[m]
A, A_1	empirical factors in the inertia source term	[-]
α_1	Phase fraction of phase 1 (water phase), empirical exponent in the inertia source term	[-]
$\alpha_{1,i,j}$	Phase fraction of phase 1 (water phase) of cross-section i during timestep j	[-]

Symbol	Description	unit
$\alpha_{1,i,j,k}$	Phase fraction of phase 1 (water phase) of element k in cross-section i during timestep j	[-]
B	empirical factor in the drag source term	[-]
β_1	empirical exponent in the drag source term	[-]
ε	Turbulent dissipation	[kg/m²s²]
	porosity	[-]
η	Surface elevation	[m]
θ_c	Critical Shields parameter	[-]
θ_i	Bed surface slope angle in the direction of i	[°]
μ	Molecular viscosity	[Ns/m²]
ν	Kinematic viscosity	[m²/s]
ν_T	Turbulent kinematic viscosity	[m²/s]
ρ	Density	[kg/m³]
ρ_0	Density of air	[kg/m³]
ρ_1	Density of water	[kg/m³]
τ	Reynolds stress tensor	[m²/s²]
$\tau_{f,i}$	Bottom shear stress in the direction of i	[N/m²]
τ_{ij}	Total shear stress	[N/m²]
$\tau_{T,ij}$	Turbulent shear stress	[N/m²]
$\tau_{V,ij}$	Viscous shear stress	[N/m²]
Ψ	Arrangement angle	[°N]
	rotation angle	[°]
ω	Specific turbulent dissipation rate	[1/s]
	angular wave frequency	[1/s]
$\mathfrak{B}$	Empirical factor in the drag source term	[-]

Superscripts	Description
$+$	Non-dimensional
$'$	Turbulent fluctuation
1	Associated to phase 1 (water phase)
B	Building, blocking
c	critical
$cell$	Associated to a computational cell
d	Associated to dissipation
dyn	dynamic
eff	effective
E	Associated to energy
f	Associated to friction
$grain$	Associated to a single grain
H	hydraulic
i	Index, direction
j	Index, direction

Superscripts	Description
k	index
m	Associated to inertia
max	maximum
mod	Modelling approach
MRE	Associated to macro-roughness elements
num	numerical
obs	observation
$overest.$	overestimated
r	Associated to reflection
ref	Associated to a reference value
S	Associated to the surface
T	Total, turbulence
$underest.$	underestimated
V	Valid, associated to viscosity
x	Longitudinal horizontal dimension

Math mode accents	Description
$*$	normalized
Δ	delta
∇	Nabla operator
$\bar{}$	Averaged over a cross-section

Abbreviations	Description
2D	Two-dimensional
3D	Three-dimensional
BE	Boussinesq equations
CFD	Computational fluid dynamics
CHL	Charles W. Harris Laboratory of the University of Washington
CM	Current meter
COBRAS	Cornell Multi-grid Coupled Tsunami model
COULWAVE	Cornell University Long and Intermediate Wave Modeling Package
DNS	Direct numerical simulation
EE	Euler equations
FEMA	Federal Emergency Management Agency
Funwave-TVD	Fully Nonlinear Boussinesq Wave Model-Total Variation Diminishing
FZK	Coastal Research Centre Hanover
GiD	Mesh generation software by CIMNE
GIS	Geographic information systems
GNU	GNU's Not Unix
GWK	Large wave flume of the Coastal Research Centre Hanover
LES	Large eddy simulation

Abbreviations	Description
LWI	Leichtweiß-Institute for Hydraulic Engineering and Water Resources
MRE	Macro-roughness elements
NLSW	Non-linear shallow water
NS	Navier-Stokes
PTHA	Probabilistic tsunami hazard assessment
RANS	Reynolds-average Navier-Stokes
SPH	Smooth particle hydrodynamics
SST	Shear stress transport
stl	stereo lithography
VOF	Volume of fluid
WG	Wave gauge

1 Introduction

1.1 Motivation

During the last two decades, two devastating tsunami events the 2004 Indian Ocean Tsunami and the 2011 Tohoku-Oki Tsunami came to high attention. The former impacted numerous coastal regions around the Indian Ocean and resulted in an extremely high number of more than 225,000 causalities (e.g. USGS, 2012). As no tsunami early warning system was in place in the Indian Ocean, no warnings were issued. In Indonesia, the first tsunami waves hit the coastal regions within approximately 30 minutes (Yalciner et al., 2005). It became clear that only a rapidly working tsunami early warning system, including detailed hazard assessment and evacuation planning, which fully integrates national and local authorities and residents, may be able to mitigate the effects of such events in the future.

During the tsunami propagation, seabed bathymetries and morphologies can cause large changes in wave height and direction. Shoals can focus waves, in some cases more than doubling wave height behind a shoal. Other bathymetric features can reduce wave heights. In addition, wave interaction with the bottom can cause wave attenuation. Flood wave propagation onshore and further inland, as it may occur in case of tsunamis, underlie further complex processes, where roughness and associated energy dissipation play a major role. The correct consideration of these effects is essential for the prediction of tsunami height and inundation extent. Especially in urban areas, small-scale topographic patterns such as vegetation and houses make estimating the terrain surface roughness severely complicated. Run-up measurements from post-tsunami field surveys suggest that such features affect the run-up height to the first order (e.g. Satake et al., 1993; Yeh et al., 1993 and Synolakis et al., 1995).

In tsunami hazard assessment the vulnerable area is usually determined using numerical models, which simulate the propagation of the estimated tsunami source energy as a wave to coastal areas, calculate the tsunami height at the shoreline and the inundation extent. Such models calculate water levels and flow velocities at discrete points in the model area. They need to account for the effects briefly mentioned above to estimate their impact on the flow. To do so, tsunami inundation numerical models need to resolve coastal communities with resolutions in the order of 5 to 30 m (e.g. Schlurmann et al., 2010; Gayer et al., 2010; Allen and Greenslade, 2016; Le Gal et al., 2018). Such models come with extremely high computational costs. This is particularly relevant in case of probabilistic approaches, where a number in the order of 1000 hypothetical events are to be calculated (Davies et al., 2017). Therefore, numerical modellers rely on simplifying assumptions, which still allow for reliable results, but at feasible cost.

It is common practice to use depth-averaged numerical models for tsunami inundation modelling. Such models are able to account for the bottom surface roughness and generally use roughness coefficients after Manning or Chezy (Eliasson, et al., 2007). Attempts were made to systematically account for MRE by developing correction factors for Manning's coefficients (e.g. Chow, 1959; Choi et al., 2009). The models often do not include individual buildings and vegetation in the terrain information because detailed up-to-date information is not available, or

the model is too coarse to resolve them. That is why, modelers must artificially increase the bottom roughness coefficients to account for these flow obstacles (e.g. Bricker et al., 2015), which are usually referred to as macro-roughness elements (MRE). Approximations for large scale models have been proposed for coastal forest (e.g. Harada and Imamura, 2000), for urban areas (e.g. Gayer et al., 2010) and based on land use classes (e.g. Leschka et al., 2011; Kaiser et al., 2011). Figure 1.1 illustrates the presence of MRE (DLR, 2008) in the town of Kuta, Indonesia (Digital Globe, 2006).

The physical principle of surface roughness is based on influencing the flow in the boundary layer of the (bottom) surface only. MRE, however, locally reduce the water depth, or even pierce the water surface. They additionally cause drag, inertia and vortex losses. Flood inundation models for urban areas relying solely on surface roughness approaches without including explicitly MRE-induced energy losses are therefore not able to represent adequately MRE and are subject to large uncertainties. Hence, the understanding of the interaction of the tsunami with buildings and vegetation needs to be improved by studying the influences of their characteristics on the propagating tsunami.

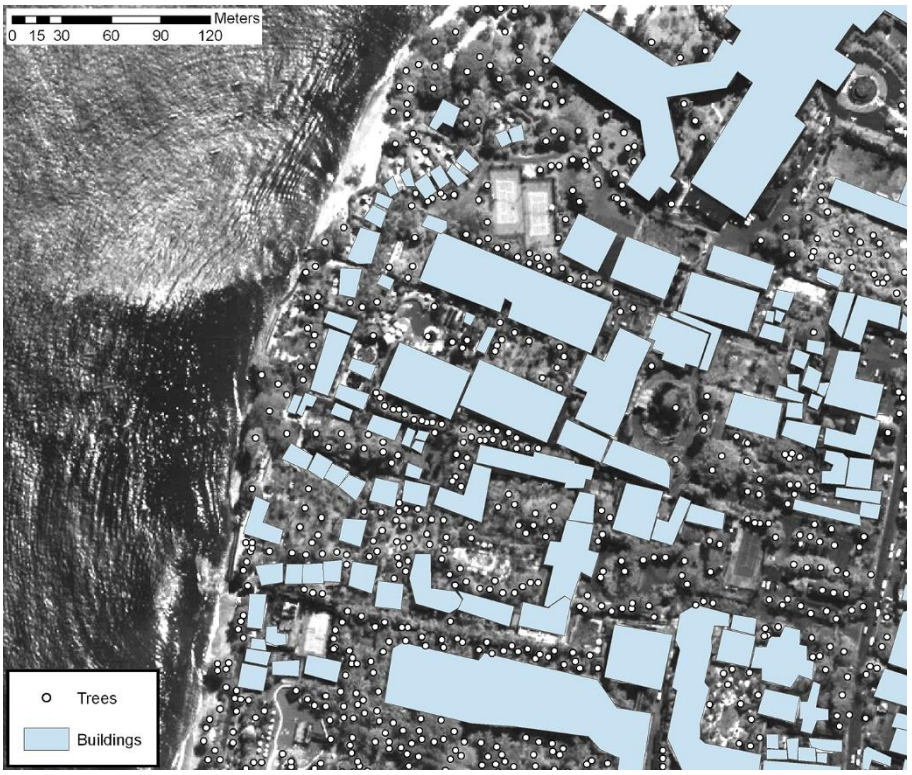

Figure 1.1. Aerial photo of Kuta, Indonesia (Digital Globe, 2006), in which buildings (blue shapes) and trees (white circles) are identified (DLR, 2008).

1.2 Objectives

The main objectives of this study are:

1. To identify buildings and vegetation parameters and their impact on the tsunami propagation, considering various flow phases of the tsunami,

2. To develop empirical formulae to describe flow resistance in dependence of easily accessible parameters of buildings and vegetation, and flow parameters, applicable in large-scale numerical models for tsunami propagation,
3. To show the performance of the developed formulae implemented in a selected NLSW model compared to laboratory data and to NLSW model with common roughness coefficients.

1.3 Scope of work

Based on the objectives, the scope of work is divided into five phases, tentatively outlined in Figure 1.2 and to be specified more precisely in the concluding section of chapter 2.

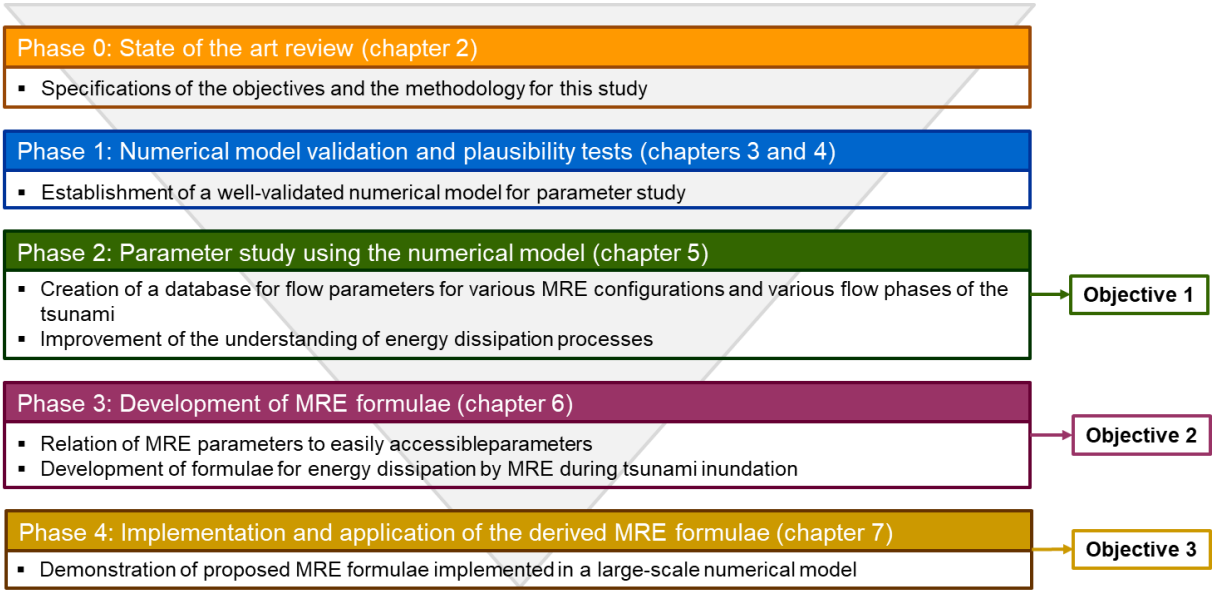

Figure 1.2. Scope and tentative phases of work.

In phase 0, the state of the art is reviewed with the aim of specifying further the objectives of this study and to develop a methodology. In phase 1, a numerical model is established and validated with the help of available physical experiments and additional plausibility tests, so that it can be used in a parameter study. In phase 2, the validated numerical model, established in phase 1, is applied in systematic parameter tests. This will lead to the identification of the impact of each parameter on the tsunami propagation during various flow phases of the tsunami (objective 1). In phase 3, a new MRE formula is developed to be used in large-scale numerical models (objective 2). In phase 4, the MRE formula is implemented in a large-scale numerical model. The results are compared to experimental data and to other roughness models to demonstrate the effect of the proposed formula (objective 3).

2 Current state of knowledge

Wave interaction with the bottom may cause energy dissipation, wave attenuation and wave breaking. Broken or unbroken waves on land, such as tsunamis or storm surges, underlie complex processes. They are influenced by natural obstacles such as dunes and coastal forests, and by manmade structures such as seawalls, dikes or buildings. Such features are examples of macro-roughness elements (MRE), which influence the flow by their geometric characteristics (e.g. Aberle and Smart, 2003) and which are smaller than the grid size of the numerical model. The current state of knowledge regarding MRE, near- and onshore flow regimes, and available methods to quantify them is reviewed in this chapter to specify more precisely the objectives and the methodology for this PhD study.

The types of MRE and the associated flow regimes are defined in section 2.1. Available sets of equations for modelling tsunami inundation are provided in section 2.2, including the methods which may be used to analyse the impact of MRE on the onshore tsunami propagation. The current knowledge on the hydrodynamic processes that mostly affect tsunami wave propagation and energy dissipation, and their consideration in numerical models, are summarized in section 2.3. Section 2.4 gives an overview of available methods to describe the energy dissipation during tsunami inundation. Based on the results, the objectives and methodologies of this PhD study are specified more precisely in section 2.5.

2.1 Types of macro-roughness elements and associated flow regimes

The representation of natural obstacles as MRE and their characteristics (e.g. shape), which are not described by the bathymetry and topography data, is difficult to standardize. The MRE shape may vary for example from relatively plane surfaces for dunes to more complex surfaces for vegetation resulting in a high number of flow obstructions of small scale. The flow regime of the onshore propagating tsunami may be affected by the characteristics of such obstacles and other MRE and need to be understood for its adequate quantification. Furthermore, the availability of such characteristics is an important condition.

In this section, the flow regimes of the approaching tsunami are generally discussed. Among the MRE, it is distinguished between vegetation and man-made structures. Their characteristics and implications to the flow are described. An indication of methods for obtaining MRE parameters is provided at the end of this section.

2.1.1 Tsunami flow regimes

Eye-witness reports and video observations of the 2004 Indian Ocean Tsunami and the 2011 Tohoku-Oki Tsunami documented the run-up and the draw-down phase and indicated flow velocities u between 2 m/s and 11 m/s (Fritz et al., 2006, 2012). Such flow velocities result in high Reynolds numbers

$$Re = \frac{ul_0}{\nu} \tag{2-1}$$

with the characteristic length l_0 and the kinematic viscosity ν, clearly indicating the dominance of drag over viscous effects. For example, Re > 10,000 indicates clearly drag domination (referring to the Shields diagram). During the 2004 Indian Ocean tsunami, videos documented the interaction of the flow with buildings in Banda Aceh, Indonesia (Borrero et al. 2006). Velocity time series indicated that the tsunami front velocity was rapidly increased with increasing flow depth. The flow velocity doubled within 25 s. Froude numbers

$$Fr = \frac{u}{\sqrt{gh}} \tag{2-2}$$

with the acceleration due to gravity g and the flow depth h ranged between 0.61 and 1.04, and indicate the presence of both subcritical and supercritical flow regimes during tsunami inundation (Fritz, et al., 2006). Soares-Frazão and Zech (2008) distinguished between two flow phases: (i) a severe transient (supercritical) flow phase followed by (ii) a slow transient (subcritical), which is close to steady flow conditions.

In order to appropriately describe flow regimes during tsunami propagation, Madsen et al. (2008) considered tsunami time scales and propagation distances and showed that the thresholds for soliton separation are not exceeded neither in the deep ocean nor on the continental shelf, which makes simulating onshore tsunamis by solitary waves not advisable. To find alternative descriptions, constant horizontal velocity over the depth can be assumed for long wave run-up (Laitone, 1960). Such velocity distribution is found not only in tsunami surges but also in dam break waves. Ritter (1892) gave analytical equations for the celerity of the dam break wave front:

$$u = 2\sqrt{gh_0} \tag{2-3}$$

The flow depth h_x at a distance x from the dam can be estimated using

$$h_x = h_0 \left(\frac{\frac{x}{t\sqrt{gh_0}} - 2}{-3} \right)^2 \tag{2-4}$$

in which h_0 denotes the reservoir impoundment height, t the time after the dam break and g the acceleration due to gravity. This equation is valid for ideal fluids, where friction is not considered. Chanson (2006) stated that the flow properties are well approximated by Ritter's theory between (i) the most upstream extend of the initial backward characteristic and (ii) a flow region immediately behind the tip region. He supports the findings of Yeh (1991), according to which a broken tsunami wave or bore is a frequent flow regime in destructive tsunamis, which needs to be considered when investigating flooding. For the wave tip region, Castro-Orgaz and Chanson (2017) discussed the validity of Ritter's solution and found that the analytical model by

Whitham/Dressler/Chanson (see e.g. Chanson, 2009) can reasonably well predict the bore propagation, if the positive wave is the main concern. They state that the free-surface profile in the wave tip region can be described according to Chanson (2009) but requires accurate calibration of the equivalent sand roughness height, which is used in the analytical model.

The flows resulting from such flooding interact with various types of MRE, which are mainly vegetation and man-made structures as described in the following.

2.1.2 Vegetation

Coastal vegetation is known for having a damping effect on incoming waves and tsunamis. It can be grouped into wooden vegetation, cultivated fields, grasslands, weeds and scrubs. When assessing the detailed hydraulic performance of vegetation, highly detailed and costly computational models must be used which is not feasible in large-scale modelling. Therefore, several studies were conducted to define the key characteristics of different vegetation structures and to estimate the impact on tsunami inundation from these characteristics (Oumeraci, 2006).

Components, that might resist a tsunami wave and induce vortices of larger scale to the flow, are mainly trunks, roots and the canopy as a whole. The shape of the constitutive components such as leaves, and branches strongly changes in the flow and therefore have a reduced impact on the flow. In case of planted vegetation, where the plants are often placed in rows, the retardation effects of the plants are restricted to those distinct vegetation bands while the flow in the gaps between the rows is relatively unhindered (Green, 2005).

Different types of vegetation were investigated by Aida (1977; as reported in Latief and Hadi, 2007) who distinguished between dense, relatively dense, nearshore vegetation including trees and smaller vegetation. Tanaka et al. (2007) classified eight types of trees from field surveys in Thailand. They can be distinguished based on the tree height and the tree width, and the existence of roots above terrain.

The effect of mangroves on wave attenuation were studied by means of simplified vegetation models. Irtem et al. (2009) and Huang et al. (2011) used rigid cylinders. Ismail et al. (2012) distinguished between canopy, trunk and roots. The authors highlighted the correlation between (i) wave run-up and (ii) density and width of the mangrove forest. Strusinska-Correia et al. (2013) presented a mangrove parametrization based on biomechanical and structural properties, which are relevant for damping both solitary waves and tsunami bores. Husrin (2013) outlined that the submergence of mangrove vegetation is crucial because the root, trunk and canopy zone have different hydraulic influences on the flow, and each zone consists of different rigidities, diameters and other plant characteristics. He suggested that submerged volume and projection area can be helpful indicators for the amount of vegetation interacting with the flow. Maza et al. (2015b) also found a high correlation between regular/irregular wave damping and vegetation density. They introduced the plant parameter standing biomass, which can be useful for large scale numerical simulations.

Investigating uniform vegetation arrangements might lead to underestimating the drag forces when generalized and applied to random arrangements, which are found in nature (Maza et al.,

2015a). Furthermore, in natural vegetation, trunks are rarely parallel to each other so that at various heights, various relative distances between the trunks are found, which results in different flow regimes over the flow depth (Younis et al., 2016).

2.1.3 Man-made structures

Man-made structures in coastal areas are mainly buildings, infrastructure such as bridges and coastal protection structures such as sea walls and dikes. Sea walls and dikes are large structures with the purpose of blocking the flow. Kotani et al. (1998) recommended to include these structures in the bathymetry. Therefore, they will not be considered as MRE but included in the bathymetry in this work. Buildings mainly consist of frame structures and walls. Tsunami wave heights of a few meters would demolish walls easily, but depending on the flow depth and velocity, the frame structures might resist. Therefore, the representation of man-made structures by its individual structural components is very difficult and demand for simplifications.

Bridge piers were investigated by Wei et al. (2015). They studied forces on the piers, which were represented by cylindrical, squared and diamond shapes. Buildings are often represented using rectangular shapes. Soares-Frazão and Zech (2008) investigated the interaction of a dam-break wave with an idealized city and observed wave impacts on structures, or higher water rise following wave reflection against a structure. Flow separation can occur at the corners. In case of a group of aligned MRE, at the most upstream MRE row a hydraulic jump was observed, while the flow depth between the MRE was still low. With increasing flow depth between the MRE, the supercritical conditions changed to subcritical. In case of a rotated MRE group, complex interactions between the flows occurred at each crossroad, and the city was progressively filled with water.

Rueben et al. (2011) performed optical measurements of tsunami inundation through a 1:50 idealized model of the town of Seaside, Oregon, in the laboratory. They found that the overall effect of macro-roughness was to decrease the bore propagation speed by 40 % relative to a setting without MRE. Buildings were idealized as impermeable rectangular blocks.

Schlurmann et al. (2010) investigated the impact of MRE for a case study of the city of Padang using a numerical model and found that MRE reduce the inundated area by approximately 36 %. Goseberg (2013) performed physical and three-dimensional (3D) numerical experiments of flow through different arrangements of idealized buildings and observed that the staggered and rotated configuration results in lower velocities compared to the aligned configurations, leading to higher flow velocity between the MRE. Strong currents may form especially in spaces which are orientated in flow direction, for example streets. The flow is characterised by accelerations and decelerations due to sudden narrowing and widening in between the MRE area. This process increases with increasing permeability of the wave facing MRE area and with increasing non-linearity of the incident waves and directly affects wave run-up. Energy is dissipated from the flow through collision of the flow with the MRE which can be affiliated to transversal interactions due to the element orientation. In case of staggered and rotated configurations, the run-up was reduced by up to approximately 20 %.

2.1.4 Selection of macro-roughness parameters

MRE parameters should be easily identifiable to facilitate any application of derived formulae. They can be available from satellite imagery, aerial photography, geographic information systems (GIS), authorities or surveys.

A key role in simplifying MRE parameterisation is played by remote sensing. While vegetation can be highly automated using mainly spectral and texture information, automated mapping of urban impervious surfaces (roads, buildings, etc.) is not entirely available. Many attempts have been made (see e.g. Kunapo, et al., 2005) but so-called building footprint detection remains a field of active research (Rasmussen, 2020). A recent example for automatic detection of impervious structures is available from DHI (2020).

Macro-roughness elements (MRE) generally consist of vegetation and man-made structures:

- *Vegetation* needs to be considered differently at various heights due to its heterogeneous shape consisting of root system (mangroves), trunk (forest) and canopy (forest and mangroves). Furthermore, its rigidity and its (mostly) random arrangement influence the flow.
- *Man-made structures* can block the flow and also accelerate and decelerate it, particularly in the case of aligned arrangements, depending on the distance between MRE.

As simplified shapes representing onshore MRE, circular, squared and diamond-shaped MRE may be considered.

The detection of MRE parameters via remote sensing is the most convenient method. While vegetation is easily identifiable, methods for building footprint detection exist, but are currently an active field of research.

The similarities between tsunami waves and dam break waves in both space and time scales suggest that the representation of the onshore tsunami as a bore is more appropriate than as a solitary wave. Ritter's theory of the bore shape is a good approximation outside the wave tip region.

2.2 Modelling energy dissipation in flow with macro-roughness elements

The total energy in a progressive wave consists of potential and kinetic energy. Potential energy results from the displacement of the free water surface and the kinetic energy is due to the wave-induced motion of the water particles. This total energy and its transmission are important when examining how waves change while propagating shoreward (Dean & Dalrymple, 1991).

The Euler equations (EE) provide a description of the free water surface elevation and water particle velocities u for inviscid fluids in the three-dimensional (3D) space and time t and read

$$\nabla \cdot u = 0 \tag{2-5}$$

$$\frac{\partial u}{\partial t} + u(\nabla \cdot u) = -\frac{1}{\rho}\nabla p + g \tag{2-6}$$

In these equations, ρ is the fluid density, p is the pressure and g is the acceleration due to gravity. On the left-hand side of equation (2-6), the first term is the temporal variation and the second term is the convection of the fluid. They represent the inertia of the volume. On the right-hand side, the first term is the internal source term, in which $\frac{p}{\rho}$ is the specific thermodynamic work, and the second term is the external source term representing the body acceleration acting on the fluid, e.g. due to gravity. The EE build the basis for the Navier-Stokes (NS) equations, the non-linear shallow-water equations (NLSW) and the Boussinesq equations (BE), which are presented in the following section. The presentation of the equations is followed by a description of methods to determine energy reflection, transmission and dissipation.

For the sake of completeness, it is mentioned that Smooth Particle Hydrodynamics (SPH) techniques become increasingly popular and are applied in recent tsunami impact studies (St-Germain et al., 2014; Wei et al, 2015; Yang et al., 2016; Wang et al., 2018). However, considering Dalrymple and Rogers (2006) and Shao (2006) as the first application in coastal engineering, SPH techniques are still new compared to NS methods, which have a 20 year longer history (e.g. van Gent et al., 1994) in coastal engineering (Higuera et al., 2014a). SPH techniques are therefore not considered in this study.

2.2.1 Navier-Stokes, non-linear shallow-water and Boussinesq equations

A. Navier-Stokes equations

Numerical models have the advantage of providing flow parameters in the entire domain in a pre-defined spatial and temporal resolution. Such detailed flow descriptions can hardly or not fully be gained from physical experiments. In real flow cases, shear stresses need to be considered. This is particularly the case when fluid-structure interaction is of interest, where the flow is close to a boundary and where it decelerates. The problem of velocity reduction in boundary layers can only be solved with a higher order equation, which arises from the consideration of dynamic viscosity μ. In analogy to elasticity, viscosity can be described using shear stresses. Their implementation into the EE leads finally to the Navier-Stokes (NS) equations (Navier, 1822; Cauchy, 1823; Poisson, 1829; Saint-Venant, 1837; Stokes, 1845). This system of equations for the 3D case is composed of one equation for mass conservation (2-7) and three equations for momentum conservation for incompressible flow of a fluid with constant density(2-8):

$$\nabla \cdot u = 0 \tag{2-7}$$

$$\frac{\partial u}{\partial t} + u(\nabla \cdot u) - \frac{1}{\rho}\mu\nabla^2 u = -\nabla h \tag{2-8}$$

The first two terms of the left-hand side of equation (2-8) and the right-hand side are similar to equation (2-6). Both (internal and external) source terms are combined defining the hydraulic head $\nabla h = \frac{1}{\rho}\nabla p - g$. The third term of the left-hand side is the viscous stress term, which acts

as a diffusion of momentum. The expression $\mu\nabla^2 u = 2\mu\nabla \cdot S$ is the viscous stress tensor with the strain rate tensor S.

For laminar flow, viscous shear stress is governed by the Newtonian shear stress relationship. For turbulent flows, where the velocities and pressures fluctuate about mean values due to the presence of eddies, equation (2-8) is modified to describe the mean ($\bar{u}_i$) and the fluctuating quantities (u_i') separately, in order to facilitate their use. When further multiplying with the fluid density ρ, these modifications lead to the Reynolds-averaged Navier-Stokes momentum equation (RANS):

$$\rho\frac{\partial \bar{u}_i}{\partial t} + \rho\bar{u}_j\frac{\partial \bar{u}_i}{\partial x_j} = -\frac{\partial p}{\partial x_i} + \frac{\partial}{\partial x_j}\left(2\mu S_{ij} - \rho\overline{u_j' u_i'}\right) \tag{2-9}$$

The bar denotes time-averaged mean values and the apostrophe denotes the turbulent fluctuations. $\overline{u_j' u_i'}$ is the time-averaged rate of momentum transfer due to the turbulence. $\rho\overline{u_j' u_i'}$ is the Reynolds-stress tensor. There is no explicit solution for this set of equations yet. They have to be solved iteratively, which is time consuming. The equations can be formulated for different fluids making them also appropriate for multi-phase calculations. In such case, RANS models have a phase-surface capturing scheme, such as the Volume of Fluid (VOF) method. RANS-VOF method is successfully been applied in coastal engineering (e.g. Higuera et al., 2014a, 2014b). Codes commonly used in academic groups are open source packages such as OpenFOAM, COBRAS or CADMAS Surf 3D.

There are more accurate methods than RANS-VOF methods such as direct numerical simulations (DNS) and large eddy simulations (LES) (e.g. Sridhar, 2019). However, they are both excluded from this study due to their considerably higher computational costs, making them not feasible for the planned systematic parameter study. Due to the still excessively high computational costs of RANS codes, hybrid methods have been developed which make use of simplifying assumptions in model areas located further away from the area of interest. For example, (i) shallow-water equations used in the far-field are coupled with the incompressible NS equation for vertical velocity distribution in the near-field (Erduran and Kutija, 2003), (ii) fully non-linear potential flow equations are coupled with NS equations (Grilli, 2008) or (iii) two-dimensional (2D) incompressible NS equations with 3D compressible NS equations (Elsafti and Oumeraci, 2017).

B. Non-linear shallow-water equations

Simplifying assumptions led to the development of 2D (depth-averaged) equations for inviscid fluids, which can be solved explicitly. The typical linear shallow-water equations are

$$\frac{\partial \eta}{\partial t} + \frac{\partial}{\partial x_i}[(\eta + d)u_i] = 0 \tag{2-10}$$

$$\frac{\partial u_i}{\partial t} + u_i\frac{\partial u_i}{\partial x_i} + g\frac{\partial \eta}{\partial x_i} = 0 \tag{2-11}$$

with the water surface elevation η, the still water depth d, the space dimensions x_i, the depth-averaged flow velocity u_i, both in the directions of $i = \{x, y\}$, the acceleration due to gravity g and the time t.

Large values of wave steepness H/L with wave height H and wave length L suggest that the small-amplitude assumption is questionable. Then, based on the work of Friedrichs (1948), Lowell (1949), Keller (1958), Stoker (1948) and Carrier and Greenspan (1958), the non-linear shallow water (NLSW) theory has to be applied, which takes into account the interaction with the bottom over variable total water depth $h = d + \eta$ and total shear stress τ_{ij}. The NLSW equations read

$$\frac{\partial h}{\partial t} + \frac{\partial h u_i}{\partial x_i} = 0 \tag{2-12}$$

$$\frac{\partial u_i h}{\partial t} + \frac{\partial u_i^2 h}{\partial x_i} + \frac{\partial u_i u_j h}{\partial x_j} + gh\frac{\partial h}{\partial x_i} - \frac{h}{\rho}\left(\frac{\partial \tau_{ii}}{\partial x_i} + \frac{\partial \tau_{ij}}{\partial x_j}\right) = ghS_{0,i} - S_{f,i} \tag{2-13}$$

(DHI, 2021). On the left-hand side of the momentum equation (2-13), the first term is the temporal variation term, the second is the flux convection term, the third is the cross-momentum term, the fourth is the gravity term and the fifth is the turbulent shear stress term. τ_{ij} is the sum of the viscous shear stress $\tau_{V,ij}$ and the turbulence shear stress $\tau_{T,ij}$

$$\tau_{ij} = \tau_{V,ij} + \tau_{T,ij} \tag{2-14}$$

with

$$\tau_{V,ij} = \mu\frac{\partial u_i}{\partial x_i}, \tau_{T,ij} = \mu_T\frac{\partial u_i}{\partial x_i} \tag{2-15}$$

where $\tau_{T,ij} \gg \tau_{V,ij}$. The turbulent viscosity μ_T is also known as eddy viscosity. In the right-hand side of equation (3-13), $S_{0,i} = sin\theta_i$ is the bed surface slope, defined as an upward slope for the angle between the bed and the horizontal $\theta_i > 0$. $S_{f,i}$ is the bed friction (in analogy to the bed slope often referred to as friction slope) and can be expressed as

$$S_{f,i} = \frac{\tau_{f,i}}{\rho} \tag{2-16}$$

with the fluid density ρ and the bottom shear stress

$$\tau_{f,i} = \frac{1}{2}\rho f|u_i|u_i \tag{2-17}$$

In this equation, f is a friction factor associated with the primary cover layer which is assumed to be constant. It is related to the complicated flow pattern over the primary cover layer and needs to be determined empirically (Kobayashi, 1987). This theory has been found to be adequate for modelling surface elevation, overland flow, river and lake hydrodynamics, and long wave run-up, as well as estuarine and coastal circulation. They are extensively applied in tsunami modelling (see also section 2.4).

NLSW models can handle (i) non-linear effects in very shallow water, (ii) robustly wetting and drying and (iii) are simpler and computationally more efficient at larger scales than other types of 2D depth-averaged models. They cannot completely/adequately reproduce the fully turbulent flow (3D by nature) at the scale required to resolve the processes underlying the energy dissipation by MRE.

Although 3D Navier-Stokes models with a proper turbulence closure model seem more appropriate, they are computationally unaffordable for large scale applications in practice. Therefore, the question of most interest should be how and to which extent such NLSW models could be improved to properly account for the flow resistance induced by MRE.

For advancing in this direction, an appropriate NLSW model is to be selected. For tsunami applications, several NLSW models exist, for example open source models ANUGA Hydro (Nielsen et al., 2005), COMCOT (Liu et al., 1998), MOST (Titov & Synolakis, 1995), GeoClaw (Clawpack Development Team, 2020), TsunAWI (e.g. Rakowsky et al., 2013), TUNAMI (Imamura et al., 2006) and TELEMAC-2D (EDF-R&D, 2014). Their characteristics in terms of accessibility, discretization method and implemented non-linear effects are summarized in Table 2.1.

Table 2.1. Overview of considered open source NLSW models.

Model	Accessibility	Discretization			Considered processes and effects		
		Finite differences	Finite volumes	Finite elements	Spatially varying onshore bottom roughness	Wave breaking	Wave dispersion
ANUGA Hydro	GNU General Public License	-	✓	-	✓	-	-
COMCOT	GNU General Public License	✓	-	-	✓	✓	✓
GeoClaw	Berkeley Software Distribution License	-	✓	-	-	-	-
MOST	Upon request	✓	-	-	-	-	-
TELEMAC-2D	GNU General Public License	-	✓	✓	✓	-	-
TsunAWI	No license	-	-	✓	✓	-	-
TUNAMI	Upon request	✓	-	-	✓	-	-

Compared to other NLSW models, COMCOT has the advantage of including empirically energy dissipation due to wave breaking and dispersion. It is modifiable and freely available under

the GNU General Public License. Furthermore, it solves the NLSW equations on a structured grid, which simplifies the implementation of new empirical relations.

C. Boussinesq equations

The ratio between water depth d and wave length L, the relative depth d/L, determines whether waves are dispersive or non-dispersive and whether the wave celerity, length and height are affected by the bottom. For tsunami, Kajirua (1963) introduced a criterion to determine whether or not the dispersion effect should be taken into consideration using the following parameter:

$$P_a = \left(\frac{6h}{x}\right)^{1/3} \frac{L_0}{h} \tag{2-18}$$

where the travel distance is x and L_0 is the length of the tsunami source measured along the direction of propagation. For $P_a < 4$, the dispersion effect is not negligible. When the dispersion term is required, one has to switch from NLSW equations to the Boussinesq equations (BE).

The existence of long finite-amplitude waves of permanent form propagating in shallow water has first been recognized by Boussinesq (1871). He developed a set of equations assuming the pressure to be hydrostatic so that vertical water particle accelerations are small and imposing a horizontal velocity on the flow to make it steady with respect to the moving reference frame. Peregrine (1967) derived equations of motion for long waves in water of varying depth, including non-linear terms, which correspond to the BE for water of constant depth. Assuming a solitary wave on a beach of uniform slope $S_{0,i}$ with water in the region $x_i > 0$ and $d(x_i) = S_{0,i}x_i$, the BE are

$$\frac{\partial \eta}{\partial t} + \frac{\partial}{\partial x_i}\left[(\eta + S_{0,i}x_i)u_i\right] = 0 \tag{2-19}$$

$$\frac{\partial u_i}{\partial t} + u_i\frac{\partial u_i}{\partial x_i} + \frac{\partial \eta}{\partial x_i} = \frac{1}{3}S_{0,i}^2 x_i^2 \frac{\partial}{\partial t}\frac{\partial^2 du_i}{\partial x_i^2} + S_{0,i}^2 x_i \frac{\partial}{\partial t}\frac{\partial du_i}{\partial x_i} \tag{2-20}$$

Initially, the BE described a wave in water of constant depth and limited the description to waves of small amplitude. Both assumed that density differences are sufficiently small to be neglected except in terms, where they are multiplied by gravity g. Based on equations (2-19) and (2-20), the cnoidal wave theory was developed by Korteweg and de Vries (1895). A particular case of these waves is given by the solitary wave theory. It is the most elementary solution of the BE (Russel, 1844; Miles, 1981; Fenton, 1988). Additional terms for the momentum equations (2-20) are available and may be included to account e.g. for wave breaking (Madsen et al., 1997a, 1997b; Kennedy et al., 2000).

In research, for example the open source BE codes Coulwave (Lynett and Liu, 2008) and Funwave-TVD (Shi et al., 2013) are among the most commonly used Boussinesq-type models, applicable to model tsunami inundation. However, their application on bathymetries with arbitrary shape comprises often stability problems, which makes it difficult to develop a showcase applicable to a wide range of tsunami inundation scenarios.

2.2.2 Reflection, transmission and dissipation

Analysing reflection, transmission and dissipation is one way to determine the influence of MRE on the flow. The ratio of incident and transmitted waves or of the incident and reflected wave to obtain a measure for energy transmission and reflection and eventually, dissipation, are determined. This is shown by Oumeraci and Köther (2009) on the example of submerged wave absorbers by analysing wave signals in the far-field seaward H_r (reflected wave height) and landward H_t (transmitted wave height) of the absorbers and set them into relation with the incident wave height H_0. The incident wave energy E_0, the reflected wave energy E_r and transmitted wave energy E_t were derived by

$$E_j = \frac{1}{8}\rho g H_j^2 \tag{2-21}$$

in which $j = \{0, r, t\}$, ρ is the density of water and g is the acceleration due to gravity. The dissipated wave energy can then be derived by

$$E_d = E_0 - (E_r + E_t) \tag{2-22}$$

Reflection, transmission and dissipation coefficients can be calculated using respectively:

$$C_r = \sqrt{\frac{E_r}{E_0}},\ C_t = \sqrt{\frac{E_t}{E_0}} \text{ and } C_d = \sqrt{\frac{E_d}{E_0}} \tag{2-1}$$

Moreover, a potential flow model, together with a new "structure parameter" (see equation (2-40)), which is required for the matching conditions at the obstacle to account for the energy losses (drag, inertia and vortex losses), was used together with linearized boundary conditions to obtain an analytical model for the prediction of the hydraulic performance of submerged porous barriers. In case that strong vorticity effects are expected, e.g. during bore propagation, turbulence plays an important role. The presence of MRE increases the turbulence (see e.g. Árnason, 2004) and, hence, the energy losses in the flow. This component would be missed out and energy losses induced by MRE would be underestimated. Therefore, a NS flow model instead of potential flow (EE) models should be applied when investigating the impact of MRE on the flow.

Bredschneider and Reid (1954) described wave transmission as a ratio between the incident wave height H_0 and the height of the transmitted wave H_t by means of bottom friction. Mazda et al. (1997) formulated the energy dissipation of swell waves through submerged mangroves in terms of bottom friction. They compared their solution to the relation of Bredschneider and Reid (1954). As their energy losses were higher, the differences were contributed to energy losses due to the mangroves.

When describing the influence of MRE on a tsunami-like bore by high-resolution RANS data, flow quantities such as flow depth and volume flux might be derived and analysed instead of wave heights. They form part of the large-scale (depth-averaged) flow models and can therefore directly be used to derive additional source terms due to MRE for such models.

Due to the implementation of viscosity and the three-dimensional coverage in space, the NS equations are capable to capture important flow phenomena associated with energy dissipation in the close surrounding of macro-roughness elements (MRE). Well-validated RANS-VOF models can substantially extend the understanding of the processes gained from physical model experiments. They are therefore appropriate for this study in order to obtain detailed flow characteristics for various MRE configurations. Among such models, OpenFOAM has the advantage of being an open source model with an active and increasing community of users.

The most efficient and mostly applied models for tsunami inundation are the NLSW models, which consider important non-linear processes such as turbulence and the interaction of the flow with the bottom and are more robust than BE models. The most appropriate NLSW model seems to be COMCOT due to its extended set of equations and convenience in implementing further extensions.

When analysing the flow to assess the impact of MRE, flow depth and volume flux of the incident and transmitted tsunami wave can be used.

2.3 Effects of beach topography on wave propagation and implications for wave modelling

Wave propagation toward the shore is essentially affected by the beach topography which is determinant for non-dissipative processes such as wave shoaling, refraction, diffraction and dispersion as well as for dissipative processes such as wave breaking. Based on analytical methods, Kânoglu and Synolakis (1998) found that small-scale bathymetry changes do impact wave run-up and that the latter is largely controlled by the beach slope. Madsen and Fuhrman (2007) highlighted the relation of the tsunami impact to the beach slope. Shimozono et al. (2012) found that during the 2011 Tohoku-Oki Tsunami, the heights and wave forms were significantly different from bay to bay in the central Sanriku coast, Japan, highlighting the importance of inner-bay topography, spanning a range from short period flooding (e.g. in Ryori Bay) and high resonance to long-lasting floods with high velocities (e.g. in Rikuzentakata).

Both dissipative and non-dissipative processes affect wave run-up and inundation. Therefore, the topographic features should be represented properly in the numerical domain. The effects caused by such features are described in this section.

2.3.1 Non-dissipative processes

Wave shoaling, refraction, diffraction and dispersion are caused by the shape of the bottom topography, which may influence the direction of wave travel and causes wave energy to be concentrated or spread out.

Shoaling and reflection can be described by the NLSW equations by including the bed topography using the bed slope $S_{0,i}$ (Kajiura, 1961; Carrier and Greenspan, 1958; Carrier, 1966). Real

shelf reflections are strongly correlated with the large-scale undulations in coastline positions (Carrier and Noiseux, 1983).

Dispersion due to the interaction of the wave with the sea bottom induces changes to the wave shape, which can be described using the extended BEs (Hamilton, 1977). Yoon and Liu (1989) added wave-current interaction. Improved linear dispersion properties allow a wider range of water depths to reasonably simulate several non-linear effects that occur in the shoaling of surface waves from deep to shallow water, including the amplification of the forced lower- and higher frequency wave harmonics and the associated increase in the horizontal and vertical asymmetry of the waves (Nwogu, 1993). Wang and Power (2011) included an algorithm to account for weakly dispersive waves in the NLSW equations.

Long wave refraction due to different sea bottom shapes such as circular bottom contours and circular sills leads to the trapping of wave energy which is essential to assess the reflection of internal waves at the edge of the sill, particularly if the incident wave angle is large enough. A sufficient condition for trapping is that there shall be a closed ray-path completely surrounding the circular island (Longuet-Higgins, 1967). If the wavelength is sufficiently small with respect to the island diameter, wave refraction and diffraction dominates over reflection. A 2D encroachment surpasses one-dimensional (1D) run-up for wave lengths less than twice the island base diameter (Lautenbach, 1970). The scattering behaviour of a conical island is related to the frequency dependence of wave amplification, which cannot be assessed using linear shallow water theory (Smith and Sprinks, 1975). Liu et al. (1985) developed a parabolic approximation to study the combined refraction/diffraction of weakly non-linear shallow-water waves.

2.3.2 Wave breaking and bottom roughness

In most circumstances, waves break as they approach the shore while unbroken waves may reach the shoreline only in case of (i) very steep beach slope, (ii) very low steepness of incident waves, and (iii) very small water depth in the foreshore so that bottom friction dissipates most of the incident wave energy. The run-up of broken solitary waves as compared to unbroken solitary waves is different (Synolakis, 1987). The quantification of energy losses due to wave breaking offshore is essential for the evaluation of run-up and inundation effects onshore.

For tsunami, onshore wave breaking has also to be considered. Referring to section 2.2.1.B, dispersion causes shorter waves to split from the long-wave crest, which is referred to as soliton fission. The shorter waves can break offshore as observed on a gentle seabed slope in shallow water along the coast during the 1983 Nihonkai-Chubu earthquake tsunami (Shuto, 1985). When soliton fission occurs, the new leading wave height increases remarkably, before breaking. After wave breaking, the height of the split wave decreases due to energy dissipation (Matsuyama et al., 2007). Many researchers investigated the observed processes. They formulated breaking criteria and suggested methods to consider wave breaking and bottom roughness, which are discussed in the following.

The ratio of the horizontal particle velocity at the free surface to the wave speed can serve as breaking criterion (Fujima et al., 1986). Titov and Synolakis (1995) pointed out, that shallow-water theory is not valid anywhere near breaking. When using the BE instead, the inclusion of

wave breaking tended to suppress the dispersion of the wave front due to the mixing caused by wave breaking (Sato, 1996). Zelt (1991) suggested to model wave breaking using the BEs, including a diffusion term in the momentum equation. Schäffer et al. (1993) developed the so-called roller surface concept to model wave breaking using the BEs. They developed an additional convective momentum term, in which the breaking criterion is related to the local slope of the water surface. Madsen et al. (1997a) derived various extensions to the BEs regarding processes taking place in the surf zone, such as linear dispersion characteristic improvements, wave breaking and moving boundary at the shoreline. Sørensen et al. (1998) extended the equations of Madsen et al. (1997b) considering wave-induced horizontal nearshore circulation, coming from wave breaking and wave-induced currents. Kennedy et al. (2000) added a dissipative term due to wave breaking to the BEs.

Wave breaking can also be assumed as point of discontinuity of the shallow-water equation, which allows to some extent to reproduce the global properties of the wave, but not local energy dissipation, which are associated with the plunging jet of the subsequent splash-up (Li and Raichlen, 2002). Madsen et al. (2008) stated that the role of wave breaking for tsunami run-up is often exaggerated. When not aiming for accurate capturing dispersion and wave-breaking and concentrating on run-up, the NLSW equations might still be capable to provide satisfactory results (Teng and Feng, 2000). Glimsdal et al. (2013) stated that undular bores may evolve during shoaling but are not included in shallow-water wave theory. Even though such bores may double the wave height locally, their effect on inundation is more uncertain because the individual crests are short and may be strongly affected by dissipation due to wave breaking. They concluded that a reasonable hazard assessment in the near-field for tsunamis of seismic origin may be based on shallow-water theory.

Kishi and Saeki (1966) found that during run-up of solitary waves, the breaking point is not related to bottom roughness. However, the influence of the bottom friction must be accounted for so that energy and momentum transported to the beach by the wave are sufficiently accurate for the prediction of wave run-up, wave loads on structures, etc. (Heitner and Housner, 1970). For larger beach slope angles $\theta = 10°$ and $\theta = 15°$, the influence of bottom friction is smaller compared to smaller slopes, because friction effects are less pronounced due to reduced wave run-up lengths. During run-up, the incident bore is transformed at the initially undisturbed shoreline into a wave that surges up the beach and consequently followed up by the backwash. This hold, when in the latter flow regimes, the shoreline acceleration approaches the value of the gravity acceleration component down the beach (Hibbert and Peregrine, 1979). Wüthrich et al. (2019) highlighted the importance of bottom roughness on determining loads induced on structures by waves - also by tsunami and dam-break waves.

Beach topography affects onshore tsunami propagation. The larger the tsunami is, the higher is its potential to cause damages in the coastal areas, and the more likely it is that wave transformation processes lead to exceedance of the critical condition for incipient wave breaking.

As a broken waves or bores represent a common flow regime in the case of destructive onshore tsunamis, it needs to be considered when investigating flooding (e.g. Yeh, 1991; Chanson et al., 2006).

The NLSW equation does not fully incorporate all processes, e.g. the modelling of undular bores. Boussinesq-type models account for more relevant processes such as wave breaking but are often difficult to apply to the wide range of natural topologies due to numerical stability issues. Therefore, NLSW models are generally preferred for modelling tsunami inundation. Not considered relevant processes have to be addressed with simplifying assumptions or by introducing additional empirical terms.

2.4 Approaches for energy dissipation by surface roughness and by macro-roughness elements

Energy is dissipated during flooding events (e.g. tsunami inundation or storm surges) while the flow interacts with the bottom and with MRE. It can be distinguished between friction, drag, vortex and inertia energy losses. The amount of dissipated energy depends on the flow conditions, bottom surface roughness as well as on MRE characteristics. Figure 2.1 gives an overview of the principal methodology to derive the relevant MRE parameters which affect the energy losses.

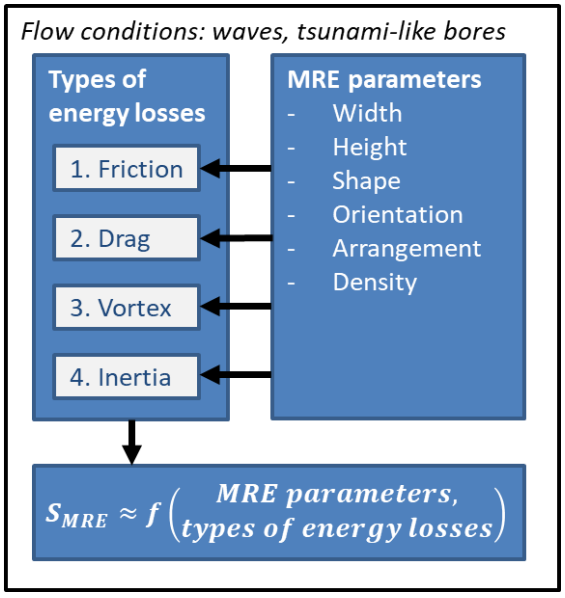

Figure 2.1. Principle methodology to assess the influence of MRE parameters on energy losses.

As indicated in Figure 2.1, the influence of MRE characteristics particularly under tsunami-like flow conditions are assessed in this section for the four indicated types of energy losses. The aim is to set the frame for developing empirical formulae to describe energy losses induced by MRE S_{MRE}, while S_{MRE} depends on the MRE parameters and flow conditions.

2.4.1 Friction losses

Friction losses in a flow field result from vortices acting on a very small-scale directly at the surface of the boundary. These vortices are not transported away from the boundary. Beside the flow conditions, friction losses also depend on the roughness of the surface and affect the vertical flow velocity profile. As such, bed friction also influences the interaction of the flow with MRE over the entire submergence depth of MRE.

Therefore, this section discusses friction in unsteady flow conditions, including waves and tsunami inundation. First, examples of general applications of friction are provided, which form the basis for attempts to consider its application to tsunami and large flow obstructions. Their application to tsunami flow conditions and their validity is discussed to derive the limitations of using the bed friction slope to account for MRE.

A. Examples of general applications

The Manning's formula

$$u = \frac{1}{n}(r_H)^{2/3}\sqrt{S_0} \tag{2-23}$$

with Manning's roughness coefficient n and the hydraulic radius r_H is generally the basis for considering friction losses in NLSW equation models. Hibbert and Peregrine (1979) indicated, that the Chézy friction terms, which can directly be related to Manning's formula in equation (2-23), are unsuited to unsteady flow problems as such terms were empirically developed from steady river flows. This consequentially applies also to n. A review of approaches valid for steady state conditions applied to open channel flow is provided in Leschka (2008).

Vionnet et al. (2004) pointed out that in practical simulations, friction coefficients, roughness values and the depth-averaged eddy viscosity will vary markedly in space and time. As n is a dimensional coefficient, it should only be applied to the channels with the cross-sectional shape they have been determined for. Furthermore, the treatment of bed friction near wet/dry boundaries results in unrealistically large predictions of the shear stress when using Manning's formula. Nevertheless, applying n for unsteady flow conditions is a widely accepted approach.

To include roughness into the NLSW momentum equation (2-13) for unsteady flow conditions, Bradford and Sanders (2002) proposed deriving the bed friction slope using

$$S_{f,i} = f_f u_i \sqrt{u_i^2 + u_j^2} \tag{2-24}$$

where

$$f_f = \frac{gn^2}{h^{1/3}} \tag{2-25}$$

is a friction coefficient, calculated using n. The flow depth h is considered as an adequate substitute for hydraulic radius r_H in the case of very wide-open channels as compared to the water

depth. It is pointed out that the flow in many regions of a typical application may not be fully rough, in which case f_f is underpredicted.

Alternatively, based on the Colebrook equation given by Haaland (1983), Bradford and Sanders (2002) used

$$f_f = \frac{0.204}{ln^2\left[Re + \frac{k_S}{14.8h}\right]} \tag{2-26}$$

in which the Reynolds number (see equation (2-1)) is related to the flow depth as characteristic length. This expression is valid for $1000 < Re < 2.5 \cdot 10^7$ and $0 < k_S/h < 0.2$. Vionnet et al. (2004) specified the friction factor by

$$f_f = \frac{1}{2 \cdot 5ln\left(\frac{11h}{k_S}\right)} \tag{2-27}$$

with Nikuradse's effective roughness height k_S.

Friction under water waves has been investigated by various researchers, which use comparable approaches as in equation (2-16), where the bottom friction slope $S_{f,i}$ depends on u^2. The friction factor f is related to the flow pattern over the primary cover layer and has to be determined empirically (Kobayashi et al., 1987). According to Kishi and Saeki (1966), a friction factor of $f = k_S/4$, might be determined for steady flow conditions. f depends on the bottom slope but not on the wave conditions. Zelt and Raichlen (1991) found that for bottom slopes steeper than θ = 20°, the surface friction does not play an important role (see also section 2.3.2).

In the context of dam failure and storm surge, Zelt and Raichlen (1991) used in their Lagrangian Boussinesq model a bottom friction expression derived by Rouse in 1946

$$S_{f,i} = -\frac{f_f}{d + \eta}\frac{\partial x}{\partial a}u|u| \tag{2-28}$$

Beside the friction coefficient f_f, $S_{f,i}$ also depends on the total water depth with the still water depth d and the surface elevation η, the Lagrangian coordinate a and u^2 They stated that the choice of the bottom friction coefficient is a difficult issue and they used f_f for calibration purposes, which is still a widely accepted method.

B. Applications to tsunami and large flow obstructions

To account also for larger obstacles, e.g. Arcement and Schneider (1989), Petryk and Bosmajian (1975) and Green (2005) developed methods to derive representative Manning's roughness coefficients n to account for flow obstructions and vegetation in vegetated flood plains. In the context of tsunami, several researchers proposed approaches to provisionally incorporate energy losses due to large obstacles by a representative Manning's n (see equation (2-23)) or Chézy value, often referred to as equivalent roughness models, first suggested by Goto and

Shuto in 1983, e.g. Latief (2000), Fujima (2001), Harada and Kawata (2005), Schupiloff and Schimmels (2006), Choi et al. (2009) and Muhari et al. (2011).

Chanson (2006) defined in his tsunami model the bottom friction slope

$$S_{f,i} = \frac{f_{DW}}{2}\frac{u_i^2 h}{D_H} \tag{2-29}$$

with the hydraulic diameter D_H and the Darcy-Weissbach friction factor f_{DW} and could reproduce the maximum flow depths in Banda Aceh (Tsuji, 2005; Borrero, 2005; Chanson, 2005) with a relatively good agreement.

By analysing energy losses of swell waves due to mangroves, Mazda et al. (1997) determined a representative friction factor in equation (2-23) by reproducing the ratio between incident and transmitted wave height by

$$f_f = \frac{d^2}{H_0 \Delta x}\left(\frac{H_0}{H_t} - 1\right) \tag{2-30}$$

with the mean (still) water depth d between the two locations for capturing the offshore wave height H_0 and the transmitted wave height H_t and the distance between both measurement points Δx. Some of the values of Manning n values for MRE representation in tsunami flooding as suggested in previous studies are summarized in Table 2.2.

Table 2.2 shows that Manning's values n for mangroves range between n = 0.01 s/m$^{1/3}$ to n = 0.095 s/m$^{1/3}$ and for urban areas between n = 0.045 s/m$^{1/3}$ and n = 0.172 s/m$^{1/3}$. The reasons for the large bandwidth of n, as discussed in Bricker et al. (2015), are related to the limited experimental data and the associated narrow range of Reynolds and Weber numbers. Despite the raised concerns regarding unsteady flow (Hibbert and Peregrine, 1979; Vionnet et al., 2004), they suggest making use of the extensive experiences in river engineering to estimate representative n values, as summarized in Leschka (2008).

The physical principle of surface roughness is still limited to well-submerged vegetation (Huthoff, 2012; Cassan et al., 2017). This limitation does not generally apply to MRE. Therefore, applying such values to tsunami inundation problems remains questionable and the application of resistance values from look-up tables in numerical investigations remains very subjective; the estimated n can thus be highly inaccurate (Hey, 1972). Therefore, the source term for considering bed friction in the NLSW equation is not suitable for generally accounting for energy losses due to MRE.

Table 2.2. Overview of Manning n values for macro-roughness element (MRE) representation in tsunami flooding as suggested in previous studies.

Application	Manning n values [s/m$^{1/3}$]	Reference
Coastal area, East coast of Japan	0.030	Wei et al. (2012)
Coastal area	0.032	Apotsos et al. (2011)
Mangroves	$0.016 + 0.17V_B^*$, V_B^*>0.07	Latief (2000)
	0.030, V_B^*<0.07	Latief (2000)
Mangroves, resistant	0.095	Kaiser et al. (2010)
Mangroves, non-resisting	0.011 – 0.031	Kaiser et al. (2010)
Forest	0.040	Goto et al. (2012)
	$\sqrt{n_0^2 + \frac{C_D}{2g} h \frac{N}{dxdy} D^{4/3}}$, with $C_D = 8.4V_B^*$+0.66	Harada and Kawata (2005)
Building	0.150	Latief, et al. (2007)
Building, resistant	0.400	Gayer et al. (2010)
Building, non-resistant	0.091	Gayer et al. (2010)
Urban area	0.130	Gayer et al. (2010)
	$\sqrt{n_0^2 + \frac{C_D}{2gD_B} \frac{A_B}{1-A_B} h^{4/3}}$, with C_D = 1.5	Koshimura et al. (2009), Muhari et al. (2011)
	0.030	Jakeman et al. (2010)
	0.050	Goto et al. (2012)
	0.050	Shimozono and Sato (2016)
Urban area (low density)	0.045	Kotani et al. (1998), Koshimura et al. (2009)
	0.053	Koshimura et al. (2009), Petryk and Bosmajian (1975)
Urban area (middle density)	0.060	Kotani et al. (1998)
	0.094	Koshimura et al. (2009), Petryk and Bosmajian (1975)
Urban area (high density)	0.080	Kotani et al. (1998)
	0.172	Koshimura et al. (2009), Petryk and Bosmajian (1975)

$V_B^* = \frac{V_B}{V_0}$: volumetric occupation, n_0: Manning value representing the bed resistance, C_D: drag coefficient, N: number of trees, D: tree diameter, A_B: fraction of bottom area occupied by buildings, D_B: width of buildings

2.4.2 Drag losses

Drag losses occur due to the work that the flow performs on the obstacle while fluid particles have to change their path when moving around the obstacle. The required energy is taken from the flow. These losses are mainly investigated by assessing the forces acting on the obstacle under various flow conditions. Figure 2.2 provides a simplified sketch of the processes and factors affecting drag losses.

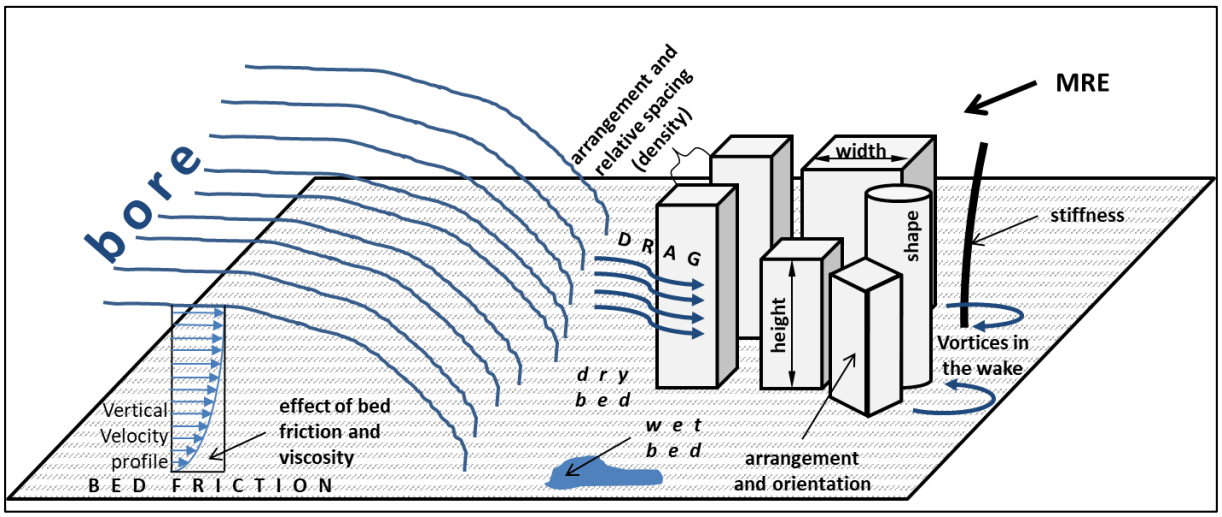

Figure 2.2. Processes and factors affecting drag losses (principal sketch).

The total forces acting on the obstacle do not only contain drag forces but also inertia forces. Furthermore, they are influenced by the bed conditions, which affect the vertical flow velocity profile due to bed friction, which is variable, e.g. when considering dry and wet beds. The amount of energy losses depends also on MRE parameters, for example on shape, size and stiffness.

In this section, drag is discussed based on examples related to tsunami-like bores. First, drag is reviewed in conjunction with other losses. Then, empirical relations are provided to estimate the drag coefficient for various MRE characteristics. Uncertainties in their application, especially under unsteady flow conditions, are highlighted to identify the MRE parameters required to describe the associated energy losses.

A. Dependency of drag from other energy losses

According to Cumberbatch (1960) and Cross (1967), who presented a solution of a tsunami-representing two-dimensional fluid wedge on a flat surface, the drag force on a wall is related to the momentum that would occur at the wall location if the wall were not present, and a gravity force:

$$F_D = \rho C_D A u^2 + \frac{1}{2}\rho g A h \tag{2-31}$$

In this equation, C_D is the drag coefficient which was shown to be a function of the incident wedge angle. Ramsden (1993) found that this equation under-predicts the measured forces due to bore impact in cases of a dry bed. A force difference of approximately 40 % between wet and dry bed was found by Al-Faesly et al. (2012), who measured tsunami-like bore-induced forces on a squared cylinder, only in case of the smallest of three tested inundation depths, while for larger inundation depths, the forces were very similar. By comparing design guidelines FEMA P646 (2008) and SMBRT (Okada et al., 2005) to loads included by a tsunami-like bore during experiments using dry and wet beds, Al-Faesly et al. (2012) found that the equation

proposed by FEMA (2008) considerably underestimated the loads, while the equation proposed in Okada et al. (2005) overestimated the loads, particularly in case of great flow depths. In unsteady flows, Petroff and Raichlen (1991) observed that the in-line force on a body can be decomposed into (i) a drag force proportional to the square of the in-line velocity, and (ii) an inertial force proportional to the fluid acceleration. Tsutsumi et al. (2000) applied this principle and analysed damaged structures along the Okushiri Island coast after the South Hokkaido earthquake tsunami on July 12, 2003. The velocity of the tsunami flow was calculated from the estimated tsunami forces using Morison's equation of a fixed body in oscillatory flow

$$F = \rho C_I V_B \frac{\partial u}{\partial t} + \frac{1}{2} \rho C_D A u|u| \tag{2-32}$$

in which C_I is the inertia coefficient, V_B is the volume of the body and A is the front face area of the body. The first term calculates the inertia force and the second term the drag force. As shown by Keulegan and Carpenter (1958), C_D and C_I vary over time. McNown and Keulegan (1959) found that this variation is related to vortex formation in the wake of the objects and depend on the duration of the flow, so that one set of coefficients appeared to be insufficient to describe forces for an entire wave. Tsutsumi et al. (2000) assumed the tsunami as a steady flow. Therefore, the inertia force was neglected, and the drag coefficient could be assumed to be constant.

Other applications of the Morison equation to tsunami studies are reported e.g. by Noji et al. (1993), Yeh (2006) and Nouri et al. (2010). Adaptations of the Morison equation (2-32) for the drag force are found by many researchers. An overview is provided in Table 2.3.

Table 2.3 Overview of drag force formulae with C_D values for different applications.

Application	Drag force formulae	Flow regime	Reference
Trees	$F_D = \frac{1}{2}\rho u^2 C_D \frac{D_{B,trunk}}{dxdy}$, with $C_D = 1.0$	river flow (steady)	Lopez and Garcia (1997)
Trees	$F_D = \frac{1}{2}\rho u\|u\| C_D \frac{ND_{B,trunk}}{\Delta z} h_{eff}$ with $C_D = 1.1$	river flow (steady)	Erduran and Kutija (2003)
Mangroves	$F_D = \frac{1}{2}\rho C_D D_B du\|u\|$, with $C_D = 1.686 \cdot 10^3 Re^{0.542}$	solitary waves, bores	Husrin et al. (2012)
Sphere	$F_D = \frac{1}{2}\rho u\|u\| C_D \frac{\pi D_B}{4}$, with $C_D^* = 0.5$ to $C_D = 1.0$	long waves	Petroff and Raichlen (1991)
Submerged filter system	$F_D = \frac{1}{2}\rho C_D^* \omega(1-\varepsilon) t_B \int_0^{h_B} u_{1,max}^2(z)dz$, with $C_D^* = \frac{1}{\omega}\frac{4}{3\pi d_B}\frac{\int_0^{d_B} C_D(z)u_{1,max}^3(z)dz}{\int_0^{d_B} u_{max}^2(z)dz}$	Regular, irregular, solitary waves	Oumeraci and Koether (2009)
Buildings	$F_D = \frac{1}{2}\rho C_D D_B du\|u\|$, with $C_D = \{2.05, 2.24\}$	Tsunami	Yeh (2006), Hashimoto and Park (2008) Árnason et al. (2009), Noji et al. (2010), Tsutsumi et al. (2010), Yen and Liu (2011)
Building	$F_D = \frac{1}{2}\rho C_D D_B (hu^2)_{max}$ with $(hu^2)_{max} = gh_{design}\left[0.125 - 0.235\frac{z}{d_{design}} + 0.11\left(\frac{z}{d_{design}}\right)^2\right]$ with $C_D = 2.0$	Tsunami	FEMA (2008)
Building	$F_{total} = \frac{1}{2}\rho g D_B[(6dz_2 - z_2^2) - (6dz_1 - z_1^2)]$	Tsunami	Okada et al. (2005)
Squared cylinders	$F_D = \frac{1}{2}\rho C_D D_B hu^2$ with $C_D = \{1.15, 1.4, 1.65\}$	Tsunami-like bore	Shafiei et al. (2016a)

D_B: building width, $D_{B,trunk}$: trunk diameter, C_D: drag coefficient, ρ: fluid density, u: flow velocity, $dxdy$: lengths of control volume, N: number of trees, z: vertical coordinate, h_{eff}: effective height of (bended) tree, h_{design}: design height, C_D^*: modified drag coefficient, ω: angular wave frequency, ε: porosity, t_B: wall thickness, h_B: height of filter system, $u_{1,max}$: maximum velocity amplitude, h: flow depth, z_1: minimum height of the pressure-exposed surface, z_2: maximum height of the pressure-exposed surface.

B. Dependency of drag from flow and MRE parameters

Morison's equation (2-32) already describes the drag-induced forces in terms of flow velocity, front face area and drag coefficient C_D. Huang et al. (2011) investigated the effect of coastal forest on solitary waves and found the drag coefficient C_D to be a key parameter. He suggested to use

$$C_D = 1.245 + 4.587\frac{V_B}{V_0 - V_B} \tag{2-33}$$

with the control volume $V_0 = d \cdot dxdy$ and the volume of trees in the flow V_B. In the aforementioned guidelines, C_D is assumed constant. In case of tsunami-like bores, Goseberg et al. (2015) showed that C_D varies over the course of the flow-structure interaction. However, C_D remained almost constant for Re > 50,000. The range of Re causing the conditions in the boundary layer to change from laminar to turbulent, known as drag crisis, which can be expected at $Re \approx$ 250,000 (e.g. White, 1991), still implies uncertainty in the selection of a constant drag coefficient.

Various researchers investigated the impact of additional MRE parameters, namely arrangement, shape, orientation to the flow, rigidity and submergence. They are discussed in the following.

Distance and arrangement

In terms of MRE parameters, the drag coefficient has been found to depend on the density of a group of cylinders, but not on the cylinder arrangement (Huang et al., 2011). In contrast, Bonakdar et al. (2014) compared physical experiments of various arrangements of cylindrical piles subject to waves. The influence of arrangement and distance on the drag coefficient was analysed at two different scales. In tandem configuration, the distance between two cylinders has practically no influence on the inline moment, while in side-by-side configuration the inline moment increases in all piles the smaller the distance between them is. This is especially true for the inner pile. Differences are more pronounced in large scale experiments, indicating that small scale experiments might tend to underestimate the influence of the arrangement.

Nouri et al. (2010) concluded that the configuration of obstacles to the flow, upstream of the structure, could have a significant effect on the exerted force on the structure. Therefore, various arrangements could be accounted for in the structural design codes for the estimation of tsunami-induced forces on structures. This suggestion is supported by Maza et al. (2015a) who indicated that generalizations obtained from uniform arrangements could lead to underestimation of wave-exerted forces, especially for configurations with low densities.

Although related to wind with comparably small Reynolds numbers, Hori (1959) investigated the pattern of drag and lift coefficients for various staggered arrangements with two cylinders. He drew the interference force coefficients for drag (C_D) and lift (C_L) for all possible arrangements of the two cylinders, which were rotated around a centre. He further indicated the direction of the interference force and the magnitude of the coefficients C_D and C_L, which is recalled in Figure 2.3.

In Figure 2.3, the six occurrences of lift and drag forces are combined so that five zones can be identified:

1. Negligible lift force and decreased drag force
2. Small repulsive lift force and decreased drag force
3. Repulsive lift force and increased drag force
4. Negligible lift force and increased drag force
5. Negative lift force and decreased drag force

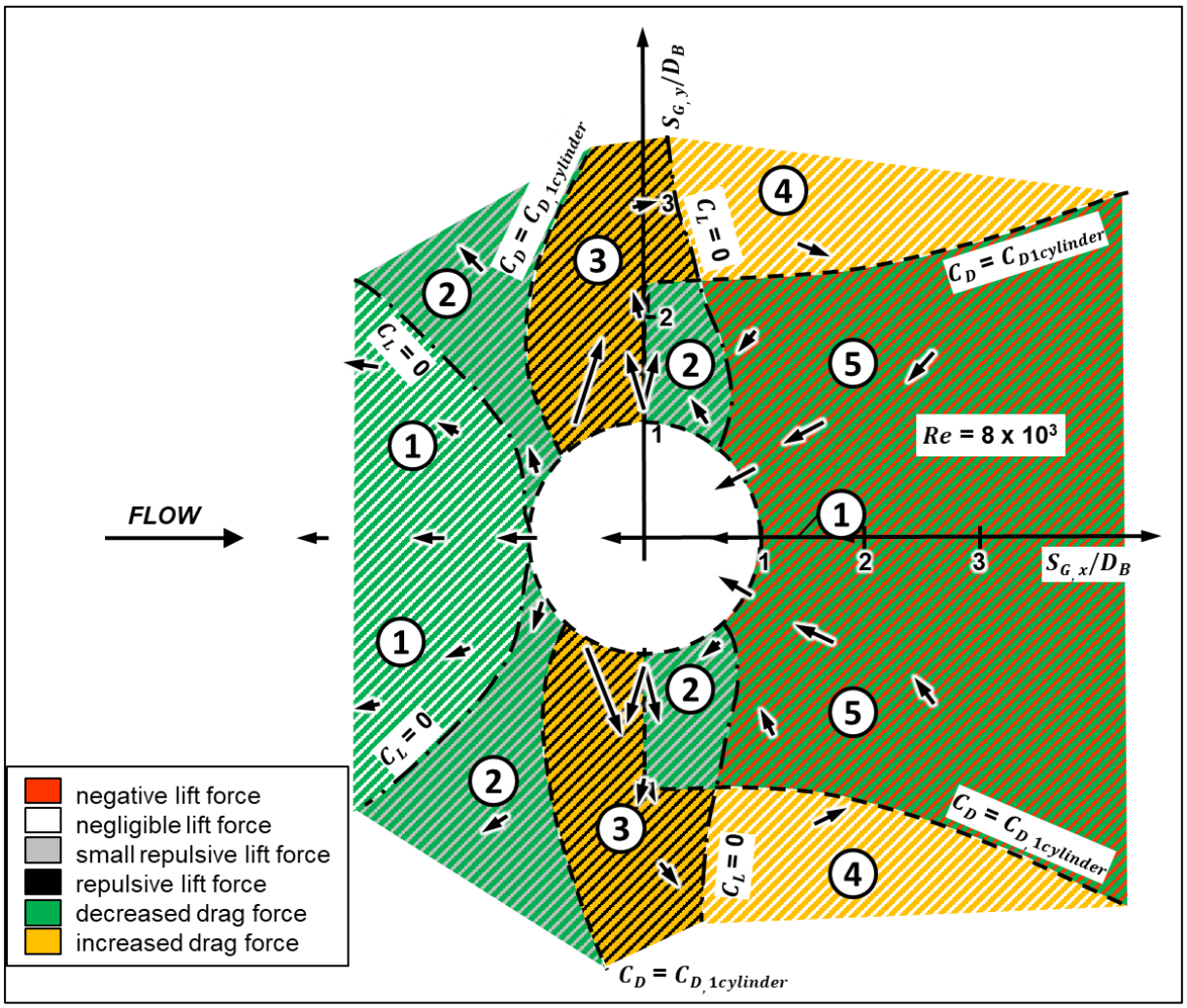

Figure 2.3. Interference force coefficients for all arrangements (redrawn from Hori (1959)).

It is seen qualitatively that the cylinders influence each other to some extent in all arrangements by means of the drag and the lift force. The arrows show the direction of the interference force.

Shape and orientation to the flow

Cassan et al. (2017) found that the ratio between MRE height h_B and diameter $D_B$influences the drag coefficient considerably. For example, when the MRE height is equal to the flow depth ($h = h_B$), then C_D is approximately twice as high as for D_B/h_B = 0.5 than for D_B/h_B = 2.0.

In case of squared cylinders, their orientation to the flow direction (rotation angle Ψ) also affects C_D (Shafiei et al., 2016). For a squared cylinder rotated by Ψ = 0°, 30° and 45°,Table 2.4 shows that the drag coefficient may vary by up to 0,5 as compared to Ψ = 0°.

Table 2.4. Maximum drag coefficients of a rotated squared cylinder (Shafiei et al., 2016).

Rotation angle Ψ [°]	Drag coefficient C_D [-]
0	1.65
30	1.4
45	1.15

Fukui et al. (2019) parameterized C_D based on a characteristic length of the MRE and the Reynolds number Re on experimental scale ($Re < 50{,}000$). The energy losses due to MRE were estimated by the drag source term

$$S_{D,i} = \frac{1}{2} C_D \frac{A_i min(h, h_B)}{dxdyh} q_i \frac{\sqrt{q_i^2 + q_j^2}}{h^2} \tag{2-34}$$

with the projected area of the MRE normal to the flow direction A_i, the flow depth h, the grid cell sizes in the directions $i = \{x, y\}$ dx and dy and the volume flux q_i and $q_j$in the direction i and j, respectively. They noted the difficulty of specifically accounting for the shape of the MRE and could not consider it in the estimation of C_D.

Rigidity and submergence

In case of flexible cylindrical MRE under waves and currents (Losada et al., 2016) and in case of rigid cylindrical MRE under steady current conditions (Cassan et al., 2017), C_D depends only to a small extent on the submergence depth.

The drag effect of vegetation was included in a NLSW equation model by Harada and Imamura (2003), who considered drag due to coastal forest during tsunami inundation. The drag coefficient was determined depending on the amount of submerged vegetation in a control volume

$$C_D = 8.4 V_B^* + 0.66 \tag{2-35}$$

with the submerged vegetation volume fraction $V_B^* = \frac{V_B}{V_0}$ for $0.01 \leq V_B^* \leq 0.07$. The drag source term due to vegetation reads

$$S_{D,i} = \frac{1}{2} C_D A_B^* u_i \sqrt{u_i^2 + u_j^2} \tag{2-36}$$

with the projected tree area fraction $A_B^* = \frac{A_B}{A_0}$ and the projected area of the control area $A_0 = dxdy = \frac{V_0}{d}$. This equation was extended by Matsutomi et al. (2006) to account for the submergence depth and the shape:

$$S_{D,i} = \frac{1}{2} C_D \frac{A_B^*}{f_{shape}} u_i \sqrt{u_i^2 + u_j^2} \frac{A_i}{D_B^2} \tag{2-37}$$

The shape is considered by the shape correction factor f_{shape} (for cylinders, $f_{cylinder} = \frac{\pi}{4}$, for squared cylinders $f_{cube} = 1$). The MRE area projected to the flow A_i is determined by

$$A_i = hD_B \text{ if } h \leq h_B \tag{2-38.a}$$

$$A_i = h_{B,trunk}D_{B,trunk} + \sqrt{\frac{1}{1-V^*_{B,foliage}}\left(hD_B^2 - h_{B,trunk}D_{B,trunk}^2\right)\left(h - h_{B,trunk}\right)} \tag{2-38.b}$$

$$\text{if } h_{B,trunk} < h \leq h_B$$

$$A_i = h_{B,trunk}D_{B,trunk} + \sqrt{\frac{1}{1-V^*_{B,foliage}}\left(h_BD_B^2 - h_{B,trunk}D_{B,trunk}^2\right)\left(h_B - h_{B,trunk}\right)} \tag{2-38.c}$$

$$\text{if } h_B < h$$

In these equations, $h_{B,trunk}$ is the trunk height, $D_{B,trunk}$ is the trunk diameter, h is the flow depth, h_B is the tree height, D_B is the tree diameter and $V^*_{B,foliage}$ is the void ratio of foliage

$$V^*_{B,foliage} = 1 - \frac{V_{B,foliage}}{V_0} \tag{2-39}$$

with the net volume of the foliage $V_{B,foliage}$. Matsutomi et al. (2006) included an additional source term for wave drag, which was neglected in the numerical simulations of inundation of vegetated areas. In these equations, it is difficult to grasp the details of the trees and to express them numerically. The accuracy of the vegetation correction terms and their computed results were determined to be low. However, to the author's knowledge, this method is the first attempt to consider losses induced by MRE, which theoretically is applicable to both vegetation and man-made structures.

These considerations show that C_D is dependent on the shape, the width/height ratio, the arrangement, the orientation to the flow direction and the Reynolds number Re. C_D might therefore been seen as "shape factor", which can be selected to be constant for Re > 50,000 (Goseberg et al., 2015).

2.4.3 Vortex losses

Vortex losses occur on the solid boundary layers of an obstacle for flows with very low Reynolds numbers (e.g. for Re > 5 in case of flow around smooth circular cylinders), where shear stresses act. Fluid particles moving in the boundary layer around the obstacle are separated from the main stream and move into the wake behind the obstacle. In case of higher Re (Re >40 in case of flow around circular cylinders), the wake becomes unstable and eventually, vortices are transported away from the obstacle (Sumer and Fredsøe, 2006). Such vortex streets have been modelled in the wake of vegetation by Marsooli et al. (2016) and by Goseberg et al. (2015) behind a squared cylinder. The impact of vortices on structures is mostly described as part of drag forces (Yeh et al., 1983).

For fully submerged walls in waves, Oumeraci and Koether (2008) developed a new structure parameter

$$S = \frac{1}{(f_D + f_V) - i f_I} \tag{2-40}$$

with the linearized modified drag coefficient f_D, the modified vortex loss coefficient f_V and the modified inertia coefficient f_I and showed that due to flow separation at the crest of the wall, vortices are induced twice during a wave cycle. It was found, that these vortices lead to energy losses which may reach up to 20 % of the total energy dissipation by the wall for moderate wave lengths and large relative wall heights. For longer waves, this effect becomes less important as the vortices are transported away from the wall. Based on the theoretical study of Stiassnie et al. (1984), the vortex loss coefficient was linearized using the Lorentz-Hypothesis, of equivalent work which lead to the expression (Oumeraci and Koether, 2008)

$$f_v = \frac{1}{\omega} \frac{2F_v}{\rho h_B t_B u_{1,max,D_B}} \tag{2-41}$$

with the angular wave frequency ω, the density of the fluid ρ, the height of the wall h_B, the thickness of the wall t_B and the horizontal flow velocity at the upper edge of the wall u_{1,max,D_B}. The dissipated energy flux due to vortices is then

$$F_v = \frac{2.79 \left(k \frac{H_0}{2}\right)^{2/3}}{\langle k(d-h_B)\{K_1^2[k(d-h_B)] + \pi^2 I_1^2[k(d-h_B)]\}\rangle^{4/3}} \frac{1}{32\pi} \rho g^2 T H_0^2 \tag{2-42}$$

with the wave number k, the incident wave height H_0, the water density ρ, the gravitational acceleration g, the wave period T, the still water depth d, the wall height h_B and Bessel functions of first order K_1 and I_1. The (originally included) influence of the wall's porosity is here neglected.

Lin (2004) found that vortex shedding plays a significant role in the solitary wave interaction with MRE. The maximum energy dissipation occurred for the ratio of MRE height to still water depth $h_B/d = 0.95$ due to vortex shedding and wave breaking. When a wave breaks, the falling water produces a plunging jet and the overturning wave crest also closes over to form a vortex tube. Vortices were measured using the V3V technique by Ting and Reimnitz (2015). The mainly observed 3D form was a vertex loop with counter-rotating and transverse vortices. The vortex loop broke when it hit the bottom. The averaged lifetime of a vortex was 0.25 to 0.5T. Instead, the kinetic energy was transported mainly due to wave-induced and turbulence velocities, predominantly in the shoreward direction. Therefore, in a tsunami-like bore, the contribution of vortices to the energy losses can considered as part of turbulence, e.g. in a RANS model (see section 2.2.1).

2.4.4 Inertia losses

Inertia is the resistance of a particle against changing its speed and/or direction and has to be considered under unsteady flow conditions. It acts like shocks to the flow. Fluid particles hit

the obstacles, while no flow pattern exists, which has already balanced with the obstacle. Its contribution to the total energy losses is often described in comparison to drag forces. In this section, the influence of the MRE shape and MRE orientation on the inertia losses is discussed.

As suggested by Petroff and Raichlen (1991), the inertia force can be determined using the first term of Morison's equation (2-32). Some applications of the inertia term are summarized in Table 2.5.

Table 2.5. Overview of inertia force formulae applications to long wave and tsunami conditions.

Application	Inertia force formulae	Flow regime	Reference
Sphere	$F_I = \rho C_I \frac{\pi D_B^3}{6} \frac{\partial u}{\partial t}$ with $C_I = 0.75$ to $C_I = 1.6$	long waves	Petroff and Raichlen (1991)
Cylinder	$F_I = \rho C_I \frac{\pi D_B^2}{4} \frac{\partial u}{\partial t}$ with $C_I = 0$[1)]	Tsunami	Tsutsumi et al. (2000)
Building	$F_I = 1.5 F_D$	Tsunami	FEMA (2008)

F_I: inertia force, ρ: fluid density, C_I: inertia coefficient, D_B: MRE width, u: flow velocity, F_D: drag force, [1)] Inertia force was regarded as negligible, assuming the tsunami as steady current.

In case of tsunami-like bores, Árnason (2004) and Al-Faesly et al. (2012) found that the initial peak of the bore impact on a squared cylinder is up to 1.5 times higher than the force after the impact (drag) which is in agreement with FEMA P646 design guidelines in Table 2.5 (FEMA, 2008), while the Japanese design guideline SMBRT (Okada et al., 2005) does not distinguish between drag and inertia force. Shafiei et al. (2016a) investigated the bore impact on rotated squared cylinders. They found high pressure peaks during the initial bore impact over a dry bed which, however, did not result in high force peaks due to the small flow depth during the un-steady flow phase. The total force during bore impact was lower than the drag forces at the maximum flow depth in all cases. As pointed out in Al-Faesly et al. (2012), the impulsive force from the initial impact of the bore front is even lower in case of an initially wet bed. Nouri et al. (2010) noted from their experiments that the initial impact force did not overshoot the drag force for the case of the cylindrical structure. In the case of diamond-shaped cylinder (= squared cylinder rotated by 45°), no force peak due to the initial bore impact was observed by Árnason (2004). By analysing the forces acting on a circular cylinder from flow field calculations during the 1993 Southwest Hokkaido Earthquake Tsunami, Tsutsumi et al. (2000) found the inertia force being negligible. Nouri et al. (2010) found that the impact duration during the experiments was approximately 0.007 s.

Inertia losses were included in the NLSW momentum equation (2-13) model by Latief (2000) and Harada and Imamura (2000), depending on the relative volume of submerged vegetation in a water volume $V_B^* = \frac{V_B}{V_0}$:

$$S_{I,i} = C_I V_B^* \frac{\partial h u_i}{\partial t} \tag{2-43}$$

with the flow depth h and the flow velocity u_i. Harada and Imamura (2003) suggested an inertia coefficient of $C_I = 1.7$.

Matsutomi et al. (2006) extended the NLSW momentum equation by

$$S_{I,i} = -C_I A_B^* \frac{\partial hu_i}{\partial t} + 2A_B^* \frac{\frac{hu_i}{D_B}\frac{\partial D_B}{\partial h} + \frac{1}{2}C_{I,i}u_i}{1 - A_B^* - 2A_B^* \frac{h}{D_B}\frac{\partial D_B}{\partial h}} \left(\frac{\partial hu_i}{\partial x_i} + \frac{\partial hu_j}{\partial x_j}\right) \quad (2\text{-}44)$$

with the projected tree area fraction $A_B^* = \frac{A_B}{A_0}$ and the tree diameter D_B. Nevertheless, the drag losses (see equation (2-36)) were assumed to be dominant compared to the inertia losses.

These studies suggest that inertia should be considered when (i) the face of the obstacle is orientated normal towards the approaching bore and (ii) structure loads are of concern. Inertia depends on the size, the shape and the arrangement of the MRE. As MRE can be of various shape and orientation, inertia is to be considered in a generally applicable MRE formulae.

Friction losses are mostly considered in NLSW equation models using (dimensional) Manning values n. Until recently, so-called equivalent roughness values are used, which account also for vegetation and man-made structures (Bricker et al., 2015). Due to its limitation to well-submerged obstacles and steady flow assumption of the Manning formula, its application to tsunami inundation models might result in large uncertainties.

Drag and inertia can be described using Morison's equation (2-32) (e.g. Petroff and Raichlen, 1991). Assuming constant drag C_D and inertia coefficients C_I implies some uncertainty. Various researchers reported on the dependency of C_D on other parameters than the shape such as on the Reynolds number Re (e.g. Keulegan & Carpenter, 1958), the density (Huang et al., 2011; Harada and Imamura, 2003), the arrangement (Bonakdar, et al. 2014), height-diameter ratio (Cassan et al., 2017), the orientation to the flow direction (Shafiei et al., 2016) and rigidity (Losada et al., 2016). This suggests the necessity to define a non-dimensional "shape factor" in order to account for the shape of MRE only. In case of small flow depth, dry or wet bed conditions affect the energy losses. However, assuming constant C_D in tsunami studies is valid for large Re (Goseberg et al., 2015).

Inertia is often neglected in tsunami studies (e.g. Tsutsumi et al., 2000; Okada et al., 2005) as the duration of the impact is extremely short (Nouri et al., 2010), but it should be considered in cases when a flat side of an obstacle faces the flow. In such cases, the impact (inertia) force can reach up to 0.5 times the drag force, particularly for an initially dry bottom. The inertia force depends on the size, the shape and the arrangement of the MRE (e.g. Árnason, 2004; Al-Faesly et al., 2012; Shafiei et al., 2016).

Vortex losses can increase to up to 20% of the total energy losses in case of waves acting on fully submerged porous walls (Oumeraci and Koether, 2008). Vortex formation and, particularly, the shedding of vortices causes fluctuations in energy losses, which are reflected in a changing C_D (McNown and Keulegan, 1959). However, in case of broken waves, the lifetime of the vortex is rather short (Ting and Reimnitz, 2015) and might be addressed as part of the turbulent kinetic energy.

2.5 Specifications of objectives and methodology for the present study

This section discusses the current state of knowledge in considering energy losses in tsunami inundation modelling to derive the objectives and the methodology for the development of a formula that considers the effect of macro-roughness elements (MRE) on tsunami inundation in large scale numerical models. Extensive studies performed in the past by various researchers have contributed to improve the understanding of processes associated with tsunami inundation and resulted in a range of empirical relations to consider energy dissipation in depth-averaged numerical codes such as NLSW and Boussinesq-type models.

The objectives of this study are derived in the following section. The implications of the current state of knowledge are summarized. Furthermore, simplifying assumptions seem necessary. They are stated and their impact is estimated. Section 2.5.2 outlines the methodology applied to derive the MRE formula.

2.5.1 Objectives

Due to the variety of processes and onshore situations, it is extremely difficult to find generally applicable methods to consider energy dissipation processes in a physically sound manner, i.e. based on the understanding of the underlying processes. Consequently, simplifying assumptions are generally required which may lead to serious limitations of the applicability of the models or unreliable modelling results. The objectives in this work are therefore:

(i) to propose and systematically validate a RANS-VOF model against laboratory data, and then
(ii) to use the validated model to create a database of flow parameters associated to various macro-roughness element (MRE) configurations as part of a parameter study;
(iii) to improve the understanding of energy dissipation processes in different groups of MRE under the prevailing flow regimes during tsunami inundation, essentially based on the results of the numerical parameter study;
(iv) to relate energy losses to MRE parameters easily determinable in the field, from data available to the authorities (Cox, 2018) or identifiable by GIS applications (see e.g. Hoonhout et al., 2015),
(v) to develop MRE formulae for the energy dissipation induced during tsunami inundation by macro-roughness in different basic configurations, and finally
(vi) to demonstrate the ability of the new formulae to predict tsunami inundation by incorporating them in a NLSW model and using this model for comparison with physical experiments.

The implications of the current state of knowledge can be summarized as follows:

- *Flow regime:* The predominant flow regime during tsunami-inundation is a broken wave, which can be reproduced as dam break wave (see section 2.1).
- *MRE parameters:* Rigid roughness elements cause more disturbance and energy losses in the flow than flexible ones. Given that buildings withstand the tsunami impact, they

can be assumed to be rigid. Rigid components of vegetation are mainly roots and trunks of trees. Therefore, the MRE parameters to be considered in this study are:

- *Shape:* While buildings mainly have a rectangular shape, rigid vegetation components have mainly circular shapes. For the elements with a rectangular shape, further distinction can be made according to their orientation related to the mean flow direction. A measure for this orientation can be the angle between their longest symmetry axis and the mean flow direction. This allows to distinguish between the flow impacting one of the faces and that on one of the edges of the rectangular elements.
- *Height:* The relative height of the roughness elements is expected to affect the degree of disturbance of the mean flow by the MRE. It is distinguished between fully and partially submerged MRE (e.g. Oumeraci and Koether, 2009).
- *Arrangement:* In coastal zones, buildings are mainly grouped in urban areas. Vegetation can be found in agriculturally used, natural and urban areas. In urban areas and agriculturally used areas, buildings and vegetation tend to be distributed in a more organized way while vegetation in natural areas follows other criteria and will be assumed randomly distributed. The arrangement of roughness elements affects flow disturbance (e.g. Green, 2005). For organized distributions, it can be distinguished between in-line and staggered configurations.
- *Density:* The density of roughness elements in a coastal zone significantly affects energy dissipation (e.g. Kotani et al., 1998).

In order to keep the variety of possible combinations for different roughness elements simple, assumptions are necessary. They are summarized in Table 2.6, which also approximately estimates their effect and importance ranking from 1 (high) to 5 (low) with regard to future research on tsunami inundation in urban areas.

The impact of these assumptions on tsunami modelling in urban areas is estimated as follows:

- *No debris flow*: Sediments, damages to buildings and other features of urban areas (e.g. cars) contribute in debris flow, which highly affect flow characteristics such as the viscosity and the density of the bore. Although its impact is expected to be high, the temporal variation of fluid characteristics will not be considered in this study. This might lead to underestimation of energy losses and overestimation of inundation extents.
- *No morphological changes of MRE*: Roughness elements experiencing tsunami impact might undergo morphological changes during the event. The temporal variation of MRE characteristics, e.g. after exceeding stability thresholds, will not be considered in this study. The impact of this assumption is expected to be considerable and might lead to overestimation of energy losses in urban areas and underestimation of inundation extents.
- *Constant length/width ratio of MRE*: The ratio of width and length of a rectangular MRE will not be varied. The impact is expected to be less important in case of coarse resolution models but might lead to local underestimation as well as local overestimation of energy losses when applied to high resolution models.

- *Only organized MRE configurations*: Only organized distributions of roughness elements which predominantly form urban coastal areas will be considered. Due to the smaller presence of vegetation in urban areas, the impact of this assumption is expected to be small. It is expected to lead to considerable underestimation of energy losses and overestimation of inundation extents, mainly when applied to purely vegetated areas.

Rigid MRE: Since rigid MRE result in higher energy losses, flexible vegetation and flexible components of rigid vegetation will not be considered. The impact of this assumption is expected to be small due to the smaller presence of vegetation in urban areas. When applied to purely vegetated areas, then considering the stiffness is important and the rigidity assumption might lead to considerable overestimation of energy losses and underestimation of inundation extents.

Table 2.6. Approximate estimation of effect of simplifying assumptions in tsunami inundation modelling in urban areas.

Assumption	**addressing literature**	**estimated effect on energy losses in large scale inundation modelling in urban areas**		**Importance rank**
		Underestimation	**Overestimation**	
No debris flow	Iverson & Denlinger (2001), Goseberg et al. (2016), Shafiei et al. (2016b)	High	-	1.
No morphological changes of MRE	-	-	Considerable	2.
Constant width/length ratio of MRE	-	Small	Small	3.
Only organized MRE configurations	Maza et al. (2015a)	Small	-	4.
Rigid MRE	Losada et al. (2016)	-	Small	5.

2.5.2 Methodology

The applied methodology with essentially four work phases and their respective primary aims is outlined in Figure 2.4.

In phase 1, a RANS model based on OpenFOAM will be established by validating the model in terms of flow regimes and fluid-structure interaction, which is described in chapter 3. Additionally, plausibility tests are performed varying arrangement and density of three cylinders to further assess the ability of the model to reproduce fluid-structure interaction. The results are compared to empirical relations found in literature. The tests are presented in chapter 4.

In phase 2, a database of simulated flow parameters associated to various MRE parameters is created. For that, flow parameters and important MRE parameters are selected, which are varied systematically. The results are investigated in detail in order to improve the understanding of

energy dissipation processes in the simulated MRE configurations. Phase 2 is described in chapter 5.

In phase 3, the most important MRE parameters are related to parameters which are accessible, for example using geographic information systems (GIS), field surveys or data available from local authorities. These parameters are used to develop simple formulae for energy dissipation by MRE during tsunami inundation. This is achieved by firstly performing a dimensional analysis, followed by identifying the most relevant MRE parameters and flow regimes and, finally, fitting of data, which is obtained from the parameter tests in phase 2. The development of the MRE formulae is presented in chapter 6.

In phase 4, the performance of the MRE formulae is demonstrated by applying the model to a well-described test case (Park et al., 2013). First, the formulae are discretized and implemented in the NLSW model COMCOT. The results are also compared to other approaches considering MRE. Phase 4 is described in chapter 7.

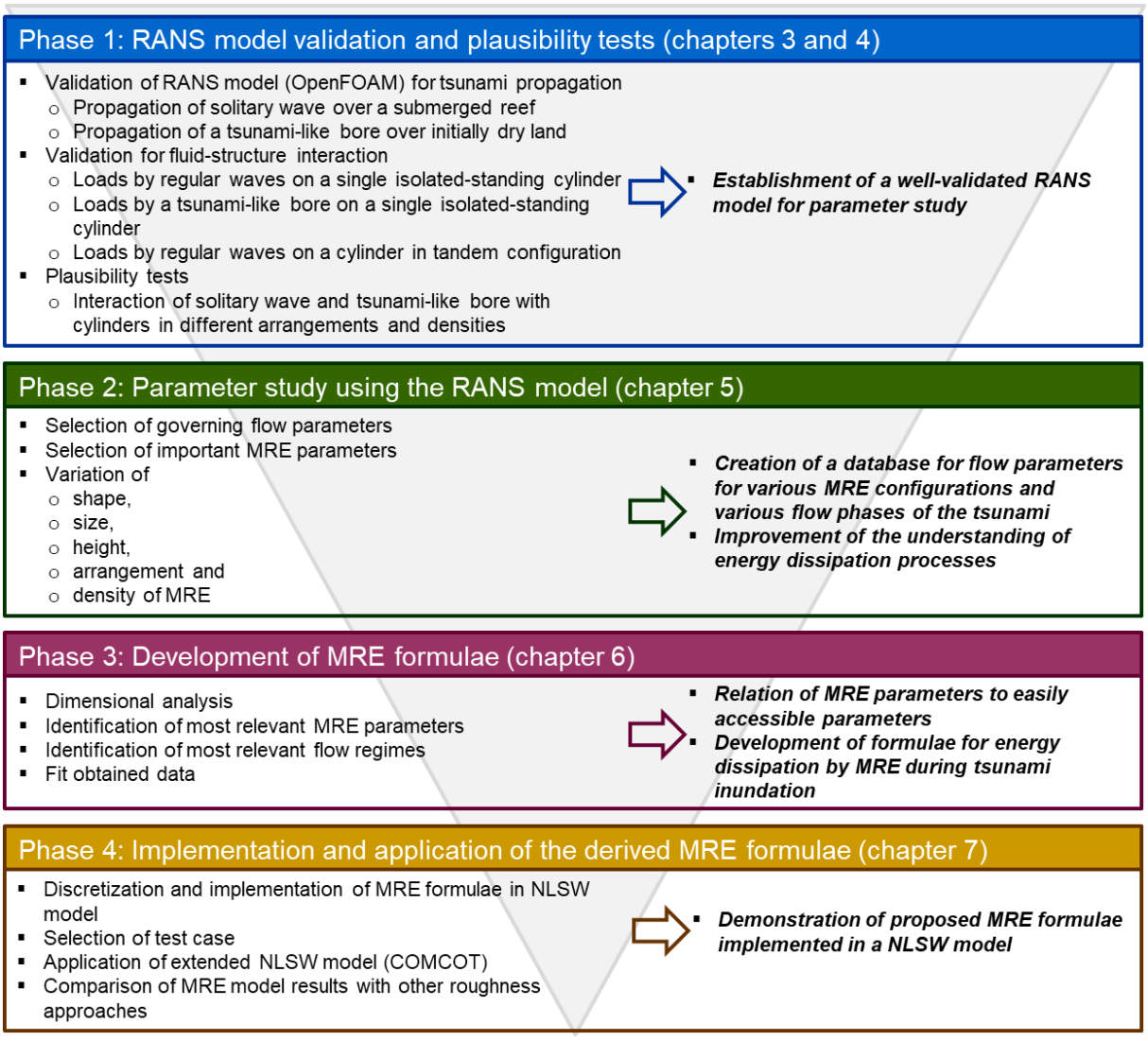

Figure 2.4. Specified methodology (left) and objectives (right) of the PhD study.

3 Numerical model and validation

Computational Fluid Dynamics (CFD) software such as three-dimensional (3D) Reynolds-averaged Navier-Stokes (RANS) models can help to improve the understanding of complex coastal processes, such as those involved in fluid-structure interaction. They can therefore be seen as tools which may ideally complement and extend physical experiments. The models solve partial differential equations by iteration and determine fluid parameters such as flow velocity and hydrostatic and hydrodynamic pressures within a virtual space, the so-called numerical domain. The latter is described by a mesh composed of a number of computational elements. The model provides averaged values which are valid for the temporal range of a time step and the spatial range of the element. Therefore, natural processes are still considered in a simplified manner only. The ability of the model to predict flow parameters as accurately as required has to be tested against analytical solutions and physical experiments, so that the model can be applied for generating numerical data for analysing the flow phenomena associated with macro-roughness elements (MRE).

In section 3.1, the CFD model OpenFOAM (OpenFOAM Foundation, 2011) to be used in this study is briefly described. The derivation of the numerical parameters such as mesh resolution and turbulence settings is provided in section 3.2. As no laboratory experiments could be performed in the frame of this study to describe in detail the flow conditions during a tsunami-like bore propagating through a group of macro-roughness elements (MRE), the CFD model is validated with regard to onshore and offshore flow regimes and the interaction of the flow with obstacles with the help of available laboratory data in section 3.3. The model is applied to reproduce the propagation of (i) a solitary wave over a submerged structure. This is followed by the investigation of the propagation of (ii) a bore over an initially dry bottom. Then, the interaction of (iii) regular waves and (iv) a bore with a single cylinder and of (v) regular waves with two cylinders in tandem configuration are tested. The concluding section of this chapter summarizes the ability and limitations of the selected numerical methods to be applied in this study.

3.1 Description of the CFD model

OpenFOAM ® is a free, open source CFD software package released and developed primarily by OpenCFD Ltd since 2004. It has a large user base across most areas of engineering and science, from both commercial and academic organizations (OpenCFD, 2018). It is to form the basis for numerical data generation in this study.

OpenFOAM uses finite volume discretization schemes to solve systems of partial differential equations ascribed on any 3D structured or unstructured mesh of polyhedral elements (OpenFOAM Foundation, 2011). The package contains the `interFoam` solver for free surface flow, which can be used for coastal applications and which also serves as a basis for wave generation extensions. In section 3.1.2 the turbulence model is discussed and section 3.1.3 introduces applied pre- and postprocessing tools.

3.1.1 Free surface flow solver *interFoam*

`interFoam` is the solver for multiphase incompressible, isothermal, immiscible flow in OpenFOAM. It solves the RANS equations for velocities u and pressure p. The interface between the two fluid phases is captured based on the volume of fluid (VOF) phase-fraction (Hirt & Nichols, 1981).

In the VOF method, the momentum equation and continuity equation are the same for both fluid phases. The physical properties of one fluid are calculated as weighted average based on the volume fraction of the two fluids in one element. The momentum equations take the form

$$\frac{\partial \rho u}{\partial t} + \nabla \cdot \rho u^2 - \nabla \mu \nabla u - \rho g = -\nabla p - F_S \tag{3-1}$$

where F_S is the surface tension, which takes place only at the free surface, g is the acceleration due to gravity, ρ is the density, μ is the molecular viscosity and t is the time.

The continuity equation is given by

$$\nabla u = 0. \tag{3-2}$$

The VOF (water) in an element is computed as

$$V_{water} = \alpha_1 V_{cell} \tag{3-3}$$

V_{cell} is the volume of the computational element and α_1 is the fluid fraction in a computational element. The values of α_1 in an element range from 1 (filled with water) to 0 (filled with the void phase, e.g. air). The (interpolated) value of 0.5 is commonly interpreted as the free surface position.

The scalar function can be computed from a separate transport equation

$$\frac{\partial \alpha_1}{\partial t} + \nabla \cdot (\alpha_1 u) = 0 \tag{3-4}$$

The `interFoam` solver uses the multidimensional universal limiter with explicit solution (MULES-VOF) method to maintain boundedness of the phase fraction independent of the underlying numerical scheme, mesh structure, etc. The compression of the surface is achieved by introducing an extra artificial compression term into the VOF equation (3-4), which then leads to

$$\frac{\partial \alpha_1}{\partial t} + \nabla \cdot (\alpha_1 u) + \nabla \cdot [\alpha_1 (1 - \alpha_1) u^1] = 0 \tag{3-5}$$

where u^1 is a velocity field suitable to compress the interface. This artificial term is active only in the interface region due to the term $\alpha_1(1 - \alpha_1)$.

The density at any point in the numerical domain is calculated as a weighted average of the volume of the two fluids as

$$\rho = \alpha_1 \rho_1 + (1 - \alpha_1)\rho_0 \tag{3-6}$$

with the density of air ρ_0 and the density of water ρ_1. The surface tension F_S is computed as

$$F_S = \sigma \kappa(x) n \tag{3-7}$$

Where n is the unit vector normal to the interface that can be calculated from

$$n = \frac{\nabla \alpha_1}{|\nabla \alpha_1|} \tag{3-8}$$

And κ is the curvature of the interface that can be calculated from

$$\kappa(x) = \nabla \cdot n \tag{3-9}$$

(Olsson and Kreiss, 2005; Olsson et al., 2007). The method is mass conservative and allows sub-grid mixing, but it also leads to interface smearing for sharp interface problems.

The free surface treatment in OpenFOAM does not account for the effects of turbulence. This is a consequence of the fact that the Reynolds-averaged approach to turbulence modelling does not match the notion of an infinitesimally thin interface between air and water. Therefore, the free surface can be viewed as a direct numerical simulation (DNS) of fluid flow.

For all wave cases, the extended solver `waveFoam` from the `waves2Foam` library has been used. It is based on the `interFoam` solver and contains additional libraries for generic wave generation and absorption. Several wave theories such as solitary waves and different order Stokes solutions for non-linear waves are implemented. Absorption works in a so-called relaxation zone, which uses an active sponge layer to damp waves and which can be applied at the outlet boundaries. For more details it is referred to Jacobsen, et al. (2012).

3.1.2 Turbulence model

Turbulence energy equation models were developed to incorporate non-local and flow history effects in the eddy viscosity. Prandtl (1945) postulated computing a characteristic velocity scale for turbulence, thus obviating the need for assuming that the mixing velocity is proportional to the mixing length. He chose the kinetic energy (per unit mass) of the turbulent fluctuations,

$$k = \frac{1}{2}\overline{u_i' u_j'} = \frac{1}{2}\left(\overline{u_x'^2} + \overline{u_y'^2} + \overline{u_z'^2}\right) \tag{3-10}$$

(CFD-wiki, 2011) as a basis for this velocity scale. It can be derived from the Reynolds-stress tensor

$$\tau_{ij} = -\overline{u_i' u_j'} = -2k \tag{3-11}$$

The quantity ε is the turbulent dissipation per unit mass and is defined by the correlation

$$\varepsilon = \nu \overline{\frac{\partial u_i'}{\partial x_k}\frac{\partial u_i'}{\partial x_k}} \tag{3-12}$$

(CFD-wiki, 2015). The most popular k-related turbulence models are introduced in the following.

A. k-ε model

The idea behind the k-ε model is to derive the exact equation for ε and to find suitable closure approximations for the exact equation governing its behaviour. The standard k-ε model (Jones and Launder, 1972) introduces the kinematic eddy viscosity

$$\nu_T = C_\mu \frac{k^2}{\varepsilon} \tag{3-13}$$

the turbulence kinetic energy equation

$$\frac{\partial k}{\partial t} + u_j \frac{\partial k}{\partial x_j} = \tau_{ij} \frac{\partial u_i}{\partial x_j} - \varepsilon + \frac{\partial}{\partial x_j}\left[\left(\nu + \frac{\nu_T}{\sigma_k}\right)\frac{\partial k}{\partial x_j}\right] \tag{3-14}$$

and the dissipation rate equation

$$\frac{\partial \varepsilon}{\partial t} + u_j \frac{\partial \varepsilon}{\partial x_j} = C_{\varepsilon 1} \frac{\varepsilon}{k} \tau_{ij} \frac{\partial u_i}{\partial x_j} - C_{\varepsilon 2} \frac{\varepsilon^2}{k} + \frac{\partial}{\partial x_j}\left[\left(\nu + \frac{\nu_T}{\sigma_\varepsilon}\right)\frac{\partial \varepsilon}{\partial x_j}\right] \tag{3-15}$$

The closure coefficients are

$$\begin{aligned} &C_{\varepsilon 1} = 1.44,\ C_{\varepsilon 2} = 1.92,\ C_\mu = 0.09,\ \sigma_k = 1.0,\ \sigma_\varepsilon = 1.3, \\ &\omega = \frac{\varepsilon}{C_\mu k} \text{ and } l = \frac{C_\mu k^{3/2}}{\varepsilon}, \end{aligned} \tag{3-16}$$

in which ω is the specific turbulent dissipation rate and l is the turbulent length scale (Wilcox, 1998).

The k-ε model is very popular and useful in case of small pressure gradients but fails in case of large adverse pressure gradients in the free-flow zone and in boundary layers (Wilcox, 1998). It overestimates increasingly the turbulent kinetic viscosity during the ongoing simulation at the interface of two phases (Devolder et al., 2017).

B. Wilcox' k-ω model

Wilcox' k-ω model enables one to account for the surface roughness and is generally more suitable to approximate the flow in the boundary layer. The kinematic eddy viscosity is derived from

$$\nu_T = \frac{k}{\omega} \tag{3-17}$$

The turbulence kinetic energy is given by

$$\frac{\partial k}{\partial t} + u_j \frac{\partial k}{\partial x_j} = \tau_{ij} \frac{\partial u_i}{\partial x_j} - \beta^* k\omega + \frac{\partial}{\partial x_j}\left[(\nu + \sigma^* \nu_T)\frac{\partial k}{\partial x_j}\right] \tag{3-18}$$

and the specific dissipation rate equation takes the form

$$\frac{\partial \omega}{\partial t} + u_j \frac{\partial \omega}{\partial x_j} = \alpha \frac{\omega}{k} \tau_{ij} \frac{\partial u_i}{\partial x_j} - \beta \omega^2 + \frac{\partial}{\partial x_j}\left[(\nu + \sigma \nu_T)\frac{\partial \omega}{\partial x_j}\right] \tag{3-19}$$

The closure coefficients and auxiliary relations are

$$\begin{aligned} &\alpha = \tfrac{13}{25},\ \beta = \beta_0 f_\beta,\ \beta^* = \beta_0^* f_{\beta^*},\ \sigma = \tfrac{1}{2},\ \sigma^* = \tfrac{1}{2}, \\ &\beta_0 = \tfrac{9}{125},\ f_\beta = \tfrac{1+70\chi_\omega}{1+80\chi_\omega},\ \chi_\omega \equiv \left|\tfrac{\Omega_{ij}\Omega_{jk}S_{ki}}{(\beta_0^*\omega)^3}\right|,\ \beta_0^* = \tfrac{9}{100}, \\ &f_{\beta^*} = \begin{cases} 1, & \chi_\omega \le 0 \\ \frac{1+680\chi_\omega^2}{1+400\chi_\omega^2}, & \chi_\omega > 0 \end{cases},\ \chi_\omega \equiv \tfrac{1}{\omega^3}\tfrac{\partial k}{\partial x_j}\tfrac{\partial \omega}{\partial x_j},\ \varepsilon = \beta^*\omega k \text{ and } l = \tfrac{\sqrt{k}}{\omega}. \end{aligned} \tag{3-20}$$

The tensors Ω_{ij} and S_{ij} in equation (3-20) are the mean-rotation and mean-strain-rate tensors defined by

$$\Omega_{ij} = \tfrac{1}{2}\left(\frac{\partial u_i}{\partial x_j} - \frac{\partial u_j}{\partial x_i}\right) \text{ and } S_{ij} = \tfrac{1}{2}\left(\frac{\partial u_i}{\partial x_j} - \frac{\partial u_j}{\partial x_i}\right) \tag{3-21}$$

respectively (Wilcox, 1998).

The k-ω formulation in the inner parts of the boundary layer makes the model directly usable through the viscous sub-layer. It is more sensitive to the inlet free stream turbulence properties (Menter, 1994). Furthermore, the turbulent kinetic viscosity tends to increase at the free surfaces during the simulations (Devolder et al., 2017).

C. k-ω-SST model

The k-ω-SST model combines the k-ε model and the k-ω formulation. The regions of a turbulent boundary layer are shown in Figure 3.1.

The axes in Figure 3.1 are defined as the dimensionless distance from the wall (Wilcox, 1998)

$$y^+ = \frac{y u_f}{\nu} \tag{3-22}$$

with the kinematic viscosity ν and the friction velocity u_f, which can be calculated using

$$u_f = \sqrt{\frac{\tau}{\rho}} \tag{3-23}$$

in which τ is the total wall shear stress at the wall and ρ is the water density. Furthermore,

$$\tau = \frac{1}{2} C_f \rho \bar{u}^2 \tag{3-24}$$

In this equation, $\bar{u}$ is a mean velocity, which has to be selected according to the type of flow. For example, it can be the depth-averaged velocity under a wave crest or the propagation velocity of a bore.

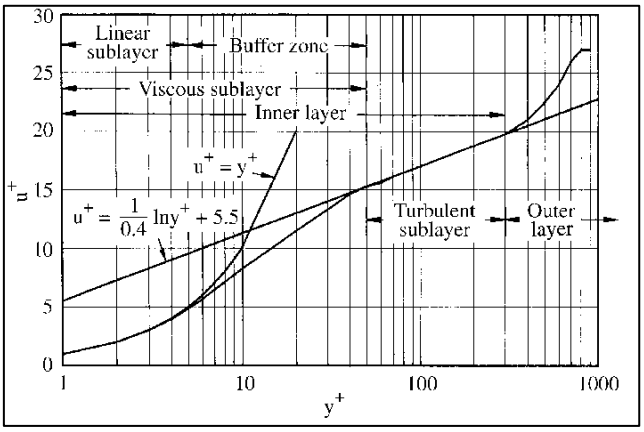

Figure 3.1. Regions of a turbulent boundary layer on an impermeable wall (Cuhadaroglu, 1997).

The skin friction coefficient (von Kármán, 1963)

$$C_f = \frac{0.583}{Re^{0.2}} \tag{3-25}$$

with the Reynolds number

$$Re = \frac{\bar{u} d}{\nu} \tag{3-26}$$

where d is the still water level and ν the kinematic viscosity. Furthermore, the dimensionless velocity (Wilcox, 1998)

$$u^+ = \frac{\bar{u}}{u_f} \tag{3-27}$$

The k-ε model is used in the outer layer and the k-ω model is applied in the inner boundary layer. The k-ω-SST model leads to significant improvements for all flows involving adverse pressure gradients and is able to accurately predict pressure-induced separation (Menter, 1994). Recently, the buoyancy-modification of the k-ω SST model seems to be a promising approach to better controlling the turbulence level in two-phase applications, which is still under development. Here, the k-ω SST model is chosen to be applied in this study.

At the walls, the turbulent kinetic energy $\frac{\partial k}{\partial n} = 0$ (zero gradient) condition applies. For ω and the eddy viscosity ν_T, the boundary conditions are given as

$$\omega = \frac{u_f}{\sqrt{\beta^*}\kappa y_p} \tag{3-28}$$

$$\nu_T = \frac{\sqrt{\beta^*}\sqrt{k} y_p}{log(Ey^+)} \tag{3-29}$$

with the dissipation term coefficient β^*, the Kármán constant κ, the distance to the first calculation point at the wall y_p. The surface roughness is considered as part of the eddy viscosity term. In relation to the non-dimensional absolute roughness height

$$k_S^+ = \frac{k_S u_f}{\nu} \tag{3-30}$$

with the absolute roughness height k_S,

$$E = 9.8 \text{ for smooth walls } (k_S^+ < 2.25) \tag{3-31.a}$$

$$E = \frac{9.8}{\left(\frac{k_S^+ - 2.25}{87.75} + C_S k_S^+\right)^{sin[0.4258log(k_S^+) - 0.811]}} \text{ for transitional roughness } (2.25 < k_S^+ < 90) \tag{3-31.b}$$

$$E = \frac{9.8}{1 + C_S k_S^+} \text{ for fully rough walls } (k_S^+ > 90) \tag{3-31.c}$$

with the roughness constant was selected C_S (OpenFOAM Foundation, 2011).

3.1.3 Pre- and post-processing tools

Numerical domain and mesh generation: The geometry is generated using "GiD", which is an interactive graphical user interface for the definition, preparation and visualization of all data related to a numerical simulation (CIMNE, 2010). The geometries are saved in stereo lithographie (stl) format.

All meshes are generated and manipulated using tools, which are part of the OpenFOAM package. First, the tool `blockMesh` is applied to build a background mesh. By default, resulting meshes are structured and consist of hexahedral elements (OpenFOAM Foundation, 2011). The background mesh is then refined where necessary, using the tools `setSet`, which identifies the regions for refinement, and `refineMesh`, which performs the refinement. Subsequently, `snappyHexMesh` is applied. The tool works in three steps. In the first step, the geometry surfaces (stl files) are used to cut out unwanted regions from the background mesh. In the second step, neighbour mesh elements are snapped to the geometry surfaces. Finally, layers are introduced to ensure the heights of the hexahedral elements at the surface, which are required for a correct estimation of the flow in the boundary layer. `snappyHexMesh` introduces new boundaries to the mesh. They are adjusted so that they match the patch names used for boundary condition specifications in the numerical setup of each simulation. Then, the mesh is renumbered using the `renumberMesh` tool, which saves communication bandwidth during the simulation.

Finally, the mesh is checked using `checkMesh` which controls the topology and the geometry (OpenFOAM Foundation, 2011).

Setup of the relaxation zones: The domain is to be filled with water using the OpenFOAM tool `setFields`. For all wave cases, the boundary conditions for the waves as well as the relaxation zones for wave dumping are to be setup. This is done using the `waves2Foam` tools `setWaveParameters` and `setWaveField` (OpenFOAMWiki, 2012).

Post-processing: While OpenFOAM is running, several post-processing tasks can be performed at the same time using implemented object functions. The water surface elevation, velocities along vertical lines and in horizontal planes as well as forces and momentums are calculated and extracted simultaneously from the simulation results.

Subsequent analyses on the results are performed using Matlab scripts. The programme Paraview (Kitware, 2012-2018) is applied for visualization. It is part of the third-party package which accompanies OpenFOAM.

In this study, the CFD model is based on the free surface RANS solver interFoam, which is part of the free software package OpenFOAM. It uses the volume of fluid (VOF) method to calculate the free surface development. For wave cases, the extended solver waveFoam (Jacobsen et al, 2012) is applied. In all cases, the k-ω-SST turbulence model (Menter, 1994) is selected as the most suitable compromise for describing turbulence in free flow and bounded flow regions.

3.2 Numerical model setup

3.2.1 Mesh

In order to save computational time, element sizes are chosen as small as necessary. In free flow regions, element sizes should match the following criteria:

In case of wakes, the approximate vortex diameter should be resolved by 10 elements (Wu, 2004).

In case of waves, the wave height should be resolved with 5 to 10 elements.

The latter criteria is derived from common practice.

At wall boundaries, element heights are determined by the wall function of the turbulence model. The methods to calculate such element heights are introduced in section 3.3. In the following, initial and boundary conditions are described.

3.2.2 Initial conditions

The fluid phase fraction α_1, the particle velocities u_x, u_y and u_z, the hydrostatic and dynamic pressures p_{stat} and p_{dyn}, the turbulent kinetic energy k, the turbulent kinetic dissipation rate ε

and the specific turbulent dissipation rate ω at the beginning of the simulation need to be set for the calculation of the first time step.

All simulations start with a fixed water level and zero velocity. According to equation (3-10), k should also be zero. The turbulence will remain zero if it is zero initially, because the production term of k in equations (3-14) and (3-18) is proportional to k. That is why the so-called initial seeding is required. A very small value of k is imposed as initial condition (Wu, 2004). k has been set to a small value of the order 10^{-2} [m²/s²]. After the first timestep, it is updated automatically. The same applies to ω. Setting ε is not required. For p_{dyn}, a buoyant distribution `buoyantPressure` has been set. It calculates the normal gradient from the local density gradient.

3.2.3 Boundary conditions

A. Inlet

The inlet boundary condition exists for all wave cases. The `waveFoam` solver (Jacobsen et al., 2012) contains a dictionary storing all required wave parameters, particularly

time shift (not required here),

- the sea level,
- wave type,
- water depth,
- soft start time (not required here),
- water depth,
- wave height,
- vector to indicate the direction of wave propagation as well as
- spatial offset, so that the wave will be generated starting from the initial water surface.

The turbulent energy is calculated using

$$k = 1.5(\bar{u}I)^2 \tag{3-32}$$

$\bar{u}$ is the mean flow velocity. It is set equal to the depth-averaged horizontal particle velocity under the wave crest. I is the turbulence intensity (CFD-Wiki, 2018), which can be estimated based on physical and numerical experiments. Wu (2004) compared turbulence intensity in a breaking wave on a sloping beach and compared his results with physical experiments of Ting and Kirby (1994). During wave breaking, I took values between 5 and 20 %. The value increased from the bottom towards the wave tip region. Away from the zone of wave breaking, I < 2.5 %. He also reported I around a squared cylinder subject to a bore and derived values between 12 and 23 %. I increased near the bore front.

The specific turbulent dissipation rate is estimated based on equation (3-32),

$$\omega = \frac{\sqrt{\sigma}}{l} \tag{3-33}$$

In this equation, it is common to set the turbulence length scale l to a certain percentage of a typical dimension of a problem. In open channel flow, l can be estimated to be 5 % of the water depth (CFD-Wiki, 2012). σ is the absolute roughness height.

In the bore cases, no inlet boundary condition is required.

B. At the wall

The flow near walls is modelled using a wall function. Based on empirical relations, a wall function estimates the flow profile, which is based on flow velocity in the free flow zone. It can further consider the wall roughness. The element size at the wall must be selected according to the turbulence model. For the distance of the centre of the first element, usually a value of the dimensionless distance from the wall $y^+ = 50$ is recommended. Another restriction is, that the non-dimensional absolute roughness height $k^+ \leq 5$ (Wilcox, 1998).

The specific turbulence dissipation rate ω at the walls is set based on k^+, using the relation

$$\omega = \frac{2500\nu}{{k_S}^2} \tag{3-34}$$

for a "slightly rough-surface boundary condition" (Wilcox, 1998) with the effective roughness height k_S, here assumed to be $k_S = 0.001$ m.

C. Outlet

At the outlet, the total pressure is calculated. For velocities, zero gradient conditions are applied. All wave cases comprise additionally a relaxation zone to damp waves before reaching the outlet. This zone length is set to be twice the wavelength.

The empirical relations introduced in this section will be used consequently to derive numerical parameters for all simulations in this study. Their validity is assessed in the following section.

3.3 Validation of the CFD model

This section presents the validation of the CFD model (OpenFOAM) in terms of its performance to predict energy losses in wave-structure interaction.

Laboratory data from the Large Wave Flume (GWK) of the Coastal Research Centre (FZK) in Hanover and the wave flume of Leichtweiß-Institute for Hydraulic Engineering & Water Resources (LWI) at TU Braunschweig involving single slender cylinders subject to regular waves (Bonakdar, 2012; Bonakdar & Oumeraci, 2014) were made available for this study. Those studies also include experiments with groups of three slender cylinders in different arrangements subject to regular waves of different wave periods. Furthermore, laboratory tests of a solitary

wave passing a submerged reef structure performed at LWI (Strusinska, 2010) and of a bore acting on a single cylinder (Árnason, 2004) performed at Charles W. Harris Laboratory of the University of Washington were made available (Yeh, 2014).

In order to check the applicability of the model, the validation is performed in five main phases:

(i) *Solitary wave over a submerged reef structure.* The model's ability to reproduce wave generation and propagation with acceptable numerical dissipation is shown by comparing the numerical results with laboratory tests of Strusinska (2010). The phase will provide recommendations on the mesh element size for wave cases.
(ii) *Bore propagation over a flat and initially dry bottom.* The model's ability to reproduce the flow associated with bore propagation over a flat bottom is shown by comparing the numerical results with the analytical solution derived by Ritter (1892). The phase will provide recommendations on the mesh element size for bore cases.
(iii) *Loads induced by regular waves on a single isolated cylinder.* The data were made available by Bonakdar (2012). The model's ability to properly calculate drag and friction forces on a cylinder under offshore tsunami conditions is demonstrated. The phase will provide recommendations on mesh element sizes in the (cylinder) MRE boundary layer for wave cases.
(iv) *Loads induced by a bore on a single isolated cylinder*. The laboratory data by Árnason (2004) are used for comparison to extend the applicability of the model to fluid structure interaction in onshore flow regimes. The results of this phase lead to mesh element sizes at the (cylinder) MRE boundary layer for bore cases.
(v) *Loads on a cylinder in tandem configuration.* The interaction of cylinders is considered by comparing the model results with laboratory data from an instrumented cylinder which was placed in the wake of another cylinder. The data was made available by Bonakdar (2012). The results of this phase should confirm the mesh element sizes for wave cases.

The obtained numerical parameters during one phase are transferred to the next phase. Only the turbulence intensity is selected individually for each phase based on literature.

Data is analysed using routines, which are essentially based on DHI's Internal Matlab Toolbox (Grode, et al., 2017). Far field parameters such as flow velocities and water levels as well as near field parameters such as moments and forces are analysed extensively. The statistical analyses are given in Appendix A.

The following sections present the results of each phase with a similar structure: First, the laboratory experiment is described, followed by the numerical setup and the results of the comparisons between laboratory and numerical data. In addition, in section 3.3.2 (phase ii), scaling tests of various mesh resolutions are performed to assess the performance of the numerical model with regard to the resolution of the elements at the bottom.

3.3.1 Solitary wave over a submerged reef structure (phase i)

A. Laboratory experiment

Experiments of solitary waves propagating over a submerged artificial reef are selected to validate the ability of the model

- to calculate friction at the bottom and
- to minimise numerical dissipation.

The experiments were carried out in the LWI wave flume which is constructed of bricks, approximately 90 m long, 2 m wide and 1.2 m high. The locations of the deployed wave gauges (WG) are shown in Figure 3.2. Waves were generated with a piston type wave maker. Their characteristics are summarized in Table 3.1. A detailed description of the experiments is given in Strusinska (2010).

Table 3.1. Wave conditions for the submerged reef experiment.

Wave type	Solitary wave
Still water depth *d* [m]	0.6
Wave height *H* [m]	0.22
Wave period *T* [s]	2.5
Wave length *L* [m]	7.189

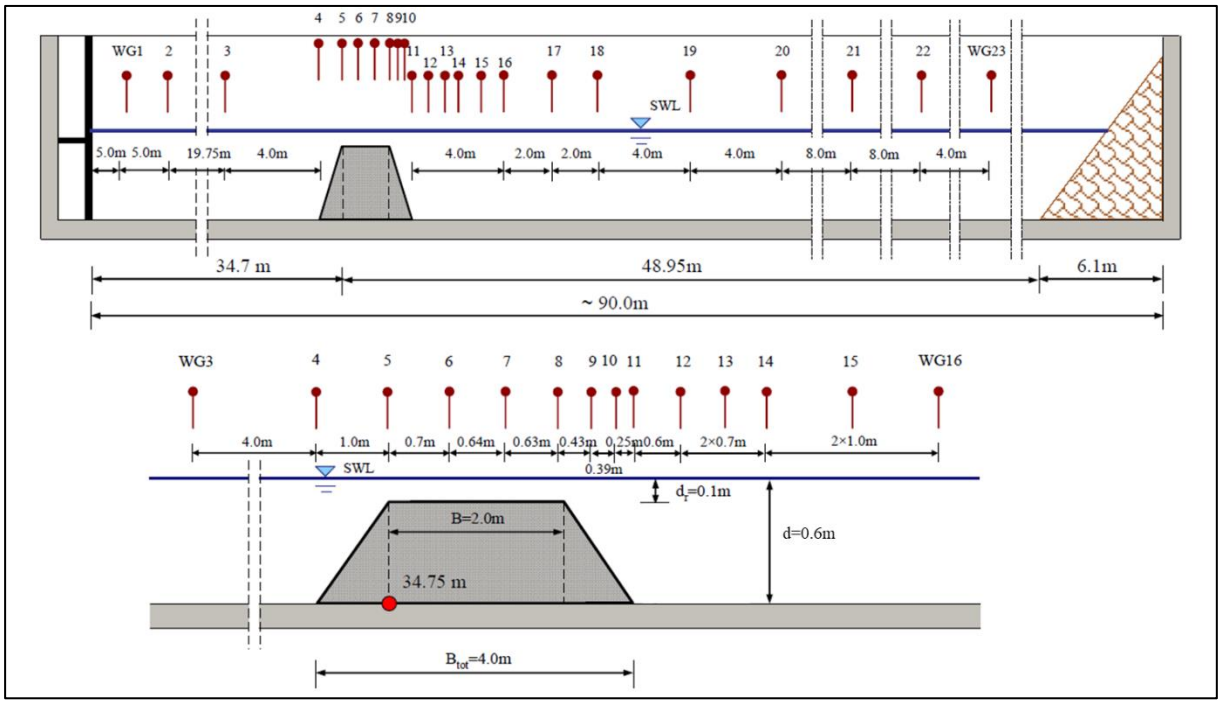

Figure 3.2. Experimental set-up in the LWI wave flume, Test no. 20 (modified from Strusinska, 2010).

B. Numerical model setup

The numerical domain represents the wave flume as exact as possible, but the width dimension is not considered. A 3D model (1 mesh element wide) is set up, neglecting 3D effects in the wave flume, such as the interaction of the wave with the lateral flume walls. Approximately, 235,000 elements (mainly hexahedrons) form the mesh. Figure 3.3 depicts the most important characteristics of the mesh.

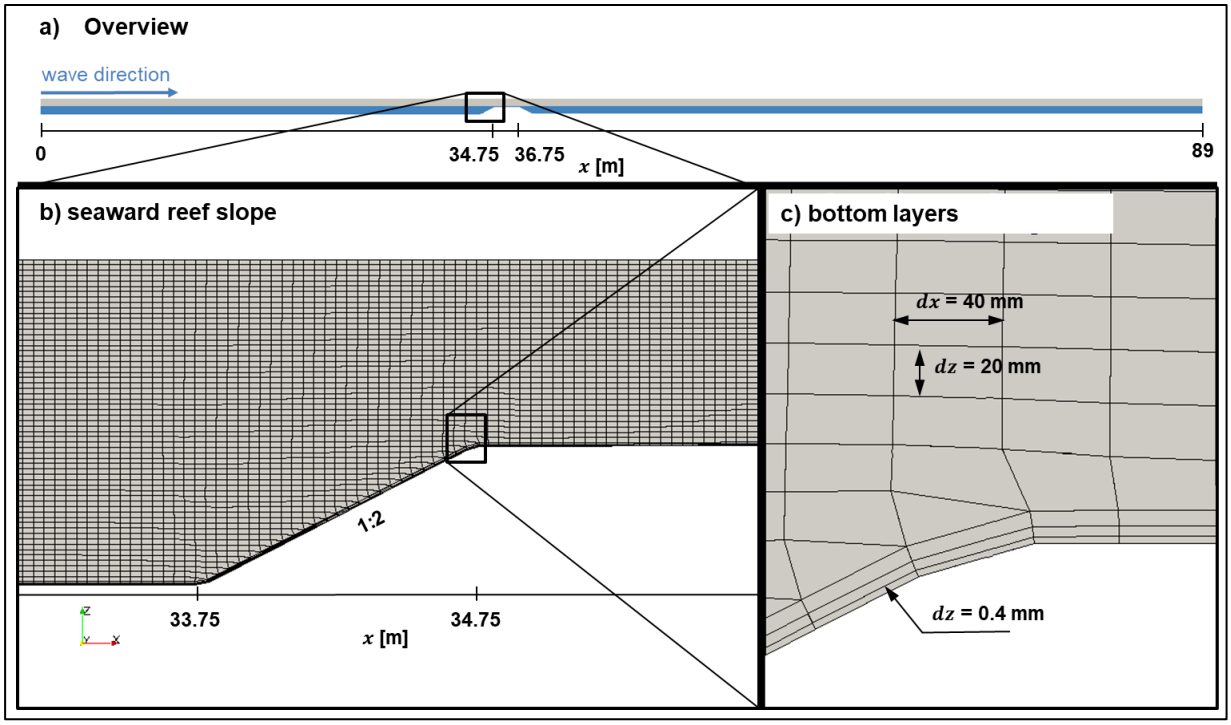

Figure 3.3. Mesh of the solitary wave case, a) overview along the entire wave flume, b) seaward reef slope, c) bottom layers.

The mesh element sizes are determined using the set of equations given in section 3.2. The height of the mesh elements at the bottom is determined by using the dimensionless distance between the first element centre and the bottom $y^+ = 50$. The transient water particle velocity parallel to the bottom under the wave crest is considered to lead to the maximal friction during a wave period. This velocity can be determined using the equation (Dean & Dalrymple, 1991)

$$\bar{u} = \sqrt{gd}\left(1 + \frac{H}{2d}\right)\left\langle -1 + \frac{H}{d}\left\{1 + \frac{H}{4d}\left[3\left(\frac{z}{d}\right)^2 - 5\right]\right\}\right\rangle \tag{3-35}$$

with the acceleration due to gravity g, the still water depth d, the wave height H and the distance from the bottom z. Furthermore, it can also be assumed, that maximum energy losses due to friction occur under the wave crest. Therefore, the velocity at the bottom is used as the mean velocity $\bar{u}$ in the Manning-Strickler equation:

$$\bar{u} = k_{St} r_H^{2/3} I_E^{1/2} \tag{3-36}$$

with the Strickler coefficient k_{St}, the hydraulic radius r_H and the energy gradient I_E. Only the maximum velocities of laboratory and numerical experiments are compared, since (i) $\bar{u}$ from

equation (3-35) is applied to estimate the maximum flow velocity and (ii) $\bar{u}$ is in equation (3-36) is only valid for steady channel flow.

According to equation (3-35), the mean particle velocity under the wave crest at the bottom is $\bar{u}$ = 2.0 m/s. As the width dimension is neglected in the numerical model, the hydraulic radius of the channel is assumed to be the still water depth $r_H = d$ = 0.6 m. As the wave flume is made from concrete, k_{St} = 90 m$^{1/3}$/s (Schroeder, 1992). Equation (3-36) then leads to an energy gradient of $I_E = \frac{\Delta z}{1m} \approx 10^{-3}$ m/m.

The friction force per unit area can then be estimated using

$$F_f = \rho g \Delta z \tag{3-37}$$

which leads to the surface shear stress of

$$\tau = \frac{F_f}{A} \tag{3-38}$$

with the unit area A = 1 m².

Applying equations (3-23) and (3-24) with a water density of ρ = 1000 kg/m³ leads to a friction velocity of u_f = 0.27 m/s and, finally, to a distance of the element centre from the wall y = 0.2 mm, so that the element height at the wall shall be 0.4 mm (see Figure 3.3.c)).

The initial wave height in the numerical simulation are adjusted using the records of WG 1 of the laboratory experiments. Based on CFD-Wiki (2018), an initial turbulence of 0.5 % for low-turbulent flow is assumed.

C. Results

The numerical simulation time and laboratory data recorder clock time are synchronized by shifting the numerical time scale with +82.53 s so that the arrival times match at WG 1.

The free surface elevations of the simulations are compared with laboratory data at the locations of WG 1, 3 (seaward of the reef), WG 7 (above the reef) and WG 16 (landward of the reef) (see Figure 3.3.a)). The calculated and measured time series at these WG are presented in Figure 3.4. The time shift between the arrival of the peak in both time series, the peak ratios, the correlation coefficient and the scatter index (see Appendix, section A.1) of the surface elevations of these WG are given in the Appendix, section A.2.

It is noted that the surface elevation at WG 1 (see Figure 3.4.a)) slightly exceeds the laboratory data. With increasing wave propagation, the surface elevation in the numerical model decreases stronger than the surface elevation in the laboratory data due to numerical dissipation. At WG 3, the wave propagated over 24.75 m, which is approximately 3.4 times the wavelength. The peak ratios PR, as a measure of the ability of the model to reproduce maximum values, reduces by 0.01 over this distance.

The wave damping coefficient can be determined from the ratio

$$K_d = \frac{H_d}{H_0} \tag{3-39}$$

with the incident wave height H_0 and the damped wave height H_d. The damped wave height is the difference between the wave height at WG 1 and 3 (see Appendix A, section A.2). This leads to a damping coefficient of K_d = 0.0044, which is K_d = 0.0013 per wavelength.

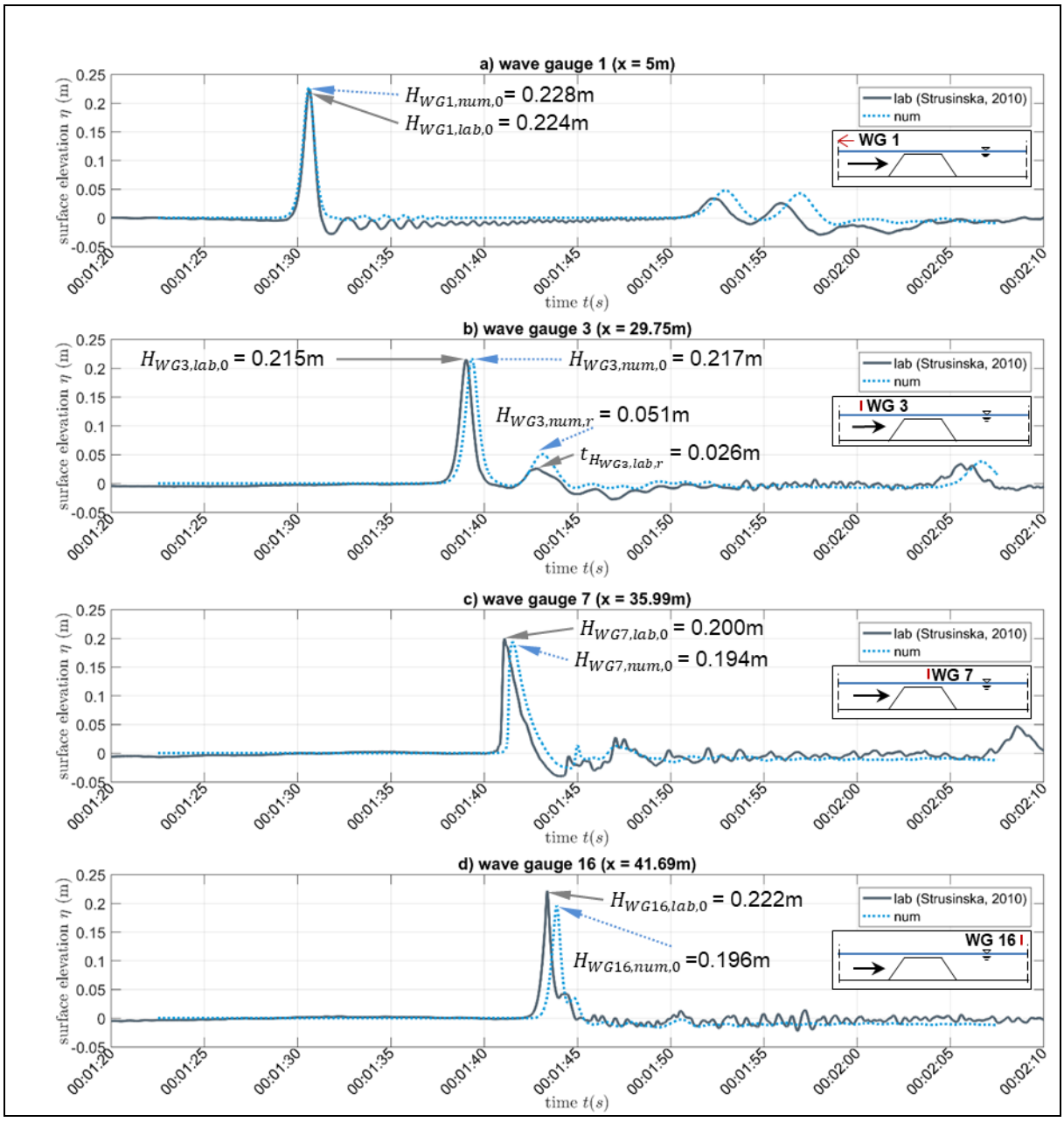

Figure 3.4. Water surface elevations at a) wave gauge WG 1, b) WG 3, c) WG 7 and d) WG 16.

At the front face of the reef structure, the wave is partially reflected, leading to waves propagating backwards towards WG 3. The reflected waves arrive at WG 3 at time stamp 1:43 min (see Figure 3.4.b)). It is seen that the reflected wave with 0.051 m is overestimated by approximately 100 %, as the laboratory data shows a wave height of 0.026 m only. These deviations might be caused by differences between the wave flume (e.g. geometrical differences) and its

numerical representation in the model. Bottom profile measurements of the flume are used and applied to build the geometry of the domain, but the exact water depth above the reef was not available. Small differences in the bottom profile between the numerical model and the laboratory might result in a different angle of the reef structure front face and change the water depth above the reef, which may cause the differences in wave reflection. Another reason might be that the reef consisted of smoother material (wood) than the flume. The estimated roughness value in the numerical model is based solely on the rougher material of the flume (concrete) so that friction in the shallow areas above the reef is overestimated.

At WG 7 (see Figure 3.4.c)), which is located above the reef structure, the wave height reduces by 0.017 m compared to WG 3. While the wave reflection is overestimated (see Figure 3.4.b)), the wave transmission is underestimated to the same extent, causing to a greater reduction of the leading wave height compared to the laboratory data, where the wave reduces by 0.015 m.

At WG 16 (see Figure 3.4.d)), the simulated height of the leading wave increases by 0.002 m compared to WG 7, while in the laboratory data, the wave height increases by 0.022 m. This is mainly dedicated to geometrical differences between the numerical model and the laboratory experiments mentioned above.

At all WG, the peak ratio is between PR = 0.88 and 1.02, revealing a good representation of the maximum wave heights. The correlation coefficient CC, as a measure of the model's ability to represent averaged values, takes values of CC > 0.9, which documents a good agreement between both data sets. It indicates that the model provides the ability to reproduce averaged values. The scatter index SI, as a measure of the model's ability to represent instantaneous values, takes values of SI > 0.7, which is very high see Appendix, section A.2), so that the model is not suited to reproduce accurately instantaneous values.

The arrival of the leading solitary wave is delayed in the numerical model. The delay, however, takes values of only 0.5 s, when propagating over a distance of approximately 37 m, which is roughly 5 wave lengths.

The numerical dissipation of the numerical model is reasonably small. The maximum wave height is reasonably well represented while instantaneous values are poorly reproduced. Uncertainties associated with the water depth above the reef structure and the reef slope might partly be responsible for the deviation in the height of the leading wave across the reef structure. It can be concluded that the numerical model calculates the wave height with peak ratio of PR = 0.88 or better and sufficiently accurate.

The mesh element size at the bottom of dz = 0.0004 m and in the free-flow zone of $dx = dy$ = 0.4 m and dz = 0.02 m and turbulence intensity of I = 0.05 % can be used for wave propagation with comparable flow velocities.

3.3.2 Bore propagation over an initially dry bottom (phase ii)

The ability of the model to represent onshore tsunami bore propagation is presented in this section. The bore is generated with a dam break mechanism, making use of the similarity between dam break and tsunami bores (Chanson, 2006). The numerical results are compared to the analytical relation derived by Ritter (1892), see section 2.1.1).

A. Analytical solution

The flow depth h_x at a distance x from the dam can be estimated using equation (2-4), which is here given for convenience:

$$h_x = h_0 \left(\frac{\frac{x}{t\sqrt{g h_0}} - 2}{-3} \right)^2 \tag{3-40}$$

in which h_0 denotes the impoundment height, t the time after the dam break and g the acceleration due to gravity (Chanson, 2006).

B. Numerical model setup

The numerical domain extends in (x, y, z) over (36, 8, 1.2) m, as shown in Figure 3.5.

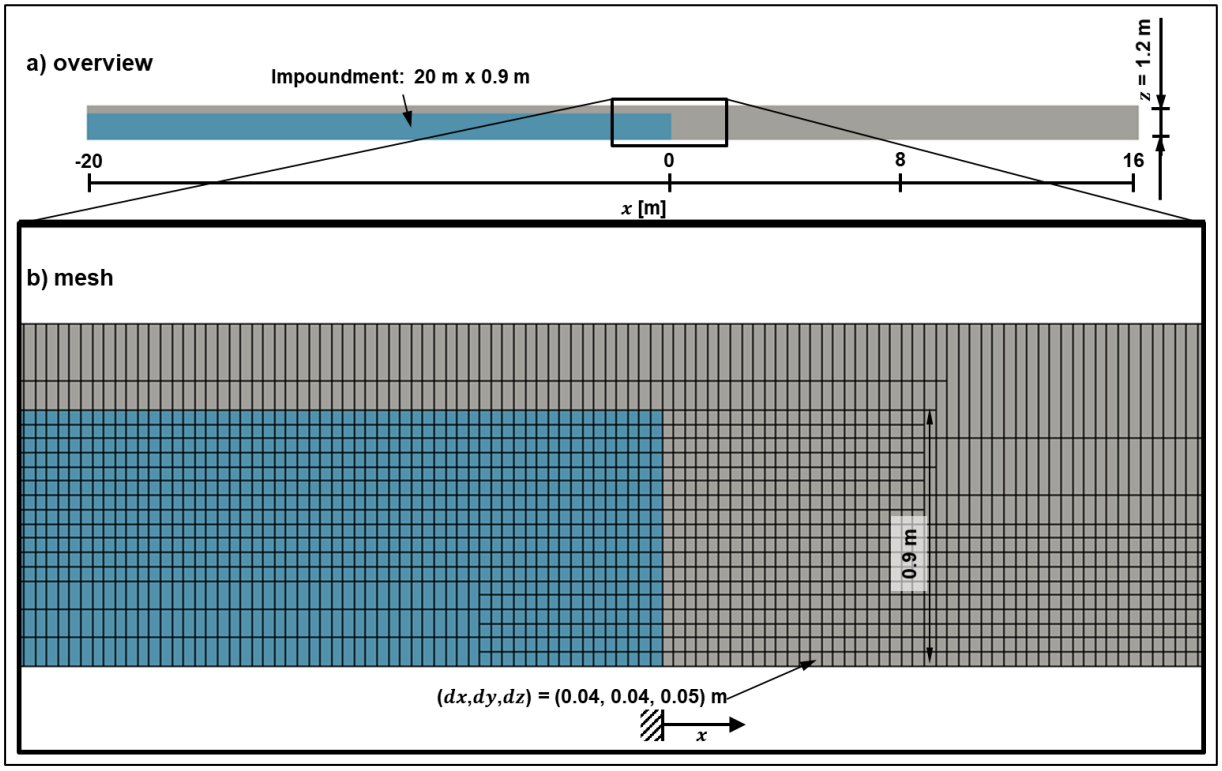

Figure 3.5. Domain and mesh for the propagation of a bore over an initially dry bottom: a) overview, b) mesh.

The initial impoundment is set at the left side of the domain and is 20 m long, 0.9 m high and takes the entire width of the domain. The bottom outside of the impoundment is left dry. Sensitivity tests on mesh element sizes, in which water levels and horizontal flow velocities are compared, lead to elements of (dx, dy, dz) = (0.04, 0.04, 0.05) m. A total of approximately 90,000 elements are used to discretize the domain. A turbulence intensity of I = 10 % is used for the bore propagation, which is a common choice for highly turbulent flow (CFD-Wiki, 2018; see also section 3.2.3.A, regarding analogy between bore and wave breaking).

It is noted that the element height dz is too coarse to calculate the flow velocities inside of the bottom boundary layer correctly.

C. Results

The comparison of the free surface position over time at a distance of 8 m (see Figure 3.5.a) from the dam is shown in Figure 3.6.

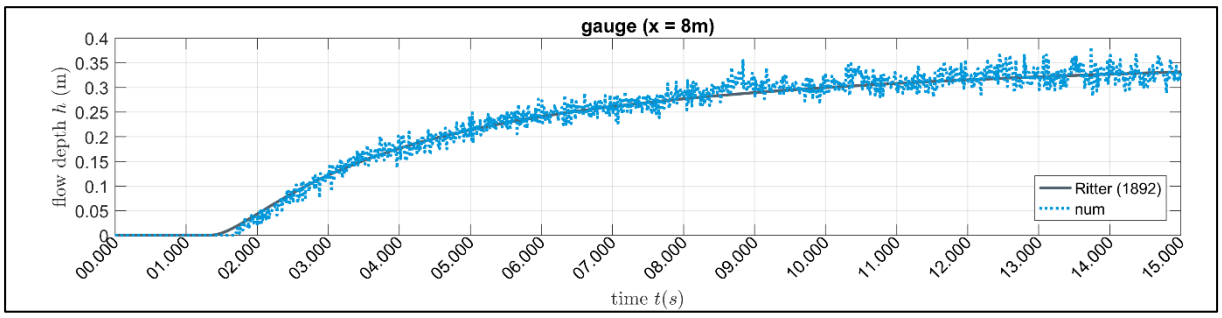

Figure 3.6. Comparison of water level of numerical and Ritter's analytical solution at x = 8 m (see Figure 3.5.a).

The numerical data consists of high fluctuations. The numerical representation of the free water surface follows the analytical Ritter solution very well. A correlation coefficient of CC = 0.99 and a scatter index of SI = 0.07 (see also Appendix, section A.3) confirm the excellent agreement with the analytical solution. Only slight deviations between the model and the analytical solution at the very bore front are noted, where, however, the analytical solution is not valid (see section 2.1.1).

D. Scaling tests

In order to assess the performance of the numerical model with regard to the resolution of the mesh elements at the bottom towards recommended values of $dz = 2 \cdot 10^{-4}$ m (see equation (3-22), assuming $dz = y$), the horizontal flux in flow direction is calculated based on simulations using three meshes, which differ in their vertical resolution. In addition to the mesh shown in Figure 3.5, in which the vertical resolution is Δz_1 = 0.05 m, the performance of meshes with Δz_2 = 0.025 and Δz_3 = 0.0125 m are investigated. The results are given in Figure 3.7.

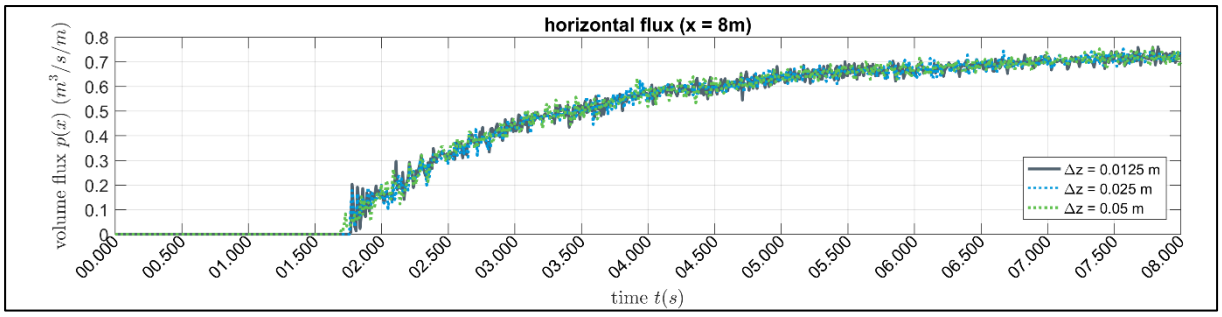

Figure 3.7. Comparison of depth-averaged velocities of three meshes with different vertical resolutions at x = 8 m (see Figure 3.5.a).

The statistical analysis of the comparison of the results obtained with the coarsest and with the finest vertical mesh resolution reveals a peak ratio of PR = 1.0, a correlation coefficient of CC = 0.99 and a scatter index of SI = 0.06, indicating that both solutions are almost identical (see Appendix, section A.8).

The numerical model is very well suited to reproduce maximum, averaged and instantaneous flow depth during the propagation of a bore over an initially dry bottom.

Mesh element sizes in the bottom boundary layer of dz = 0.05 m and a turbulence intensity I = 10 % can be used for bore propagation with comparable flow velocities.

3.3.3 Loads induced by regular waves on a single isolated cylinder (phase iii)

In this section, the overturning moments around the top suspension of a single cylinder subject to regular waves (5th order Stokes waves) are compared in order to demonstrate the model's ability to assess drag forces. The numerical simulation attempts to reproduce measurements of a physical experiment in the large wave flume (GWK) Hannover. They correspond to case 23060401 in Bonakdar (2014).

A. Laboratory experiment

The GWK Hannover is 309 m long, 5 m wide and 7 m deep. A single cylinder of diameter D = 0.324 m is suspended at a supporting structure above the wave flume. The geometric characteristics of the experiments are presented in Figure 3.8.

Figure 3.8 shows also the positions of wave gauges (WG) near the measurement pile, the current meters (CM) and the strain gauge. The selected wave conditions are given in Table 3.2.

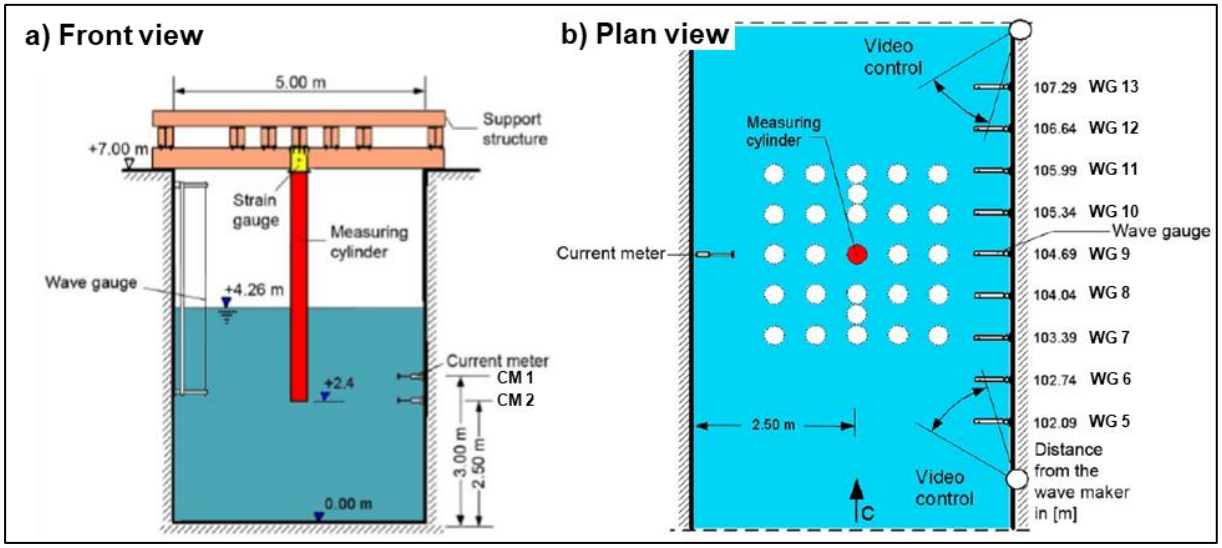

Figure 3.8. Model setup with the measuring pile: a) front view, b) top view (modified from Bonakdar, 2012).

Table 3.2. Selected test with single cylinder subject to regular waves.

Wave type	Stokes 5th order
Still water depth d [m]	4.26
Wave height H [m]	0.8
Wave period T [s]	7
Wave length L [m]	14.7

B. Numerical model setup

The numerical mesh characteristics are depicted in Figure 3.9.

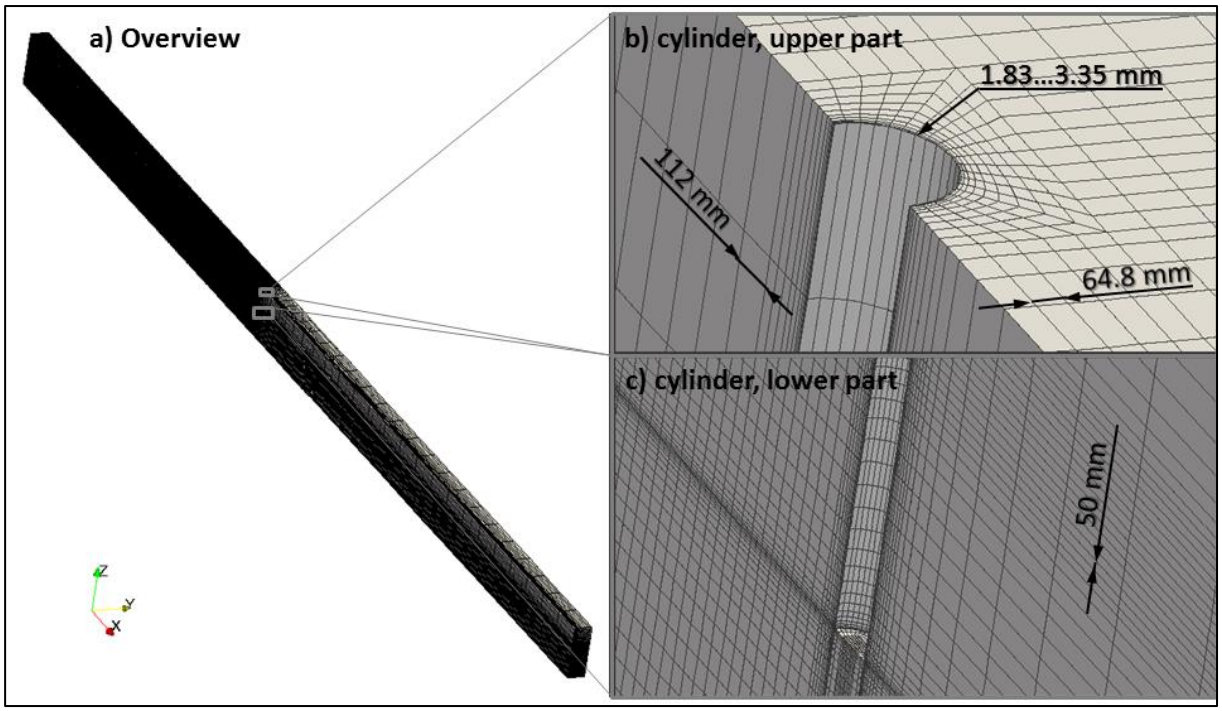

Figure 3.9. Mesh characteristics for the test with single cylinder subject to regular waves.

The entire domain covered the flume from x = 35 m to x = 200 m. 671,100 hexahedrons have been used. Due to symmetry of the domain, the latter is cut vertically along the longitudinal axis of the flume (see also Weihua et al., 2006).

The element widths at the cylinder wall dx = 0.0033 m is determined using the friction velocity-based approach, outlined in section 3.3.1.B. The Reynolds number Re in equation (3-28) is determined with the mean water particle velocity under the wave crest, which reads

$$\bar{u} = \int_0^{d+H} u(z,t)\, dz \tag{3-41}$$

In this equation, the water particle under the wave crest $u(z,t)$ can be estimated using linear wave theory (e.g. see Dean & Dalrymple, 1991)

$$u(z,t) = \frac{H\pi}{T} \frac{cosh\left[\frac{2\pi}{L}(z+d)\right]}{sinh\left(\frac{2\pi d}{L}\right)} \tag{3-42}$$

With the wave height H, the wave period T, the wavelength L, the still water depth d and the vertical distance from the bottom z. Its maximum occurs at the water surface, where $z = d + H$.

At the inlet, a turbulence intensity of I = 5 %, representing medium turbulent conditions is assumed (see CFD-Wiki, 2018; see also section 3.2.3.A with regard to unbroken waves with $I \leq 5$ % and bore interaction with a cylinder with $I \geq 12$ %).

C. Results

The numerical results are evaluated by means of surface elevations, current speeds and overturning moments around the top suspension of the measurement cylinder.

The comparisons of free surface data at the position of three WG are presented in Figure 3.10. WG 1 is located 25.54 m upstream and WG 7 is 1.3 m upstream of the measurement pile, WG 9 is located at the same horizontal position x as the measurement pile and WG 13 is located 2.6 m downstream of the measurement pile (see Figure 3.8.b)). The statistical descriptors obtained from the analyses are given in Appendix, section A.4.1).

The numerical time is shifted by 42.65 s to skip the first waves from the laboratory tests, which were still developing. Comparing the maximum wave heights at WG 1 and WG 7 and taking the wave length stated in Table 3.2 into account, the dissipation coefficient according to equation (3-39) is K_d = 0.005 per wave length, only. The first four fully developed waves are analysed (see also Appendix, section A.4.1). The laboratory data comprises slight variations in the amplitudes. The variations in wave crest and wave trough suggest that, beside the generated wave, there might have been an underlying long period wave of small amplitude in the flume. Furthermore, the last peak observed from WG 13 is higher than the previous peaks. This indicates the presence of reflections in the wave flume. Such oscillations are not present in the numerical data. Correlation coefficients of CC = 0.99, peak ratios between PR = 0.93 and

PR = 0.99 and scatter indices between SI = 0.14 and SI = 0.18 indicate that the measured wave amplitudes, phases and shapes have been very well reproduced by the numerical model.

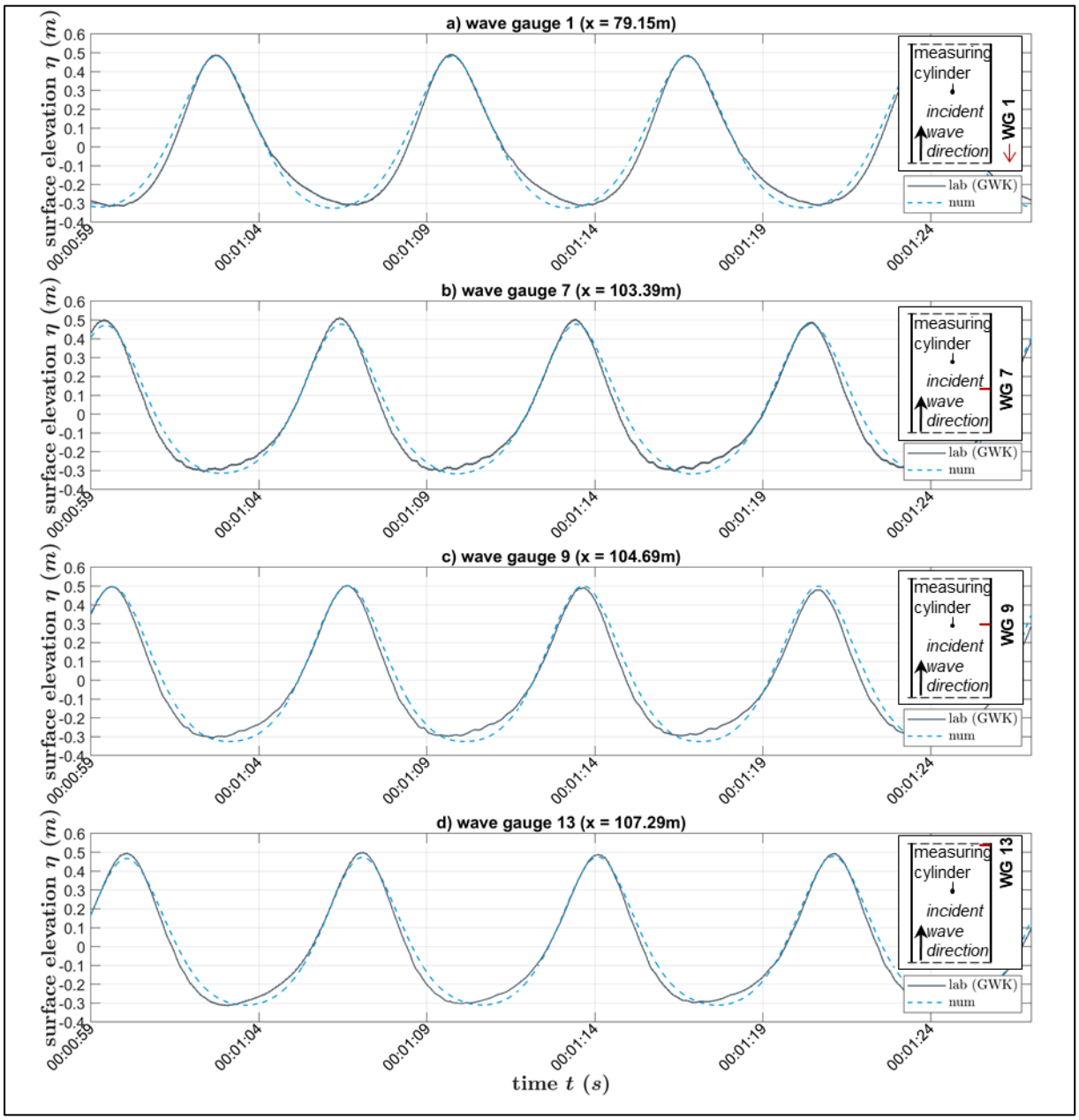

Figure 3.10. Comparison of free surface data from the test with single cylinder subject to regular waves: a) wave gauge WG 1, b) WG 7, c) WG 9 and d) WG 13.

The flow velocities are compared at the position of two CM. Their locations are shown in Figure 3.8.a). The time series of measured and calculated current speeds are shown in Figure 3.11. The statistical descriptors are given in Appendix, section A.4.2.

The measured flow velocities show similar variations as observed from the WG data. Increasing amplitudes in the last three peaks in Figure 3.11 indicate reflections from the rear wall of the

flume. Correlation coefficients of CC = 0.99, peak ratios between PR = 0.94 to 0.98 and a scatter index of SI = 0.12 to 0.14 indicate very good agreement with measured flow velocities (see Appendix, section A.4.2).

The comparison of the overturning moments around the strain gauge on the top of the measurement cylinder (see Figure 3.8.a)) are given in Figure 3.12. The statistical descriptors are provided in Appendix, section A.4.3.

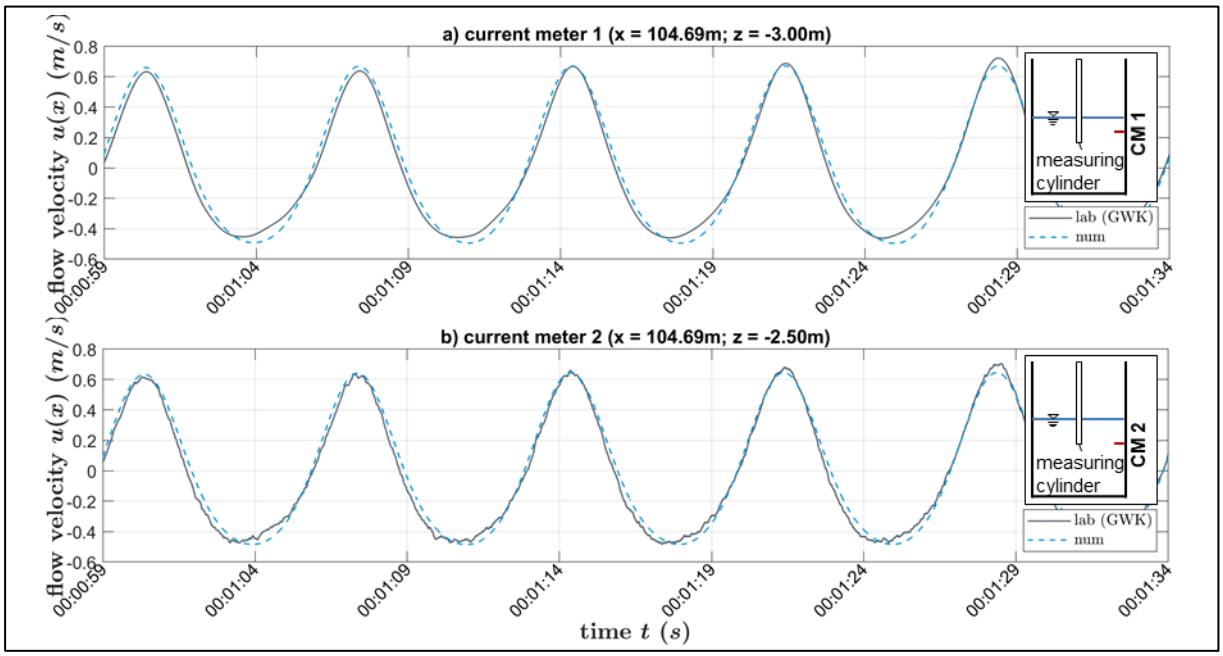

Figure 3.11. Comparison of velocity data from the test with single cylinder subject to regular waves at a) current meter CM 1 and b) CM 2.

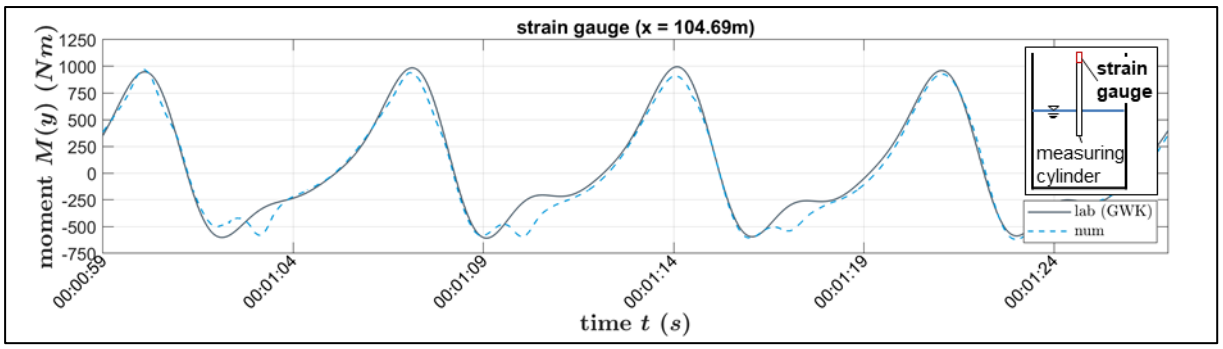

Figure 3.12 Comparison of overturning moment data from the test with single cylinder subject to regular waves.

For the comparison of the overturning moments, the calculated moments have been multiplied with 2, because the simulation only represents half of the flume (and half of the cylinder surface). The wave troughs in laboratory and numerical data show the presence of a small underlying wave of slightly smaller wave period than the “main” wave. The small wave might originate from reflection at the wave absorbing boundary in both cases, which does not suppress

the wave fully. When the "main" and the reflected wave overlap, the wave crest is slightly higher in both numerical and laboratory data. Comparisons of WG 9 data (see Appendix, section A.4.1) reveal that the wave crest corresponds to maximum moments and the wave trough to minimum moments. Hence, the wave phase representation is very good. The laboratory data shows small variations of the extreme values. For the comparison, maximum and minimum moments in the numerical data are averaged over all four fully developed simulated waves. The correlation coefficient of $CC = 0.99$ and the peak ratio of $PR = 0.98$ confirm that very good agreement is achieved between laboratory and numerical experiments.

The numerical model is very well suited to reproduce maximum and instantaneous flow depth and flow velocity, and their effects on the structure as indicated by the overturning moment due to drag caused by waves. Small deviations in the wave shape are believed to have its origin in an underlying long period wave in the experimental data and very small reflections from the numerical wave absorbing boundary.

The mesh element sizes in the (cylinder) MRE boundary layer $dx = 0.002$ m and turbulence intensity of $I = 5$ % can be used for regular wave loads on a single cylinder with comparable flow velocities.

3.3.4 Loads induced by a bore on a single vertical cylinder (phase iv)

The forces induced on a cylinder subject to a passing bore are determined in this section. Numerical results are compared to measurements obtained from laboratory experiments performed by Árnason (2004) to show the ability of the numerical model to calculate drag forces due to a bore.

A. Laboratory experiment

The laboratory experiment was conducted in the Charles W. Harris Laboratory (CHL) of the University of Washington. A diagram of the wave tank is provided in Figure 3.13 (Árnason et al., 2005).

The tank is 16.62 m long, 0.61 m wide and 0.45 m high. A gate is located 5.9 m from the tank head. In a distance of 4.9 m of the gate, a cylinder with a diameter of 0.14 m was placed. The impoundment height upstream of the gate was 0.25 m. Before the experiments, a water layer of 0.02 m was observed downstream of the gate. The gate is lifted by a piston driven by air pressure (Árnason et al., 2005).

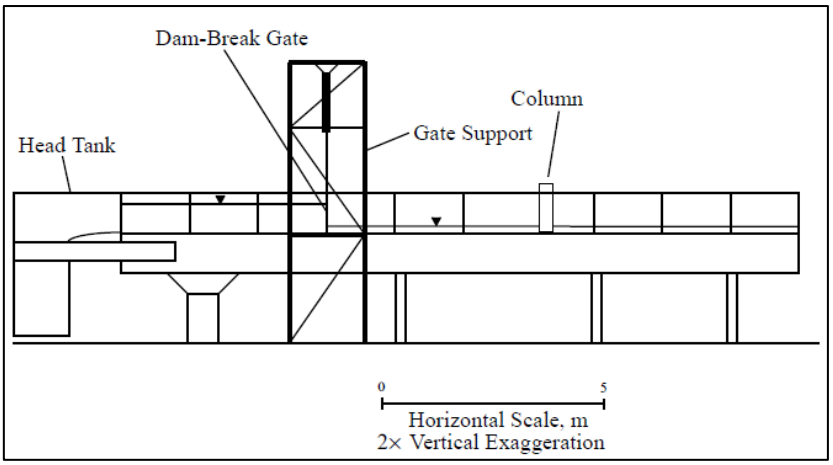

Figure 3.13. Diagram of the wave tank at Charles W. Harris Laboratory (Árnason et al., 2005).

B. Numerical model setup

The numerical model was set up as shown in Figure 3.14.

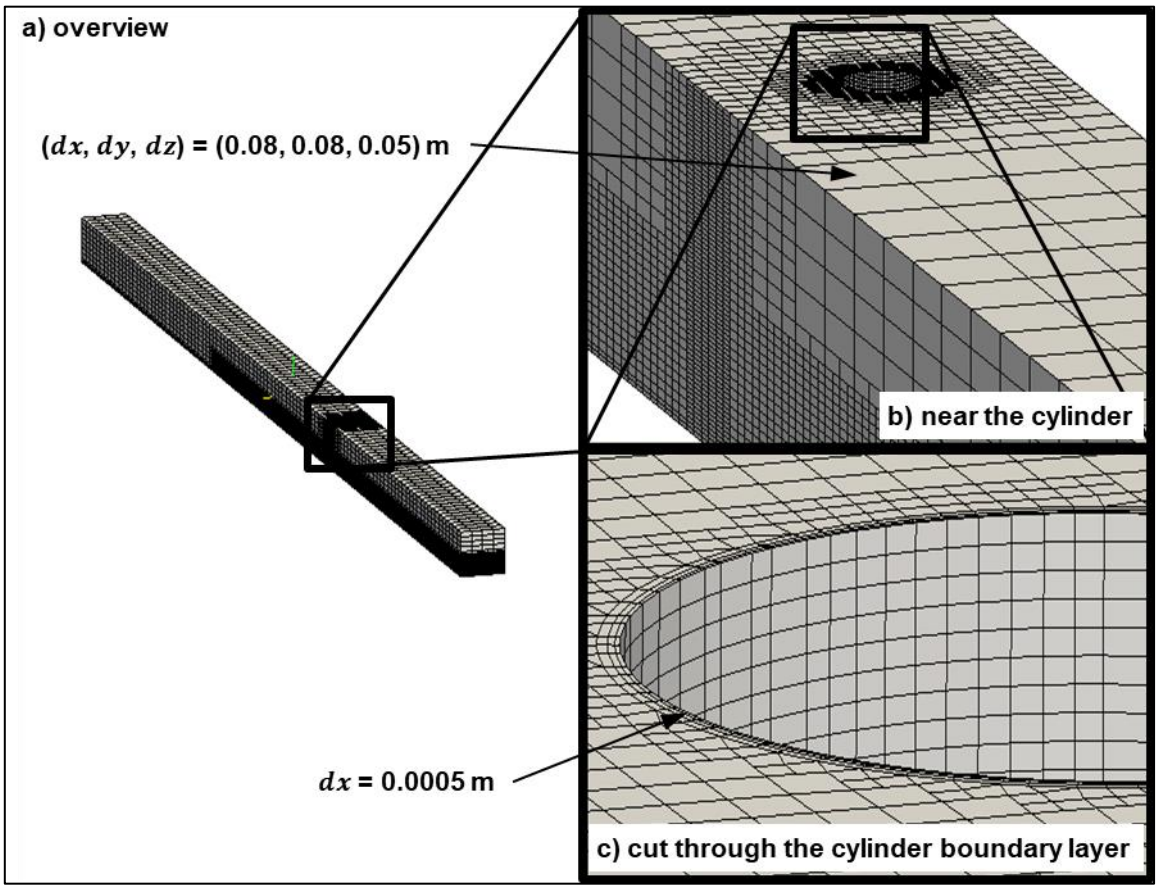

Figure 3.14. Mesh characteristics for the test with single cylinder subject to a bore, a) overview, b) detail near the cylinder and c) cut through the cylinder boundary layer.

The mesh covers the similar extent as the wave tank (see section 3.3.4.A). Predominantly hexahedral elements are used for the mesh, which is composed of approximately 206,000 elements.

The turbulence intensity is set to I = 10% representing high turbulent conditions (CFD-Wiki, 2018), similar to phase (ii) (see section 3.3.2.B). Figure 3.15 gives an overview of the locations selected for comparison of calculated and measured free surface elevation and flow velocity.

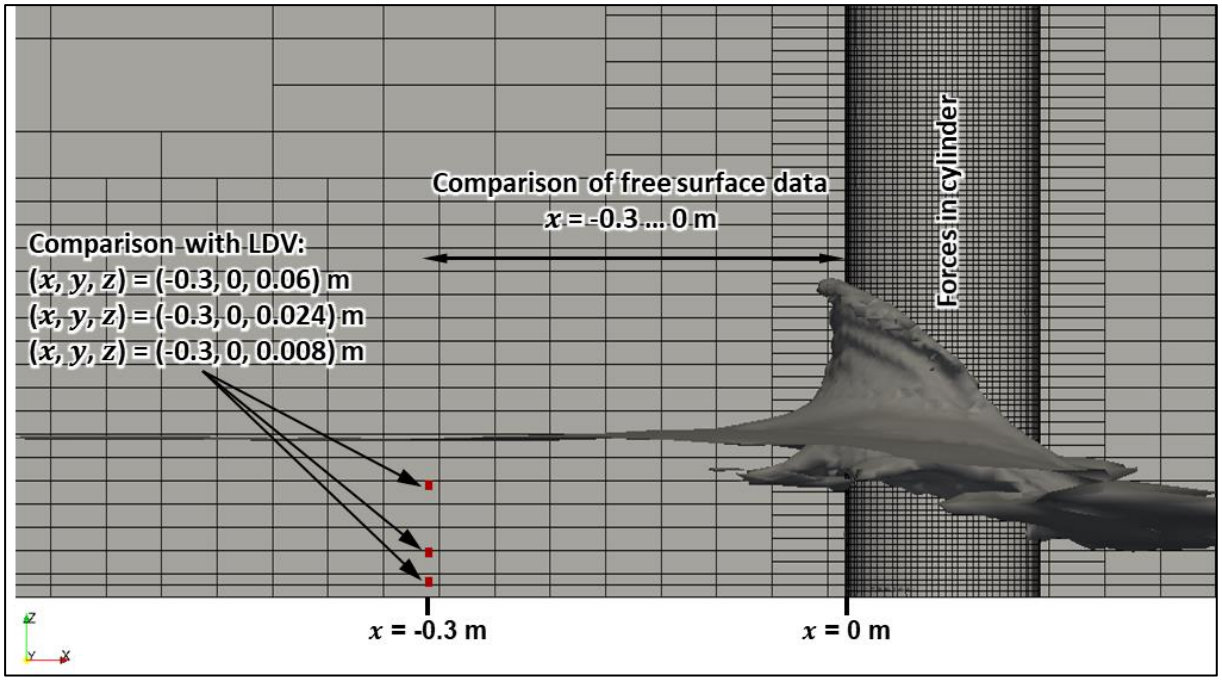

Figure 3.15. Selected locations for comparison of calculated and measured free surface elevation and flow velocity.

C. Results

The comparison of measured and calculated free surface elevations is given in Figure 3.16 for different time steps.

At the moment of maximum run-up (t = 3.5 s, see Figure 3.16.b)) laboratory data shows a value of z = 0.276 m at the cylinder front face, while the numerical model underestimates the water level with z = 0.158 m considerably. The numerical results reveal air entrainment upstream of the cylinder front face. The measurement techniques applied in the laboratory are not able to capture air below the water surface. However, a breaking of the bore front has been observed, which could potentially lead to such air entrainments (Yeh, 2014). At later time steps ($t \geq$ 3.5 s, see Figure 3.16.c) to f)), the free surface position further upstream of the cylinder face differs between laboratory observations and numerical model. It is believed to originate from the construction of the gate and have been observed in similar experiments (Nistor, 2014). The gate moves inside an ultra-high molecular weight plastic track, which is fitted into the walls of the tank (Árnason, 2004). The lateral walls and especially the plastic track prevent the water from moving evenly through the flume towards the column. It leads to diagonal waves, riding on top of the bore, which was reported by Árnason (2004). The features of the lateral walls are not included in the numerical model and, thus, these secondary effects are not captured.

The comparison of measured and calculated horizontal flow velocity $u(x)$ at three elevations (z = 0.06, 0.024 and 0.008 m) above the bottom is given in Figure 3.17.

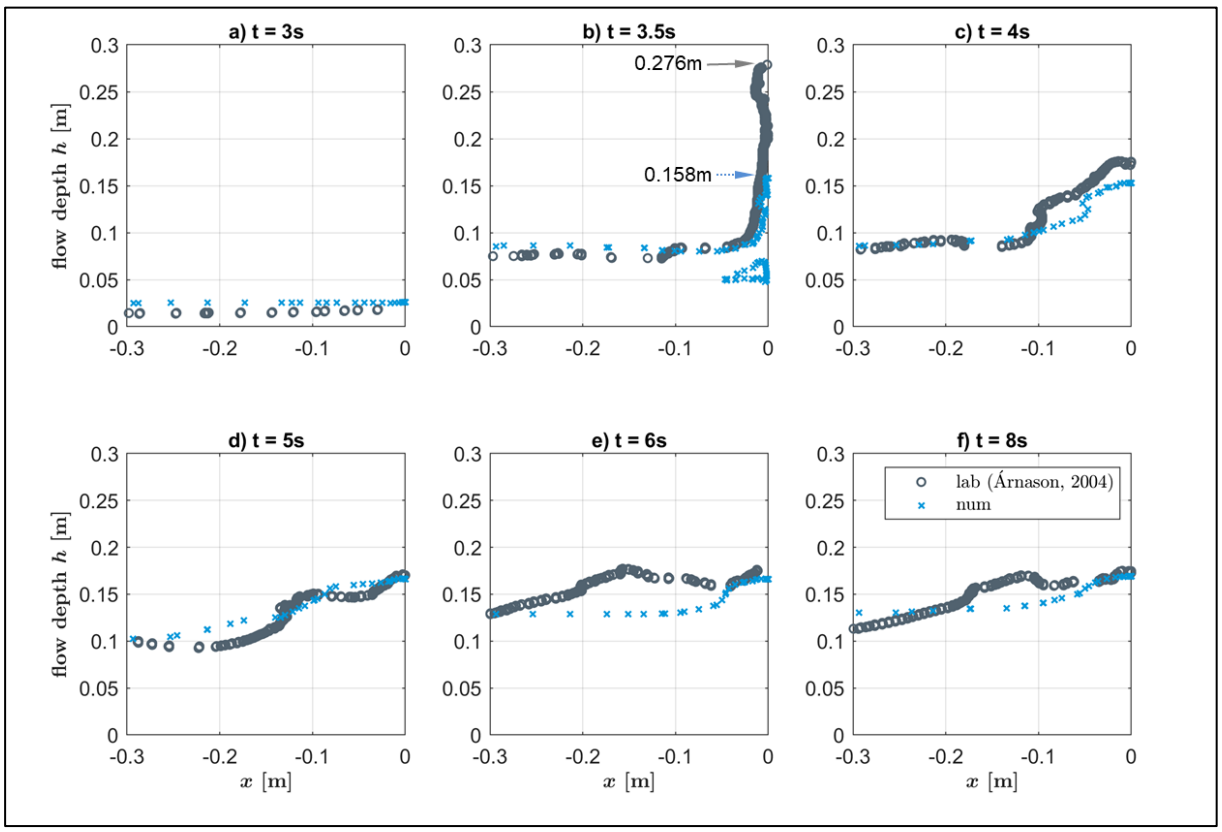

Figure 3.16. Comparisons of measured and calculated free surface elevations at the time steps a) t = 3 s, b) t = 3.5 s, c) t = 4 s, d) t = 5 s, e) t = 6 s and f) t = 8 s.

The arrival time of the bore is well predicted by the numerical model. The maximum velocity agreements are acceptable at the lowest and highest point (CM 1 and 3, see Figure 3.17.a) and c)). The peak ratios are PR = 0.85 and PR = 0.89, the correlation coefficients take value of CC = 0.82 and CC = 0.73, respectively (see Appendix, section A.4.1). The missing secondary effects caused by the gate and not represented by the numerical model (see above) are believed to be responsible for higher scatter indices. The maximum values of the flow velocities are well represented. At CM 2 which is located between the CM 1 and 3, the numerical model does not capture the maximum velocity. This results from the relatively coarse vertical mesh resolution, so that the numerical data represents average values for a relatively large computational element volume of $dxdydz = 0.8 \cdot 10^{-5}$ m³ compared to the measurement data, which represents the velocities in a very small volume in the range of 10^{-9} m³. Furthermore, the larger computational cell volume compared to the control volume of the measurements results in smoothed results so that individual peaks in the measurements resulting from small scale flow phenomena such as small vortices are not captured in the numerical model. These weaknesses of the model need to be considered when applying the model in later phases of the study.

Figure 3.18 depicts the comparison of measured and calculated forces induced by a bore on a single vertical cylinder.

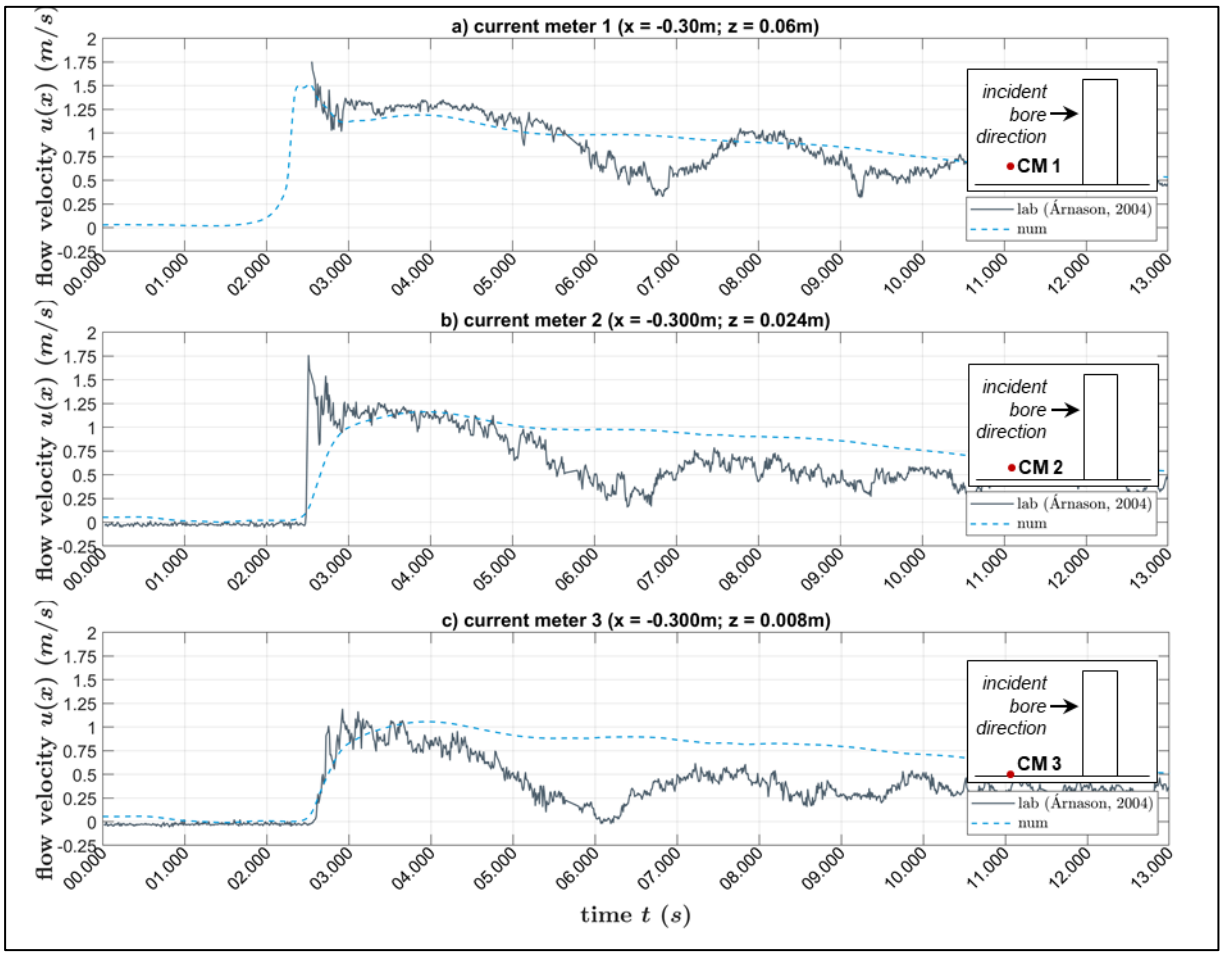

Figure 3.17. Comparison of measured and calculated horizontal flow velocity $u(x)$ at a distance from the bottom a) z = 0.06 (current meter CM 1), b) z = 0.024 (CM 2) and c) z = 0.008 m (CM 3). (see Figure 3.15 for coordinates of cylinder and CM).

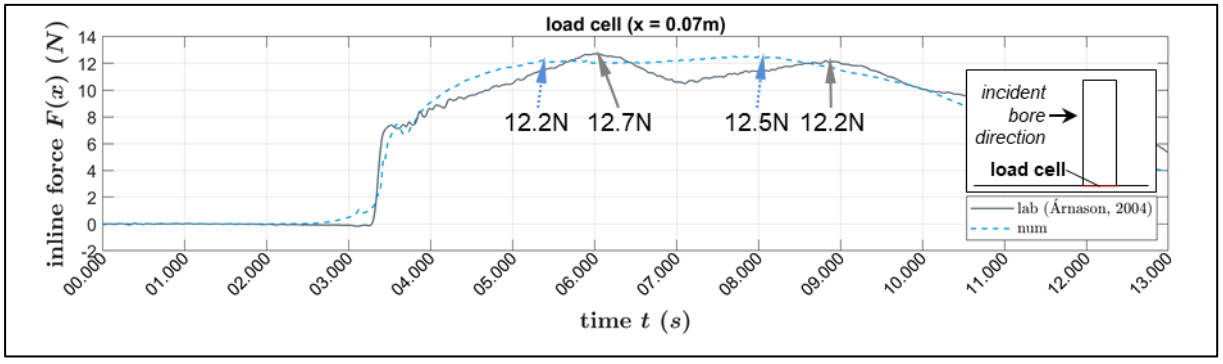

Figure 3.18. Comparison of measured and calculated force induced by a bore on a single vertical cylinder.

Measured laboratory forces exhibit two peaks. The first peak of the inline force $F(x)$ = 12.7 N is the result of the impact of the breaking bore front; the second with $F(x)$ = 12.2 N is reached at the moment of maximum run-up at the vertical cylinder. The numerical simulation captures qualitatively well this behaviour, although the peaks of $F(x)$ = 12.2 and $F(x)$ = 12.5 N are not as pronounced as their measured counterparts, likely due to the selected grid resolution. Air

entrainment might further contribute to the differences. The highly turbulent bore front involves compressible air bubbles in the impact process. They cannot be represented due to the use of an incompressible solver and due to a relatively coarse mesh resolution, which cannot capture the surfaces of the bubbles. However, the model reproduced the instantaneous increase of the force at the moment of bore impact (t = ~3.5 s) and the maximum force very well. The analyses in Appendix, section A.4.2, show that with peak ratio PR = 0.99, correlation coefficient CC = 0.98 and scatter index of SI = 0.12 a very good agreement is obtained between calculated and measured data.

When comparing flow velocities, the model leads to acceptable results. The inline forces, which represent an integrating parameter for the other flow characteristics in the near field, are very well reproduced. The model is suitable to reproduce averaged and instantaneous flow characteristics such as flow depth and flow velocities.

Element mesh sizes at the cylinder of dx = 0.00005 m and turbulence intensity of I = 10 % can be used for calculating the load on a single vertical cylinder induced by a bore with comparable flow velocities.

3.3.5 Loads induced by regular waves on vertical cylinders in tandem configuration (phase v)

Two cylinders in tandem configuration subject to regular waves (Stokes 5th order) are modelled in this section. The results are compared with laboratory data to assess the ability of the model to reproduce the moments induced by the waves on the downstream cylinder. The case is chosen because vortices induced by the upstream cylinder have to be well reproduced by the model in order to obtain a good agreement between calculated and measured wave loads on the sheltered cylinder. The configuration corresponds to case 28060404 in Bonakdar (2014).

A. Laboratory experiment

The wave characteristics are similar to those of case 23060401, described in Table 3.2 (T = 7 s, H = 0.8 m) in section 3.3.3.A. In addition to the aforementioned case, a second cylinder is suspended upstream of the measuring cylinder. The spacing S_G between both cylinders with similar shape and size with the diameter D = 0.324 m is $S_G = 1D$.

B. Numerical model setup

The model setup is similar to that in section 3.3.3.B, except that here, two cylinders are included. The only difference is that a second cylinder of similar shape and size as the instrumented downstream cylinder is installed. The numerical mesh is given in Figure 3.19.

The entire domain covered the flume from x = 35 m to 200 m. 900,000 elements (mainly hexahedrons) form the mesh. Boundary and initial conditions are the same as those presented in section 3.3.3, except turbulence settings. A turbulence intensity of 10 % for high turbulent flow

is determined from sensitivity tests (see also CFD-Wiki, 2018), which is similar to phase iv (see section 3.3.4.B).

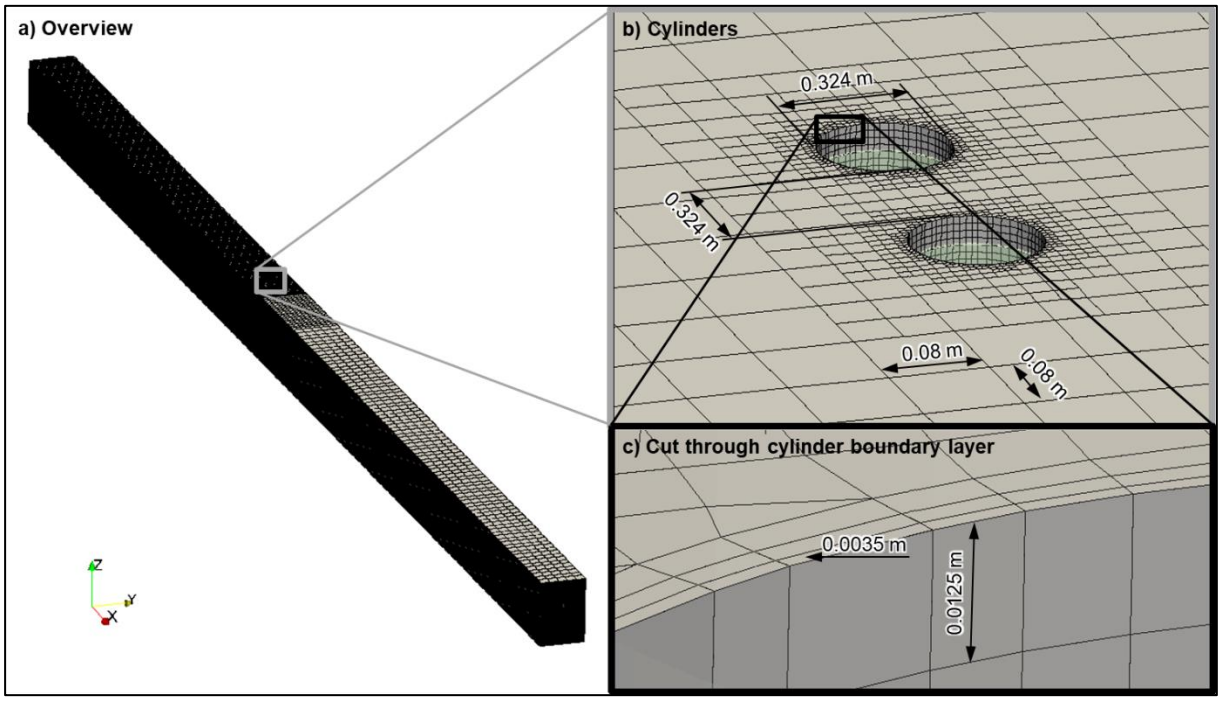

Figure 3.19. Characteristics of the mesh for the two cylinders in tandem configuration: a) overview, b) cylinders, c) cut through the cylinder boundary layer.

C. Results

The numerical results are evaluated by means of surface elevations, current speeds and overturning moments around the top suspension of the measurement cylinder.

The comparison of measured and calculated free surface elevations at three wave gauges (WG) is depicted in Figure 3.20. Similar to the experiments outlined in section 3.3.5.A, WG 1 and 7 are located upstream, WG 9 at the same horizontal position as the measurement cylinder and WG 13 is located downstream of the cylinders (see Figure 3.8 in section 3.3.3.A). The statistical descriptors of the comparison between numerical and laboratory data are given in Appendix, section A.6.1.

Between WG 1 and 3, no reduction in maximum wave height is noted. A phase shift of 43.0 s is applied to the numerical results to synchronize them with laboratory data. The peak ratios at the analysed WG vary between PR = 0.93 and 0.96, the correlation coefficient is CC = 0.99 at all WG, and the scatter index between SI = 0.15 and 0.17 (see Appendix, section A.6.1). The wave troughs in the numerical model are slightly delayed, which might be due to underlying long period wave in the wave flume (see section 3.3.3), causing a slightly asymmetric wave shape. The derived statistical descriptors confirm that the measured wave heights and wave phases are very well reproduced by the numerical model.

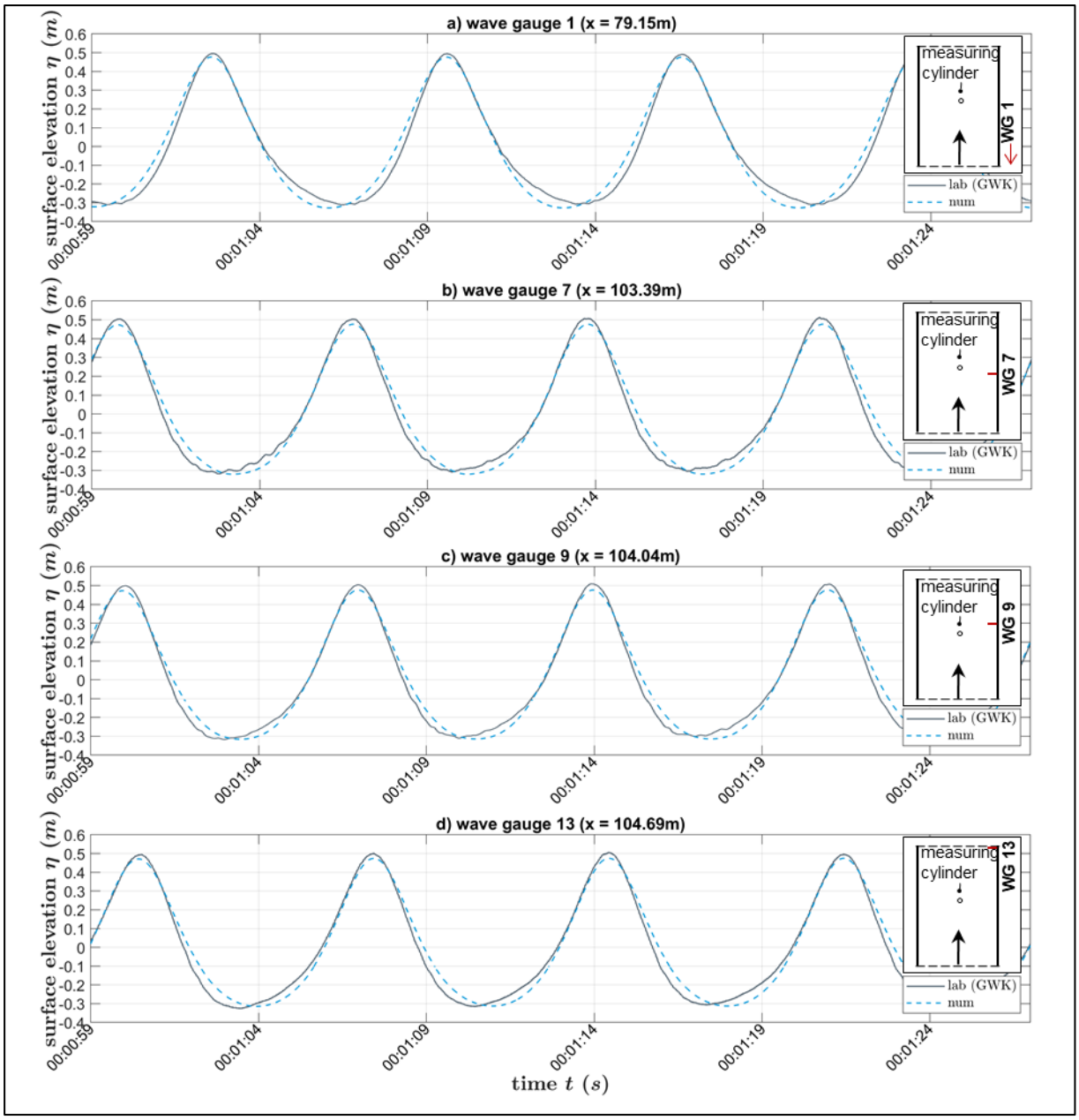

Figure 3.20. Comparison of measured and calculated free surface data for the case with two cylinders in tandem arrangement: a) wave gauge WG 1, b) WG 7, c) WG 9, d) WG 13 (see Figure 3.8 for coordinates of the measurement cylinder and wave gauges).

Figure 3.21 presents the comparison of the velocity components in the main flow direction at two current meters (CM) placed aside the instrumented cylinder (see Figure 3.8).

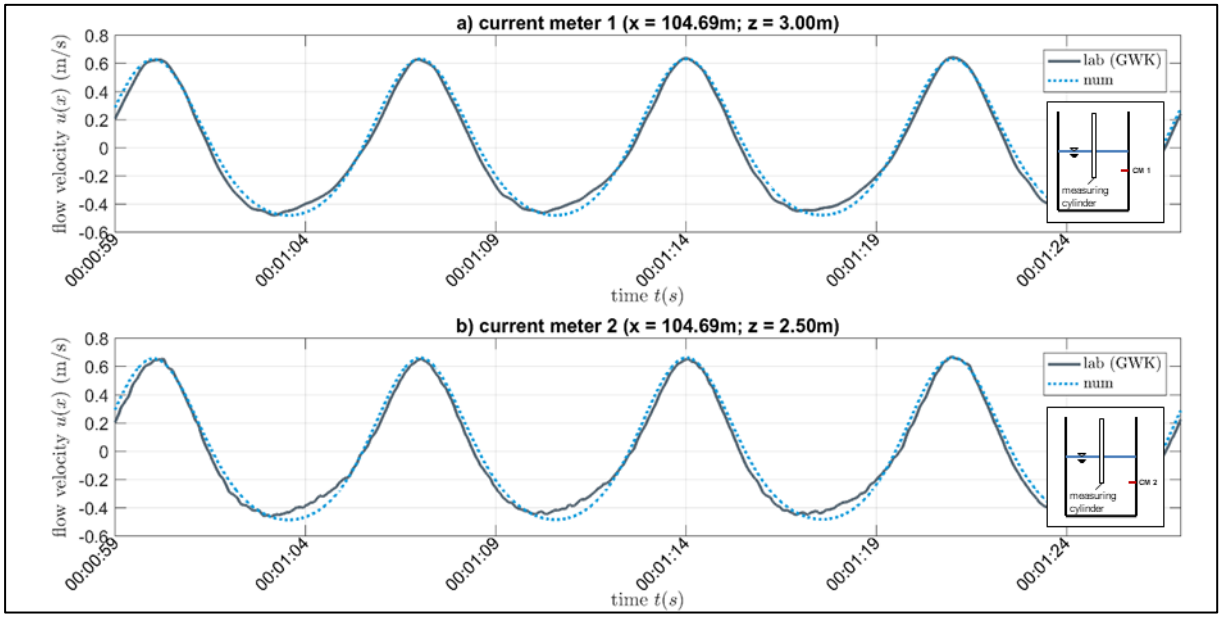

Figure 3.21. Comparison of measured and calculated flow velocities for the case with two cylinders in tandem arrangement: a) current meter CM 1, b) CM 2.

The measured peak velocities increase slightly during the course of the experiments. This is believed to be due to wave reflection from the end of the flume. Furthermore, the asymmetric wave shape leads to a slightly faster increase of flow velocities during the wave troughs. Both observations are not reproduced by the numerical simulations due to the relaxation zone near the outlet (see section 3.2.3.C). However, peak ratio PR = 0.98 to PR = 0.99, correlation coefficient CC = 0.99 and CC = 1.0 and scatter indices SI = 0.12 and SI = 0.15 indicate excellent agreement between the calculated and measured data for the first fully developed waves (see also Appendix, section A.6.2).

The comparison of the measured and calculated inline overturning moments is shown in Figure 3.22.

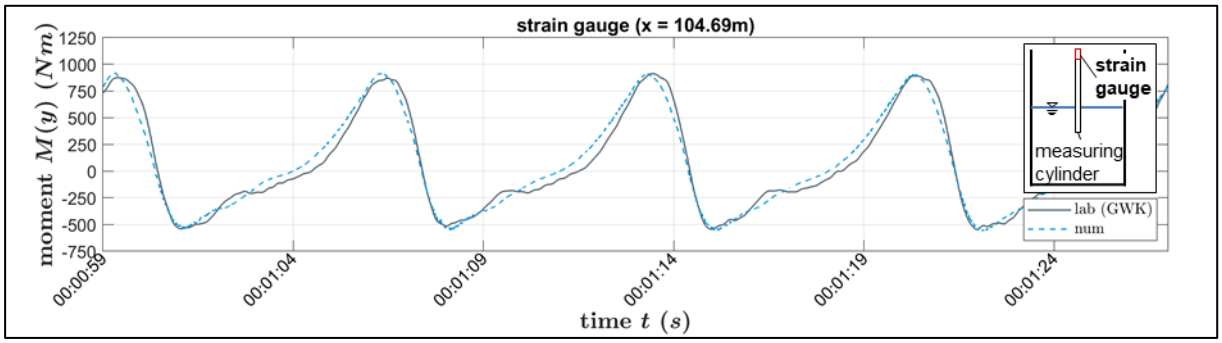

Figure 3.22. Comparison of the measured and calculated inline overturning moments for the case with two cylinders in tandem arrangement.

Peak ratio of PR = 1.01, correlation coefficient of CC = 0.99 and a scatter index of SI = 0.21 characterise very good agreement between calculated and measured moments induced by the first four fully developed waves (see Appendix, section A.6.3). The next waves lead to higher

moments, which correspond to the observations of increasing velocities during the laboratory experiments, which might originate from reflections.

Overall, very good agreement between the calculated and measured wave heights and current velocities in the far field of the two vertical cylinders in tandem arrangement and the overturning moment in the measurement cylinder downstream are noted. Deviations during the period of wave troughs might originate from underlying (parasitic) long-period waves occurring in the laboratory. The comparisons well-illustrate the ability of the numerical model to reproduce the characteristics of the flow in the wake of the upstream located cylinder with the here selected mesh element sizes and turbulence intensity of I = 10 %.

3.4 Summary and discussion

In this chapter, a CFD model based on OpenFOAM is described and validated in five phases against laboratory data for regular waves, solitary waves and bores as well as against an analytic solution for bore propagation. While the mesh characteristics follow common practice recommendations, the turbulent kinetic energy k is calculated based on the turbulence intensity I (equation (3-32)). The fluid-structure interaction is assessed in

- solitary wave over a submerged reef (phase i) with I = 0.05 %,
- bore propagation over a flat and initially dry bottom (phase ii) with I = 10 %,
- regular waves around a single isolated-standing cylinder (phase iii) with I = 5 %,
- bore around a single isolated-standing cylinder (phase iv) with I = 10 %, and
- regular waves around two cylinders in tandem configuration (phase v) with I = 10 %.

For validation, the characteristics of the wave and bore induced flow in the far field and the near field are considered. The results are summarized in Table 3.3.

Table 3.3. Evaluation of the results from the model validation (see Appendix A, section A.1).

	force/moment			**water level/wave height**			**horizontal flow velocity**		
	max.	**avg.**	**instantaneous**	**max.**	**avg.**	**instantaneous**	**max.**	**avg.**	**instantaneous**
solitary wave phase i	n.a.	n.a.	n.a.	very good	very good	acceptable	n.a.	n.a.	n.a.
regular waves phases iii & v	very good	very good	very good	very good	very good	very good	very good	very good	very good
bores phases ii & iv	very good	very good	acceptable	very god	very good	acceptable	good	very good	acceptable

n.a.=not applicable

In the far field, the damping of a solitary wave (phase i) propagating over a flat bottom is only K_d = 0.0013 per wavelength L = 7.189 m. For regular wave propagation (phase iii) K_d = 0.005

per L = 14.7 m per wavelength. In case of bore propagation over a flat bottom (phase ii), the bore propagation and surface profile is independent from the tested mesh resolutions, which proves that in the free flow zone, the mesh resolution of (dx, dy, dz) = (0.04, 0.04, 0.05) m is sufficiently small.

In the near field of the cylinders (phases iii to v) very good agreements are achieved for calculating the overturning moment as an integrated parameter of the flow characteristics for regular waves. The same applies to the bore, where drag is predominant.

However, instantaneous quantities within time series during the propagation of the bore (see section 3.3.4) are not satisfactorily reproduced. The instantaneous water levels in Figure 3.16 do not match well and the run-up on the front face of a single cylinder is underestimated. Furthermore, the current speed fluctuations observed in the measured data (see Figure 3.17) are not reflected in the numerical results, which is partly due to secondary effects during experiments, but also due to the selected vertical mesh resolution. This is also reflected in the statistical descriptors in Table 3.3 for bores phases ii & iv. Still, integrated quantities such as the inline force are well captured.

One has to take into account that the fluid-structure interaction is assessed for relatively simple configurations only. Since the validation tests of the numerical model were performed, more suitable experimental data became available such as Sivasubramanian et al. (2015), who performed experiments of flow over rectangular blocks in a channel, and Chuang et al. (2020), who conducted experiments on simplified buildings subject to a tsunami bore. These experiments provided improved insight in flow phenomena related to flow separation occurring at sharp edges in high Reynolds number flow, which are very important effects to be considered during tsunami inundation of urban areas. Unfortunately, these works could not be considered in this study anymore due to time constraints.

More complex flow patterns are expected to occur from rectangular shapes with steep pressure gradients and clear flow separation effects. This implies uncertainties with regard to the selection of turbulence intensities I to be selected for parameter tests in later phases of this study, which can only be based on experiences documented in literature. As in a RANS model, I is constant, a very high model resolution at the pressure gradient in the wake zone is required, which results in very long simulation times.It is concluded that

- the model might be appropriate to investigate the interaction of waves and bores with structures, when analysing averaged and maximum conditions, but
- uncertainty remains with regard to the interaction of flow with structures involving sharp flow separation and
- solely instantaneous data should not form part of subsequent analyses of the simulated results.

Additional systematic tests involving three circular MRE in various distances and arrangements are conducted and evaluated against experimental data with the aim to the extend the plausibility of the selected model parameters.

4 Numerical tests with three vertical cylinders in different arrangements

This chapter describes the numerical investigations of the impact of a solitary wave and a tsunami-like bore on three cylinders. The results will be possibly compared with laboratory experiments and empirical relations derived from regular wave tests to verify the numerical model applied in this study. The numerical setup is based on the numerical parameters for mesh element size and turbulence intensities as recommended in chapter 3. The focus lies on the influence of the cylinder arrangement and the spacing between them, and on the interference effect in terms of hydrodynamic forces on the cylinders.

The first section describes the numerical setup. The results of the numerical simulations are then analysed with regard to the influence of spacing in section 4.2 and arrangement in section 4.3.

4.1 Numerical setup

Three emerged vertical cylinders with diameter D_B = 0.05 m in a side-by-side arrangement, in a tandem configuration and in two staggered configurations are subject to two types of incident flow regimes: a solitary wave and a bore. These four basic arrangements in the computational domains for both flow types are depicted in Figure 4.1. Each arrangement is expressed by the arrangement angle Ψ_B, which has its origin at the bottom of the middle cylinder (cylinder 2) and spans clockwise between the flow direction and the direction in which the next cylinder is encountered. The arrangements are symmetric along the x axis, which is also the mean flow direction. The spacings between the cylinders S_G (see Figure 4.1.a)) take values of 0.5 D_B, 1 D_B, 2 D_B and 3 D_B.

The sizes of the numerical domains of the solitary wave cases (Figure 4.1.a) and the bore cases (Figure 4.1.b) are summarized in Table 4.1, the test matrix is provided in Table 4.2. and the initial conditions are provided in Table 4.3.

The domains for solitary wave simulations and bore simulations consist respectively of approximately $1.2 \cdot 10^6$ and $1.0 \cdot 10^6$ elements, of which more than 90 % are hexahedral elements. Only between the boundary layer at the cylinders and the free flow zone some tetrahedral wedges, prisms and polyhedrons are introduced by the mesh generation software snappyHexMesh to adapt the mesh to the shape of the cylinders. A part of the mesh is given exemplarily for staggered 1 configuration in Figure 4.2. The cell sizes for various regions of the mesh are summarized in Table 4.4.

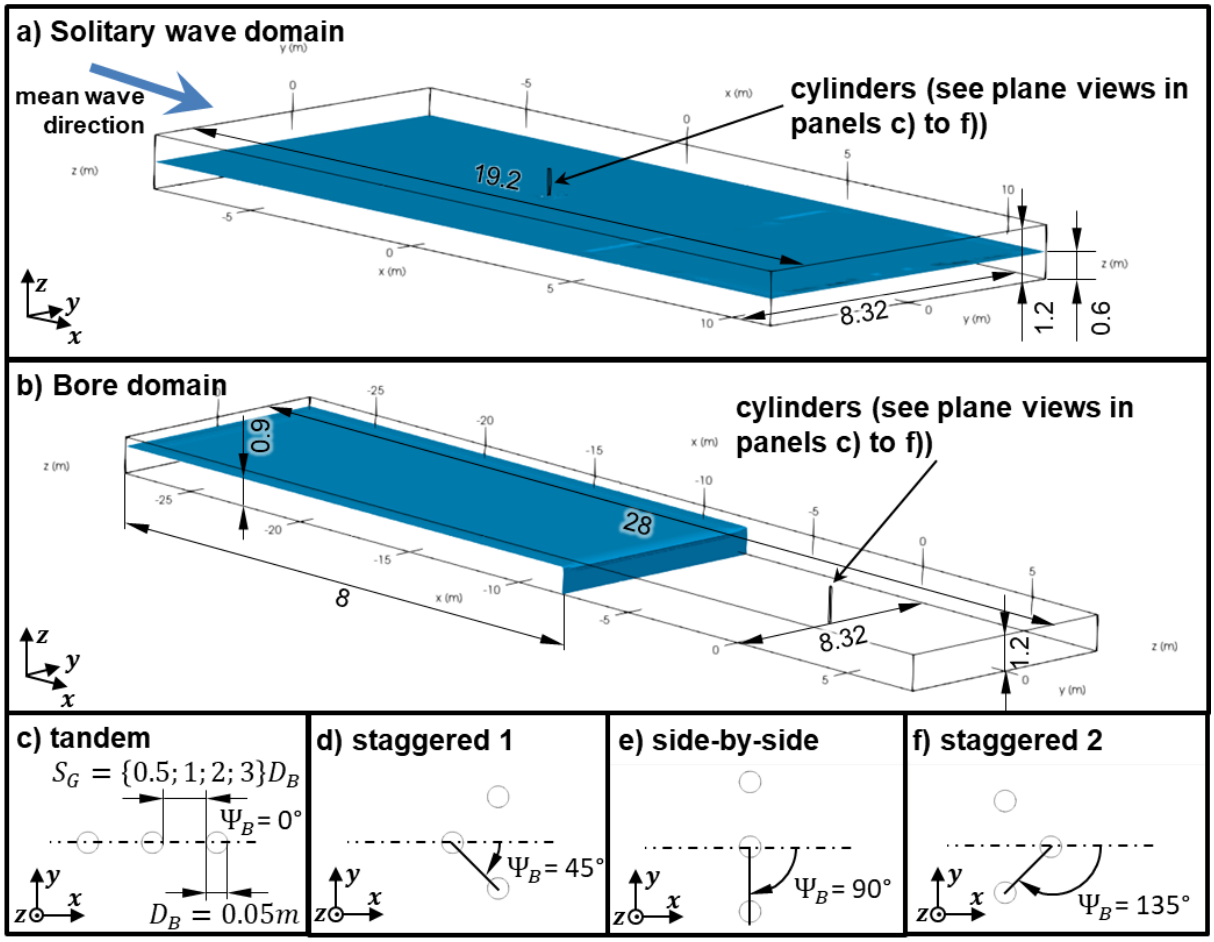

Figure 4.1. Basic arrangements of the three vertical cylinders and numerical domains. a) solitary wave domain, b) bore domain, c) tandem arrangement, d) staggered 1 arrangement, e) side-by-side, f) staggered 2 (all dimensions in meter).

Table 4.1. Sizes of the numerical domains of the three cylinder configurations (see Figure 4.1).

	Solitary wave	**Bore**
x	19.2 m	36 m
y	8.32 m	8.32 m
z	1.2 m	1.2 m

Table 4.2. Test matrix of configurations of three cylinders subject to solitary wave and tsunami-like bore.

arrangement Ψ_B **spacing S_G**	**Tandem $\Psi_B = 0$**	**Staggered 1 $\Psi_B = 45°$**	**Side-by-side $\Psi_B = 90°$**	**Staggered 2 $\Psi_B = 135°$**
0.025 m	Three cylinders combined in 4 arrangements (see Figure 4.1.c) to f)) x 4 spacings subject to (i) a solitary wave and (ii) a tsunami-like bore (see Table 4.3) (total: 32 cases)			
0.05 m				
0.1 m				
0.15 m				

Table 4.3. Initial conditions of three cylinder configurations (see Figure 4.1).

	Initial conditions
Solitary wave	Still water depth d = 0.6 m Wave height H = 0.22 m relative water depth d/L = 0.08 (shallow-water wave conditions)
bore	Impoundment length L_0 = 20 m Impoundment height h_0 = 0.9 m

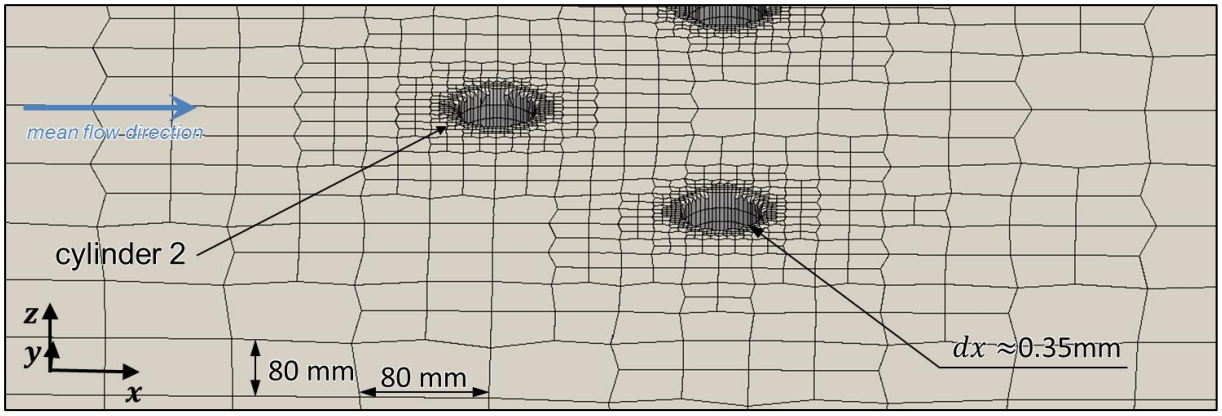

Figure 4.2. Detail of the mesh with three cylinders in staggered 1 configuration.

Table 4.4. Mesh element sizes in numerical domains of the solitary wave and bore cases.

	dx [m]	dy [m]	dz [m]	
			solitary wave	**bore**
free flow zone	0.08	0.08	0.02	0.025
bottom boundary	0.08	0.08	0.02	0.0125
cylinder boundaries	$0.35 \cdot 10^{-3}$		0.02	0.0125

The mesh element sizes, summarized in Table 4.4, base on the validation results obtained in chapter 3 (see Figure 3.19 for wave cases and Figure 3.14 for bore cases).

The k-ω-SST turbulence model is applied and turbulence intensities of I = 10 % for both flow regimes are selected (see sections 3.1.2.C, 3.3.4.B and 3.3.5.B).

During the simulations, the free surface elevations, the local velocities in a layer around the cylinders and the depth-averaged velocities upstream and in the wake of the cylinders are extracted. Forces and moments on all cylinders are calculated.

To also comparatively evaluate the impact of the cylinders on the flow field, a case is prepared with similar domain extent, initial and boundary conditions, but without cylinders. Furthermore, one case with a single isolated-standing cylinder is used to compare the inline forces in various configurations with the inline forces acting on the single cylinder.

4.2 Effect of spacing between the cylinders on inline forces

In this section, the spacing between the cylinders S_G is varied between 0.5 D_B and 3 D_B. For each cylinder group, the inline forces $F(x)_i$ on each cylinder i are determined.

The maximum inline force $F(x)_{i,max}$ acting on each cylinder within the group is normalized by the maximum inline force on a single, isolated-standing cylinder $F(x)_{single,max}$, being exposed to the same hydraulic conditions as the cylinder group. The normalized maximum inline force $F(x)^*_{i,max}$ can then be derived using the relation

$$F(x)^*_{i,max} = K_G = \frac{F(x)_{i,max}}{F(x)_{sinlge,max}} \tag{4-1}$$

$F(x)^*_{i,max}$ can be interpreted as interference coefficient K_G. The time series of the inline forces on a single isolated-standing cylinder which is subject to the solitary wave and the bore are illustrated in Figure 4.3.

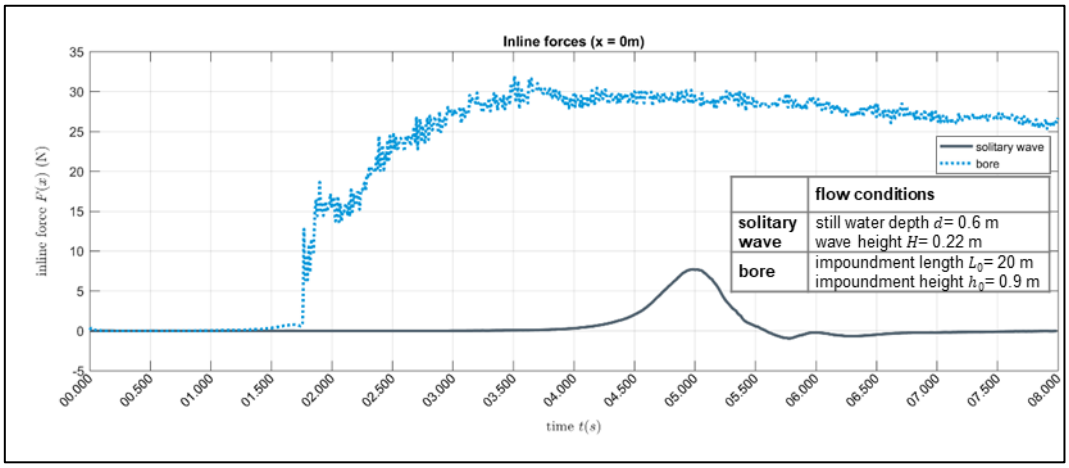

Figure 4.3. Time series of inline forces in a single cylinder subject to a) solitary wave, b) bore.

It should be noted that in case of the bore, the calculated inline force time series comprises turbulent fluctuations. This has also been reported from physical experiments, e.g. Árnason (2004). He identified spikes in measured data and considered them as outliers and filtered them out. In contrast, numerical data does not comprise such outliers to be filtered out, but shows also fluctuations, which are influenced by the mesh resolution. That is why a moving average filter (similar to the measured data) is applied. It takes the form

$$\begin{aligned} F(x,t)_{sinlge,avg} &= \frac{1}{N}F(x,t)_{sinlge} + \frac{1}{N}F(x,t-1)_{sinlge} \\ &+ \frac{1}{N}F(x,t-2)_{sinlge} + \cdots + \frac{1}{N}F(x,t-N)_{sinlge} \end{aligned} \tag{4-2}$$

in which t is the temporal index and N is the number of considered previous timesteps. The time series of inline forces of all simulated cases are provided in Appendix B. Like for the

normalized maximum inline forces in equation (4-1), the corresponding normalized maximum overturning moment is defined as

$$M(y)^*_{max} = \frac{M(y)_{i,max}}{M(y)_{sinlge,max}} \tag{4-3}$$

where $M(y)_{i,max}$ is the maximum overturning moment acting on cylinder i in the cylinder group (e.g. Bonakdar, 2014) and $M(y)_{sinlge,max}$ is the maximum overturning moment on a single isolated-standing cylinder subject to similar hydraulic conditions. Similar to equation (4-1), this ratio represents the interference of the cylinders. It is noted that when comparing K_G in equation (4-1) with $M(y)^*_{max}$ in equation (4-3), that in the latter, also the distance of the resulting force on the cylinder from the base of each cylinder might change. This is the case, for example, in tandem configuration, where the cylinders 2 and 3 are located in the wakes of the upstream cylinders 1 and 2, respectively. Therefore, $M(y)^*_{max}$ might slightly differ from K_G.

The maximum flow velocities around the cylinder group $u(x)_{i,max}$ were normalized by the maximum flow velocities determined from cases without any cylinder $u(x)_{max}$ with the relation

$$u^*(x)_{max} = \frac{u(x)_{i,max}}{u(x)_{max}} \tag{4-4}$$

The following sections present the relations of spacing and arrangements by means of inline forces and horizontal flow velocities for the four basic arrangements in Figure 4.1.

4.2.1 Tandem configuration (Ψ_B = 0°)

The interference coefficient K_G in equation (4-1) of the three cylinders in tandem arrangement subject to a solitary wave and a bore is presented in Figure 4.4 and Table 4.5.

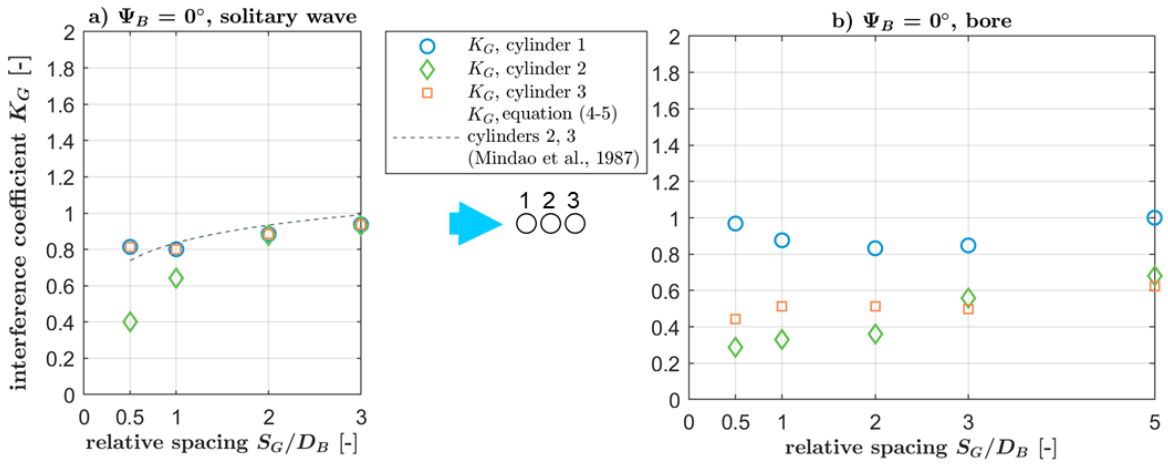

Figure 4.4. Interference coefficients K_G of three cylinders in tandem arrangement (Ψ_B = 0°) subject to a) solitary wave compared to experimental data (Mindao et al., 1987), b) bore.

Table 4.5. Interference coefficients K_G of three cylinders in tandem arrangement subject to a solitary wave and a bore.

	Solitary wave			**Bore**		
S_G/D_B	**cylinder 1**	**cylinder 2**	**cylinder 3**	**cylinder 1**	**cylinder 2**	**cylinder 3**
0.5	0.81	0.40	0.64	0.97	0.29	0.44
1.0	0.80	0.64	0.84	0.88	0.33	0.51
2.0	0.88	0.88	0.95	0.83	0.36	0.51
3.0	0.94	0.93	0.96	0.85	0.56	0.50

In the solitary wave cases (Figure 4.4.a)), the deviation between the inline forces on the cylinders is greater the closer the cylinders stand together. With a spacing of S_G/D_B = 0.5, the greatest force can be observed on the most upstream cylinder (cylinder 1); the smallest force can be observed on the middle cylinder (cylinder 2). With increasing distance, the forces on all cylinders increase, while the middle cylinder remains the most sheltered. At a spacing of 3 D_B, the differences between the cylinders are very small and close to the forces acting on the single cylinder. This effect can be explained when investigating the flow fields around the cylinders by means of normalized maximum horizontal flow velocities $u^*(x)_{max}$ (see equation 4-4) in Figure 4.5.

The maximum horizontal flow velocities $u(x)_{max}$ are extracted in horizontal planes at half still water depth 0.5 d. Bluish areas indicate areas of decreased flow velocities and reddish areas indicate increased flow velocities. The different patterns of increased flow velocities aside the cylinders confirm the differences observed for the forces on the cylinders. They differ more the closer the cylinders stand together. It is further noted that with spacings of 0.5 D_B and 1 D_B (Figure 4.5.a) and Figure 4.5.b), respectively) the middle cylinder (cylinder 2) does not comprise of laterally increased flow velocities as it is noted for larger spacings. This observation originates from the protective role which the cylinders 1 and 3 fulfil in case of small spacings.

It is noted that also the most upstream located cylinder 1 benefits from cylinders located in its wake the smaller the distance is. Vortex losses occur in the wake of an obstacle (see section 2.4.3), which can take values of 20 % of total losses (Oumeraci and Koether, 2008). The reduction of vortex losses leads to interference coefficients $K_G < 1$. In case of small distances between the cylinders, such vortices cannot form, and the water is forced to move around the group of cylinders. Vortices can only form in the wake of the most downstream cylinder, which is the reason for higher K_G values for cylinder 3 compared to cylinder 2.

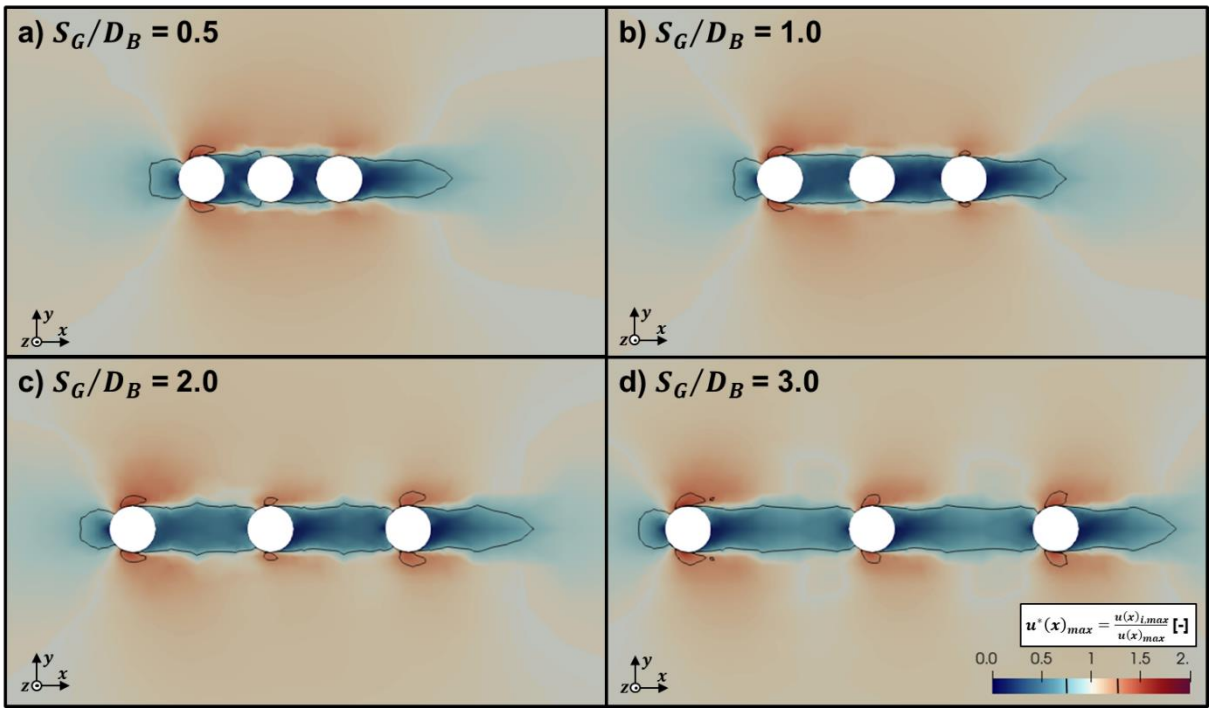

Figure 4.5. Normalized maximum horizontal flow velocities $u^*(x)_{max}$ around cylinders in tandem arrangement (Ψ_B = 0°) subject to a solitary wave. The black line indicates 25 % higher or lower maximum flow velocities compared to the case without cylinders.

The results in Figure 4.4 and Table 4.5 are compared to the empirical relations derived by Mindao et al. (1987), given by

$$K_G = 0.836 + 0.141 ln\left(\frac{S_G}{D_B}\right) \tag{4-5}$$

in which S_G/D_B is the relative spacing between the neighbouring cylinders. It is noted that in this relation, the number of cylinders and wave conditions are not considered. Therefore, it can only be interpreted as an indication for a trend for forces related to cylinder spacings. The trend indicated by Mindao et al. (1987) is matched by the here obtained numerical results.

In the bore case, the deviation between the inline forces in all cylinders is higher for small spacings between the cylinders. The most upstream cylinder receives the highest force which is similar to the force acting on a single cylinder. For spacings smaller than 3 D_B, the middle cylinder is the most protected, which indicates that the presence of cylinder 3 downstream of cylinder 2 also contributes to the protection of the middle cylinder in a group in tandem configuration. At 3 D_B, the most upstream cylinder still receives the highest force, whereas the order of forces in the following cylinders switches so that cylinder 3 receives the smallest load. Cylinder 3 does not contribute to the protection of cylinder 2 and the cylinders start to behave like isolated standing cylinders. For a spacing of 5 D_B, cylinder 1 receives similar loads as an isolated standing cylinder, whereas the cylinders 2 and 3 are still protected. The maximum horizontal flow velocities $u^*(x)_{max}$ around the cylinders are presented in Figure 4.6.

The zones, in which the flow velocity in the bore decreases, extend further downstream than in the solitary wave cases, because in general, the velocity in the bore is higher. Once the flow is deflected by the first cylinder forcing the particles to move around the cylinder on both sides, they travel a longer distance before joining downstream. The wake is therefore longer than in the solitary wave cases and the cylinders 2 and 3 benefit from the shelter of the first cylinder over greater distances than in the solitary wave cases.

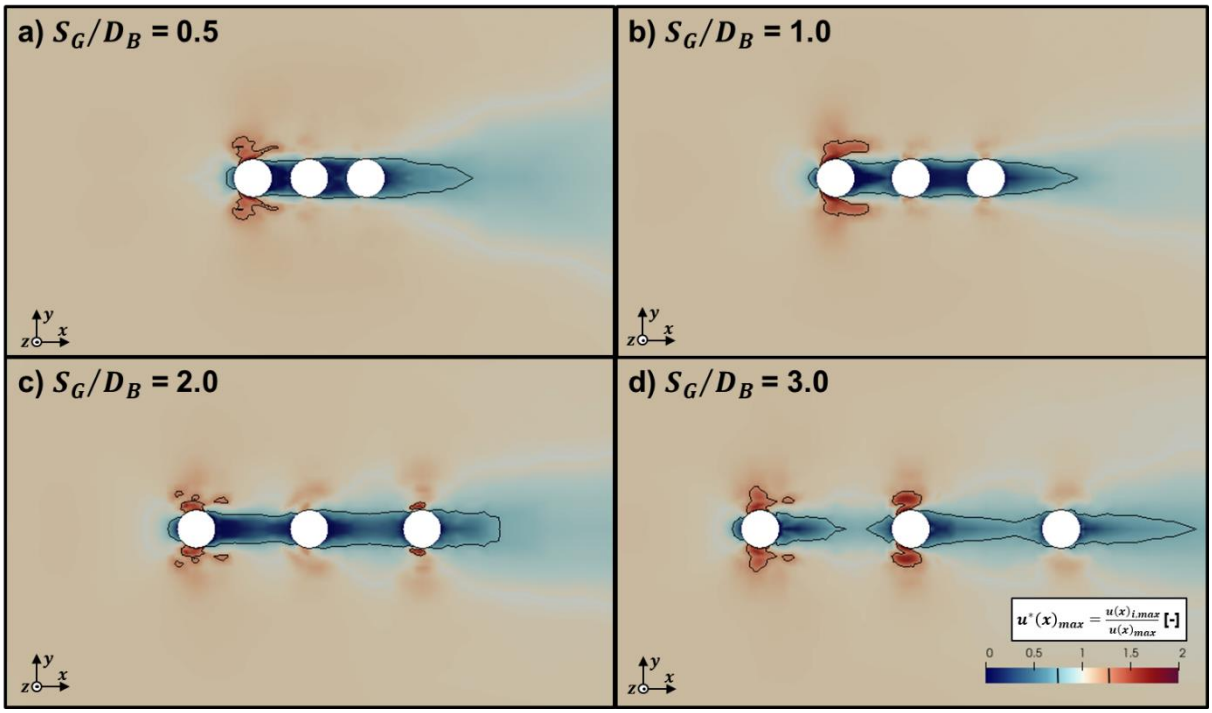

Figure 4.6. Normalized maximum horizontal flow velocities $u^*(x)_{max}$ around cylinders in tandem arrangement (Ψ_B = 0°) subject to a bore. The black line indicates 25 % higher or lower maximum flow velocities compared to the case without cylinders.

In tandem arrangement, the middle cylinder experiences the smallest inline force in both flow regimes (bore and solitary wave), whereas the most upstream cylinder experiences the highest.

For the solitary wave simulations, the forces on the cylinders are more sensitive to the relative spacing S_G/D_B compared to the bore cases. The differences between the forces on the cylinders vanish when the spacing increases to 3 D_B. The here determined interference effect compares well with the observations made by Mindao et al. (1987) and Oumeraci and Koether (2008).

For the bore simulations, the most upstream located cylinder receives comparable forces to a single cylinder for $S_G/D_B \geq 5$, although the difference between the forces in the downstream located cylinders is still apparent.

The numerical model provides results which, in case of solitary wave simulations, can be related to experimental data. In case of bore simulations, the results seem reasonable but cannot be related to experimental data.

4.2.2 Staggered 1 (Ψ_B = 45°)

The normalized maximum inline forces acting on three cylinders as a ratio of inline forces on a group of cylinders to the inline forces on a single cylinder can be interpreted as interference coefficient K_G. For cylinders in the staggered 1 arrangements (Ψ_B = 45°) subject to a solitary wave and a bore, K_G is presented in Figure 4.7 and Table 4.6.

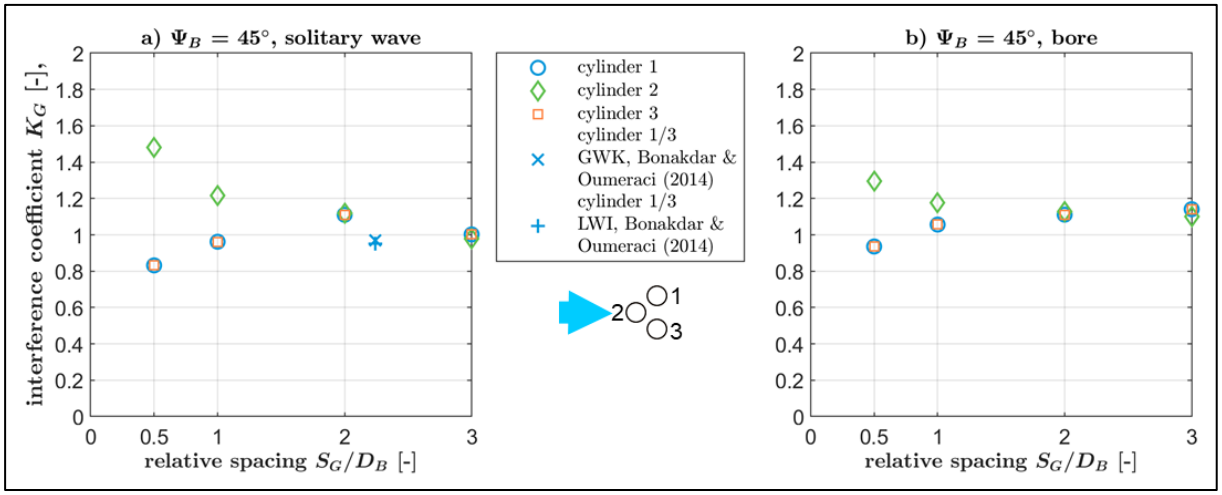

Figure 4.7. Interference coefficient K_G for three cylinders in staggered 1 arrangement (Ψ_B = 45°) subject to a) solitary wave (including laboratory data by Bonakdar & Oumeraci, 2014), b) bore.

Table 4.6. Interference coefficient K_G for three cylinders in staggered 1 arrangement subject to a solitary wave and a bore.

	Solitary wave			Bore		
S_G/D_B	cylinder 1	cylinder 2	cylinder 3	cylinder 1	cylinder 2	cylinder 3
0.5	0.83	1.48	0.83	0.94	1.29	0.94
1.0	0.96	1.22	0.96	1.06	1.18	1.06
2.0	1.11	1.12	1.11	1.11	1.13	1.11
3.0	1.00	0.98	1.00	1.14	1.10	1.14

In the solitary wave cases, the deviation between the inline forces on the cylinders is greater the closer the cylinders stand together. At a relative spacing of S_G/D_B = 0.5, the greatest force can be observed on the middle cylinder (cylinder 2); the cylinders at the sides receive smaller loads. With increasing distance, the forces approach the value of the single cylinder. At a spacing of S_G/D_B = 2.0, the maximum forces are similar on all three cylinders and higher than on a single cylinder. Referring to Figure 2.3, it is noted that cylinders 1 and 3 are located in zone 4 of cylinder 2, in which the drag force is increased and the lift force is negligible while in case of smaller relative spacings the drag force is decreased and the lift force is negligible (zone 5), which explains interference coefficients K_G > 1. Furthermore, cylinder 2 is located in zone 2, where drag forces are reduced but lift forces are increased. Compared to the other relative spacings in Figure 4.7.a), it is seen that the drag force dominates over the lift force the smaller the relative spacing is, so that K_G > 1 in case of S_G/D_B = 2.0.

When the distance increases further, then the differences between the cylinders become very small and the forces take values similar to those of the single cylinder, so that $K_G \approx 1$. This is supported by Figure 4.8, where the maximum normalized flow velocities $u^*(x)_{max}$ velocities around the cylinders indicate independent cylinder behaviour for a spacing $S_G/D_B \geq 2$.

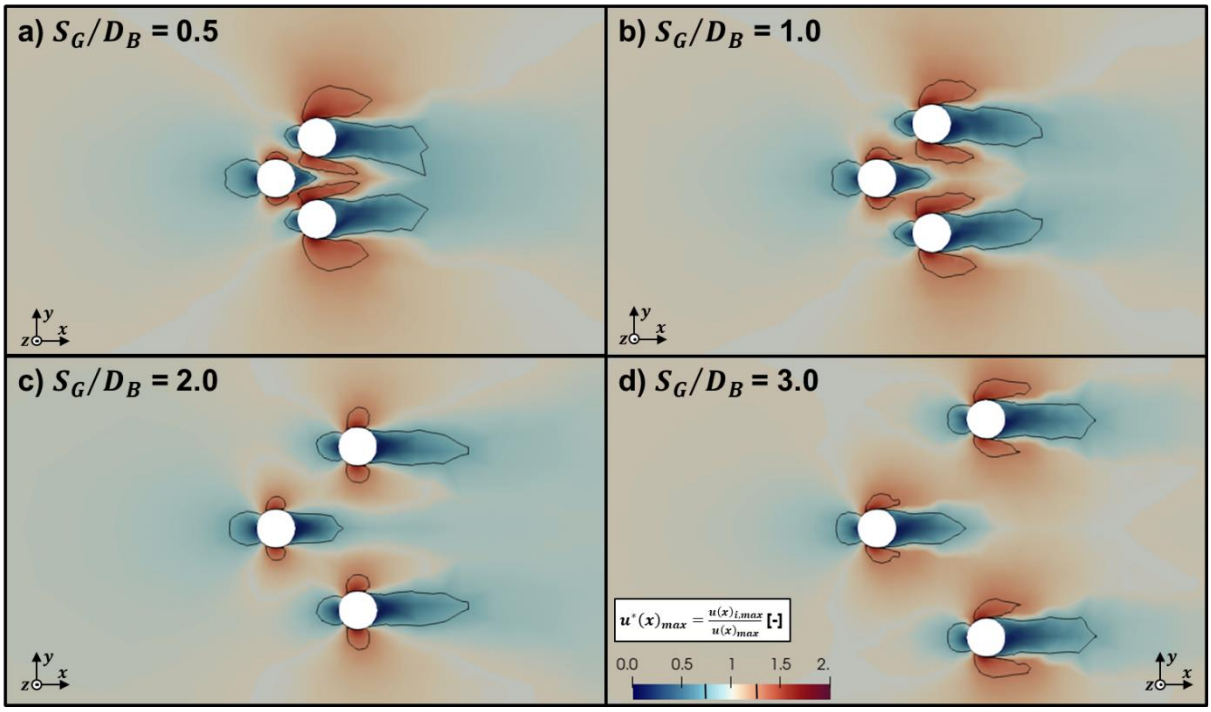

Figure 4.8. Normalized maximum horizontal flow velocities $u^*(x)_{max}$ around cylinders in staggered 1 arrangement (Ψ_B = 45°) subject to a solitary wave. The black line indicates 25 % higher or lower maximum flow velocities compared to the case without cylinders.

In the case of small cylinder spacing (Figure 4.8.a)), the zone of reduced flow velocities in the wake of cylinder 2 cannot develop due to the presence of the cylinders 1 and 3. The outer lateral zones of cylinders 1 and 3 comprise higher flow velocities than the inner lateral zones. This indicates that water particles move to a large extent around the group of cylinders.

In the case of larger spacing, flow patterns around each cylinder are more similar, indicating that water particles move through the cylinder group and around each single cylinder. The middle cylinder can provide shelter for the outer recessed cylinders only for spacings up to 2 D_B.

For further verification, Figure 4.7a includes laboratory data by Bonakdar (2014), in which normalized maximum overturning moments $M^*(y)_{max}$ (see equation (4-2)) of 15 regular wave cases in two wave flumes (GWK in Hanover and LWI at TU Braunschweig) are analysed in a similar way. The laboratory setup is different to the numerical setup predominantly in two aspects:

- The cylinders are mounted at the top.
- The cylinders do not reach the bottom.

The differences are assumed to be negligible for relative comparisons performed here.

In the physical experiments, at a distance of 2.242 D_B, $M^*(y)_{max}$ = 0.996 and at a distance of 6.728 D_B (not shown), $M^*(y)_{max}$ = 1.07 on the outer cylinder. In Bonakdar (2014), K_G varied for the recessed cylinder (comparable with cylinder 1 or 3 in this study) between K_G = 0.87 and K_G = 1.18 for staggered arrangements. He concluded that K_G is independent from structural and wave parameters. Therefore, the ranges of K_G in the experimental and numerical data should be compared rather than the averaged values reported in Bonakdar and Oumeraci (2014). The here obtained K_G for the cylinders 1 and 3 between K_G = 0.83 and K_G = 1.11 compares reasonably well with the above-mentioned range of laboratory data.

In the bore case, the deviation between the inline forces in all cylinders in Figure 4.7.b) is higher for small spacings. The middle cylinder receives the highest loads. At 2 D_B, all cylinders are subject to almost the same force. It is noted that at a distance of 3 D_B, the interference coefficient $K_G \approx 1.2$ at all cylinders, although one would expect a trend towards 1.0. This trend is not clearly sized in the results. On one hand, there is still water which moves around the entire group of cylinders so that in the wake of each cylinder a lower water level is observed. On the other hand, at the distance of ~3 D_B, the run-up at the front faces of the three cylinders is similar to the runup on the isolated standing cylinder. This results in a higher hydrostatic pressure in each cylinder so that the forces acting on the three cylinders exceed the forces acting on the isolated standing cylinder. For clarification, forces on cylinder 2 are compared with the single cylinder force. They are represented in Figure 4.9.

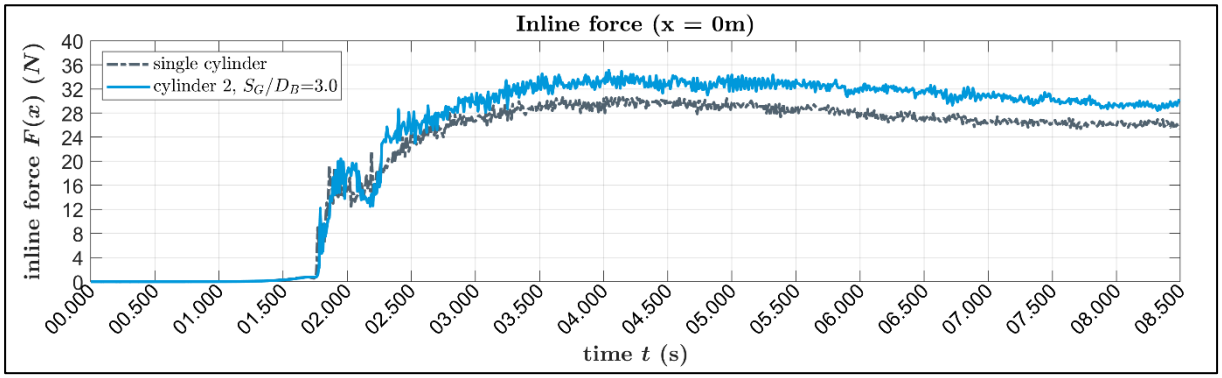

Figure 4.9. Time series of bore forces on a single cylinder and cylinder 2 in staggered 1 (Ψ_B= 45°) arrangement with relative spacing S_G/D_B = 3.0.

The time series reveals that at the moment of bore impact the forces in both cases are similar. With increasing flow depth over time, the forces in cylinder 2 standing in a group in staggered 1 arrangement increase more than in the simulation with a single cylinder. The maximum forces are noted at $t \approx 4.0$ s. The flow depth h are extracted between cylinders 1 and 2 (see Figure 4.1.d)) and, at the same position, in the single cylinder case. The time series of h are analysed and presented in Figure 4.10 (note that the position of the single cylinder is at cylinder 2, see Figure 4.1.d)).

The position of data extraction is indicated in Figure 4.10.a). It is seen that the water depth h is larger higher in the staggered 1 arrangement case. In both cases, the velocities between z = 0 and 0.18 m are similar, but in the staggered 1 case, there is a water layer between z = 0.2 m and

z = 0.25 m apparent, which moves slower, but which also contributes to the cylinder forces acting in the staggered 1 case. A physical interpretation is that the interference between the cylinders leads to increased drag forces in the recessed cylinders stand outside of the wake of cylinder 2. This is the case for relative spacings $S_G/D_B \geq 2$. Referring to Figure 2.3 (modified from Hori, 1959), the cylinders 1 and 3 are located mainly in zones 4 with increased drag forces. Cylinder 2 is subject to interference with two recessed cylinders. It seems that zone 3 (increased drag forces) extents further upstream in case of the interaction of three cylinder. However, Figure 2.3 only describes the interference between a total of two cylinders and can therefore not be applied for explaining the here observed effects.

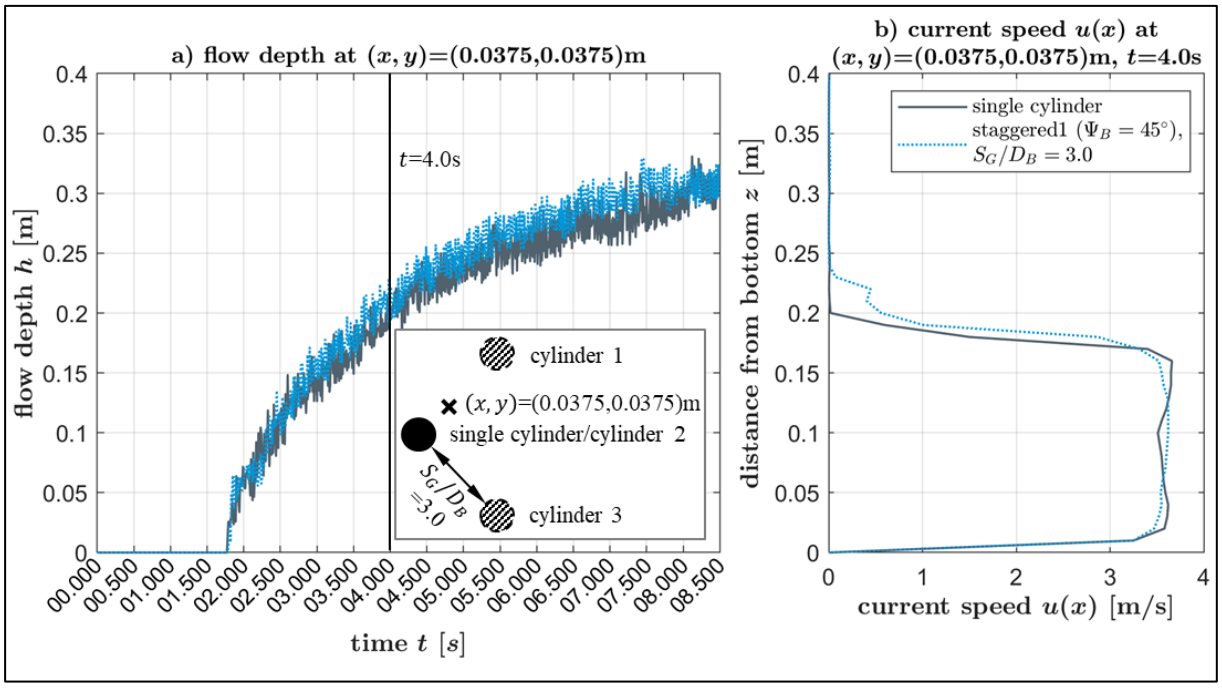

Figure 4.10. a) Flow depth h at (x, y) = (0.0375, 0.0375) m in the staggered 1 (Ψ_B = 45°) configuration (3 D_B case) and at the same position in the single cylinder case, b) horizontal velocities $u(x)$ at the same position at t = 4.0 s.

The normalized maximum horizontal flow velocities around the cylinders are given in Figure 4.11.

As observed for the solitary wave cases, the water particles tend to move around the group of cylinders when the spacing between the cylinders is small (S_G/D_B < 2 in Figure 4.11.a)), which is indicated by the greater zones of increased flow velocities at the outer sides of the cylinders 1 and 3.

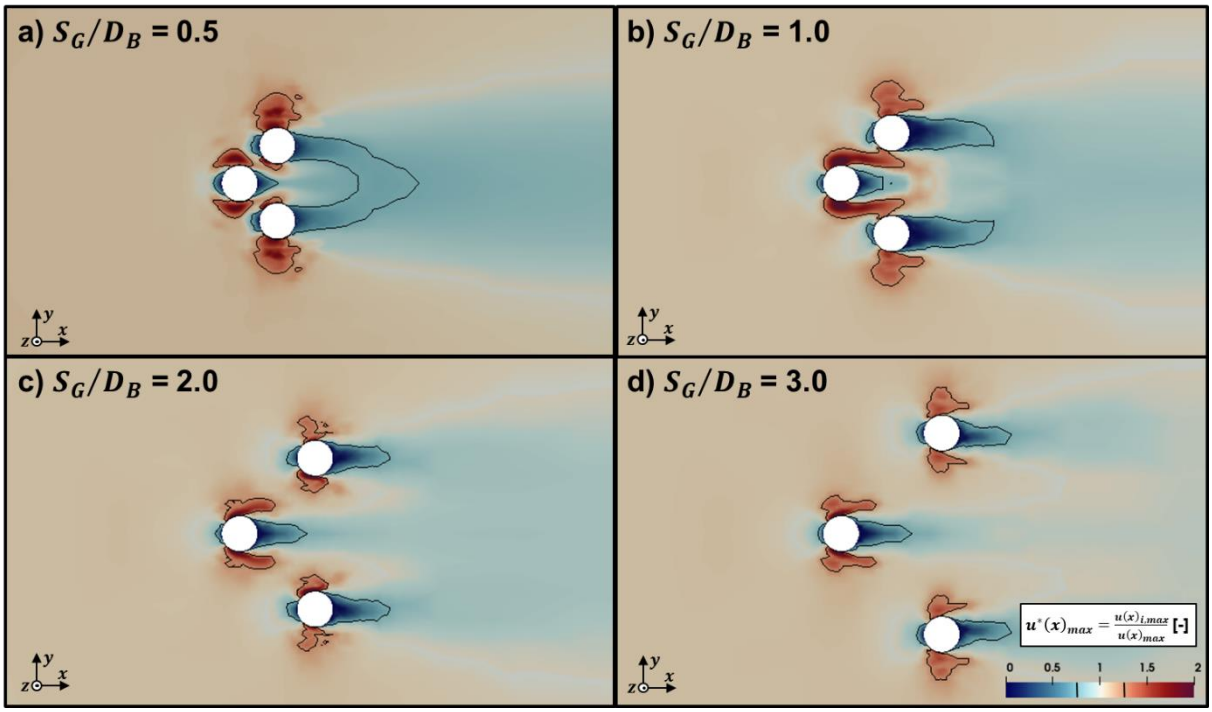

Figure 4.11. Normalized maximum horizontal flow velocities $u^*(x)_{max}$ around cylinders in staggered 1 arrangement (Ψ_B = 45°) subject to a bore. The black line indicates 25 % higher or lower maximum flow velocities compared to the case without cylinders.

In staggered 1 arrangement, the middle cylinder experiences the highest force in both flow regimes. The interference between the cylinders is similar for all cylinders for relative spacings of $S_G/D_B \geq 2$.

For the wave cases, for $S_G/D_B < 2$, the differences are more pronounced compared to the bore cases. The here determined range of the interference coefficients between K_G = 0.88 and K_G = 1.11 of cylinders in waves compares reasonably well with experimental data reported in Bonakdar (2014).

For the bore cases, the cylinder forces still differ from those on a single cylinder at a distance of 3 D_B. For $S_G/D_B \geq 2$, increased drag forces in the recessed cylinders can be explained by the interference diagram of Hori (1959) in Figure 2.3. The increased drag forces of cylinder 2 for spacings $S_G/D_B \geq 2$ might be related to overlapping of interference of three cylinders, but no experimental data was found to confirm this assumption.

The numerical model seems to provide reasonable results, although direct comparison with experimental data is difficult, as (i) in case of waves, experimental data comprises a wide range of results and (ii) no experimental data is found for bores.

4.2.3 Side-by-side (Ψ_B = 90°)

The interference coefficient of three cylinders in side-by-side arrangement subject to a solitary wave and a bore are presented in Figure 4.12 and Table 4.7.

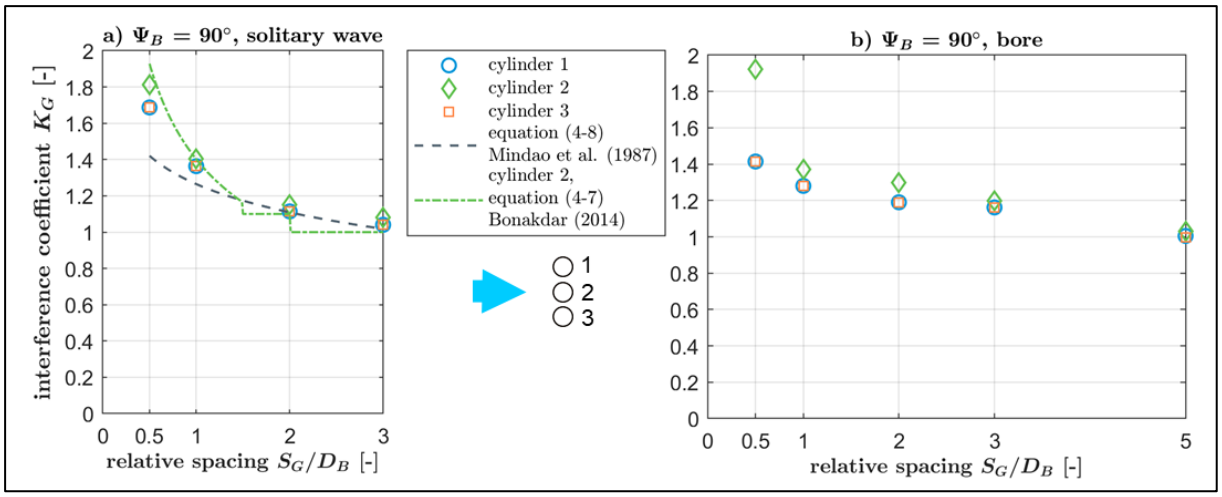

Figure 4.12. Interference coefficient K_G for three cylinders in side-by-side arrangement (Ψ_B = 90°) subject to a) solitary wave (including empirical relations of Mindao et al., 1987 and Bonakdar, 2014), b) bore.

Table 4.7. Interference coefficient K_G for three cylinders in side-by-side arrangement (Ψ_B = 90°) subject to a solitary wave and a bore.

	Solitary wave			**Bore**		
S_G/D_B	**cylinder 1**	**cylinder 2**	**cylinder 3**	**cylinder 1**	**cylinder 2**	**cylinder 3**
0.5	1.69	1.81	1.69	1.41	1.92	1.41
1.0	1.36	1.40	1.36	1.28	1.37	1.28
2.0	1.11	1.15	1.11	1.19	1.30	1.19
3.0	1.04	1.08	1.04	1.16	1.20	1.16

In the solitary wave cases (Figure 4.12.a)), the forces acting on the cylinders decrease with increasing distance. The middle cylinder (cylinder 2) receives the highest load. Differences between the cylinders vanish with increasing distance. The phenomenon can be explained with the help of the flow field around the cylinders, which is presented in Figure 4.13.

The lengths of the wakes downstream of the cylinders (bluish areas) indicates that at smaller distances the wakes downstream of the middle cylinder (cylinder 2) comprise smaller maximum normalized flow velocities than downstream of the outer cylinders 1 and 3. Furthermore, the zones of increased flow velocities aside each cylinder overlap in case of small spacings $S_G/D_B < 3$ so that the motion of water particles around each cylinder is hindered. This leads to increased forces on each of the cylinders, especially in the middle one.

The interference coefficients K_G of the solitary wave cases are compared to empirical relations derived by Bonakdar (2014) for a side-by-side arrangement. For the middle cylinder, the interference coefficient can be expressed

$$\begin{aligned} &\text{for } S_G/D_B \leq 1.5 \text{ and } KC{>}13 \quad && K_G = 1.4\left(\frac{S_G}{D_B}\right)^{-0.46} exp(52.7KC^{-2.22}) \\ &\text{for } 1.5 < S_G/D_B \leq 2 && K_G = 1.1 \text{ and} \\ &\text{for } S_G/D_B > 2 && K_G = 1.0. \end{aligned} \tag{4-6}$$

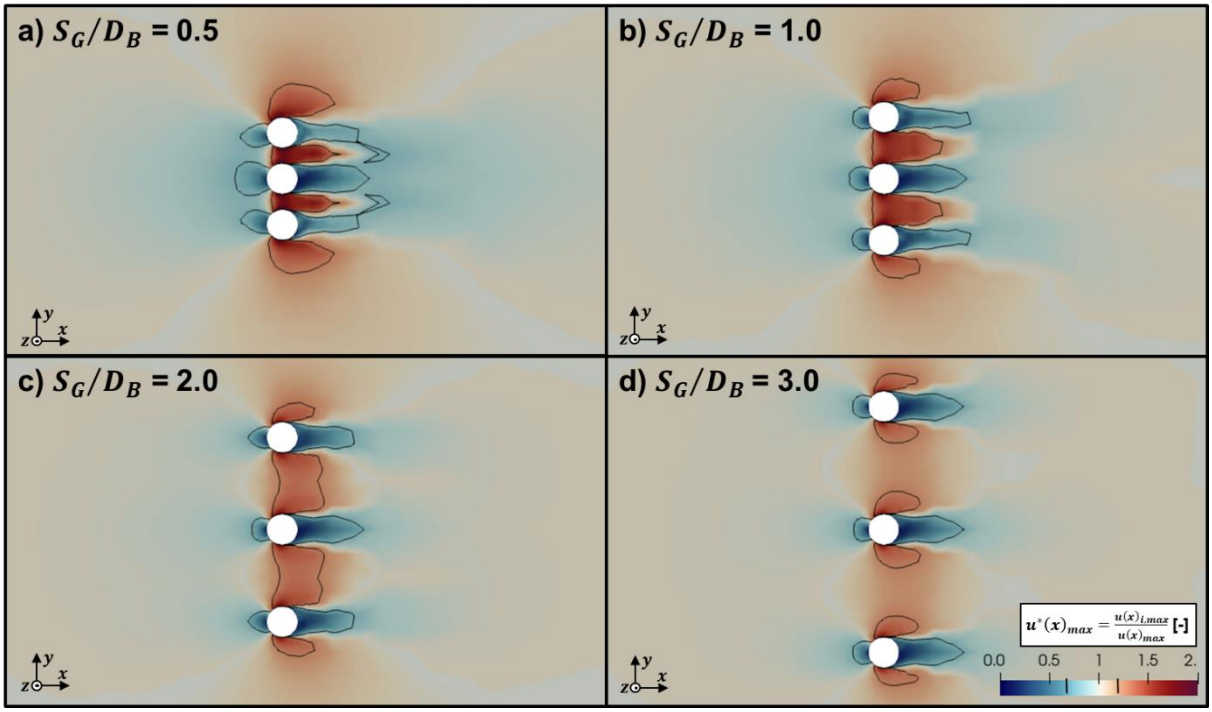

Figure 4.13. Normalized maximum horizontal flow velocities $u^*(x)_{max}$ around cylinders in side-by-side arrangement (Ψ_B = 90°) subject to a solitary wave. The black line indicates 25 % higher or lower maximum flow velocities compared to the case without cylinders.

Mindao et al. (1987) determined for a side-by-side arrangement.

$$K_G = 1.265 - 0.225ln\left(\frac{S_G}{D_B}\right) \tag{4-7}$$

which is the averaged value of one outer pile (either cylinder 1 or 3) and the middle pile (cylinder 2). Equation (4-8) was derived from tests with various heights and periods of regular waves. Therefore, the comparison with the here performed solitary wave tests is understood as an indication of trends, only. In the numerical results, a similar trend is noted. The numerical model results for the middle cylinder agree very well with the empirical relation by Bonakdar (2014).

In the bore cases, the differences between the cylinders are more apparent than in the solitary wave cases. Furthermore, the forces are higher in all cylinders than in a single cylinder. This is confirmed by the flow field, given in Figure 4.14.

The interference between the cylinders hinders the water particles to move around the individual cylinders as they would do around a single isolated-standing cylinder. The water particles

moving towards neighbouring cylinders have less space available. This leads to higher water levels at the upstream cylinder faces and higher velocities in the gaps between them. Zdravkovich (1977) reported a similar behaviour from his investigation of side-by-side arranged cylinders subject to wind. He found that such behaviour is independent from the Reynolds number Re and that the cylinders influence each other even at a relatively large spacing of S_G/D_B = 5.

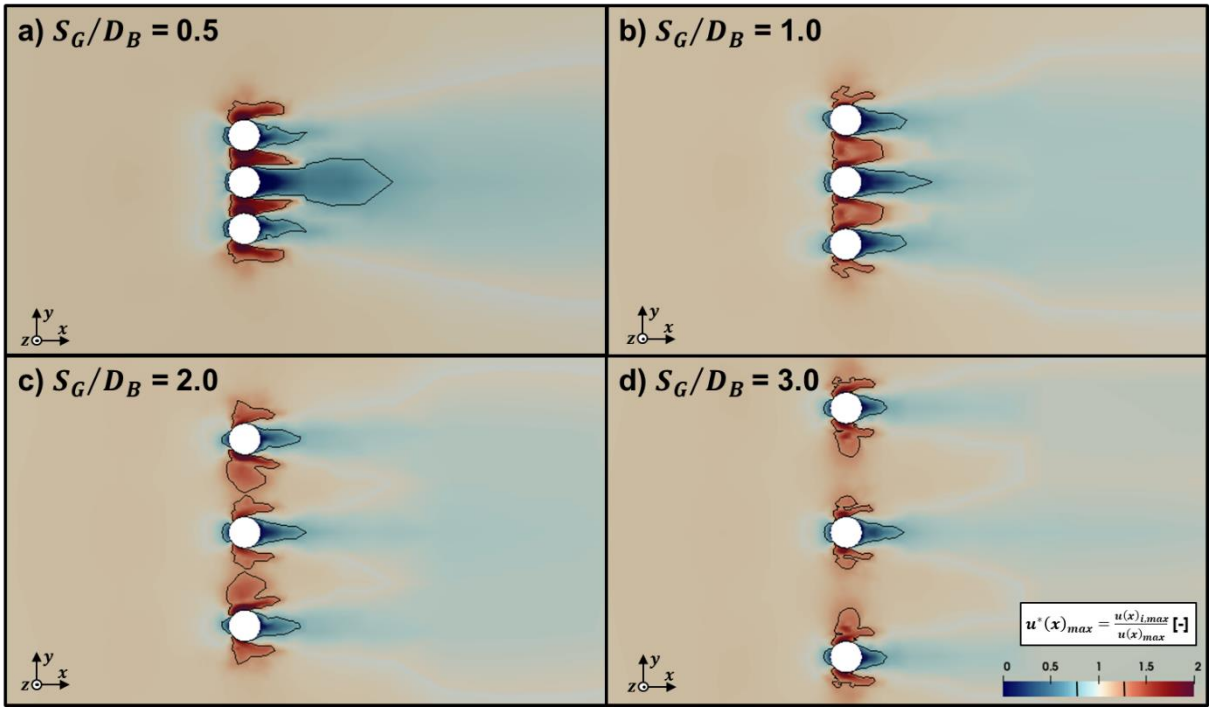

Figure 4.14. Normalized maximum horizontal flow velocities $u^*(x)_{max}$ around cylinders in side-by-side arrangement (Ψ_B = 90°) subject to a bore. The black line indicates 25 % higher or lower maximum flow velocities compared to the case without cylinders.

In side-by-side arrangement, the middle cylinder experiences the highest load under both flow regimes (bore and solitary wave). The differences between the cylinders are more pronounced in the bore cases.

For the solitary wave cases, the interference coefficients K_G compare reasonably well with empirical relations derived by Mindao et al. (1987) and Bonakdar and Oumeraci (2014). The interference effect vanishes with spacing of ~3 D_B,

For the bore cases, the influence of neighbouring cylinders vanishes with spacing of ~5 D_B, which agrees with the findings of Zdravkovich (1977).

The numerical model provide reliable results for wave simulation cases, while for the bore cases, the results seem reasonable but cannot be related to experimental data.

4.2.4 Staggered 2 (Ψ_B = 135°)

The interference coefficients K_G of three cylinders in staggered 2 arrangement subject to a solitary wave and a bore are presented in Figure 4.15 and Table 4.8.

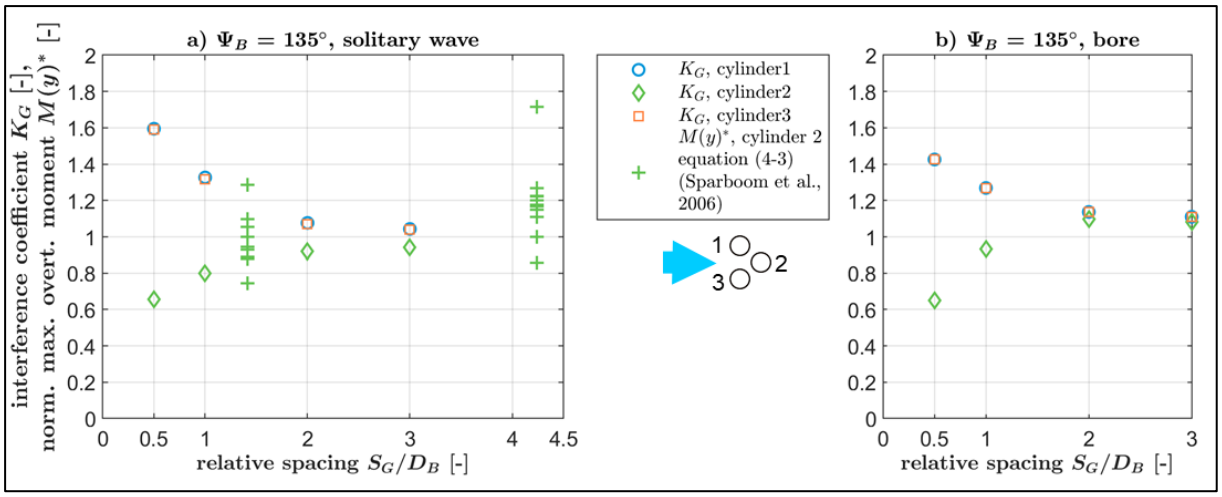

Figure 4.15. Interference coefficient K_G in three cylinders in staggered 2 arrangement (Ψ_B = 135°) subject to a) solitary wave compared to the normalized maximum overturning moment $M(y)^*$ (Sparboom et al., 2006), b) bore.

Table 4.8. Interference coefficient K_G in three cylinders in staggered 2 arrangement (Ψ_B = 135°) subject to a solitary wave and a bore.

	Solitary wave			**Bore**		
S_G/D_B	**cylinder 1**	**cylinder 2**	**cylinder 3**	**cylinder 1**	**cylinder 2**	**cylinder 3**
0.5	1.69	1.81	1.69	1.43	0.65	1.43
1.0	1.36	1.40	1.36	1.27	0.93	1.27
2.0	1.11	1.15	1.11	1.14	1.10	1.14
3.0	1.04	1.08	1.04	1.11	1.08	1.11

In the solitary wave cases, the deviation between the inline forces on the cylinders is greater the closer the cylinders stand together. With a spacing of S_G/D_B = 0.5, the greatest force can be observed on the outer cylinders; the smallest force can be observed on the middle cylinder (cylinder 2). For S_G/D_B = 1, considerable differences between K_G are still noted, which was not observed by Bonakdar (2014), who re-analysed tests with similar configurations (S_G/D_B = 1.414 and S_G/D_B = 4.243) using regular waves (Sparboom et al., 2006). In the re-analysis, no influence of the cylinder position in staggered arrangements was noted, which suggests that K_G should be similar for all three cylinders.

Sparboom et al. (2006) reported overturning moments $M(y)^*$ in slender piles subject to regular waves for this configuration from measurements in the large wave flume Hanover for the above mentioned relative spacings and for a single cylinder, from which the normalized overturning moment $M(y)^*$ on cylinder 2 was determined (see equation (4-3)). The measurements comprise wave heights between H = 0.8 to H = 1.4 and wave periods between T = 4 s and T = 8 s. The measurements do not show a clear correlation between $M(y)^*$ and H or T. Therefore, they can

only indicate a range of values, in which also fall the here determined values for K_G for the solitary wave.

In this study, the forces acting on cylinder 2 are the smallest compared to those acting on the outer cylinders (cylinders 1 and 3). This indicates that in this study, more fluid particles move around the entire group than between the cylinders 1 and 3, and therefore, both cylinders provide shelter for cylinder 2.

This indication is confirmed by the flow fields, showing normalized maximum horizontal flow velocities around the cylinders, which are given in Figure 4.16.

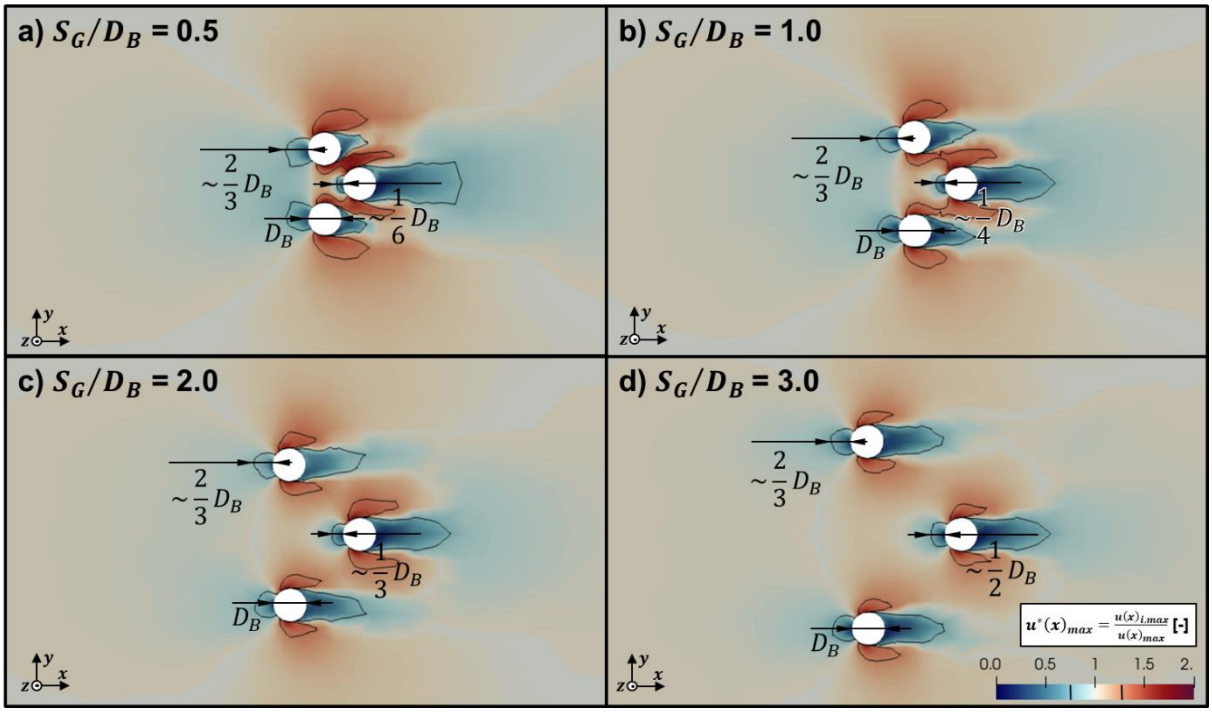

Figure 4.16. Normalized maximum horizontal flow velocities $u^*(x)_{max}$ around cylinders in staggered 2 arrangement subject to a solitary wave. The black line indicates the 25 % higher or lower maximum flow velocities compared to the case without cylinders.

For spacing S_G/D_B = 1 (Figure 4.16.b), the zone of small flow velocities at the upstream part of the face of the middle cylinder (cylinder 2) is still smaller compared to the outer cylinders (cylinders 1 and 3), suggesting that the approaching flow is still influenced (decreased). For relative spacings S_G/D_B > 1, the wakes and zones of increased velocities aside the cylinders show comparable patterns, but the zone of small flow velocities upstream of the middle cylinder is still smaller than those upstream of the outer cylinders. For S_G/D_B = 3, the differences in K_G between the cylinders are very small. They take values close to the forces of the single isolated cylinder.

In the bore cases, the forces show a similar behaviour, but at a distance of 3 D_B they are slightly higher than those acting on a single cylinder. This is in accordance with the observations of the normalized maximum flow velocities around the cylinders in Figure 4.17.

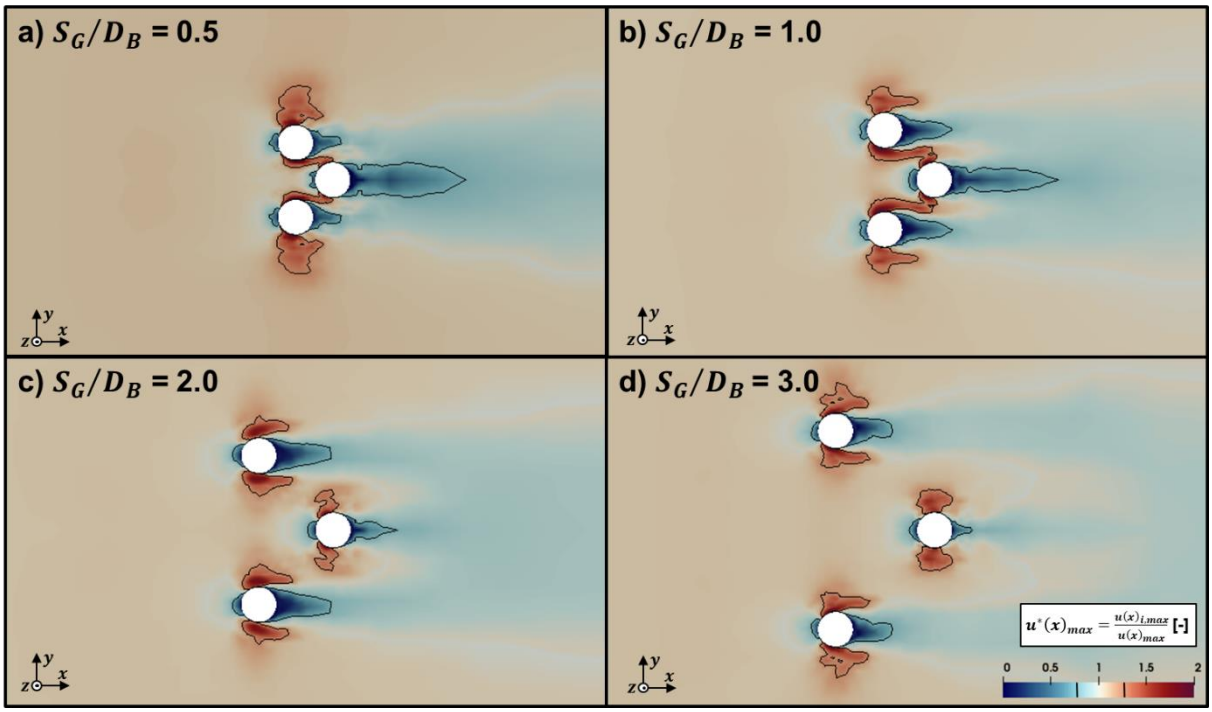

Figure 4.17. Normalized maximum horizontal flow velocities $u^*(x)_{max}$ around cylinders in staggered 2 arrangement subject to a bore. The black line indicates 25 % higher or lower maximum flow velocities compared to the case without cylinders.

Because the flow is forced to move around the outer cylinders, they receive higher loads than the middle cylinder. For relative spacings $S_G/D_B > 2$, inline forces in all cylinders exceed inline forces of the single cylinder. A possible interpretation is that presence of cylinder 2 can still lead to increased flow depth in the area spanned between the three cylinders so that increased hydrostatic pressure acting on cylinder 2 results in higher inline forces. As a further consequence, the approaching flow is forced to move around the cylinder group, resulting in higher hydrodynamic pressure in the outer cylinders 1 and 3. However, it needs to noted that no experimental data is available to support this assumption.

For the staggered 2 arrangement, the influence of the spacing seems comparable in both flow regimes (bore and solitary wave). At a spacing of $3D_B$, the cylinders act almost independently.

For the solitary wave cases, measurements of overturning moments $M(y)^*$ reported in Sparboom et al. (2006) with similar arrangements comprise a wide range of the interference coefficient K_G, which compares well with the determined interference effects.

For the bore cases, the cylinder forces still differ from those on a single cylinder at a spacing of $3D_B$. Higher forces in all cylinders compared to the single cylinder might be caused by the flow disturbing effect of cylinder 2.

The results of the numerical model might be reasonable, but due to the absence of experimental data, no evidence for reliable model performance can be found in the investigation of this arrangement.

4.3 Effect of arrangement on inline forces

The interference coefficient K_G, derived from inline forces acting on cylinders in the mean flow direction with a relative spacing of S_G/D_B = 0.5 are shown in Figure 4.18, with S_G/D_B = 1.0 in Figure 4.19, with S_G/D_B = 2.0 in Figure 4.20 and with S_G/D_B = 3.0 in Figure 4.21 as a function of the four basic arrangements in Figure 4.1.c) to f) for both flow regimes (solitary waves and bores).

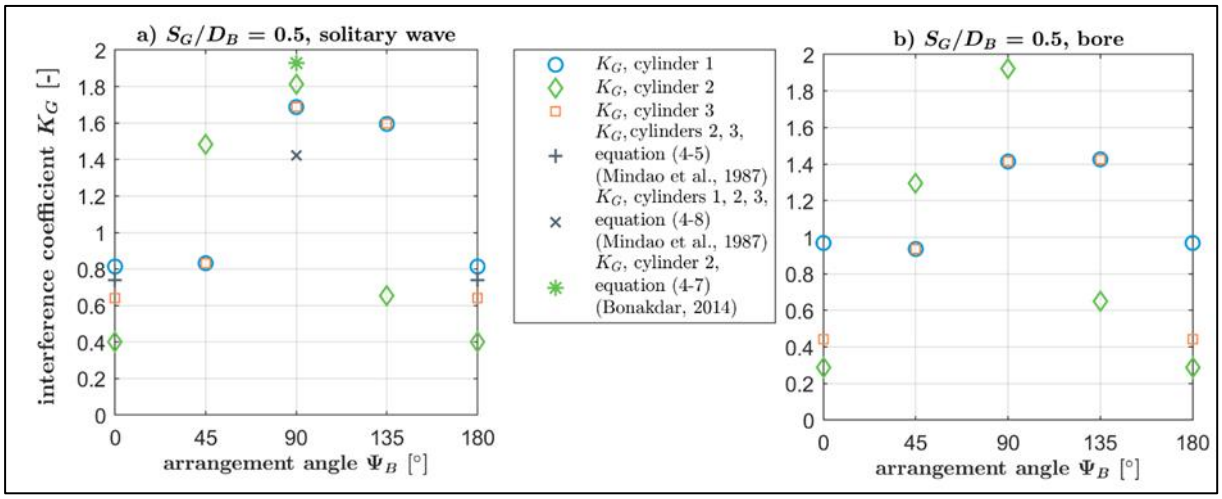

Figure 4.18. Interference coefficient K_G of three cylinders for arrangement angles Ψ_B = 0° and Ψ_B = 180° with a relative spacing of S_G/D_B = 0.5 subject to a) solitary wave (including empirical relations of Mindao et al., 1987 and Bonakdar, 2014), b) bore. For definition of arrangements, see Figure 4.1.

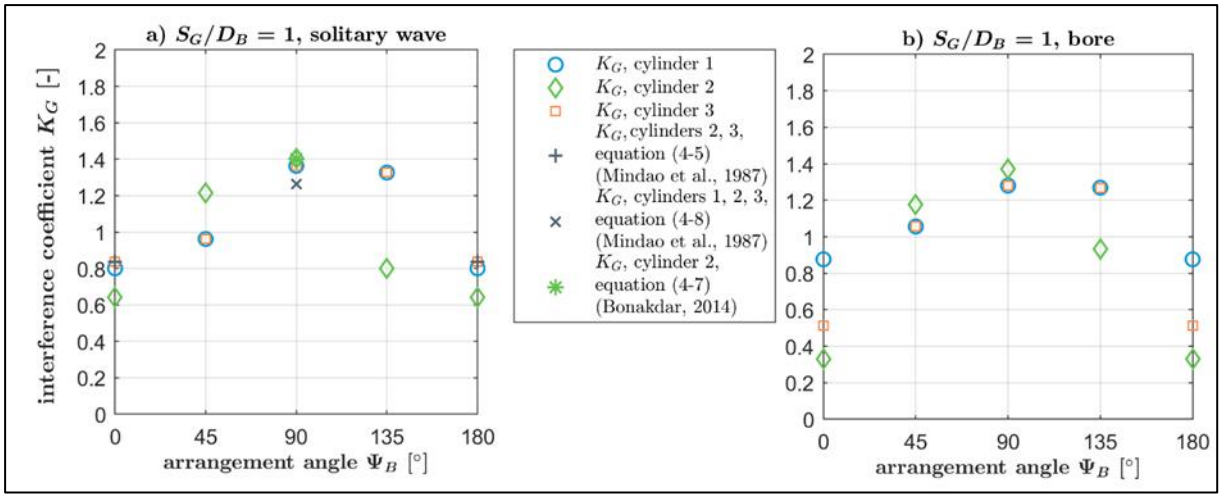

Figure 4.19. Interference coefficient K_G of three cylinders for arrangement angle Ψ_B = 0° and Ψ_B = 180° with a relative spacing of S_G/D_B = 1.0 subject to a) solitary wave (including empirical relations of Mindao et al., 1987 and Bonakdar, 2014), b) bore. For definition of arrangements, see Figure 4.1.

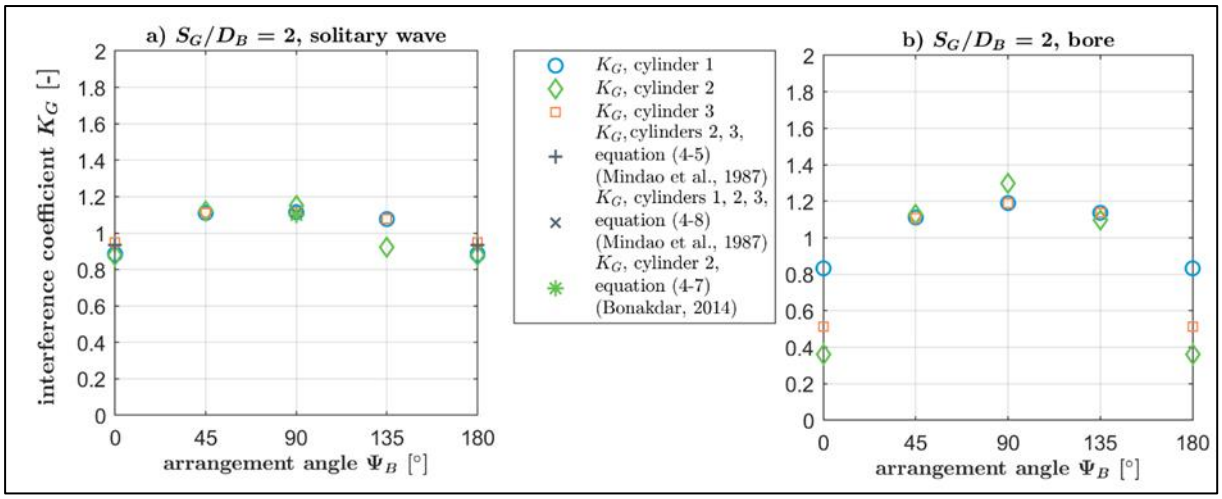

Figure 4.20. Interference coefficient K_G of three cylinders for arrangement angle Ψ_B = 0° and Ψ_B = 180° with a relative spacing of S_G/D_B = 2.0 subject to a) solitary wave (including empirical relations of Mindao et al., 1987 and Bonakdar, 2014), b) bore. For definition of arrangements, see Figure 4.1.

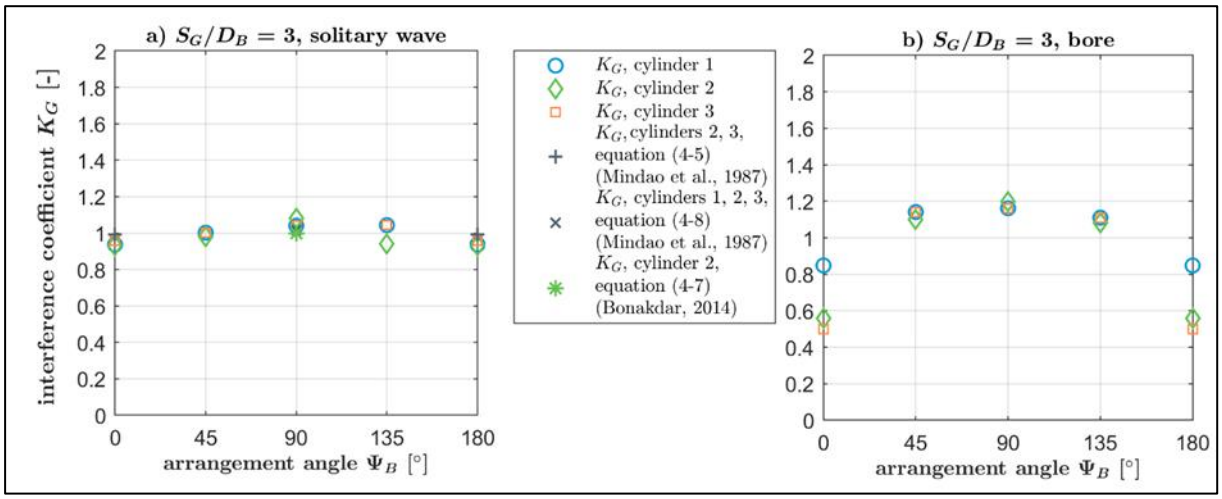

Figure 4.21. Interference coefficient K_G of three cylinders for arrangement angle Ψ_B = 0° and Ψ_B = 180° with a relative spacing of S_G/D_B = 3.0 subject to a) solitary wave (including empirical relations of Mindao et al., 1987 and Bonakdar, 2014), b) bore. For definition of arrangements, see Figure 4.1.

In Figure 4.18.a) and b), the forces on all cylinders increase as soon as the arrangement angle $\Psi_B > 0°$, which corresponds to the tandem arrangement. They are maximal when $\Psi_B \sim 90°$ (side-by-side arrangement). When $0° < \Psi_B < 90°$, the middle cylinder (cylinder 2) is the first at which the wave or the bore arrives. Compared to the load on cylinder 2, the outer cylinders 1 and 3 receive smaller loads as they are sheltered by cylinder 2. For the arrangement angle $\Psi_B \sim 90°$, the outer cylinders are located outside of the shelter zone of cylinder 2 and they receive loads higher than found on a single isolated-standing cylinder. When $\Psi_B = 180°$, the situation is equal to $\Psi_B = 0°$ and all cylinders stand in tandem arrangement. When $90° < \Psi_B < 180°$, the outer cylinders are the first at which the wave or bore arrives. With increasing Ψ_B they provide more shelter for the middle cylinder. In tandem arrangement (Ψ_B = 0°

or Ψ_B = 180°) the upstream located cylinder receives the highest load. Qualitatively, the observations are similar for both flow types (solitary wave and bore). However, the difference between the cylinders is more pronounced for bores. Particularly the upstream cylinder, at which the bore arrives, receives higher loads than in case of the solitary wave. Furthermore, it provides more shelter for the following cylinders than it is the case for a solitary wave. In case of bores, these effects can be noted at larger cylinder spacings, too, as shown in Figure 4.19, Figure 4.20 and Figure 4.21. However, they tend to vanish with increasing spacing. While in the solitary wave case for a relative spacing of S_G/D_B = 3.0 all cylinders show similar behaviour as with a single, isolated-standing cylinder (see Figure 4.21.a)). In case of the bore, the upstream cylinder in tandem arrangement provides still considerable shelter for the downstream located cylinders whereas in all other arrangements the difference between the cylinders vanishes.

For both solitary wave and tsunami-like bore cases, the effect of the arrangement on the forces on the cylinders increases with smaller relative spacing S_G/D_B:

- *For tandem arrangement (Ψ_B = 0°)*, the middle cylinder (cylinder 2) is the most sheltered, while the outer cylinders (cylinders 1 and 3) receive higher loads, which do not exceed the forces acting on a single cylinder (interference coefficient K_G < 1). For the most upstream located cylinder 1, K_G < 1 mainly due to the reduction of vortex losses and cylinders 2 and 3 due to sheltering.
- *For staggered 1 arrangement (Ψ_B = 45°)*, the middle cylinder receives the highest loads (K_G > 1), while the forces acting on the outer cylinders are smaller compared to a single cylinder (K_G < 1).
- *For side-by-side arrangement (Ψ_B = 90°)*, all cylinders experience higher loads than the single cylinder (K_G > 1). The increase of inline forces is most pronounced in the middle cylinder (cylinder 2).
- *For staggered 2 arrangement (Ψ_B = 135°)*, outer cylinders located further upstream than the middle cylinder, seem to protect the middle cylinder in case of relative spacings S_G/D_B < 3, so that for the outer cylinders K_G > 1 and for the middle cylinder K_G < 1.

The influence of the arrangement is more pronounced in the bore cases than in the solitary wave cases.

4.4 Summary and conclusions

Forces on three cylinders in different arrangements and spacings are systematically analysed and possibly compared to experimental data (Bonakdar & Oumeraci, 2014; Sparboom et al., 2006), empirical relations (Bonakdar, 2014; Mindao et al., 1987) and observations made by Hori (1959). Thereby, the numerical model is evaluated for more complicated flow fields than those in chapter 3. The numerical model is setup using the numerical parameters for element size in the free flow and bounded flow zone and for the turbulence model as derived in chapter 3.

By examining each arrangement individually and varying the spacing between the cylinders, the following key results are obtained:

- *Tandem (Ψ_B = 0°):* The middle cylinder experiences the smallest force in both flow regimes (bore and solitary wave), whereas the upstream located cylinder experiences the highest. In all cases and for all cylinders is the interference coefficient K_G < 1. In the case of a solitary wave, the differences between the forces on the cylinders vanish when the spacing increases to 3 D_B, whereas in the bore case the difference between the forces on the most upstream located and the downstream located cylinders is still apparent. The here determined interference effect of cylinders in waves can be related to observations made by Mindao et al. (1987) and Oumeraci and Koether (2008).
- *Staggered 1 (Ψ_B = 45°):* The middle cylinder experiences the highest load (K_G > 1) in both flow regimes. The forces acting on the outer cylinders 1 and 3 are smaller compared to a single cylinder (K_G < 1). The differences between the cylinders vanishes when the distance reaches 2 D_B. With smaller spacing, the differences are more pronounced in the solitary wave cases, whereas in bore cases with spacing 3 D_B, the cylinder forces still differ from those of a single cylinder. For the solitary wave cases, the range of computed K_G agrees well with the experimental data of Bonakdar (2014). For the bore cases, K_G > 1 for $S_G/D_B \geq 2$ can only partly be explained with the help of the interference diagram by Hori (1959) in Figure 2.3.
- *Side-by-side (Ψ_B = 90°):* All cylinders experience higher loads than the single cylinder (K_G > 1). The middle cylinder experiences the highest load under both flow regimes (bore and solitary wave). The differences between the cylinders are more pronounced in the bore cases. In the solitary wave cases, the interference vanishes with a spacing of ~3 D_B, while for bores the influence of neighbouring cylinders vanishes with spacing of ~5 D_B. The computed interference coefficients K_G for the solitary wave cases compare reasonably well with the empirical formulae of Mindao et al. (1987) and Bonakdar and Oumeraci (2014).
- *Staggered 2 (Ψ_B = 135°):* The influence of the spacing seems comparable for both flow regimes (bore and solitary wave). The outer cylinders located further upstream than the middle cylinder, seem to protect the middle cylinder in case of relative spacings S_G/D_B < 3, so that for the outer cylinders K_G > 1 and for the middle cylinder K_G < 1. At a spacing 3 D_B, the cylinders act almost independently. For the solitary wave cases, comparisons with the range of measurements reported in Sparboom et al. (2006) cannot provide confidence in the here obtained results. For the bore cases, the absence of experimental data lets the here provided physical interpretations unconfirmed.

The here obtained results can partly be confirmed with measurements (Bonakdar & Oumeraci, 2014) and empirical relations (Mindao et al., 1987; Bonakdar, 2014). The numerical model is able to provide plausible results in case of slightly more complex flow fields involving three

cylinders in various arrangements than in cases, which were available for validation, where the flow interacts with one or two cylinders, only[1].

However, some uncertainty remains as no comparisons with rectangular shapes in groups could be made, because to the authors knowledge, no measurements of forces acting on rectangular-shaped cylinders standing in a group. Such configurations lead to steeper velocity gradients and flow separation in the wakes, which are expected in the parameter tests reported in the following chapter. The resulting empirical formulae of this study should therefore be extensively compared to well-described experimental data and in situ measurements before applying it in tsunami studies.

In future research, physical experiments investigating forces acting on groups of elements of rectangular shapes are essential to confirm and improve the understanding of fluid-structure interaction in urban areas.

[1] The numerical model was applied to quantify the influence of spacing and arrangement on the inline forces in Leschka et al., 2014.

5 Flow through the macro-roughness elements of different configurations

The interaction of a tsunami-like bore with macro-roughness elements (MRE) of different configurations is investigated to assess the effect of the most relevant parameters on energy losses during tsunami inundation or similar floods.

First, the scale for the hydraulic conditions in the bore and the characteristic lengths associated with the MRE are considered. On this basis, a programme of numerical tests using the three-dimensional CFD model, as described and validated respectively in sections 3.1 and 3.3, is then outlined. In the testing programme, the following MRE parameters are varied individually: shape, relative width, arrangement angle, relative height and relative spacing. Finally, the effect of each parameter variation on the propagation of the bore is analysed and quantified, and conclusions of the results are drawn.

5.1 Model scale

Three-dimensional (3D) CFD simulations in full scale require extensive computational resources due to the size of the model and to the small cell sizes that are required in the bounded flow region. Therefore, the numerical simulations are performed in model scale. The similitude law of Froude is considered for scaling while the similitude of Reynolds is needed to assess possible scale effects due to the non-similarity of the viscous forces in the Froude model.

5.1.1 Froude number

For an undistorted model, the Froude similitude requires that the Froude number Fr of the model is the same as at full scale:

$$Fr_{obs} = \frac{u(x)_{obs}}{\sqrt{gh_{obs}}} = \frac{u(x)_{num}}{\sqrt{gh_{num}}} = Fr_{num} \tag{5-1}$$

in which $u(x)$ is the free stream velocity in the mean flow direction x, g is the acceleration due to gravity and h is the flow depth. The subscript obs denotes observations of real conditions at full scale whereas the subscript num denotes the corresponding numerical model parameters.

After the 2004 Indian Ocean tsunami, Borrero (2005) reported that maximum flow depths h_{obs} between 4.2 to 9 m were witnessed in Banda Aceh (Indonesia). Lavigne et al. (2006) estimated the maximum propagation speed $u(x)_{obs}$ of the tsunami to be higher than 13.5 m/s near the shoreline. Based on video analysis, Chanson (2006) concluded that during the inland tsunami propagation, the surge advanced with a speed of 1.5 to 1.6 m/s in a street of Banda Aceh, which is believed to be 1.5 to 3 km inland and close to the maximum inundation line. It was further reported that the surge appeared to progress through the streets section by section in a disorganized manner. This behaviour might have been induced by turbulence and the presence of debris in the fluid.

For the following analyses, a flow depth of 9 m (Borrero et al., 2005) and a free stream flow velocity of 13.5 m/s (Lavigne et al., 2006) are considered near the shoreline and 0.2 m flow depth and 1.5 m/s (Chanson, 2006) flow velocity near the maximum inundation line are assumed to span the range of flow parameters during tsunami inundation.

It is further noted that natural or man-made structures can most effectively induce energy losses during tsunami inundation, when they resist the tsunami impact. According to FEMA (1979), buildings can be grouped into three categories, depending on the construction material. The damage classes of these building categories for different volume fluxes (q in m³/s/m) are given in Table 5.1.

Table 5.1. Building stability/damage under different flow conditions (FEMA, 1997).

Volume Flux $q(x)$		**Building category**		
		Masonry, concrete and brick structures	**Wood-framed structures, anchored**	**Wood-framed structures, unanchored**
Damage class	**no damage**	< 3 m³/s/m	< 3.1 m³/s/m	< 2.1 m³/s/m
	partial damage	3 - 7 m³/s/m	3.1 - 7 m³/s/m	2.1 - 3.1 m³/s/m
	total damage	> 7 m³/s/m	> 7 m³/s/m	> 3.1 m³/s/m

Combining both considerations, (i) the encountered flow conditions and (ii) the stability criteria, the framework for the numerical experiments can be set as shown in Figure 5.1.

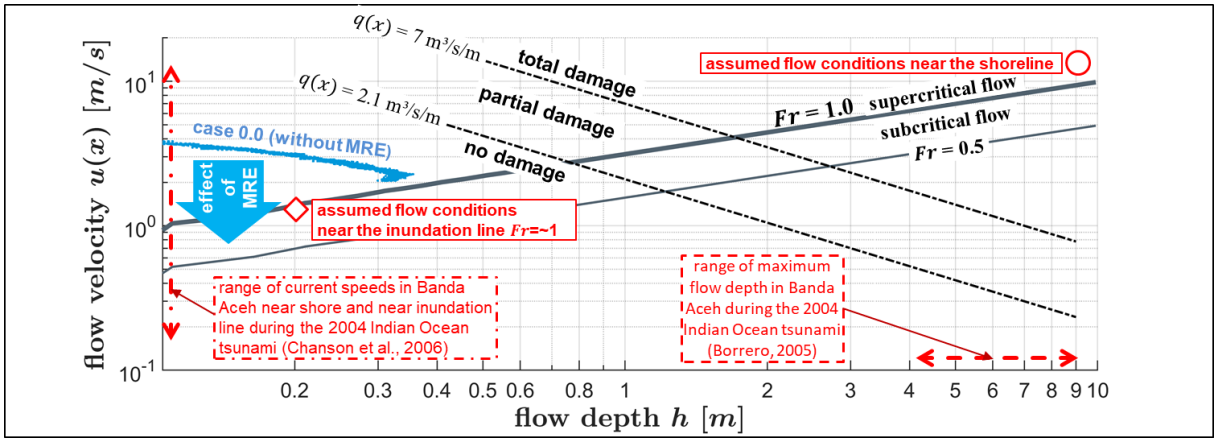

Figure 5.1. Damage criteria and Froude numbers for a range of hydraulic conditions (observations after the 2004 Indian Ocean Tsunami are indicated with the red arrows). The blue line indicates the flow conditions of case 0.0 (without any MRE). Volume flux thresholds for damage criteria (FEMA, 1997) are indicated by the dash-dot lines. The thick black line separates subcritical and supercritical flow conditions.

In Figure 5.1, flow conditions under which no damage occurs ($q(x)$ < 2.1 m³/s/m) and conditions under which each type of structure will be totally damaged ($q(x)$ > 7 m³/s/m) are separated using black dash-dotted isolines. The red arrows indicate reported observations after the 2004 Indian Ocean tsunami (Borrero, 2005; Chanson, et al., 2006). The thick black line (Fr = 1) separates subcritical from supercritical flow regimes. Based on the described observations of the 2004 Indian Ocean Tsunami, the Froude numbers Fr_{obs} range from ca. 1 (~0.2 m flow

depth, 1.5 m/s flow velocity, near the maximum inundation line) to ca. 1.4 (h_{obs}~9 m flow depth, 13.5 m/s flow velocity), as indicated in Figure 5.1 with a red ◇ and a red ○, respectively.

The selected hydraulic conditions for case 0.0 (without any MRE) are indicated by the thick blue line in Figure 5.1 and are similar to the conditions described in section 3.3.2. The maximum flow depths h_{num} at a distance of x = 8 m from the 0.9 m deep impoundment is 0.357 m. Taking into account the observed flow depth h_{obs}, the ratio of h_{num}/h_{obs} = 0.357 m/9 m results in a model scale of 1:25.

The evolution in time of the Froude number is calculated using the flow depth and the depth-averaged flow velocity in a distance of x = 8 m from the impoundment, using equation (5-1). The result is shown in Figure 5.2.

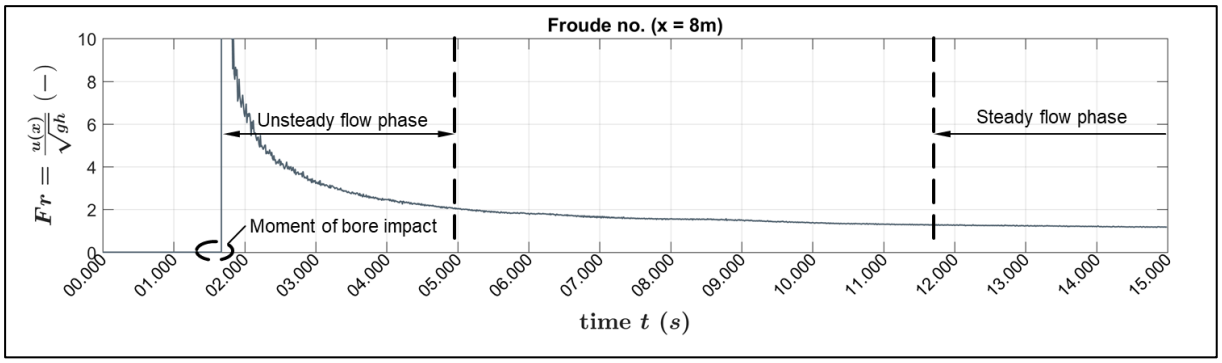

Figure 5.2. Evolution in time of Froude number Fr at a distance of x = 8 m downstream of the impoundment.

The moment of impact at t = ~2 s is characterized by an abrupt increase of Fr up to a very high value of Fr > 10, while (i) the flow depth at the bore tip is still small and (ii) the speed is very high. In the course of bore propagation, the conditions stabilize. Relatively stable conditions can be found at the end of the time series, where Fr < 2.

The selected flow conditions in case of no MRE are classified as supercritical. It is expected that including MRE will lead to a slowdown of the flow velocity and an increase of the flow depth, particularly upstream of the front row of MRE. Both will result in a decreasing Fr so that subcritical flow conditions (Fr < 1) will prevail.

Considering the Froude similitude, the selected hydraulic conditions are appropriate to represent a tsunami-like bore propagating over an initially dry bottom in model scale. Compared to the 2004 Indian Ocean Tsunami in Banda Aceh and the 2011 Tohoku Tsunami, the selected model scale is ~1:25.

5.1.2 Reynolds number

The ratio between inertial and viscous forces acting on the MRE's is described by the Reynolds number Re. The Reynolds similitude requires that Re' is the same in the model and at full scale:

$$Re'_{obs} = \frac{u_{f,obs} D_{B,obs}}{\nu_{obs}} = \frac{u_{f,num} D_{B,num}}{\nu_{num}} = Re'_{num} \tag{5-2}$$

where Re' is associated with the friction velocity at the MRE u_f and with the MRE width D_B as the characteristic length, and ν is the kinematic viscosity. The subscript obs denotes observations of real conditions whereas the subscript num denotes the corresponding numerical model parameters. As the Froude similitude must be applied (free surface flow) and as it is hardly possible to apply Reynolds similitude simultaneously, scale effects due to the non-scaled viscous forces in the Froude model occur. These scale effects in the Froude model decrease with increasing Re values, which can be achieved for example when u_f and/or D_B are increased to approach the rough turbulent flow regime.

This context was extensively investigated in the field of sediment transport, where friction influences the suspension of sediment grains. The drag force acting on the grain is determined by means of the friction velocity acting directly on the grain surface (skin friction). The exposed grain will not move as long as the friction velocity is smaller than a critical friction velocity u'_{fc}. This dependency is expressed by the critical Shields parameter

$$\theta_c = \frac{u'^2_{fc}}{(s-1) g D_{grain}} \tag{5-3}$$

which determines the behaviour of the grain. In this equation, s is a gravity constant, usually close to 2.65, g is the acceleration due to gravity and D_{grain} is the grain diameter. The behaviour of the Shields parameter as a function of the Reynolds number based on the friction velocity Re' is depicted in Figure 5.3.

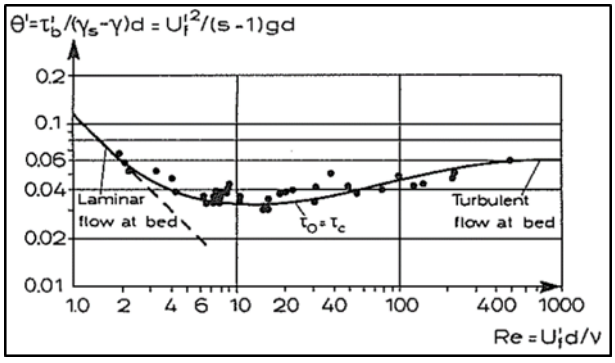

Figure 5.3. Shields diagram giving the threshold value θ_c (denoted as θ') as a function of the friction-based Reynolds number Re', here denoted as Re. The grain diameter D_{grain} is denoted as d (Fredsøe and Deigaard, 1992)

No scale effects are expected if θ_c (in Figure 5.3 denoted as θ') remains constant over Re' (in Figure 5.3 denoted as Re). In Figure 5.3 it is noted that for $Re' > 1000$, the critical Shields parameter θ_c remains constant with further increase of Re' . For the selected hydraulic conditions, the free stream velocity $u(x)$ does not fall below 2 m/s. The friction velocity u_f on a MRE can be determined based on the set of equations given in section 3.2 (equations (3-23) to (3-26)).

Taking note of the analogy of the friction acting on the grain to the friction acting on the MRE, the minimum MRE width D_B is selected. Hence, as long as the MRE width D_B > 3 mm and the flow velocities $u(x)$ > 2 m/s, Re' > 1000. By selecting D_B = 0.04 m, Re' is calculated in a distance of x = 8 m from the initial impoundment, using equation (5-2). The evolution in time of the Reynolds number is shown in Figure 5.4.

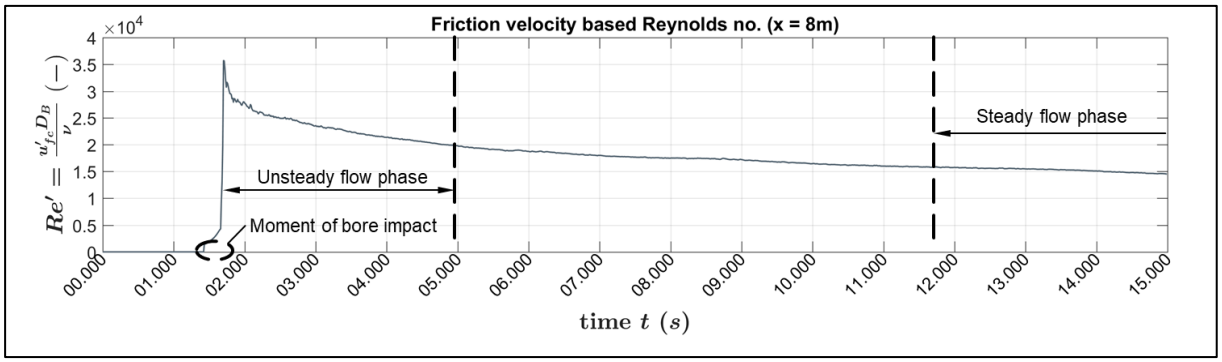

Figure 5.4. Evolution in time of Reynolds number Re' at a distance of x = 8 m downstream of the impoundment.

Figure 5.4 reveals that during the bore propagation, Re' takes values between 36,000 (at the bore front, denoted as unsteady conditions) and 15,000 (in a later phase with steady conditions), so that no scale effects from viscosity are expected.

The selected flow conditions and MRE dimensions result in a Froude model scale of 1:25. Viscous forces are negligibly small, and form (or pressure) drag dominate over viscous drag. The flow conditions in the model 1:25 are appropriate to represent a tsunami-like bore propagating over an initially dry bottom without noticeable scale effects due to viscous forces.

5.2 Numerical testing Programme

Various configurations of macro-roughness elements (MRE) subject to a tsunami-like bore are investigated. The experimental programme comprises variations of a basic configuration, for which the parameters of the MRE are defined as follows:

Shape: As inundation modelling is mainly applied in populated areas, the largest MRE's are buildings, which face the coastline with one side. That is why squared (cubic) shapes are selected to form the basic shape.

Relative width D_B/h_{max}*:* For the basic configuration, a characteristic width D_B = 0.04 m is selected, which is suitable to assess losses due to combined drag and inertia (during unsteady conditions) and drag (during nearshore steady conditions) (see section 5.1.2).

Arrangement angle Ψ*:* Coastal urban areas exhibit streets which are often orientated parallel and perpendicular to the coastline. Hence, the in-line arrangement (Ψ = 0°) is chosen as a basic arrangement.

Relative spacing S_G/D_B: The density of MRE (e.g. buildings) in coastal urban areas can be described by their relative spacing S_G/D_B which may vary from very small values of less than 1 in case of narrow streets to values greater than 5 in case of wide alleys or parks. Therefore, an average relative spacing of S_G/D_B = 2.0 is chosen for the basic configuration.

Relative height h_B/h_{max}: Only during the most devastating tsunamis the maximum bore height h_{max} may exceed the height of the buildings h_B. Thus, $h_B/h_{max} > 1$ (emergent MREs) is chosen for the basic configuration.

In the numerical tests, besides the selected basic configuration each parameter is varied individually, while all the other parameters are kept constant. The testing programme is summarized in Table 5.2.

Table 5.2. Numerical testing programme. The black highlighted cells indicate the parameter variations. The grey row highlights the basic configuration.

<table>
<tr><th></th><th>shape
[-]</th><th>relative width
D_B/h_{max}
[-]</th><th>arrangement
Ψ
[°]</th><th>relative spacing
S_G/D_B
[-]</th><th>relative height
h_B/h_{max}
[m]</th></tr>
<tr><td>0.0</td><td colspan="5">Flow without any MRE</td></tr>
<tr><td>0.1</td><td>cubic</td><td rowspan="3">0.112</td><td colspan="2" rowspan="3">Single MRE at x = 8 m</td><td rowspan="3">≫ 1</td></tr>
<tr><td>0.2</td><td>circular</td></tr>
<tr><td>0.3</td><td>diamond</td></tr>
<tr><td>1.0</td><td>cubic</td><td>0.112</td><td>in-line (0°)</td><td>2.0</td><td>≫ 1</td></tr>
<tr><td>1.1</td><td>circular</td><td rowspan="2">0.112</td><td rowspan="3">in-line (0°)</td><td rowspan="4">2.0</td><td rowspan="8">≫ 1</td></tr>
<tr><td>1.2</td><td>diamond</td></tr>
<tr><td>2.1</td><td rowspan="10">cubic</td><td>0.232</td></tr>
<tr><td>2.2</td><td>0.464</td></tr>
<tr><td>3.1</td><td rowspan="8">0.112</td><td>st (26.565°)</td></tr>
<tr><td>3.2</td><td>staggered (45°)</td></tr>
<tr><td>4.1</td><td rowspan="6">in-line (0°)</td><td>0.5</td></tr>
<tr><td>4.2</td><td>1.0</td></tr>
<tr><td>4.3</td><td>3.0</td></tr>
<tr><td>4.4</td><td>4.0</td></tr>
<tr><td>5.1</td><td rowspan="4">2.0</td><td>1</td></tr>
<tr><td>5.2</td><td>0.75</td></tr>
<tr><td>5.3</td><td>0.5</td></tr>
<tr><td>5.4</td><td>0.25</td></tr>
</table>

Case 1.0 represents the basic configuration defined above. The case 0.0 represents the reference case without any MRE, which also provides the maximum flow depth h_{max} = 0.357 m for all cases. The testing programme comprises variations of the MRE parameters shape (cases 1.0 to 1.2). Three shapes are considered: (i) cubic cylinder with cylinder sides facing the flow (referred to as cubic), (ii) circular cylinder (referred to as cylindrical) and (iii) cubic cylinder with cylinder edges facing the flow (referred to as diamond). Furthermore, relative width (cases 2.1 to 2.2), arrangement (cases 3.1 to 3.2), relative spacing (cases 4.1 to 4.4) and relative height (cases 5.1 to 5.4) are investigated. The testing programme allows to generate the database of impacts of various MRE configurations on energy losses.

To understand the group effect of MRE, the cases 0.1 to 0.3 contain only one single, isolated standing MRE each, which is located in a downstream distance of x = 8 m from the impoundment for comparison. The flow fields around the MRE generated in the different cases 0.1 to 5.4 are compared to the flow field of the case without MRE (case 0.0), so that the influence of each MRE parameter on the bore propagation can be quantified. This will finally lead to a formulation of a new source term for the non-linear shallow water (NLSW) equations used in large-scale 2D models.

The numerical testing programme comprises 19 simulations, in which the influence of MRE parameters shape, relative width, arrangement, relative spacing and relative height on the bore propagation are investigated. Each parameter is varied individually, while keeping all other parameters constant as selected for the basic configuration. By comparing the results with the reference case without any MRE, the impact of each MRE parameter on the bore propagation can be quantified, so that a new source term for the NLSW equations can finally be developed.

5.3 Numerical setup and simulations

The general numerical setup including the computational domain, mesh characteristics in the free flow region and in the close vicinity of the macro-roughness elements (MRE), the initial and the boundary conditions are similar for all cases of the numerical testing programme (see section 5.2). Only the MRE parameters must change to ensure that numerical effects such as dissipation are comparable in all cases and cannot pollute the comparisons of the cases which will form the basis for the development of the MRE formula.

On the example of the basic configuration (case 1.0) as a role model for all other cases, this section outlines the computational domain and mesh characteristics. Furthermore, the initial and boundary conditions are described.

5.3.1 Computational domain and mesh of the basic configuration

The computational domain of the basic configuration is exemplarily outlined in Figure 5.5 (refer to case 1.0 in Table 5.2) as it forms the role model for the setups of all MRE configurations.

Figure 5.5.a) depicts the top view of the situation described in the basic configuration case. The tsunami-like bore propagates towards the zone of MRE at x_0 = 6.4 m from left to right.

It becomes apparent, that the arrangement pattern is the same in lateral (y) direction. Along each central line between two neighbouring MRE in x direction, full symmetry exists. Therefore, the numerical domain is reduced to comprise only one row of MRE, which is orientated in x direction. The side view of the domain is shown in Figure 5.5.b). At the lateral boundaries, symmetry boundary conditions are imposed.

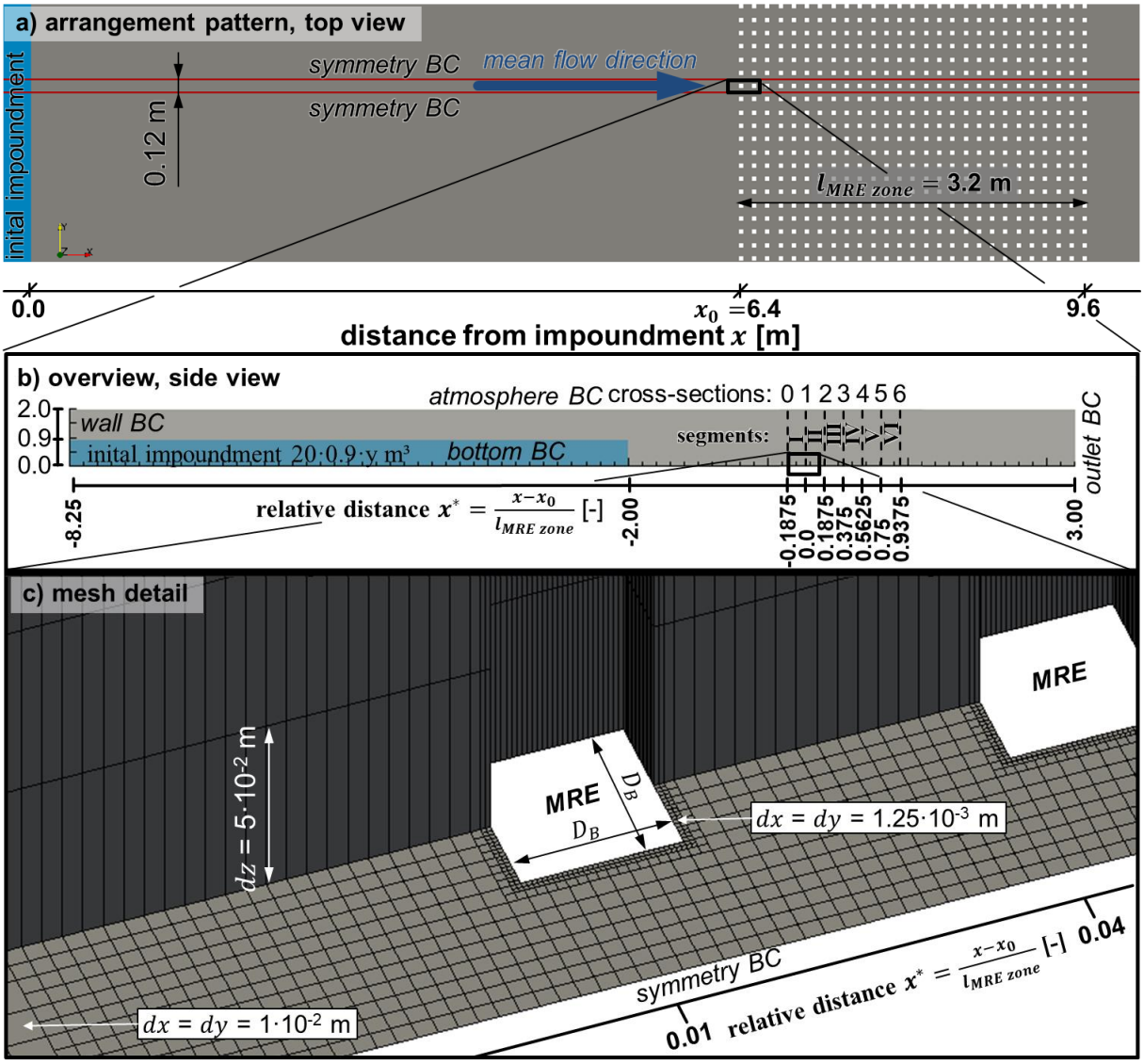

Figure 5.5. Computational domain of the basic configuration (case 1.0): a) arrangement pattern (top view), b) overview of the numerical domain (side view; the vertical orange lines mark the location of analysed cross-sections), c) mesh detail.

The distance from the impoundment is normalized with the length of the MRE zone using the relation

$$x^* = \frac{x - x_0}{l_{MRE\ zone}} \tag{5-4}$$

with the length of the MRE zone $l_{MRE\ zone}$ = 9.6 m – 6.4 m (see also Figure 5.5.a). $x^* < 0$ indicates regions upstream of the MRE zone, $0 < x^* < 1$ regions inside the MRE zone and $x^* > 1$ outside the MRE zone.

The details of the mesh are presented in Figure 5.5.c). The numerical domain of the basic configuration (case 1.0) is discretized using approximately 300,000 elements. The number of cells vary between 296,440 elements (case 1.0, basic configuration, see Table 5.2) and 2,650,000 (case 3.1, arrangement angle Ψ = 26.565°). On average, 725,000 elements are used (for

runtimes see section 5.3.5). The element sizes in the free flow zone are similar to the sizes used in section 3.3.3. In the bounded flow region, larger cell sizes need to be used then initially derived from the validation in section 3.3.4. Otherwise, it would not be possible to stay in a feasible range of simulation time of 10 days on average for each case.

The following sections discuss the implications of using the symmetry boundary condition and the increased cell sizes in the bounded flow region.

5.3.2 Implications of the approach of making use of the symmetry in lateral direction

To evaluate the performance of the approach which makes use of the symmetry in lateral direction, a comparison of the numerical results of two setups is conducted. One simulation comprises a 0.12 m wide numerical domain (see Figure 5.5.a)) with one row of MRE, whereas the other simulation uses a 0.36 m wide domain with three rows of MRE. The time series of the volume flux in the cross-sections between $x^* = 0$ and 1 (Figure 5.5.b) and the maximum normalized forces (as the sum of viscous and drag forces) of both simulations are compared. The results are presented in the Appendix, section A.7. An exemplary time series of volume flux in the middle of the MRE zone ($x^* = 0.5$) is shown in Figure 5.6.

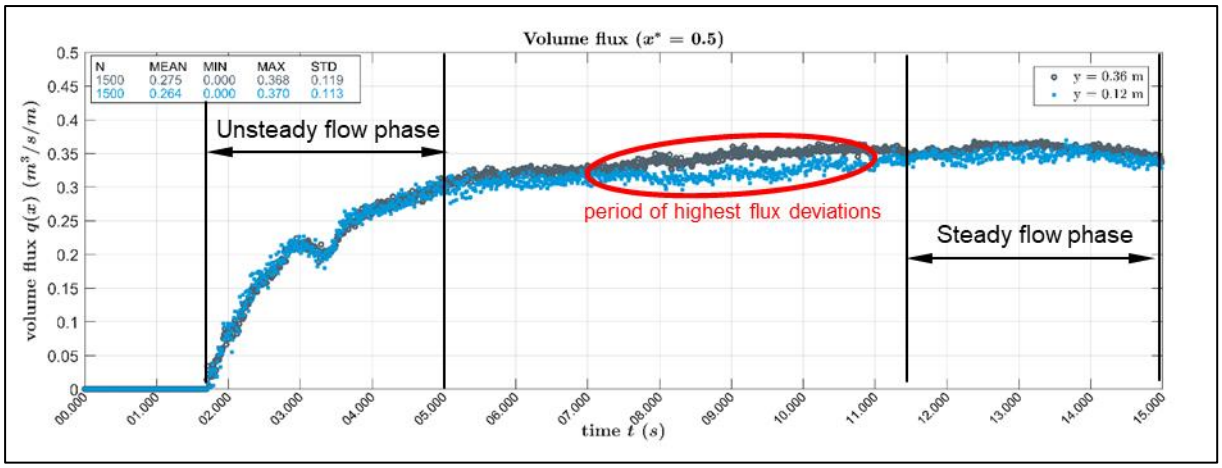

Figure 5.6. Time series of volume flux at $x^* = 0.5$ using a 0.36 m wide domain (three MRE rows) and a 0.12 m wide domain (one MRE row). The period of the highest flux deviations is indicated red.

It is noted that there is a shift of approximately 0.025 m³/s/m between 7 and 11 s of the time series, revealing that in this period, the volume flux is underestimated by ~5 % when using only one row instead of three rows of MRE. This deviation occurs in all cross-sections and is acceptable given (i) that a significantly lower computational time is required and (ii) that the analysed flow phases can be selected to be outside the period of the greatest deviations between $t = 5$ s and $t = 11$ s. The maximum values are still reproduced well. Scatter indices of 0.05, correlation coefficients between 0.99 and 1.00 and peak ratios between 0.98 and 1.04 indicate a very good agreement between both simulation results (see Appendix, section A.7).

Referring to section 3.4, Table 3.3, the numerical model provides reliable results for maximum and averaged values and acceptable results for instantaneous values. Making use of the symmetry in lateral direction, the performance of the numerical model to reproduce instantaneous values decreases by less than 5 %. For reproducing averaged values, the performance of the model decreases by ca. 1 %, which is acceptable.

5.3.3 Implications due to the use of increased cell sizes in the bounded flow region

In the bounded flow region, element sizes take values of $dx = 1.25 \cdot 10^{-3}$ m, which is considerably smaller than in the free flow region (see Figure 5.5.c). For the calculation of forces, the normalized element size is usually recommended to take values of $y^+ = 50$ (see also section 3.2.3 for the requirements on cell sizes at walls). Considering a maximum free flow velocity of $u(x)_{max} \approx 3$ m/s at time $t = 5$ s, when the maximum force is calculated (see section 3.2.3), an element size in the boundary layer of $\Delta x \approx 0.64 \cdot 10^{-3}$ m would be required. For the presence of partially more than 50 MRE (case 5.1), using such small element sizes would result in unfeasibly long simulation times. As the volume flux is investigated to assess the influence of the MRE on the bore propagation, coarser meshes may be applied to increase the efficiency of the simulations. The solutions of different mesh sizes ($dx = 1.25 \cdot 10^{-3}$ and $dx = 0.625 \cdot 10^{-3}$ m) are compared in various cross-sections and are reported in the annex, section A.8.2. An exemplary time series in the middle of the MRE zone ($x^* = 0.5$) is shown in Figure 5.7.

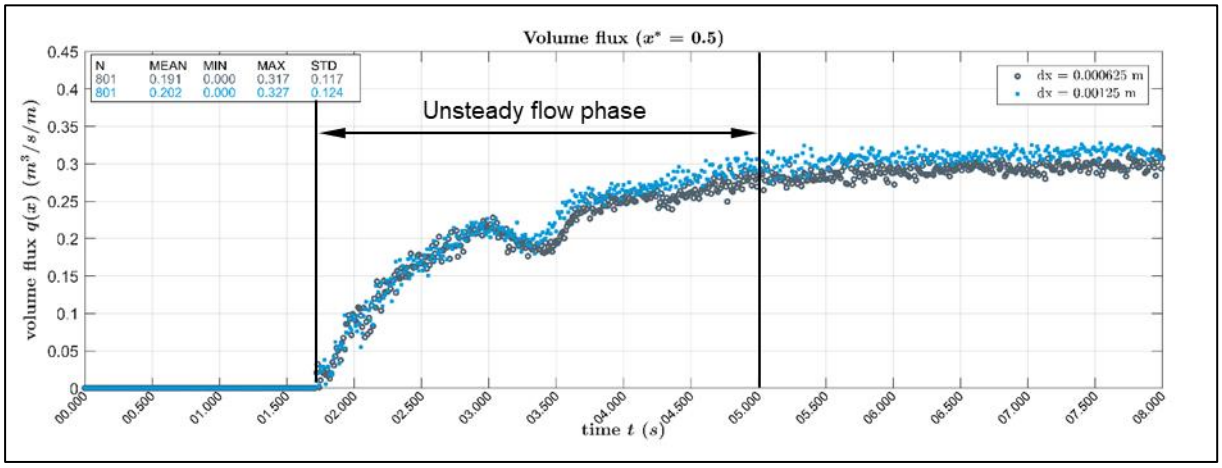

Figure 5.7. Time series of volume flux at $x^* = 0.5$ using cell sizes of $dx = 0.625 \cdot 10^{-3}$ m and $dx = 1.25 \cdot 10^{-3}$ m in the bounded flow region.

Until $t = 3$ s, no deviation between the volume fluxes are obtained for the two mesh sizes. For $t > 3$ s, deviations are apparent. The volume fluxes tend to be overestimated by $q(x) \approx 0.01$ m/s³/m when using the coarser mesh. These deviations are noted in each of the analysed cross-sections. Scatter indices between $SI = 0.07$ and $SI = 0.08$ (in one case 0.15) and correlation coefficients between $CC = 0.99$ and $CC = 1.00$ show generally very good agreement between the instantaneous values of both simulations. Peak ratios between $PR = 1.03$ and $PR = 1.07$ show that maximum volume fluxes are slightly overestimated by the simulation using the coarser mesh.

Referring to Section 3.4, Table 3.6, the numerical model provides reliable results for maximum and averaged values and acceptable results for instantaneous values. When using increased cell sizes in the bounded flow region, the performance of the model to reproduce instantaneous values decreases by ca. 8 %. For reproducing averaged values, the performance decreases by ca. 1 %, which is acceptable.

5.3.4 Boundary and initial conditions

The numerical parameters are selected according to the validations as shown in sections 3.3.2 and 3.3.4 and are summarized in Table 5.3.

Table 5.3. Numerical parameters selected for the boundary conditions. For a detailed description of the specific boundary conditions, refer to the OpenFOAM documentation (OpenFOAM Foundation, 2011).

Boundary	**Dynamic pressure p_{dyn} [kg m^{-1} s^{-2}]**	**velocity u [m s^{-1}]**	**Turbulent kinetic energy k [m^2 s^{-2}]**	**Specific dissipation ω [s^{-1}]**	**Turbulent kinematic viscosity ν_T [m^2 s^{-1}]**	**Phrase fraction α_1 [-]**
wall	$\frac{\partial p_{dyn}}{\partial n} = 0$	$u = 0$	$\frac{\partial k}{\partial n} = 0$	$\omega = \frac{u_f}{\sqrt{\beta^*}\kappa y_p}$	$\nu_T = \frac{\sqrt{\beta^*}\sqrt{k} y_p}{log(E y^+)}$	$\frac{\partial \alpha_1}{\partial n} = 0$
bottom						
cube						
outlet	$p + \frac{1}{2}\rho\lvert\bar{u}\rvert^2 = 0$	$\frac{\partial u}{\partial n} = 0$		$\frac{\partial \omega}{\partial n} = 0$	$\frac{\partial \nu_T}{\partial n} = 0$	
atmosphere						
symmetry	symmetryPlane					

E: see section 3.1.2, equation (3-31.a-c), n: distance normal to the direction of the boundary, u_f: friction velocity, y_p: distance to first calculation point at wall, y^+: dimensionless distance from a wall in the boundary layer, β^*: dissipation term coefficient, κ: Kármán constant.

For further details on deriving the numerical parameters of the boundary conditions it is referred to section 3.2.3.

In the initial stage of the simulation, all velocities are set equal to zero. Phase fraction α_1 (water) is zero in the entire domain except at the 0.9 m deep impoundment between x = -20 m and 0 m, where α_1 = 1.

5.3.5 Numerical simulations

The simulations were performed on two computers one with 8 and one with 16 cores. Runtimes on 16 cores varied between 29 hours for case 5.4 (smallest MRE height) and 61.3 days for case 3.1. The average runtime for the cases was 10.5 days (see also see section 5.3.1).

Reynolds numbers $Re(D_H)$, based on the hydraulic diameter D_H as sketched in Figure 5.8, took values between 9,000 (case 4.1, smallest spacing during the steady flow phase, see Table 5.2) and 110,000 (case 4.4, greatest spacing during unsteady flow phase, see Table 5.2) so that in all cases, turbulent conditions are noted.

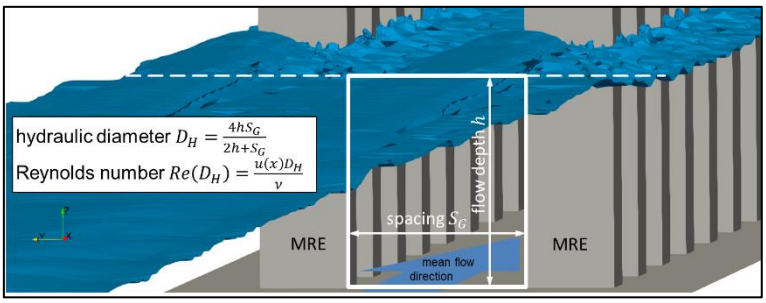

Figure 5.8 Definition of the hydraulic diameter for the calculation of the Reynolds number Re.

Compared to the validated numerical model, the setups comprise larger cells in the bounded flow region and make use of the symmetry boundary condition. The model's accuracy to reproduce averaged values is affected by less than 2 %.

5.4 Analysis procedure

To assess the hydraulic conditions near the macro-roughness elements (MRE), flow velocities $u(x)$ and water levels h are extracted from the 3D numerical model results at various cross-sections. The result analysis is done in two steps: (i) analysis of the maximum flow velocities and (ii) analysis of changes in the flow field between cross-sections in the MRE zone.

In the first step, statistical analysis of flow velocities are extracted at z = 0.05 m above the bottom in order to better understand the impact of the MRE on the flow field. The maximum flow velocities are then analysed and compared to the flow fields of reference case 0.0 without any MRE.

In the second step, use is made of the fact that $u(x)$ and h are parts of the non-linear shallow-water (NLSW) equations (see section 2.2.1). These quantities are extracted at various cross-sections which separate the segments I to VI (see Figure 5.5.b)). Segment I is located upstream of the MRE zone (between the cross-sections located at x^* = {-0.1875; 0}, segment II is the most upstream segment of the MRE zone (between the cross-sections located at x^* = {0; 0.1875}) and the segments III to VI are located inside the MRE zone (between the cross-sections at x^* ={0.1875; 0.375; 0.5625; 0.75; 0.9375}, see Figure 5.5.b)). Each cross-section between two neighbouring segments can be interpreted as a cell face of a grid cell of a large-scale 2D model.

The analysis procedure comprises spatial integration of the 3D model results within each cross-section in section 5.4.1 and temporal integration based on the distance of each cross-section in section 5.4.2 and thereby bridges the gap between the scales of the (small-scale) detailed 3D model and the large-scale 2D model. The propagation of the bore through the MRE zone is described by deriving the rate of flow parameter change between the cross-sections as described in section 5.4.3. The impact of each parameter is then estimated by analysing the change rates by means of statistical descriptors as explained in section 5.4.4. In section 5.4.5, the impact of

local flow effects and the position of the MRE relative to the cross-sections on the analysis results is discussed.

5.4.1 Spatial averaging

Each cross-section i is defined here as a narrow volume of known size

$$V_i = X_i Y_i Z_i \tag{5-5}$$

with $X = \Delta x_{i,max}$ = 0.01 m is the maximum length of a cell in x direction within the cross-sectional volume. Y is the width and Z is the height of the cross-section. Y and Z are equal to the height and the width of the numerical 3D domain (see Figure 5.5). Accordingly, V_i is defined to be independent from the presence of the MRE inside of the cross-sections.

The numerical solver is extended in this way that it writes the volume $V_{i,k}$ of each numerical element k beside the calculated quantities such as the water phase fraction of each cross-section element $\alpha_{1,i,j,k}$ and the flow velocity $u_{i,j,k}$ at time step j. In this way, the averaged water fraction of each cross-section can be determined using

$$\alpha_{1,i,j} = \frac{\sum_{k=1}^{n} \alpha_{1,i,j,k} V_{i,k}}{V_i} \tag{5-6}$$

and the horizontal volume flux through the cross-section is

$$q(x)_{i,j} = \frac{\sum_{k=1}^{n} \alpha_{1,i,j,k} u(x)_{i,j,k} V_{i,k}}{X_i Y_i} \; [m^3/s/m] \tag{5-7}$$

The water depth averaged over each cross-section is calculated using

$$\bar{h}_{i,j} = \alpha_{1,i,j} Z_i \tag{5-8}$$

The averaged flow velocity of the water perpendicular to the cross-section reads

$$\overline{u(x)}_{i,j} = \frac{q(x)_{i,j}}{\bar{h}_{i,j}} \tag{5-9}$$

5.4.2 Temporal averaging

It is obvious that the spatial integration and averaging in space in equations (5-7) to (5-9) should be combined with temporal averaging of the numerical results so that the degree of detail in the results is well-balanced between space and time. The ratio between spatial and temporal frames should be close to the flow velocity

$$\frac{dx}{dt} \approx \overline{u(x)}_{i,j} \tag{5-10}$$

In other words, it means that the time frame dt cannot be longer than the time which a real fluid particle needs to travel the distance dx (Courant-Friedrichs-Lewy criterion). The latter is adopted here to ensure that all flow phenomena in the 3D model are properly transferred into a large-scale 2D model. The maximum averaging period dt_{max} can then be selected based on the distance between the cross-sections dx and the maximum (space-) averaged flow velocity $\overline{u(x)}_{i,j,max}$.

The volume fluxes at each cross-section are calculated with the equation

$$\overline{q(x,dt)}_{i,j} = \frac{\sum_{j=t_1}^{t_2} \overline{q(x)}_{i,j}}{dt} \tag{5-11}$$

with $t_2 = t_1 + dt$. The time interval dt is selected based on the maximum depth-averaged flow velocity $\overline{u(x)}_{i,j,max}$ and the distance between the cross-sections dx = 0.6 m (see Figure 5.5.b) in each case. Time step dt is then applied to all time series of flow depth, flow velocity and volume flux.

5.4.3 Propagation of the bore through the MRE zone

The propagation through the MRE zone is qualitatively analysed by means of the maximum flow velocities in a distance from the bottom of z = 0.05 m.

Furthermore, quantitative analyses of the changes of the flow depth, depth-averaged flow velocity and volume flux between the cross-sections i just upstream and inside the MRE zone (see Figure 5.5.b)) are performed and described, using their mean values. The changes between neighbouring cross-sections are derived by using the relations

$$\begin{aligned} \Delta\bar{h} &= \bar{h}_{i+1} - \bar{h}_i \\ \Delta\overline{u(x)} &= \overline{u(x)}_{i+1} - \overline{u(x)}_i \\ \Delta\overline{q(x)} &= \overline{q(x)}_{i+1} - \overline{q(x)}_i \end{aligned} \tag{5-12}$$

This is done for both unsteady and steady flow phases (see Figure 5.2 and Figure 5.4):

- *The unsteady phase* starts with the arrival of the bore front t_1, defined here as the moment when the flow depth exceeds h = 0.05 m. The periods for determining the mean values span from t_1 to $(t_1 + 3s)$.
- *The steady phase* is characterized by constant flow conditions, which is defined here as the moment of maximum flow depth t_2. The periods for determining the mean values span from $(t_2 - 1.5s)$ to $(t_2 + 1.5s)$.

As for the volume flux and the flow depth, only integrated values are used in these analyses, the bar in the notation of these parameters will be omitted hereafter for convenience and easier readability.

5.4.4 Assessment of the impact of each MRE parameter on the bore propagation

For each parameter variation (see section 5.2, Table 5.2), the mean values of the volume flux during a period of 3 s within (i) the unsteady and (ii) the steady phase of bore propagation are derived for segments located upstream of the MRE zone ($x^* < 0$, see Figure 5.5) and inside the MRE zone ($x^* > 0$). For each of the five parameter variations, four standard deviations

(i) Upstream of MRE zone, steady conditions
(ii) Upstream of MRE zone, unsteady conditions
(iii) Inside MRE zone, steady conditions
(iv) Inside MRE zone, unsteady conditions

are derived, which allow a quantitative evaluation of the effect of each parameter on the bore propagation.

Statistical analyses allow the evaluation of the impact of each MRE parameter on the energy losses. The mean of the mean values of the changes of the volume flux $\Delta q(x)/\Delta x$ within the segments (see Figure 5.5b) indicates the average impact of the MRE on the flux reductions of the investigated cases. Their standard deviations represent the bandwidth of the impact. The higher the standard deviations the higher is the impact of the MRE parameter on the flux reduction. The relative standard deviation relates the bandwidth to the average impact level of the investigated cases. However, very small mean values result in high relative standard deviations, and thus in an apparently pronounced importance of the MRE parameter. Hence, the standard deviation of the mean values is used for the evaluation.

5.4.5 Local flow effects and influence of the position of the MRE inside the cross-sections

It is noted that due to the variation of the arrangement angle (cases 3.1 and 3.2) and the relative spacing on one hand and constant distances and orientations of the cross-sections on the other hand, local flow effects in the vicinity of the MRE can influence the analysis results in (fixed) cross-sections. The problem is depicted in Figure 5.9.

Figure 5.9 shows the flow velocities $u(x)$ in a horizontal plane at approximately 0.5 h in the MRE zone. It further shows the cross-sections i and the flow depth h. It is seen that the local flow velocities in the longitudinal gaps of the MRE (in the wakes downstream of the MRE) are considerably lower than in the lateral gaps. It is apparent, that the flow conditions in the MRE zone do not vary considerably between cross-sections i = 1 and i = 2. The cross-section i = 1 is located between two rows of MRE and the cross-section i = 2 goes through a MRE row.

The flow depth $h_{i=1,j}$ during the timestep j is obtained by the equations (5-8). In these equations, k is the index of the elements located in the cross-section i. At cross-section i = 2, however, the analysis leads to smaller flow depth than observed, due to the position of the MRE inside the cross-section, indicated by the white rectangles. The water volume in cross-section i = 2 is smaller than in cross-section i = 1. In both cross-sections, however, according to equation (5-6), the water volume is divided by the cross-section volume V_i (see equation (5-5)), which is equal for all cross-sections of each case. Therefore, $h_{i=1,j} > h_{i=2,j}$.

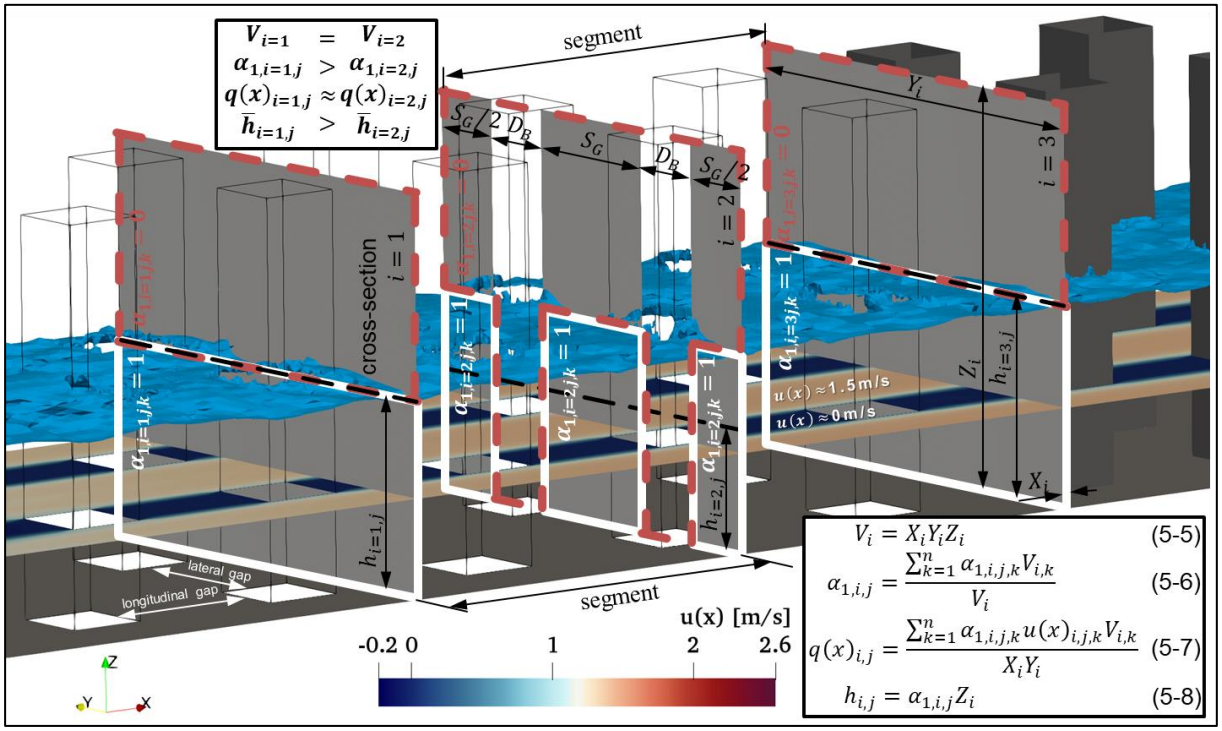

Figure 5.9. Position of cross-sections relative to MRE.

The volume flux $q(x)_{i,j}$ during timestep j is obtained by equation (5-7). In cross-section $i = 1$, the volume flux $q(x)_{i=1,j}$ is averaged over zones with high flow velocities (lateral gaps) and low flow velocities (longitudinal gaps), while in cross-section $i = 2$, the volume flux $q(x)_{i=2,j}$ is only averaged over zones with high flow velocities (lateral gaps). Due to the small contribution of the longitudinal gaps to the water volume passing cross-section $i = 1$, it is comparable to the water volume passing cross-section $i = 2$. As all cross-sections of a case have the same size. $X_i Y_i$ is equal for both cross-sections and consequently, also the volume flux $q(x)_{i=1,j} \approx q(x)_{i=2,j}$.

When looking at cross-section $i = 2$ in Figure 5.9, then it becomes apparent that the differences in flow depth between cross-section $i = 1$ and $i = 2$, $(h_{2,j} - h_{1,j})$ is negative, while the differences in flow depth between cross-sections $i = 2$ and $i = 3$, $(h_{3,j} - h_{2,j})$ is positive, so that the average of both differences is $(h_{3,j} - h_{1,j}) \approx 0$. Therefore, the influence of the position of the MRE relative to the cross-sections becomes decreasingly important when the results can be averaged over larger regions of the MRE zone.

The 3D model results are analysed within virtual cross-sections. The scale difference between the 3D model and the 2D model is bridged by spatial and temporal integration and averaging. Beside the qualitative description of the maximum flow velocities, the mean values of the flow depth, depth-averaged flow velocities and volume fluxes are analysed.

Local flow effects induced by the MRE inside analysed cross-sections can pollute the analysis results but can be minimized by averaging. The effect of each parameter on the bore propagation is evaluated using the standard deviation of the mean values of each individual case.

5.5 Analysis of the results for the effect of MRE parameters on bore propagation and flow

This section presents the analysis of flow fields from the numerical simulations to better understand the effect of each MRE parameter variation, so that the most important parameters are selected for including them in the MRE formula. The simulation results are included in Appendix C.

First, a reference case without MRE (case 0.0) is presented to which all flow fields around the MRE will be related. This case is also used to evaluate the uniformity of the bore propagation through the MRE zone. The reference case takes the effective roughness height k_S = 0.001 m into account (see section 3.2.3), which is kept unchanged for all cases. In section 5.5.2, the flow fields around single isolated standing MRE (cases 0.1 to 0.3) are discussed. They serve as a reference for showing the effects of MRE standing in groups in the sections 5.5.2 to 5.5.6, where the flow velocities of MRE configurations varying the shape, the relative width, the arrangement, the relative spacing and the relative height are discussed. Furthermore, these sections provide an analysis of flow parameters through cross-sections placed within the MRE zone (see Figure 5.5) during the steady and unsteady flow phase, so that the relevance of each MRE parameter can specifically be evaluated with regard to space and time for consideration in the MRE formula as part of the NLSW momentum balance equation.

5.5.1 Reference case for flow without any macro-roughness elements (Case 0.0)

From the simulation of the case without MRE, flow depths h, flow velocities $u(x)$ and volume fluxes $q(x)$ have been averaged at six cross-sections over the entire width of the numerical domain. Their positions are marked in Figure 5.5.b). The time series are presented in Figure 5.10. The maximum values are summarized in Table 5.4.

The flow depth in Figure 5.10.a) gradually increases for ca. 10 s after the arrival of the bore and then starts to decrease slightly. The maximum flow depth decreases with increasing distance x from the impoundment from $h_{1,max}$ = 0.34 m at x^* = 0 to $h_{6,max}$ = 0.328 m at x^* = 0.9375 (Table 5.4).

The depth-averaged flow velocities increase abruptly to the maximum at the time of the bore arrival and then decrease gradually (Figure 5.10.b). The maximum flow velocity increases slightly with increasing distance x^* from the impoundment, from $u(x)_{1,max}$ = 4.93 m/s at x^* = 0 to $u(x)_{3,max}$ = 5.02 m/s at x^* = 0.375, before decreasing to $u(x)_{6,max}$ = 4.78 m/s at x^* = 0.9375 (Table 5.4).

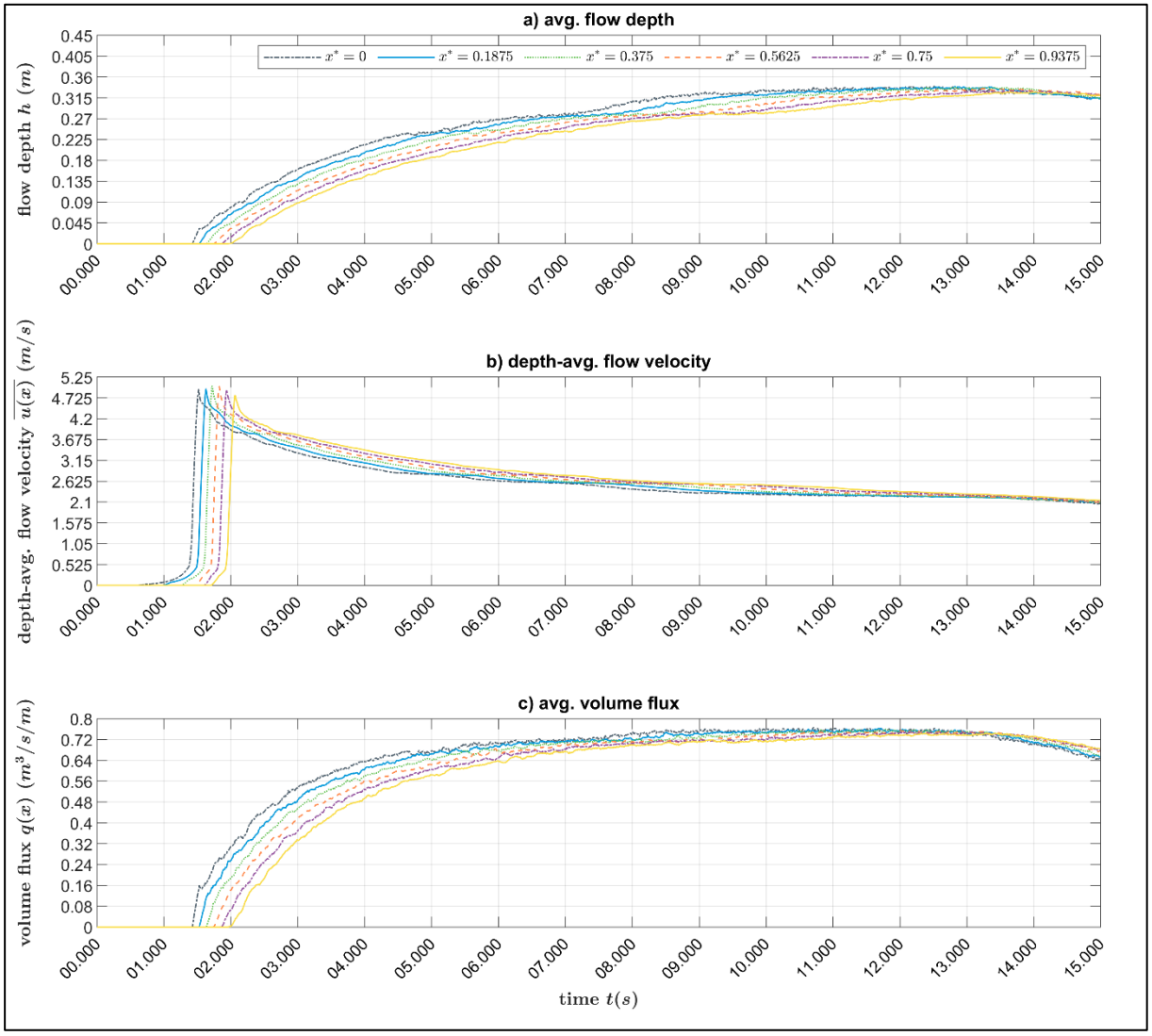

Figure 5.10. Evolution in time of flow parameters at cross-sections x^* = {0; 0.1875; 0.375; 0.5625; 0.75; 0.9375}, case 0.0 (reference case without any MRE): a) flow depths, b) depth-averaged flow velocities and c) volume fluxes.

Table 5.4. Maximum averaged flow depth, maximum depth-averaged flow velocities and maximum flow velocities 0.05 m above the bottom, and max. volume flux for case 0.0 (reference case for flow without any MRE).

Cross-section i [-]	**1**	**2**	**3**	**4**	**5**	**6**	**Mean**	**STDEV**	**Rel. STDEV**
Relative distance from impoundment x^* [-]	0	0.1875	0.375	0.5625	0.75	0.9375			
Maximum avg. flow depth $h_{i,max}$ [m]	0.340	0.340	0.338	0.335	0.330	0.328	0.335	0.005	0.014
Maximum avg. flow velocity $u(x)_{i,max}$ [m/s]	4.93	4.95	5.02	5.01	4.93	4.78	4.94	0.079	0.016
Maximum volume flux $q(x)_{i,max}$ [m³/s/m]	0.766	0.763	0.759	0.755	0.749	0.744	0.756	0.008	0.010

The volume flux decreases gradually (Figure 5.10.c). It is noted that within the first 5 s after bore arrival (between t_1 = 1.44 … 2.02 s to t_2 = 6.44 … 7.02 s) the flux increases, while subsequently the flux is relatively stable for the next 7.5 s (between t_2 to t_3 = 13.94 … 14.52 s). When both parameters flow depth and flow velocity are decreasing (after t_3), the volume flux (as the product of both parameters) decrease more than the individual parameters. The volume flux decreases from $q(x)_{1,max}$ = 0.766 m³/s/m at x^* = 0 to $q(x)_{1,max}$ = 0.756 m³/s/m at x^* = 0.9375 m³/s/m.

The uniformity of the bore during its propagation between x^* = 0 and x^* = 1 is analysed by means of the relative standard deviation of the extracted values for maximum flow depth, maximum flow velocity and maximum volume flux. It takes values between 0.010 for volume fluxes and 0.016 for maximum flow velocities. This confirms that the variation of the bore over the propagation (compare to Figure 5.6) is very low.

5.5.2 Effect of macro-roughness element shape (Cases 0.1 – 0.3 & 1.0 – 1.2)

For a qualitative assessment of the flow fields around single isolated-standing MRE of different shapes at x = 8 m (x^* = 0.5), the maximum flow velocities of each case $x.x$ $u_{case\ x.x,max}$ are normalized with maximum flow velocities $u_{0.0,max}$ of reference case 0.0 using the relation

$$u^*_{max} = \frac{u_{case\ x.x,max}}{u_{0.0,max}} \tag{5-13}$$

and extracted in a horizontal plane at z = 0.05 m above the bottom. Figure 5.11 represents the maximum normalized flow velocities u^*_{max} around a single isolated-standing single MRE of different shapes (with the same width D_B = 0.04 m).

The pattern of maximum flow velocities in the mean flow direction reveals the presence of a wake downstream of the MRE and a zone of increased flow velocities at the lateral sides of each MRE. The wakes downstream of each MRE and the upstream zone, where the flow is blocked by the MRE, differ in both shape and size among the three differently shaped MRE:

- *The cubic element* in Figure 5.11.a) affects the flow in a zone slightly wider than the MRE and up to a downstream distance of 4 to 5 D_B from the MRE. Upstream of the MRE, the length of the blocked flow zone with flow velocities smaller than 25 % of the mean flow is $l_B \approx 1/3\ D_B$. The width of the accelerated flow in the lateral vicinity of the MRE with flow velocities greater than 25 % of the mean flow velocity is $l_A \approx 1 D_B$.
- *The cylindrical element* in Figure 5.11.b) deflects the flow laterally, but the flow follows the round shape of the MRE so that after its separation the flow re-joins downstream of the cylinder at a distance of less than 2 D_B. Upstream of the MRE, the length of the blocked flow zone is $l_B \approx 1/6\ D_B$.
- *The diamond-shaped element* in Figure 5.11.c) deflects the flow to both lateral sides but due to the sharp edges, the flow continues to propagate further in the lateral direction. The flow re-joins after its separation downstream of the element at a distance of more than 5 D_B. Upstream of the MRE, the length of the blocked flow zone is $l_B \approx 1/4\ D_B$.

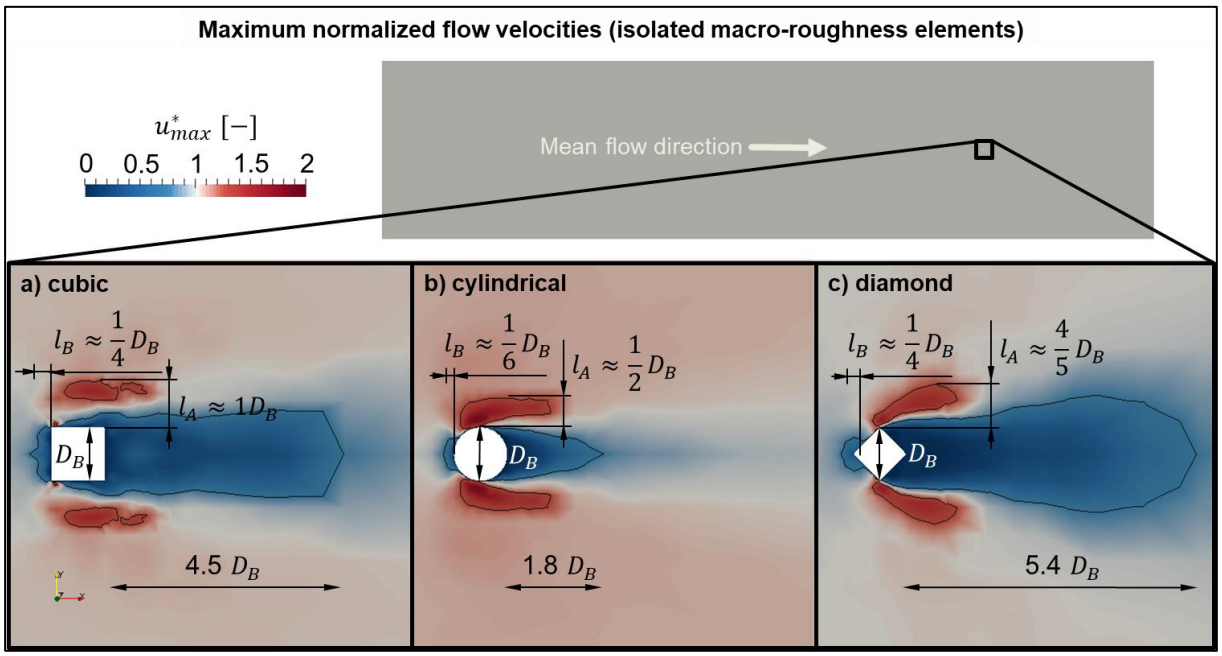

Figure 5.11. Normalized maximum flow velocities $u^*_{case0.x,max} = u_{case0.x,max}/u_{0.0,max}$ in the mean flow direction 0.05 m above the bottom around an isolated a) cubic (case 0.1), b) cylindrical (case 0.2) and c) diamond-shaped MRE (case 0.3).

The length of the blocked flow zone l_B can be related to the drag coefficients C_D of the three MRE shapes. By normalizing l_B with D_B, it can be seen that when l_B/D_B increases, C_D increases also. Both C_D and l_B/D_B are provided in Table 5.5 for the three MRE shapes.

Table 5.5. Drag coefficients (Hashimoto & Park, 2008)

	Cube	**Diamond**	**Cylinder**
Normalized length of blocked flow zone l_B/D_B	1/3	1/4	1/6
Drag coefficient C_D [-]	2.05	1.55	1.2

Similar to the assessment of the flow fields around a single isolated-standing MRE, the maximum velocities of the flow through the group of MRE at z = 0.05 m above the bottom are presented in Figure 5.12.b), c), d), for cubic, circular and diamond-shaped elements, respectively. The relative spacing between the MRE is S_G/D_B = 2.0. The time series of flow depths, velocities and fluxes are given in Appendix, section C.1.2 for the basic configuration and section C.1.3 for the other two investigated shapes.

The flow fields through the entire MRE zone of Figure 5.12.b) to Figure 5.12.d) are described and compared in the following. Detailed representations of the flow field in the close vicinity of the MRE located in the most upstream MRE row are presented in Figure 5.12.e) to Figure 5.12.g) and compared to the flow fields around a single isolated standing MRE to better understand the impacts of the MRE shape when standing in groups.

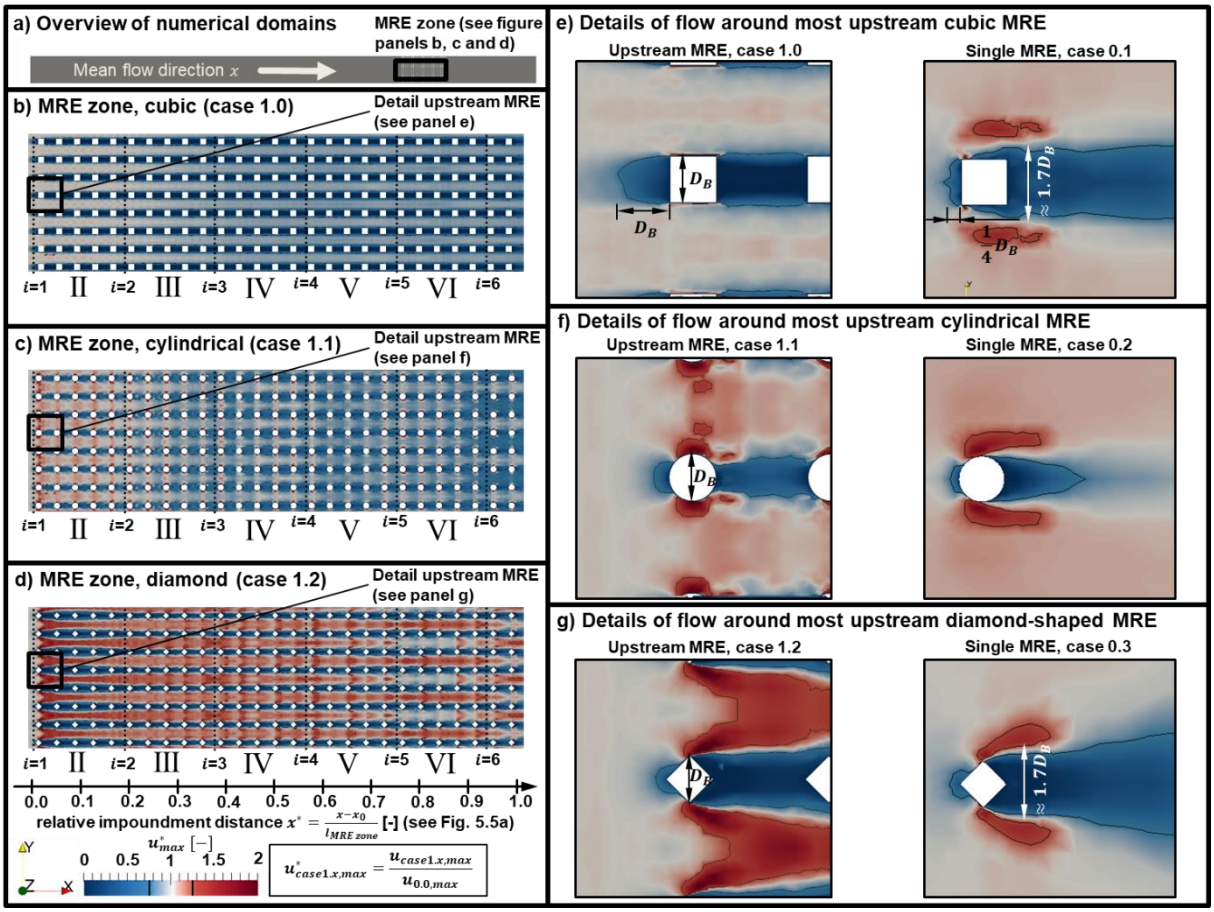

Figure 5.12. Effect of shape on normalized maximum flow velocities $u^*_{case1.x,max} = u_{case1.x,max}/u_{0.0,max}$ in mean flow direction at z= 0.05 m above the bottom through MRE: a) Overview of numerical domains, MRE zone: b) cubic (case 1.0), c) cylindrical (case 1.1), d) diamond (case 1.2), Details of flow around upstream MRE: e) cubic (case 1.0) vs. case 0.1, f) cylindrical (case 1.1) vs. case 0.2, g) diamond (case 1.2) vs. case 0.3. The dotted lines symbolize the cross-sections i and the Roman numbers II to VI symbolize the segments between them (see Figure 5.5.b).

Flow through the cubic MRE (case 1.0)

The flow through the cubic MRE in Figure 5.12.b) is separated by the most upstream cubes in segment II. In the middle of the lateral gaps, the flow velocity is slightly increased compared to the undisturbed flow velocity of case 0.0 ($u^*_{max} > 1$). It decreases during the propagation through the MRE zone due to the interaction with the MREs. In the longitudinal gaps, the flow velocity is very small due to the blocking effect of the most upstream MRE ($u^*_{max} \ll 1$).

A more detailed representation of this situation is given in Figure 5.12.e) (left). The flow separation can be observed already at a distance of more than $1D_B$ upstream of the first cubes, as at this distance the flow velocity drops below 75 % of the values of the undisturbed flow field in case 0.0 (blue area inside the u^*_{max} = 0.75 contour line). The water moves through the lateral gaps (located between the MRE normal to the mean flow direction) with a slightly increased flow velocity. The highest velocities can be observed in the middle of the lateral gaps. In the longitudinal gaps (between the MRE in the mean flow direction), the flow is blocked by the cube located upstream of each gap. This leads to zones with lower flow velocities with a width

of approximately $1D_B$. This separation is initiated by the first row of upstream cubes. Further downstream, the cubes are located in the wakes of the upstream cubes where the flow velocities are low. Therefore, it can be assumed that energy losses due to the downstream located MRE are considerably lower than at the most upstream located MRE row. For comparison, the flow field around the single cubic MRE (see Figure 5.11.a) is conveniently provided in Figure 5.12.c) (right). The flow is less hindered by the single MRE and the extent of flow velocity drop below 75 % is $1/4\ D_B$, only. Furthermore, the absence of neighbouring MRE allows for the formation of a high flow zone with flow velocities of more than 25 % higher than the undisturbed velocities (red area inside the black contour lines) and a wider wake of approximately $1.7D_B$. The fluid viscosity and the interference of the wake with the downstream-located MRE are responsible for the fact that the presence of neighbouring MRE results in MRE acting as a group, which leads to a higher drop in the velocity than the flow field around the single MRE (Figure 5.11.a) would suggest.

Flow through the cylindrical MRE (case 1.1)

The flow approaching the cylindrical MRE in Figure 5.12.c) is also separated by the most upstream located cylinders. In the lateral gaps, the flow velocity is increased to a higher extent then in case of the cubic MRE (Figure 5.12.b). It is further observed that the flow velocity does not decrease gradually as in case of the cubes. An increase of maximum flow velocities is noted close to the cylinders approximately at x^* = 0.5 (in segment IV) and at x^* = 0.75 (at cross-section i = 5) (every $\approx 18D_B$). This suggests the presence of a vertical oscillatory motion, which is observed also for example in form of the vortex shedding in the wake of an obstacle. However, such repeating pattern are not apparent for cubic MRE (see Figure 5.12.b). Therefore, it is assumed that this effect is related to the shape of the obstacle: The cylindrical shape introduces a stronger lateral component to the flow close to the element faces (see also section 4.2.1) while the cube front face is normal to the flow direction and therefore less deflecting. In the longitudinal gaps, the flow velocity is decreased but to a lesser extent than for cubic MRE.

A more detailed representation of the flow field around one MRE in the most upstream row of MRE is given in Figure 5.12.f) (left). u^*_{max} drops below 75 % of the undisturbed flow velocity (case 0.0) (blue area inside the black contour line) upstream of the front face in a distance of approximately 0.5 D_B, indicating that the bore can propagate closer towards the upstream cylinder than in the case of the cubes. Higher velocities can be observed in the lateral gaps between the upstream cylinders and close to the lateral sides of the cylinders, whereas in case of the cubes higher velocities occur in the middle of the lateral gaps. In the longitudinal gaps, lower velocities are noted, but the low velocity zones are narrower than for cubes due to the more streamlined shape of the cylinder. This suggests that cylindrical MRE located more downstream can cause larger energy losses than cubic MRE, because parts of the cylindrical MRE remain unsheltered. Compared to the flow field of the single cylinder in Figure 5.12.f) (right), the size of the slow flow zone upstream of the cylinder front face is larger. Due to the neighbouring cylinders in Figure 5.12.f) (left), the formation of a high flow zone as observed in Figure 5.12.f) (right), is hindered. Due to the more streamlined shape of the cylinder, the width of the wake is less than 1 D_B.

Flow through the diamond-shaped MRE (case 1.2)

The flow approaching the diamond-shaped MRE in Figure 5.12.d) is separated at the most upstream row of diamonds. The flow is deflected towards the lateral gaps so that comparably high flow velocities u^*_{max} occur in the most upstream part of the MRE zone. Comparable to the flow through the cylinders is, however, the oscillation pattern of the highest flow velocities, which is induced by the deflecting diamond faces. In the longitudinal gaps, the flow velocities are higher than in case of the cubes but smaller than in case of the cylinders. Between the upstream located four diamonds (x^* = 0.01 to 0.12), the flow deflection leads to a wider zone of low velocities than in the cases of the previously described shapes. An oscillatory velocity pattern can be noted which is even more obvious than in the case of the flow through the cylinders. Here, higher flow velocities are noted approximately at x^* = 0.4 (near cross-section i = 3), 0.58 (near cross-section i = 4) and 0.9 (in segment VI). Although the flow is deflected laterally, there is still a clear separation between zones of higher velocities and zones of lower velocities in the lateral gaps. The latter are slightly wider than in case of the diamond MRE. Therefore, it can be assumed that in these zones the energy losses in the bore are lower, while in the zones thinner than the diamond MRE, the energy losses should be higher.

A more detailed representation of the flow field around one MRE in the most upstream row of MRE is given in Figure 5.12.g) (left). u^*_{max} drops below 75 % of the undisturbed flow velocity (case 0.0) (blue area inside the black contour lines) at a distance of the front face of ca. 0.25 D_B only, showing that the flow separation occurs very close to the front edge of the diamonds, compared to the cubic and cylindrical shapes. The flow is deflected by the front faces, which are orientated in an angle of 45° to the mean flow direction. At the lateral upstream-orientated diamond faces, high velocities can be observed. This behaviour is similar to the flow through cylinders, where the flow is also more deflected than blocked. Higher velocities are noted in the middle of the gaps and near the lateral edges, which is also similar to the observations of flow through the cylinders. However, the velocity gradients in the lateral gaps are higher than in case of cylinders and cubes. The wake downstream of the MRE is approximately 1 D_B wide, while in case of the isolated standing diamond in Figure 5.12.g) (right), its width increases to approximately 1.7 D_B, which is similar to the cube in Figure 5.12.e) (right).

The representation of the flow fields in Figure 5.12 indicate that the channelling effect is noticeable in all configurations. The channel is the widest for the cylinders, where the shape is more streamlined than the other shapes, and it is the smallest for diamonds, where deflection plays the most dominant role. Compared to a single isolated MRE, the group effect decreases the width of the wakes downstream of the MRE.

It is seen that the MRE located further downstream can differently contribute to the energy losses due to their presence in areas with high flow velocities. Therefore, the spatial changes of the flow parameters flow depth h, depth-averaged flow velocity $u(x)$ and volume flux $q(x)$ need to be analysed throughout the entire length of the MRE zone. Furthermore, in order to differentiate between drag and inertia effects, which are to be represented in the prospective MRE formula, a distinction is made between the flow regimes of bore propagation.

The spatial change of mean flow depths $\frac{\Delta h}{\Delta x}$, mean depth-averaged flow velocities $\frac{\Delta u(x)}{\Delta x}$ and mean volume fluxes $\frac{\Delta q(x)}{\Delta x}$ during the unsteady and steady phase in the two upstream segments I and II and five segments II to VI inside the MRE zone are provided in Figure 5.13. The mean values of the volume flux changes represented in Figure 5.13 are given in Table 5.6. The mean values and standard deviations of the volume flux change for each individual case are provided for the unsteady and the steady flow phase in the Appendix, section C.2. The higher the standard deviation, the higher is the impact of the investigated parameter shape in the particular zone and flow phase.

Table 5.6. Statistics of the mean values of volume flux changes at the upstream edge (segments I and II) and inside the MRE zone (segments III to VI) for the variation of the shape. For drag coefficient C_D refer to Hashimoto & Park (2008).

Mean values of changes of volume flux $\Delta q(x)/\Delta x$		**Unsteady**		**Steady**		**average**
		I, II	**III to VI**	**I, II**	**III to VI**	
Case 1.0	**Cube (C_D= 2.05) [m³/s/m]**	-0.163	-0.017	-0.345	-0.010	-0.134
Case 1.1	**Cylinder (C_D= 1.2) [m³/s/m]**	-0.036	-0.072	-0.177	-0.004	-0.073
Case 1.2	**Diamond (C_D= 1.55) [m³/s/m]**	-0.079	-0.094	-0.316	0.013	-0.119
Mean of the mean values [m³/s/m²]		-0.093	-0.061	-0.279	0.000	-0.108
Standard deviation [m³/s/m²]		**0.052**	**0.040**	**0.090**	**0.012**	**0.048**
Relative standard deviation [-]		-0.567	-0.653	-0.321	-29.8	-7.828

Unsteady phase of bore propagation

- *In Figure 5.13.a)*, upstream of the MRE zone in segment I, the flow depth increases due to backwater effects. The increase of flow depth takes values between $\Delta h/\Delta x$ = 0.58 (cubes) and 0.1 m/m (diamonds), while for cylinders, the flow depth increases by $\Delta h/\Delta x$ = 0.12 m/m, indicating that the flow is mainly blocked by the cubes, while diamonds and cylinders also deflect the flow. In segment II, the flow depth drops by up to 0.55 m/m for the cubes, while for the cylinders and diamonds almost no decrease in water depth is apparent as the flow is deflected. The further the flow progresses through the MRE zone, the lesser are the changes in flow depth. During further bore propagation, the change in flow depth becomes smaller. From segment IV onwards, $\Delta h/\Delta x$ = -0.04 m/m for the cubes and $\Delta h/\Delta x$ = -0.02 m/m for the cylinders. Particularly, the diamonds reduce the flow depth throughout the entire MRE zone by approximately $\Delta h/\Delta x$ = -0.08 m/m.
- *In Figure 5.13.c)*, the flow velocity in segment I decreases between $\Delta\overline{u(x)}/\Delta x$ = 1.4 m/s/m for the cylinders and $\Delta\overline{u(x)}/\Delta x$ = 4.6 m/s/m for the cubes, while for the diamonds, the flow velocity decreases by $\Delta\overline{u(x)}/\Delta x$ = 2.4 m/s/m. In the most upstream segment in the MRE zone segment II, the flow velocity increases considerably by $\Delta\overline{u(x)}/\Delta x$ = 1.6 m/s/m only for the cubes, while it decreases when propagating through diamonds and cylinders. This is because the flow is partly blocked by the cubes in segment I. In the lateral gaps between the cubes, however, the propagating water is not hindered by the shape of the cubes leading to a channelling of the flow so

that on average, the flow velocity is higher than upstream of the MRE zone, which contains also the blocked water. In case of the cylinders and diamonds, the flow is blocked to a lesser extent in segment I, which is why the deviation from the flow in segment II is smaller. It is noted that the higher the blocking in segment I the smaller is the increase of the flow velocity of the propagating part of the bore in segment II. While the bore is propagating further through the MRE zone, the deviation between the cross-sections becomes smaller for all shapes. It reaches values of $\Delta\overline{u(x)}/\Delta x$ = -0.15 m/s/m (for the diamonds).

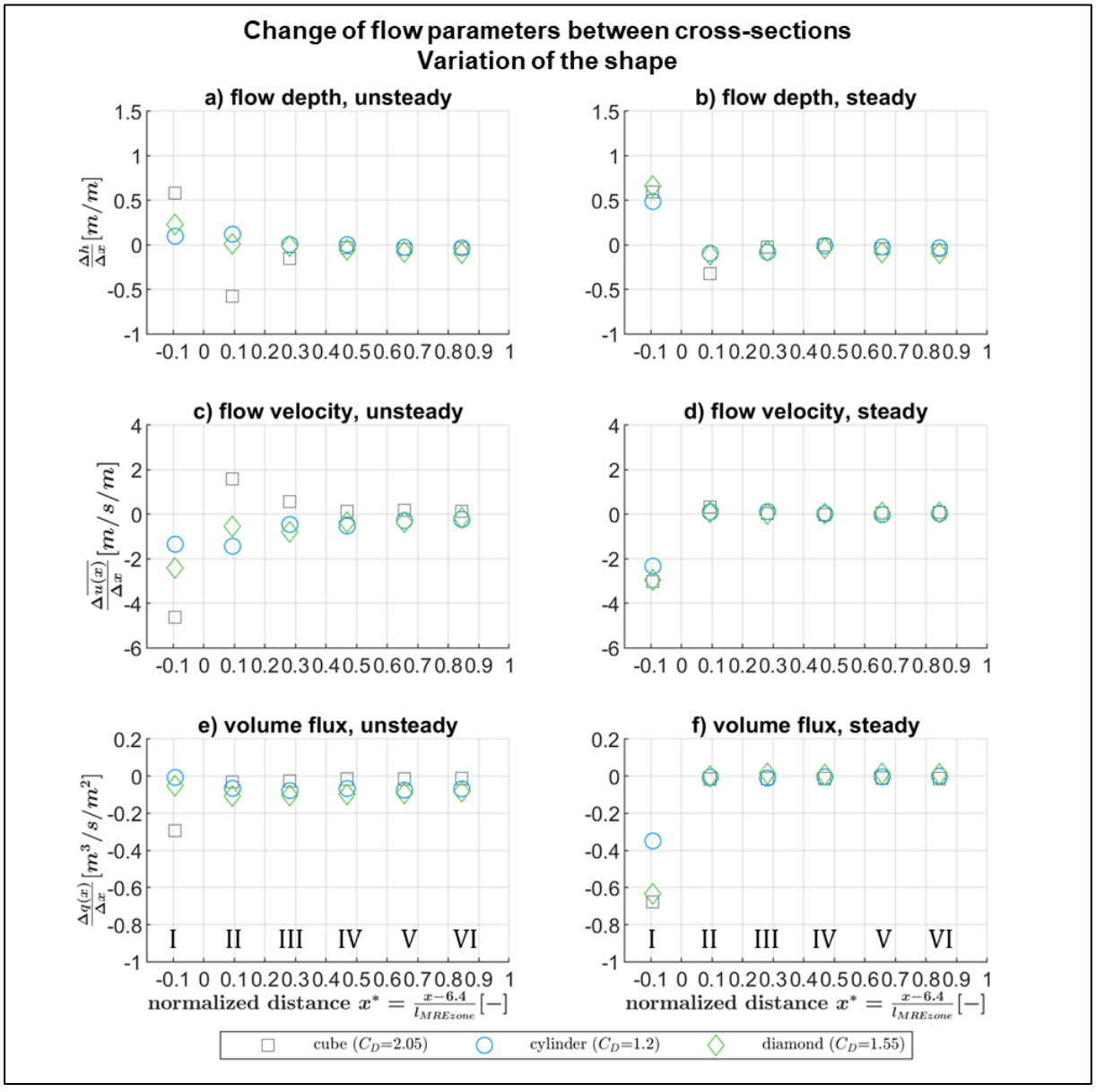

Figure 5.13. Effect of shapes (symbolized using drag coefficient C_D) on the change of the flow parameters between cross-sections in the segments I to VI: a) flow depth during the unsteady phase, b) flow depth during the steady phase, c) depth-averaged flow velocity during the unsteady phase, d) depth-averaged flow velocity during the steady phase, e) volume flux during the unsteady phase, f) volume flux during the steady phase.

- *In Figure 5.13.e)*, the volume flux in segment I decreases between $\Delta q(x)/\Delta x$ = -0.01 m³/s/m² in case of the cylinders and $\Delta q(x)/\Delta x$ = -0.29 m³/s/m² for the cubes. During further propagation through the segments II to VI, the reduction of the volume flux for the cubes is between $\Delta q(x)/\Delta x$ = -0.02 m³/s/m² and $\Delta q(x)/\Delta x$ = -0.01 m³/s/m² as the flow passes the in-line standing cubes. In case of the cylinders and diamonds, volume flux reduction still reaches $\Delta q(x)/\Delta x$ = -0.08 m³/s/m² and $\Delta q(x)/\Delta x$ = -0.10 m³/s/m², respectively, indicating that the deflected flow approaches the MRE in the downstream rows so that they still contribute to the reduction of the volume flux.

These observations can be related to the drag coefficients C_D of the single MRE (see Table 5.5), particularly in the upstream segments I and II: The higher C_D, the higher the flux reduction. This holds true also when forming the average values of these segments in Table 5.6, while flux reduction inside the MRE zone in segments II to VI does not seem to be related to C_D.

Steady phase of bore propagation

- *In Figure 5.13.b)*, upstream of the MRE zone in segment I, the flow depth varies between $\Delta h/\Delta x$ = 0.49 and $\Delta h/\Delta x$ = 0.66 m/m. Inside the MRE zone (segments III to VI), the flow depth reduces between $\Delta h/\Delta x$ = 0 m/m (cubes) and $\Delta h/\Delta x$ = -0.09 m/m (diamonds). The difference between the cases is smaller than during the unsteady phase and seems less dependent from the shape.
- *In Figure 5.13.d)*, the flow velocities are reduced between $\Delta\overline{u(x)}/\Delta x$ = -3.03 m/s/m by cubes and $\Delta\overline{u(x)}/\Delta x$ = -2.33 m/s/m by cylinders in segment I due to backwater effects. The difference between the shapes is less pronounced than during the unsteady phase of bore propagation. In the most upstream segment II of the MRE zone, the flow velocity increases in case of the cubes by $\Delta\overline{u(x)}/\Delta x$ = 0.33 m/s/m, while for all other the velocities change only by values between $\Delta\overline{u(x)}/\Delta x$ = 0.11 m/s/m in case of the cylinder and $\Delta\overline{u(x)}/\Delta x$ = 0.09 m/s/m in case of the diamond. The difference between the cases is smaller than during the unsteady phase and seems less dependent from the shape.
- *In Figure 5.13.f)*, the volume flux is reduced in segment I between $\Delta q(x)/\Delta x$ = -0.68 m³/s/m² in case of cubes and $\Delta q(x)/\Delta x$ = -0.35 m³/s/m² for the diamonds. Inside the MRE zone, the volume flux remains almost constant in all cases with at most $\Delta q(x)/\Delta x$ = -0.01 m³/s/m², suggesting that during the steady flow phase of the bore, only small energy losses occur.

These observations can be related to the drag coefficients C_D in the segments I and II upstream of the MRE, where the highest C_D lead to the highest volume flux reduction, which can be seen from the mean values of changes of volume flux in Table 5.6. The standard deviation of the mean values in Table 5.6 reveals that the highest impact of the shape is found under steady flow conditions in the upstream segments of the MRE zone (standard deviation of $\Delta q(x)/\Delta x$ = 0.09 m³/s/m²), while the least impact is noted during steady flow conditions inside the MRE zone (standard deviation of $\Delta q(x)/\Delta x$ = 0.012 m³/s/m²). On average, the standard deviation of the fluxes when varying the shape is $\Delta q(x)/\Delta x$ = 0.048 m³/s/m².

Flow patterns vary considerably with the tested MRE shapes. The cubes cause energy losses mainly due to the blockage of the flow, while the losses induced by cylindrical and diamond-shaped elements are mainly due to flow deflection. The cubes cause a more pronounced channelling effect which leads to a smaller reduction of the flow velocities in the lateral gaps between the MRE compared to the cylinders and diamond-shaped MRE. Upstream of the MRE, the cubes lead to the highest energy losses and the cylinders to the lowest. Inside the MRE zone, the diamonds lead to the highest energy losses and the cubes to the lowest.

In the unsteady phase of bore propagation, energy losses can be observed mainly upstream of the MRE zone for cubic MRE. The volume flux reduction is considerably smaller for the other shapes.

In the steady phase of bore propagation, energy losses are mainly identified upstream of the MRE zone while inside the MRE zone, no noticeable energy losses are observed.

The disturbance of the bore propagation can be related to the drag coefficient C_D of the single MRE in the upstream segments I and II of the MRE zone during the unsteady and the steady phase of bore propagation. The highest C_D leads to the highest volume flux reduction while the smallest C_D results in the smallest volume flux reduction (see Table 5.6).

5.5.3 Effect of the relative macro-roughness element width (Cases 1.0, 2.1 & 2.2)

The width of the MRE D_B is related to the maximum averaged flow depth h_{max} at normalized distance from the impoundment x^* = 0.5. Only cubic MRE are exemplarily considered below, as they represent the predominant shape in urban areas (buildings). The normalized maximum flow velocities u^*_{max} in the mean flow direction at z = 0.05 m above the bottom are presented in Figure 5.14. The time series of flow depths, velocities and volume fluxes are given in Appendix, sections C.1.2 and C.1.4 for the basic configuration and the variations of the relative width, respectively.

Flow through MRE zone with D_B/h_{max} = 0.116 (case 1.0)

Figure 5.14.b) represents the basic configuration case 1.0 with a relative width D_B/h_{max} = 0.116. Details of the flow field are depicted in comparison with the flow field around a single MRE (case 0.1) in Figure 5.14.e) (see section 5.5.2 for detailed description).

Flow through MRE zone with D_B/h_{max} = 0.232 (case 2.1)

In Figure 5.14.c), where the relative width of the cubic elements of the basic configuration is doubled to D_B/h_{max} = 0.232, the greater lateral gaps between the MRE (normal to the mean flow direction) lead to increasing flow velocities. As the lateral gap widths are also doubled, the areas of increased flow velocities are not necessarily located in the middle of the lateral gaps. Towards the centre of the lateral gaps, the flow velocity decreases towards the undisturbed flow velocity. It is further noted that the flow velocity does not decrease gradually towards the end of the MRE zone but shows an increase in the analysed horizontal plane in segment VI (see

also cases 1.1. and 1.2 in section 5.5.2). In the longitudinal gaps between the MRE (in mean flow direction), the flow velocity decreases similarly to the basic configuration. The cubes located further downstream from the most upstream row are almost fully located inside the wake of the upstream cubes suggesting their small contributions to energy losses.

A detailed view on the flow field of the most upstream MRE is provided in Figure 5.14.f) (left). It is seen that the flow separation at the front face of the MRE leads to an area of reduced flow velocities with a length of approximately $1/4\ D_B$, which is considerably less than in the basic configuration and comparable to the length upstream of the single MRE (see Figure 5.14.f).

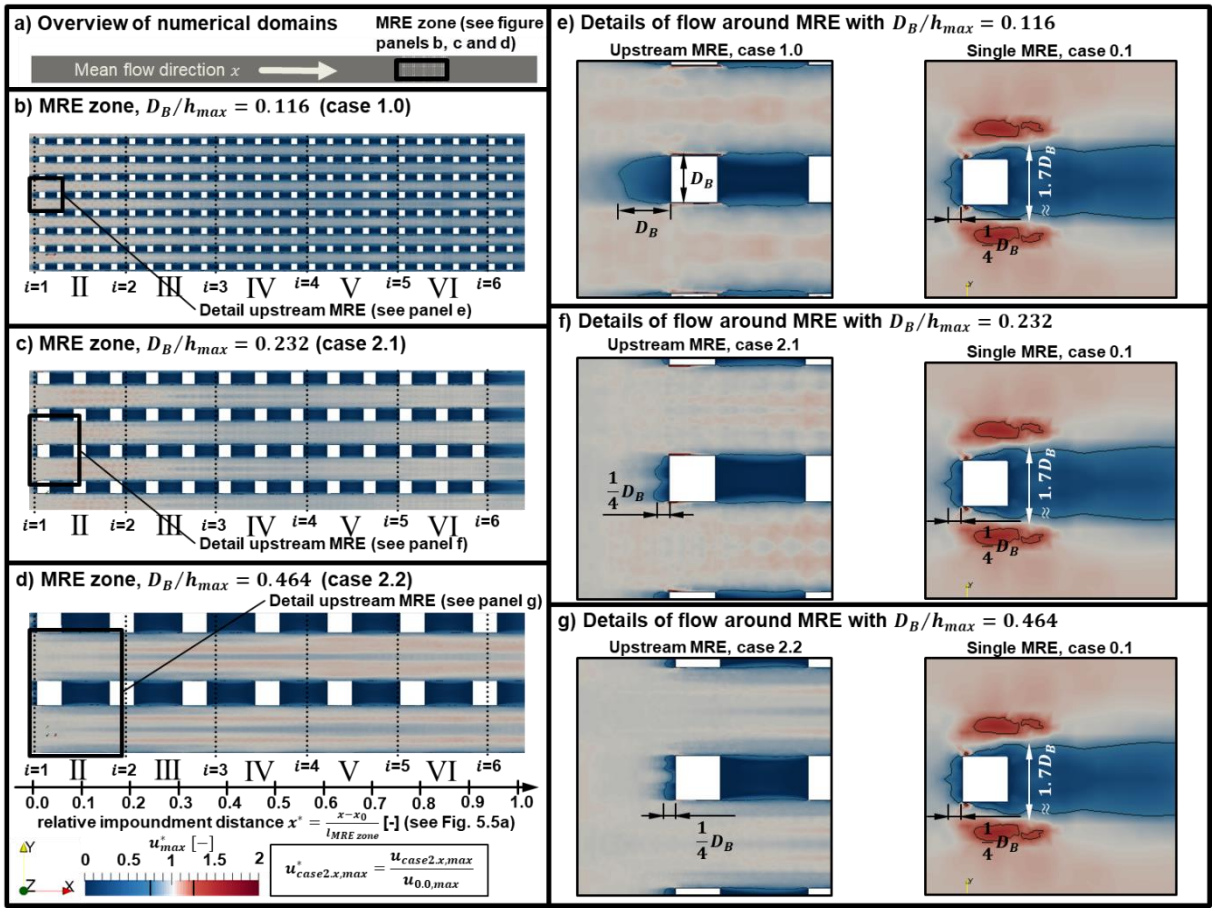

Figure 5.14. Effect of relative widths D_B/h_{max} on normalized maximum flow velocities $u^*_{case2.x,max} = u_{case2.x,max}/u_{0.0,max}$ in mean flow direction at z= 0.05 m above the bottom through MRE: a) Overview of numerical domains, MRE zone: b) D_B/h_{max} = 0.116 (case 1.0), c) D_B/h_{max} = 0.232 (case 2.1), d) D_B/h_{max} = 0.464 (case 2.2), Details of flow around upstream MRE: e) D_B/h_{max} = 0.116 (case 1.0) vs. case 0.1, f) D_B/h_{max} = 0.232 (case 2.1), g) D_B/h_{max} = 0.464 (case 2.2). The dotted lines symbolize the cross-sections i (see Figure 5.5.b).

Flow through MRE zone with D_B/h_{max} = 0.464 (case 2.2)

In Figure 5.14.d), where the relative width of the MRE is further doubled to D_B/h_{max} = 0.464, the areas of increased flow velocities in the lateral gaps are not located in the middle of the gaps. The lateral distance between the cubes is here even wider than in the previous cases so that the influence of the MRE on the flow field reduces towards the middle of the gap. In the

longitudinal gaps, a decrease of flow velocities can be observed which is comparable to the previous cases.

A detailed view on the flow field of the most upstream MRE is provided in Figure 5.14.g). The flow separation is observed at the comparable distance as for case 2.1 at approximately $1/4\ D_B$ upstream of the MRE's front face.

The change rates of the mean flow depth $\frac{\Delta h}{\Delta x}$, mean depth-averaged flow velocity $\frac{\Delta \overline{u(x)}}{\Delta x}$ and mean volume flux $\frac{\Delta q(x)}{\Delta x}$ during the unsteady and steady phase in the upstream segment I and in the following five segments II to VI inside the MRE zone are provided in Figure 5.15. The mean values of the volume flux changes, its standard deviations and its relative standard deviations are given in Table 5.7. The mean values of $\frac{\Delta q(x)}{\Delta x}$ for each individual case are provided for the unsteady and the steady flow phase in the Appendix, section C.2.

Table 5.7. Statistics of the mean values of flux changes at the upstream edge (segments I and II) and inside the MRE zone (segments III to VI) for the variation of the relative width D_B/h_{max}.

Mean values of changes of volume flux $\Delta q(x)/\Delta x$		**Unsteady**		**Steady**		**average**
		I, II	**III to VI**	**I, II**	**III to VI**	
Case 1.0	**D_B/h_{max}=0.116 [m³/s/m]**	-0.163	-0.017	-0.345	-0.010	-0.134
Case 2.1	**D_B/h_{max}=0.232 [m³/s/m]**	-0.158	-0.012	-0.314	-0.011	-0.124
Case 2.2	**D_B/h_{max}=0.464 [m³/s/m]**	-0.153	-0.002	-0.285	0.002	-0.108
Mean of the mean values [m³/s/m]		-0.158	-0.009	-0.315	-0.006	-0.122
Standard deviation [m³/s/m]		**0.004**	**0.008**	**0.024**	**0.006**	**0.011**
Relative standard deviation [m³/s/m]		-0.025	-0.935	-0.077	-0.993	-0.508

Unsteady phase of bore propagation

- *In Figure 5.15.a),* upstream of the MRE zone in segment I, the flow depth increases between $\Delta h/\Delta x$ = 0.43 m/m for D_B/h_{max} = 0.116 and $\Delta h/\Delta x$ = 0.58 m/m for D_B/h_{max} = 0.464 due to backwater effects. In segment 2, only water which was not blocked can propagate. Therefore, the flow depth decreases between $\Delta h/\Delta x$ = -0.58 m/m for D_B/h_{max} = 0.116 and $\Delta h/\Delta x$ = -0.53 m/m for D_B/h_{max} = 0.464. The rate of flow depth reduction decreases while the bore propagates further through the MRE zone. It is noted that the differences between the here compared cases are relatively small.
- *In Figure 5.15.c),* the flow velocity decreases between $\Delta\overline{u(x)}/\Delta x$ = -4.4 m/s/m and $\Delta\overline{u(x)}/\Delta x$ = -4.6 m/s/m in the most upstream segment I and thereby is comparable in all three cases. In the first segment inside the MRE zone (segment II), the flow velocity increases more the greater the relative width is, as in case of D_B/h_{max} = 0.116, $\Delta\overline{u(x)}/\Delta x$ = 1.6 m/s/m, in case of D_B/h_{max} = 0.232, $\Delta\overline{u(x)}/\Delta x$ = 2.3 m/s/m and in case of D_B/h_{max} = 0.464, $\Delta\overline{u(x)}/\Delta x$ = 3.1 m/s/m. This is because the boundary layer near the MRE has a smaller influence on the flow velocities extracted in the cross-sections the greater the relative width is. The differences in flow velocities between the segments decrease with further bore propagation.

- *In Figure 5.15.e)*, the volume flux decreases in the most upstream segment I in all cases by $\Delta q(x)/\Delta x$ = 0.29 to $\Delta q(x)/\Delta x$ = 0.30 m³/s/m² and thereby does not vary significantly with the relative width of the MRE. Inside the MRE zone (segments II to VI), the flow depth varies similarly along the MRE zone in all cases, showing that the width of the MRE does have only little influence on the volume flux.

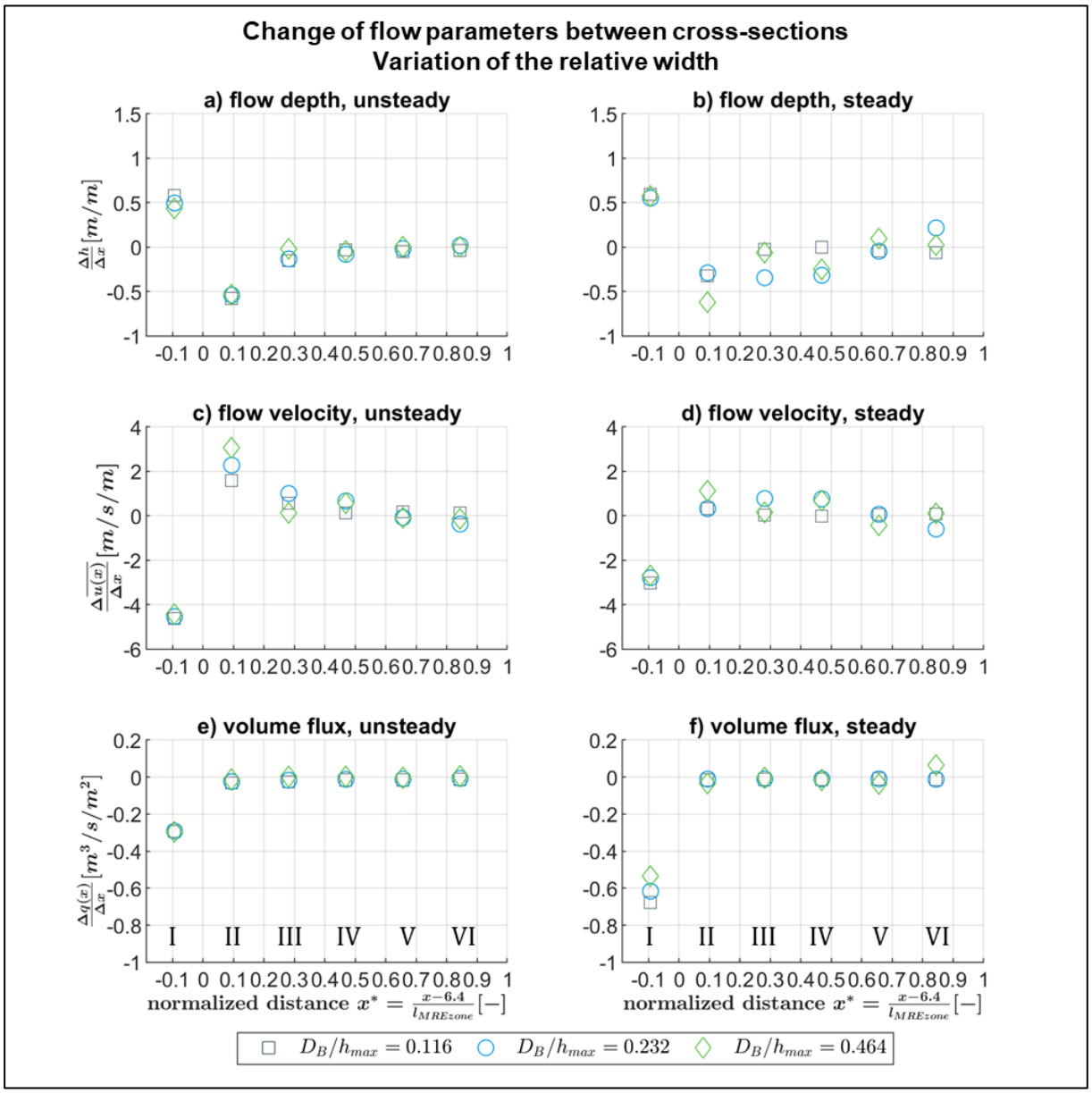

Figure 5.15. Effect of relative width D_B/h_{max} on the change of the flow parameters between cross-sections in the segments I to VI: a) flow depth during the unsteady phase, b) flow depth during the steady phase, c) depth-averaged flow velocity during the unsteady phase, d) depth-averaged flow velocity during the steady phase, e) volume flux during the unsteady phase, f) volume flux during the steady phase.

The observations indicate that the dependency of the flow through the MRE zone from the relative width D_B/h_{max} is very small. This is confirmed by Table 5.7, where the mean value of the flux reduction in the upstream segments I and II is by $\Delta q(x)/\Delta x$ = -0.158 m³/s/m² and the

standard deviation of the mean value is only 0.004 m³/s/m². In case of the segments inside the MRE zone, both the mean value and its standard deviation is with $\Delta q(x)/\Delta x$ = -0.009 m³/s/m² and $\Delta q(x)/\Delta x$ = 0.008 m³/s/m², respectively, very small.

Steady phase of bore propagation

- *In Figure 5.15.b)*, upstream of the MRE zone, the change of flow depth takes values between $\Delta h/\Delta x$ = 0.59 m/m and $\Delta h/\Delta x$ = 0.55 m/s, which are comparable to the values obtained for the unsteady flow phase. In the segments II to VI, the flow depths decrease in all cases but to a lesser extent the further the bore propagates through the MRE zone. The flow depth reduction is in all cases similar, but some exceptions are noted: In segment II, the flow depth in case of D_B/h_{max} = 0.464 decreases more than the other two cases (see Figure 5.14.d). In segment III, similar observations are made in case for D_B/h_{max} = 0.232 (see Figure 5.14.c). In segment IV, in both of these cases the flow depth decreases more than in case of D_B/h_{max} = 0.116. The reason is the location of the MRE. If the cross-section between the segments passes a MRE or is closely located in the wake of a MRE, the averaged flow depth is smaller than in the other cases. Only the basic configuration (case 1.0) with D_B/h_{max} = 0.116 guarantees the same relative position of the MRE to each of the cross-sections while in all other cases, the local effects around individual MRE can disturb the pattern (see section 5.4.5). In such cases, the deviations are interpreted as outliers rather than being influenced by the relative width.
- *In Figure 5.15.d)*, the flow velocity reduction in the upstream segment I is with values between $\Delta\overline{u(x)}/\Delta x$ = -2.7 and $\Delta\overline{u(x)}/\Delta x$ = -3.0 m/s/m comparable. All cases show a smaller backwater effect compared to the unsteady phase. Inside the MRE zone (segments II to VI) almost no change in the flow velocity is noted in all cases due to the channelling effect. Exceptions are noted due to the location of the MRE, particularly when it is located in a close distance downstream of a cross-section.
- *In Figure 5.15.f)*, the volume flux decreases in segment I between $\Delta q(x)/\Delta x$ = -0.68 m³/s/m² in case of D_B/h_{max} = 0.116 and $\Delta q(x)/\Delta x$ = -0.54 m³/s/m² in case of D_B/h_{max} = 0.464 due to a smaller impact of the boundary layer on the bore propagation (see above) and, therefore, depends slightly on D_B/h_{max}. In the further downstream segments II to VI, almost no change in volume flux is noted in all cases.

The observations indicate that the reduction of the volume flux is barely influenced by the relative width D_B/h_{max}. Referring to Table 5.7, this is confirmed for the segments I and II is by the small standard deviation of the mean value of $\Delta q(x)/\Delta x$ = 0.024 m³/s/m². In case of the segments inside the MRE zone, the standard deviation of the mean value is with $\Delta q(x)/\Delta x$ = 0.006 m³/s/m² even smaller. On average, the standard deviation of the volume fluxes when varying the relative MRE width is $\Delta q(x)/\Delta x$ = 0.011 m³/s/m², which is considerably less than when varying the shape.

The flow velocity patterns at z = 0.05 m show in all cases zones of higher flow velocities in the lateral gaps and lower velocities in the longitudinal gaps. In case of the largest distance between the MRE, the effect of the MRE starts to decrease towards the middle of the lateral gaps. In all cases, a channelling effect is noted, so that the flow velocities in the lateral gaps are almost maintained through the entire length of the MRE zone.

In the unsteady phase of bore propagation, energy losses are caused mainly upstream of the MRE zone. There is no clear correlation of the energy losses and the relative size of the MRE.

In the steady phase of bore propagation, energy losses are noted upstream of the MRE zone and show a small dependency from the relative size of the MRE.

The disturbance of the bore propagation indicates a small relation to the relative size of the MRE, as indicated by very small standard deviations of the mean values in Table 5.7. The standard deviations of the mean values are considerably smaller than in case of the shape variation in section 5.5.2, indicating that the variation of the relative width of the MRE has a relatively small influence on the energy losses.

5.5.4 Effect of the arrangement of macro-roughness elements (Cases 1.0, 3.1 & 3.2)

The maximum flow velocities in mean flow direction at z = 0.05 m above the bottom normalized by the case without MRE (case 0.0) for the investigated variations of the arrangement angle Ψ are presented in Figure 5.16. Only cubic MRE, being the predominant shape in urban areas, are exemplarily considered. The time series of flow depths, flow velocities and volume fluxes are given in Appendix, sections C.1.2 and C.1.5 for the basic configuration and the variations of the arrangement (cases 3.1 and 3.2), respectively.

Flow through MRE zone with arrangement angle Ψ = 0° (case 1.0)

Figure 5.16.b) represents the basic configuration (case 1.0) with the arrangement angle Ψ = 0°. Details of the flow field are provided in comparison with the flow field around a single MRE (case 0.1) in Figure 5.16.e). For a detailed description of the flow field it is referred to section 5.5.2.

Flow through MRE zone with arrangement angle Ψ = 26.565° (case 3.1)

In Figure 5.16.c), compared to the basic configuration in case 1.0, the group of MRE is rotated by an angle of Ψ = 26.565°. Due to this rotation, the MRE downstream of the most upstream row of MRE are located outside its sheltering wake. Furthermore, the front face of the MRE is now inclined so that the flow is less blocked and more deflected. Therefore, areas with high flow velocity can form. Due to the presence of more unsheltered MRE in the flow compared to case 1.0, the flow velocity decreases strongly during the bore propagation through segment II.

A detailed view on the flow field of the most upstream MRE is provided in Figure 5.16.f). The flow separation is noted closer to the upstream faces compared to case 1.0. The area of flow velocities, which is less than 75 % of the undisturbed flow field in case 0.0 is approximately

$1/4\ D_B$ long. The reason is that the inclined front faces partly deflect the flow, while in basic configuration the front faces are predominantly blocking the flow. Particularly at the deflecting MRE faces, high flow velocities can be observed (see also case 1.2, Figure 5.12.c)). The flow is directed towards the further downstream located rows of MRE and is there deflected again. This repeating process leads to a redirection of the entire flow field by the arrangement angle Ψ. From segment III onwards, the dominant flow direction adapted to Ψ. Hence, the MRE provide shelter for the further downstream located MRE.

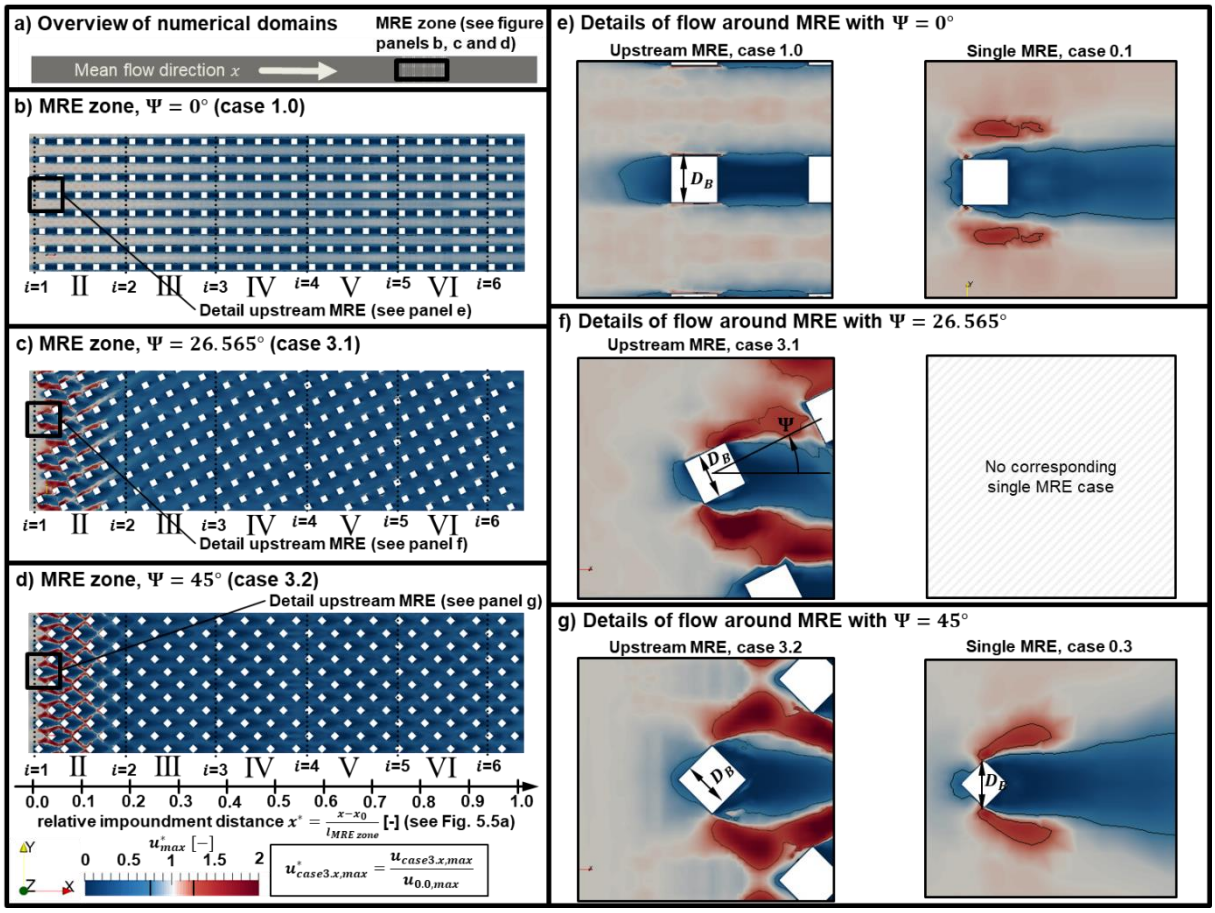

Figure 5.16. Effect of arrangements Ψ on normalized maximum flow velocities $u^*_{case3.x,max} = u_{case3.x,max}/u_{0.0,max}$ in mean flow direction at z = 0.05 m above the bottom through: a) Overview of numerical domains, MRE zone: b) Ψ = 0° (case 1.0), c) Ψ = 26.565° (case 3.1), d) Ψ = 45° (case 3.2), Details of flow around upstream MRE: e) Ψ = 0° (case 1.0) vs. case 0.1, f) Ψ = 26.565° (case 3.1), g) Ψ = 45° (case 3.2) vs. case 0.3. The dotted lines symbolize the cross-sections i (see Figure 5.5.b).

Flow through MRE zone with arrangement angle Ψ = 45° (case 3.2)

In Figure 5.16.d), the group of MRE is rotated by Ψ = 45°, due to which half of the MRE are moved out of the shelter of the further upstream located MRE. As the MRE itself are also rotated, the cube with flow-facing sides turns into a diamond with a flow-facing edge, so that the sides deflect the flow, which is comparable to case 1.2 (see Figure 5.12.d). However, here in case 3.2, the rotation of the entire MRE group leads to a staggered arrangement as the distance

between the MRE is smaller than in case 1.2. Therefore, higher velocities than in the undisturbed flow field occur only in segment II.

A more detailed representation of the flow field around a MRE in the most upstream located row is provided in Figure 5.16.g), together with the representation of the flow field around a single diamond-shaped MRE (equal to the representation in Figure 5.12.g). Although in both representations, the MRE have slightly different sizes (in case 3.2, the width is $\sqrt{2}D_B$ due to the rotation and in case 0.3 the width is D_B), the flow fields can qualitatively be compared. As the water is deflected on the front faces and joins the water which is approaching the lateral gaps in mean flow direction in both representations, the flow velocity increases in the lateral gaps of the most upstream located MRE, which leads to a comparable flow pattern as the deflection on the front faces of the single MRE. until the water is blocked by the front faces of the further downstream located MRE.

The spatial change of mean flow depths $\frac{\Delta h}{\Delta x}$, mean depth-averaged flow velocities $\frac{\Delta \overline{u(x)}}{\Delta x}$ and mean volume fluxes $\frac{\Delta q(x)}{\Delta x}$ during the unsteady and steady phase in the upstream segment I and five segments II to VI inside the MRE zone are provided in Figure 5.17. The mean values of the volume flux changes, its standard deviations and its relative standard deviations are given in Table 5.8. The mean values and standard deviations of the volume flux change for each individual case are provided for the unsteady and the steady flow phase in the annex, section C.2.

Table 5.8. Statistics of the mean values of flux changes at the upstream edge (segments I and II) and inside the MRE zone (segments III to VI) for the variation of the arrangement angle Ψ.

Mean values of changes of volume flux $\Delta q(x)/\Delta x$		**Unsteady**		**Steady**		**average**
		I, II	**III to VI**	**I, II**	**III to VI**	
Case 1.0	**Ψ = 0° [m³/s/m²]**	-0.163	-0.017	-0.345	-0.010	-0.134
Case 2.1	**Ψ = 26.565° [m³/s/m²]**	-0.226	-0.048	-0.445	0.020	-0.175
Case 2.2	**Ψ = 45° [m³/s/m²]**	-0.215	-0.078	-0.439	-0.003	-0.184
Mean of the mean value [m³/s/m²]		-0.201	-0.048	-0.410	0.002	-0.164
Standard deviation [m³/s/m²]		**0.028**	**0.025**	**0.046**	**0.013**	**0.028**
Relative standard deviation [-]		-0.14	-0.53	-0.11	5.36	1.146

Unsteady phase of bore propagation

- *In Figure 5.17.a)*, upstream of the MRE zone in segment I, the flow depth increases between $\Delta h/\Delta x$ = 0.58 m/m for Ψ = 0° and $\Delta h/\Delta x$ = 0.47 m/m for Ψ = 26.565° due to backwater effects. In segment II, only water which was not blocked can propagate. Therefore, the flow depth decreases between $\Delta h/\Delta x$ = -0.58 m/m for Ψ = 0° considerably more than in case of the rotated MRE, where $\Delta h/\Delta x$ = -0.30 m/m for Ψ = 26.565° and $\Delta h/\Delta x$ = -0.32 m/m for Ψ = 45°. The rate of flow depth reduction decreases during further bore propagation through the MRE zone in the sections III to VI. In this part of the MRE zone, there are differences between the three arrangement angles notable, but no clear pattern of the differences is seen. The differences are related to the positions of the MRE near the cross-sections between the segments and local flow effects (see section 5.4.5).

- *In Figure 5.17.c)*, the flow velocities decrease in the upstream segment I between $\Delta\overline{u(x)}/\Delta x$ = -3.8 m/s/m (for Ψ = 26.565°) and $\Delta\overline{u(x)}/\Delta x$ = -4.6 m/s/m (in the basic configuration with Ψ = 0°). It is noted that the decrease of the flow velocity is related to the increase in flow depth. The same applies to the increase of flow velocity in segment II, which corresponds to the decrease of the flow depth. In the further downstream located segments, the flow velocity decreases less with further bore propagation and no clear differences between the arrangement angels are noted.

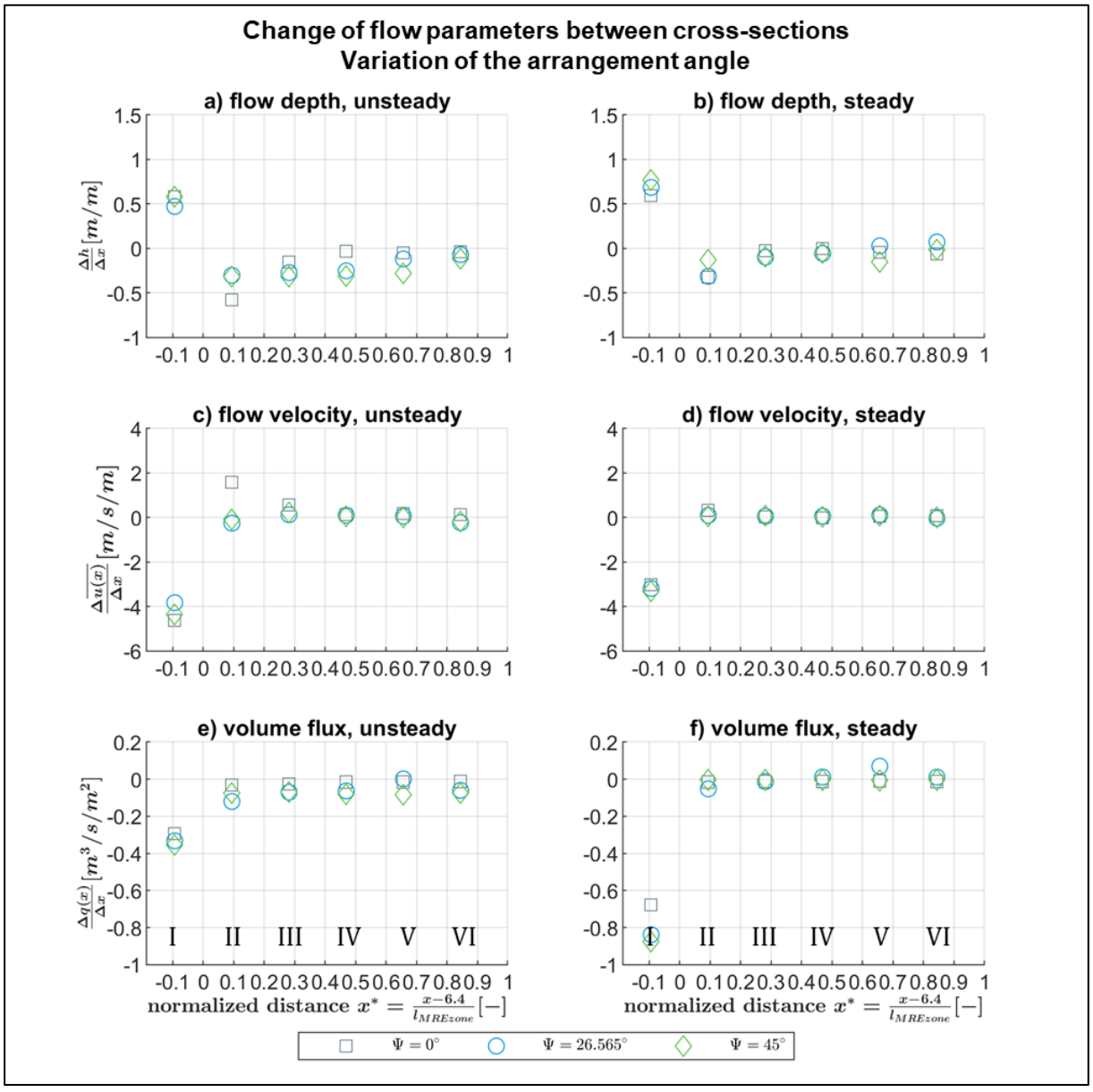

Figure 5.17. Effect of arrangement angles Ψ on the change of the flow parameters between cross-sections in the segments I to VI: a) flow depth during the unsteady phase, b) flow depth during the steady phase, c) depth-averaged flow velocity during the unsteady phase, d) depth-averaged flow velocity during the steady phase, e) volume flux during the unsteady phase, f) volume flux during the steady phase.

- *In Figure 5.17.e)*, in the upstream segment I the volume flux decreases with $\Delta q(x)/\Delta x$ = -0.36 m³/s/m² the most in case of the greatest arrangement angle Ψ = 45° and the least in case of Ψ = 0° with $\Delta q(x)/\Delta x$ = -0.29 m³/s/m². The reduction of the volume flux decreases with further propagation of the bore through the MRE zone. Similar to the development of flow depth and velocity, differences between the cases are dedicated to local flow effects due to the presence of the MRE close to the cross-sections (see section 5.4.5).

These observations are reflected in Table 5.8. In the upstream segments I and II, the cases with an arrangement angle Ψ > 0° are comparable to each other and result in greater volume flux reduction than the case with Ψ = 0°. Inside the MRE zone in the segments III to VI, the volume flux reduction is clearly related to the arrangement angle. Although the flux reduction rates in the individual segments are polluted with local flow effects, the averaged flux reduction rates are related to the arrangement angle.

Steady phase of bore propagation

- *In Figure 5.17.b)*, upstream of the MRE zone in segment I, the flow depth increases in a range from $\Delta h/\Delta x$ = 0.59 m/m in case of Ψ = 0° to $\Delta h/\Delta x$ = 0.77 m/m in case of Ψ = 45°. This range is slightly bigger than during the unsteady phase. In the most upstream segment in the MRE zone (segment II), the flow depth decreases with $\Delta h/\Delta x$ = -0.31 m/m and $\Delta h/\Delta x$ = -0.32 m/m in the cases of Ψ = 0° and Ψ = 26.565°, respectively, to a similar extent, while for Ψ = 45°, the flow depth reduces only by $\Delta h/\Delta x$ = -0.13 m/m only. Further downstream, the impact of the MRE on the flow depth decreases similarly in all cases to small values between $\Delta h/\Delta x$ = 0.00 m/m and $\Delta h/\Delta x$ = -0.05 m/m. Larger deviations from these values in the segments V and VI are dedicated to the presence of MRE inside the cross-sections (see Figure 5.16.b), c) and section 5.4.5).
- *In Figure 5.17.d)*, the flow velocities in segment I decrease between $\Delta\overline{u(x)}/\Delta x$ = -3.0 m/s/m and $\Delta\overline{u(x)}/\Delta x$ = -3.3 m/s/m and are comparable to each other. Further downstream, the velocities remain almost constant as only very small reductions rates of $\Delta\overline{u(x)}/\Delta x$ = 0.1 m/s/m differ only slightly among each other.
- *In Figure 5.17.f)*, the volume flux in segment I is reduced by $\Delta q(x)/\Delta x$ = -0.68 m³/s/m² (for Ψ = 0°) and $\Delta q(x)/\Delta x$ = -0.88 m³/s/m² (for Ψ = 45°) and, thus, the flux reduction rate is related to the arrangement angle. This reduction is more than two times greater than during the unsteady phase. Further downstream, the volume flux varies between the cross-section between $\Delta q(x)/\Delta x$ = -0.01 and $\Delta q(x)/\Delta x$ = 0.01 m³/s/m². Only in case of Ψ = 26.565° the flux reduction rate can take values up to $\Delta q(x)/\Delta x$ = 0.07 m³/s/m² due to local flow effects.

Similar to the unsteady case, the standard deviation of the change of the volume flux $\Delta q(x)/\Delta x$ in the upstream segments I and II of the cases with the arrangement angle Ψ > 0° are comparable to each other and are greater than for the case with Ψ = 0°, as it is seen from Table 5.8. Inside the MRE zone, the changes remain very small and no clear correlation between Ψ and $\Delta q(x)/\Delta x$ are noted. Referring to the standard deviations in Table 5.8, the highest impact of Ψ

is seen in the upstream segments I and II under steady flow conditions, while the least impact is noted inside the MRE zone (segments III to VI) under steady flow conditions. On average, the standard deviation of the fluxes when varying the relative MRE width is $\Delta q(x)/\Delta x$ = 0.028 m³/s/m², which is higher than when varying the relative MRE width, but less when compared to when varying the shape.

The disturbances of the flow patterns increase with increasing arrangement angle Ψ and hinders the flow to develop a channel-like flow pattern.

During the unsteady phase of the bore propagation, energy losses are mainly caused at the front face of the most upstream MRE, resulting in a backwater effect, and to a smaller extent inside the MRE zone. There, the flux reduction is correlated with the arrangement angle.

During the steady phase of bore propagation, energy losses are noted mainly at the front face of the most upstream MRE zone as well, but they exceed the losses during the unsteady phase approximately by factor 2, while the losses inside the MRE zone are negligible.

The correlation of the energy losses with the arrangement angle is noted only inside the MRE zone during unsteady flow conditions, where the energy losses are smaller than at the front face of the most upstream MRE. In the segments I and II, in which arrangement angles of Ψ > 0° lead to the greater flux reduction than for Ψ = 0°, the energy losses are comparable to each other, which is seen in Table 5.8. The standard deviations are smaller than compared to the variation of the shape (see section 5.5.2), but still considerably greater than in case of the relative width variation (see section 5.5.3).

5.5.5 Effect of the relative spacing between macro-roughness elements (Cases 1.0, 4.1 to 4.4)

The normalized maximum flow velocities in the mean flow direction at z = 0.05 m above the bottom normalized by the case without MRE (case 0.0) for the investigated variations of the relative spacing S_G/D_B between the MRE are presented in Figure 5.18. Only cubic MRE, being the predominant shape in urban areas, are considered. The time series of flow depths, velocities and fluxes are given in Appendix, section C.1.2 for the basic configuration and section C.1.6 for the other four investigated relative spacings.

Flow through the MRE zone with S_G/D_B = 0.5 (case 4.1)

Figure 5.18.b) provides the flow field for the relative spacing S_G/D_B = 0.5. The permeability of the MRE zone is reduced to 1/3 of the area upstream of the roughness elements. Compared to the other cases 4.x, the boundary layer of the MRE influence the flow field to a large extent so that only small flow velocities are noted inside the MRE zone.

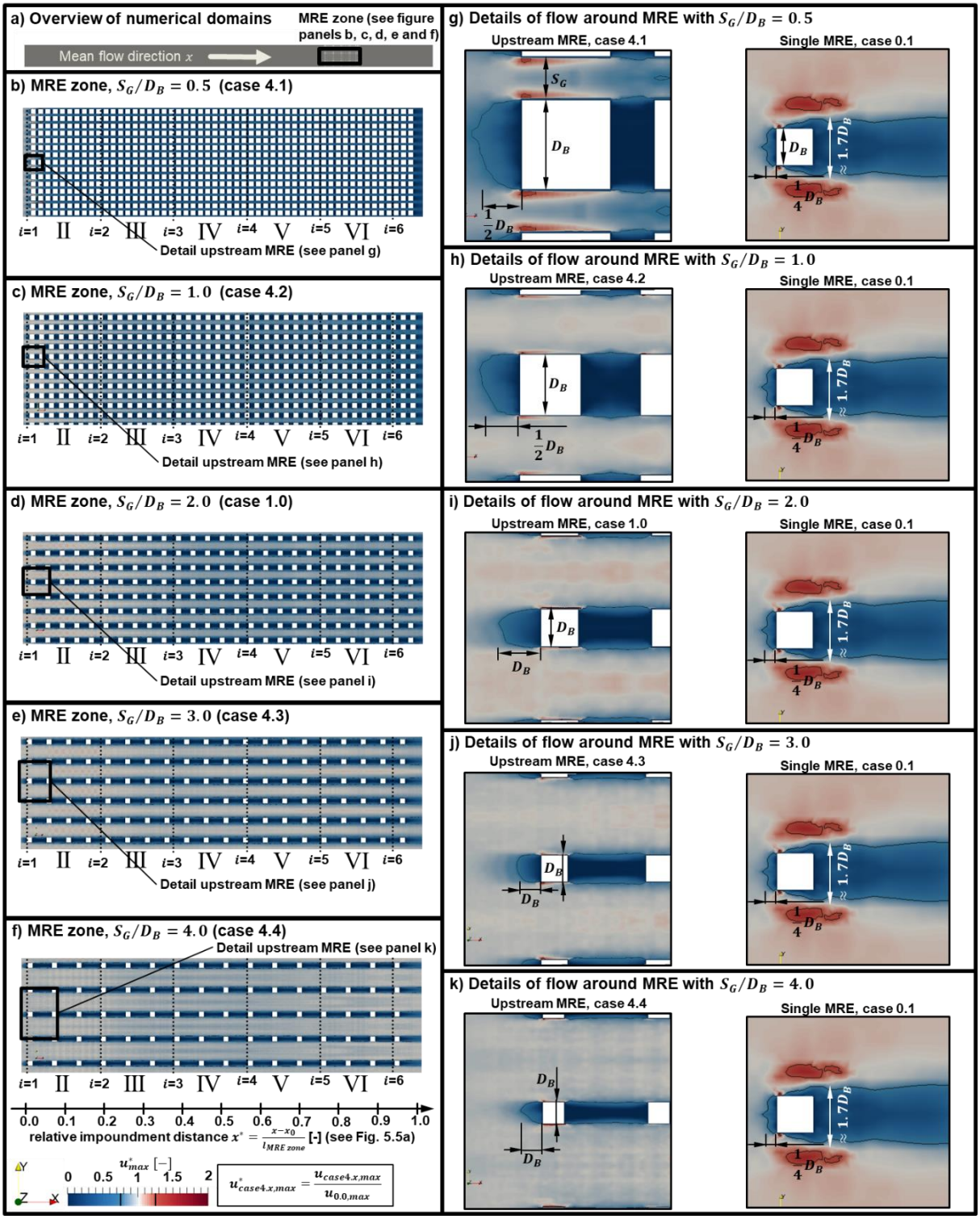

Figure 5.18. Effect of relative spacings S_G/D_B on normalized maximum flow velocities $u^*_{case4.x,max} = u_{case4.x,max}/u_{0.0,max}$ in mean flow direction at z= 0.05 m above the bottom through MRE: a) Overview of numerical domains, MRE zones: b) S_G/D_B = 0.5 (case 4.1), c) S_G/D_B = 1.0 (case 4.2), d) S_G/D_B = 2.0 (case 1.0), e) S_G/D_B = 3.0 (case 4.3), f) S_G/D_B = 4.0 (case 4.4), Details of flow around upstream MRE: g) S_G/D_B = 0.5 (case 4.1) vs. case 0.1, h) S_G/D_B = 1.0 (case 4.2) vs. case 0.1, i) S_G/D_B = 2.0 (case 1.0) vs. case 0.1, j) S_G/D_B = 3.0 (case 4.3) vs. case 0.1, k) S_G/D_B= 4.0 (case 4.4) vs. case 0.1. The dotted lines symbolize the cross-sections i (see Figure 5.5.b).

Figure 5.18.g) represents a detailed view on the flow field around a MRE located in the most upstream row of MRE. The flow field is compared to the one around the single MRE of case 0.1. The contour line of flow velocities of 75 % of the undisturbed flow field (in case 0.0) is used as indicator for the flow separation upstream of the most upstream located MRE. Its length is approximately $1/2\ D_B$, which is as double as long as in the single MRE. In the lateral gaps, the highest flow velocities are noted at the side faces of the most upstream MRE row. They can take values of more than 125 % of the undisturbed flow field. In the longitudinal gaps, the flow velocities are very small. The large difference between flow velocities in longitudinal and lateral gaps show a channelling effect.

Flow through the MRE zone with S_G/D_B = 1.0 (case 4.2)

In Figure 5.18.c), where the relative spacing S_G/D_B = 1.0, the permeability of the MRE zone is reduced to 1/2 of the area upstream of the roughness elements. In contrast to case 4.1, higher flow velocities than in the case 0.0 without MRE are found in the lateral gaps of the MRE in segment II.

A detailed view on the flow field of the most upstream MRE is provided in Figure 5.18.h). Upstream of the front face of the MRE, the area with flow velocities of less than 75 % of the undisturbed flow velocity in case 0.0 is approximately $1/2\ D_B$ long. In the middle of the lateral gaps, flow velocities take larger values than in the narrower case 4.1, but at the side faces of the first MRE row, the flow velocities are increased to a lesser extent.

Flow through the MRE zone with S_G/D_B = 2.0 (case 1.0)

Figure 5.18.d) represents the basic configuration case 1.0 with a relative width S_G/D_B = 2.0. Details of the flow field are depicted in comparison to the flow field around a single MRE (case 0.1) in Figure 5.18.i). For a detailed description it is referred to section 5.5.2.

Flow through the MRE zone with S_G/D_B = 3.0 (case 4.3)

Figure 5.18.e) provides the flow field in the MRE zone with a relative spacing of S_G/D_B = 3.0, so that the permeability of the MRE zone increased to 3/4. The flow velocities increase in the lateral gaps, especially in the area of the first rows of MRE. Further downstream, the flow velocities decrease slightly. However, higher flow velocities than in the case 0.0 without MRE are found in the middle of the lateral gaps in all segments of the MRE zone.

A detailed view on the flow field of the most upstream MRE is provided in Figure 5.18.j). The area with flow velocities of less than 75 % of the undisturbed flow velocity in case 0.0 upstream of the front face of the MRE is approximately 1 D_B long. The flow velocity in the lateral gaps does not show a clear increase of the flow velocity towards the middle of the gap, which is due to the large width of the gap and the relatively small ratio of blocking MRE front faces.

Flow through the MRE zone with S_G/D_B = 4.0 (case 4.4)

Figure 5.18.f) provides the flow field in the MRE zone with a relative spacing of S_G/D_B = 4.0. The permeability of the MRE zone is 4/5. It is seen that in the relatively wide lateral gaps the flow velocity first increases with increasing distance from the lateral sides of the MRE and then

decreases towards the middle of the gaps. This has been noted in the case of large relative widths S_G/h_{max} as well (see section 5.5.3), where $S_G/h_{max} \geq 0.464$. Here, S_G/h_{max} = 0.928. It can be assumed that the highest velocities occur in a certain distance from the roughness elements. As long as the lateral gaps are $S_G/h_{max} < 0.464$, the maximum velocities are found in the middle of the gaps. In case of wider lateral gaps, the flow velocities decrease again towards the middle of the gap and approach values similar to the reference case.

Figure 5.18.k) represents a detailed view on the flow field around a MRE located in the most upstream row of MRE. Flow separation, indicated by the contour line of flow velocities of 75 % of the undisturbed velocities (case 0.0), is noted at an upstream distance from the front face of the most upstream MRE of approximately $1D_B$. Although in the lateral gaps the flow velocities are not considerably higher than in the undisturbed case due to the high permeability of the MRE zone, there is still a clear separation of the flow in the lateral gaps and the longitudinal gaps, where very low flow velocities of less than 75 % of case 0.0 are noted.

The spatial change of mean flow depths $\frac{\Delta h}{\Delta x}$, mean depth-averaged flow velocities $\frac{\Delta \overline{u(x)}}{\Delta x}$ and mean volume fluxes $\frac{\Delta q(x)}{\Delta x}$ during the unsteady and steady phase in the upstream segment I and five segments II to VI inside the MRE zone are provided in Figure 5.19. The mean values of the volume flux changes, its standard deviations and relative standard deviations are provided in Table 5.9. The mean values of the volume flux change for each individual case are provided for the unsteady and the steady flow phase in the Appendix, section C.2.

Table 5.9. Standard deviations of mean values of volume flux changes upstream and inside the MRE zone for the variation of the relative spacing S_G/D_B.

Mean values of changes of volume flux $\Delta q(x)/\Delta x$		**Unsteady**		**Steady**		**mean**
		I, II	**III to VI**	**I, II**	**III to VI**	
Case 4.1	**S_G/D_B = 0.5 [m³/s/m²]**	-0.275	0.004	-0.281	-0.007	-0.140
Case 4.2	**S_G/D_B = 1.0 [m³/s/m²]**	-0.218	-0.006	-0.271	-0.010	-0.126
Case 1.0	**S_G/D_B = 2.0 [m³/s/m²]**	-0.163	-0.017	-0.345	-0.010	-0.134
Case 4.3	**S_G/D_B = 3.0 [m³/s/m²]**	-0.128	-0.028	-0.284	-0.008	-0.112
Case 4.4	**S_G/D_B = 4.0 [m³/s/m²]**	-0.097	-0.034	-0.211	-0.004	-0.086
Mean of the mean values [m³/s/m²]		-0.176	-0.016	-0.278	-0.008	-0.120
Standard deviation [m³/s/m²]		**0.064**	**0.014**	**0.043**	**0.002**	**0.030**
Relative standard deviation [-]		-0.361	-0.845	-0.153	-0.277	-0.409

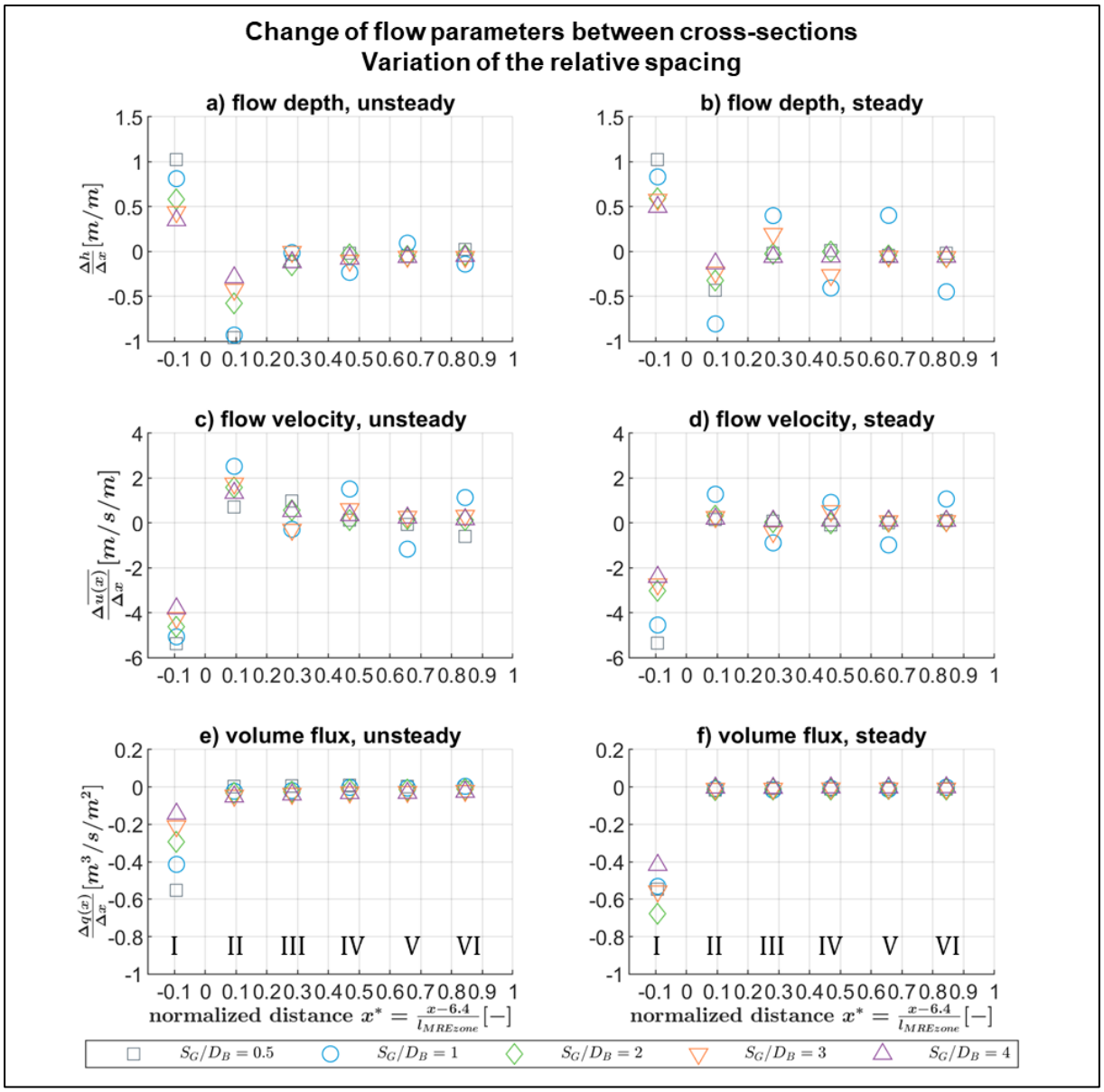

Figure 5.19. Effect of relative spacing S_G/D_B on the change of the flow parameters between cross-sections in the segments I to VI: a) flow depth during the unsteady phase, b) flow depth during the steady phase, c) depth-averaged flow velocity during the unsteady phase, d) depth-averaged flow velocity during the steady phase, e) volume flux during the unsteady phase, f) volume flux during the steady phase.

Unsteady phase of bore propagation

- *In Figure 5.19.a)*, the flow depth increases upstream of the MRE zone in segment I due to backwater effects. The increase is with $\Delta h/\Delta x$ = 1.01 m/m the greatest in case of the smallest spacing of S_G/D_B = 0.5 and with $\Delta h/\Delta x$ = 0.35 m/m the smallest in case of the greatest spacing of S_G/D_B = 4.0. In the most upstream segment II in the MRE zone, the water depth decreases with $\Delta h/\Delta x$ = -0.96 m/m the most in case of S_G/D_B = 0.5 as only a relatively small amount of water can propagate through the most upstream row of MRE. The more S_G/D_B increases the least becomes the reduction rate of the flow depth.

It is with $\Delta h/\Delta x$ = -0.29 m/m the smallest in case of S_G/D_B = 4.0. Inside the MRE zone (segments III to VI), the flow depth reduction decreases while the bore propagates further, but to a much lesser extent as in the upstream segments. The observations can be explained with the channelling effect. As soon as the bore propagates through the lateral gaps in the most upstream row of MRE, the way for the water remains relatively undisturbed as all MRE's located further downstream are located in the wakes of the upstream MRE's and thereby are mostly sheltered by them. Therefore, no clear dependency from S_G/D_B is noted inside the MRE zone. The case with S_G/D_B = 1.0 shows a slightly oscillating pattern, which is related to the presence of the MRE inside the cross-sections (see Figure 5.18.b), leading to a higher flow depth reduction, when a MRE is located at the outlet of a segment and, hence, the water content is smaller due to local flow effects induced by MRE located close or inside the cross-sections (see section 5.4.5). This is the case for segment I, III and V. In contrast, the segments with a MRE located at the inlet section show smaller flow depth reduction (segments II and IV).

- *In Figure 5.19.c)*, the flow velocity decreases upstream of the MRE zone in segment I due to backwater effects. The decrease is with $\Delta\overline{u(x)}/\Delta x$ = -5.4 m/s/m the greatest in case of S_G/D_B = 0.5 and the smallest with $\Delta\overline{u(x)}/\Delta x$ = -3.8 m/s/m in case of S_G/D_B = 4.0. Inside the MRE zone (segments II to VI), no clear dependency of the flow velocity change to S_G/D_B can be observed due to local flow effects (see section 5.4.5).
- *In Figure 5.19.e)*, the volume flux decreases upstream of the MRE zone in segment I due to backwater effects. The decrease is with $\Delta q(x)/\Delta x$ = -0.55 m³/s/m² the greatest in case of S_G/D_B = 0.5 and with $\Delta q(x)/\Delta x$ = -0.14 m³/s/m² in case of S_G/D_B = 4.0. Inside the MRE zone (segments II to VI), the reduction of volume flux takes values of less than $\Delta q(x)/\Delta x$ = -0.05 m³/s/m² and is relatively small in all investigated cases.

These observations are reflected by the statistical analyses summarized in Table 5.9. The impact of the relative spacing in the upstream segments during unsteady flow conditions is with a standard deviation of $\Delta q(x)/\Delta x$ = 0.064 m³/s/m² considerably greater than inside the MRE zone with a standard deviation of $\Delta q(x)/\Delta x$ = 0.014 m³/s/m².

Steady phase of bore propagation

- *In Figure 5.19.b)*, upstream of the MRE zone in segment I, the mean values for the change in flow depth show a comparable behaviour as during the unsteady phase (see Figure 5.19.a). In the downstream segments, the oscillating effect of the MRE in the cross-sections is more pronounced than during the unsteady flow conditions.
- *In Figure 5.19.d)*, comparable observations to the unsteady flow conditions (see Figure 5.19.c) are made.
- *In Figure 5.19.f)*, upstream of the MRE zone in segment I, the volume flux reduces in case of the smallest relative spacing of S_G/D_B = 0.5 by $\Delta q(x)/\Delta x$ = -0.547 m³/s/m² and in case of the greatest relative spacing of S_G/D_B = 4.0 with $\Delta q(x)/\Delta x$= -0.417 m³/s/m². The greatest volume flux reduction, however, is found for S_G/D_B = 2.0 with $\Delta q(x)/\Delta x$ = -0.677 m³/s/m². The reason for this inconsistency is related to the extent of the backwater effect, which for the smallest relative spacings S_G/D_B = 0.5 and S_G/D_B = 1.0 during steady flow conditions extents further upstream than segment I.

Consequently, the inlet cross-section of segment I already exhibits a reduced volume flux. Therefore, the flux reduction over the length of the cross-section Δx takes smaller values in these configurations. Inside the MRE zone (segments II to VI), almost no change in volume flux is observed.

These observations are reflected in Table 5.9, where under steady flow conditions the standard deviation of the volume flux changes in the segments I and II takes a value of 0.043 m³/s/m² and inside the MRE zone in the segments III to VI 0.002 m³/s/m² only. In contrast to the previously investigates MRE parameter variations of the shape, the relative width and the arrangement angle, the highest impact of the relative spacing is here noted during the unsteady flow phase. The standard deviation of the volume flux change in the segments I and II is with 0.064 m³/s/m² greater than during the steady flow conditions. On average, the standard deviation of the fluxes when varying the relative MRE width is $\Delta q(x)/\Delta x$ = 0.030 m³/s/m², which is higher than when varying the arrangement, but less when compared to when varying the shape.

The flow patterns show a channelling effect for all considered relative spacings S_G/D_B between the MRE. With increasing lateral spacing, the flow velocity increases towards the middle of the lateral gaps. For a relative spacing $S_G/D_B > 3$, the flow velocity decreases towards the middle and takes values similar to the reference case.

During the unsteady phase of bore propagation, energy losses increase with decreasing spacing of the MRE, mainly due to blockage of the flow upstream of the MRE zone.

During the steady phase of bore propagation, energy losses are noted almost only upstream of the MRE zone. For relative spacings $S_G/D_B < 2$, the backwater effect extents over the upstream segment I.

For the tested configurations, energy losses increase with decreasing relative spacing S_G/D_B under both unsteady and steady flow conditions for $S_G/D_B > 1$ in the upstream segments I and II and, less pronounced, inside the MRE zone during unsteady flow conditions. The impact of the relative spacing on the energy losses is slightly smaller than in case of the shape. During unsteady flow conditions, its impact is higher than the one of the arrangement angle. During steady flow conditions, it is slightly smaller. On average, the impact of the relative spacing is second to the variation of the shape.

5.5.6 Effect of the relative height of macro-roughness elements (Cases 1.0, 5.1 to 5.4)

The height of the roughness elements h_B is related to the maximum bore height h_{max} = 0.345 m at x^* = 0.5 (see section 5.5.1, Table 5.4). The maximum flow velocity in the mean flow direction x is normalized by the maximum flow velocity of the case without any MRE (case 0.0) u^*_{max} at z = 0.05 m above the bottom. Like in the previous section, only cubic MRE are considered. The results of four configurations with relative heights h_B/h_{max} = 0.25, 0.5, 0.75, 1.0 and a basic configuration $h_B/h_{max} \gg 1$ are presented in Figure 5.20. The time series of flow

depths, flow velocities and volume fluxes are given in Appendix, section C.1.2 for the basic configuration and section C.1.7 for the other four investigated relative heights.

Flow through the MRE zone with $h_B/h_{max} \gg 1$ (case 1.0)

Figure 5.20.b) provides the flow field of the basic configuration with $h_B/h_{max} \gg 1$. Details of the flow field are depicted in comparison with the flow field around a single MRE (case 0.1) in Figure 5.20.g). For a detailed description it is referred to section 5.5.2.

Flow through the MRE zone with $h_B/h_{max} = 1$ (case 5.1)

Figure 5.20.c) provides the flow field of case 5.1 with $h_B/h_{max} = 1$. The area of low flow velocities is wider and the area of high flow velocities in the lateral gaps is narrower compared to the basic configuration (see Figure 5.20.b).

A detailed view on the flow field around the most upstream MRE is provided in Figure 5.20.h). The presence of the MRE cause increased flow depths on the upstream side of the MRE so that the MRE are overflown. Due to the presence of the MRE, the flow depth in the wake is smaller so that the overflowing water is falling down downstream of the MRE and partly at the sides of the MRE. This induces a vertical velocity component in the flow field. As the motion of the water in the close lateral distance of the MRE is disturbed by the induction of additional vortices by the overflowing water, energy is taken out from the flow so that the flow velocity in the mean flow direction is reduced. Therefore, in the lateral gaps only a narrower part remains with increased flow velocities. The additional vertical vortices lead to short sections of increased horizontal flow velocities, which are located in an angle of approximately 45° downstream of the MRE (see Figure 5.20.h), where velocities higher than 125 % of the undisturbed flow velocities can occur. In the longitudinal gaps, the flow velocities are very low so that a channelling effect in the lateral gaps can still be noted. The flow velocity decreases with increasing propagation distance.

Flow through the MRE zone with $h_B/h_{max} = 0.75$, $h_B/h_{max} = 0.5$ and $h_B/h_{max} = 0.25$ (cases 5.2, 5.3 and 5.4)

Figure 5.20.d), e) and f) provide the flow field of case 5.2, 5.3 and 5.4 with $h_B/h_{max} = 0.75$, $h_B/h_{max} = 0.5$ and $h_B/h_{max} = 0.25$, respectively. In the lateral gaps, the width of the area of low and high flow velocities is comparable to the case of $h_B/h_{max} = 1$, indicating that similar processes during overflow of the MRE take place.

Detailed views on the flow fields around the most upstream MRE are provided in Figure 5.20.i), j) and k). The short sections of high flow velocities are noted as in the previously described case, but here, the flow velocities increase with decreasing MRE height. Increasing height of the MRE lead to an increased shelter for the downstream-located MRE and, consequently, to less flow velocity reduction. As long as the MRE are overflown ($h_B/h_{max} \leq 1$), then higher MRE result in higher flow obstruction.

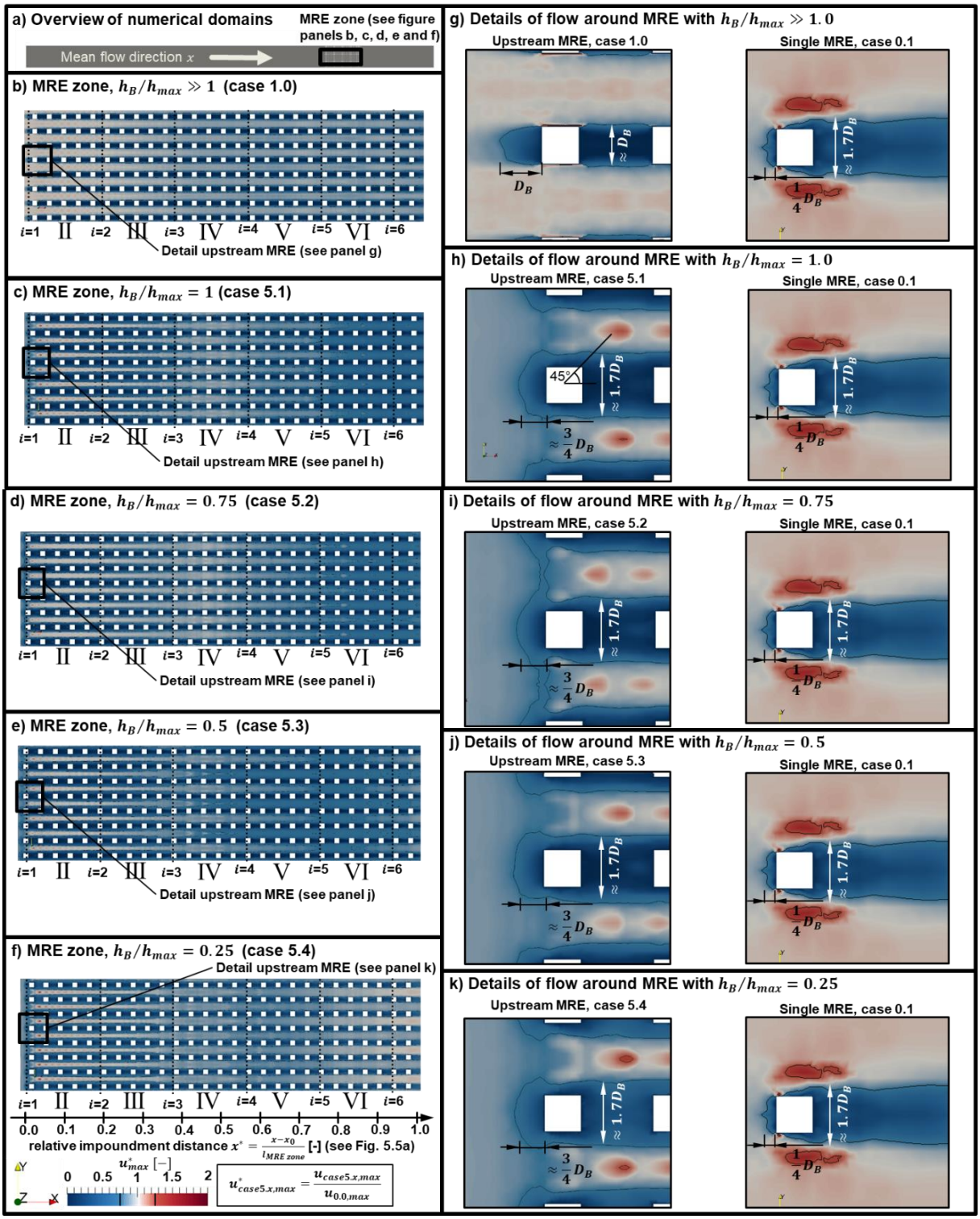

Figure 5.20. Effect of relative height h_B/h_{max} on normalized maximum flow velocities $u^*_{case5.x,max} = u_{case5.x,max}/u_{0.0,max}$ in mean flow direction at z = 0.05 m above the bottom through MRE: a) Overview of numerical domains, MRE zones: b) $h_B/h_{max} \gg 1.0$ (case 1.0), c) h_B/h_{max} = 1.0 (case 5.1), d) h_B/h_{max} = 0.75 (case 5.2), e) h_B/h_{max} = 0.5 (case 5.3), f) h_B/h_{max} = 0.25 (case 5.4), Details of flow around upstream MRE: g) $h_B/h_{max} \gg 1.0$ (case 1.0) vs. case 0.1, h) h_B/h_{max} = 1.0 (case 5.1), i) h_B/h_{max} = 0.75 (case 5.2), j) h_B/h_{max} = 0.5 (case 5.3), k) h_B/h_{max} = 0.25 (case 5.4). The dotted lines symbolize the cross-sections i (see Figure 5.5.b).

The spatial change of mean flow depths $\frac{\Delta h}{\Delta x}$, mean depth-averaged flow velocities $\frac{\Delta \overline{u(x)}}{\Delta x}$ and mean volume fluxes $\frac{\Delta q(x)}{\Delta x}$ during the unsteady and steady phase in the upstream segment I and five segments II to VI inside the MRE zone are provided in Figure 5.21. The mean values of the volume flux changes, its standard deviations and relative standard deviations are provided in Table 5.10. The mean values of the volume flux change for each individual case are provided for the unsteady and the steady flow phase in the Appendix, section C.2.

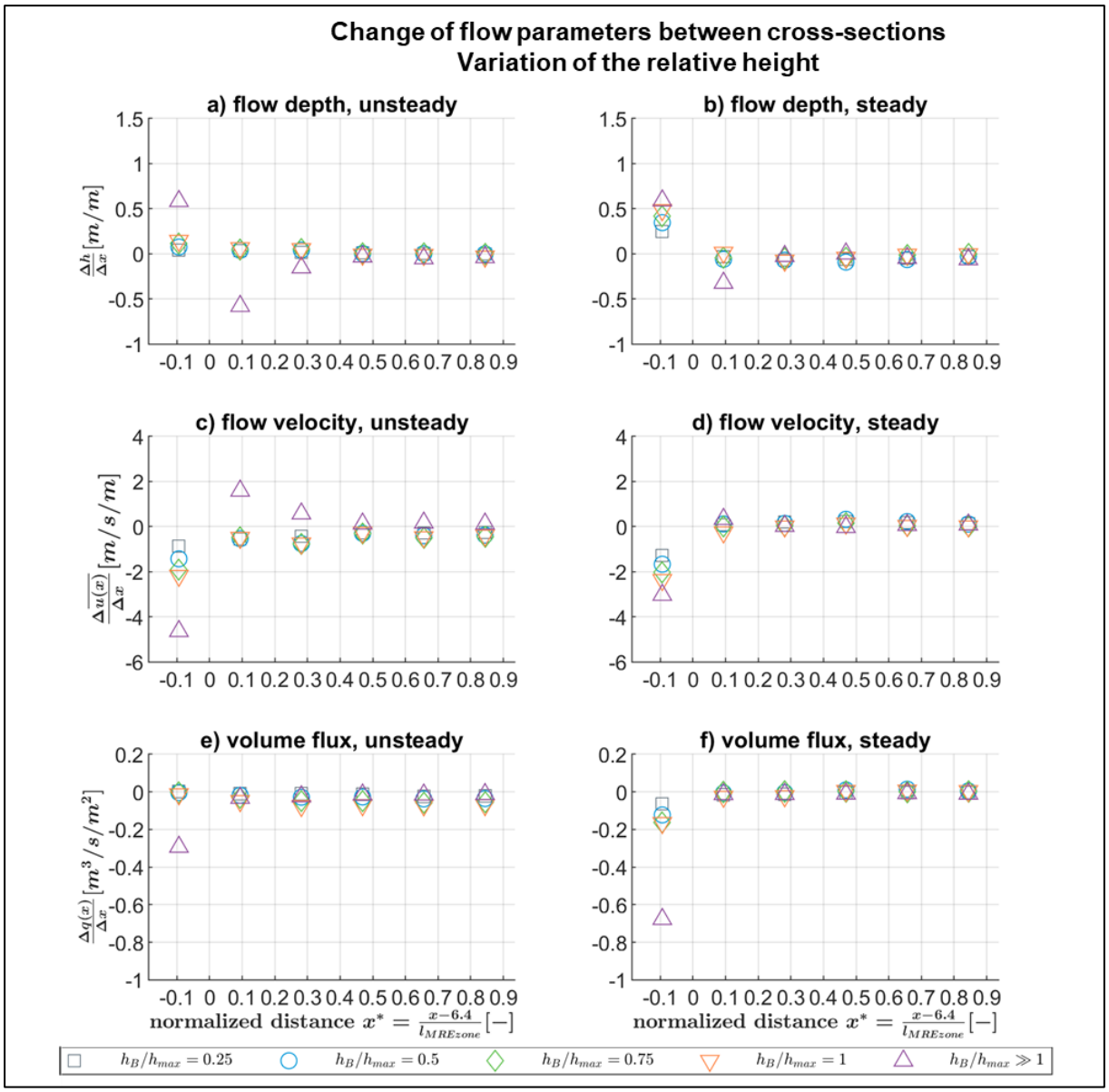

Figure 5.21. Effect of relative height h_B/h_{max} on the change of the flow parameters between cross-sections in the segments I to VI: a) flow depth during the unsteady phase, b) flow depth during the steady phase, c) depth-averaged flow velocity during the unsteady phase, d) depth-averaged flow velocity during the steady phase, e) volume flux during the unsteady phase, f) volume flux during the steady phase.

Table 5.10. Statistics of the mean values of flux changes at the upstream edge (segments I and II) and inside the MRE zone (segments III to VI) for the variation of the relative MRE height (h_B/h_{max}).

Mean values of changes of volume flux $\Delta q(x)/\Delta x$		**Unsteady**		**Steady**		**mean**
		I, II	**III to VI**	**I, II**	**III to VI**	
Case 5.1	**h_B/h_{max} = 0.25 [m³/s/m²]**	-0.001	-0.015	-0.039	-0.005	-0.015
Case 5.2	**h_B/h_{max} = 0.5 [m³/s/m²]**	-0.011	-0.032	-0.065	0.006	-0.025
Case 5.3	**h_B/h_{max} = 0.75[m³/s/m²]**	-0.017	-0.052	-0.080	0.003	-0.036
Case 5.4	**h_B/h_{max} = 1.0 [m³/s/m²]**	-0.031	-0.072	-0.095	-0.001	-0.050
Case 1.0	**$h_B/h_{max} \gg$ 1.0 [m³/s/m²]**	-0.163	-0.017	-0.345	-0.010	-0.134
Mean of the mean values [m³/s/m²]		-0.045	-0.037	-0.125	-0.001	-0.052
Standard deviation [m³/s/m²]		**0.060**	**0.022**	**0.112**	**0.006**	**0.050**
Relative standard deviation [-]		-1.346	-0.576	-0.896	-4.054	-1.718

During the unsteady phase of bore propagation

- *In Figure 5.21.a)*, upstream of the MRE zone in segment I, the flow depth increases considerable in the emerged case (basic configuration, case 1.0). It changes by a rate of $\Delta h/\Delta x$ = 0.58 m/m due to the backwater effect. The submerged cases (5.1-5.3) show flow depth changes between $\Delta h/\Delta x$ = 0.04 and $\Delta h/\Delta x$ = 0.14 m/m and the change are hereby considerably smaller. The smallest values are found for the smallest relative height, while it is increasing with increasing MRE heights. In segment II, which is the most upstream segment of the MRE zone, the flow depth decreases only for the emerged case with $\Delta h/\Delta x$ = -0.58 m/m (case 1.0). The submerged cases, the flow depth increases by values between $\Delta h/\Delta x$ = 0.03 m/m (case 5.1) and $\Delta h/\Delta x$ = 0.06 m/m (case 5.4). The higher the MRE, the more the flow depth increases. With further propagation of the bore through the MRE zone, the rates of change tend towards zero.
- *In Figure 5.21.c)*, the depth-averaged flow velocity decreases in segment I in all cases. The reduction rate is with $\Delta\overline{u(x)}/\Delta x$ = -0.86 m/s/m the smallest in case of the smallest MRE (case 5.1). It increases gradually to $\Delta\overline{u(x)}/\Delta x$ = -2.2 m/s/m for the tallest submerged MRE (case 5.4) and doubles to $\Delta\overline{u(x)}/\Delta x$ = -4.6 m/s/m for the emerged case (case 1.0). In segment II, the flow velocity increases only in the emerged case by a rate of $\Delta\overline{u(x)}/\Delta x$ = 1.59 m/s/m. In the submerged cases, the flow velocity further decreases by rates between $\Delta\overline{u(x)}/\Delta x$ = -0.56 m/s/m and $\Delta\overline{u(x)}/\Delta x$ = -0.47 m/s/m, indicating that the differences between the submerged cases are relatively small. The flow velocity reduction is decreasing towards values between $\Delta\overline{u(x)}/\Delta x$ = -0.26 and $\Delta\overline{u(x)}/\Delta x$ = -0.39 m/s/m (the lowest for the smallest and the highest for the tallest). In the emerged case, the flow velocity is increased inside the MRE zone due to the channelling effect and the rate of increase becomes smaller with further bore propagation and takes values between $\Delta\overline{u(x)}/\Delta x$ = 1.6 and $\Delta\overline{u(x)}/\Delta x$ = 0.12 m/s/m.
- *In Figure 5.21.e)*, the volume flux varies between $\Delta q(x)/\Delta x$ = -0.01 m³/s/m² and $\Delta q(x)/\Delta x$ = 0 m³/s/m² in the submerged cases and, hence, does not change considerably. In the emerged case (case 1.0), the volume flux reduces by $\Delta q(x)/\Delta x$ = -0.29 m³/s/m². In the most upstream segment of the MRE zone (segment II), the volume flux changes by values between $\Delta q(x)/\Delta x$ = -0.00 m³/s/m² and $\Delta q(x)/\Delta x$ = -0.07 m³/s/m² in the submerged cases, depending on the MRE height

(higher reduction for the taller MRE). In the emerged case, the volume flux changes by only $\Delta q(x)/\Delta x$ = -0.03 m³/s/m², because a channelling effect can develop. It is noted that in the submerged cases, the rate of volume flux reduction does not decrease significantly during further bore propagation through the MRE zone, indicating that also the further downstream located MRE contribute to the energy losses, as long as they are submerged.

These observations are also reflected by the statistical analyses of the mean values of volume flux changes in Table 5.10. During the unsteady phase of bore propagation, the standard deviation of the mean values of the segments I and II of $\Delta q(x)/\Delta x$ = 0.06 m³/s/m² is higher than for the segments III to VI with $\Delta q(x)/\Delta x$ = 0.02 m³/s/m².

During the steady phase of bore propagation

- *In Figure 5.21.b)* upstream of the MRE zone (segment I), the flow depth increases in the submerged cases between $\Delta h/\Delta x$ = 0.25 m/m for the smallest MRE (case 5.1) and $\Delta h/\Delta x$ = 0.48 m/m for the highest MRE (case 5.4). In the emerged case (case 1.0), the flow depth increases by $\Delta h/\Delta x$ = 0.59 m/m. Compared to the unsteady phase, the flow depth shows a higher sensitivity against the height of the MRE. In segment II, the submerged cases show only small changes of the flow depth between $\Delta h/\Delta x$ = -0.06 m/m and $\Delta h/\Delta x$ = 0.01 m/m, while in the emerged case, the flow depth decreases by $\Delta h/\Delta x$ = -0.32 m/m. Inside the MRE zone (segments III to VI), the range in which the flow depth changes takes values between $\Delta h/\Delta x$ = 0.01 and $\Delta h/\Delta x$ = -0.09 m/m and remains almost constant in all cases. In the emerged case, the change in flow depth reduces towards $\Delta h/\Delta x$ = 0 m/m.
- *In Figure 5.21.d),* the depth-averaged flow velocities decrease in segment I in all cases. In relation to the MRE height, the values range between $\Delta\overline{u(x)}/\Delta x$ = -1.3 m/s/m (case 5.1) and $\Delta\overline{u(x)}/\Delta x$ = -3.0 m/s/m (case 5.4). In the further downstream located sections II to VI, the flow velocity remains almost constant and changes within the relatively small range from $\Delta\overline{u(x)}/\Delta x$ = 0.33 m/s/m and $\Delta\overline{u(x)}/\Delta x$ = -0.25 m/s/m and decreases with further propagation through the MRE zone.
- *In Figure 5.21.f),* the volume flux decreases in segment I in the submerged cases between $\Delta q(x)/\Delta x$ = -0.06 m³/s/m² (case 5.1) and $\Delta q(x)/\Delta x$ = -0.17 m³/s/m² (case 5.4), depending on the MRE height. The flux reduction is here larger than during the unsteady phase of bore propagation. In the emerged case (case 1.0), $\Delta q(x)/\Delta x$ = -0.68 m³/s/m², is considerably higher than for the submerged cases. The emerged case does not allow overflow and thereby results in higher flow blocking. With further bore propagation through the MRE zone, the flux reduction is between $\Delta q(x)/\Delta x$ = 0 m³/s/m² and $\Delta q(x)/\Delta x$ = -0.02 m³/s/m² only, suggesting that in case of the submerged cases, a layer of low flow velocities is developed, while the water above this layer can propagate without considerable disturbance. In the emerged case, the channelling effect is responsible for the small flux reduction inside the MRE zone.

The observations can be related to the statistical analyses, provided in Table 5.10. During the steady phase of bore propagation, the standard deviation of the mean values of the volume flux

change rate takes with 0.112 $m^3/s/m^2$ a considerably higher value in the upstream segments I and II than with 0.006 $m^3/s/m^2$ in the segments III to VI. In the upstream segments, the value exceeds the standard deviation of the mean value during the unsteady phase of bore propagation by approximately factor 2, while for the downstream segments, the standards deviation of the steady flow conditions is considerably smaller than the value of the unsteady flow condition (0.022 $m^3/s/m^2$). On average, the standard deviation of the volume fluxes when varying the relative MRE height is 0.050 $m^3/s/m^2$, which is higher than when varying the relative spacing, but less when compared to when varying the shape.

The higher the macro-roughness elements (MRE) are compared to the water depth, the more sheltered are the downstream located MRE. For submerged MRE, the areas of low flow velocities increase with increasing relative MRE height indicating higher flow resistance with increasing relative MRE height. They exceed the width of the slow flow area of the emerged case so that inside the MRE zone, higher flow resistance than in the emerged case are noted.

In the upstream segments of the MRE zone (segments I and II), the energy losses in the submerged cases are very small compared to those in the emerged case during both the unsteady and the steady flow phase of bore propagation. They increase with increasing relative MRE height. During the steady phase, the energy losses exceed the values of the unsteady phase by factor 2.

In the MRE zone (segments III to VI) during the unsteady phase of bore propagation, energy losses of the submerged cases increase with increasing relative MRE height and tend to exceed the energy losses of the emerged case. During steady flow conditions the energy losses in the submerged cases are very small, without indicating a clear correlation.

The impact of the relative MRE height on the energy losses exceeds the impact of the relative spacing, the arrangement angle and the relative width of the MRE and is comparable to the impact of the MRE shape.

5.6 Summary and concluding remarks

In this chapter, numerical tests are performed at a model scale to analyse the effect of five parameters of the macro-roughness elements (MRE) on the propagation of a tsunami-like bore over an initially dry bottom during bore arrival (unsteady phase) and during stabilised conditions (steady phase) of the bore propagation. Model conditions are selected based on the 2004 Indian Ocean tsunami and the 2011 Tohoku tsunami at a scale of approximately 1:25. In all cases, the turbulent flow regime is obtained.

The flow through the tested MRE configurations (shape, relative width, arrangement angle, relative spacing and relative height) are described by means of flow depths, depth-averaged velocities and volume fluxes through cross-sections within and upstream of an area of similar MRE. The impact of each parameter variation on the change rate of volume flux is assessed using the standard deviation of the mean values. The following conclusions are derived:

- *The shape (C_D)* is on average the most important parameter inside the MRE zone during unsteady flow conditions, as indicated by the standard deviation of the volume flux change rate of 0.04 m³/s/m².
- *The arrangement angle Ψ* during steady flow conditions inside the MRE zone is only slightly more important than the other parameters, which is indicated by the relatively small standard deviation of 0.013 m³/s/m².
- *The relative spacing (S_G/D_B)* is the most important parameter during the unsteady flow conditions in the upstream part of the MRE zone.
- *The relative height (h_B/h_{max})* is the most important parameter during the steady flow conditions in the upstream part of the MRE zone.
- The most important region for assessing the energy losses is represented by the upstream segments I and II, especially during the steady flow conditions.
- Considering all flow conditions and all locations, the relative MRE height h_B/h_{max} (with the averaged standard deviation of 0.050 m³/s/m²) and the MRE shape (with the averaged standard deviation of 0.048 m³/s/m²) have the highest impact on the bore propagation, while the relative width (D_B/h_{max}) with averaged standard deviation of 0.011 m³/s/m² seems to be the least important parameter.
- During the steady phase of bore propagation in the inner MRE zone, the standard deviations of volume flux changes between 0.002 m³/s/m² (variation of S_G/D_B) and 0.013 m³/s/m² (variation of Ψ) only. This indicates that during this situation all parameters are less important for developing the MRE formula.

For further analyses of the energy losses due to the parameter variations, the statistical analyses above indicate that the empirical relations for estimating the energy losses during the bore propagation should

- distinguish between upstream region and region inside the MRE zone,
- distinguish between steady and unsteady flow conditions and
- make use of the four MRE parameters: shape, arrangement angle, relative spacing and relative height.
- The analyses need to be performed using various distances between the cross-sections to minimize local flow effects due to the presence of the MRE near or inside the cross-sections.
- The inner MRE zone during the steady phase of bore propagation should not be considered for deriving the MRE formula.

6 Formula for the effects of macro-roughness elements on the propagation of a tsunami-like bore over initially dry land

The analysis of macro-roughness elements (MRE) subject to a tsunami-like bore is extended in this chapter to assess the influence of MRE parameters on bore propagation in terms of depth-averaged flow parameters, which are used in non-linear shallow water (NLSW) models. The results from the parameter study in Chapter 5 are analysed further, and a formula is developed for the prediction of the energy losses due to MRE as a function of the most relevant parameters of the flow and the MRE. Such a formula represents a source term which is needed in any NLSW model as it describes the contribution of the MRE-induced energy losses.

In section 6.1, the analysis procedure is outlined. The data from the numerical parameter study (see Appendix, section D.2) is analysed in several cross-sections upstream and inside the MRE to obtain the differences in volume flux and flow depth compared to the reference case without MRE. These differences are then used in section 6.2 to determine two source terms due to drag and inertia. Based on the results of the parameter study in Chapter 5 and the dimensional analysis (see Appendix, section D.1), dimensionless numbers are used to relate the effect of MRE parameters on the bore propagation in section 6.3. In section 6.4, the MRE formula is developed. In section 6.5, the MRE formula is applied to a distinct flow regime and evaluated using statistical descriptors.

6.1 Methodology for CFD data analysis

The methodology for data analysis relies closely on the quantities used in depth-averaged numerical models for large-scale applications (see Section 2.2.1), which are

- flow depth h
- volume flux q.

Moreover, it relies on the fact that the propagation of a tsunami-like bore over a horizontally flat and initially dry bottom without MRE can adequately be described by traditional non-linear shallow-water (NLSW) equation models, which commonly account for energy losses due to bottom friction (S_{fx}, S_{fy}) and turbulent shear stress (τ_{xx}, τ_{xy}, τ_{yy}) as indicated in equation (2-13). However, the energy losses S_{MRE} due to the presence of MRE of different arrangements, shapes, heights and densities are not represented by the NLSW equations. In analogy to equation (2-13) in section 2.2.1, the energy losses S_{MRE} will be added as source terms to the momentum equations, here given for the flow along the direction of x

$$\frac{\partial q(x)}{\partial t} + \frac{\partial}{\partial x}\left(\frac{q(x)^2}{h} + gh^2 - \frac{h}{\rho}\tau_{xx}\right) = -S_{fx} + S_{MRE} = S_{total} \tag{6-1}$$

where

$$q(x) = u(x)h \tag{6-2}$$

is the volume flux in the direction of x with the flow velocity $u(x)$, t is the time, h is the flow depth, g is the acceleration due to gravity and ρ is the density of the fluid.

Comparing equation (6-1) to equation (2-13), some changes are noted:

- The bed surface slope $S_{0,i} = sin\theta_i$ of the NLSW equations is here zero which is why the term $ghS_{0,i}$ is removed.
- As the numerical experiments, outlined in section 5.3, are designed for analysing the bore propagation in mean flow direction x, symmetry boundary conditions are used on the lateral sides of the numerical domain (see Figure 5.5), so that
  - no differences in the flow velocities u_j can be assumed, leading to the cross-momentum term $\frac{\partial u_i u_j h}{\partial x_j} = \frac{\partial u(x)u(y)h}{\partial y} = 0$, and
  - the turbulence term $-\frac{h}{\rho}\left(\frac{\partial \tau_{ii}}{\partial x_i} + \frac{\partial \tau_{ij}}{\partial x_j}\right) = -\frac{h}{\rho}\left(\frac{\partial \tau_{xx}}{\partial x} + \frac{\partial \tau_{xy}}{\partial y}\right) = -\frac{h}{\rho}\frac{\partial \tau_{xx}}{\partial x}$

The viscous and turbulence stresses (see equation (2-14)) can then be estimated

$$\tau_{xx} = -\rho u(x)' u(x)' \tag{6-3}$$

with the turbulent flux oscillations

$$u(x)' = I(x)u(x) \tag{6-4}$$

and the turbulence intensity $I(x)$.

The systematic variations of the aforementioned parameters (see section 5.2) in the CFD models result in empirical relations describing the impact of each parameter. Eventually, their combination results in the source terms.

In accordance with chapter 5, two flow regimes will be considered:

- unsteady phase of bore propagation (period during bore impact) and
- quasi-steady phase of bore propagation (relatively stable current conditions).

The unsteady phase of bore propagation is characterized by a high gradient in flow depth h and high flow velocities $u(x)$ at the bore front, while the gradient of flow depth $\frac{\partial h}{\partial x}$ is minimal during the quasi-steady phase of bore propagation. The flow phases are selected by analysing the time series at each investigated cross-section (see e.g. the time series obtained from the basic configuration in the Appendix, Section C.1.2). The selection of a representative time frame for each of the conditions is consistent with the procedure described in section 5.4. The following procedure is seen as a continuance and is applied in this chapter. The flow chart is given in Figure 6.1.

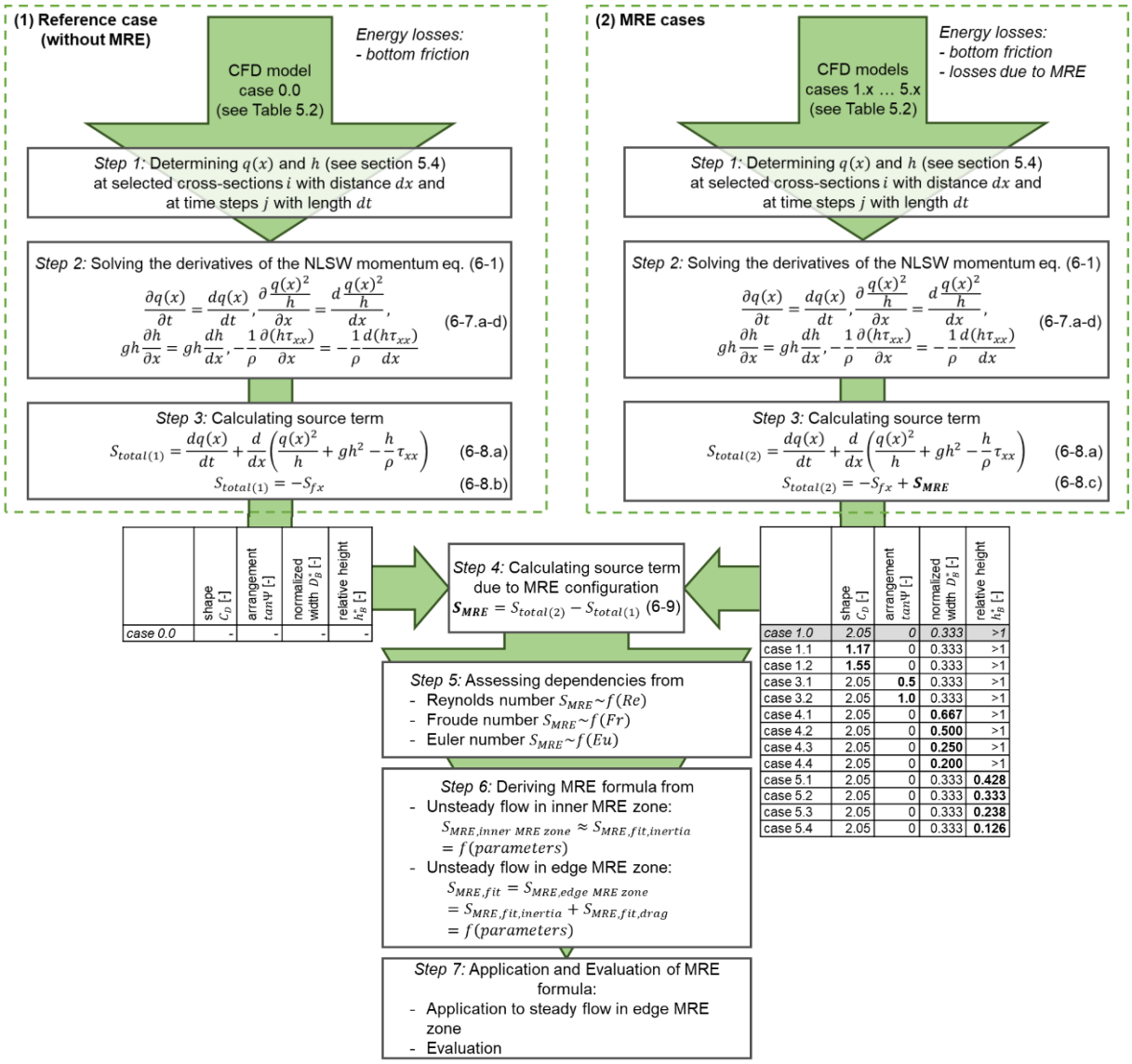

Figure 6.1. Flow chart of the analysis procedure to derive the source term S_{MRE} describing the energy losses due to macro-roughness elements (MRE) from the data obtained from CFD modelling.

The left branch of the flow chart describes the processing of CFD data derived from the simulation of the *reference case* (case 0.0), including only effects which are fully represented by the traditional NLSW equation, namely bottom friction and turbulent shear stress. The right branch of the flow chart describes the processing of the CFD data of all cases in which the MRE are included (cases 1.x to 5.x). The following steps are performed for each individual case in the left and the right branch of Figure 6.1.

Step 1: Determining volume flux q(x) *and flow depth* h *at selected cross-sections*

During the CFD simulations (refer to the cases summarized in Figure 6.1), the flow velocities $u(x)$ and the fluid phase content α_1 are derived for each computational element. In section 5.4,

they are extracted and averaged at selected cross-sections i, which are located between the neighbouring cross-sections $i-1$ and i and at the timesteps j and $j+1$ spanning the time step length dt. As a result, the flow parameters volume flux $q(x)$ and flow depth h become available for each i and j and can be used in the (discretized) NLSW momentum equation.

In analogy to section 5.5 it is distinguished between the edge MRE zone (segments I and II) and the inner MRE zone (segments III to VI). They will be separately analysed for the description for the energy losses due to MRE. These zones are depicted in Figure 6.2.

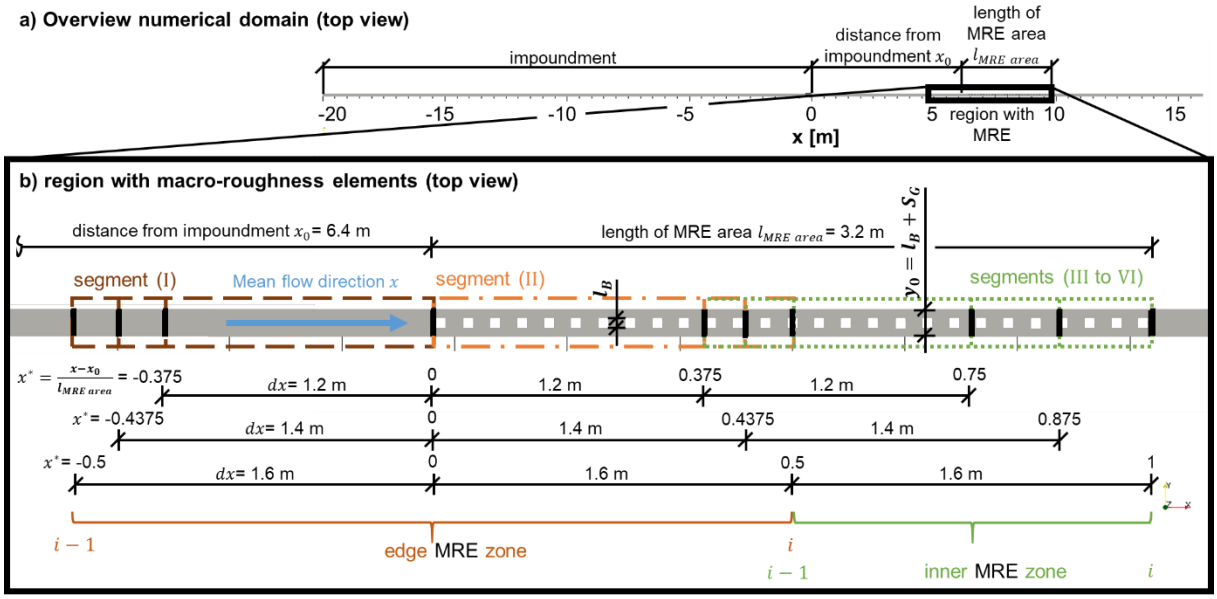

Figure 6.2. Selected cross sections in the edge zone and the inner zone of the area of macro-roughness elements (MRE): a) Overview of numerical domain, b) area of MRE. Segments I (dashed) and II (dash-dotted) form the edge zone and segments III to VI (dotted) is the inner zone of MRE. The vertical black bars indicate the selected cross-sections & the squares indicate the MRE.

By considering only two zones (edge zone and inner zone), the source term in the NLSW model needs to distinguish basically between two situations:

1. the upstream unit area contains MRE (similar to the actual cell) – only losses observed in the inner zone are to be considered
2. the upstream unit area does not contain MRE (in contrast to the actual cell) – also the losses which are only associated to the most upstream located row or MRE are considered.

Consequently, the source term needs to be composed from two additive terms.

It is further mentioned that at the downstream edge of the MRE zone, no separate solution is formulated. Pasha & Tanaka (2017) observed in laboratory experiments an undular hydraulic jump leading to energy losses between only 1.4 and 6.4 % of the total losses. To the author's knowledge, such phenomenon was never reported from nature, where other effects e.g. due to debris or due to natural bottom features may superimpose the formation of an undular hydraulic

jump. Therefore, and because the reported energy losses are relatively small, the downstream edge of the MRE zone is not explicitly considered in this study.

As previously mentioned in this section, data was extracted and averaged from the CFD model as described in section 5.4, but the aim here is to obtain only single averaged values per case per zone, so that less cross-sections are to be selected for further analyses as shown in Figure 6.2.

In Figure 6.2, three lengths of unit areas dx = {1.2, 1.4, 1.6} m are shown. Each of these dx result in different distances between the cross-sections and different distances to individual MRE, which may affect the flow fields in the cross-sections (see section 5.4.5). In order to minimize these local effects, the analyses are performed for all three dx and the results are averaged. To represent the energy losses in the edge zone, volume fluxes $q(x)$ and flow depths h are determined for the inlets $(i-1)$ and the outlets i for each dx as follows:

$$q(x)_{i-1} = \frac{q(x)_{x^*=-0.375} + q(x)_{x^*=-0.4375} + q(x)_{x^*=-0.5}}{3} \tag{6-5.a}$$

$$q(x)_{i} = \frac{q(x)_{x^*=0.375} + q(x)_{x^*=0.4375} + q(x)_{x^*=0.5}}{3} \tag{6-5.b}$$

$$h_{i-1} = \frac{h_{x^*=-0.375} + h_{x^*=-0.4375} + h_{x^*=-0.5}}{3} \tag{6-5.c}$$

$$h_{i} = \frac{h_{x^*=0.375} + h_{x^*=0.4375} + h_{x^*=0.5}}{3} \tag{6-5.d}$$

For the inner zone, $q(x)$ and h for $i-1$ and i are determined using the relations

$$q(x)_{i-1} = \frac{q(x)_{x^*=0.375} + q(x)_{x^*=0.4375} + q(x)_{x^*=0.5}}{3} \tag{6-6.a}$$

$$q(x)_{i} = \frac{q(x)_{x^*=0.75} + q(x)_{x^*=0.875} + q(x)_{x^*=1}}{3} \tag{6-6.b}$$

$$h_{i-1} = \frac{h_{x^*=0.375} + h_{x^*=0.4375} + h_{x^*=0.5}}{3} \tag{6-6.c}$$

$$h_{i} = \frac{h_{x^*=0.75} + h_{x^*=0.875} + h_{x^*=1}}{3} \tag{6-6.d}$$

It is pointed out that although the sets of equations (6-5) and (6-6) might remind on discretization techniques in numerical modelling as an approximation for the derivatives of $q(x)$ and h at discrete points i, here it represents rather snapshots of the flow field on discrete locations instead of an approximation of the derivative terms. This is because in numerical modelling, the derivatives of $q(x)$ and h are extrapolated (in case of explicit methods) or iterated (in case of implicit methods), while here $q(x)$ and h are already available from CFD simulations (acknowledging that the derived data is merely approximated as well, but on a finer scale, at which the MRE are fully resolved).

Step 2: Solving the derivatives of the left-hand side of the NLSW momentum equation (6-1)

The flow parameters $q(x)$ and h are used to solve the derivatives of the left-hand side of NLSW momentum equation (6-1) as follows:

$$\frac{\partial q(x)}{\partial t} = \frac{dq(x)}{dt} = \frac{q(x)_{i,j+1} - q(x)_{i,j}}{t_{j+1} - t_j} \tag{6-7.a}$$

$$\frac{\partial}{\partial x}\frac{q(x)^2}{h} = \frac{d}{dx}\frac{q(x)^2}{h} = \frac{\frac{q(x)_{i,j}^2}{h_{i,j}} - \frac{q(x)_{i-1,j}^2}{h_{i-1,j}}}{x_i - x_{i-1}} \tag{6-7.b}$$

$$\frac{\partial}{\partial x} g h^2 = g h \frac{dh}{dx} = \frac{g\left(h_{i,j} + h_{i-1,j}\right)\left(h_{i,j} - h_{i-1,j}\right)}{2(x_i - x_{i-1})} \tag{6-7.c}$$

$$\begin{aligned} -\frac{\partial}{\partial x}\frac{h}{\rho}\tau_{xx} = -\frac{1}{\rho}\frac{d(h\tau_{xx})}{dx} &= \frac{d(hI(x)^2 u(x)^2)}{dx} \\ &= \frac{I(x)^2\left(\frac{q(x)_{i,j}^2}{h_{i,j}} - \frac{q(x)_{i-1,j}^2}{h_{i-1,j}}\right)}{(x_i - x_{i-1})} \end{aligned} \tag{6-7.d}$$

Equation (6-7.d) uses the relations provided in the equations (6-2), (6-3) and (6-4). The index *j* specifies the timestep. For each dx, the corresponding j is derived according to the Courant-Friedrichs-Lewy (CFL) criterion (see section 5.4.2).

Step 3: Calculating the source terms

The source terms are calculated from the left-hand side of equation (6-1) using the terms determined in Step 2. Then, the equation reads

$$\begin{aligned} S_{total} = &\frac{q(x)_{i,j+1} - q(x)_{i,j}}{t_{j+1} - t_j} + \frac{\left(\frac{q(x)_{i,j}^2}{h_{i,j}} - \frac{q(x)_{i-1,j}^2}{h_{i-1,j}}\right)}{x_i - x_{i-1}} \\ &+ \frac{g\left(h_{i,j} + h_{i-1,j}\right)\left(h_{i,j} - h_{i-1,j}\right)}{2(x_i - x_{i-1})} \\ &- \frac{I(x)^2\left(\frac{q(x)_{i,j}^2}{h_{i,j}} - \frac{q(x)_{i-1,j}^2}{h_{i-1,j}}\right)}{x_i - x_{i-1}} \end{aligned} \tag{6-8.a}$$

$$S_{total(1)} = -S_{fx} \tag{6-8.b}$$

$$S_{total(2)} = -S_{fx} + S_{MRE} \tag{6-8.c}$$

In the left branch of Figure 6.1, $S_{total(1)}$ can only contain losses due to bottom friction S_{fx}, because no MRE are included (S_{MRE} = 0), which is resulting in equation (6-8.b). In contrast, in the right branch of Figure 6.1, $S_{total(2)}$ includes also the losses induced by the MRE (S_{MRE}), resulting in equation (6-8.c)

Step 4: Calculating the source terms due to MRE configurations

By subtracting the losses of the right branch in Figure 6.1, $S_{total(1)}$, including only the energy losses of the case without MRE, from the left branch $S_{total(2)}$, also including the losses due to MRE,

$$S_{MRE} = S_{total(2)} - S_{total(1)} \tag{6-9}$$

only the losses due to the MRE remain.

Step 5: Assessing dependencies from non-dimensional variables

The source terms $S_{total(1)}$ and $S_{total(2)}$ are directly obtained from the right-hand side of equation (6-8.a) and form the database for deriving the MRE formula as NLSW source term. In analogy to the derivation of empirical formulae from laboratory tests (e.g. Husrin, 2013), it is attempted in Step 6 to proceed similarly using non-dimensional variables obtained from dimension analysis (see Appendix, section D.1): Reynolds number Re, Froude number Fr and Euler number Eu.

Step 6: Deriving MRE formula

In order to assess the influence of the investigated MRE parameters,

$$S_{MRE,fit} \approx f(MRE\ parameters) \tag{6-10}$$

Following the structure of the Morrison equation (2-32)

$$S_{MRE,fit} = S_{MRE,fit,inertia} + S_{MRE,fit,drag} \tag{6-11.a}$$

$$S_{MRE,fit,inertia} = f\left(\rho C_I V_B \frac{\partial \frac{q(x)}{h}}{\partial t}, MRE\ parameters\right) \tag{6-11.b}$$

$$S_{MRE,fit,drag} = f\left(\frac{1}{2}\rho C_D A_B \left(\frac{q(x)}{h}\right)^2, MRE\ parameters\right) \tag{6-11.c}$$

where ρ is the density of the fluid, C_I is the inertia coefficient, V_B is the volume of the MRE, and $\frac{\partial(q(x)/h)}{\partial t}$ is the local acceleration of the fluid, C_D is the drag coefficient and A_B is the front face area of the submerged part of the MRE.

Chapter 5 has clearly shown that inertia contributes to energy losses (i) at the upstream edge and (ii) in the inner MRE zone during the unsteady flow phase of bore propagation (see Table 5.10). In contrast, during the steady flow phase, considerable losses are only observed at the upstream edge of the MRE zone. By distinguishing between these two regions, the source terms $S_{MRE,fit,inertia}$ and $S_{MRE,fit,drag}$ are developed consecutively as shown in Figure 6.3.

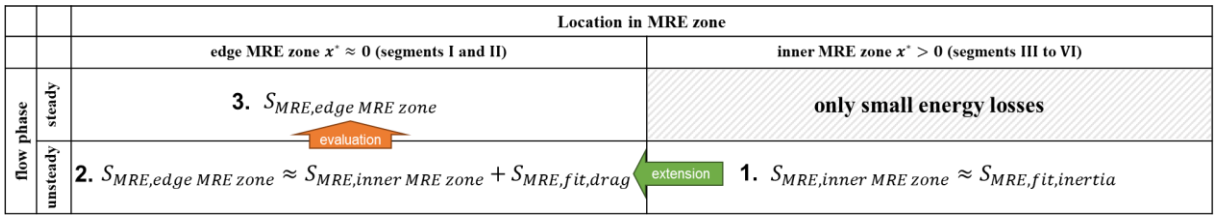

Figure 6.3. Procedure for the consecutive development of the source terms $S_{MRE,fit,inertia}$ and $S_{MRE,fit,drag}$ and evaluation (see Figure 6.2 for definition of zones).

First, the source term due to inertia $S_{MRE,fit,inertia}$ is derived individually in the inner MRE zone during the unsteady phase of bore propagation, because during the steady phase, no considerable drag is observed in this region. Consequently, the solution for S_{MRE} is valid during the steady phase as well.

It is further acknowledged that each MRE parameters is describing the MRE in conjunction with the other MRE parameters. Therefore, their effects on the energy losses are formulated as a product. By varying individually each parameter separately, the impact of each parameter can be included in the fit one after the other. In each of these steps, the complexity of the equation, but also the sensitivity of the MRE formula to the MRE configuration increases. The fits are done in MS Excel as it provides the possibility to easily link cells and graphs. By changing coefficients manually, their effect on the fit can be evaluated by statistical descriptors and visually, so that the best match of various attempts can be selected.

Secondly, the source term $S_{MRE,fit,inertia}$ is applied to the edge MRE zone. Fitting is performed similarly as stated above. The deviation of $S_{MRE,fit,inertia}$ from the source term S_{MRE} (obtained from CFD data) is interpreted as drag losses $S_{MRE,fit,drag}$.

Step 7: Application and evaluation of MRE formula

It is noted that in the consecutive development of the MRE formula, inertia effects cannot be fully excluded as they are present to some extent also in the here called “steady” phase (but in fact quasi-steady), as the flow cannot be seen as ideally steady. Therefore, the MRE formula is also applied to the steady phases of bore propagation so that the performance of the fit $S_{MRE,fit}$ is evaluated for all relevant conditions, as indicated in Figure 6.3.

The data from the CFD parameter tests are transferred and processed to represent depth-averaged data by spatial and temporal averaging (refer to sections 5.4.1 and 5.4.2), which are used to calculate the derivatives of the NLSW equation.

The MRE-induced energy losses are to be derived from each CFD simulation case by subtracting the energy losses obtained from a *reference case* without any MRE (case 0.0), in which only losses due to bottom friction and turbulent shear stress are present, from the total energy losses.

The source terms are to be derived for two distinct conditions during the unsteady phase of bore propagation: (i) in the inner MRE zone and (ii) in the edge MRE zone.

In order to evaluate the applicability of the formulae for the entire period of bore propagation, the formulae for the source terms are to be applied in the edge MRE zone during the steady phase of bore propagation.

6.2 Calculating the source terms from CFD data (Steps 1 to 4)

This section contains the steps 1 to 4, in which the energy losses due to the MRE S_{MRE} are determined from each CFD simulation case by analysing the flow parameters h and $q(x)$ in various cross-sections (step 1). The values are used to solve the derivatives in the left-hand side of the NLSW momentum equation (step 2) to determine the source term on the right-hand side (step 3). Finally, the MRE source term S_{MRE} is isolated by subtracting the bottom friction source term (step 4). S_{MRE} forms the data basis for deriving the MRE formula. S_{MRE} is derived for various flow phases and locations in the MRE zone to describe the bore propagation.

In section 6.2.1, the flow and macro-roughness parameters are defined. In section 6.2.2, special attention is paid on the turbulence intensity selection, which dominates the shear-stress derivative term. Then, the source terms are calculated for the unsteady phase of bore propagation in the inner MRE zone (section 6.2.3), for the unsteady phase of bore propagation in the edge MRE zone (section 6.2.4) and for the steady phase of bore propagation in the edge MRE zone (section 6.2.5).

6.2.1 Definition of flow and macro-roughness parameters

The flow and MRE parameters for developing the source terms are selected in this way that they can be determined relatively easily, preferably using satellite imagery, aerial photography, from available geographic information systems (GIS) or from local/regional/national authorities (see section 2.1.4). They are defined in Figure 6.4 for both emerged and submerged MRE.

All MRE and flow parameters are interpreted as averaged values and valid for the entire unit area $dxdy$, where dx and dy are the unit length and unit width, respectively. S_G is the spacing between the MRE, D_B is the width of the MRE and h_B is the height of the MRE. Only the part of the MRE is taken into account, which is subject to the flow and referred to as effective height of the MRE

$$h_{B,eff} = min\left(h_{eff}, h_B\right) \tag{6-12}$$

with the effective flow depth

$$h_{eff} = f_{eff} h \tag{6-13}$$

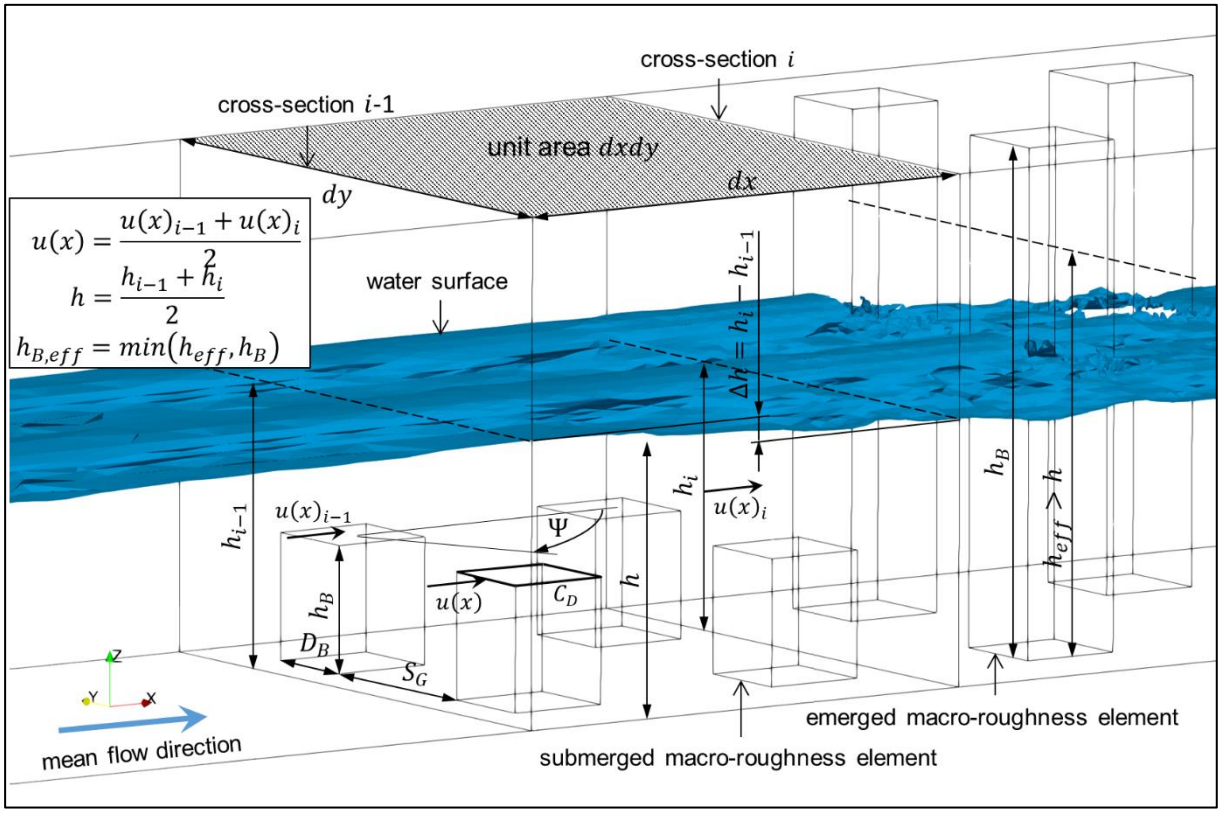

Figure 6.4. Definition of flow and macro-roughness parameters for both emergent and submerged MRE.

which is larger than the flow depth h. This is expressed by a factor f_{eff}, because it can be expected that e.g. due to the run-up of the bore on a front face of a MRE, also MRE parts located above the (spatially averaged) water surface contribute to the energy losses. In equation (6-14), h is determined as the average of the flow depth at the upstream and the downstream cross-section $i-1$ and i

$$h = \frac{h_{i-1} + h_i}{2} \tag{6-14}$$

The effective height of the MRE $h_{B,eff}$ is normalized by the flow depth h resulting in relative effective MRE height

$$h^*_{B,eff} = \frac{h_{B,eff}}{h} = \frac{min(h_{eff}, h_B)}{h} \tag{6-15}$$

The width of the MRE D_B in Figure 6.4 is normalized by the sum of MRE width and spacing $(D_B + S_G)$. The normalized MRE width, which might be interpreted as blockage ratio of the flow, reads

$$D^*_B = \frac{D_B}{D_B + S_G} \tag{6-16}$$

The arrangement angle Ψ in Figure 6.4 is defined as the angle between the mean flow direction and the orientation of the group of MRE.

6.2.2 Selection of the turbulence intensity

In accordance with the conclusions derived from chapter 5, the MRE parameters should be related to the source terms in equation (6-9) by using the data obtained from the parameter tests during the steady and unsteady phases of bore propagation at the upstream edge and inner zone of MRE (see Figure 6.2). The energy losses during the unsteady phase of bore propagation are assessed in the inner MRE zone first, before they are derived in the edge MRE zone (see Figure 6.3). The impact of using various turbulence intensities I with various unit lengths dx are discussed.

In equation (6-8.a), the turbulence intensity $I(x) = \frac{\sqrt{(u(x)')^2}}{\overline{u(x)}}$ is to be selected. In this relation, $\overline{u(x)}$ is the mean flow velocity and $u(x)'$ is the turbulent velocity fluctuation in x direction. Wu (2004) investigated turbulence effects in breaking waves in detail by means of numerical simulations and laboratory experiments. Depending on the height over the bottom and the downstream distance from the breaking point values between I = 0.05 and I = 0.2 are reported. Considering the propagating bore as a broken wave, similarities in turbulence characteristics might be expected. Árnason (2004) investigated the bore impact on a circular cylinder and reported values of up to I = 0.325 in the centreline of the cylinder and between I = 0.03 and I = 0.064 elsewhere. To assess the impact of this choice on the source terms S_{MRE}, a sensitivity test is performed, using $I(x) = \{0,0.01,0.025,0.05, 0.1, 0.2,0.35\}$. Exemplarily, a unit length of dx = 1.4 m as the medium length (see Figure 6.2) is used. The results are provided in the Appendix, section D.2.2. A graphical representation of the results during unsteady flow conditions in the inner and the edge zone as well as during steady flow conditions in the edge zone are provided in Figure 6.5.

It is noted that in case of selecting $I(x)$ = 5 %, the contribution of the turbulent shear stress term to the source term S_{MRE} is on average 0.3 %, only. For $I(x)$ = 10 %, the contribution to S_{MRE} is 5.7 %. In both cases, the impact of the choice on the source term is considered small. A turbulence intensity of $I(x)$ = 10 % seems an adequate choice as being valid for unit areas $dxdy$. This choice acknowledges that high turbulence is likely to occur in the wakes of the MRE, while it is expected to decrease further away from the MRE.

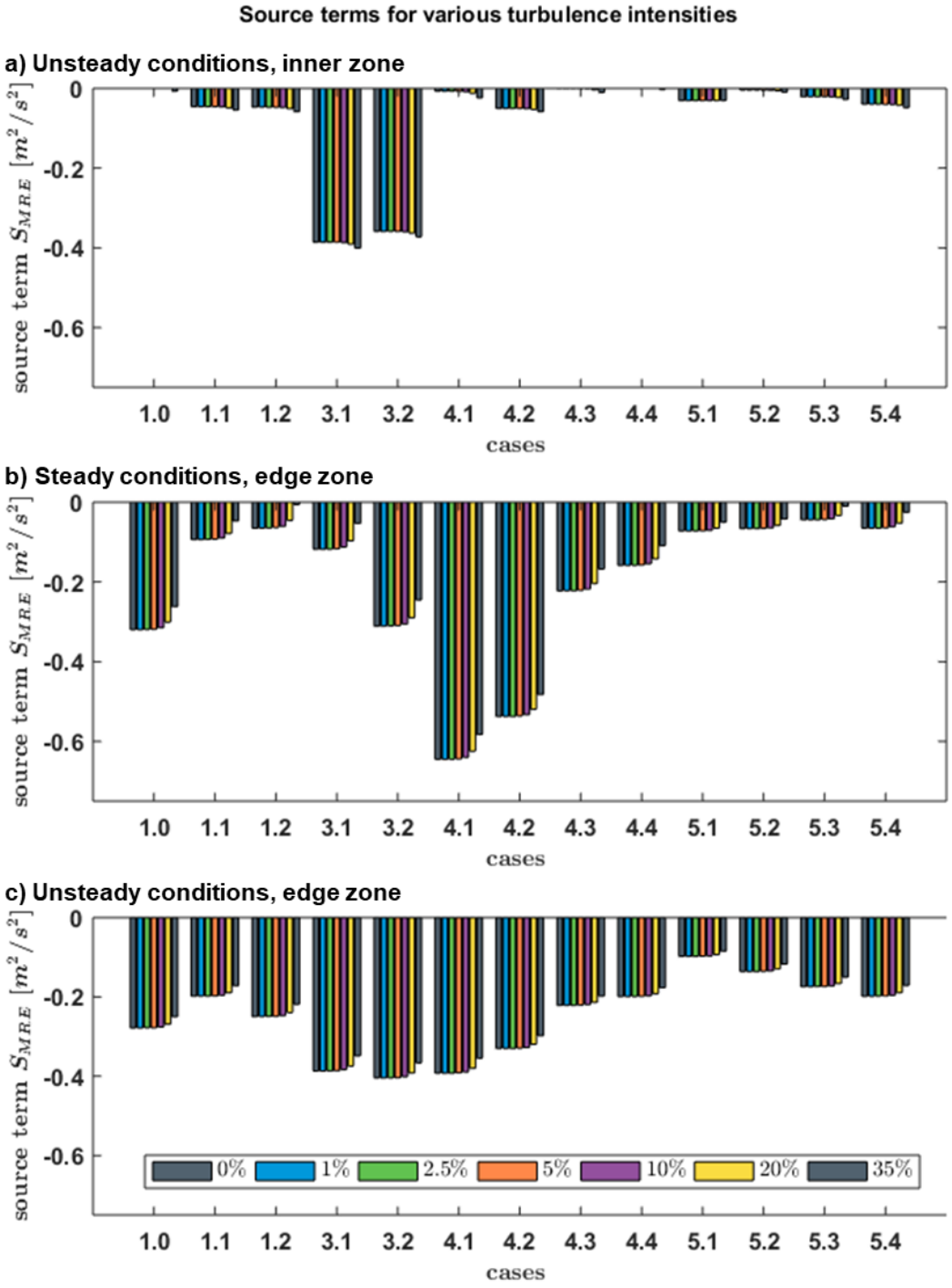

Figure 6.5. Comparison of derived source terms using various turbulence intensities I for a) unsteady conditions in the inner MRE zone, b) steady conditions in the edge MRE zone and c) unsteady conditions in the edge MRE zone.

6.2.3 Unsteady phase of bore propagation in the inner MRE zone

The source terms S_{MRE} are calculated for various unit lengths dx = 1.2 m, 1.4 m and 1.6 m using a turbulence intensity of $I(x)$ = 10 % during the unsteady phase of bore propagation in

the inner MRE zone as summarized in Figure 6.6. Full data is provided in the Appendix, section D.2.1.

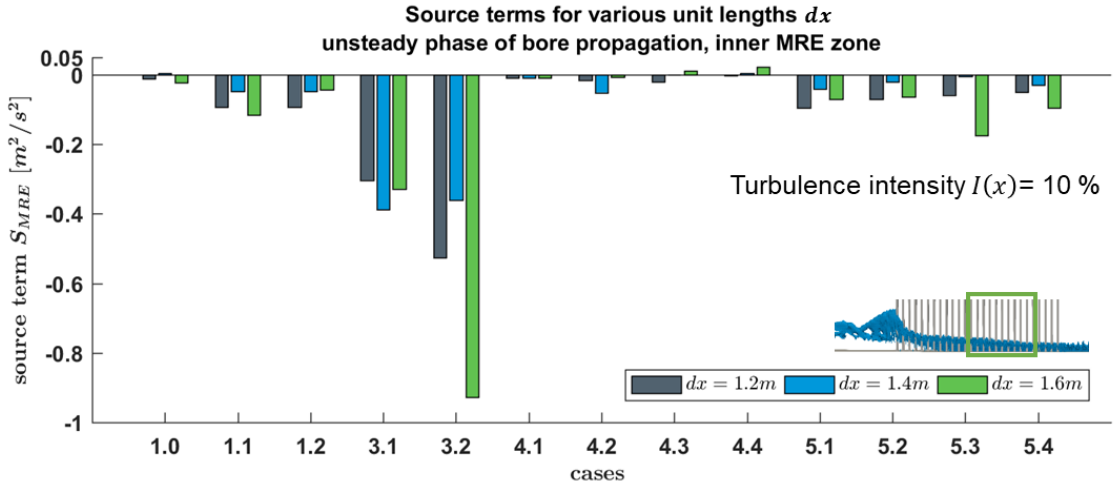

case	*1.0*	1.1	1.2	3.1	3.2	4.1	4.2	4.3	4.4	5.1	5.2	5.3	5.4
Shape (drag coefficient C_D) [-]	*2.05*	**1.2**	**1.55**	2.05	2.05	2.05	2.05	2.05	2.05	2.05	2.05	2.05	2.05
Arrangement angle Ψ [°]	*0*	0	0	**26.57**	**45**	0	0	0	0	0	0	0	0
Normalized width D_B^* [-]	*0.333*	0.333	0.333	0.333	0.333	**0.667**	**0.500**	**0.250**	**0.200**	0.333	0.333	0.333	0.333
Height h_B [m]	$\gg h$	$\gg h$	$\gg h$	$\gg h$	$\gg h$	$\gg h$	$\gg h$	$\gg h$	$\gg h$	**0.215**	**0.161**	**0.108**	**0.054**
Mean source term S_{MRE} [m²/s²]	*-0.010*	-0.085	-0.061	-0.339	-0.605	-0.009	-0.024	-0.003	0.008	-0.068	-0.052	-0.079	-0.059
Standard deviation $STDEV$ [m²/s²]	*0.014*	0.035	0.028	0.043	0.291	0.001	0.023	0.016	0.012	0.028	0.027	0.087	0.034
Relative standard deviation RSD [%]	*141*	41	45	13	48	13	98	536	154	40	52	110	57

Figure 6.6. Source term S_{MRE} for dx = 1.2 m, 1.4 m and 1.6 m in the inner MRE zone ($x^* > 0$) during the unsteady phase of bore propagation (see Figure 6.3), its mean values S_{MRE}, standard deviations $STDEV$ and relative standard deviations RSD.

The analyses using different dx lead to considerably different results, as the position of the MRE relative to the cross-sections influences the results differently. This is discussed in section 5.4.5. It is shown that mainly the flow depth $h_{i,j}$ in cross-section i and at timestep j is affected. Consequently, the source term calculation equation (6-8.a) is also affected. The variation of the source term $\bar{S}_{MRE}(dx)$ is expressed by the standard deviation, which is with $STDEV$ = 0.291 m²/s² the greatest in case 3.2 (arrangement angle $\Psi = 45°$) and with $STDEV$ = 0.001 m²/s² the smallest in case 4.1 ($D_B^* = 2/3$).

The relative standard deviation RSD relates the variation in $S_{MRE}(dx)$ to the mean value. Values of RSD > 100 % reveal that the mean energy loss is less than the variation which originates from different dx. Therefore, the source terms for the cases 1.0, 4.3, 4.4 and 5.3 are understood as being less reliable and fitting of these parameters during these flow conditions should be omitted.

The shape, represented by the drag coefficient C_D, is related to the source term S_{MRE}. The smallest drag coefficient C_D = 1.2 (case 1.1) leads to the highest mean value of the source term $\bar{S}_{MRE}$ = -0.085 m²/s² and the greatest drag coefficient C_D = 2.05 (case 1.0) leads to the smallest $\bar{S}_{MRE}$ = -0.010 m²/s². The reason is that more streamlined shapes allow the water to flow around the MRE, leading to smaller wakes, so that further downstream MRE are more subjected to the flow than in case of C_D = 2.05, where the flow is mainly blocked and where the channelling effect is more pronounced (see section 5.5.2).

The arrangement angle Ψ variation is found being related to the source term S_{MRE} as an increasing Ψ leads to an continuous increase of the mean value of $\bar{S}_{MRE}$ from $\bar{S}_{MRE}$ = -0.010 m²/s² for Ψ = 0° (case 1.0) to $\bar{S}_{MRE}$ = -0.605 m²/s² for Ψ = 45° (case 3.1).

The normalized width D_B^* seems independent from the source term as the greatest mean value of the source term is with $\bar{S}_{MRE}$ = -0.024 m²/s² found for the second greatest normalized width (case 4.2). It is further noted that all $S_{MRE}(dx)$ are the smallest of all cases. The channelling effect, observed in section 5.5.5, is responsible for this phenomenon.

The height h_B seems independent from the source term as long as the MRE are submerged, because the greatest mean value of the source term is with $\bar{S}_{MRE}$ = -0.079 m²/s² found for the second smallest height (case 5.3) and the smallest source term is with $\bar{S}_{MRE}$ = -0.052 m²/s² noted for the third highest MRE (case 5.2). The difference in $\bar{S}_{MRE}$ between the cases is comparably small, e.g., when comparing with the source term of case 3.1. This gives rise to the interpretation of the flow field in section 5.5.6, where the presence of a boundary layer of low flow velocities is developed over the submerged MRE and limits the disturbance of the flow.

6.2.4 Unsteady phase of bore propagation in the edge MRE zone

The source terms S_{MRE} are calculated for various unit lengths dx = 1.2 m, 1.4 m and 1.6 m using a turbulence intensity of I = 10 % during the unsteady phase of bore propagation in the edge MRE zone. The results are summarized in Figure 6.7. Full data is provided in the Appendix, section D.2.1.

In all cases, the energy losses S_{MRE} are smaller in cases of larger unit lengths dx, which is according to the expectations resulting from equations (6-7.b) to (6-7.d), where dx is the denominator. The energy losses occur mainly at the most upstream row of MRE in the edge MRE zone (see chapter 5). The standard deviation of the source terms using various dx takes values between $STDEV$ = 0.021 m²/s² (case 5.4) and $STDEV$ = 0.049 m²/s² (case 4.1) and are greater than the mean value of the source term $\bar{S}_{MRE}$ in all cases.

The relative standard deviation takes values between RSD = 5.9 % and RSD = 22 %, which is relatively small when compared to the inner MRE zone (see section 6.2.3). It is seen that under the here investigated conditions, local flow effects apparently do not affect the solutions, as it is the case in the inner MRE zone.

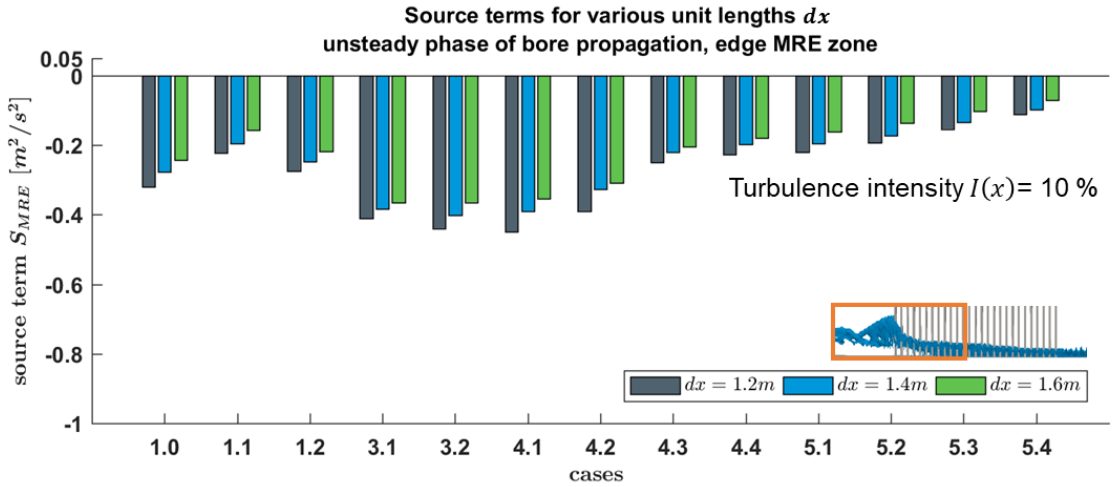

case	1.0	1.1	1.2	3.1	3.2	4.1	4.2	4.3	4.4	5.1	5.2	5.3	5.4
Shape (drag coefficient C_D) [-]	2.05	**1.2**	**1.55**	2.05	2.05	2.05	2.05	2.05	2.05	2.05	2.05	2.05	2.05
Arrangement angle Ψ [°]	0	0	0	**26.57**	**45**	0	0	0	0	0	0	0	0
Normalized width D_B^* [-]	0.333	0.333	0.333	0.333	0.333	**0.667**	**0.500**	**0.250**	**0.200**	0.333	0.333	0.333	0.333
Height h_B [m]	$\gg h$	$\gg h$	$\gg h$	$\gg h$	$\gg h$	$\gg h$	$\gg h$	$\gg h$	$\gg h$	**0.215**	**0.161**	**0.108**	**0.054**
Mean source term S_{MRE} [m²/s²]	-0.279	-0.194	-0.248	-0.390	-0.405	-0.401	-0.344	-0.226	-0.203	-0.193	-0.167	-0.130	-0.093
Standard deviation $STDEV$ [m²/s²]	0.039	0.034	0.029	0.023	0.038	0.049	0.042	0.023	0.024	0.029	0.029	0.026	0.021
Relative standard deviation RSD [%]	14	18	12	5.9	9.3	12	12	10	12	15	17	20	22

Figure 6.7. Source term S_{MRE} for dx = 1.2 m, 1.4 m and 1.6 m in the edge MRE zone ($x^* \approx 0$) during the unsteady phase of bore propagation (see Figure 6.3), its mean values S_{MRE}, standard deviations $STDEV$ and relative standard deviations RSD.

The shape, expressed as drag coefficient C_D, correlates with $\bar{S}_{MRE}$ as for case 1.2 with the smallest value for C_D = 1.2, $\bar{S}_{MRE}$ = -0.194 m²/s² is also the smallest. $\bar{S}_{MRE}$ is continuously increasing to $\bar{S}_{MRE}$ = -0.279 m²/s² for case 1.0 with C_D = 2.05. This is opposite to the unsteady phase of bore propagation in the inner MRE zone, where the smallest C_D leads to the greatest $\bar{S}_{MRE}$ and vice versa.

The arrangement angle Ψ variation also correlates with $\bar{S}_{MRE}$, as for Ψ = 0° (case 1.0), $\bar{S}_{MRE}$ = -0.279 m²/s². $\bar{S}_{MRE}$ increases continuously to $\bar{S}_{MRE}$ = -0.405 m²/s² for Ψ = 45° (case 3.2).

The normalized width D_B^* is related to $\bar{S}_{MRE}$ as the greatest D_B^* = 0.667 (case 4.1) leads to the greatest $\bar{S}_{MRE}$ = -0.401 m²/s². $\bar{S}_{MRE}$ is continuously decreasing with decreasing D_B^*. The smallest D_B^* = 0.200 (case 4.4) leads to the smallest $\bar{S}_{MRE}$ = -0.203 m²/s².

The height h_B correlates with $\bar{S}_{MRE}$ as the greatest h_B = 0.215 m (case 5.1) results in the greatest $\bar{S}_{MRE}$ = -0.193 m²/s². $\bar{S}_{MRE}$ is continuously decreasing with a decreasing h_B. The smallest h_B = 0.054 (case 5.4) leads to the smallest $\bar{S}_{MRE}$ = -0.093 m²/s².

6.2.5 Steady phase of bore propagation in the edge MRE zone

The source terms S_{MRE} are calculated for various unit lengths dx = 1.2 m, 1.4 m and 1.6 m using a turbulence intensity of I = 10 % during the steady phase of bore propagation in the edge MRE zone. The results are summarized in Figure 6.8. Full data is provided in the Appendix, section D.2.1.

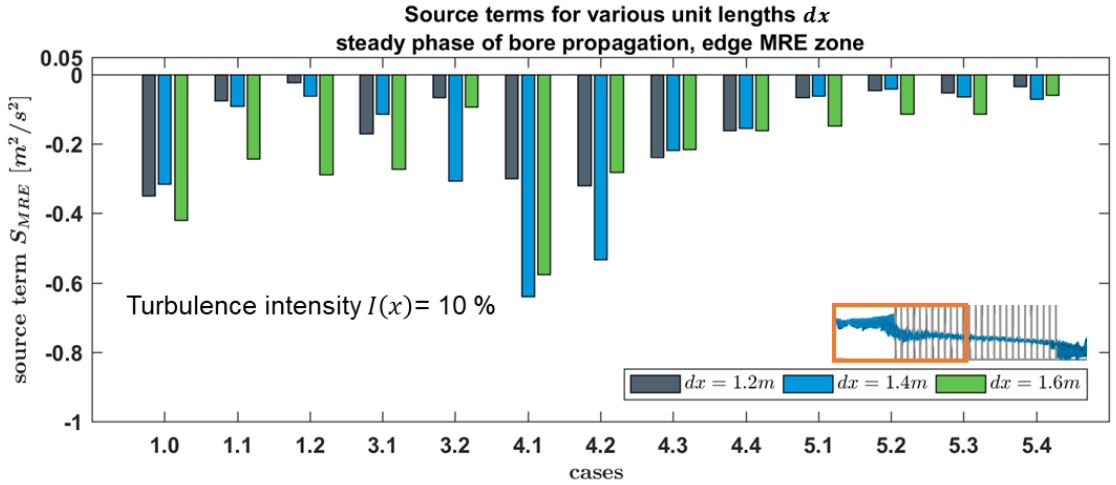

case	*1.0*	1.1	1.2	3.1	3.2	4.1	4.2	4.3	4.4	5.1	5.2	5.3	5.4
Shape (drag coefficient C_D) [-]	*2.05*	**1.2**	**1.55**	2.05	2.05	2.05	2.05	2.05	2.05	2.05	2.05	2.05	2.05
Arrangement angle Ψ [°]	*0*	0	0	**26.57**	**45**	0	0	0	0	0	0	0	0
Normalized width D_B^* [-]	*0.333*	0.333	0.333	0.333	0.333	**0.667**	**0.500**	**0.250**	**0.200**	0.333	0.333	0.333	0.333
Height h_B [m]	$\gg h$	$\gg h$	$\gg h$	$\gg h$	$\gg h$	$\gg h$	$\gg h$	$\gg h$	$\gg h$	**0.215**	**0.161**	**0.108**	**0.054**
Mean source term S_{MRE} [m²/s²]	*-0.361*	-0.136	-0.123	-0.185	-0.155	-0.506	-0.378	-0.223	-0.159	-0.092	-0.067	-0.077	-0.054
Standard deviation $STDEV$ [m²/s²]	*0.044*	0.076	0.117	0.066	0.108	0.148	0.111	0.010	0.004	0.015	0.027	0.034	0.040
Relative standard deviation RSD [%]	*12*	56	95	36	70	29	29	4.4	2.2	28	35	50	43

Figure 6.8. Source term S_{MRE} for dx = 1.2 m, 1.4 m and 1.6 m in the edge MRE zone ($x^* \approx 0$) during the steady phase of bore propagation (see Figure 6.3), its mean values S_{MRE}, standard deviations $STDEV$ and relative standard deviations RSD.

The energy losses vary considerably for various unit lengths dx, particularly in case 4.1 (D_B^* = 0.667), where the standard deviation of the source terms using various dx is $STDEV$ = 0.148 m²/s² due to the position of the MRE relative to the cross-sections (see section 5.4.5).

The relative standard deviation takes values between RSD = 2.2 % (case 4.4) and RSD= 95 % (case 1.2), which is smaller then compared to the inner MRE zone (see section 6.2.3). It is seen that under the here investigated conditions, local flow effects affect the solutions to a lesser extent than in the inner MRE zone.

The shape, expressed by means of the drag coefficient C_D, does not seem to be correlated to the mean value of the source term $\bar{S}_{MRE}$ as the smallest C_D = 1.2 (case 1.1) leads to the second

smallest $\bar{S}_{MRE}$ = -0.136 m²/s² and the second smallest C_D = 1.55 (case 1.2) leads to the smallest $\bar{S}_{MRE}$ = -0.123 m²/s². However, as the standard deviation of case 1.2 is with $STDEV$ = 0.117 m²/s² relatively high (RSD = 95 %), local flow effects might have polluted the results so that a correlation between $\bar{S}_{MRE}$ and C_D is here not excluded.

The arrangement angle Ψ correlates with $\bar{S}_{MRE}$ as the smallest Ψ = 0° (case 1.0) leads to the greatest $\bar{S}_{MRE}$ = -0.361 m²/s² and the greatest Ψ = 45° (case 1.2) leads to the smallest $\bar{S}_{MRE}$ = -0.123 m²/s². This is because the rotated MRE deflect water to a higher extent while in case of Ψ = 0° the flow is blocked (see also section 5.5.4).

The normalized width D_B^* is related to $\bar{S}_{MRE}$ as the greatest D_B^* = 0.667 (case 4.1) leads to the greatest $\bar{S}_{MRE}$ = -0.506 m²/s². $\bar{S}_{MRE}$ is continuously decreasing with decreasing D_B^*. The smallest D_B^* = 0.200 (case 4.4) leads to the smallest $\bar{S}_{MRE}$ = -0.159 m²/s².

The height h_B seems to be correlated to $\bar{S}_{MRE}$, because the greatest h_B = 0.215 m (case 5.1) leads to the greatest $\bar{S}_{MRE}$ = -0.092 m²/s² and the smallest h_B=0.054 m (case 5.4) leads to the smallest $\bar{S}_{MRE}$ = -0.054 m²/s². The heights in between these extremes, h_B=0.161 m (case 5.2) and h_B = 0.108 m (case 5.3) take values of $\bar{S}_{MRE}$ = -0.067 m²/s² and $\bar{S}_{MRE}$ = -0.077 m²/s², respectively, which indicate that $\bar{S}_{MRE}$ is not continuously decreasing. However, the difference between the $\bar{S}_{MRE}$ of the cases 5.2 and 5.4 is small when comparing to the standard deviation of up to $STDEV$ = 0.034 m²/s². Therefore, it is assumed that local flow effects might have polluted the here presented results to some extent (see section 5.4.5).

Source term S_{MRE} is derived during the unsteady phase of bore propagation in the inner MRE zone and in the edge MRE zone, and during the steady phase of bore propagation only in the edge MRE zone. The analyses are performed for various unit lengths dx and a turbulence intensity I = 10 %.

During the unsteady phase of bore propagation in the inner MRE zone, the arrangement angle Ψ is the dominant factor for S_{MRE}, while at the edge MRE zone, S_{MRE} is considerably influenced by the shape, the arrangement angle Ψ, the normalized width D_B^* and the height h_B of the MRE.

Local flow effects induced by the MRE inside analysed cross-sections are noted particularly when varying D_B^* in the inner MRE zone and during the steady phase of the bore propagation in the edge MRE zone, in which spatial differences between the cross-sections have a higher impact on S_{MRE} than during the unsteady flow phase.

6.3 Assessing the dependencies from non-dimensional variables (Step 5)

In this section, step 5 is performed, where the dependencies of S_{MRE} from the non-dimensional variables Reynolds number Re, Froude number Fr and Euler number Eu are discussed to derive their implications for the fitting procedure in step 6.

Based on the dimensional analysis (see the Appendix, section D.1), the source terms S_{MRE} obtained during the steady and unsteady phases of bore propagation at the upstream edge and inner zone of MRE (see Figure 6.2) are related to

$$Re = \frac{ul_2}{\nu} = \frac{\frac{q(x)}{h}h}{\nu} \tag{6-17.a}$$

$$Fr = \frac{u^2}{l_1 a} = \frac{\left(\frac{q(x)}{h}\right)^2}{hg}, Fr = \frac{\frac{q(x)}{h}}{\sqrt{hg}} \tag{6-17.b}$$

$$Eu = \frac{F}{u^2 l_2^2 \rho} = \frac{p}{\left(\frac{q(x)}{h}\right)^2 \rho}, Eu = \frac{dp}{\left(\frac{q(x)}{h}\right)^2 \rho} \tag{6-17.c}$$

with the flow velocity $u(x) = \frac{q(x)}{h}$, the characteristic length $l_1 = h$, which is the flow depth, the characteristic length l_2 (which is interpreted as the square root of the MRE front face area, so that $l_2^2 = A$), the pressure force F, the pressure $p = \frac{F}{A}$, the acceleration $a = g$, the fluid density ρ and the pressure gradient dp.

Froude number Fr (ratio of flow inertia to gravity) can be used to assess the unsteady phase of bore propagation. Inertia is interpreted as a deviation of the flow velocity over time.

Reynolds number Re (ratio of drag forces to viscous forces) is associated with drag and can be used to describe the steady phase of bore propagation.

Euler number Eu (ratio of pressure gradient to inertia-deviation of flow velocity over space) is related to dynamic pressure differences, which occur between the upstream faces of the MRE, where the flow is slowed down, and beside the MRE near the lateral faces, where high flow velocities occur. Referring to section 5.5, high velocity gradients are mainly observed in the edge zone of the MRE. Such velocity gradients can be expected during steady and unsteady flow conditions. It is noted that they occur inside the unit areas $dxdy$ on sub-grid scale and are not captured by the cross-sections in which the flow parameters are calculated. Therefore, it is difficult to use Eu in the source term S_{MRE}. However, here, drag consists predominantly of form drag, which dominates over friction drag in high Re flow (which is the case here). Form drag results from the pressure distribution over the MRE. Therefore, the pressure force in equation (6-17.c) can be set equal to the drag force component of equation (6-11.c)

$$F_{drag} = \frac{1}{2}\rho C_D A_B \left(\frac{q(x)}{h}\right)^2 = Eu \cdot u^2 l_2^2 \rho = F_{pressure} \tag{6-18}$$

If further the characteristic length l_2 in equation (6-17.c) is expressed as

$$l_2 = \sqrt{A_B} = \sqrt{D_B \, min(h, h_B)} \tag{6-19}$$

with the front face area A_B as a product of the MRE width D_B and the submerged part of the MRE height h_B, then it can be shown that $Eu = \frac{1}{2} C_D$. So, as long as C_D is part of the solution, Eu is implicitly accounted for and does not need to be explicitly considered in the further analysis.

6.3.1 Inertia during the unsteady flow phase of bore propagation in the inner MRE zone

The Froude number Fr in equation (6-17.b) is related to the inertia component of the energy losses S_{MRE}. It is related to the unsteady phase of bore propagation (see Figure 6.3). The dependency between S_{MRE} and Fr is shown in Figure 6.9. The figure shows the mean values of the analysis, which is repeated for various unit lengths dx = {1.2, 1.4, 1.6} m (see also Figure 6.2). The complete data set is given in Appendix D (for the definition of the MRE parameters see Figure 6.4).

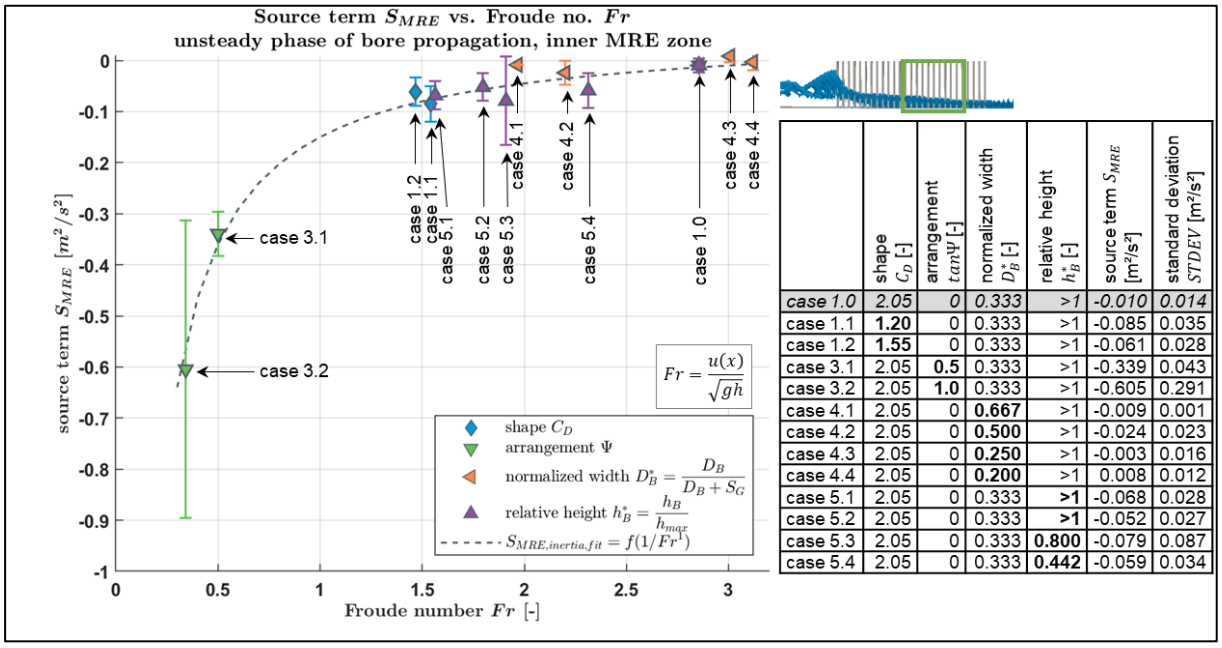

	shape C_D [-]	arrangement $tan\Psi$ [-]	normalized width D_B^* [-]	relative height h_B^* [-]	source term S_{MRE} [m²/s²]	standard deviation $STDEV$ [m²/s²]
case 1.0	*2.05*	*0*	*0.333*	*>1*	*-0.010*	*0.014*
case 1.1	**1.20**	0	0.333	>1	-0.085	0.035
case 1.2	**1.55**	0	0.333	>1	-0.061	0.028
case 3.1	2.05	**0.5**	0.333	>1	-0.339	0.043
case 3.2	2.05	**1.0**	0.333	>1	-0.605	0.291
case 4.1	2.05	0	**0.667**	>1	-0.009	0.001
case 4.2	2.05	0	**0.500**	>1	-0.024	0.023
case 4.3	2.05	0	**0.250**	>1	-0.003	0.016
case 4.4	2.05	0	**0.200**	>1	0.008	0.012
case 5.1	2.05	0	0.333	**>1**	-0.068	0.028
case 5.2	2.05	0	0.333	**>1**	-0.052	0.027
case 5.3	2.05	0	0.333	**0.800**	-0.079	0.087
case 5.4	2.05	0	0.333	**0.442**	-0.059	0.034

Figure 6.9. Source terms S_{MRE} vs. Froude number during unsteady conditions in the inner MRE zone (segments III to VI) for different dx (For the definition of the MRE parameters see Figure 6.4) . The error bars indicate the standard deviations.

The data in Figure 6.9 shows a clear dependency of the source term S_{MRE} from the Froude number Fr and can be expressed as $S_{MRE,inertia,fit} = \frac{-0.21}{Fr} + 0.06$. When investigating individual parameter variations, the following observations are made:

The shape variations (expressed by drag coefficient C_D) are not directly related to S_{MRE}. For (inverse) proportionality, Fr for the case with C_D = 2.05 (case 1.0) should be smaller than for case 1.2 with C_D = 1.55. For an explanation, it is first to note that inside the MRE zone, the flow velocities vary largely over a cross-section (which is also indicated in section 5.4.5) and that the MRE are located in slow flow regions. Second, it is referred to section 5.5.2, where the flow

fields around the MRE of various shapes are discussed (e.g. Figure 5.12, showing maximum normalized flow velocities u^*_{max} between the MRE). It is seen that even if the averaged flow velocities in the cross-sections are similar, the flow approaching the front face(s) of an individual MRE inside the cross-section vary considerably. u^*_{max} is much smaller in case of cubic MRE (case 1.0) than in case of diamond-shaped (case 1.2) or cylindrical MRE (case 1.1). Therefore, the here used averaged flow velocity used in Froude number Fr cannot lead to a direct relation of C_D to S_{MRE}. Because the energy losses with S_{MRE} < 0.1 m²/s² are very small, which is approximately the range of uncertainty of $2 \cdot STDEV$ = 0.07 m²/s² (see Figure 6.6), the influence of the shape on S_{MRE} is neglected here.

Regarding the normalized height h^*_B variations, it is noted that the submerged cases with h^*_B = 0.442 and h^*_B = 0.800 (cases 5.4 and 5.3, respectively, see Figure 6.9) lead to higher energy losses than the fully emerged case 1.0, because additional flow disturbance can be induced downstream of the MRE, when the MRE are overflown. It is further noted, that the cases 5.1 and 5.2 appear to be emerged during the investigated conditions (see Figure 6.9) for the averaged flow depth h = 0.118 m and h = 0.112 m, respectively. Therefore, one would expect similar energy losses as for the fully emerged case 1.0, but in contrast, both cases show higher energy losses than case 1.0, suggesting that some MRE between the investigated cross-sections might still be overflown.

This is shown by investigating the analysed time step ∂t (see equation (6-7.a)) exemplary for a unit length dx= 1.4 m in the inner MRE area for case 5.1, in which the averaged flow depth is h = 0.118 m and the MRE height h_B = 0.215 m. For deriving the source terms, the time step is determined as shown in section 5.4.2. The maximum flow velocity occurs in the outlet cross-section at t_j= 2.68 s, leading to a time step of dt = 0.33 s, so that dt ends at t_{j+1} = 3.01 s. The bore propagation during this period is depicted in Figure 6.10.

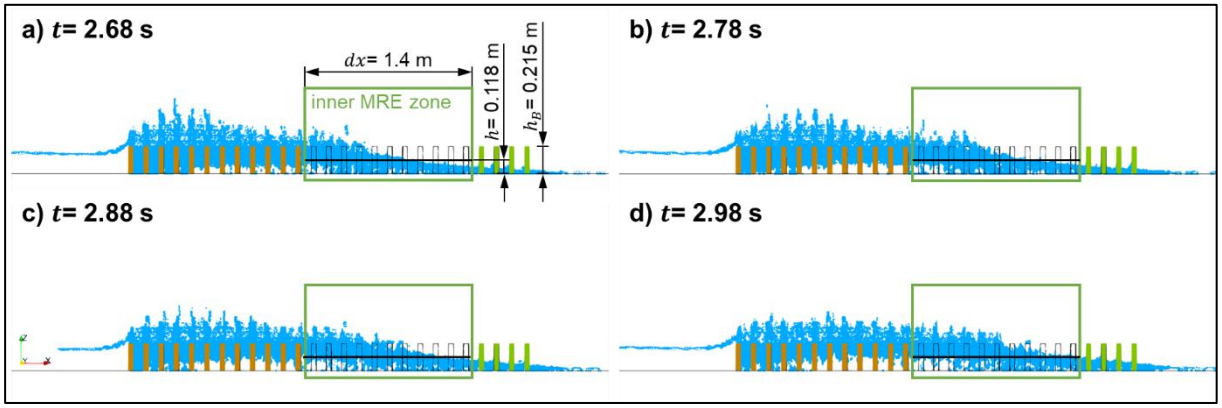

Figure 6.10. Unit length dx with overflown MRE during a time step dt = 0.33 s for the unsteady phase of bore propagation: a) t = 2.68 s, b) t = 2.78 s, c) t= 2.88 s and d) t = 2.98 s.

During this period, some of the MRE are overflown, leading to additional flow disturbance, although the averaged h is smaller than h_B. This suggests that even if the MRE height is almost double as high as the flow depth, additional energy losses can still be induced compared to the fully emerged cases (e.g. case 1.0).

It is suggested that the factor f_{eff} (see equation (6-13)) should account for the spatial deviations of the flow depth during the unsteady phase of the bore propagation, which may also include effects such as run-up on the front faces of the MRE. Here, h_B = 0.215 m, so that $f_{eff} = h_B/h$ = 1.82.

The energy losses obtained from the cases 5.3 and 5.4, which are fully submerged during the investigated flow condition, are proportional to the relative height, as one would expect: greater h_B in case 5.3 leads to greater S_{MRE} compared to case 5.4. The energy losses take values of S_{MRE} > -0.1 m²/s² and are very small.

Regarding the normalized width D_B^* variations, in contrast to expectations, the lowest value of D_B^* = 0.2 (case 4.4) is not associated with the lowest value of S_{MRE}, and the largest value of D_B^* = 0.667 (case 4.1) is not associated with the largest value of S_{MRE}. The reason for the observed inconsistencies lies mainly in the presence of the MRE near the cross-sections, because the MRE influences the local flow velocities and flow depths, which may have a significant effect on the averaged flow parameters at the cross-sections (see also section 5.4.5).

The variation of the arrangement angle Ψ (cases 3.1 and 3.2) causes energy losses of S_{MRE} < -0.3 m²/s². S_{MRE} is proportional to arrangement angle Ψ which is by far the most important parameter to describe the energy losses in the inner MRE zone during the unsteady phase of the bore propagation (see also section 5.5.4).

6.3.2 Drag during the steady phase of bore propagation in the edge MRE zone

The Reynolds number Re in equation (6-17.a) is associated with the square root of the MRE front face area (see equation (6-19)). The dependency between the source term S_{MRE} during the steady phase of bore propagation in the edge MRE zone (see Figure 6.3) and the $Re(l_2)$ is depicted in Figure 6.11. The figure shows the mean values of the analysis, which is repeated for various unit lengths dx = 1.2 m, 1.4 m and 1.6 m (see also Figure 6.2). For the definition of the MRE parameters please refer to Figure 6.4.

By visual inspection of Figure 6.11, clear dependencies of the energy losses S_{MRE} from $Re(l_2)$ can be identified. It seems that for the variations of the relative height h_B^* and the arrangement angle Ψ, the dependency of S_{MRE} from Re can be expressed as $S_{MRE,drag,fit2}(h_B^*, \Psi) = 10^{-16} Re^3 + 0.01$, while for the variation of the normalized width D_B^*, the dependency is rather $S_{MRE,drag,fit1}(D_B^*) = \frac{-1.3 \cdot 10^{10}}{Re^2} + 0.28$. When investigating individual parameter variations further, the following observations are made:

The normalized MRE width D_B^* (cases 4.1 to 4.4) clearly appears to have the greatest influence on the energy losses S_{MRE}, but it is noted that Re only varies between $1.3 \cdot 10^5$ and $1.85 \cdot 10^5$.

Regarding the arrangement angle Ψ (cases 3.1 and 3.2), it is noted that increasing Ψ leads to a reduction of S_{MRE}, which is the opposite from the behaviour observed in the inner MRE zone (see section 6.3.1). It becomes clear that the most upstream MRE row in the edge MRE zone

becomes more permeable due to the rotation of MRE group by Ψ (see also section 5.5.4), which leads to smaller energy losses compared to the arrangement, in which Ψ = 0° (case 1.0).

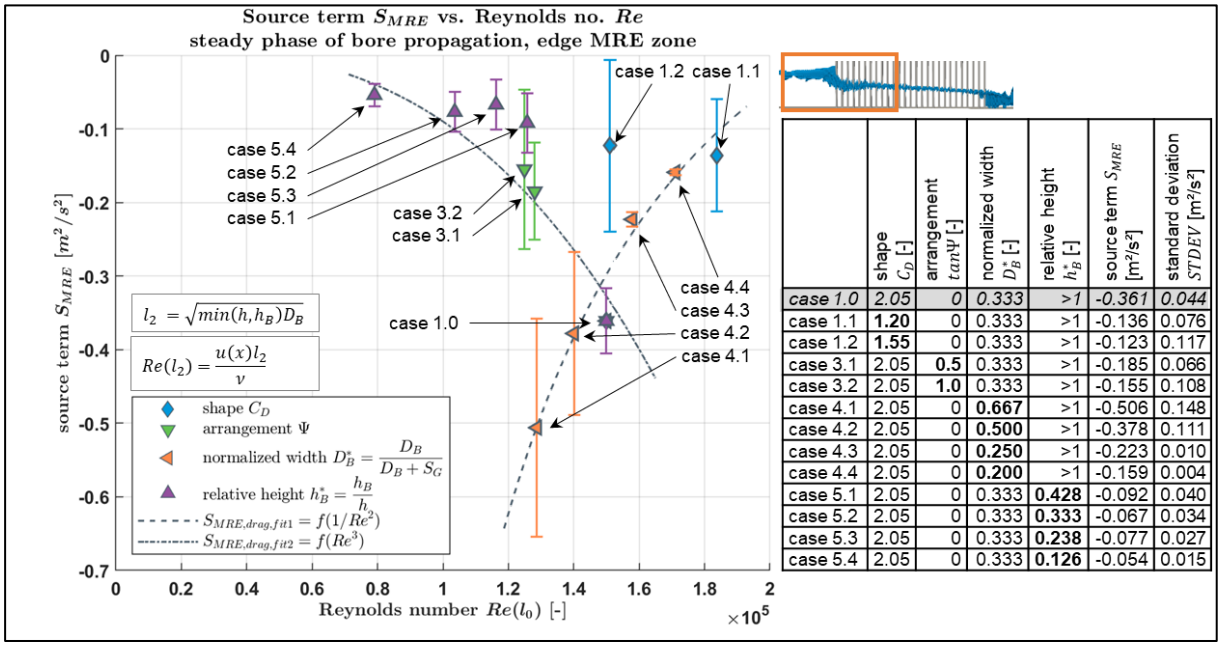

	shape C_D [-]	arrangement $tan\Psi$ [-]	normalized width D_B^* [-]	relative height h_B^* [-]	source term S_{MRE} [m²/s²]	standard deviation $STDEV$ [m²/s²]
case 1.0	*2.05*	*0*	*0.333*	*>1*	*-0.361*	*0.044*
case 1.1	**1.20**	0	0.333	>1	-0.136	0.076
case 1.2	**1.55**	0	0.333	>1	-0.123	0.117
case 3.1	2.05	**0.5**	0.333	>1	-0.185	0.066
case 3.2	2.05	**1.0**	0.333	>1	-0.155	0.108
case 4.1	2.05	0	**0.667**	>1	-0.506	0.148
case 4.2	2.05	0	**0.500**	>1	-0.378	0.111
case 4.3	2.05	0	**0.250**	>1	-0.223	0.010
case 4.4	2.05	0	**0.200**	>1	-0.159	0.004
case 5.1	2.05	0	0.333	**0.428**	-0.092	0.040
case 5.2	2.05	0	0.333	**0.333**	-0.067	0.034
case 5.3	2.05	0	0.333	**0.238**	-0.077	0.027
case 5.4	2.05	0	0.333	**0.126**	-0.054	0.015

Figure 6.11. Source terms S_{MRE} vs. Froude number during steady conditions in the upstream edge of the MRE zone (segments I and II) for different dx (see Figure 6.4 for definition of MRE parameters). The error bars indicate the standard deviations.

Regarding the shape variations (expressed by the drag coefficient C_D), no clear dependency is seen between energy losses S_{MRE} and Reynolds number Re. On one hand, case 1.0 using C_D = 2.05 (cubic shape) leads to the greatest S_{MRE}. Case 1.1 with C_D = 1.2 (cylindrical shape) leads to greater S_{MRE} than case 1.2 with C_D = 1.55 (diamond-shaped), so that S_{MRE} is not proportional to C_D. On the other hand, Re is considerably higher in case 1.1 than in case 1.2, for which Re is slightly higher than in case 1.0, so that $Re \propto f(C_D)$. This is in agreement with the observation made in section 5.5.2, where it is noted that in case 1.2 the flow is more deflected by the front faces of the diamond than blocked. Therefore, it allows for higher (averaged) flow velocities between the MRE, but also considerably smaller flow velocities at the front faces of the diamond-shaped MRE, resulting in smaller S_{MRE}. This explains why the energy losses in case 1.2 with $S_{MRE,case1.2\ (C_D=1.55)}$ = -0.123 m²/s² are slightly smaller than in the case 1.1 with $S_{MRE,case1.1\ (C_D=1.2)}$ = -0.136 m²/s². However, referring to Figure 6.11, it needs to be mentioned that the standard deviations $(STDEV)$ due to local flow effects in case 1.2 (C_D = 1.55) and case 1.1 (C_D = 1.2) take high values of $STDEV$= 0.117 m²/s² and $STDEV$ = 0.076 m²/s², respectively. Comparing it to the difference between the calculated energy losses between both cases 1.1 and 1.2, $\Delta S_{MRE} = |S_{MRE,case1.1} - S_{MRE,case1.2}|$= 0.013 m²/s, it imposes high uncertainty on any quantitative conclusion.

Regarding the relative height h_B^* variations in cases 5.2 and 5.3, respectively with h_B^* = 0.238 and h_B^* = 0.333, an inconsistency is seen as the energy losses S_{MRE} seem to increase with increasing Re, which is opposite to the tendency noted for the cases 5.1 and 5.4, where S_{MRE}

decreases with increasing Re. This observation might be due to local flow effects as discussed in section 5.4.5, because the absolute difference between both mean energy losses in cases 5.2 and 5.3, $\Delta S_{MRE} = \left|S_{MRE,case5.2} - S_{MRE,case5.3}\right|$= 0.01 m²/s² is smaller than the standard deviation $STDEV$ = 0.033 m²/s² (see Figure 6.11). The energy losses for the cases with h_B^* < 0.5 take values of S_{MRE} > -0.1 m²/s², only. However, the differences in S_{MRE} among the cases varying h_B^* are relatively small, which might be related to the formation of a boundary layer with low flow velocities (see section 5.5.6).

It is noted that (i) two parameters h_B^* and Ψ can be related to Re^3, while one parameter D_B^* is related to $1/Re^2$. Furthermore, (ii) the change in Re in Figure 6.11 is dominated by the spacing S_G (relative standard deviation of S_G of the cases 1.0 and 4.1 to 4.4 is RSD = 0.80), while the flow depth h and the volume flux $q(x)$ change only slightly (see Table D.6, where the relative standard deviation of $u(x) = q(x)/h$ of the cases 1.0 and 4.1 to 4.4 is RSD = 0.17, only). As (iii) S_G forms part of D_B^* (see equation (6-16)), the dependency of the energy losses from $1/Re^2$ is neglected and are related to D_B^* and Re directly. Assuming constant kinematic viscosity of the fluid, Re depends mainly on D_B^*, h_B^*, S_G and $q(x)/h$, so that Re is considered implicitly.

Clear dependencies are observed of the source terms S_{MRE} from:

- *Froude number Fr in the inner MRE zone during the unsteady phase of bore propagation*: Only the variation of the arrangement angle Ψ leads to considerably high energy losses of S_{MRE} < -0.3 m²/s², which is approximately three times higher than for all other parameters with only S_{MRE} > -0.1 m²/s². The shape shows an inverse proportionality. For considering the MRE height h_B, an effective flow depth of $h_{eff} \approx 1.8h$ is suggested to account for runup on the front face of the MRE and for flow depth variation in a computational cell. The normalized width D_B^* is not correlated to Fr due to the channelling effect.
- *Reynolds number Re in the edge MRE zone during the steady phase of bore propagation:* The normalized width D_B^* shows the strongest correlation with Re. Ψ is inversely correlated to Re due to the higher permeability of the most upstream located MRE row due to the rotation of the MRE group. The relative MRE height h_B^* shows a small correlation to Re due to the pollution of data with local flow effects and a boundary layer with low flow velocities. The drag coefficient C_D (describing the shape of the MRE) cannot be related to S_{MRE} as (i) C_D does not account for effects such as deflection of flow towards the downstream-located MRE and (ii) high standard deviations of the source terms exclude any conclusion due to the high uncertainty.
- *Euler number Eu* cannot be used directly in the fits for the source term $S_{MRE,fit}$ because the pressure differences at the MRE faces are acting on smaller scale than the unit length dx. However, Eu is indirectly accounted for, when considering the shape of the MRE by using C_D.

The inertia term correlates with $1/Fr$. The drag term is related to Re through D_B^*, h_B^*, the spacing S_G and the flow velocity $q(x)/h$.

6.4 Deriving MRE formula (step 6)

According to equation (6-11.a-c) and the results of the dimensional analysis in Appendix D, the source term will be derived in this section. Based on the Morison equation (equation (2-32)), the source term will have the following structure:

$$S_{MRE,fit} = S_{MRE,fit,inertia} + S_{MRE,fit,drag} \tag{6-20.a}$$

$$S_{MRE,fit,inertia} = \frac{\partial q(x)}{\partial t} \cdot f\left(\frac{1}{Fr}\right) \cdot f(\Psi) \tag{6-20.b}$$

$$S_{MRE,fit,drag} = -\frac{\partial D_B^*}{\partial x} \cdot f\left(\frac{\partial\, D_B^*}{\partial x}\right) \cdot f\left(h_{B,eff}^*\right) \cdot \frac{q(x)^2}{h} \cdot \frac{1}{2} f(C_D) \cdot f(\Psi) \tag{6-20.c}$$

The equations comprise functions f of the parameters

- change of normalized MRE width $\frac{\partial D_B^*}{\partial x}$ with the normalized width D_B^* (see equation (6-16)),
- relative effective height $h_{B,eff}^*$ (see equation (6-15)),
- the MRE shape (represented by the drag coefficient C_D),
- the arrangement angle Ψ and
- the Froude number Fr (see equation (6-17.b)).

It is noted that equation (6-20.b) considers the dependency of energy losses from Ψ, as discussed in section 6.3.1, and the dependency from the inverse Fr as shown in Figure 6.10.

Equation (6-20.c) agrees well with the form of equation (6-11.c). The factor $\frac{1}{2}$, which forms part of the drag term in the Morison equation (2-32) with C_D, originates from the considerations of the Euler number (see section 6.3). The factor $\frac{q(x)^2}{h} = u(x)^2 h$ with the unit [m³/s²] is required to maintain the units of the source term $S_{MRE,fit,drag}$ [m²/s²] as the spatial derivative $\frac{\partial}{\partial x}$ imposes the unit [1/m].

The source terms are developed by sequential fitting of the CFD data obtained from the variation of each parameter. According to equation (6-20.c), $S_{MRE,fit,drag}$ is only applied in the edge MRE zone due to the factor $\frac{\partial D_B^*}{\partial x}$, which is zero in the inner MRE zone. Therefore, $S_{MRE,fit,inertia}$ is developed first in the inner MRE zone during the unsteady phase of bore propagation. The edge MRE zone is then considered to estimate the drag contribution, $S_{MRE,fit,drag}$, to the total term $S_{MRE,fit}$. Finally, the source term $S_{MRE,fit,drag}$ is applied to the edge MRE zone during the steady phase of bore propagation. The solutions are evaluated using three statistical descriptors: correlation coefficient CC, covariance cov and root mean square error $RSME$ as defined in section A.1 of the Appendix.

The following sections will systematically focus on the effects of the MRE parameters on the source term S_{MRE}, including the statistical evaluation of the fits in two idealized situations:

during unsteady phase of bore propagation in the inner MRE zone (section 6.4.1) and during unsteady phase of bore propagation in the edge MRE zone (section 6.4.2).

6.4.1 Source term within the inner MRE zone during the unsteady phase of bore propagation

In this section, the source term $S_{MRE,fit}$ (see equation (6-20.a)) consists of the inertia component only, because the drag component is zero in the inner MRE zone.

Arrangement angle function $f(\Psi)$: Based on the data in Figure 6.12, cases 1.0, 2.1 and 2.2, and Froude number Fr in equation (6-17.b), the fitted function for Ψ reads

$$f(\Psi) = [\mathrm{A}_1 - cos(4\Psi)]^{\alpha_1} \tag{6-21}$$

with A_1 = 1.3 and α_1 = 0.33, so that equation (6-20.b) reads

$$S(\Psi)_{MRE,fit,inertia} = \frac{\partial q(x)}{\partial t}\frac{\sqrt{gh}}{\frac{q(x)}{h}}[1.3 - cos(4\Psi)]^{0.33} \tag{6-22}$$

The arrangement angle function $f(\Psi)$ must not be zero because, otherwise $S(\Psi)_{MRE,fit,inertia} = 0$ (i.e. no inertia losses). Furthermore, $f(\Psi)$ should be equal in case of Ψ = 0° and Ψ = 90°. Assuming an evenly distributed arrangement with equal MRE's with equal widths D_B in x and y direction, it becomes clear that the arrangement angle between Ψ = 0° and Ψ = 45° covers all possible situations. The minimum losses should occur at Ψ = 0° ($cos(0°)$ = 1) and the maximum losses at Ψ = 45° ($cos(4 \cdot 45°)$ = -1).

Compared to the inertia term in equation (6-11.b), it is noted that equation (6-22) does not explicitly include the fluid density ρ, inertia coefficient C_I nor the fluid volume V_B. ρ is excluded from all NLSW momentum equation terms but the turbulent shear stress by multiplying them with $\frac{1}{\rho}$ (e.g. see equation (2-13)). V_B is related to the normalized MRE width D_B^*, for which no considerable contribution to the energy losses are found (see section 6.3.1) and is omitted, so that only the volume flux $q(x)$ can be related to the volume in the inertia term of the Morison equation (2-32). C_I may be interpreted as acceleration due to the change of flow direction due to Ψ, so that $C_I = f(\Psi)$.

The fit in equation (6-22) is visually and statistically evaluated in Figure 6.12.

The arrangement variations in the cases 3.1 and 3.2 (Figure 6.12) lead to source terms $S(\Psi)_{MRE,fit,inertia}$ which are estimated with equation (6-22) with a difference of not more than 2.2 %, except for case 1.0, where the deviation is 139 %. The fit is derived from three averaged values from a total of nine data points (see section 6.2.3). Particularly because the context of Ψ to $S(\Psi)_{MRE,fit,inertia}$ is provided by trigonometric functions and thereby setting a strict framework for the fit, this is assumed to suffice.

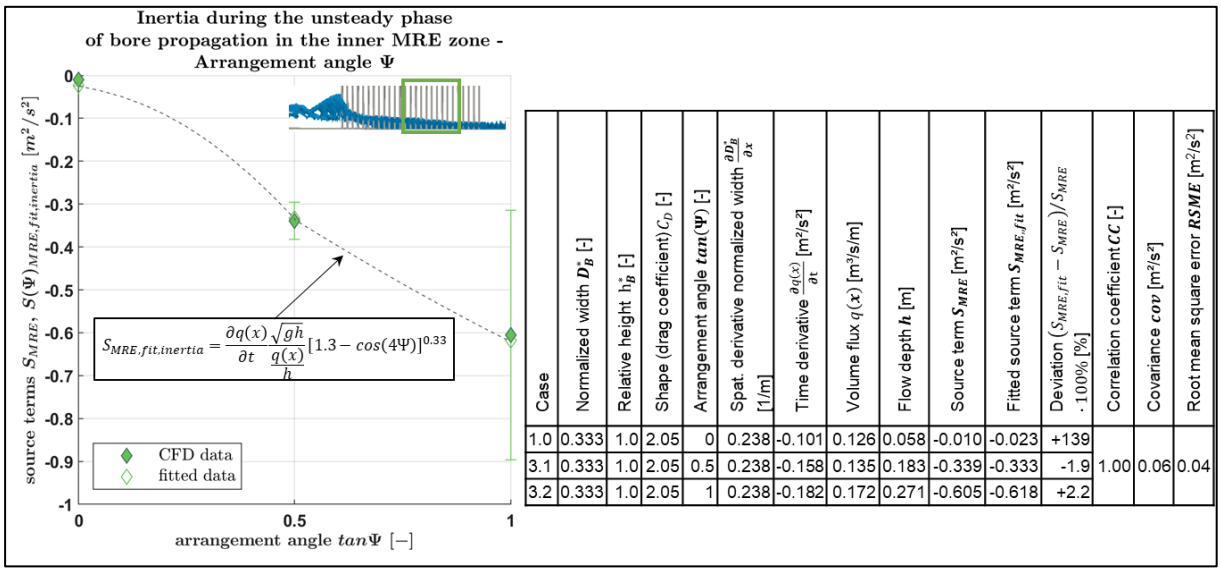

Case	Normalized width D_B^* [-]	Relative height h_B^* [-]	Shape (drag coefficient) C_D [-]	Arrangement angle $tan(\Psi)$ [-]	Spat. derivative normalized width $\frac{\partial D_B^*}{\partial x}$ [1/m]	Time derivative $\frac{\partial q(x)}{\partial t}$ [m²/s²]	Volume flux $q(x)$ [m³/s/m]	Flow depth h [m]	Source term S_{MRE} [m²/s²]	Fitted source term $S_{MRE,fit}$ [m²/s²]	Deviation $(S_{MRE,fit} - S_{MRE})/S_{MRE} \cdot 100\%$ [%]	Correlation coefficient CC [-]	Covariance cov [m²/s²]	Root mean square error $RSME$ [m²/s²]
1.0	0.333	1.0	2.05	0	0.238	-0.101	0.126	0.058	-0.010	-0.023	+139			
3.1	0.333	1.0	2.05	0.5	0.238	-0.158	0.135	0.183	-0.339	-0.333	-1.9	1.00	0.06	0.04
3.2	0.333	1.0	2.05	1	0.238	-0.182	0.172	0.271	-0.605	-0.618	+2.2			

Figure 6.12. Effect of MRE arrangement angle Ψ on the source term S_{MRE} in the inner MRE zone (segments III to VI) during the unsteady phase of bore propagation, including the statistical evaluation of the fit $S(\Psi)_{MRE,fit,inertia}$.

Although the (relative) deviation is large, it is acceptable because of the very small energy losses in these cases, which differ in the fit by only 0.023 m²/s², which is inside the uncertainty range due to local flow effects of $2 \cdot STDEV$ = 0.028 m²/s² (see Figure 6.9). The correlation coefficient of CC = 1.00 confirms excellent ability of the fit $S(\Psi)_{MRE,fit,inertia}$ to follow the variability of S_{MRE}. The covariance of cov = 0.06 m²/s², expressing the balance between under- and overestimation of the fit, is reasonably small and the root mean square error $RMSE$ = 0.04 m²/s² is also small.

6.4.2 Source terms in the edge MRE zone during the unsteady phase of bore propagation

In this section, the source term $S_{MRE,fit,inertia}$ (equation (6-22)), developed in section 6.4.1 by fitting data points in the inner MRE zone, is extended by the drag term $S_{MRE,fit,drag}$, which is only valid in the edge MRE zone due to the spatial derivative term for the normalized MRE width $\frac{\partial D_B^*}{\partial x}$ in equation (6-20.c)). Due to this structure of $S_{MRE,fit,drag}$, its consideration in the NLSW momentum equation is restricted to the edge MRE zone only, so that the here extended equation (6-20.a) is applicable to both the inner and the edge MRE zone. The fits for each parameter variation, which is added to equation (6-22), are presented in the following.

In this section, the change of the normalized MRE width $\frac{\partial D_B^*}{\partial x}$ is incorporated into equation (6-22) first, followed by the adaptation of the source term fit $S_{MRE,fit}$ to account for the variation of the relative effective MRE height $h_{B,eff}^*$, the MRE shape (considered by the drag coefficient C_D) and the arrangement angle Ψ.

Change of normalized MRE width function $f\left(\frac{\partial D_B^*}{\partial x}\right)$: Based on the data in Figure 6.13 of the cases 1.0 and 4.1 to 4.4, the fitted function for the change of the normalized MRE width reads

$$f\left(\frac{\partial D_B^*}{\partial x}\right) = \mathrm{B}_1 \left(\frac{\partial D_B^*}{\partial x}\right)^{\beta_1} \tag{6-23}$$

with $\mathrm{B}_1 = 0.8$ and $\beta_1 = 1$, so that the fitted source term for drag (see equation (6-20.c)

$$S\left(\frac{\partial D_B^*}{\partial x}\right)_{MRE,fit,drag} = -0.8 \frac{\partial D_B^*}{\partial x} \frac{q(x)^2}{h} \tag{6-24}$$

The empirical coefficient $\mathrm{B}_1 = 0.8$ includes all effects of the MRE height, shape and arrangement angle, which are constant in the cases 1.0 and 4.1 to 4.4. The visual and statistical evaluations of equation (6-24) are provided in Figure 6.13.

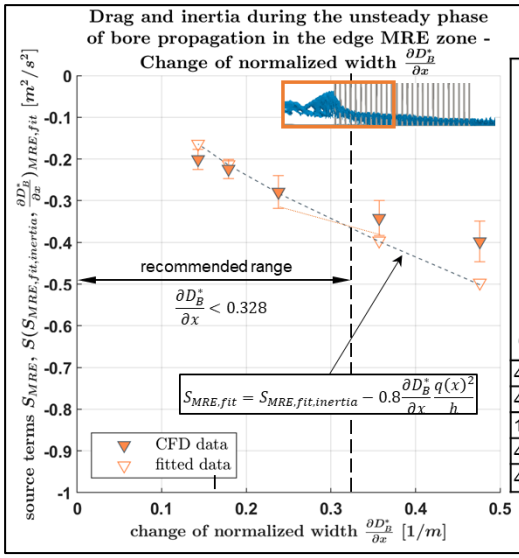

Case	Normalized width D_B^* [-]	Relative height h_B^* [-]	Shape (drag coefficient) C_D [-]	Arrangement angle $tan(\Psi)$ [-]	Spat. derivative normalized width $\frac{\partial D_B^*}{\partial x}$ [1/m]	Time derivative $\frac{\partial q(x)}{\partial t}$ [m²/s²]	Volume flux $q(x)$ [m²/s/m]	Flow depth h [m]	Source term S_{MRE} [m²/s²]	Fitted source term $S_{MRE,fit}$ [m²/s²]	Deviation $(S_{MRE,fit} - S_{MRE})/S_{MRE}$ ·100% [%]	Correlation coefficient CC [-]	Covariance cov [m²/s²]	Root mean square error $RSME$ [m²/s²]
4.1	0.667	1.0	2.05	0	0.476	-0.079	0.434	0.340	-0.398	-0.508	+25			
4.2	0.500	1.0	2.05	0	0.357	-0.061	0.412	0.277	-0.342	-0.405	+16			
1.0	0.333	1.0	2.05	0	0.238	-0.046	0.384	0.220	-0.279	-0.287	0	1.00	0.01	0.05
4.3	0.250	1.0	2.05	0	0.179	-0.029	0.362	0.187	-0.224	-0.218	-5.1			
4.4	0.200	1.0	2.05	0	0.143	-0.018	0.334	0.163	-0.201	-0.168	-18			

Figure 6.13. Effect of the change of normalized width $\frac{\partial D_B^*}{\partial x}$ on the source term S_{MRE} in the edge MRE zone (segments I and II) during the unsteady phase of bore propagation, including the statistical evaluation of the fit $S(D_B^*)_{MRE,fit}$.

In Figure 6.13, it is noted that for large changes of the normalized width $\frac{\partial D_B^*}{\partial x}$ (cases 4.1 and 4.2), the fit overestimates the energy losses $S_{MRE,fit}$ by up to 25 %. In case of small $\frac{\partial D_B^*}{\partial x}$ (case 4.4), the energy losses are underestimated by 18 %. The correlation coefficient of $CC = 1.00$ indicates excellent ability of the fit to reflect the variability of CFD data. The covariance of $cov = 0.01$ m²/s² is very small, expressing the very good balance between overestimation and underestimation of the considered values. The root mean square error $RMSE = 0.05$ m²/s² is acceptable.

It can be seen that the fit works best in for cases 1.0 and 4.3, in which the deviation is only 3 %. By taking into account the range of uncertainty due to local flow effects, which is expressed as

standard deviations in Figure 6.7, and which are depicted as error bars in Figure 6.13, a recommended range for the fit can be defined. For this purpose, the lower ends of the range of uncertainties are linearly interpolated between neighbouring values of the source term S_{MRE}, resulting in a threshold for the application of the fit.

It is concluded that in general a relatively good ability of the fit to reproduce the CFD data can be noted, but large changes in the relative width D_B^* lead to an overestimation of the energy losses. Good results are expected, as long as the ratio between unit length dx and the change of the relative width $\frac{\partial D_B^*}{\partial x}$ < 0.328 1/m. This means that for a good reproduction of the energy losses in the edge MRE zone (e.g. at the coastline), the cell size in the NLSW model should be selected to take values in the range of $dx \geq 3D_B^* \cdot 1$ m. Even in case of very densely covered areas with D_B^* = 0.9 (90 % blockage in case of emerged MRE), a cell size of dx > 2.7 m is recommended, which represents an extremely fine resolution in NLSW models. Such resolution is too fine to consider for example houses as MRE as they can be resolved by the grid. Therefore, the threshold $\frac{\partial D_B^*}{\partial x}$ < 0.328 1/m does practically not restrict the application of the fit.

Relative effective MRE height function $f\left(h_{B,eff}^*\right)$: The fitted function for considering the normalized effective height $h_{B,eff}^*$ (see equations (6-13) and (6-15)) reads

$$f\left(h_{B,eff}^*\right) = \mathrm{B}_2 \left(\frac{min(2h, h_B)}{h}\right)^{\beta_2} \tag{6-25}$$

with B_2 = 1 and β_2 = 1, so that the fitted source term for drag losses (see equation (6-20.c) due to $\frac{\partial D_B^*}{\partial x}$ and $h_{B,eff}^*$ reads

$$S\left(\frac{\partial D_B^*}{\partial x}, h_{B,eff}^*\right)_{MRE,fit,drag} = -0.8 \frac{\partial D_B^*}{\partial x} \frac{q(x)^2}{h} \frac{min(h_B, 2h)}{h} \tag{6-26}$$

With reference to equation (6-10) and the discussion on the variability of the flow depth inside the unit area during the unsteady phase of bore propagation in section 6.3.1, it is noted that the fit is considerably improved by setting f_{eff} in equation (6-13) to f_{eff} = 2.0. The value is close to the previously in section 6.3.1 determined value of f_{eff} = 1.82 to account for the variability of flow depth inside a computational cell and thereby implies that the height of the MRE h_B affects the energy losses even if h_B is 100% higher than the flow depth h, e.g. due to run-up of water on the front face of the MRE.

The visual and statistical evaluations of equation (6-26) are provided in Figure 6.14.

For all cases, the fit $S_{MRE,fit}$ deviates from the energy losses S_{MRE} between -3 % and +15 %. The largest overestimation of S_{MRE} is noted for cases 5.1, where the MRE height is close to the water surface and where MRE is partly overflown. The correlation coefficient CC = 0.98 is very good. The covariance of cov = 0.00 m²/s² states, that under- and overestimation are well-balanced over the range of the considered values of relative effective height $h_{B,eff}^*$. The root mean square error $RMSE$ = 0.02 m²/s² confirms the very good fit.

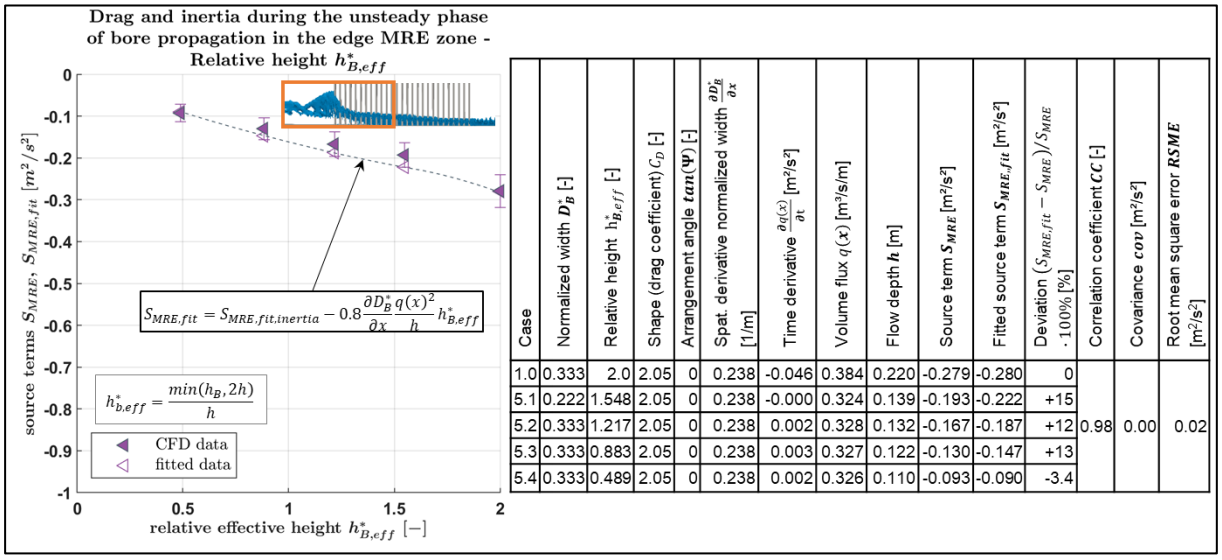

Case	Normalized width D^*_B [-]	Relative height $h^*_{B,eff}$ [-]	Shape (drag coefficient) C_D [-]	Arrangement angle $tan(\Psi)$ [-]	Spat. derivative normalized width $\frac{\partial D^*_B}{\partial x}$ [1/m]	Time derivative $\frac{\partial q(x)}{\partial t}$ [m²/s²]	Volume flux $q(x)$ [m³/s/m]	Flow depth h [m]	Source term S_{MRE} [m²/s²]	Fitted source term $S_{MRE,fit}$ [m²/s²]	Deviation $(S_{MRE,fit} - S_{MRE})/S_{MRE} \cdot 100\%$ [%]	Correlation coefficient CC [-]	Covariance cov [m²/s²]	Root mean square error $RSME$ [m²/s²]
1.0	0.333	2.0	2.05	0	0.238	-0.046	0.384	0.220	-0.279	-0.280	0			
5.1	0.222	1.548	2.05	0	0.238	-0.000	0.324	0.139	-0.193	-0.222	+15			
5.2	0.333	1.217	2.05	0	0.238	0.002	0.328	0.132	-0.167	-0.187	+12	0.98	0.00	0.02
5.3	0.333	0.883	2.05	0	0.238	0.003	0.327	0.122	-0.130	-0.147	+13			
5.4	0.333	0.489	2.05	0	0.238	0.002	0.326	0.110	-0.093	-0.090	-3.4			

Figure 6.14. Effect of the normalized effective height $h^*_{B,eff}$ on the source term S_{MRE} in the edge MRE zone (segments I and II) during the unsteady phase of bore propagation, including the statistical evaluation of the fit $S(D^*_B, h^*_{B,eff})_{MRE,fit}$.

MRE shape (described by C_D): Based on the data in Figure 6.15, cases 1.0 to 1.2, the fitted function for considering the effect of the MRE shape (described by the drag coefficient C_D) reads

$$f(C_D) = \mathrm{B}_3 {C_D}^{\beta_3} \tag{6-27}$$

with B_3 = 0.5 and β_3 = 1. It is noted that the factor B_3 is in agreement with the considerations regarding the Euler number Eu (see section 6.3) and the drag force in the Morison equation (2-32). The fitted source term for considering drag losses due to the normalized $\frac{\partial D^*_B}{\partial x}$, $h^*_{B,eff}$ and C_D reads

$$S\left(\frac{\partial D^*_B}{\partial x}, h^*_{B,eff}, C_D\right)_{MRE,fit,drag} = -0.39\frac{\partial D^*_B}{\partial x}\frac{q(x)^2}{h}h^*_{B,eff}C_D \tag{6-28}$$

The visual and statistical evaluations of equation (6-28) are provided in Figure 6.15.

The fit is derived from three averaged values from a total of nine data points (see section 6.2.4). The fitted source term $S_{MRE,fit}$ underestimates the source S_{MRE} term derived from CFD data by up to 19 % in case 1.2 of diamond-shaped MRE. In the cases 1.0 and 1.1 (cubic and cylindrical), the underestimation is 2.1 % or less. The correlation coefficient of CC = 0.85 indicates the deficit of using a (constant) drag coefficient in the fit in representing the energy losses in case 1.2, which does not account for deflection, but it is still in a reasonable range. The covariance cov = 0.00 m²/s² is very small and root mean square error $RMSE$ = 0.03 m²/s² is small, too.

The statistical descriptors confirm a good agreement for the variation of the shape.

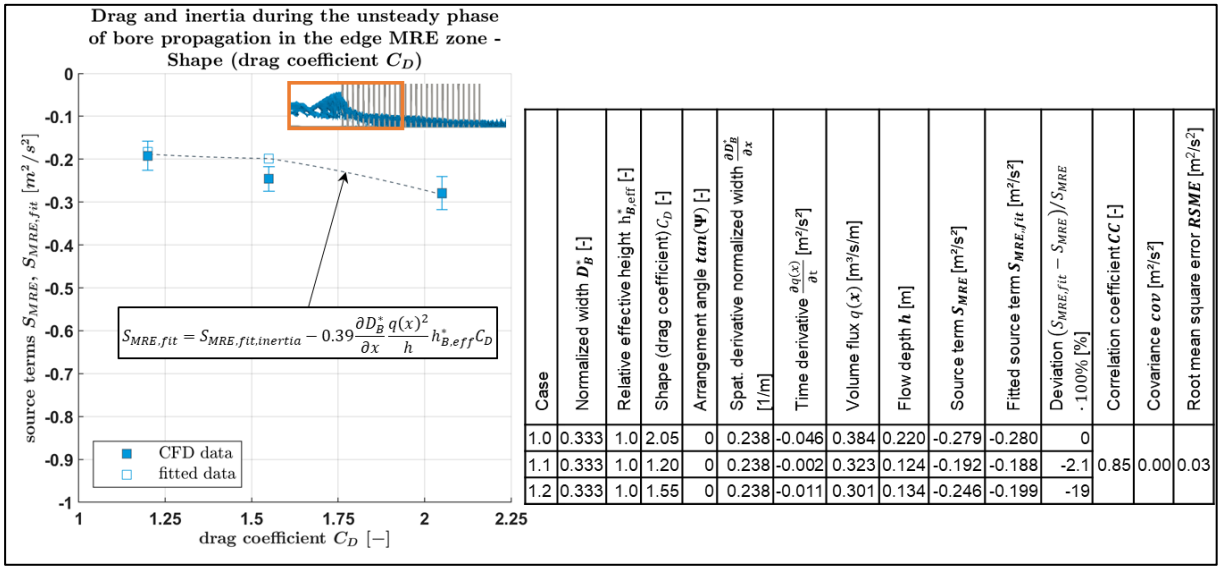

Case	Normalized width D_B^* [-]	Relative effective height $h_{B,eff}^*$ [-]	Shape (drag coefficient) C_D [-]	Arrangement angle Ψ [-]	Spat. derivative normalized width $\frac{\partial D_B^*}{\partial x}$ [1/m]	Time derivative $\frac{\partial q(x)}{\partial t}$ [m²/s²]	Volume flux $q(x)$ [m³/s/m]	Flow depth h [m]	Source term S_{MRE} [m²/s²]	Fitted source term $S_{MRE,fit}$ [m²/s²]	Deviation $(S_{MRE,fit} - S_{MRE})/S_{MRE} \cdot 100\%$ [%]	Correlation coefficient CC [-]	Covariance cov [m²/s²]	Root mean square error $RSME$ [m²/s²]
1.0	0.333	1.0	2.05	0	0.238	-0.046	0.384	0.220	-0.279	-0.280	0			
1.1	0.333	1.0	1.20	0	0.238	-0.002	0.323	0.124	-0.192	-0.188	-2.1	0.85	0.00	0.03
1.2	0.333	1.0	1.55	0	0.238	-0.011	0.301	0.134	-0.246	-0.199	-19			

Figure 6.15. Effect of the drag coefficient C_D on the source term S_{MRE} in the edge MRE zone (segments I and II) during the unsteady phase of bore propagation, including the statistical evaluation of the fit $S\left(D_B^*, h_{B,eff}^*, C_D\right)_{MRE,fit}$.

Arrangement angle Ψ: Based on the data in Figure 6.16, cases 1.0, 2.1 and 2.2, the fitted function for considering the arrangement angle Ψ reads

$$f(\Psi) = \{1 - \mathrm{B}_4[1 - cos(4\Psi)]\}^{\beta_4} \tag{6-29}$$

With B_4 = 0.3 and β_4 = 0.1. The function considers that its smallest value must be $f(\Psi)$ = 1, which is the case, if the arrangement angle Ψ = 0° ($cos(0°) = 1$). The maximum impact is expected, if Ψ = 45° ($cos(4 \cdot 45°) = -1$). $f(\Psi)$ increases with larger Ψ values, which is controlled by the factor B_4. The condition of $\mathrm{B}_4 < 0.5$ applies to prevent that the sign of $f(\Psi)$ can change. It is further considered that increasing Ψ (up to 45°) leads to a reduction of the energy losses, which is also noted in Figure 6.11.

The fitted source term for considering drag losses due to the normalized $\frac{\partial D_B^*}{\partial x}$, $h_{B,eff}^*$, C_D and Ψ reads

$$S\left(D_B^*, h_{B,eff}^*, \mathrm{C}_D, \Psi\right)_{MRE,fit,drag} = -0.39\frac{\partial D_B^*}{\partial x}\frac{q(x)^2}{h}h_{B,eff}^* C_D[0.7 + 0.3cos(4\Psi)]^{0.1} \tag{6-30}$$

The visual and statistical evaluations of this fit are provided in Figure 6.16.

The fit underestimates the energy losses for arrangement angles Ψ of up to approximately 20 % (Ψ = 26.565°), while the deviations for Ψ = 0° and Ψ = 45° are with 0 % and +2.2 % very small. The correlation coefficient of CC = 0.75 reveals that the fit has deficits in following the trend of the MRE data. The covariance as a balance between underestimation and overestimation cov = 0.00 is very small and the root mean square error $RMSE$ = 0.05 is acceptable.

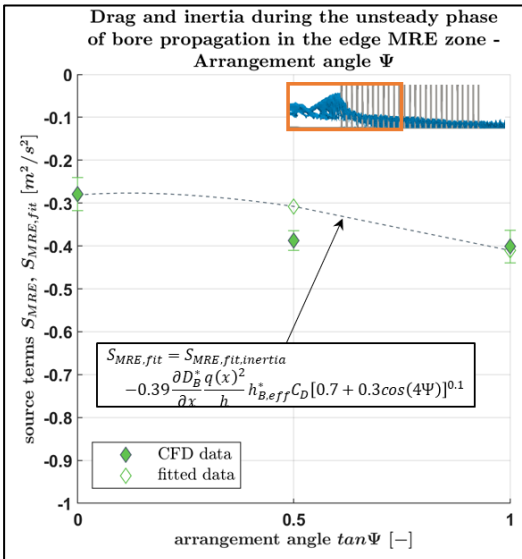

Case	Normalized width D_B^* [-]	Relative effective height $h_{B,eff}^*$ [-]	Shape (drag coefficient) C_D [-]	Arrangement angle $tan(\Psi)$ [-]	Spat. derivative normalized width $\frac{\partial D_B^*}{\partial x}$ [1/m]	Time derivative $\frac{\partial q(x)}{\partial t}$ [m²/s²]	Volume flux $q(x)$ [m³/s/m]	Flow depth h [m]	Source term S_{MRE} [m²/s²]	Fitted source term $S_{MRE,fit}$ [m²/s²]	Deviation $(S_{MRE,fit} - S_{MRE})/S_{MRE}$ ·100% [%]	Correlation coefficient CC [-]	Covariance cov [m²/s²]	Root mean square error $RSME$ [m²/s²]
1.0	0.333	2.0	2.05	0	0.238	-0.046	0.384	0.220	-0.279	-0.280	0			
3.1	0.333	2.0	2.05	0.5	0.238	-0.092	0.366	0.260	-0.387	-0.308	-20	0.75	0.00	0.05
3.2	0.333	2.0	2.05	1	0.238	-0.111	0.447	0.353	-0.401	-0.410	+2.2			

Figure 6.16. Effect of the arrangement angle Ψ on the source term S_{MRE} in the edge MRE zone (segments I and II) during the unsteady phase of bore propagation, including the statistical evaluation of the fit $S\left(D_B^*, h_{B,eff}^*, C_D, \Psi\right)_{MRE,fit}$.

The following formulae for energy losses due to drag and inertia are developed in analogy to the Morrison equation:

$$S_{MRE,fit} = S_{MRE,fit,inertia} + S_{MRE,fit,drag} \tag{6-31.a}$$

$$S_{MRE,fit,inertia} = \frac{\partial q(x)}{\partial t}\frac{\sqrt{gh}}{\frac{q(x)}{h}}[1.3 - cos(4\Psi)]^{0.33} \tag{6-31.b}$$

$$S_{MRE,fit,drag} = -0.4\frac{\partial D_B^*}{\partial x}\frac{q(x)^2}{h} h_{B,eff}^* C_D[0.7 + 0.3cos(4\Psi)]^{0.1} \tag{6-31.c}$$

in which the relative effective height is defined as $h_{B,eff}^* = \frac{min(2h, h_B)}{h}$, taking into account that, due to flow depth variations in a unit area and due to run-up on the front faces of the MRE, higher parts of the MRE of up to twice the flow depth contribute to the energy losses.

The source term (equation (6-31.b)) is expected to describe the inertia losses by relating the impact to the arrangement angle Ψ very well due to the small root mean square error $RSME$ = 0.04 m²/s².

The drag loss term (equation (6-31.c)) slightly underestimates the effects of the change of the normalized width $\frac{\partial D_B^*}{\partial x}$ and the effects of the shape (represented by C_D) in the range of $RSME$ = 0.03 m²/s² and Ψ in the range of $RSME$ = 0.05 m²/s², while the representation of the influence of the relative effective height $h_{B,eff}^*$ seems to be very well confirmed by $RSME$ = 0.02 m²/s².

In total, it is expected that the energy losses are slightly underestimated by the MRE formula, mainly due to deficits in describing the shape by drag coefficient C_D.

6.5 Application and evaluation of MRE formula (step 7)

The formula derived from two idealized situations of the bore propagation in the MRE zone is applied to a third situation: the steady flow phase in the edge MRE zone, thereby showing the formula's applicability for the entire period of bore propagation, consisting of the unsteady and steady flow phases in the edge and the inner MRE zone, while energy losses during the steady phase of bore propagation in the inner MRE zone (the fourth and last possible idealized situation) seem to be the least decisive for evaluating the MRE formula (as concluded from chapter 5). The three combinations of flow phases and locations are then analysed by statistical descriptors to show the performance of the MRE formula during bore propagation.

In section 6.5.1, the derived MRE formula is applied to the edge MRE zone during steady phase of bore propagation. In section 6.5.2, performance of the MRE formula is assessed by means of statistical descriptors for three flow conditions.

6.5.1 Source terms in the edge MRE zone during steady phase of bore propagation

Equation (6-30) is applied to the steady phase of bore propagation in the edge of the MRE zone (see also Figure 6.3) and evaluated for each parameter variation in this section.

The impact of local flow effects is considered by calculating the source term S_{MRE} for various unit lengths dx = {1.2, 1.4, 1.6} m. As local flow effects are associated with the position of the MRE and cross-sections, the here noted impacts correspond to the situation in section 6.3.2, in which the steady phase of bore propagation in the edge MRE zone ($x^* \approx 0$) is addressed.

Shape C_D: Figure 6.17 presents S_{MRE} and the results of the fitting equation (6-30) due to drag and inertia during the steady phase of bore propagation, when varying the shape (expressed as drag coefficient C_D).

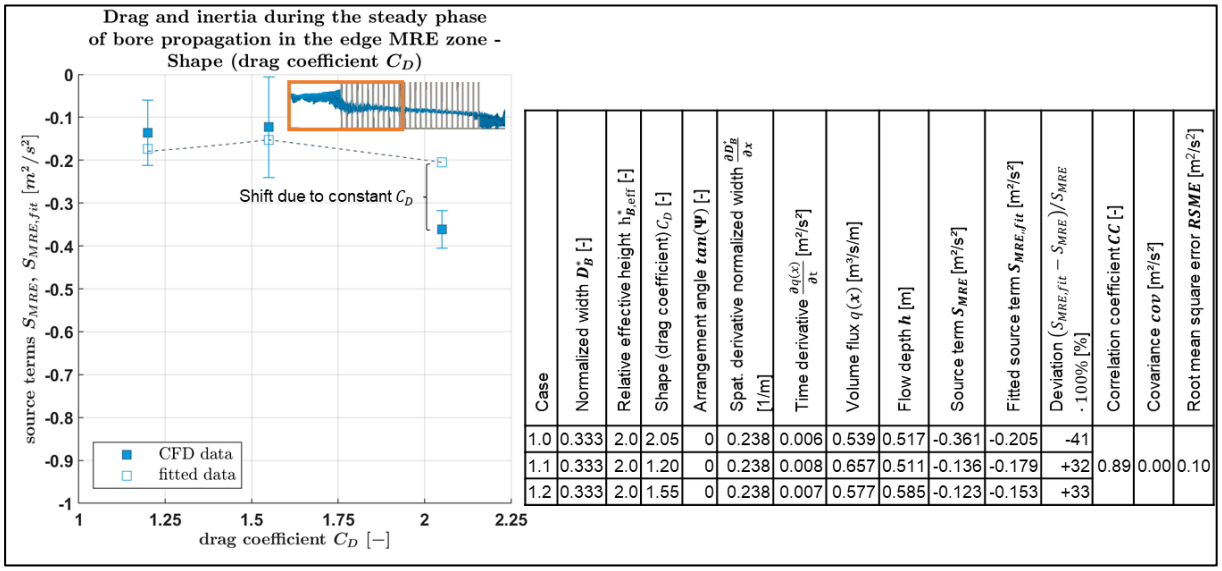

Case	Normalized width D_B^* [-]	Relative effective height $h_{B,eff}^*$ [-]	Shape (drag coefficient) C_D [-]	Arrangement angle $tan(\Psi)$ [-]	Spat. derivative normalized width $\frac{\partial D_B^*}{\partial x}$ [1/m]	Time derivative $\frac{\partial q(x)}{\partial t}$ [m²/s²]	Volume flux $q(x)$ [m³/s/m]	Flow depth h [m]	Source term S_{MRE} [m²/s²]	Fitted source term $S_{MRE,fit}$ [m²/s²]	Deviation $(S_{MRE,fit} - S_{MRE})/S_{MRE} \cdot 100\%$ [%]	Correlation coefficient CC [-]	Covariance cov [m²/s²]	Root mean square error $RSME$ [m²/s²]
1.0	0.333	2.0	2.05	0	0.238	0.006	0.539	0.517	-0.361	-0.205	-41			
1.1	0.333	2.0	1.20	0	0.238	0.008	0.657	0.511	-0.136	-0.179	+32	0.89	0.00	0.10
1.2	0.333	2.0	1.55	0	0.238	0.007	0.577	0.585	-0.123	-0.153	+33			

Figure 6.17. Effect of the drag coefficient C_D on the source term S_{MRE} in the edge MRE zone (segments I and II) during the steady phase of bore propagation, including the statistical evaluation of the fit $S_{MRE,fit}$.

In case 1.0 (basic configuration), the fitted source term is 41 % smaller than the source term derived from the CFD data, while for the other shapes cylinder and diamond the energy losses overestimated between 35 % and 33 %, respectively. The fit is barely able to reproduce the relation between the energy losses S_{MRE} and the drag coefficient C_D. As pointed out in section 6.3.2, no clear correlation between both parameters are seen. However, the fitted source term is able to reproduce the trend of S_{MRE}, that the basic configuration case 1.0 (C_D = 2.05) leads the highest energy losses and the diamond configuration case 1.2 (C_D = 1.55) to the smallest. This is reflected by the good CC = 0.93 and the very low cov = 0.00 m²/s². The $RMSE$ = 0.09 m²/s² is, however, relatively high when compared with absolute values of S_{MRE} between -0.123 m²/s² (case 1.2) and -0.361 m²/s² (case 1.0).

When comparing the here obtained results for the steady phase of bore propagation with the results for the unsteady flow phase (see section 6.4.2), then it becomes clear that the combination of drag and inertia components works better under unsteady conditions. In other words, it reproduces the energy losses in the bore front better than in the later “quasi-steady” current. Goseberg et al. (2015) investigated drag in transient flow, showing that smaller flow velocities result in higher C_D. Here, however, it is not accounted for variable C_D. Using a constant drag coefficient for both flow phases might contribute to the here observed differences.

Arrangement angle Ψ: Figure 6.18 presents S_{MRE} and the results of the fit (equation (6-30)) due to drag and inertia during the steady phase of bore propagation, when varying the arrangement angle Ψ).

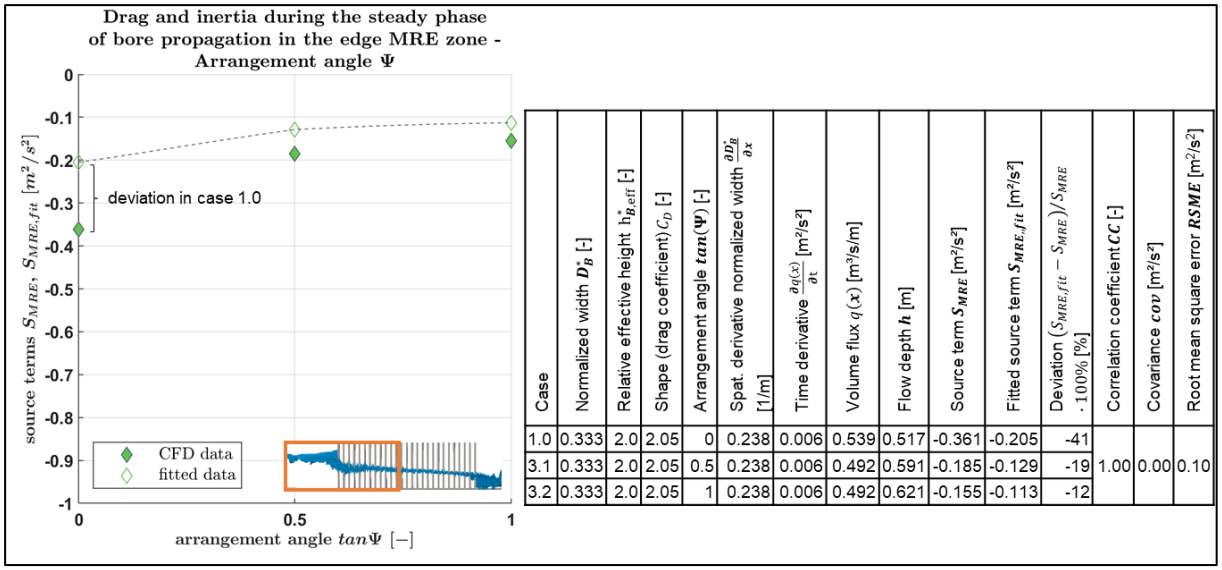

Case	Normalized width D_B^* [-]	Relative effective height $h_{B,eff}^*$ [-]	Shape (drag coefficient) C_D [-]	Arrangement angle $tan(\Psi)$ [-]	Spat. derivative normalized width $\frac{\partial D_B^*}{\partial x}$ [1/m]	Time derivative $\frac{\partial q(x)}{\partial t}$ [m²/s²]	Volume flux $q(x)$ [m³/s/m]	Flow depth h [m]	Source term S_{MRE} [m²/s²]	Fitted source term $S_{MRE,fit}$ [m²/s²]	Deviation $(S_{MRE,fit} - S_{MRE})/S_{MRE}$ ·100% [%]	Correlation coefficient CC [-]	Covariance cov [m²/s²]	Root mean square error $RSME$ [m²/s²]
1.0	0.333	2.0	2.05	0	0.238	0.006	0.539	0.517	-0.361	-0.205	-41			
3.1	0.333	2.0	2.05	0.5	0.238	0.006	0.492	0.591	-0.185	-0.129	-19	1.00	0.00	0.10
3.2	0.333	2.0	2.05	1	0.238	0.006	0.492	0.621	-0.155	-0.113	-12			

Figure 6.18. Effect of the arrangement angle Ψ on the source term S_{MRE} in the edge MRE zone (segments I and II) during the steady phase of bore propagation, including the statistical evaluation of the fit $S_{MRE,fit}$.

The fitted energy losses $S_{MRE,fit}$ obtained from the cases 1.0, 3.1 and 3.2 underestimate the energy losses S_{MRE} between 12 % and 41 %. The considerable underestimation is reflected by $RMSE$ = 0.10 m²/s². The trend is still well reproduced, which is confirmed by CC = 1.00 and cov = 0.00 m²/s², showing similar variability in both data sets.

The deviation originates mainly from the shift in the basic configuration, while the influence of Ψ on S_{MRE} is reflected in $S_{MRE,fit}$ reasonably well. This indicates that the reason for this underestimation is less related to Ψ, but more to other parameters such as shape and normalized width.

Change of normalized MRE width $\frac{\partial D_B^*}{\partial x}$: Figure 6.19 presents S_{MRE} and the results of the fit (equation (6-30)) due to drag and inertia during the steady phase of bore propagation, when varying the change of the normalized width $\frac{\partial D_B^*}{\partial x}$.

With increasing $\frac{\partial D_B^*}{\partial x}$, the deviation of $S_{MRE,fit}$ increases as well. While in case of the smallest $\frac{\partial D_B^*}{\partial x}$ (case 4.4) S_{MRE} is slightly overestimated by 5.1 %, it is increasingly underestimated up to 41 % in case 1.0. The value of $RMSE$ = 0.13 m²/s² is relatively high, when compared to S_{MRE}. The trend of S_{MRE} is well reproduced, which is expressed by CC = 0.94 and cov = 0.01 m²/s². Compared to the unsteady flow phase (see section 6.4.2), where the fit tends to overestimate the energy losses for high $\frac{\partial D_B^*}{\partial x}$ and underestimates the energy losses for small $\frac{\partial D_B^*}{\partial x}$, the fit shows

the opposite trend: increasing $\frac{\partial D_B^*}{\partial x}$ leads to increasing underestimation while in case of unsteady conditions, increasing $\frac{\partial D_B^*}{\partial x}$ leads to increasing overestimation of S_{MRE} (compare to Figure 6.13).

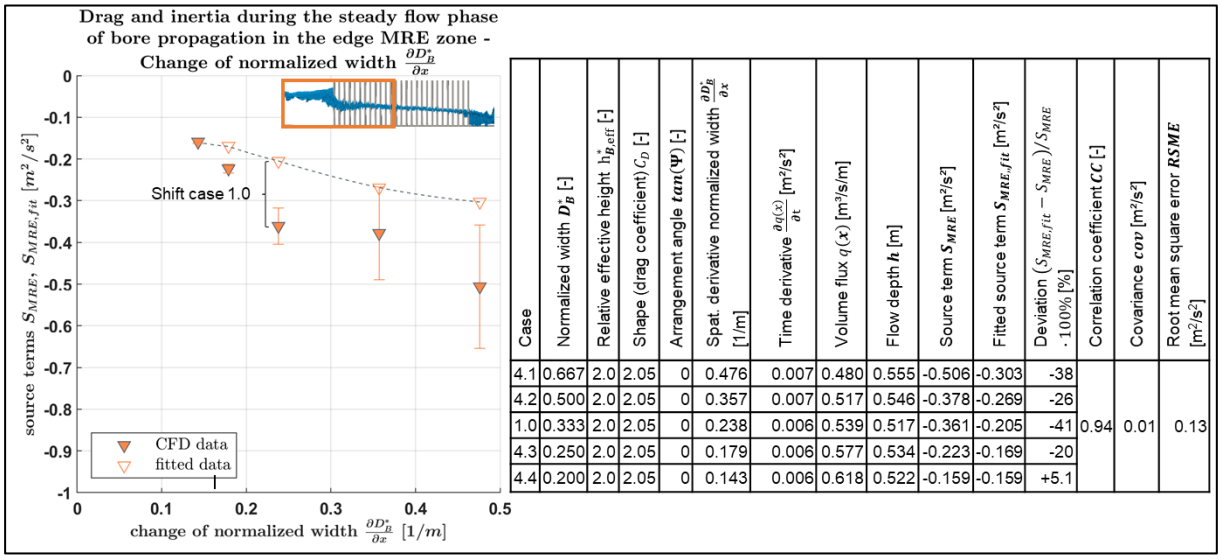

Case	Normalized width D_B^* [-]	Relative effective height $h_{B,eff}^*$ [-]	Shape (drag coefficient) C_D [-]	Arrangement angle $tan(\Psi)$ [-]	Spat. derivative normalized width $\frac{\partial D_B^*}{\partial x}$ [1/m]	Time derivative $\frac{\partial q(x)}{\partial t}$ [m²/s²]	Volume flux $q(x)$ [m³/s/m]	Flow depth h [m]	Source term S_{MRE} [m²/s²]	Fitted source term $S_{MRE,fit}$ [m²/s²]	Deviation $(S_{MRE,fit} - S_{MRE})/S_{MRE}$ ·100% [%]	Correlation coefficient CC [-]	Covariance cov [m²/s²]	Root mean square error $RSME$ [m²/s²]
4.1	0.667	2.0	2.05	0	0.476	0.007	0.480	0.555	-0.506	-0.303	-38			
4.2	0.500	2.0	2.05	0	0.357	0.007	0.517	0.546	-0.378	-0.269	-26			
1.0	0.333	2.0	2.05	0	0.238	0.006	0.539	0.517	-0.361	-0.205	-41	0.94	0.01	0.13
4.3	0.250	2.0	2.05	0	0.179	0.006	0.577	0.534	-0.223	-0.169	-20			
4.4	0.200	2.0	2.05	0	0.143	0.006	0.618	0.522	-0.159	-0.159	+5.1			

Figure 6.19. Effect of the change of the normalized width $\frac{\partial D_B^*}{\partial x}$ on the source term S_{MRE} in the edge MRE zone (segments I and II) during the steady phase of bore propagation, including the statistical evaluation of the fit $S_{MRE,fit}$.

Relative effective MRE height $h_{B,eff}^*$: Figure 6.20 presents S_{MRE} and the results of the fit (equation (6-30)) due to drag and inertia during the steady phase of bore propagation, when varying the relative height.

With increasing relative effective height $h_{B,eff}^*$, the deviation of the fitted source term $S_{MRE,fit}$ from source term derived from CFD data S_{MRE} increases. It is noted that, except in case 1.0 (basic configuration), in all cases 5.1 to 5.4, the MRE are well submerged, taking values of $h_{B,eff}^* < 0.5$. For the smallest $h_{B,eff}^* = 0.126$ (case 5.4), which also results in the smallest S_{MRE}, $S_{MRE,fit}$ underestimates S_{MRE} by 45 %. Otherwise, $S_{MRE,fit}$ takes values within the standard deviation of the source term S_{MRE}, which is indicated as error bars in Figure 6.20. In the basic configuration, the deviation between S_{MRE} and $S_{MRE,fit}$ originates from using a constant drag coefficient C_D in equation (6-30), which ignores the effect of deflection.

When evaluating $S_{MRE,fit}$, the root mean square error $RMSE = 0.07$ m²/s² is considerable high and originates furthermost from the deviation in case 1.0, which can be related to the usage of a drag coefficient. However, the correlation coefficient $CC = 0.99$ and the covariance $cov = 0.01$ m²/s² confirm a very good reproduction of the trend of S_{MRE}.

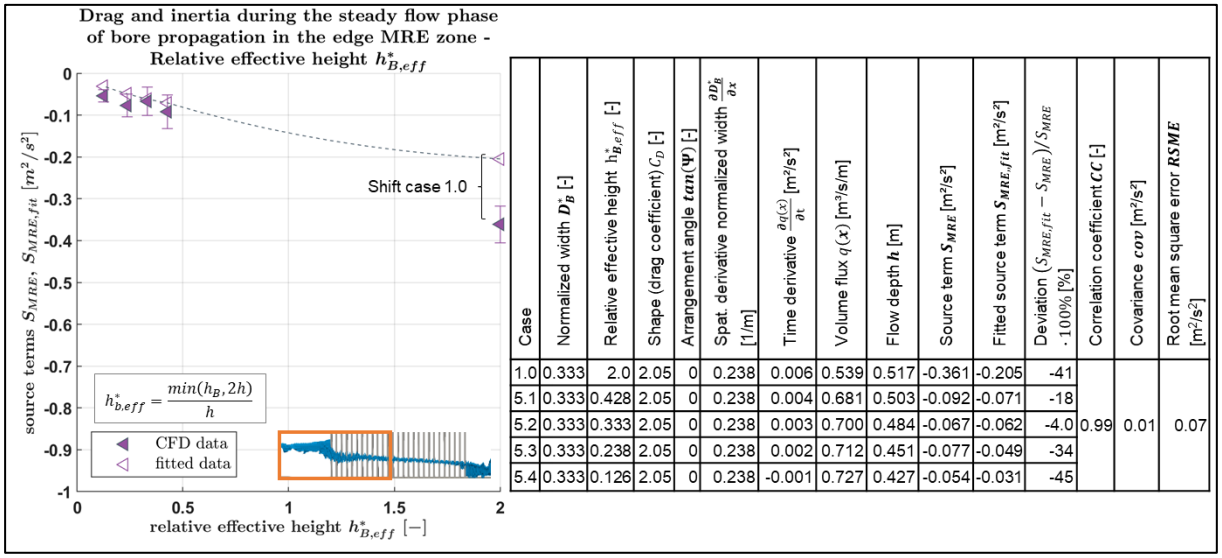

Case	Normalized width D_B^* [-]	Relative effective height $h^*_{B,eff}$ [-]	Shape (drag coefficient) C_D [-]	Arrangement angle $tan(\Psi)$ [-]	Spat. derivative normalized width $\frac{\partial b_B^*}{\partial x}$ [1/m]	Time derivative $\frac{\partial q(x)}{\partial t}$ [m²/s²]	Volume flux $q(x)$ [m²/s/m]	Flow depth h [m]	Source term S_{MRE} [m²/s²]	Fitted source term $S_{MRE,fit}$ [m²/s²]	Deviation $(S_{MRE,fit} - S_{MRE})/S_{MRE} \cdot 100\%$ [%]	Correlation coefficient CC [-]	Covariance cov [m²/s²]	Root mean square error $RSME$ [m²/s²]
1.0	0.333	2.0	2.05	0	0.238	0.006	0.539	0.517	-0.361	-0.205	-41			
5.1	0.333	0.428	2.05	0	0.238	0.004	0.681	0.503	-0.092	-0.071	-18			
5.2	0.333	0.333	2.05	0	0.238	0.003	0.700	0.484	-0.067	-0.062	-4.0	0.99	0.01	0.07
5.3	0.333	0.238	2.05	0	0.238	0.002	0.712	0.451	-0.077	-0.049	-34			
5.4	0.333	0.126	2.05	0	0.238	-0.001	0.727	0.427	-0.054	-0.031	-45			

Figure 6.20. Effect of the change of the relative effective height $h^*_{B,eff}$ on the source term S_{MRE} in the edge MRE zone (segments I and II) during the steady phase of bore propagation, including the statistical evaluation of the fit $S_{MRE,fit}$.

6.5.2 Evaluation of the MRE formula for three relevant flow situations

In total, the MRE formula is applied to the three flow conditions shown in Figure 6.3. Figure 6.21 provides the scatter plots for a) the unsteady phase of bore propagation in the inner MRE zone (situation for developing the inertia source term of the MRE formula (6-31.b), b) the unsteady phase of bore propagation in the edge MRE zone (situation for developing the drag source term of the MRE formula (6-31.c) and c) the steady phase of bore propagation in the edge MRE zone (independent situation for applying the MRE formula, as presented in section 6.5.1).

The covariance is cov = 0.02 m²/s² during the unsteady phase of bore propagation in the inner MRE zone (Figure 6.21.a) or less. The correlation coefficient is CC = 0.92 during the steady phase of bore propagation in the edge MRE zone (Figure 6.21.c) or higher. For this configuration, the root mean square error $RSME$ = 0.10 m²/s² and the $BIAS$ = 0.07 m²/s² are the highest. Note that positive $BIAS$ expresses an underestimation of the (negative) energy losses. The analyses performed in the sections 6.4.1 and 6.4.2, show that equations (6-31.a-c) lead to good agreements between the fitted source term $S_{MRE,fit}$ and the source term derived from the CFD parameter tests S_{MRE} during the three situations in Figure 6.3.

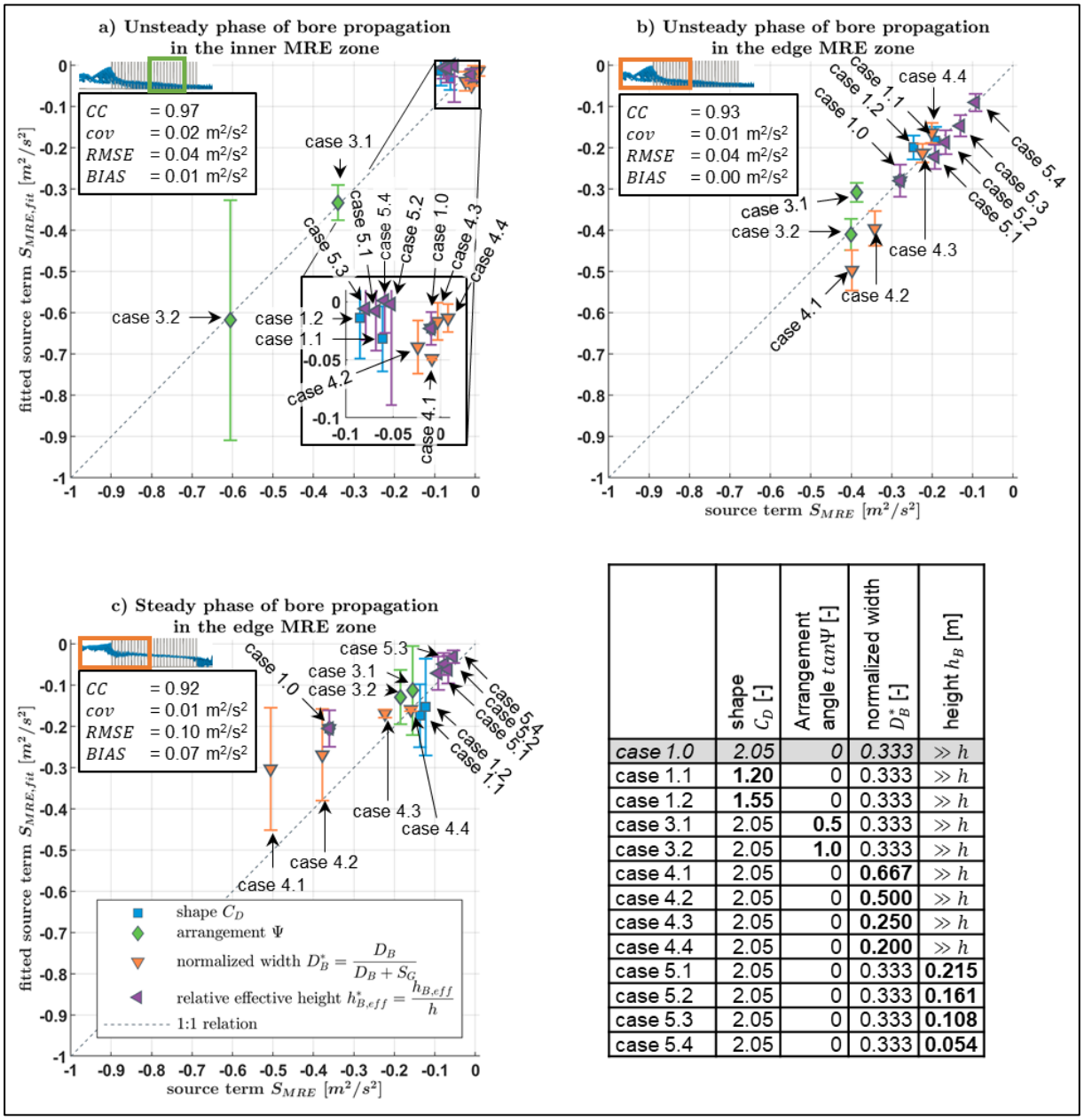

	shape C_D [-]	Arrangement angle $tan\Psi$ [-]	normalized width D_B^* [-]	height h_B [m]
case 1.0	*2.05*	*0*	*0.333*	$\gg h$
case 1.1	**1.20**	0	0.333	$\gg h$
case 1.2	**1.55**	0	0.333	$\gg h$
case 3.1	2.05	**0.5**	0.333	$\gg h$
case 3.2	2.05	**1.0**	0.333	$\gg h$
case 4.1	2.05	0	**0.667**	$\gg h$
case 4.2	2.05	0	**0.500**	$\gg h$
case 4.3	2.05	0	**0.250**	$\gg h$
case 4.4	2.05	0	**0.200**	$\gg h$
case 5.1	2.05	0	0.333	**0.215**
case 5.2	2.05	0	0.333	**0.161**
case 5.3	2.05	0	0.333	**0.108**
case 5.4	2.05	0	0.333	**0.054**

Figure 6.21. Scatter plots fitted source $S_{MRE,fit}$ term over the original source term S_{MRE}: a) Inertia during the unsteady phase of bore propagation, b) Drag and inertia during the unsteady phase of bore propagation in the edge MRE zone, c) Drag and inertia during the steady phase of bore propagation in the edge MRE zone.

6.6 Summary and concluding remarks

This chapter outlines the development of source terms for the non-linear shallow-water (NLSW) equations describing the effect of macro-roughness elements (MRE) on the energy losses during tsunami inundation. The energy losses due to the MRE S_{MRE} are determined from each CFD simulation case by analysing the flow parameters h and q in various cross-sections

to solve the derivatives NLSW momentum equation. The MRE source term is isolated by subtracting the bottom friction source term.

The MRE source terms are derived for two situations and evaluated in a third situation which are assumed to represent the relevant situations during the propagation of the bore through the MRE zone:

1. Unsteady phase of bore propagation in the inner MRE zone (to derive the inertia term of the MRE formula),
2. Unsteady phase of bore propagation in the edge MRE zone (to derive the drag term of the MRE formula) and
3. Steady phase of bore propagation in the edge MRE zone (to evaluate the inertia term and drag term of the MRE formula).

The turbulence intensity is carefully selected to be I = 10 % based on sensitivity tests and by repeating the analysis for three unit lengths dx to minimize the impact of local effects, e.g. due to the presence of MRE inside the analyses cross-sections.

The dependencies from non-dimensional variables are assessed by selecting two distinct situations:

- The unsteady phase of bore propagation in the inner MRE zone can be related to the Froude number Fr. This configuration is selected to obtain the energy losses due to inertia. Clear correlations are seen for the variation of the arrangement angle Ψ.
- The steady phase of bore propagation in the edge MRE zone can be related to the Reynolds number Re. This configuration is selected to obtain the energy losses due to drag. Clear correlations are seen for the variations of Ψ, the normalized width MRE D_B^* and the relative MRE height h_B^*, while no correlation is seen for the variation of the drag coefficient C_D, which is used to describe the shape of the MRE.

The underlying assumptions for deriving the MRE formula are:

- Reynolds numbers does not fall below Re = 50,000.
- The MRE shape can be described by a constant drag coefficient C_D:
  - Buildings: $C_D = 2.05$,
  - Rigid vegetation: $C_D = 1.2$
- Vortex losses can be described as part of the turbulence.
- In large-scale modelling, man-made structures can be represented by squared shapes and stiff vegetation by cylinders.
- All MRE are stiff.
- MRE are impermeable and undestroyable.
- No debris is floating with the tsunami bore.
- Onshore, the tsunami bore moves over a dry bottom.
- The onshore region consists of structured arrangements of MRE as usually found in urban areas.

The MRE formula is obtained as follows:

$$S_{MRE,fit} = S_{MRE,fit,inertia} + S_{MRE,fit,drag} \quad \text{(6-31.a)}$$

$$S_{MRE,fit,inertia} = \frac{\partial q(x)}{\partial t} \frac{\sqrt{gh}}{\frac{q(x)}{h}} [1.3 - cos(4\Psi)]^{0.33} \quad \text{(6-31.b)}$$

$$S_{MRE,fit,drag} = -0.4 \frac{\partial D_B^*}{\partial x} \frac{q(x)^2}{h} h_{B,eff}^* C_D [0.7 + 0.3cos(4\Psi)]^{0.1} \quad \text{(6-31.c)}$$

With the volume flux $q(x)$, the time t, the acceleration due to gravity g, the flow depth h, the dimension x and the relative effective height $h_{B,eff}^* = \frac{min(2h,h_B)}{h}$ with the MRE height h_B.

The evaluation of the MRE formula is performed for the aforementioned conditions 1. to 3 (see Figure 6.21). The correlation coefficient varies between CC = 0.92 and CC = 0.97. The formula tends to underestimate the energy losses as expressed by $BIAS$, taking values between $BIAS$ = 0.00 m²/s² and $BIAS$ = 0.01 m²/s² during the unsteady phase of bore propagation and $BIAS$ = 0.07 m²/s² during the steady phase of bore propagation (taking note that positive $BIAS$ indicate underestimation of energy losses). Therefore, it can be expected that the inundation extent will be overestimated slightly, so that when applying the MRE formula to inundation modelling, conservative results will be obtained.

To the author's knowledge, the MRE formula is the first representation of energy losses for large scale modelling, which directly depends on a number of MRE parameters, including man-made structures. It is to improve the results of models, which do not resolve individual obstacles such as buildings, as applied for example in probabilistic hazard assessment.

The limitations of the MRE formula are:

- Reynolds numbers must not fall below Re = 50,000.
- The cell size should be selected so that the change of the relative width $\frac{\partial D_B^*}{\partial x}$ < 0.328 1/m.
- The energy losses during the steady phase of bore propagation are considerably underestimated.
- Application to unstructured rigid vegetation (e.g. coastal forests) can lead to underestimation of the energy losses.

Further research is required to assess the impact of flow deflection towards neighbouring MRE. The here obtained results suggest that using a constant drag coefficient cannot fully represent the energy losses in groups of MRE. It is pointed out that the drag force is acting against the flow direction only, and it is therefore only a 1D representation of the inner MRE forces during steady conditions. A second component acting in lateral direction is needed to fully describe the shape influence of the MRE standing in a group. Such "lateral" component is known as lift force in aerodynamics (see e.g. Hori, 1959), which reflects the asymmetric deviations in the flow field surrounding the MRE. The shape coefficient needs to address both inner forces the

drag and the lift-like force. The drag force results in flow blockage while the lift-like force results in flow deflection. Furthermore, the shape coefficient needs to be Re-independent.

7 Application of the new formulae to laboratory experiments and comparison with standard models

The new marco-roughness element (MRE) formula is implemented in the non-linear shallow-water (NLSW) model COMCOT v1.7, and the so modified model is then applied to reproduce a well-described physical experiment, to demonstrate its ability to predict the inundation extent during the onshore propagation of a tsunami-like bore. A comparative analysis is performed by considering the results from (i) the modified COMCOT model using the new MRE formula, (ii) the COMCOT model using two standard roughness models based on Manning coefficient n, (iii) physical experiments. These comparisons are made for different model grid resolutions in order (i) to relate the MRE results to experimental data and common roughness approaches, (ii) also to obtain indications on the sensitivity of the modified COMCOT model to the grid resolution and finally (iii) to derive recommendations for the applications of the MRE formula as implemented in the COMCOT model.

In section 7.1, the physical experiment is introduced, and the implications of the obtained data are discussed. In section 7.2, the methodology is outlined which allows the evaluation of various roughness models with various grid resolutions. The numerical setups are developed in section 7.3 and the results are provided and discussed in section 7.4.

7.1 Physical experiment

In this section, the physical experiments are introduced which form the basis for the evaluation of the roughness models.

First, the experimental setup is described. Section 7.1.2 gives the measurements performed during the experiments and section 7.1.3 discusses the implications for using the obtained measurement data for evaluating the numerical results.

7.1.1 Experimental setup

Rueben et al. (2011) conducted laboratory experiments on tsunami inundation through the urban area in Seaside, Oregon. The physical experiments were conducted in the Tsunami Wave Basin at the O.H. Hinsdale Wave Research Laboratory, Oregon State University. The idealized hydraulic model, constructed at 1:50 scale, was designed to study tsunami flow over and around macro-roughness elements (MRE) to observe, among others, the effect of building shape and density on tsunami inundation and to develop a data set for the evaluation of the next generation of numerical models. The fixed-bed experiments focused on the initial inundation zone along an urban waterfront so that the flow among several individual buildings could be observed. The design tsunami condition corresponds to the estimated tsunami wave height for the 500-year Cascadia Subduction Zone (CSZ) tsunami for this region (USGS, 2006).

The experimental area is given in Figure 7.1. The background images are satellite imagery of Seaside and a photo of the plan view of the physical model, including the onshore measurement locations (modified from Park et al., 2013).

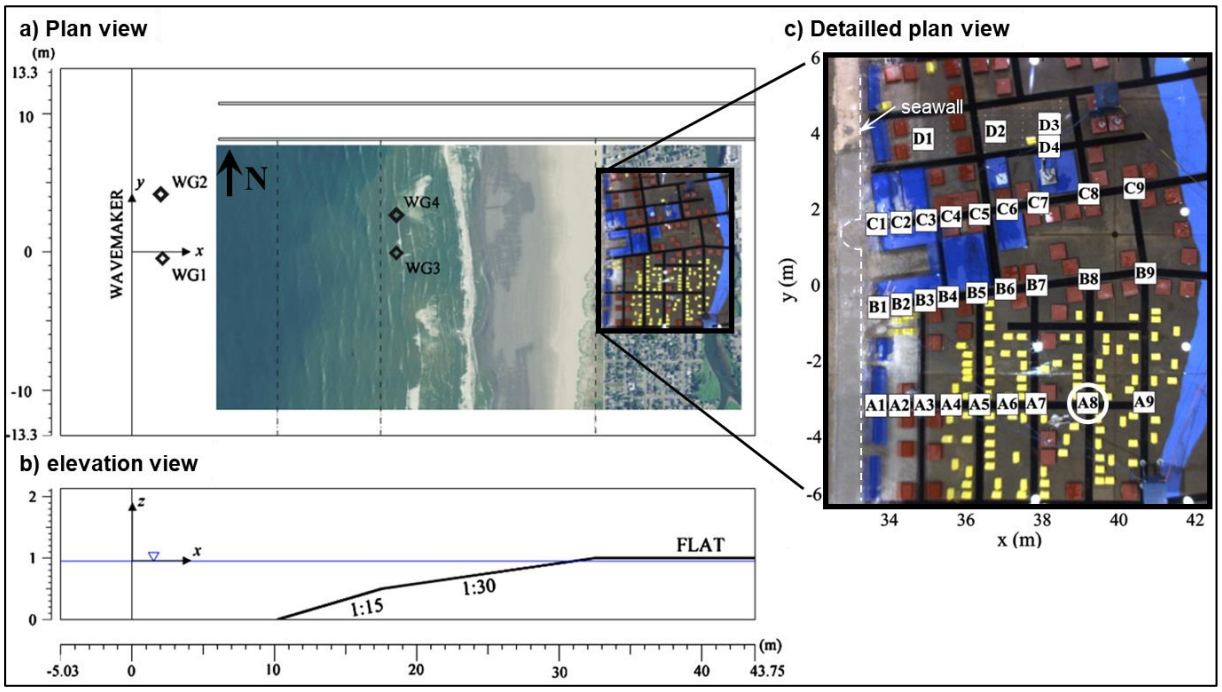

Figure 7.1. Physical model in the Tsunami Wave basin: a) Plan view with satellite imagery (Source: Google), a laboratory photo providing the scale of the Seaside model, b) elevation view and c) a detailed plan view of macro-roughness elements of the physical model, annotated with measurement locations and the seawall (white dashed line) (modified from Park et al., 2013). The white circle marks the measurement location A8, which is selected to provide the time for analysing the inundation extent.

In Figure 7.1.a), the origin of the x and y axes were centred on the piston-type wavemaker, with x positive towards the shore and y positive to the north. The rectangular basin was 48.8 m long, 26.5 m wide, and 2.1 m deep. The idealized bathymetry for Seaside was constructed of smooth concrete with a flat finish. The bottom roughness height in the wave basin was estimated to be k_S = 0.1 – 0.3 mm (Rueben et al., 2011).

In Figure 7.1.b), the profile of the experimental model consisted of a 10 m horizontal section near the wavemaker with a water depth of 0.97 m, an 8 m wide section with a 1:15 slope, a 15 m wide section with a 1:30 slope, on which the still water level intersected, and another 11 m wide horizontal section which extended to the back wall (Park et al, 2013).

In Figure 7.1.c), three different types of buildings are represented in the experimental model where blue coloured blocks indicate large hotels or commercial buildings, brown blocks are light commercial buildings and yellow blocks represent residential houses. The white dashed line indicates the location of a 0.04 m high seawall. The thick solid black lines between the blocks represent city streets. The buildings were positioned on the flat ground using aerial imagery and field survey data; they were fixed in place on the upper horizontal section to ensure test repeatability.

At prototype scale, the characteristic wave height corresponded to the 10 m tsunami height (Rueben et al., 2011).

7.1.2 Measurements

In the offshore region, four wave gauges (WG1–WG4) were fixed in the basin (see Figure 7.1).

In the onshore region,

- free water surface,
- flow velocity and
- bore front positions

were recorded. Four pairs of co-located ultra-sonic surface WG and acoustic-Doppler velocimeter sensors were used to measure the free water surface and the flow velocity in lines A, B, C, and D, simultaneously (see Figure 7.1). WG indicated with A were located on a city street parallel to the primary inundation flow direction and numbered sequentially from 1 to 9, as the measurement locations move inland. The streets are now referred to as street A, street B, street C and street D, respectively. WG indicated with B and C were on streets inclined approximately 10° to the flow direction, were flanked by hotels or commercial buildings, and numbered the same as line A. WG indicated with D are located mostly behind buildings and only had 4 measurement locations. Through the experiment, the sensors in the streets A, B, and C moved in unison from positions 1 through 9 and have the same number of repetitions for streets A, B, and C at a given location (Park, et al., 2013). In total, there were 35 measurement locations. Their positions and the number of measurements trials obtained at each location are specified in Table 7.1.

Furthermore, Rueben et al. (2011) provided the positions of the bore front during inundation at several time steps from video recordings. Due to the spatial limitations of the experimental facility, the bore reaches the rear walls during the experiments so that the maximum inundation extent could not be determined.

Table 7.1. Measurement locations and number of total and valid trials, N_T and N_V, respectively (Park et al., 2013). The coordinates of the measurement location A8 are highlighted as bold numbers.

Num.	WG		Line A		Line B		Line C		Number of trials for A, B, C		Line D			
	x [m]	y [m]	x [m]	y [m]	x [m]	y [m]	x [m]	y [m]	N_T [-]	N_V [-]	x [m]	y [m]	N_T [-]	N_V [-]
1	2.086	-0.515	33.61	-3.19	33.72	-0.59	33.81	1.51	53	48	35.12	3.71	53	48
2	2.068	4.065	34.10	-3.19	34.22	-0.53	34.55	1.60	11	10	36.68	3.89	33	26
3	18.618	0.000	34.53	-3.18	34.68	-0.47	35.05	1.69	12	12	38.09	4.07	18	5
4	18.618	2.860	35.04	-3.18	35.18	-0.41	35.56	1.77	12	4	38.14	3.59	28	20
5	-	-	35.54	-3.19	35.75	-0.32	36.05	1.85	18	5	-	-	-	-
6	-	-	36.36	-3.2	36.64	-0.23	37.05	1.99	7	6	-	-	-	-
7	-	-	37.77	-3.2	37.77	-0.07	38.24	2.19	6	3	-	-	-	-
8	-	-	39.22	-3.2	39.22	0.14	39.21	2.34	8	7	-	-	-	-
9	-	-	40.68	-3.23	40.67	0.27	40.40	2.58	9	4	-	-	-	-
Total								-	136	99		-	136	99

7.1.3 Implications for the numerical model evaluations

As the maximum inundation extent could not be determined, only (i) the flow depth, (ii) the flow velocity and (iii) the bore front at several moments might be used for evaluating numerical models. In the onshore region, the buildings reflect and deflect the flow. This leads to very heterogenous flow conditions resulting in high variations of the flow depth and flow velocity so that the measured values are only representative for small areas.

In order to reproduce the experimental data, the numerical model would require a high resolution that enables for distinguishing between the (very local) flow conditions. As the MRE formula is to be evaluated on various model resolutions, only the bore front location at several moments is suitable for comparisons.

The model resolution not only affects the degree of detail in which the onshore area is represented. It also affects the representation of flow characteristics, which are (i) of even smaller scale then onshore terrain characteristics, e.g. eddies and gradients of the surface elevation at the bore front, and which are (ii) independent from the roughness model. For example, the gradient of the surface elevation at the bore front influences the flow velocity at the bore front and, hence, the propagation speed of the bore. The coarser the grid at the bore front is, the slower the bore. In other words, the evaluation of the roughness formulation in the numerical model by means of the position to which the bore could propagate with its calculated speed, is polluted by the resolution of the numerical grid and other model characteristics which add to numerical dissipation in each model. Therefore, the numerical dissipation (including the effect

induced by using various grid resolutions) needs to be removed from the comparisons of various roughness models.

The well-described physical experiments on tsunami inundation of the idealized town of Seaside, Oregon, (Rueben et al., 2011) form the basis for evaluating the new MRE source term formula and common roughness models. Due to the spatial constraints of the experimental facility, the flow parameters (e.g. depth, velocity, bore front locations) can be analysed only at selected time steps before the maximum inundation extent. Because the roughness approaches are to be evaluated for various grid resolutions, numerical dissipation needs to be considered.

7.2 Methodology for the evaluation of various roughness approaches

The bore front position obtained during the physical experiments (see section 7.1) is used to evaluate the results of several non-linear shallow water (NLSW) roughness models: (i) *no bottom friction (NF)* (no Manning's n layer), (ii) *Constant bottom friction (CF)* (constant Manning's n values for offshore and onshore), (iii) *Variable bottom friction (VF)* (n for offshore and onshore considering buildings) and (iv) *New MRE formula* (see section 6.4). CF and VF models are examples for the so-called equivalent roughness models (see section 2.4.1.B).

Due to the spatial constraints of the experimental facility, the inundation extent is analysed at a specific moment of time. The selection of these moments is also influenced by the model grid resolution. The influence of the grid resolution on the comparison is removed by the here outlined methodology to allow evaluating the isolated effect of each of the tested roughness approaches.

Section 7.2.1 briefly summarizes the main characteristics of the NLSW model COMCOT, which is used for testing the new MRE formula and the above-mentioned common roughness models. Section 7.2.2 outlines the methodology for setting up the numerical models so that the effect of numerical dissipation can be removed from the comparisons. Section 7.2.3 presents the data analysis procedure for extracting the representative bore front for the evaluation.

7.2.1 Implementation of the MRE formula in COMCOT

COMCOT (Cornell multi-grid coupled tsunami model) is a NLSW model, which is maintained by GNS Science (Wang & Power, 2011). Since the 1990s it is in further development and applied at numerous tsunami-prone areas for modelling tsunami inundation, such as New Zealand, Indonesia and Japan. It is selected for implementing the MRE formula due to its wide application, availability, modifiability and inclusion of empirically energy dissipation due to wave breaking and dispersion (see section 2.2.1.B). Here, version 1.7 is used which is the latest fully tested available version.

The NLSW equations are solved on staggered regular grids using cartesian or spherical coordinates. The solution can be derived on one or on multiple (nested) grids. The solutions are derived using a leap-frog finite difference scheme for all but the nonlinear convective schemes, where an upwind scheme is used. The coastline is moved dynamically using a moving boundary scheme, separating dry and wet cells. Spatially varying friction values (Manning's values n) can be incorporated in the model. In addition to other NLSW models, the energy dissipation due to wave breaking is estimated by an eddy viscosity model.

The details of the discretization of the MRE formula (equation (6-31.a) to c)) and its implementations are given in the Appendix, section E.1.

7.2.2 Numerical setups

The numerical models vary in the roughness approach: (i) no bottom friction (NF), (ii) constant bottom friction (CF), (iii) variable bottom friction (VF) and (iv) MRE including constant friction and in the grid resolution. CF and VF model can be understood as two examples for equivalent (friction) roughness models discussed in section 2.4.1.B.

The following considerations are needed to allow a specific evaluation of the roughness models:

(i) The numerical model scale is 1:1; i.e. the experimental data have to be transferred from the laboratory scale 1:50 to full-scale.
(ii) A numerical reference model (based on COMCOT) is established for a grid resolution dx = 5 m, which is fine enough to resolve individual buildings to determine the bore speed including the effect of numerical dissipation as a whole. By comparing the roughness models with this reference model, all aspects of numerical dissipation can be excluded from the discussion for dx = 5 m, because they are assumed to be similar in all models including the reference model.
(iii) To determine the isolated effect of grid resolution variation on the results, the NF model is applied to determine the bore speed on various dx.

The methodology needs to reflect these considerations so that similar flow conditions are provided at the shoreline for all cell sizes and roughness approaches. It is outlined in Figure 7.2.

Step 1: Establish numerical reference (BR model, dx = 5 m)

Referring to Figure 7.2, the building-representing (BR) model at scale 1:1 is with dx = 5 m fine enough to represent all buildings as part of the bathymetry. The hydrodynamics of the physical experiments is reproduced by calibrating the inlet boundary condition which consists of the (upscaled) wave signal at WG1, so that the flow depth in the middle of the coastline at B1 is reproduced. This is necessary to ensure that the beach-facing buildings are overflown as observed in the physical experiment. This is achieved by scaling the wave signal by $h_{WG1,mod,dx=5m} = f_{mod} \cdot 50 h_{WG1,exp}$. The factor "50" is for bridging the gap between the experimental and the reference model scale. The factor f_{mod} is to make up for all overrated dissipations occurring in the BR model during bore propagation from WG1 to B1.

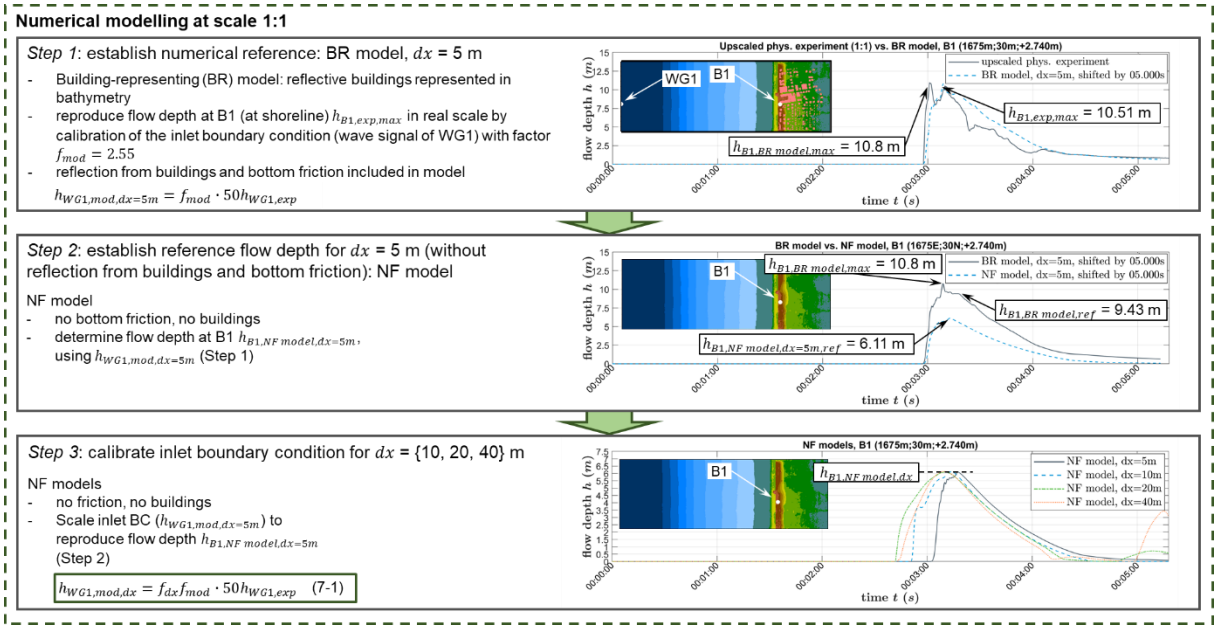

Figure 7.2. Procedure for creating the numerical setups based on the physical experiments of Park at al., (2013).

Step 2: Establish reference flow depth for dx = 5 m

The numerical reference model including all initial and boundary conditions, forms the basis for the no friction (NF) model with dx = 5 m so that no bottom friction and no buildings influence the flow depth at B1. The resulting flow depth of the NF model $h_{B1,NF\ model,dx=5m}$ = 6.11 m is used as reference flow depth when varying grid resolutions dx.

Step 3: Calibrate inlet boundary condition for dx = {10, 20, 40} m

The NF model with dx = 5 m forms the basis for the NF models for grid resolutions dx = {10, 20, 40} m, where only the bathymetry is exchanged. The simulations result in flow depths at B1 $h_{B1,NF\ model,dx}$, which differ from the one with dx = 5 m because of varying dx, only. In order to provide the similar flow depth at the shoreline for each dx, the inlet boundary condition (based on WG1) is calibrated using the factor f_{dx}, so that the inlet boundary is derived by

$$h_{WG1,mod,dx} = f_{dx} f_{mod} \cdot 50 h_{WG1,exp} \quad (7\text{-}1)$$

f_{dx} is given in Table 7.2.

Table 7.2. Grid factors for scaling the inlet boundary condition for various grid resolutions dx.

Grid resolution dx [m]	Grid factor f_{dx}
5	1.000
10	0.694
20	0.596
40	0.443

The derived inlet boundary conditions are applied to each roughness model with the corresponding grid resolution. All numerical models are able to transport similar waves from the inlet boundary to the shoreline with B1 so that the inundation of the bore can be discussed in terms of the roughness approach in the model, isolated from numerical dissipation.

7.2.3 Data analysis

As the maximum inundation extent cannot be analysed, an appropriate timestep is to be extracted from the results, which is comparable to a selected timestep from the numerical reference (BR model). The following considerations are made:

(i) A timestep is selected from the reference BR model, at which in none of the roughness models NF, CF, VF and MRE the bore front reaches the rear wall yet.
(ii) As the bore speed is slightly different due to using various grid resolutions dx, the inundation time needs to be selected accordingly.

The data analysis procedure needs to reflect these considerations. It is outlined in Figure 7.3.

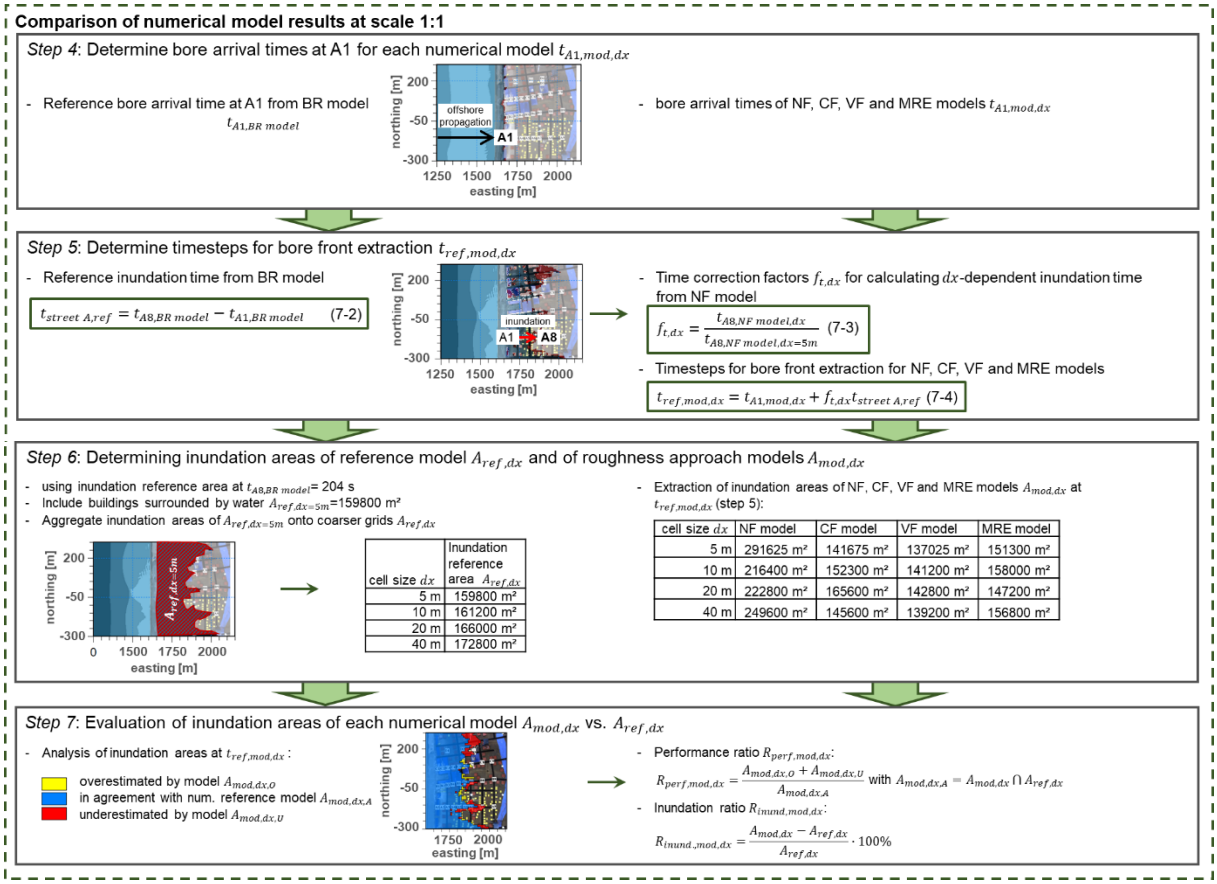

Figure 7.3. Data analysis procedure for the comparison of numerical model results.

In Figure 7.3, the reference BR model provides the inundation area at a timestep to be selected from the model results. The corresponding timestep from the roughness models with various cell sizes dx need to be extracted and evaluated by performing the following steps:

Step 4: Determine bore arrival times at A1 for each numerical model $t_{A1,mod,dx}$

As the numerical models provide similar flow conditions at the shoreline, a WG is to be selected to assess the timestep for the conditions at the start of the inundation process. A1 is selected as it is located in the only street which is orientated exactly in mean flow direction.

Step 5: Determine timesteps for bore front extraction $t_{ref,mod,dx}$

The reference inundation is selected at the moment when the bore front arrives at the A8 using the numerical reference BR model, which at best reproduces the physical experiments by including the buildings in the bathymetry. The arrival time at A8 is $t_{A8,BR\ model}$ = 204 s. The reference inundation time for bore propagation from A1 at $t_{A1,BR\ model}$ = 183 s to A8 along "Street A" is then determined to be

$$t_{street\ A,ref} = t_{A8,BR\ model} - t_{A1,BR\ model} \tag{7-2}$$

which is $t_{street\ A,\ ref}$ = 21 s, valid as reference inundation time for models with dx = 5 m.

To account for slightly varying bore speeds with varying cell sizes dx, a time correction factor is determined using NF models, which only differs in dx. The arrival times at A8 (see Figure 7.1.b) are determined for each model and the ratio between the arrival times of various dx $t_{A8,NF\ model,dx}$ to the arrival time of the model with dx = 5 m $t_{A8,NF\ model,dx=5m}$ is used to determine the time correction factor

$$f_{t,dx} = \frac{t_{A8,NF\ model,dx}}{t_{A8,NF\ model,dx=5m}} \tag{7-3}$$

The timesteps for extracting the bore front is then determined using the relation

$$t_{ref,mod,dx} = t_{A1,mod,dx} + f_{t,dx} t_{street\ A,ref} \tag{7-4}$$

The timesteps for each model are given in the Appendix, section E.2.

Step 6: Determine inundation areas

The reference inundation area at $t_{A8,BR\ model} = A_{ref,dx=5m}$= 159800 m², which is valid for all models using dx = 5 m. In this area, the buildings are manually added, which are fully surrounded by the water, buildings which are surrounded partly, are added partly as well. For details, please refer to Leschka (2020).

The reference inundation area for the remaining cell sizes dx = {10, 20, 40} m is derived by aggregating the areas on coarser grids. The flow depths obtained on the dx = 5 m grid are interpolated onto the next coarser grid dx = 10 m using the relation

$$h_{i',j'} = \frac{\sum_{i=1}^{2}\sum_{j=1}^{2} h_{i,j}}{4} \tag{7-5}$$

With the flow depth in cell (i,j) of the smaller grid $h_{i,j}$ and the flow depth in cell (i',j') of the coarser grid $h_{i',j'}$. The cell (i',j') is part of the inundation area on the coarser grid $A_{ref,dx}$ if $h_{i',j'} > 0$ (see Wang & Powers, 2011).

Step 7: *Evaluate inundation areas of each model*

The inundation areas of the roughness inundation models $A_{mod,dx}$ are overlaid with the dx-corresponding reference inundation areas $A_{ref,dx}$ so that three types of inundation areas can be determined for each model:

- Overlapping inundation areas, where both models are in agreement
  $A_{mod,dx,A} = A_{mod,dx} \cap A_{ref,dx}$,
- Areas, which are inundated in the reference ref but not in the roughness models mod, so that the inundation is underestimated
  $A_{mod,dx,U} = \emptyset \cap A_{ref,dx}$ and
- Areas which are not inundated in the reference but are determined as inundated in the roughness models, so that the inundation is overestimated
  $A_{mod,dx,O} = A_{mod,dx} \cap \emptyset$.

Jakeman et al. (2010) suggested two measures to quantify the agreement between the observed and the modelled inundation in terms of (i) not captured inundated area and (ii) simulated inundation area which falls outside the observed inundated area separately. To evaluate a model's performance, it is favourable to combine both measures. Here, two ratios are suggested, which combine over- and underestimation each and which might be useful for two different purposes:

The performance ratios of the model mod with the grid resolution dx

$$R_{perf,mod,dx} = \frac{A_{mod,dx,O} + A_{mod,dx,U}}{A_{mod,dx} \cap A_{ref,dx}} \tag{7-6}$$

This ratio considers that for example in terms of local hazard assessment and evacuation planning, overestimation of the inundation extent is equally bad as underestimation. The closer the value is to zero, the better is the model performing. Using this ratio does not reveal if the model mod generally overpredicts or underpredicts the inundation extent. The ratio is more relevant for finer grid resolutions, where it can be distinguished for example between streets and building areas, e.g. for local hazard assessment.

The relative inundation error of the model mod with the grid resolution dx is

$$RIE_{mod,dx} = \frac{A_{mod,dx} - A_{ref,dx}}{A_{ref,dx}} \cdot 100\% \tag{7-7}$$

This ratio generally assesses the agreement between model and reference. It can be interpreted as relative standard deviation, taking note that only one timestep is considered, which makes

caring about the sign of the absolute difference between model and reference in the numerator of equation (7-7) obsolete (see Appendix A.1). The closer the value is to zero, the better is the agreement between both datasets. The advantage of this ratio is that it indicates underestimation and overestimation of the model. If $RIE_{mod,dx} < 0$, then the model mod underestimates the inundation extent, while mod overestimates it if $RIE_{mod,dx} > 0$. The ratio is useful for coarser models, where a more general overview is required, e.g. by insurances or in regional or global hazard assessment.

In order to determine the impact of numerical dissipation on the results, a numerical reference case of scale 1:1 with a grid resolution of dx = 5 m is established which provides comparable flow depths to the physical experiment at scale 1:50. For coarser grid resolutions, the inlet boundary condition is manipulated by adjusting the wave height so that the flow depths at the shoreline are maintained.

During the analysis of the results, the appropriate timesteps for extracting the bore front are determined by considering the propagation times of the bore at various grid resolutions.

7.3 Numerical model setups

The numerical model setups, based on the physical experiments described in section 7.1, are introduced in this section. The results of the COMCOT models, including the new MRE formula (see section 7.2.1), referred to as MRE models, are evaluated against reference data and compared to common COMCOT models (i) without any roughness consideration or (ii) with considerations of friction losses, only, to show the improvement due to the new MRE formula.

The COMCOT models are named as follows:

- *MRE model*: a constant Manning value n is applied representing the bottom roughness and the MRE formula, developed in chapter 6.
- *No friction (NF) model*: no bottom friction is included in COMCOT.
- *Constant friction (CF) model*: a constant Manning's n value is applied to the entire onshore section
- *Varying friction map (VF) model*: A land-use based approach considering the presence of individual buildings is reflected in a spatially varying map of n.

The reference data is obtained based on a building-representing (BR) model. In contrast to the physical experiments, the scale for all models is selected to be 1:1. The reasons for using the real scale for numerical modelling are (i) that numerous common models and recommendations were already published, and (ii) Reynolds number Re > 50,000 are obtained in the onshore region already for low flow velocities, which is required to use constant drag coefficients C_D in the MRE model (see section 2.4.2). For example, referring to equation (2-1), a flow depth of 0.2 m (threshold for dangerous flow depth for humans in FEMA, 2008) and a spacing between buildings of 5 m (grid size in the BR model), flow velocities in the order of 0.3 m/s lead to Re > 50,000.

All models are setup on various numerical grids of different resolutions to assess the applicability of the new MRE formula on various numerical grids, the following grid resolutions are prepared:

- dx = 5 m
- dx = 10 m
- dx = 20 m
- dx = 40 m

The bathymetries of the four grid resolutions are equal for all models (NF, CF, VF, MRE) except the BR model. The BR model bathymetry resolves the buildings and requires a fine resolution of 5 m x 5 m. An overview of the numerical models is provided in Table 7.3.

Table 7.3. Overview of numerical models.

Model	Grid resolution dx [m]	Buildings resolved in the bathymetry	Bottom friction	MRE layers
BR	5	Yes	n = 0.02 s/m$^{1/3}$	No
NF	5	No	Not included	No
	10			
	20			
	40			
CF	5	No	Offshore: n = 0.02 s/m$^{1/3}$ Onshore: n = 0.05 s/m$^{1/3}$	No
	10			
	20			
	40			
VF	5	No	Offshore: n = 0.02 s/m$^{1/3}$ Onshore: n = 0.02 s/m$^{1/3}$ … 0.4 s/m$^{1/3}$	No
	10			
	20			
	40			
MRE	5	No	n = 0.02 s/m$^{1/3}$	Yes
	10			
	20			
	40			

In section 7.3.1, the numerical reference BR model setup is provided, followed by the NF model in section 7.3.2, the commonly used equivalent (friction) roughness models in section 7.3.3 and the MRE model in section 7.3.4. Details on all model setups are provided in Leschka (2020).

7.3.1 Numerical reference BR model (step 1)

The BR model includes the buildings in the elevation data (bathymetry). Thereby, the model accounts for the heights of the buildings and considers them, like in the physical experiments as impermeable, and undestroyable structures.

A perspective representation of the bathymetry, with the georeferenced image draped onto the bathymetry surface and the view of the experimental setup from the same perspective (modified

from Rueben, et al., 2011) are shown in Figure 7.4 to provide a visual impression on the comparability of both models.

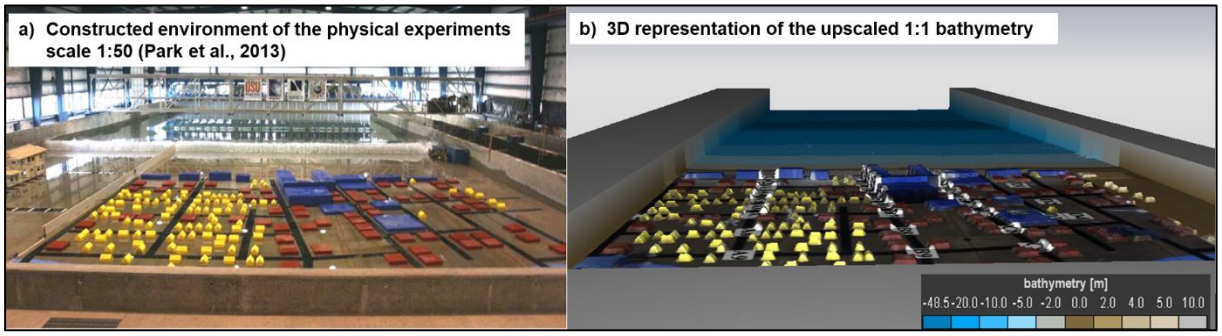

Figure 7.4. Visual comparison of the Seaside experiments. a) constructed environment of the physical experiments (modified from Rueben, et al., 2011), b) 3D representation of the upscaled 1:1 bathymetry with draped georeferenced top view image (see Figure 7.1).

The bottom friction is estimated using Manning's value n = 0.02 s/m$^{1/3}$. The value is comparable to large scale tsunami studies (e.g. Leschka et al., 2011; Gayer et al., 2010 and Kaiser, et al., 2011), which use n = 0.02 s/m$^{1/3}$ offshore, representing the bottom material, but it is high compared to comparisons of depth-averaged numerical models at scale 1:50 (Park et al., 2013), where n = 0.005 s/m$^{1/3}$ was found to provide the best match to the here selected experiments (using COULWAVE). Such deviations in n between physical experiments and large-scale depth-averaged models are noted by Bricker et al. (2015).

The boundary conditions are defined as "open", requiring a definition of the water surface elevation at all wet boundary points, which are found only at the western boundary. The remaining boundaries consist of bathymetry elevations well above the water levels obtained during the simulations, so that they remain always dry and do not require formulation of boundary conditions. The western boundary condition is determined from WG1 data of the physical experiments. An additional factor f_{mod} = 2.55 is required to reproduce the wave height at the shoreline. The relatively high factor is required to compensate the numerical dissipation during the bore propagation from the inlet BC to the shoreline for this grid resolution. The reason for such high factor is also due to the selection of the Manning's value of n= 0.02 s/m$^{1/3}$, which is appropriate to account for the bottom roughness in a natural environment (e.g. Gayer et al., 2010; Kaiser et al., 2011), but it is too high to represent the bottom roughness of the concrete surface in the experiments. Therefore, the inlet wave needs to be higher at the inlet so that at B1, the flow depth is still comparable to the upscaled flow depth of the physical experiments (see Leschka, 2020).

7.3.2 NF model (steps 2 and 3)

In the NF model, no source term for estimating the bottom friction losses are included.

The bathymetries are prepared for the grid resolutions dx = {5, 10, 20, 40} m (Leschka, 2020). Figure 7.5 shows exemplarily the bathymetry with the resolution of dx = 10 m.

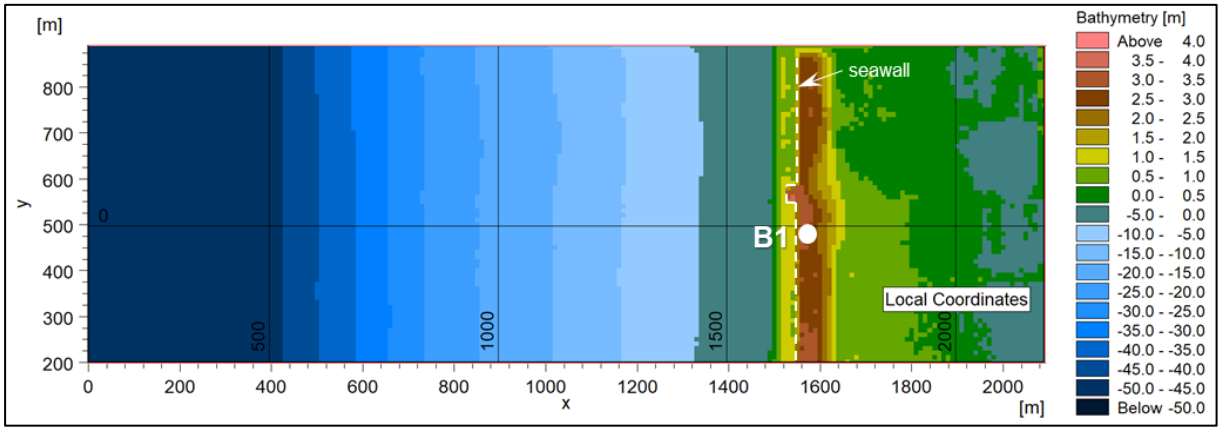

Figure 7.5. Bathymety with grid resolution dx = 10 m. The white-dotted line indicates the 2 m high seawall.

The reference flow depth at B1 for the grid resolution dx = 5 m $h_{B1,NF\ model,dx=5m}$ *(step 2)* is obtained using the same inlet boundary condition is similar to the BR model (see section 7.3.1) and takes the value

- $h_{B1,NF\ model,dx=5m}$= 6.11 m.

It is smaller than in the BR model, because no flow blocking and/or reflection from buildings can occur.

Calibration of the inlet boundary condition for various cell sizes dx (step 3) is performed to maintain the reference flow depth at the shoreline (see Leschka, 2020). They are provided in Figure 7.6.

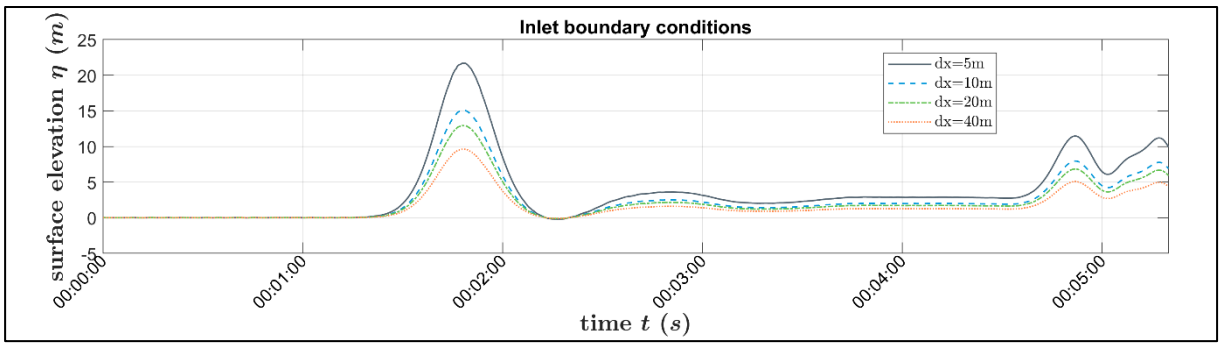

Figure 7.6. Inlet boundary conditions for various cell sizes dx.

7.3.3 Equivalent roughness models

The constant friction (CF) model comprises Manning's n values assembling the bottom friction of the experiments offshore and onshore. After careful consideration (see Leschka, 2020), n = 0.02 s/m$^{1/3}$ is chosen for the offshore region and for the onshore region n = 0.05 s/m$^{1/3}$ (e.g. Goto et al., 2012).

The building-representing varying friction map (VF) model considers the presence of individual buildings (see Leschka et al., 2011; Gayer et al., 2010 and Kaiser, et al., 2011) in case of the

smallest grid resolution dx = 5 m. Manning's n = 0.4 s/m$^{1/3}$ is used to account for buildings, while for the remaining areas, n = 0.02 s/m$^{1/3}$ (similar to the offshore region due to similarity of the bottom material). As the coarser grid sizes cannot resolve the individual buildings, n is derived by weighted averaging for each cell, depending on the fraction which is covered by the buildings A^*_{MRE}. For details on the procedure, it is referred to Gayer et al. (2010).

7.3.4 MRE model

The MRE model setups for various grid resolutions dx consist of the same bathymetries as the NF model (see section 7.3.2) and in addition, a constant friction for considering solely the bottom friction and data layers for

- MRE coverage A^*_{MRE} [-],
- MRE drag coefficient C_D [-],
- MRE height h_B [m] and
- MRE arrangement angle Ψ [°N, clockwise].

The bottom friction is represented by

- a constant Manning's n = 0.02 s/m$^{1/3}$.

in the entire numerical domain. Hereby, it is considered that the basin's roughness height (see section 7.1) is scaled up to prototype scale and takes values between k = 5 mm and k = 15 mm. The corresponding n can be taken from literature, e.g. Schneider (1992) or Chow (1959). A detailed discussion on the choice of n is provided in Leschka (2020).

Four additional MRE layers are to be prepared. An example for such layers in the onshore section for a grid resolution dx = 10 m, which is too coarse to represent individual buildings in the bathymetry, are presented in Figure 7.7.

The MRE coverage A^*_{MRE} layer of a computational cell in Figure 7.7.a) is derived from the normalized width D^*_B as defined in equation (6-16) by

$$A^*_{MRE} = max[(D^*_B)^2, 1] = \frac{A_{MRE}}{A_0} \tag{7-8}$$

with the area occupied by MRE A_{MRE} and the reference area A_0, e.g. a computational cell $A_0 = dxdy$. It is noted that $\frac{A_{MRE}}{A_0}$ could result in $A^*_{MRE} > 1$ in cases where MRE are greater than the computational cell. Therefore, the maximum A^*_{MRE} in each cell needs to be limited to not exceed A^*_{MRE} = 1.

Here it is assumed that the blocking of the flow by the MRE is equal for all flow directions. For the MRE coverage map of the other grids it is referred to Leschka (2020).

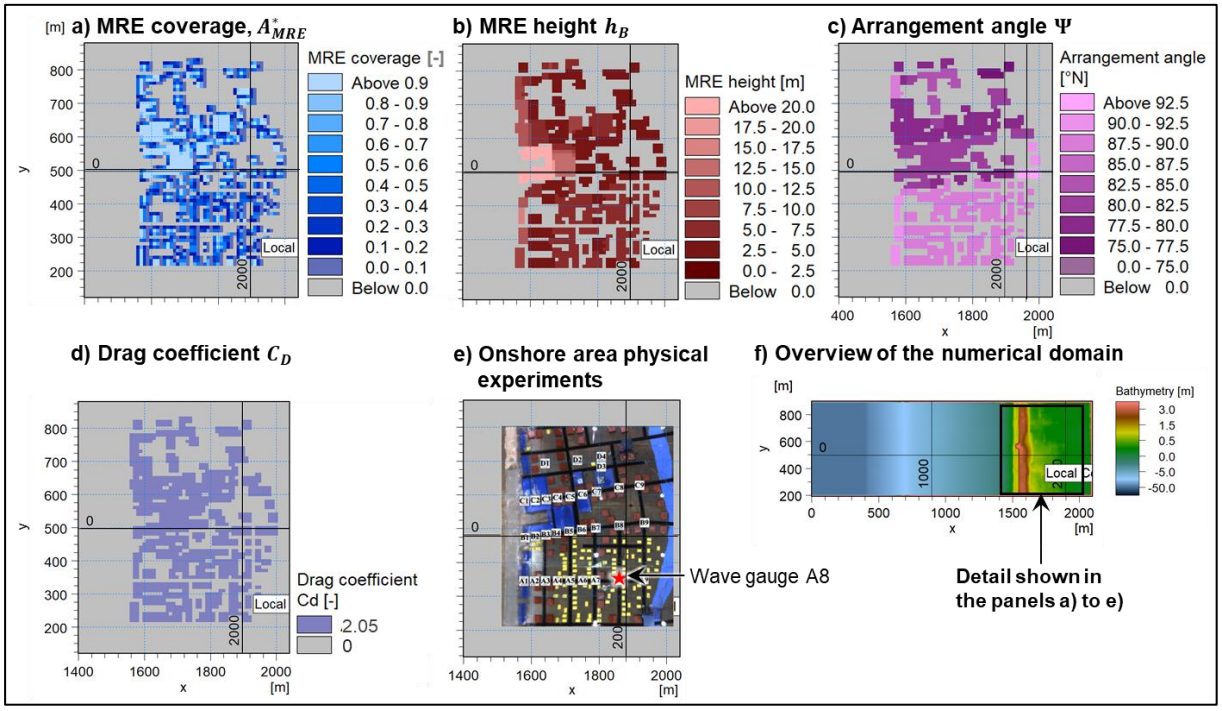

Figure 7.7. Input layers for MRE model: a) MRE coverage A^*_{MRE}, b) MRE height h_B, c) arrangement angle Ψ, d) MRE shape (drag coefficient C_D), e) Onshore area of the physical experiments (modified from Rueben, et al., 2011), f) Overview of the numerical domain. The thin black lines indicate the horizontal and vertical coordinates of the physical experiments [m].

The MRE height h_B layer in Figure 7.7.b) are prepared based on the A^*_{MRE} layer. As soon as $A^*_{MRE} > 0$, a value for h_B is assigned to the computational cell

$$h_B = \frac{\sum_{i=1}^{m} h_{B,i} A^*_{MRE,i}}{\sum_{i=1}^{m} A^*_{MRE,i}} \tag{7-9}$$

With the number of MRE-covered data points i in the computational cell. It is highlighted, that there are cells, which comprise weighted interpolated values of h_B due to the presence of buildings of different h_B inside one cell. Areas without buildings are excluded from the interpolation (see Leschka, 2020 for details).

The arrangement angle Ψ layer in Figure 7.7.c) is prepared based on the A^*_{MRE} layer. Similar to the h_B layer, Ψ are averaged over each computational cell by weighted averaging with the MRE coverage of the computational cell, $A^*_{MRE,i}$

$$\Psi = \frac{\sum_{i=1}^{m} \Psi_i A^*_{MRE,i}}{\sum_{i=1}^{m} A^*_{MRE,i}} \tag{7-10}$$

and by excluding the areas without MRE.

The drag coefficient C_D, represented in Figure 7.7.d) is applied to all these cells, in which $A^*_{MRE} > 0$. As in these experiments, only buildings are present in the onshore area, its shape is represented by the drag coefficient

- C_D = 2.05

(see section 6.6).

The numerical reference BR model is prepared to reproduce the flow depths at the shoreline at scale 1:1. The selected Manning's n value of 0.02 is more comparable to large scale tsunami inundation studies than to n values which are determined for the experimental scale (Bricker et al., 2015; Park et al., 2013).

For the NF, CF, VF and MRE models, n is chosen based on literature (e.g. Goto et al., 2012, Gayer et al., 2012).

The MRE model uses the same n as the BR model as the buildings are represented by their parameters height h_B, MRE coverage A^*_{MRE} , arrangement angle Ψ and drag coefficient C_D.

7.4 Results

The inundation extent derived by MRE models, no friction (NF) models and common roughness models (constant friction-CF, variable friction map-VF) are compared to the reference inundation in order to evaluate the performance of each model and to discuss advantages and limitations of the new MRE formula.

In section 7.4.1, the simulated data is postprocessed based on the analysis procedure outlined in section 7.2.3. In section 7.4.2, the results are compared by means of two quality indicators (also defined in section 7.2.3).

7.4.1 Post-processing of the results (steps 4 to 6)

The procedure for analysing the results of the numerical simulations using the NF, CF, VF and MRE models is performed based on section 7.2.3.

The arrival times for each flow condition (step 4) are provided in Table 7.4.

Table 7.4. Bore arrival times at A1 of models BR, CF, VF and MRE with cell sizes dx= {5, 10, 20, 40} m $t_{A1,mod,dx}$.

	arrival times at A1 $t_{A1,mod,dx}$ [s]			
cell size dx [m]	**BR model**	**CF model**	**VF model**	**MRE model**
5	183	186	184	184
10	-	173	171	171
20	-	163	163	163
40	-	164	164	164

The timestep for bore front extraction (step 5) from each model are given in Table 7.5. The arrival times at A8 in the NF model $t_{A8,NF\ model,dx}$ and the time correction factors to consider

the change of numerical dissipation when using various grid resolutions dx in the NF model $f_{t,dx}$ are provided in the Appendix, section E.2.

Table 7.5. Times for bore front extraction from roughness model results $t_{ref,mod,dx}$ for various cell sizes dx.

cell size dx [m]	times for bore front extraction $t_{ref,mod,dx}$ [s]			
	NF model	**CF model**	**VF model**	**MRE model**
5	204	208	206	206
10	180	192	191	191
20	170	182	181	181
40	201	185	185	185

The inundation areas (step 6) of the numerical reference BR model $A_{ref,dx}$ and the inundation areas of the NF, CF, VF and MRE models $A_{mod,dx}$ at timestep $t_{ref,mod,dx}$ (step 5) are provided in Table 7.6.

Table 7.6. Reference inundation areas of the BR model $A_{ref,dx}$ and inundation areas of the roughness models $A_{mod,dx}$ at timestep $t_{ref,mod,dx}$.

cell size dx [m]	Reference inundation area of the BR model $A_{ref,dx}$ [m²]	Inundation area $A_{mod,dx}$ [m²]			
		NF model	**CF model**	**VF model**	**MRE model**
5	159800	291625	141675	137025	151300
10	161200	216400	152300	141200	158000
20	166000	222800	165600	142800	147200
40	172800	249600	145600	139200	156800

7.4.2 Comparisons of various roughness models on various grid resolutions (step 7)

The extent of wetted areas at representative analysis times t_{A8} for various model resolutions dx are determined qualitatively and quantitatively. The inundation extent on various grid resolutions dx are depicted in Figure 7.8. The reference inundation areas $A_{ref,dx}$ are represented by the blue areas and the bore front extracted from the NF, CF, VF and MRE model are depicted as lines.

In Figure 7.8.a), which presents the inundated areas for the models using a grid resolution of dx = 5 m, the NF model highly overestimates the reference inundation $A_{ref,dx=5m}$ by 83 %. The CF model reproduces the inundation very well, except along the streets, where the inundation is underestimated, so that in total, the inundation extent is underestimated by 13 %. The VF model underestimates the inundation extent between and along the streets by 15 %. The MRE model reproduces the inundation extent between the streets very well and slightly underestimates the inundation along the streets so that the correctly determined inundation area is underestimated by 8 %.

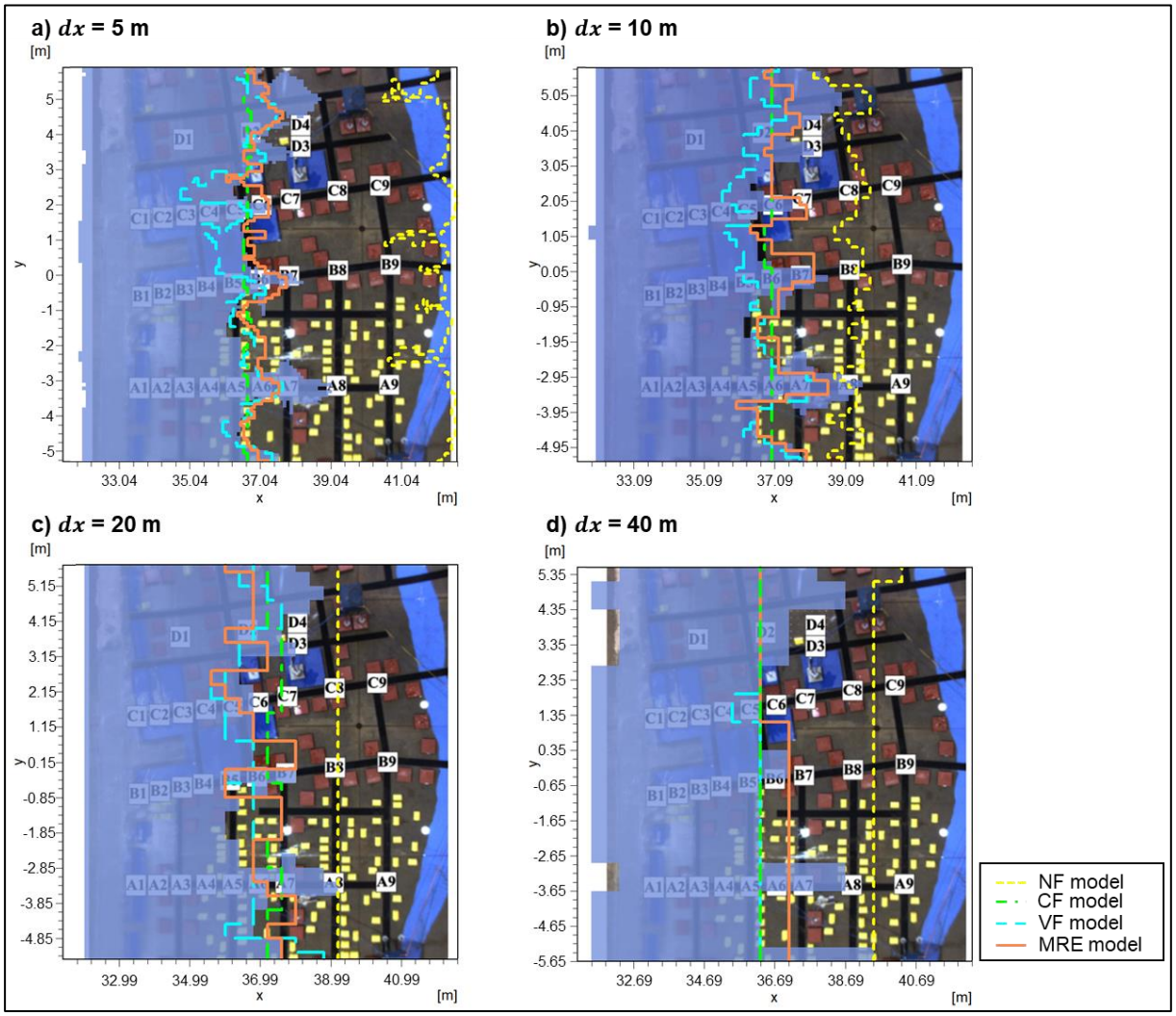

Figure 7.8. Inundated areas at the representative analysis times $t_{dx,A8}$ for various model resolutions: a) dx = 5 m, b) dx = 10 m, c) dx = 20 m, d) dx = 40 m. The blue areas represent the reference inundations $A_{ref,dx}$. The extracted bore front from the NF, CF, VF and MRE models are depicted as lines.

In Figure 7.8.b), which presents the inundated areas for the models using a grid resolution of dx = 10 m, the NF model overestimates the inundation extent $A_{ref,dx=10m}$ by 34 % considerably. The CF model overestimates the inundation between the streets slightly and underestimates the inundation extent along the streets, so that the correctly predicted inundated area is underestimated by 13 %. The VF model underestimates the inundated area by 14 % and the MRE model by only 7 %.

In Figure 7.8.c), which presents the inundated areas for the models using a grid resolution of dx = 20 m, the NF model overestimates the inundation extent by 34 %, the CF model underpredicts the inundated area by 8 % and the VF model results by 17 % and, thus, lead to comparable observations as in Figure 7.8.b). The MRE model overestimates the inundation extent in the low-density residential areas (y coordinate < 0) and underestimates the inundation extent in

the high-density residential areas (y coordinate > 0), so that the inundated area is underestimated by 15 %.

In Figure 7.8.d), which presents the inundated areas for the models using a grid resolution of dx = 40 m, the NF model overestimates the inundation extent $A_{ref,dx=40m}$ with 44 % considerably as for smaller dx. The CF model and the VF model represent the inundation extent between the buildings in the low-density residential area (y coordinate < 0) very well and underestimate the inundation extent in the high-density area so that the inundated area is underestimated by 16 % and 19 %, respectively. The propagation of the bore along the streets is not notable in the results due to the coarse resolution. The MRE model slightly overestimates the inundation between the streets by approximately 17 % and underestimates the inundation along the streets by approximately 25 % in the low-density residential area. In the high-density area, the inundation extent is underestimated by approximately 10 %. In total the MRE model underestimates the inundated area by 15 %.

The inundated areas of the models are quantitatively compared to the reference inundation area using the performance ratio $R_{perf,mod,dx}$ (see equation (7-6)) and the inundation ratio $RIE_{mod,dx}$ (see equation (7-7)). The results are summarized in Table 7.7. Furthermore, $R_{perf,mod,dx}$ and $RIE_{mod,dx}$ are depicted in Figure 7.9 and Figure 7.10, respectively.

The closer $R_{perf,mod,dx}$ and $RIE_{mod,dx}$ are to zero, the better is the model result. $RIE_{mod,dx} > 0$ indicate overestimation and $RIE_{mod,dx} < 0$ underestimation. In Figure 7.9, all tested roughness models lead to significantly better results than the no friction (NF) model as they reach performance ratios between $R_{perf,MRE\ model,5m}$ = 0.127 and $R_{perf,VF\ model,40m}$ = 0.241. It is noted that the MRE model leads to the best performance ratios of $R_{perf,MRE\ model,5m}$ = 0.127 and $R_{perf,MRE\ model,5m}$ = 0.129 for cell sizes of dx = 5 m and dx = 10 m, respectively, while for larger cell sizes, the constant friction (CF) model leads to the best results with $R_{perf,CF\ model,20m}$ = 0.176 and $R_{perf,CF\ model,40m}$ = 0.187.

In Figure 7.10, all tested roughness models lead to considerably better results than the no friction (NF) model as they reach performance ratios between $RIE_{VF\ model,40m}$ = -19 % and $RIE_{CF\ model,20m}$ = -0.2 %. The best results are obtained by the MRE model, when using cell sizes dx = {5, 10, 40} m with $RIE_{MRE\ model,5m}$ = -5.3 %, $RIE_{MRE\ model,10m}$ = -2.0 % and $RIE_{MRE\ model,40m}$ = -9.3 %. A reason for the relatively good performance of the CF model might be that the used Manning's coefficient n = 0.005 s/m$^{1/3}$ was calibrated in on physical experiments (Kotani et al., 1998), which might work well particularly for dx = 20 m, which is already coarse enough to distinguish between low density and high-density residential areas. However, the selection of n works not that well anymore when increasing the cell size to dx = 40 m.

The comparison of the MRE model with the no friction (NF) model, the constant friction (CF) model and the variable friction (VF) model reveals that under the here tested and well-defined laboratory conditions, the model leads to comparable results as the friction models, which apply Manning's values n based on experience or calibration (CF and VF model).

Table 7.7. Comparison of inundated areas obtained from the numerical simulations using various roughness models and various cell sizes dx. The best results of each dx are highlighted as bold numbers.

Roughness model	**Cell size dx [m]**	**Performance ratio $R_{perf,mod,dx}$ [-]**	**Relative inundation error $RIE_{mod,dx}$ [%]**
NF	5	0.84	+83
	10	0.35	+34
	20	0.35	+34
	40	0.44	+44
CF	5	0.17	-11
	10	0.16	-5.5
	20	**0.18**	**-0.2**
	40	**0.19**	-16
VF	5	0.18	-14
	10	0.19	-12
	20	0.23	-14
	40	0.24	-19
MRE	5	**0.13**	**-5.3**
	10	**0.13**	**-2.0**
	20	0.23	-11
	40	0.24	**-9.3**

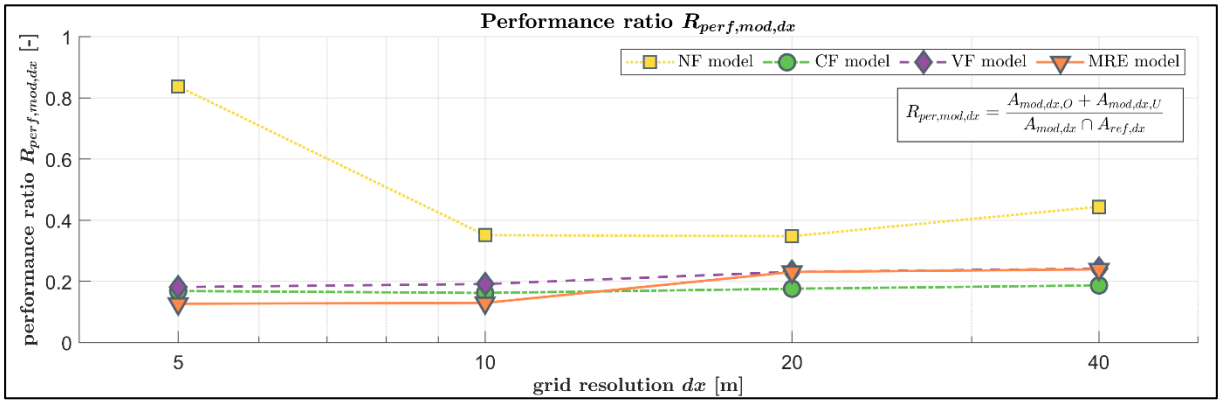

Figure 7.9. Performance ratios $R_{perf,mod,dx}$ of various roughness models for various grid resolutions.

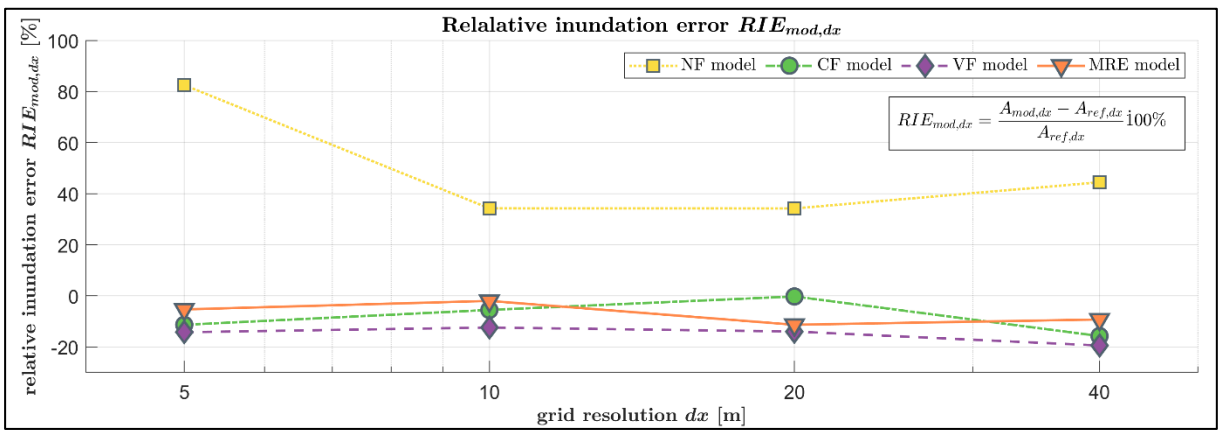

Figure 7.10. Relative inundation errors $RIE_{mod,dx}$ of various roughness models for various grid resolutions.

The MRE model exceeds the performance of pure friction models, when using small grid sizes, where it can still be distinguished between residential building areas and streets ($R_{perf,MRE\ model,5m}$ = 0.13 vs. $R_{perf,CF\ model,5m}$ = 0.17), and when using coarse grids in the order of dx = 40 m ($RIE_{MRE\ model,40m}$ = -9.3 % vs. $RIE_{CF\ model,40m}$ = -16 %). An exception is found for dx = 20 m, where the calibrated CF model led to the best results ($RIE_{MRE\ model,20m}$ = -11 % vs. $RIE_{CF\ model,40m}$ = -0.2 %).

7.5 Summary and conclusions

This chapter describes the application of the new macro-roughness element (MRE) formula incorporated in the non-linear shallow-water (NLSW) model COMCOT v1.7 as well as the comparison of the model results with a reference model based on physical experiments and common roughness models for various grid resolutions.

In order to account for MRE, the extended code requires the use of additional data layers

- MRE drag coefficient C_D (buildings: C_D = 2.05),
- MRE height h_B,
- MRE arrangement angle Ψ and
- MRE coverage A^*_{MRE}

The well-described physical experiments of a tsunami-like bore inundating the town of Seaside, Oregon, (Rueben et al., 2011) form the basis for evaluating the new MRE formula and common roughness approaches. Due to the spatial constraints of the experimental facility, only the inundation extent at selected timesteps before reaching the maximum inundation extent can be analysed. Because the roughness models are to be evaluated for various grid resolutions, numerical dissipation needs to be considered.

The methodology for evaluating the results of various roughness models involves the determination of the impact of the numerical dissipation on the results. A numerical reference building-representing (BR) model of scale 1:1 with a grid resolution of dx = 5 m is established which provides comparable flow depths to the physical experimental at scale 1:50. For coarser grid resolutions, the inlet boundary conditions are calibrated so that the flow depths at the shoreline are maintained. During the analysis of the results, the appropriate timesteps for extracting the bore front are determined by considering the propagation times of the bore at various dx.

The numerical models using various roughness approaches (i) the implemented new MRE formula and (ii) two roughness models based on Manning coefficient n: constant n (CF model), variable n (VF model), and (iii) no roughness consideration at all (NF model) are considered and set up using resolutions dx = {5, 10, 20, 40} m.

The results are analysed in terms of the inundation extent for all models and grid resolutions mentioned above. Two indicators are applied for quantitative result comparison. They take into account (i) the spatial distribution of the inundation extent, recommended to be applied for high

resolution models (e.g. for local hazard assessment or evacuation planning), and (ii) the deviation from inundated area sizes, recommended to be applied for low resolution models on very large scale (e.g. for regional/global hazard assessment).

In general, all three roughness models (CF, VF and MRE) lead to good and comparable results as indicated for example by the relative inundation error $RIE_{mod,dx}$, taking values between $RIE_{MRE\ model,40m}$ = -9.3 % vs. $RIE_{VF\ model,40m}$ = -19 %). The accuracy of the MRE model (i.e. with the implemented new MRE formula) exceeds that of the CF and VF models. Its clear advantage over the latter models is furthermore, that the energy losses contributed by the MRE are determined by a physically based formula and the MRE model does not rely on calibration like in the other tested roughness approaches.

The new MRE formula could prove its applicability to tsunami inundation modelling in the here selected example.

As for any other new method, further comparisons of the here proposed model with field observations are recommended to ensure a safe application of the formula.

8 Summary and outlook

The main objective of this study was to develop a new formula (MRE formula) which relates the energy losses of the flow to easily determinable macro-roughness elements (MRE), and which can be used in common depth averaged models such as NLSW models.

Five steps were required to reach this objective:

1. Select and validate a three-dimensional CFD model to be used for a parameter study
2. Investigate the flow around MRE by varying the MRE parameters to improve the understanding of energy dissipation processes and create a database
3. Develop a new MRE formula to be applied in Step 5 as a source term in an NLSW model
4. Implement the MRE formula in a large-scale tsunami model and apply the model to a well-described test case to demonstrate the performance of the proposed MRE formula as compared to the current approaches

8.1 Summary of key results

8.1.1 RANS model validation and plausibility tests

For application in the parameter study, a RANS model was validated by comparing the results with available experimental data in five phases by consecutively adapting the numerical parameters such as mesh element sizes and turbulence parameters, starting from relatively simple models to describe the flow regime over variable depth and further, incorporating fluid-structure interaction to extend the models applicability.

The following results were obtained:

- The k-ω-SST model was selected to estimate turbulence as a well-established turbulence model, applicable in the free-flow and bounded flow zones. For fluid-structure interaction, a turbulence intensity of I = 10 % has proved successful.
- The results of further model applications to various arrangements and distances of circular cylinders provided results, which, to a large extent, could be related to existing experimental data and empirical formulae (e.g. Mindao et al, 1987; Bonakdar and Oumeraci, 2014).
- The numerical model is suitable to investigate the interaction of waves and bores with structures under the condition, that only averaged and maximum values without consideration of the instantaneous flow fields are analysed. Uncertainty remains on the performance of the model in cases of sharp flow separation in groups of sharp-edged MRE, for which no experimental data was available.

8.1.2 Parameter study

To understand the impact of MRE parameters on the energy losses during tsunami inundation, a programme consisting of a total number of 19 test cases was developed to identify separately the effects of MRE shape, relative width, arrangement, relative spacing and relative height on energy losses during the propagation of a tsunami-like bore.

The following key results were obtained:

- It is to be distinguished between upstream region and region inside the MRE zone and between steady and unsteady conditions of the bore propagation.
- The following MRE parameters are important for determining the energy losses: relative height, shape, relative spacing and arrangement angle.
- The analyses need to be performed using various distances between the cross-sections to minimize local flow effects due to the presence of the MRE near or inside the cross-sections.
- The inner MRE zone during the steady phase of bore propagation is less relevant than during the unsteady phase and, than the edge MRE zone during both flow phases and should thus not be considered for deriving the MRE formula.

8.1.3 Development, application and limitations of the new MRE formula

To determine the MRE formula for the NLSW model, the flow is described in terms of flow depth h and volume flux $q(x)$ and incorporated as an additional source terms in the NLSW momentum equation. The source terms are derived (i) in the upstream edge of the MRE zone for the steady and unsteady phases of bore propagation and (ii) in the inner MRE zone for the unsteady phase only.

To demonstrate the performance of the MRE formula, the formula is implemented in the NLSW model COMCOT. Measurements of physical experiments (Park et al., 2013) are compared with COMCOT simulations using (i) the MRE formula, and (ii) bottom friction-based source terms often referred to as “equivalent roughness models”.

The key results are summarized as follows:

- The MRE formula takes the form:
  Equation (6-26.a): $S_{MRE,fit} = S_{MRE,fit,inertia} + S_{MRE,fit,drag}$ with:
  - Equation (6-26.b): $S_{MRE,fit,inertia} = \frac{\partial q(x)}{\partial t} \frac{\sqrt{gh}}{\frac{q(x)}{h}} [1.3 - cos(4\Psi)]^{0.33}$
  - Equation (6-26.c):

$$S_{MRE,fit,drag} = -0.4 \frac{\partial \frac{D_B}{D_B + S_G}}{\partial x} \frac{q(x)^2}{h} \frac{min(2h, h_B)}{h} C_D [0.7 + 0.3cos(4\Psi)]^{0.1}$$

- The MRE model is expected to produce conservative results with regard to the inundation extent.
- The effect of debris, morphological changes and flexibility of MRE are still neglected (as in common inundation models).

- The MRE model does not rely on tedious calibration, which is required for common models relying on bottom friction only.
- The MRE model leads to comparable results as the common "equivalent roughness models", which apply Manning's values n based on experience and individual calibration.
- The MRE might exceed the performance of pure friction models when using small grid sizes, thereby distinguishing between residential areas and streets, and coarse grids in the order of dx = 40 m.

The limitations of the new MRE formula might be summarized as follows:

- It is applicable for Re > 50,000 due to the use of the drag coefficient to describe the shape of the MRE.
- The lateral effects of the shape (flow deflection) on the energy losses are not explicitly quantified.
- The mesh element size should be selected such that the changes of the relative MRE width remain small ($\frac{\partial \frac{D_B}{D_B+S_G}}{\partial x}$ < 0.328 1/m).
- The energy losses during the steady phase of bore propagation are considerably underestimated by up to 45 %.
- The energy losses determined in areas dominated by coastal vegetation might be underestimated between 0 % and 85 % (in case of very dense vegetation, see Maza et al, 2015a).
- The influence of morphological changes and flexibility of MRE are not considered, which might lead to an overestimation of energy losses.
- The influence of debris is not considered, which might lead to an underestimation of energy losses.

8.2 Outlook

This study might contribute to enhance the understanding of the relative importance of the MRE parameters on tsunami inundation. The new MRE formula considers energy losses due to drag and inertia generally applicable in urban areas. The new formula demonstrated its applicability in a comparison with well-documented physical experiments.

The MRE formula does not consider MRE width/length ratios, random MRE arrangements and flexible vegetation. Further consideration of these issues might lead to an improved formula for flood-prone urban areas and to a reduction of its conservatism in coastal forest applications. Furthermore, the MRE formula is to be tested in real-scale applications to confirm the improvement in tsunami inundation modelling which was demonstrated by reproducing laboratory experiments.

Based on the results and their limitations, the topics recommended for future research may be ranked as follows:

1. Physical experiments investigating forces acting on at least three rectangular shaped structures standing in groups of various configurations are essential to confirm and improve the understanding of the interaction of tsunami-like bores with MRE, particularly those found in urban areas.
2. Flow deflection towards neighbouring MRE should be investigated for a range of Reynolds numbers including $Re < 50{,}000$. The investigation should lead to a new dimensionless group shape coefficient. The drag coefficient C_D has historically been used to describe the impact of a fluid on individual structures. Instead, a "group shape coefficient" shall be formulated for describing the impact of structures on the fluid. The group shape coefficient should not only (one-dimensionally) account for resistance in flow direction (drag) but also for flow deflection lateral to the flow direction (in the second dimension).
3. The impact of debris on the inundation process should be investigated. Less-resistant obstacles such as cars, trash bins or furniture can noticeably change flow velocities and flow depths. From a large-scale Eulerian perspective, the fluid fraction debris should lead to spatially variable fluid parameters density and viscosity. The results are expected to improve not only inundation modelling but also the estimates of damages on property and infrastructure.
4. The interaction of morphological changes of MRE (e.g. due to damage, erosion) and the inundation process should be investigated. Tsunamis generally cause damages to MRE so that their consideration as undamaged in inundation modelling might lead to fully incorrect results. For example, the exceedance of stability thresholds could trigger MRE to vanish and instead, increase density and viscosity of the fluid.

References

1. Abbasi, W.S., Islam, S.U., Rahman and H., 2019. Proximity effects on characteristics of flow around three inline square cylinders, Math. Prob. Eng., 2019, 1752803, 14p, https://doi.org/10.1155/2019/1752803.
2. Aberle, J. and Smart, G.M., 2003. The influence of roughness structure on flow resistance on steep slopes. J. Hydraul. Res., 41(3), 259-269.
3. Al-Faesly, Palermo, D., Nistor, I. and Cornett, A., 2012. Experimental Modeling of Extreme Hydrodynamic Forces on Structural Models. Int. J. Protective Structures, 3(4), 477-505.
4. Apotsos, A., Buckley, M., Gelfenbaum, G., Jaffe, B. and Vatvani, D., 2011. Nearshore Tsunami Inundation Model Validation: Toward Sediment Transport Applications. Pure Appl. Geophys., 168, 2097-2119.
5. Arcement Jr., G.J. and Schneider, V.R., 1989. Guide for Selecting Manning's Roughness Coefficients for Natural Channels and Flood Plains. USGS WSP2339, metric version.
6. Árnason, H., 2004. Interactions between an Incident Bore and a Free-Standing Coastal Structure. PhD thesis, University of Washington, USA.
7. Árnason, H., Petroff, C. and Yeh, H., 2009. Tsunami Bore Impingement onto a Vertical Column. J. Disaster Res., 4(6), 391-403.
8. Bonakdar, L. and Oumeraci, H, 2012. Interaction of Waves and Pile Group-Supported Offshore Structures: A Large Scale Model Study. In Proc. of the International Society of Polar and Offshore Engineers Conference ISOPE 2012.
9. Bonakdar, L., 2014. Pile Group Effect on the Wave Loading of a Slender Pile, PhD thesis, Fac. Architecture, Civil Engineering and Environmental Sciences, TU Braunschweig, Germany.
10. Bonakdar, L. and Oumeraci, H., 2014. Small and large scale experimental investigations of wave loads on a slender pile within closely spaced neighbouring piles. In Proc. of the 33rd International Conference on Ocean, Offshore and Arctic Engineering, 8-13 June 2014, San Francisco, USA.
11. Borrero, J.C., 2005. Field Survey of Northern Sumatra and Banda Aceh, Indonesia after the Tsunami and Earthquake of 26 December 2004. Seismol. Res. Lett., 76, 312-320.
12. Borrero, J.C., Synolakis, C.E. and Fritz, H.M., 2006. Field Surveys of northern Sumatra after the tsunami and earthquake of 26 December 2004, Earthquake Spectra, 22(S3), S93-S104.
13. Bradford, S.F. and Sanders, B.F., 2002. Finite-Volume Method for Shallow-Water Flooding of Arbitrary Topography. J. Hydraul. Eng.-ASCE, 128 (3), 289-298.
14. Bricker, J.B., Gibson, S., Takagi, H. and Imamura, F., 2015. On the Need for Larger Manning's Roughness Coefficients in Depth-Integrated Tsunami Inundation Models. Coastal Eng. J., 57 (2), 1550005-1-1550005-13.

15. Carrier, G.F., 1966. Gravity waves on water of variable depth. J. Fluid Mech., 24 (4), 641-659.
16. Carrier, G.F. and Greenspan, H.P., 1958. Water waves of finite amplitude on a sloping beach. J. Fluid Mech., 17, 97-109.
17. Carrier, G.F. and Noiseux, C.F., 1983. The reflection of obliquely incident tsunamis. J. Fluid Mech., 133, 147-160.
18. Cassan, L., Roux, H. and Garambois, P.-A., 2017. A Semi-Analytical Model for the Hydraulic Resistance Due to Macro-Roughnesses of Varying Shapes and Densities. Water, 9, 637, doi: 10.3390/w9090637.
19. CFD-Wiki, 2011. Turbulence kinetic energy, https://www.cfd-online.com/Wiki/Turbulence_kinetic_energy, last accessed: 20 January 2019.
20. CFD-Wiki, 2012. Turbulence length scale, https://www.cfd-online.com/Wiki/Turbulence_length_scale, last accessed: 20 January 2019.
21. CFD-Wiki, 2015. Turbulence dissipation rate, https://www.cfd-online.com/Wiki/Turbulence_dissipation_rate, last accessed: 20 January 2019.
22. CFD-Wiki, 2018. Turbulence intensity, https://www.cfd-online.com/Wiki/Turbulence_intensity, last accessed: 20 January 2019.
23. Chanson, H., 2006. Tsunami surges on dry coastal plains: Application of dam break wave equations. Coast. Eng. J., 48 (4), 355-370.
24. Chanson, H., 2009. Application of the method of characteristics to the dam break problem. J. Hydraul. Res., 47 (1), 41-49. Doi: 10.3826/jhr.2009.2865.
25. Choi, J., Ko, K.O. and Yoon, S.B., 2009. 3D numerical simulation for equivalent resistance coefficient for flooded built-up areas. In: Proc. of the 5th International Conference on Asian and Pacific Coasts, Tan, S.K. and Huang, Z. (Eds.), 13-18 October 2009, Singapore.
26. Chuang, W.-L., Chang, K.-A., Kaihatu, J., Cienfuegos, R. and Mokraini, C., 2020. Experimental study of force, pressure, and fluid velocity on a simplified coastal building under tsunami bore impact. Nat. Hazards, 103, 1093-1120, https://doi.org/10.1007/s11069-020-04027-3.
27. CIMNE, 2010. GiD Referene Manual. International Center for Numerical Methods in Engineering (CIMNE), Barcelona, Spain.
28. Clawpack Development Team, 2020. Clawpack Version 5.7.1, http://www.clawpack.org, doi: 10.5281/zenodo.4025432.
29. Cox, 2018. Personal communication, 2 August 2018.
30. Cross, R.H., 1967. Tsunami surge forces, J. Waterw. Harbor Div.-ASCE, 93 (4), 201-231.
31. Cumberbatch, E., 1960. The impact of a water wedge on a wall. J. Fluid Mech., 7, 353-374.
32. Dalrymple, R.A. and Rogers, B.D., 2006. Numerical modeling of water waves with the SPH method. Coastal Eng., 24, 233-257.
33. Davletshin, V.K. and Lappo, D.D., 1986. Tsunami forces exerted on vertical cylindrical barriers. Fluid Mech.-Soviet Res., 15 (3), 137-147.

34. Dean, R.G. and Dalrymple, R.A., 1991. Water Wave Mechanics for Engineers and Scientists, Advanced Series on Ocean Engineering, World Scientific, Singapore.
35. DHI, 2021. Flow Model and MIKE 21 Hydrodynamic and Transport Module Scientific Documentation.https://manuals.mikepoweredbydhi.help//2021/Coast_and_Sea/MIKE_21_Flow_FM_Scientific_Doc.pdf. Last accessed: 22 May 2021.
36. DHI, 2020. Urban mapping. https://www.dhi-gras.com/solutions/urban-mapping/, last accessed: 20 February 2020.
37. EDF-R&D, 2014. Telemac Modelling system 2D Hydrodynamics TELEMAC-2D Software Release 7.0 User Manual, http://www.opentelemac.org/downloads/MANUALS/TELEMAC-2D/telemac-2d_user_manual_en_v7p0.pdf. December 2014.
38. Eliasson, J., Kjaram, S.P., Holm, S.L., Gudmundsson, M.T. and Larsen, G., 2007. Large hazardous floods as translator waves. Environm. Modell. Softw., 22, 1392-1399.
39. Elsafti, H. and Oumeraci, H., 2017. Analysis and classification of stepwise failure of monolithic breakwaters. Coast. Eng., 121, 221-239.
40. Erduran, K.S. and Kutija, V., 2003. Quasi-three-dimensional numerical model for flow through flexible, rigid, submerged and non-submerged vegetation. J. Hydroinform., 5 (3), 189-202.
41. FEMA, 1979. The floodway: A guide for community permit officials. US Federal Insurance Administration, Community Assistance Series, N. 4, 1979.
42. FEMA, 2008. Guidelines for Design of Structures for Vertical Evacuation from Tsunamis. FEMA P646, Washington DC, USA.
43. Fenton, J.D., 1988. The numerical solution of steady water wave problems. Comp. Geosci., 14 (3), 357-368.
44. Fredsøe, J. and Deigaard, R., 1992. Mechanics of Coastal Sediment Transport, Advanced Series on Ocean Engineering-Volume 3, P.L.-F. Liu (Ed.), World Scientific, Singapore.
45. Fritz, H.M., Borrero, J., Synolakis, C.E. and Yoo, J., 2006. 2004 Indian Ocean tsunami flow velocity measurements from survivor videos. Geophys. Res. Lett., 33, L24605, DOI: 10.1029/2006GL026784.
46. Fritz, H.M., Phillips, D., Okayasu, A., Shimozono, T., Liu, H., Mohammed, F., Skanavis, V., Synolakis, C.E. and Takahashi, T., 2012. The 2011 Japan tsunami current velocity measurements from survivor videos at Kesennuma Bay using LiDAR. Geophys. Res. Lett., 39, L00G23, DOI: 10.1029/2011GL050686.
47. Fujima, K., 2001. Long wave propagation on large roughness. In: Proc of ITS 2001, 891-895.
48. Fujima, K., Goto, C. and Shuto, N., 1986. Accuracy of nonlinear disperse long wave equations. JSCE, 369 (II-5), 223-232.
49. Gayer, G., Leschka, S., Nöhren, I., Larsen, O. and Günther, H., 2010. Tsunami inundation modelling based on detailed roughness maps on densely populated areas. Nat. Hazards Earth Syst. Sci., 10, 1679-1687, doi: 10.5194/nhess-10-1679-2010.

50. Glimsdal, S., Pedersen, G.K., Harbitz, C.B. and Løvholt, F., 2013. Disperson of tsunamis: does it really matter? Nat. Hazards Earth Syst. Sci., 13, 1507-1526.
51. Goseberg, N., 2013. Reduction of maximum tsunami run-up due to the interaction with beachfront development-application of single sinusoidal waves. Nat. Hazards Earth Syst. Sci., 13, 2991-3010.
52. Goseberg, N., Bremm, G., Schlurmann, T., Nistor, I., 2015. A transient approach flow acting on a square cylinder-Flow pattern and horizontal forces. E-proceedings of the 36th IAHR World Congress, 28 June – 3 July, 2015, The Hague, The Netherlands.
53. Goseberg, N., Stolle, J., Nistor, I. and Shibayama, T., 2016. Experimental analysis of debris motion due the obstruction from fixed obstacles in tsunami-like flow conditions. Coastal Eng., 118, 35-49.
54. Goto, K., Fujima, K., Sugawara, D., Fujino, S., Imai, K., Tsudaka, R., Abe, T. and Haraguchi, T., 2012. Field measurements and numerical modeling for the run-up heights and inundation distances of the 2011 Tohoku-oki tsunami at Sendai Plain, Japan. Earth Planets Space, 64, 1247-1257.
55. Green, J.C., 2005. Modelling of flow resistance in vegetated streams: review and development of new theory. Hydrol. Process., 19, 1245-1259.
56. Grilli, S., 2008. On the development and application of Hybrid Numerical Models in Nonlinear Free Surface Hydrodynamics. In Proc. of the 8th International Conference on Hydrodynamics, P. Ferrant and Chen X.B. (Eds.), Nantes/France, September 2008.
57. Grode, P.D., et al., 2017. DHI's Internal Matlab Toolbox.
58. Hamilton, J., 1977. Differential Equations for long-period gravity waves on fluid of rapidly varying depth. J. Fluid Mech., 83 (2), 289-310.
59. Harada, K. and Imamura, F., 2000. Experimental study on the resistance by mangrove under the unsteady flow. In: Proc. of the 1st Congress of APACE, 975-984.
60. Harada, K. and Imamura, F., 2003. Evaluation of tsunami reduction by control forest and possibility of its use for mitigation. In: Proc. of Coast. Eng.-JSCE, 341-345. (in Japanese)
61. Harada, K. and Kawata, Y., 2005. Study on Tsunami Reduction effect on Coastal forest due to Forest Growth. Annuals of Disas. Prev. Res. Inst., Kyoto Univ., No. 48C, 2005.
62. Hashimoto, H. and Park, K., 2008. Two-dimensional urban flood simulation: Fukuoka flood disaster in 1999. WIT Trans. Ecol. Environment, 118, 59-67.
63. Heitner, K.L. and Housner, G.W., 1971. Numerical model for tsunami run-up. J. Waterw. Div.-ASCE, 96 (WW3), 701-719.
64. Hey, R.D., 1972. An analysis of some of the actors influencing the hydraulic geometry of river channels. PhD thesis, University of Cambridge, UK.
65. Hibberd, S. and Peregrine, D.H., 1979. Surf and run-up on a beach: a uniform bore, J. Fluid Mech., 95 (2), 323-345.
66. Higuera, P., Lara, J.L. and Losada, I.J., 2014a. Three-dimensional interaction of waves and porous coastal structures using OpenFOAM®. Part I: Formulation and validation. Coast. Eng. 83, 243-258.

67. Higuera, P., Lara, J.L. and Losada, I.J., 2014b. Three-dimensional interaction of waves and porous coastal structures using OpenFOAM®. Part II: Application. Coast. Eng., 83, 259-270.
68. Hirt, C.W. and Nichols, B.D., 1981. Volume of Fluid (VOF) method for the dynamics of free boundaries. J. Comput. Phys., 39, 201-225.
69. Hoerner, S.F., 1965. Fluid Dynamic Drag, Hoerner Fluid Dynamics, Bricktown, New Jersey.
70. Hoonhout, B.M., Radermacher, M., Baart, F. and van der Maarten, L.J.P., 2015. An automated method for semantic classification of regions in coastal images. Coast. Eng., 105, 1-12.
71. Hori, E., 1959. Experiments on flow around a pair of parallel circular cylinders. In Proc. 9th Japan National Congress for Applied Mechanics, Tokyo, 231-234.
72. Huang, Z., Yao, Y., Sim, S.Y. and Yao, Y., 2011. Interaction of solitary waves with emergent, rigid vegetation. Ocean Eng., 38, 1080-1088.
73. Husrin, S., Strusinska, A. and Oumeraci, H., 2012. Experimental study on tsunami attenuation by mangrove forest. Earth Planets Space, 64, 973-989.
74. Husrin, S., 2013. Attenuation of Solitary Waves and Wave Trains by Coastal Forest. PhD thesis, TU Braunschweig and University of Florence.
75. Huthoff, F., 2012. Theory of flow resistance caused by submerged roughness elements. J. Hydraul. Res., 50 (1), 10-17.
76. Imamura, F., Yalciner, A.C. and Ozyurt, G., 2006. Tsunami modelling manual.
77. Irtem, E., Gedik, N., Kabdasli, M.S. and Yasa, N.E., 2009. Coastal forest effects on tsunami run-up heights. Ocean Eng., 36(3-4), 313-320.
78. Ismail, H., Abd Wahab, A.K. and Alias, N.E., 2012. Determination of mangrove forest performance in reducing tsunami run-up using physical models. Nat. Hazards, 63, 939-963.
79. Jacobsen, N.G., Furmann, D.R. and Fredsøe, J., 2012. A wave generation toolbox for the Open-Source CFD Library: OpenFOAM. Int. J. Numerl. Meth. Fluids, 70 (9), 1073-1088, DOI 10.1002/fld.2726.
80. Jakeman, J.D., Nielsen, O.M., van Putten, K., Mleczko, R., Burbidge, D. and Hospool, N., 2010. Towards spatially distributed quantitative assessment of tsunami inundation models. Ocean Dynamics, 60, 1115-1138, doi: 10.1007/s10236-010-0312-4.
81. Jones, W.P. and Launder, B.E., 1972. The Prediction of Laminarization with a Two-Equation Model of Turbulence. Int. J. Heat Mass Transfer, 15, 301-314.
82. Kajiura, K., 1961. On the partial reflection of water waves passing over a bottom of variable depth. Inter. Union of Geodesy and Geophys. Monograph, 24, Tsunami Symposia, 206-230.
83. Kajiura, K., 1963. The leading wave of a tsunami. Bull. Earthquake Res. Inst., 41, 535-571.
84. Kandasamy, K. and Narayanasamy, R., 2005. Coastal mangrove forest mitigated tsunami. Estuar. Coast. Shelf Sci., 65, 601-606.

85. Kânoglu, U. and Synolakis, C.E., 1998. Long wave runup on piecewise linear topographies. J. Fluid Mech., 374, 1-28.
86. Kennedy, A.B., Chen, Q., Kirby, J.T., and Dalrymple, R.A., 2000. Boussinesq Modeling of Wave Transformation, Breaking, and Runup. I: 1D. J. Waterw. Port Coastal Ocean Eng.-ASCE, 126 (1), 39-47.
87. Keulegan, G.H. and Carpenter, L.H., 1958. Forces on cylinders and plates in an oscillating fluid. J. Res. Nat. Bur. Stand., 60 (5), 423-440.
88. Kishi, T. and Saeki, H., 1966. The shoaling, breaking and runup of the solitary wave on impermeable rough slopes. 10th Conference on Coastal Engineering. In: Proc. of 10th Conference on Coastal Engineering 1, 322-348, New York, USA.
89. Kitware (2012-2018). ParaView – Open Source Scientific Visualization. http://www.paraview.org/, last accessed: 20 January 2019.
90. Korteweg, D. and de Vries, G., 1895. On the change of the form of long waves advancing in a rectangular canal, and on a new type of long stationary waves. Phil. Mag., 39, 422-443.
91. Koshimura, S., Oie, T., Yanagisawa, H. and Imamura, F., 2009. Developing fragility functions for tsunami damage estimation using numerical model and post-tsunami data from Banda Aceh, Indonesia. Coast. Eng. J., 51(3), 243-273.
92. Kotani, M., Imamura, F. and Shuto, N., 1998. Tsunami run-up simulation and damage estimation using GIS. In: Proc. of Coast. Eng., JSCE, 45(1), 356-360 (in Japanese).
93. Kouwen, N., 1992. Modern Approach to Design Grassed Channels. J. Irrig. Drain Eng.-ASCE, 118 (5), 733-743.
94. Krautwald, C., 2017. Implementation of the effect of macro-roughness elements in a depth-averaged numerical model. M.Sc. thesis, Leichtweiß-Institute for Hydraulic Engineering and Water Resources, TU Braunschweig, Germany.
95. Kunapo, J., Sim, P.T. and Chandra, S., 2005. Towards automation of impervious surface mapping using high resolution orthophoto. Applied GIS, 1(1), 1-19. https://doi.org/10.2014/ag050003.
96. Laitone, E.V., 1960. The second approximation to cnoidal and solitary waves. J. Fluid Mech., 9 (3).
97. Latief, H., 2000. Study on tsunamis and their mitigation by using a green belt in Indonesia. PhD thesis, Tohoku University, Sendai, Japan.
98. Latief, H. and Hadi, S., 2007. Thematic paper: The role of forests and trees in protecting coastal areas against tsunamis. Braatz, S. , Fortuna, S., Broadhead, J. and Leslie, R. (Eds.). ISBN: 978-974-7946-95-6.
99. Latief, H., Sunendar, H., Gusman, A.R. and Panca, Y., 2007. Current Tsunami Research Activities in Indonesia. South China Sea Tsunami Workshop, 5-7 December 2007, Academica Sinica, Taiwan.
100. Lautenbach, C.C., 1970. Gravity wave refraction by islands. J. Fluid Mech., 41 (3), 655-672.
101. Lavigne, F., Paris, R., 2006. Le tsunami du 26 décembre 2004 en Indonésie. Report TSUNARISQUE 2005-2006 for Centre National de la Recherche Scientifique.

102. Leschka, S., 2008. Present state of knowledge for modelling large roughness effects on tsunami propagation, run-up and inundation. Report, 29 August 2008.
103. Leschka, S., 2020. Comparison of the MRE model and equivalence roughness models with physical experiments. Report, 5 March 2020.
104. Leschka, S., Thévenin, D., Zähringer, K. and Lehwald, A., 2007. Fluid Dynamics and Mixing Behavior of a SMX-Type Static Mixer. J. Visual., 10(4), 342-342, doi: 10.1007/BF03181889.
105. Leschka, S., Oumeraci, H. and Larsen, O., 2014. Hydrodynamic Forces on a Group of Three Emerged Cylinders by Solitary Waves and Bores: Effect of Cylinder Arrangements and Distances. J. Earthquake Tsunami, 8 (3), 1440005 (36 pages), doi: 10.1142/S1793431114400053.
106. Li, Y. and Raichlen, F., 2002. Non-breaking and breaking solitary wave run-up. J. Fluid Mech., 456, 295-318.
107. Lin, P., 2004.A numerical study of solitary wave interaction with rectangular obstacles. Coast. Eng., 51, 35-51.
108. Liu, P.L.-F., Yoon, S.B. and Kirby, J.T., 1985. Nonlinear refraction-diffraction of waves in shallow water. J. Fluid Mech., 153, 185-201.
109. Liu, P.L.-F., Woo, S.-B. and Cho, Y.-S., 1998. Computer Programs for Tsunami Propagation and Inundation, Report, Cornell University, Ithaka, USA.
110. Longuet-Higgins, M.S., 1967. On the trapping of wave energy round islands. J. Fluid Mech., 29 (4), 781-821.
111. Lopez, F. and Garcia, M., 1997. Open Cannel Flow Through Simulated Vegetation: Turbulence Modelling and Sediment Transport. Hydrosystems Laboratory, Department of Civil Engineering, University of Illinois, USA.
112. Losada, I.J., Maza, M. and Lara, J.L., 2016. A new formulation for vegetation-induced damping under combined waves and currents. Coast. Eng., 107, 1-13.
113. Lynett, P.J., Liu, P.L.-F., Sitanggang, K.I. and Kim, D.-H., 2008. Modeling Wave Generation, Evolution, and Interaction with Depth-Integrated, Dispersive Wave Equations COULWAVE Code Manual Cornell University Long and Intermediate Wave Modeling Package v. 2.0. http://isec.nacse.org/models/users_guide/coulwave.pdf, last accessed: 23 August 2019.
114. Madsen, P.A., Sørensen, O.R. and Schäffer, H.A., 1997a. Surf zone dynamics simulated by a Boussinesq type model. Part I. model description and cross-shore motion of regular waves. Coast. Eng., 32, 255-287.
115. Madsen, P.A., Sørensen, O.R., and Schäffer, H.A., 1997b. Surf zone dynamics simulated by a Boussinesq type model. Part II: surf beat and swash oscillations for wave groups and irregular waves. Coast. Eng., 32, 289-319.
116. Madsen, P.A. and Fuhrman, D.R., 2007. Analytical and numerical models for tsunami run-up. In: Kundu, A. (Ed.), Tsunami and Nonlinear Waves, 209-236, Springer, Berlin, Heidelberg, Germany.

117. Madsen, P.A., Fuhrman, D.R. and Schäffer, H., 2008. On the solitary wave paradigm for tsunamis. In: Proc. of the 31st International Conference On Coastal Engineering, 31 August-5 September 2008, Hamburg, Germany.
118. Marsooli, R., Orton, P.M., Georgas, N. and Blumberg A.F., 2016. Three-dimensional hydrodynamic modeling of coastal flood mitigation by wetlands. Coast. Eng., 111, 83-94.
119. Matsutomi, H., Ohnuma, K., Suzuki, A., and Imai, K., 2006. Governing equations for inundated flow in vegetated area and similarity laws for tree trunks. In Proc. of the 30th International Conference on Coastal Engineering, San Diego, USA.
120. Matsuyama, M., Ikeno, M., Sakakiyama, T. and Takeda, T., 2007. A study of Tsunami Wave Fission in an Undistorted Experiment. Pure Appl. Geophys., 164, 617-631.
121. Maza, M., Lara, J.L. and Losada, I.J., 2013. A coupled model of submerged vegetation under oscillatory flow using Navier-Stokes equations. Coast. Eng., 80, 16-34.
122. Maza, M., Lara, J.L. and Losada, I.J., 2015a. Tsunami wave interaction with mangrove forests: A 3-D numerical approach. Coast. Eng., 98, 33-54.
123. Maza, M., Lara, J.L. and Losada, I.J., Ondiviela, B., Trinogga, J. and Bouma, T.J., 2015b. Large-scale 3-D experiments of wave and current interaction with real vegetation. Part 2: Experimental analysis. Coast. Eng., 106, 73-86.
124. Miles, J., 1981. The Korteweg-de Vries equation: A historical essay. J. Fluid Mech., 106, 131-147.
125. Mindao, G., Lihua, H., Shaoshu, S., 1987. Experimental study for the wave forces on pile groups due to regular waves. In Proc. 2nd International Conference of Coastal and Port Engineering in Developing Countries (COPEDEC), China Ocean Press, Beijing, pp 1956-1965.
126. Muhari, A., Imamura, F., Koshimura, S. and Post, J., 2011. Examination of three practical run-up models for assessing tsunami impact on highly populated areas. Nat. Hazards Earth Syst. Sci., 11, 3107-3123, doi: 10.5194/nhess-11-3107-2011.
127. Nanía, L.S., Gómez, M. and Dolz, J., 2004. Experimental study of the dividing flow in steep street crossings. J. Hydraul. Res., 42(4), 406-412.
128. Nielsen, O., Roberts, S., Gray, D., McPherson, A. and Hitchman, A., 2005. Hydrodynamic modelling of coastal inundation. Zerger, A. and Argent, R. M. (Eds.), In: Proceedings of International Congress on Modelling and Simulation. MODSIM 2005, 518-523.
129. Nistor, I., 2014. Personal communication, June 16, 2014, Seoul/South Korea.
130. Nouri, Y., Nistor, I. and Palermo, D., 2010. Experimental investigation of tsunami impact on free standing structures. Coast. Eng. J.-JSCE, 52 (1), 43-70.
131. Nwogu, O., 1993. Alternative form of Boussinesq Equations for nearshore Wave Propagation. J. Waterw. Port Coastal Ocean Eng.-ASCE, 119 (6), 618-638.
132. Okada, T., Sugano, T., Ishikawa, T., Ohgi, T., Takai, S. and Hamabe, C., 2005. Structural Design Method of Buildings for Tsunami Resistance (SMBTR), a code proposed by The Building Technology Research Insititute of The Building Center of Japan.
133. Olsson, E. and Kreiss, G., 2005. A conservative level set method for two phase flow. J. Comput. Phys., 210, 225-246.

134. Olsson, E., Kreiss, G. and Zahedi, S., 2007. A conservative level set method for two phase flow II. J. Comput. Phys., 225, 785-807.
135. OpenCFD, 2018. About OpenFOAM, http://openfoam.com, last visited: 19 January 2019.
136. OpenFOAM Foundation, 2011. OpenFOAM 2.1.0. The Open Source CFD Tool Box User Guide, 2011. OpenFOAM Foundation, http://www.openfoam.org/archive/2.1.0/docs/.
137. OpenFOAMWiki, 2018. Contrib/waves2Foam. http://openfoamwiki.net/index.php/Contrib/waves2Foam, last accessed: 20 January 2019.
138. Oumeraci, 2006. Near- and Onshore Tsunami Effects-Knowledge Base Generation and Model Development. Background Paper for DFG Geokommission, 20 November 2006.
139. Oumeraci, H. and Koether, G., 2009. Hydraulic performance of a submerged wave absorber for coastal protection. In: Nonlinear Wave Dynamics-Selected Papers of the Symposium held of Philip L.-F. Liu's 60th Birthday P.J. Lynett (Ed.), 31-65, World Scientific, 2009.
140. Park, H., Cox, D.T., Lynett, P.J., Wiebe, D.M. and Shin, S., 2013. Tsunami inundation modeling in constructed environments: A physical and numerical comparison of free-surface elevation, velocity, and momentum flux. Coast. Eng., 79, 9-21.
141. Park, H. 2017. Re: Data set of tsunami inundation through an urban waterfront, E-Mail to c.krautwald@tu-braunschweig.de, 5 Sep 2017, 17:09 MESZ.
142. Park, H., 2018. Re: Data set of tsunami inundation through an urban waterfront, E-Mail to sle@dhigroup.com, 27 Sep 2018, 18:05 MESZ.
143. Pasha, G.A. and Tanaka, N., 2017. Undular hydraulic jump formation and energy loss in a flow through emergent vegetation of varying thickness. Ocean Eng., 141, 308-325.
144. Peregrine, D.H., 1967. Long waves on a beach. J Fluid Mech, 27 (4), 815-827.
145. Petroff, C.M. and Raichlen, F., 1991. Effect of Sheltering on Spheres in Long Waves. J. Waterw. Port Coastal Ocean Eng., 117 (3), 264-283.
146. Prandtl, L., 1945. Über ein neues Formelsystem für die ausgebildete Turbulenz. Nachr. Acad. Wiss., Goettingen, Germany.
147. Rakowsky, N., Androsov, A., Fuchs, A., Harig, S., Immerz, A., Danilov, S., et al., 2013. Operational tsunami modelling with TsunAWI-Recent developments and applications. Nat. Hazards Earth Sys. Sci., 13, 1629-1642, doi: 10.5194/nhess-13-1629-2013.
148. Ramsden, J.D., 1993. Tsunamis: Forces on a Vertical Wall Caused by Long Waves, Bores, and Surges on a Dry Bed. PhD thesis, California Institute of Technology, USA.
149. Rasmussen, M.L., 2020. RE: Buildings and vegetation from satellite images. E-Mail from R.E. Borgstrøm to sle@dhigroup.com, 28 January 2020, 21:03 CET.
150. Ritter, A., 1892. Die Fortpflanzung der Wasserwellen. Verein Deutscher Ingenieure, 36 (2.a), 947-954, (in German).
151. Rueben, M., Holman, R., Cox, D.T., Shin, S., Killian, J. and Stranley, J., 2011. Optical measurements of tsunami inundation through an urban waterfront modeled in a large-scale laboratory basin. Coast. Eng., 58, 229-238.

152. Russel, J., 1844. Report on waves. British association of the Advancement of Science, London.
153. Sato, S., 1996. Numerical simulation of 1993 Southwest Hokkaido earthquake tsunami around Okushiri Island. J. Waterw. Port Coastal Ocean Eng.-ASCE, 122 (5), 209-219.
154. Schäffer, H.A., Madsen, P.A. and Deigaard, R., 1993. A Boussinesq model for waves breaking in shallow water. Coast. Eng., 20, 185-202.
155. Schlurmann, T., Kongko, W., Goseberg, N., Natawidjaja, D.H. and Sieh, K., 2010. Near-field tsunami hazard map Padang, West Sumatra: Utilizing high resolution geo-spatial data and reasonable source scenarios. In: Lynett, P. and Smith, J.M. (Eds.), Proc. of the 32nd International Conference on Coastal Engineering, 30 June- 5 July 2010, Shanghai, China.
156. Schroeder, W., 1992. Wasserbau. In: K.-J. Schneider (Editor), Bautabellen. Werner-Verlag, Duesseldorf, Germany.
157. Sellin, R.H., Bryant, T.B. and Loveless, J.H., 2003. An improved method for roughening floodplains on physical river models. J. Hydraul. Res., 41 (1), 3-14.
158. Shafei, S., Melville, B.W. and Shamseldin, A.Y., 2016. Experimental investigation of tsunami bore impact force and pressure on a square prism. Coast. Eng., 110, 1-16.
159. Shao, S., 2006. Incompressible SPH simulation of wave breaking and overtopping with turbulence modelling. Int. J. Numer. Methods Fluids, 50, 597-621.
160. Shi, F., Kirby, T.J., Harris, J.C. and Grilli, S., 2013. Funwave-TVD Fully Nonlinear Boussinesq Wave Model with TVD Solver Documentation and User's Manual. https://fengyanshi.github.io/build/html/index.html. Last accessed: 23 August 2019
161. Shimozono, T., Sato, S., Okayasu, A., Tajima, Y., Fritz, H.M., Liu, H. and Takagawa, T. Propagation and inundation characteristics of the 2011 Tohoku tsunami on the central Sanriku coast. Coast. Eng. J., 54, 1250004-1-1250004-17, DOI: 10.1142/S0578563412500040.
162. Shimozono, T. and Sato, S., 2016. Coastal vulnerability analysis during tsunami-induced levee-overflow and breaching by a high-resolution flood model. Coast. Eng., 107, 116-126.
163. Shuto, N., 1985. The Nihokai-Chuubu earthquake tsunami on the north Akita coast, Coast. Eng. Japan, JSCE, 28, 255-264.
164. Sivasubramanian, M., Kanna, P.R., Muthukannan, M. and Uthayakumar, M., 2015. Experimental investigation on flow through a confined rectangular channel mounted with square blocks. J. Eng. Sci. Tech., 10(2), 212-223.
165. Sridhar, A., 2019. Large-eddy Simulation of Turbulent Boundary Layers with Spatially Varying Roughness. PhD Thesis, California Institute of Technology, Pasadena, California.
166. Smith, R. and Sprinks, T., 1975. Scattering of surface waves by a conical island. J. Fluid Mech., 72 (2), 373-384.
167. Soarez-Frazão, S. and Zech, Y., 2008. Dam-break flow through an idealized city. J. Hydraul. Res., 46(5), 648-658, DOI: 10.3826/jhr.2008.3164.

168. Sørensen, O.R., Schäffer, H.A., and Madsen, P.A., 1998. Surf zone dynamics simulated by a Boussinesq type model. III. Wave-induced horizontal nearshore circulations. Coast. Eng., 33, 155-176.
169. Sparboom, U., Hildebrandt, A. and Oumeraci, H., 2006. Group interaction effects of slender cylinders under wave attack. In: Proc. of the 30th International Conference On Coastal Engineering, San Diego, CA.
170. St. Germain, P., Nistor, I., Townsend, R. and Shibayama, T., 2014. Smoothed-Particle Hydrodynamics Modeling of Structures Impacted by Tsunami Bores. J. Waterway Port Coastal Ocean Eng., 140, 66-81.
171. Strusinska, A., 2010. Hydraulic Performance of an impermeable submerged structure for tsunami damping. PhD Thesis, TU Braunschweig, Germany.
172. Strusinska-Correia, A., Husrin, S. and Oumeraci, H., 2013. Tsunami damping by mangrove forest: A laboratory study using parameterized trees. Nat. Hazards. Earth Syst. Sci., 13, 483-503.
173. Sumer, B.M. and Fredsøe, J., 2006. Hydrodynamics around cylindrical structures. Advanced Series on Ocean Engineering Volume 26, Revised Edition, World Scientific, Singapore.
174. Synolakis, C.E., 1987. The runup of solitary waves. J. Fluid Mech., 185, 523-545.
175. Teng, M.H. and Feng, K., 2000. Long Wave Run-Up on Sloping Beaches. Tassoulas, J. L. 14th Engineering Mechanics Conference.
176. Ting, F.C.K. and Kirby, T.J., 1994. Observation of undertow and turbulence in a laboratory surf zone. Coast. Eng., 24, 51-80.
177. Ting, F.C.K. and Reimnitz, J., 2015. Volumetric velocity measurements of turbulent coherent structures induced by plunging regular waves. Coast. Eng., 104, 93-112.
178. Titov, V.V. and Synolakis, C.E., 1995. Modeling of Breaking and Nonbreaking Long-Wave Evolution and Runup using VTCS-2. J Waterw. Port Coastal Ocean Eng.-ASCE, 121 (6), 308-316.
179. Tsutsumi, A., Shimamoto, T., Kawamoto, E., and Logan, J.M., 2000. Nearshore Flow Velocity of Southwest Hokkaido Earthquake Tsunami. J. Waterw. Port Coastal Ocean Eng., 126 (3), 136-143.
180. USGS, 2012. Magnitude 9.1-Off the West Coast of Sumatra, US Geological Survey, https://web.archive.org/web/20120817004055/http://earthquake.usgs.gov/earthquakes/eqinthenews/2004/us2004slav/#summary, last updated on June 20, 2012.
181. Vionnet, C.A., Tassi, P.A., and Martín Vide, J.P., 2004. Estimates of flow resistance and eddy viscosity coefficients for 2D modelling on vegetated floodplains. Hydrol. Process., 18, 2907-2926.
182. van Gent, M.R.A., Tonjes, P., Petit, H.A.H. and van den Bosch, P., 1994. Wave action on and in permeable structures. Coast. Eng. Proc., 1739-1753.
183. von Kármán, T., 1963. Aerodynamics. McGraw-Hill.
184. Wang., D., Shao, S., Li, S., Shi, Y., Arikawa, T. and Zhang, H., 2018. 3D ISPH erosion model for flow passing a vertical cylinder. J. Fluids Structures, 78, 374-399.

185. Wang, X. and Power, W., 2011. COMCOT: A Tsunami Generation, Propagation and Run-up Model. GNS Report 2011/43, 129p.
186. Wei, Y., Chamberlin, C., Titov, V.V., Tang, L. and Bernard, E.N., 2012. Modeling of the 2011 Japan Tsunami: Lessons for Near-Field Forecast. Pure Appl. Geophys., DOI 10.1007/s00024-012-0519-z.
187. Wei, Z., Dalrymple, R.A., Hérault, A., Bilotta, G. Rustico, E. and Yeh, H., 2015. SPH modeling of dynamic impact of tsunami bore on bridge piers. Coast. Eng., 104, 26-42.
188. Weihua, M., Irschik, K., Wu, T.-R., Liu, P. L.-F., Oumeraci, H., 2006. A 3D numerical model for computing non-breaking wave forces on slender piles. MIT, USA, Journal of Engineering Mathematics, in Review.
189. White, F.M., 1991. Viscous Fluid Flow. 2nd edition, McGraw Hill, Inc., ISBN: 0-07-069712-4
190. Wilcox, D.C., 1998. Turbulence Modeling for CFD. DCW Industries, Inc., La Cañada, USA.
191. Wu, T.-R., 2004. A numerical study of three-dimensional breaking waves and turbulence effects. PhD thesis, Cornell University, Ithaca, USA.
192. Wüthrich, D., Pfister, M. and Schleiss, A.J., 2019. Effect of bed roughness on tsunami-like waves and induced loads on buildings. Coast. Eng., 152, 103508.
193. Yang, X., Liu, M., Peng, S. and Huang, C., 2016. Numerical modeling of dam-break flow impacting on flexible structures using an improved SPH-EBG method. Coast. Eng., 108, 56-64.
194. Yeh, H., 1991. Tsunami Bore Runup. Nat. Hazards, 4, 209-220.
195. Yeh, H., 2006. Tsunami loading. International workshop on fundamentals of coastal effects of tsunamis, Hilo, Hawaii.
196. Yeh, H., 2014. E-Mail conversation.
197. Yeh, T.T., Robertson, B. and Mattar, W.M., 1983. LDV measurements near a vortex shedding strut mounted in a pipe. J. Fluids Eng., 105, 185-196.
198. Yen, S.C. and Liu, J.H., 2011. Wake flow behind two side-by-side square cylinders. Int. J. Heat Fluid Flow, 32(1), 41-51.
199. Yoon, S.B. and Liu, P.L.-F., 1989. Interactions of currents and weakly nonlinear water waves in shallow water. J. Fluid Mech., 205, 397-419.
200. Younis, M.Y., Alam, M.M. and Zhou, Y., 2016. Flow around two non-parallel tandem cylinders. Phys. Fluids, 28, 125106.
201. Zdavkovich, M.M., 1977. Review of flow interference effects between two circular cylinders in various arrangements, Journal of Fluids Engineering, ASME, 99, 618-633.
202. Zelt, J.A., 1991. The run-up of nonbreaking and breaking solitary waves. Coast. Eng., 15, 205-246.
203. Zelt, J.A. and Raichlen, F., 1991. Overland Flow from Solitary Waves. J. Waterw. Port Coastal Ocean Eng., 117 (3), 247-263.

Appendix A Model Validation

This appendix provides details on the three-dimensional numerical model. The validations cover all physical aspects which the model is supposed to replicate satisfactorily, particularly the propagation of waves and tsunami-like bores and their interaction with single and groups of obstacles. Additional assumptions and model adaptations were necessary to efficiently apply the model to the extensive test programme. For example, modifications to the element size in the boundary layer of the obstacles and the use of special boundary conditions. The validity of these adaptations is shown in additional tests.

First, the quality indices are described, which are used to evaluate the performance of numerical models. The following sections describe the model validation in fife phases. The first three phases deal with wave conditions. The propagation of the solitary wave over a submerged reef is depicted, followed by 5th order Stokes waves at a single cylinder and two cylinders in tandem arrangement. Then, the propagation of a bore over an initially dry bottom is investigated, followed by the interaction of a bore with a single cylinder. The validity of the use of the symmetry boundary condition is shown. Furthermore, the impact of increasing the cell size in the boundary layer of the obstacles on the flux is presented. Finally, the uniformity of the undisturbed bore over several distances is shown.

A.1 Definition of statistical descriptors and quality indices

To the author's knowledge, there are no defined standards available for model validation in the field of wave structure interaction. Therefore, this section is based on criteria which are commonly applied for numerical model validation for offshore applications. This section has been modified from metocean reports produced by DHI.

To obtain an objective and quantitative measure of how well the numerical data compare to the laboratory data a number of statistical indicators or quality indices (QIs) are calculated. Prior to the comparisons the numerical data are synchronized to the time step of the laboratory data so that both time series have equal length and overlapping time stamps. For each valid laboratory data point, measured at time t, the corresponding numerical value is identified using linear interpolation between the model time steps before and after time t. The comparisons of the synchronized laboratory and numerical data are illustrated in figures describing:

- Time series plot incl. statistics
- Scatter plot incl. sorted data and QIs

The QIs are described below and their definitions are listed in Table A.1.

Most of the QIs are based on all data points and should hence be considered as averaged measures for the entire data set.

The mean value of a dataset $MEAN$ is the averaged value. The standard deviation $STDEV$ is the averaged deviation of all values from the mean value and is a measure for the data range.

The relative standard deviation RSD relates the data range to the mean value: Small values show a relatively small range, while large values indicate a relatively large range.

The $BIAS$ is the mean difference between the numerical and laboratory data and AME is the mean of the absolute difference. The root-mean-square error $RMSE$ is the root mean square of the difference. They are dimensional measures for the similarity of two time series and have to be interpreted in relation to the quantities of the time series. The smaller the values the higher the similarity of two time series.

The scatter index SI is a non-dimensional measure of the difference calculated as the unbiased $RMSE$ relative to the mean value of the observations. In open water, an SI below 0.2 is usually considered a small difference (excellent agreement). In confined areas where wave heights are generally lower, a slightly higher SI may be acceptable.

The correlation coefficient CC is a non-dimensional measure reflecting the degree to which the variation of the first variable is reflected in the variation of the second variable. A value close to 0 indicates very limited or no correlation between the two data sets, while a value close to 1 indicates a very high or perfect correlation. Typically, a CC above 0.9 is considered as a high correlation (good agreement).

The peak ratio PR is the average of the N_{peak} highest calculated values divided by the average of the N_{peak} highest measured values. $PR < 1$ means a general underestimation of the calculated peak events and $PR > 1$ an overestimation.

The regression line slope and intercept $REGS$ and $REGI$, respectively, are found from a linear fit to the data points in a least square sense (Q-Q fit). A regression line slope different from 1 may indicate a trend in the difference.

The covariance cov is a measure for the joint variability of two datasets. If the sign is positive, then both datasets show the same trend of increasing or decreasing. The smaller the value is, the higher is the agreement of both datasets. It can be interpreted as CC without normalization and shows therefore the absolute mean deviation.

Table A.1. Definition of quality indices (LAB = laboratory, NUM = numerical model).

Abbreviation	Description	Definitions
N	Number of validation observations	–
$MEAN$	Mean of model data	$MEAN(NUM) = \overline{NUM} = \frac{1}{\mathrm{N}}\sum_{\mathrm{i=1}}^{\mathrm{N}} \mathrm{NUM_i}$
$STDEV$	Standard deviation	$STDEV(NUM) = \sqrt{\frac{\sum_{\mathrm{i=1}}^{\mathrm{N}}(\mathrm{NUM_i} - \overline{NUM})^2}{N}}$
RSD	Relative standard deviation	$RSD(NUM) = \left\lvert\frac{STDEV(NUM)}{\overline{NUM}}\right\rvert \cdot 100\%$
$BIAS$	Mean of difference	$BIAS = \frac{1}{\mathrm{N}}\sum_{\mathrm{i=1}}^{\mathrm{N}}(\mathrm{NUM} - \mathrm{LAB})_\mathrm{i}$
AME	Mean of absolute difference	$AME = \frac{1}{\mathrm{N}}\sum_{\mathrm{i=1}}^{\mathrm{N}}(\lvert\mathrm{NUM} - \mathrm{LAB}\rvert)_\mathrm{i}$
$RMSE$	Root mean square of difference	$RMSE = \sqrt{\frac{1}{\mathrm{N}}\sum_{\mathrm{i=1}}^{\mathrm{N}}(\mathrm{NUM} - \mathrm{LAB})_\mathrm{i}^{\,2}}$
SI	Scatter index (unbiased)	$SI = \frac{\sqrt{\frac{1}{\mathrm{N}}\sum_{\mathrm{i=1}}^{\mathrm{N}}(\mathrm{NUM} - \mathrm{LAB} - \mathrm{BIAS})_\mathrm{i}^{\,2}}}{\mathrm{MEAN}}$
CC	Correlation coefficient	$CC = \frac{\sum_{\mathrm{i=1}}^{\mathrm{N}}(\mathrm{LAB_i} - \overline{LAB})(\mathrm{NUM_i} - \overline{\mathrm{NUM}})}{\sqrt{\sum_{\mathrm{i=1}}^{\mathrm{N}}(\mathrm{LAB_i} - \overline{LAB})^2 \sum_{\mathrm{i=1}}^{\mathrm{N}}(\mathrm{NUM_i} - \overline{\mathrm{NUM}})^2}}$
$PR(N_{peak})$	Peak ratio of N_{peak} events	$PR = \frac{\sum_{\mathrm{i=1}}^{\mathrm{N_{peak}}} \mathrm{NUM_i}}{\sum_{\mathrm{i=1}}^{\mathrm{N_{peak}}} \mathrm{LAB_i}}$
cov	Covariance	$cov = \frac{\sum_{i=1}^{N}(NUM_i - \overline{NUM})(LAB_i - \overline{LAB})}{N}$

A.2 Solitary wave over a submerged reef structure (phase i)

This section presents comparisons of a solitary wave propagating over a submerged reef by means of three-dimensional numerical model simulations and laboratory data from the wave flume at Leichtweiß-Institute at the Technical University of Braunschweig, described in Strusinska (2010). The numerical data is compared with the laboratory data in front of the structure (gauges 1 and 3), above the structure (gauges 7 and 8) and downstream of structure (gauges 16 and 19). The time series of these gauges are provided in Figure A.1. The scatter plots, including the statistical descriptors (see section A.1), are given in Figure A.2.

For the scatter plots and the statistical indicators, the numerical data is shifted so that the peaks of the numerical and the laboratory time series occur at the same time. The time shifts dt, the number of compared data points N, the peak ratio PR, the correlation coefficient CC and the scatter index SI are provided in Table A.2.

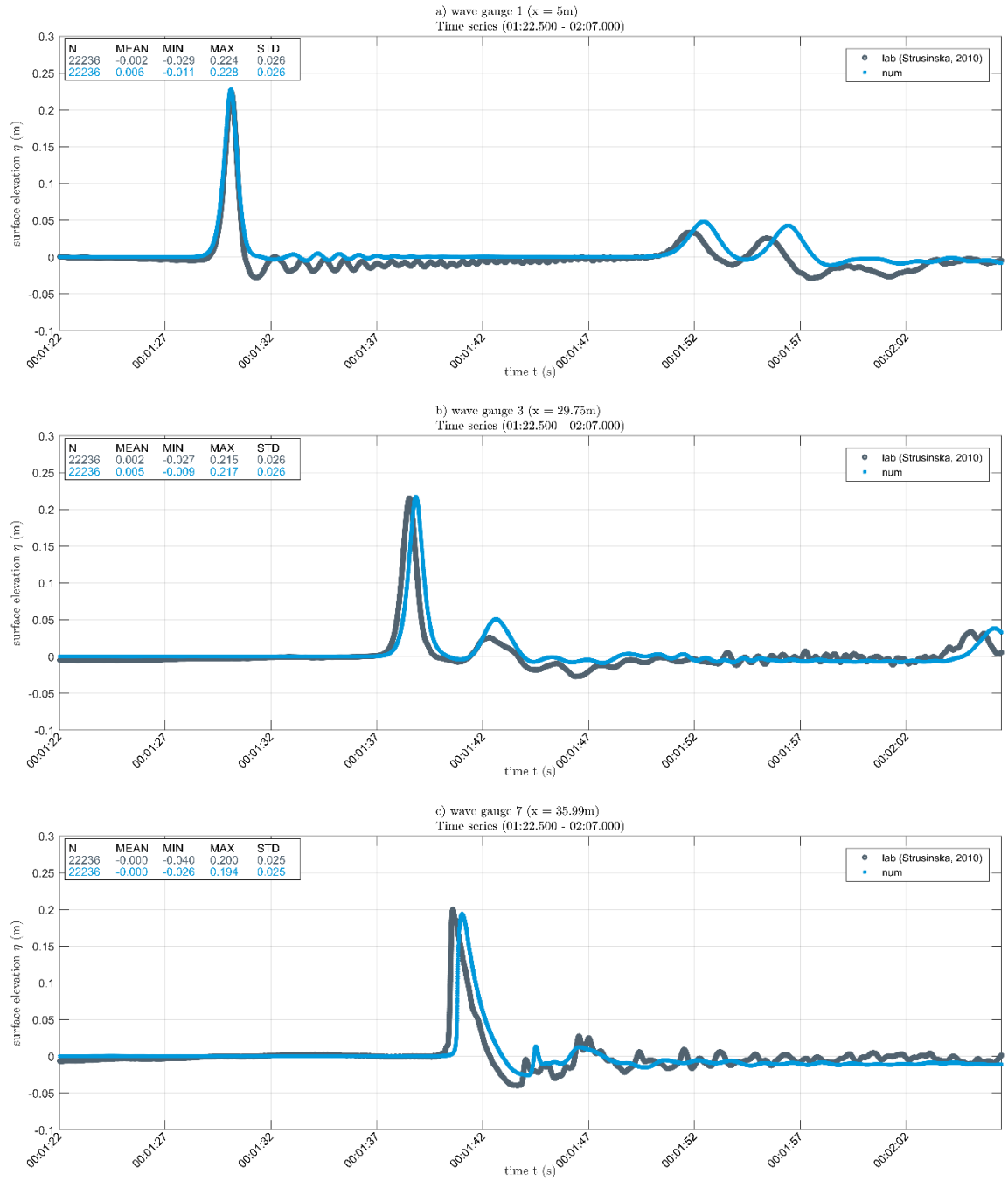

Figure A.1. Time series surface elevations of laboratory and numerical data. a) wave gauge 1, b) wave gauge 3, c) wave gauge 7, d) wave gauge 8, e) wave gauges 16, f) wave gauge 19.

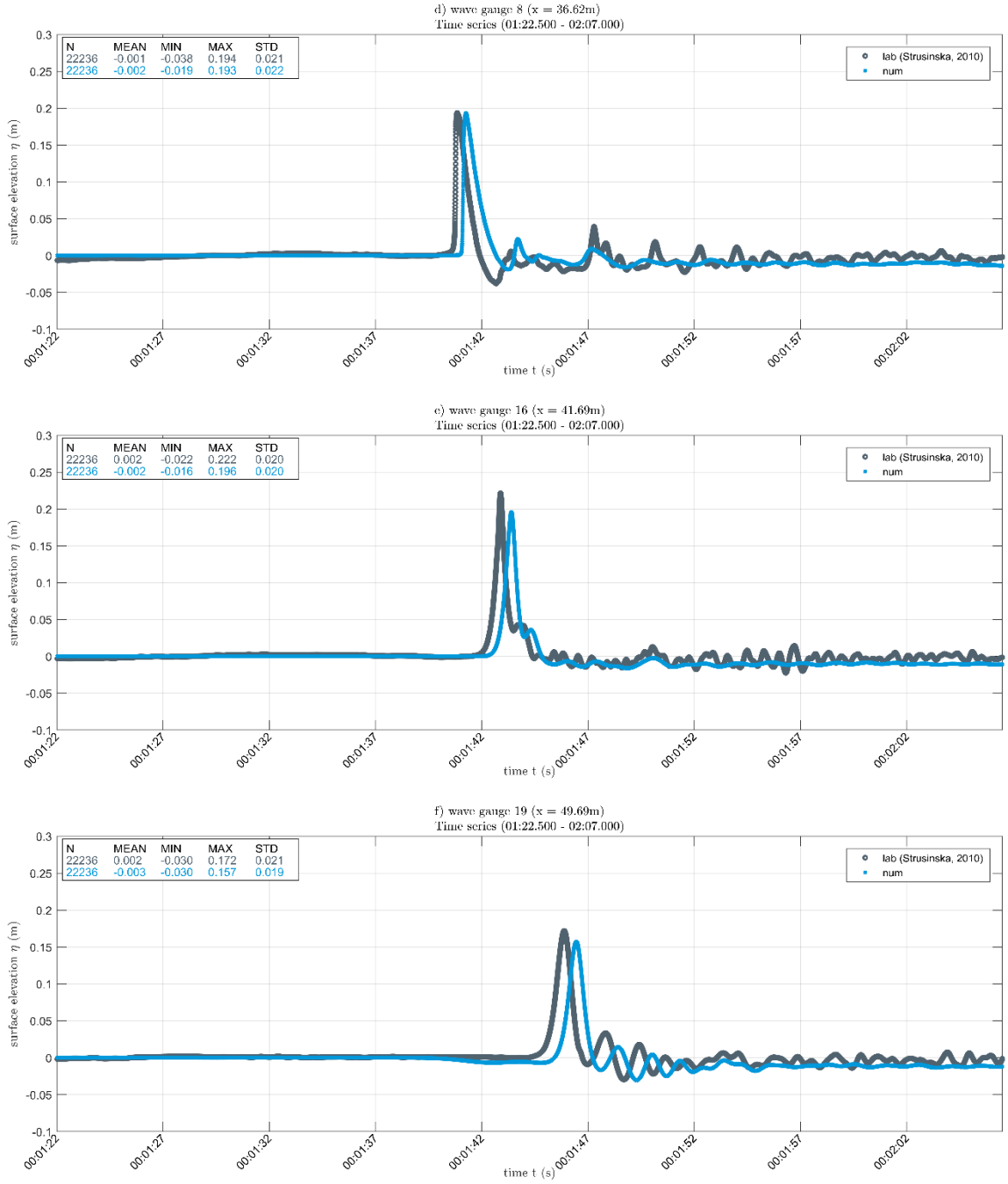

Figure A.1 (continued)

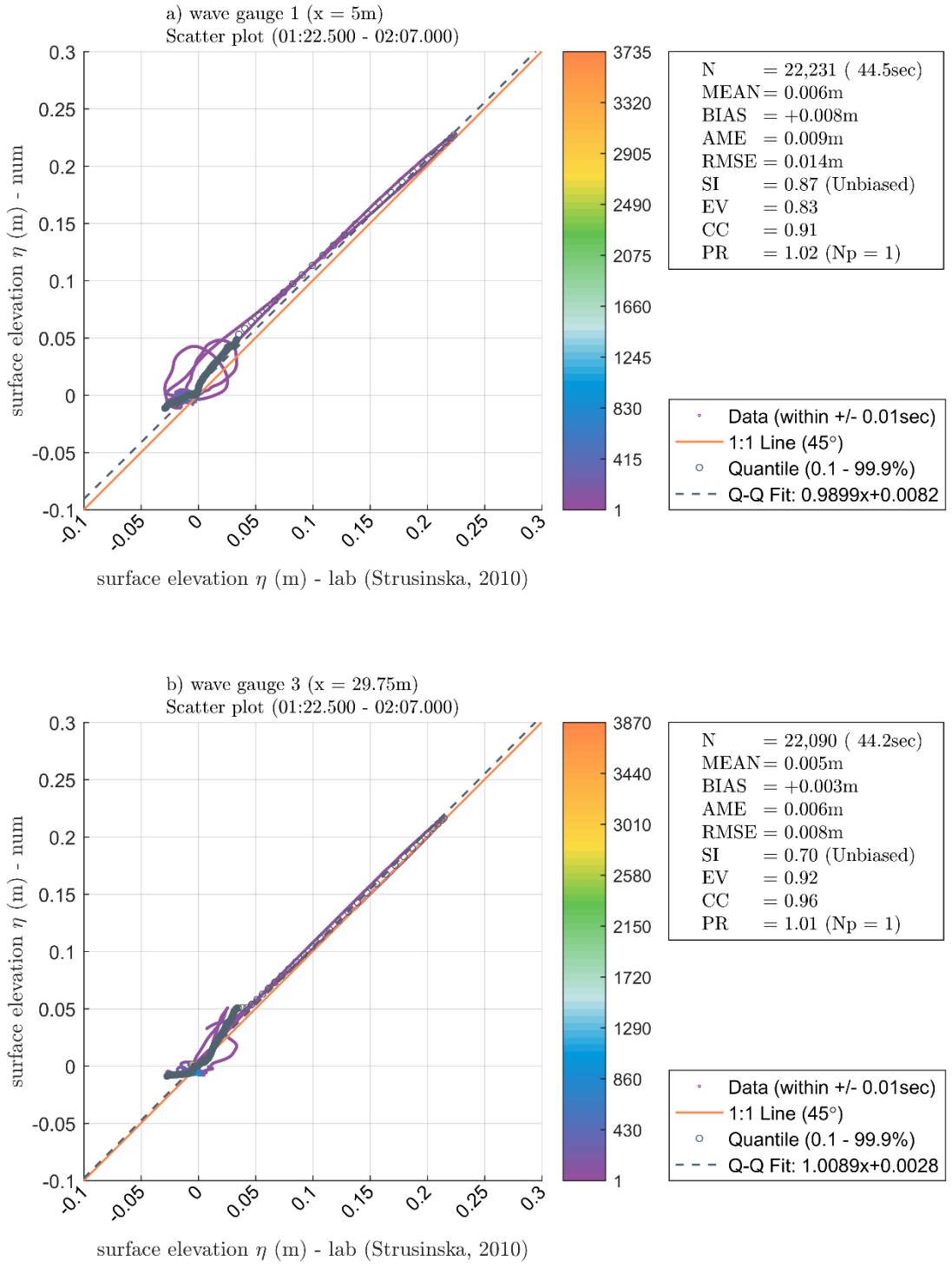

Figure A.2. Scatter plots of surface elevations of the numerical model over the laboratory data at a) wave gauge 1, b) wave gauge 3, c) wave gauge 7, d) wave gauge 8, e) wave gauge 16, f) wave gauge 19.

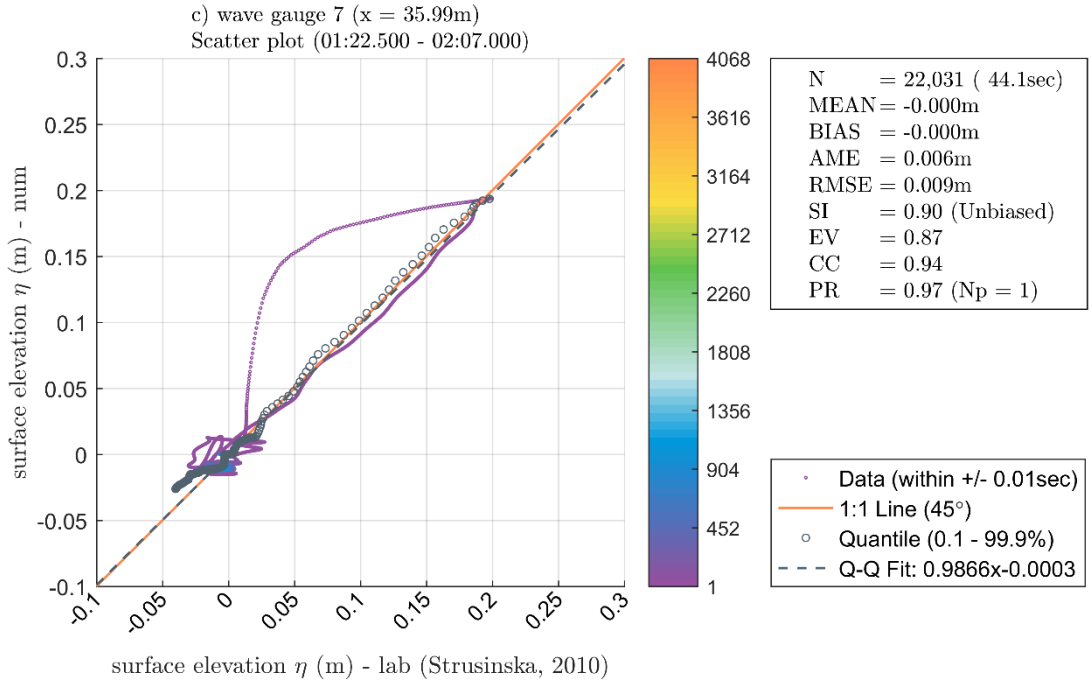

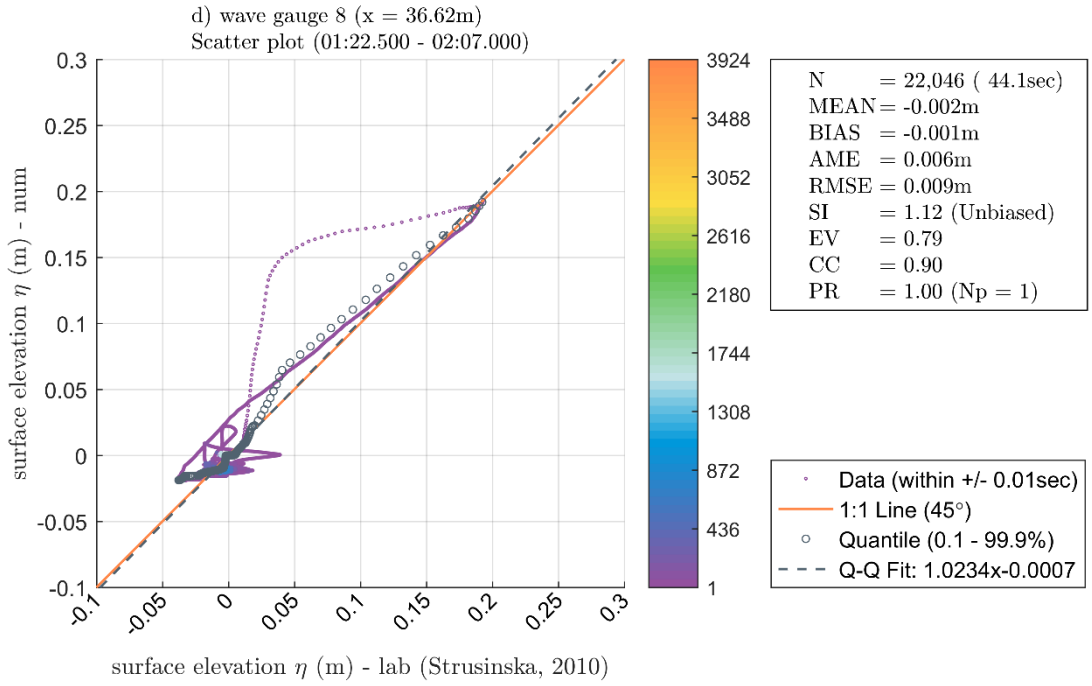

Figure A.2 (continued)

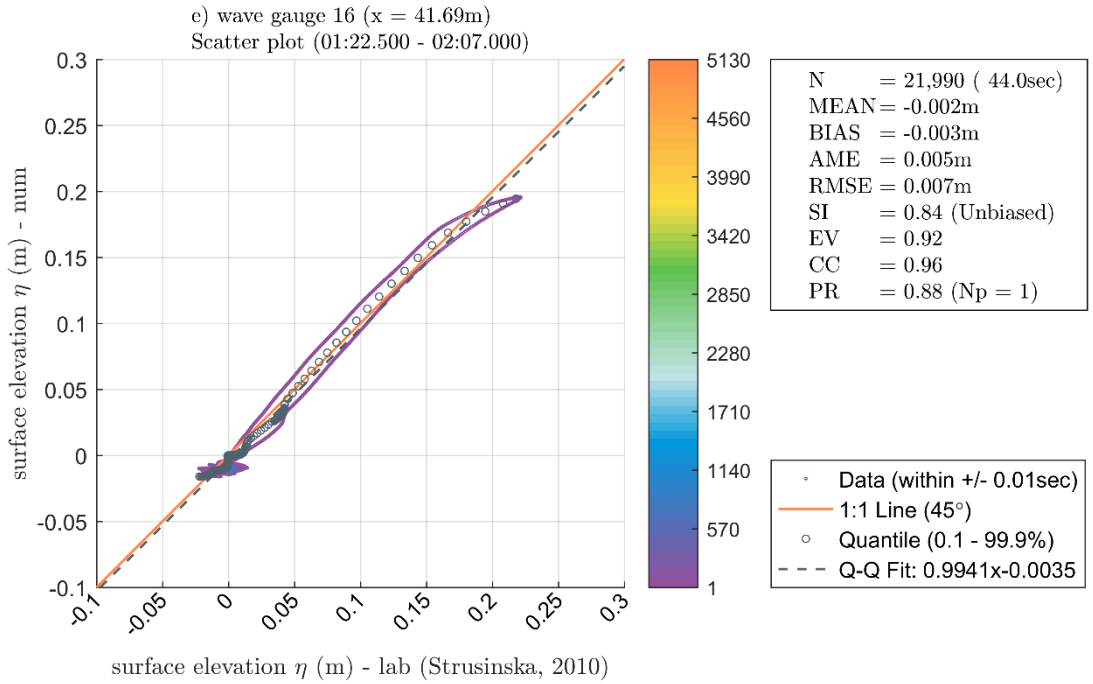

Figure A.2 (continued)

Table A.2 Time shift, number of data points, peak ratio, correlation coefficient and scatter index of laboratory and numerical data.

gauge	$t(num)$ [s]	$t(lab)$ [s]	$dt = \mathrm{t(num)} - \mathrm{t(lab)}$ [s]	N [-]	PR [-]	CC [-]	SI [-]
1	8.12	8.13	-0.01	22231	1.02	0.91	0.87
3	16.86	16.542	0.32	22090	1.01	0.96	0.7
7	19.04	18.596	0.44	22031	0.97	0.94	0.9
8	19.26	18.85	0.41	22046	1	0.9	1.12
16	21.41	20.888	0.52	21990	0.88	0.96	0.84
19	24.46	23.884	0.58	21960	0.92	0.97	0.72

A.3 Bore propagation over an initially dry bottom (phase ii)

The propagation of the tsunami-like bore over an initially dry bottom is compared against the empirical solution obtained by Ritter (1892). The bore is generated simulating a dam-break scenario with an initial impoundment. The flow depths in 8 m from the impoundment gate x are compared in Figure A.3. The figure shows the timeseries of the flow depth, the scatter plot and resulting quality indices (see section A.1). The statistical descriptors peak ratio PR, correlation coefficient CC and scatter index SI are given in Table A.3.

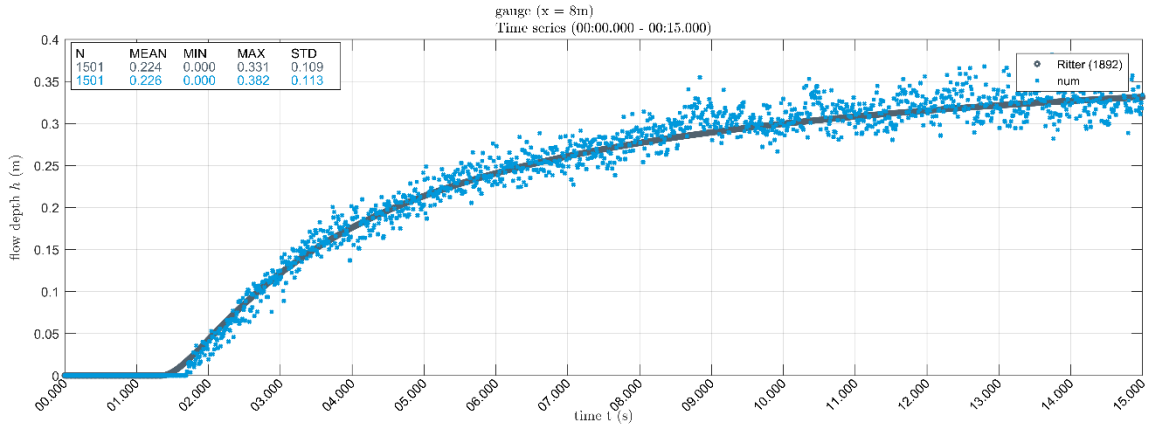

Figure A.3. Time series of flow depths of analytical (Ritter, 1892) and numerical data at x= 8 m distance from the impoundment.

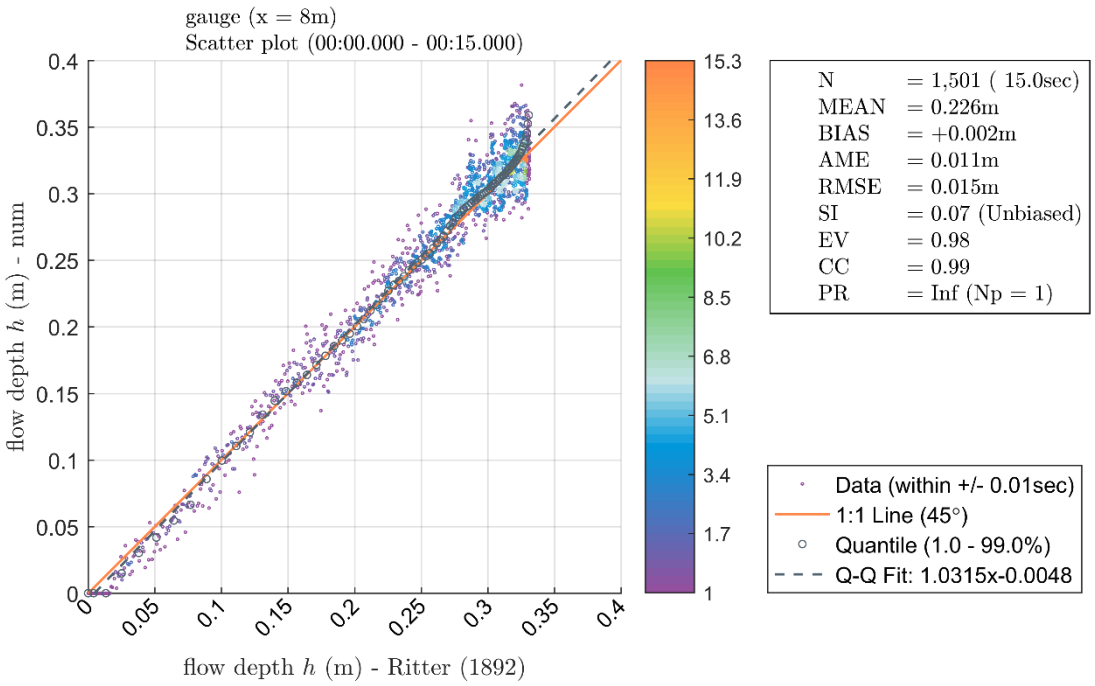

Figure A.4. Scatter plots of flow depths of analytical (Ritter, 1892) and numerical data at x = 8 m distance from the impoundment.

Table A.3. Differences in arrival times, peak ratios, correlation coefficient and scatter index of the comparison of analytical and calculated flow depth at x = 8 m.

gauge	x [m]	$t(num)$ [s]	$t(lab)$ [s]	$dt = \mathrm{t(num)} - \mathrm{t(lab)}$ [s]	PR [-]	CC [-]	SI [-]
1	8	1.67	1.35	0.32	Inf	0.99	0.07

A.4 5th order Stokes wave at a single cylinder (phase iii)

The propagation of 5th order Stokes waves through the large wave flume (GWK) of the FKI in Hanover, passing a single cylinder, is illustrated in this section. Laboratory data (see Bonakdar,

2014; case 23060401) is compared with the results of the three-dimensional numerical model. First, wave gauge data is compared, followed by a comparison of currents and the overturning moment. Each figure shows the timeseries of the surface elevation at the wave gauge, the scatter plot and resulting quality indices (see section A.1) and a frequency of occurrence diagram of several surface elevations.

A.4.1 Wave gauges

Surface elevation data obtained from laboratory and numerical wave gauges are shown inFigure A.5, comprising of the time series at the wave gauges WG 1 and 7 upstream of the cylinder, WG 9 at the same longitudinal coordinate x as the cylinder and at WG 13, located downstream of the cylinder. The corresponding scatter plots are given in Figure A.6. The statistical descriptors peak ratio PR, correlation coefficient CC and scatter index SI are summarized in Table A.3.

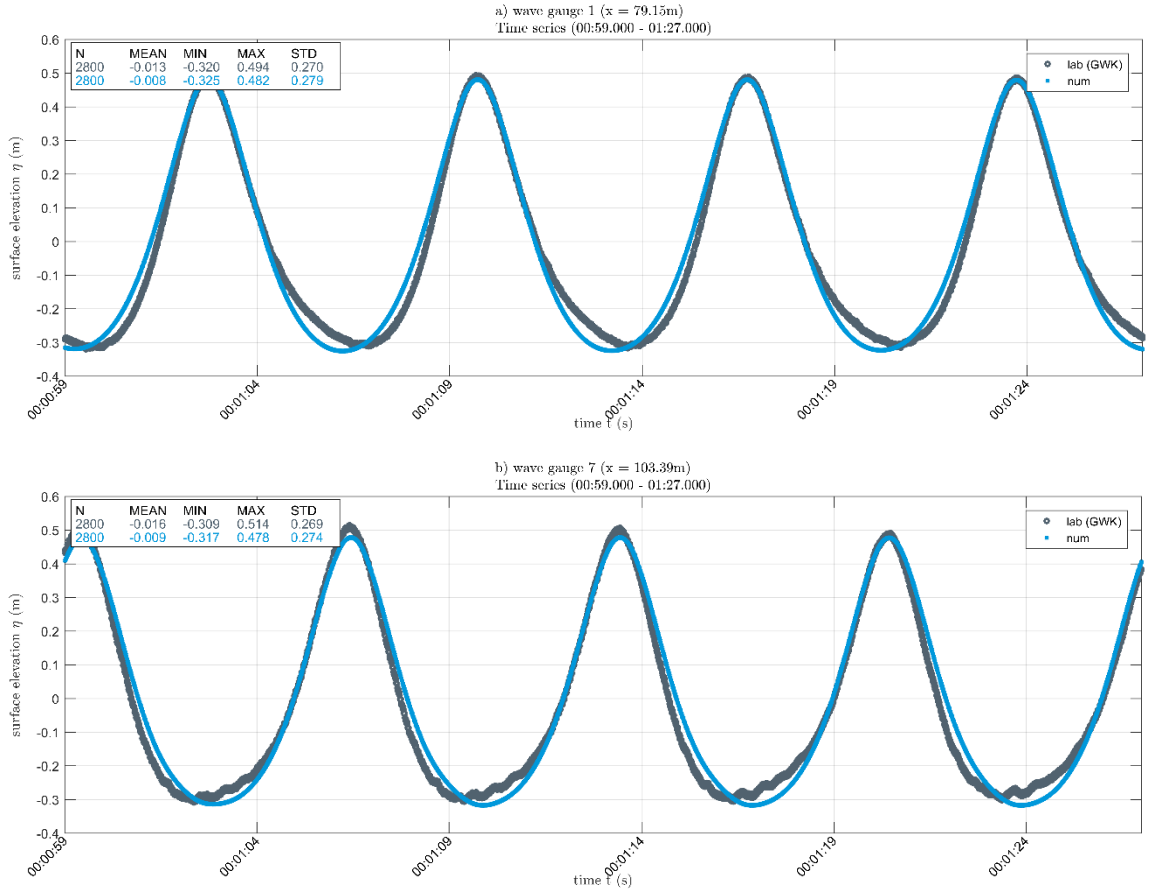

Figure A.5. Comparison of measured and simulated time series of surface elevations at a) wave gauge WG 1, b) WG 7, c) WG 9 and d) WG 13.

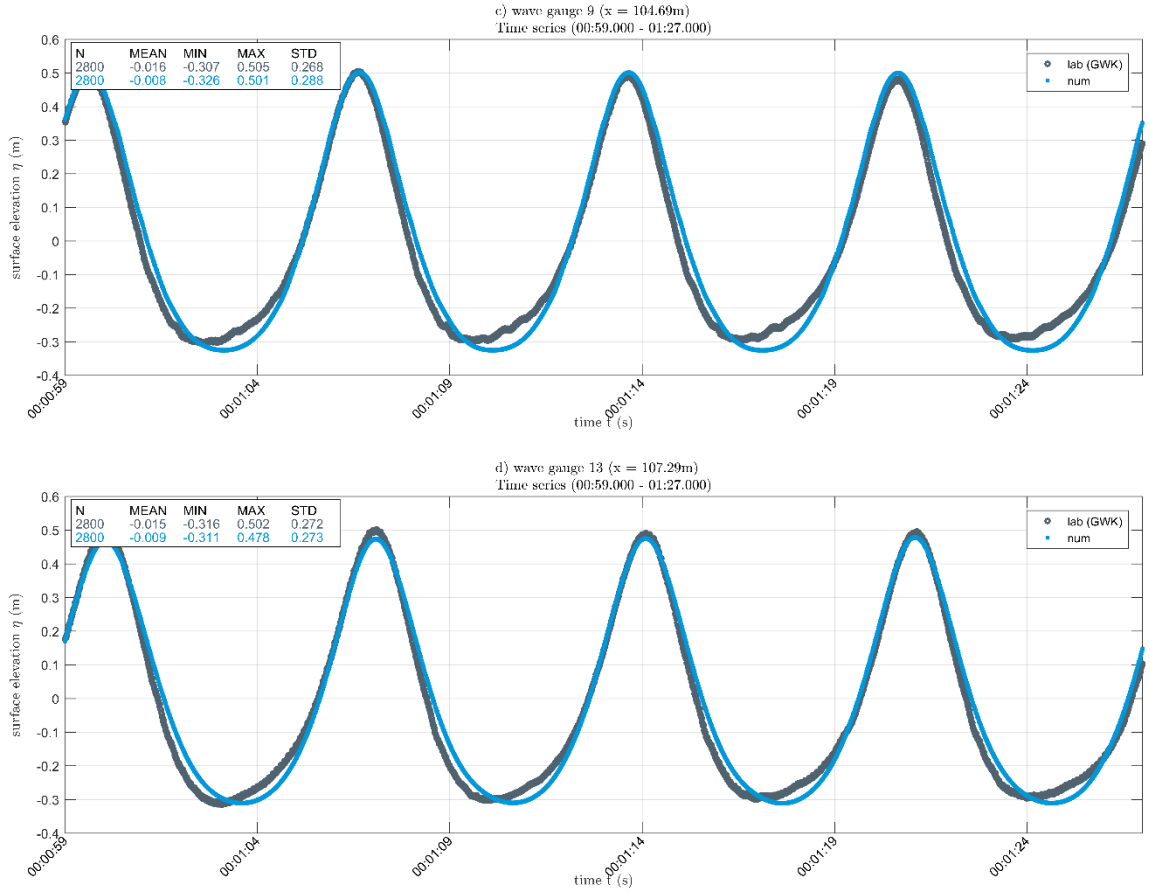

Figure A.5. (continued)

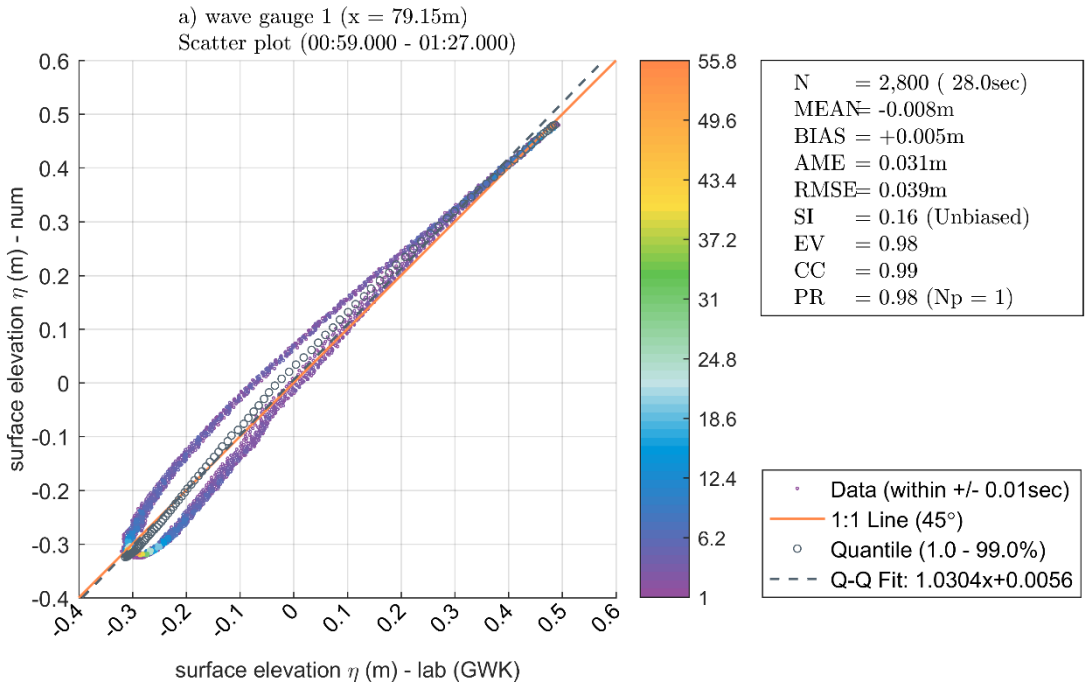

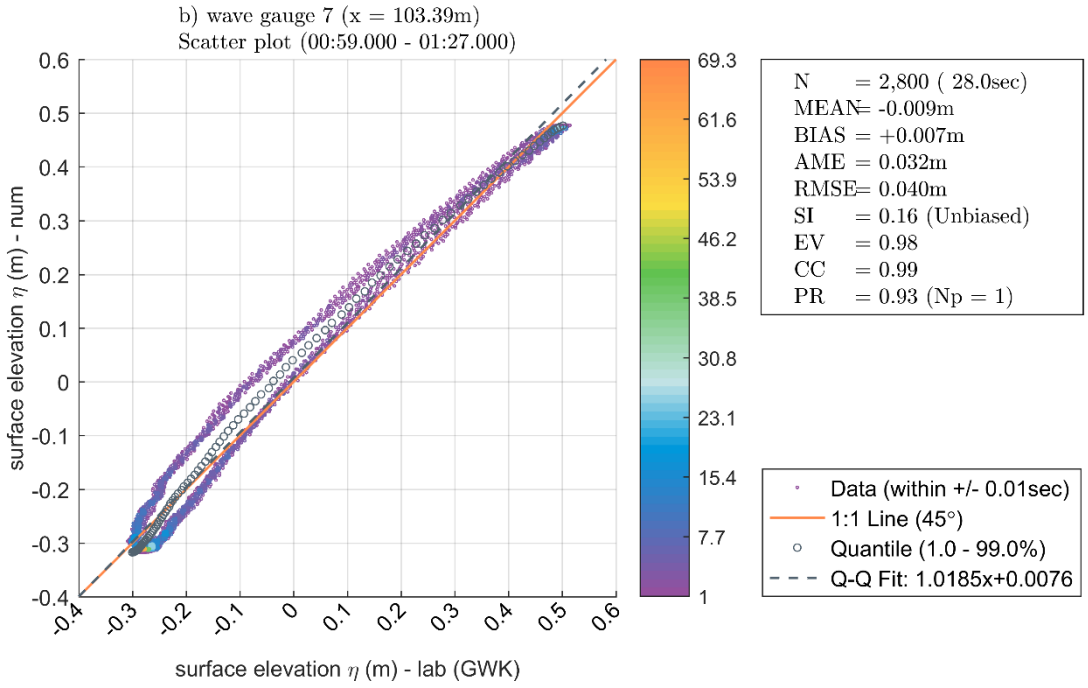

Figure A.6. Scatter plots of flow depths of measured and simulated time series of surface elevations at a) wave gauge WG 1, b) WG 7, c) WG 9 and d) WG 13.

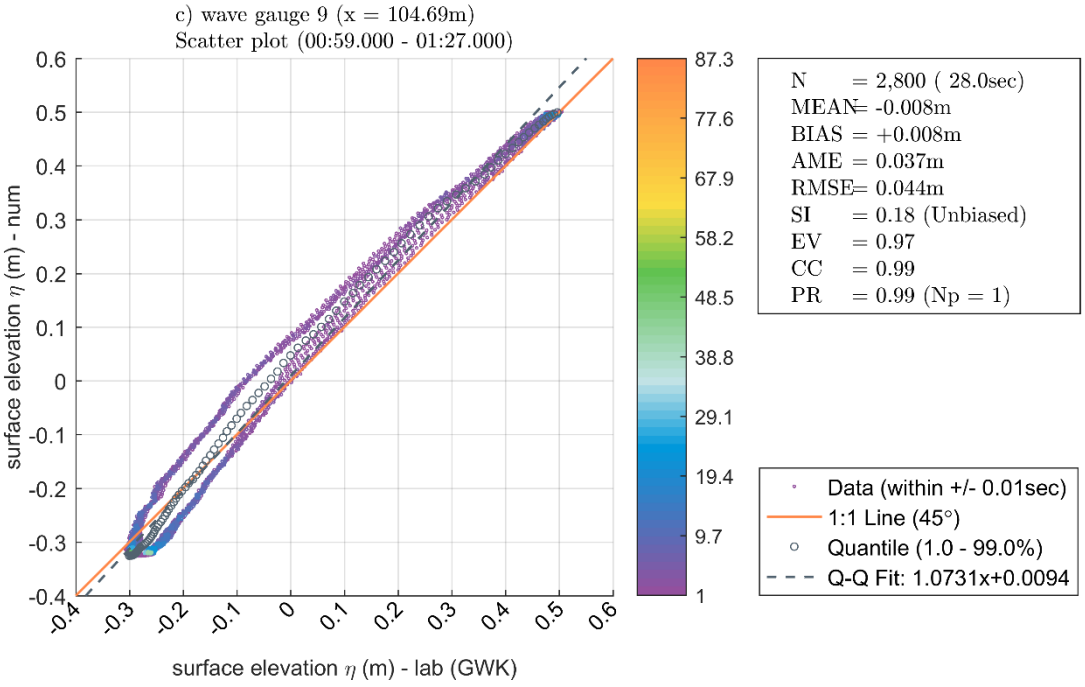

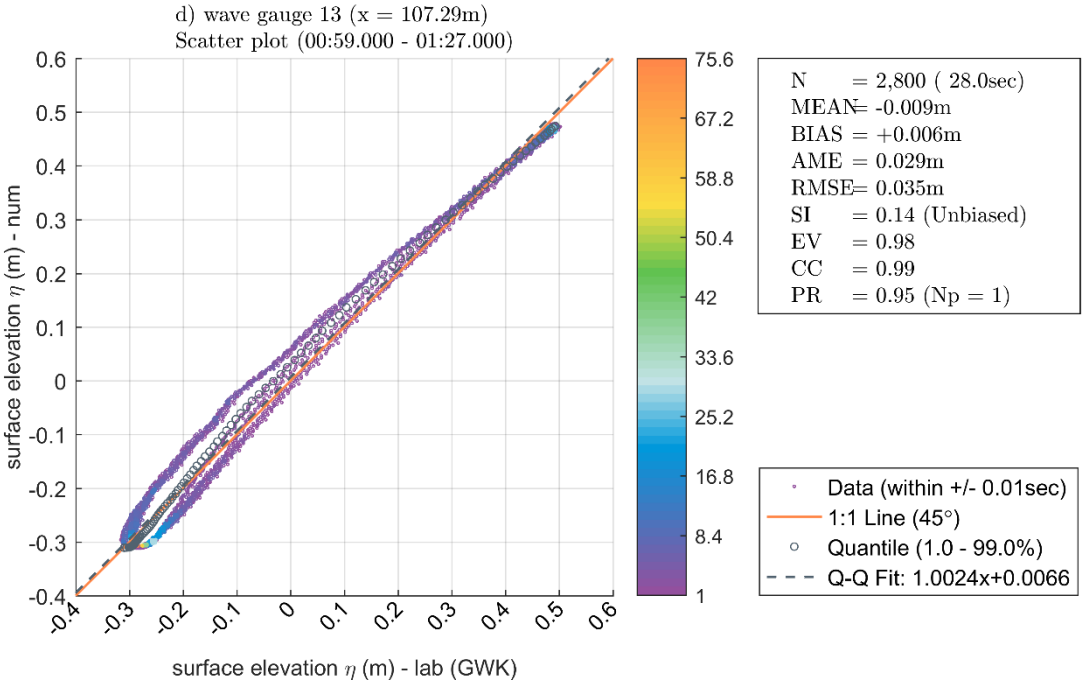

Figure A.6 (continued)

Table A.4. Peak ratios, correlation coefficient and scatter index of the comparison of measured and calculated surface elevations at the wave gauges WG 1, WG 7, WG 9 and WG 13.

gauge	x [m]	N [-]	PR [-]	CC [-]	SI [-]
1	79.15	2800	0.98	0.99	0.16
7	103.39	2800	0.93	0.99	0.16
9	104.69	2800	0.99	0.99	0.18
13	107.29	2800	0.95	0.99	0.14

A.4.2 Current meters

Current velocity data obtained from two laboratory and numerical current meters (CM) beside the cylinder are presented. The time series are shown in Figure A.7 and the scatter plots are given in Figure A.8. The statistical descriptors peak ratio PR, correlation coefficient CC and scatter index SI are provided in Table A.5.

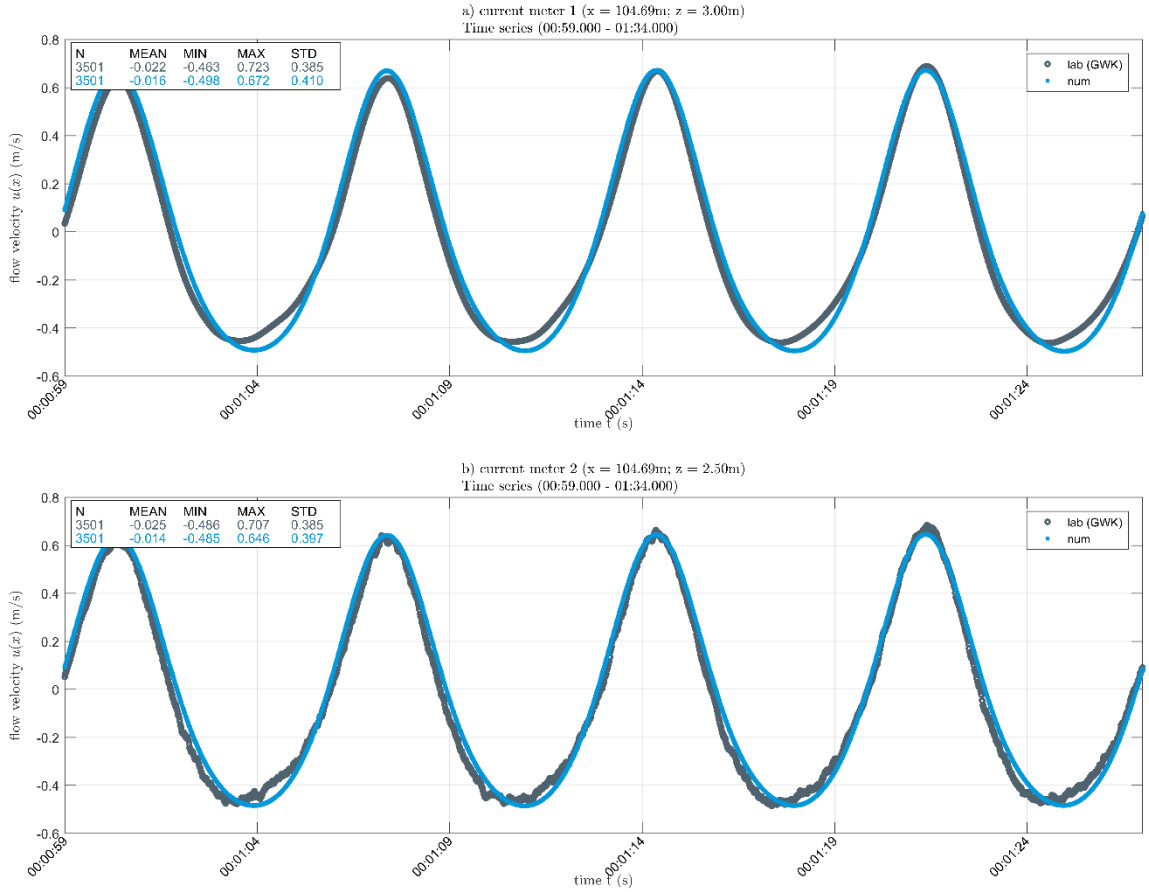

Figure A.7. Comparison of measured and simulated time series of flow velocities at a) current meter CM 1 and b) CM 2.

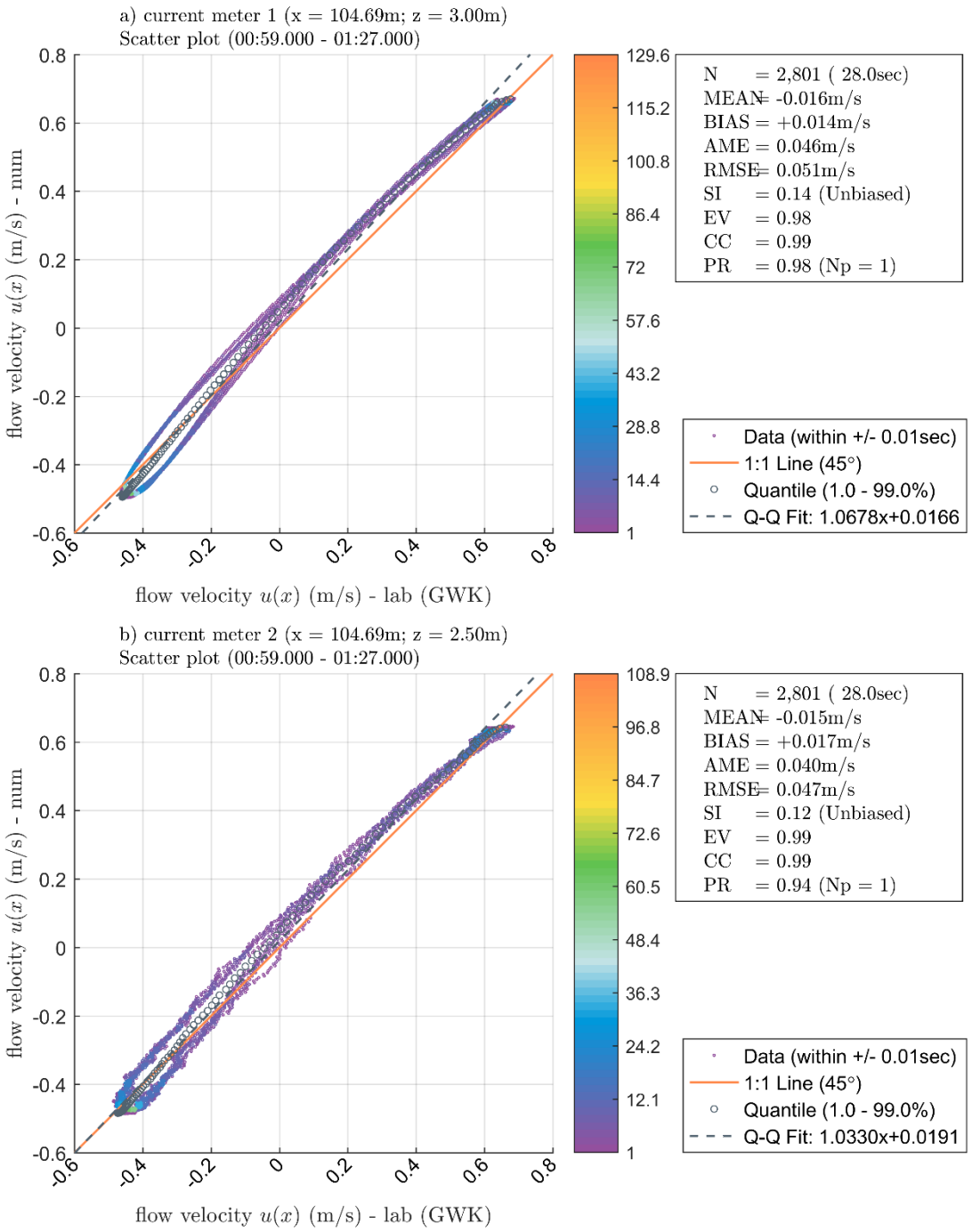

Figure A.8. Scatter plots of the comparison of measured and calculated current speeds at a) current meter CM 1 and b) CM 2.

Table A.5. Peak ratios, correlation coefficient and scatter index of the comparison of measured and calculated current speeds at the current meters CM 1 and CM 2.

Current meter	x [m]	z [m]	N [-]	PR [-]	CC [-]	SI [-]
1	104.69	2.5	2801	0.98	0.99	0.14
2	104.69	3.0	2801	0.94	0.99	0.12

A.4.3 Strain gauge

The overturning moments around the top suspension of the cylinder obtained from laboratory and numerical strain gauges are compared in this section. Figure A.9 provides the time series and Figure A.10. The statistical descriptors peak ratio PR, correlation coefficient CC and scatter index SI are provided in Table A.6.

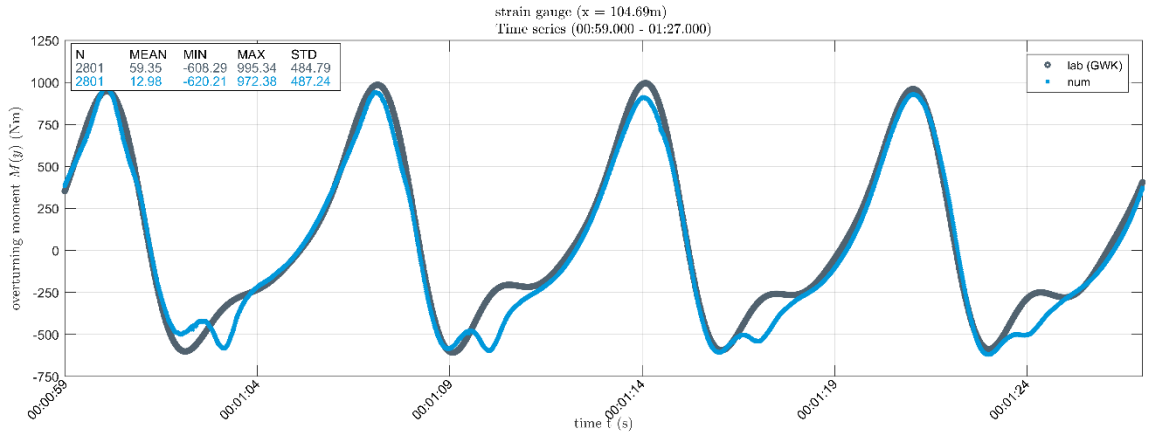

Figure A.9. Comparison of measured and simulated time series of overturning moments.

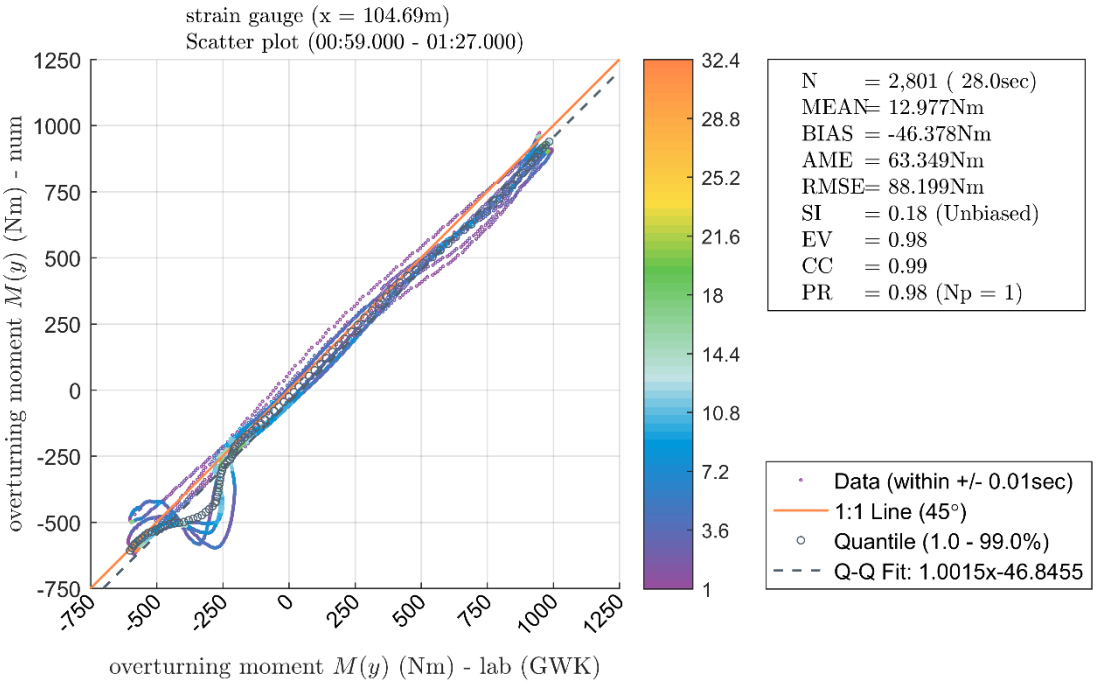

Figure A.10. Scatter plot of the comparison of measured and calculated overturning moments in the strain gauge.

Table A.6. Peak ratios, correlation coefficient and scatter index of the comparison of measured and calculated overturning moments at the strain gauge.

Strain gauge	x [m]	N [-]	PR [-]	CC [-]	SI [-]
1	104.69	2801	0.98	0.99	0.18

A.5 Bore at a single cylinder (phase iv)

This section shows a comparison of current velocities obtained from laboratory and numerical current meters (CM); and of forces obtained from a load cell included in both experimental methods. Laboratory data originates from experiments in the Charles W. Harris Laboratory (CHL) of the University of Washington, described in Árnason (2004). Each figure shows the timeseries of the surface elevation at the wave gauge, the scatter plot and resulting quality indices (see section A.1) and a frequency of occurrence diagram of several surface elevations.

A.5.1 Current meters

The comparison of both, laboratory and numerical current speeds are given in this section. The time series and scatter plots are presented in Figure A.11 and Figure A.12, respectively. The statistical descriptors are summarized in Table A.7.

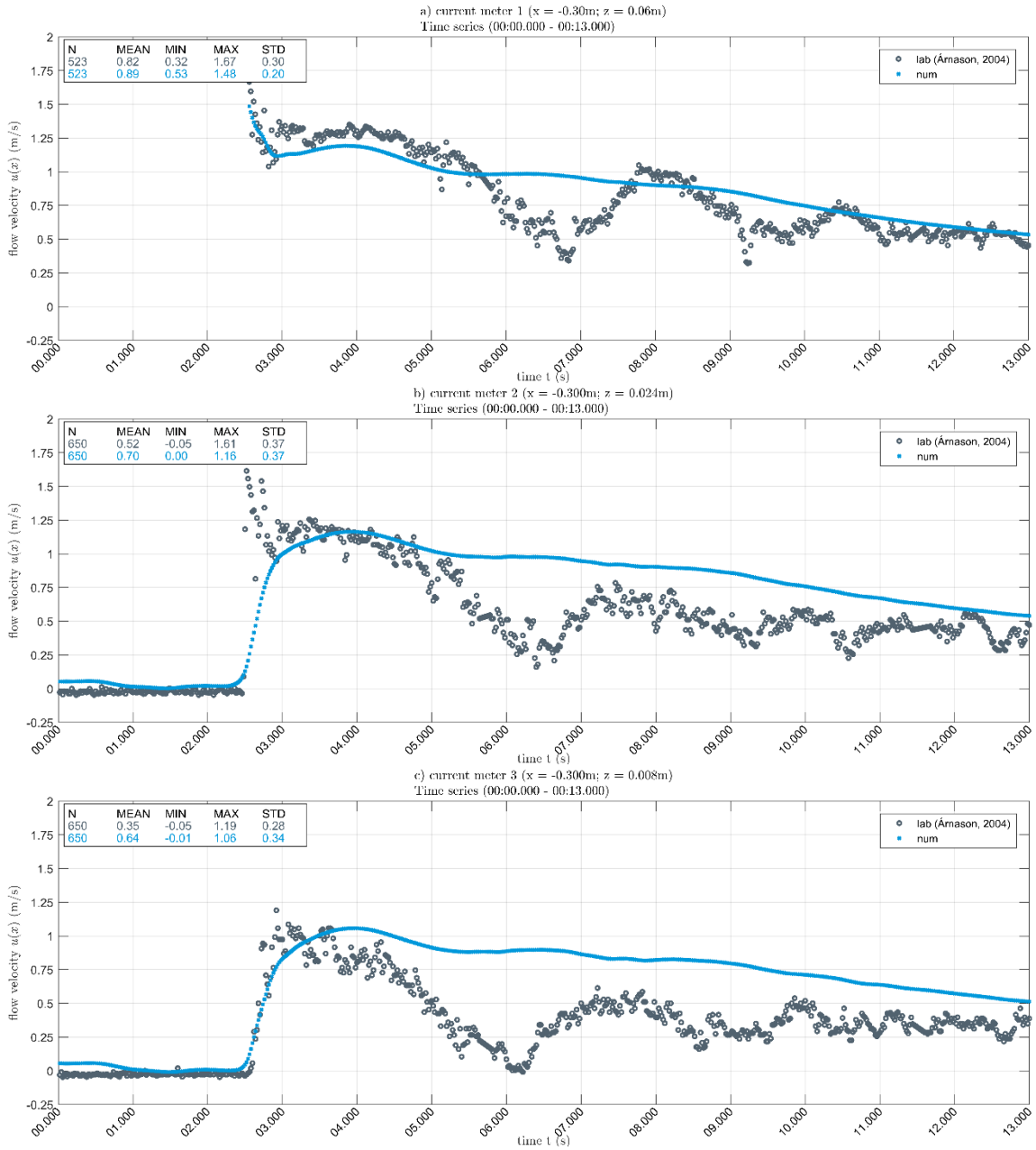

Figure A.11. Comparison of measured and simulated time series of flow velocities at a) current meter CM 1, b) CM 2 and c) CM 3.

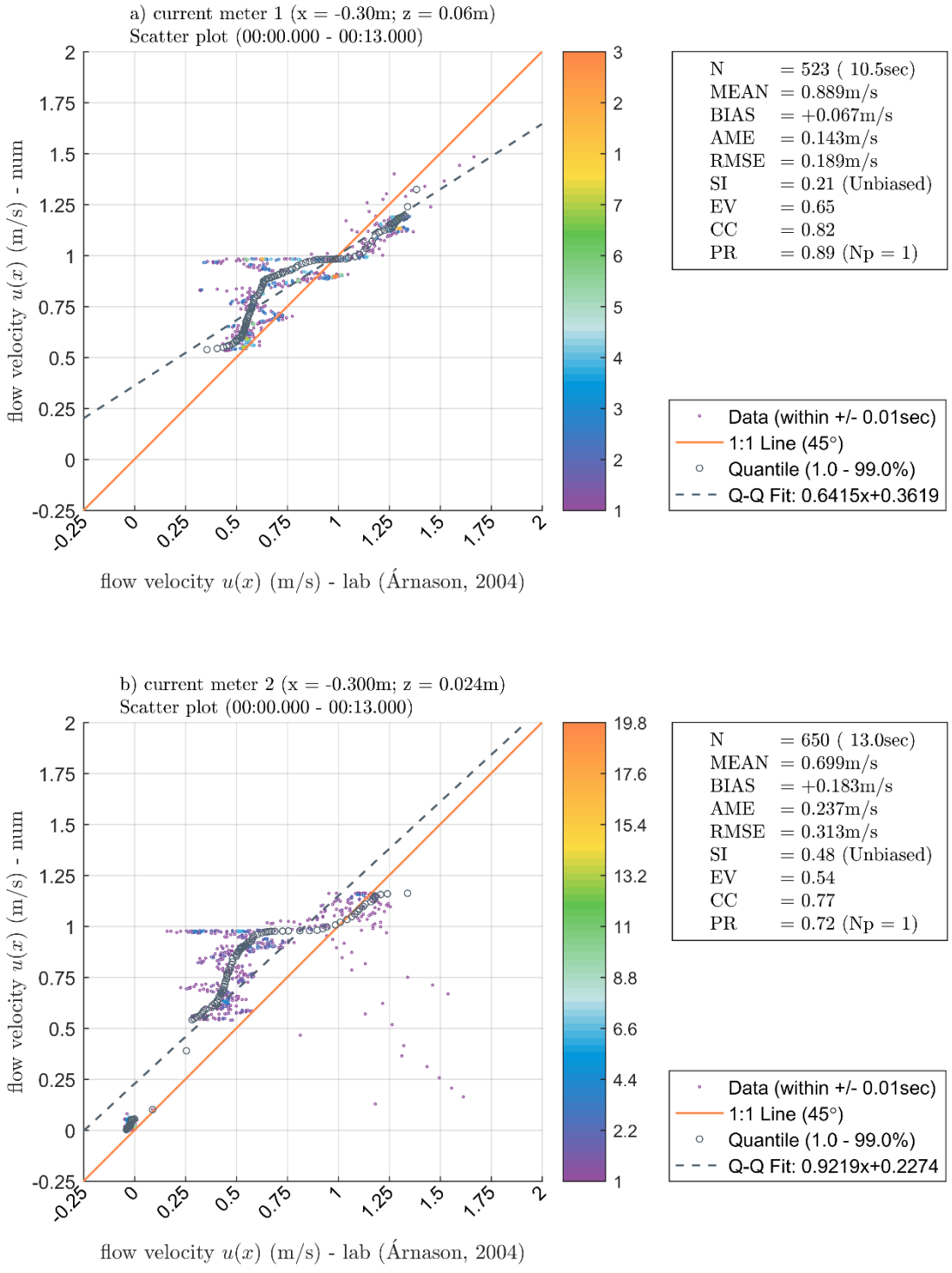

Figure A.12. Scatter plots of the comparison of measured and calculated flow velocities in current meters a) CM 1, b) CM 2 and c) CM 3.

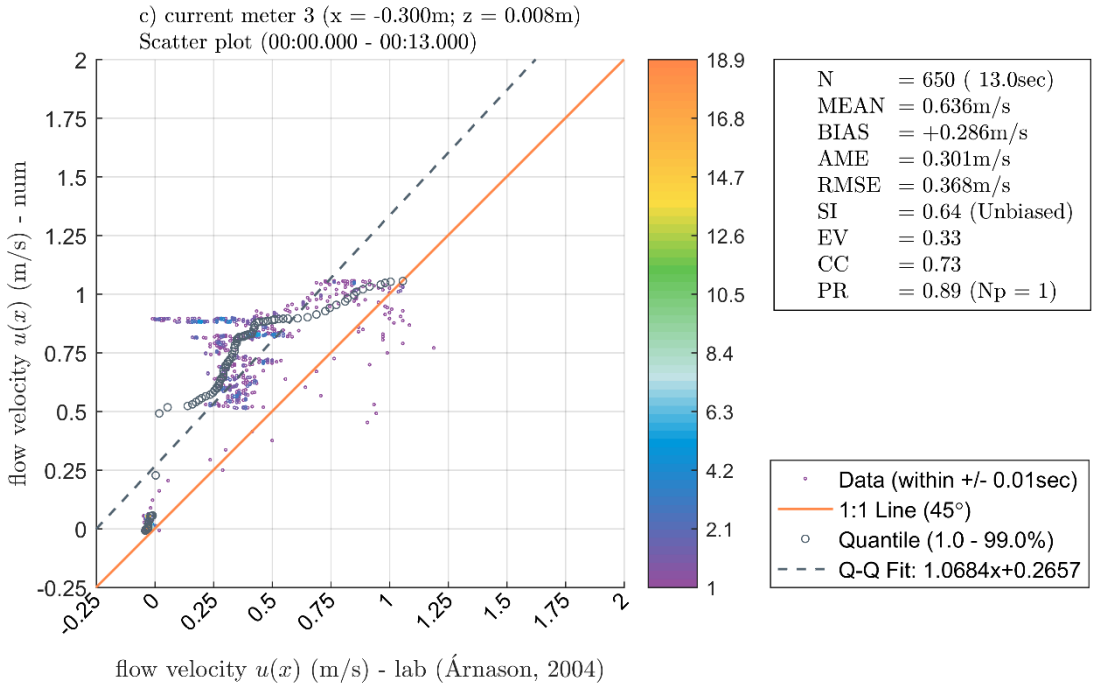

Figure A.12. (continued)

Table A.7. Peak ratios, correlation coefficient and scatter index of the comparison of measured and calculated overturning moments at the strain gauge.

Current meter	x [m]	z [m]	N [-]	PR [-]	CC [-]	SI [-]
1	-0.3	0.06	523	0.89	0.82	0.21
2	-0.3	0.024	650	0.72	0.77	0.48
3	-0.3	0.008	650	0.89	0.73	0.64

A.5.2 Load cell

The comparison of both, laboratory and numerical inline forces are given in this section. The time series are shown in Figure A.13.

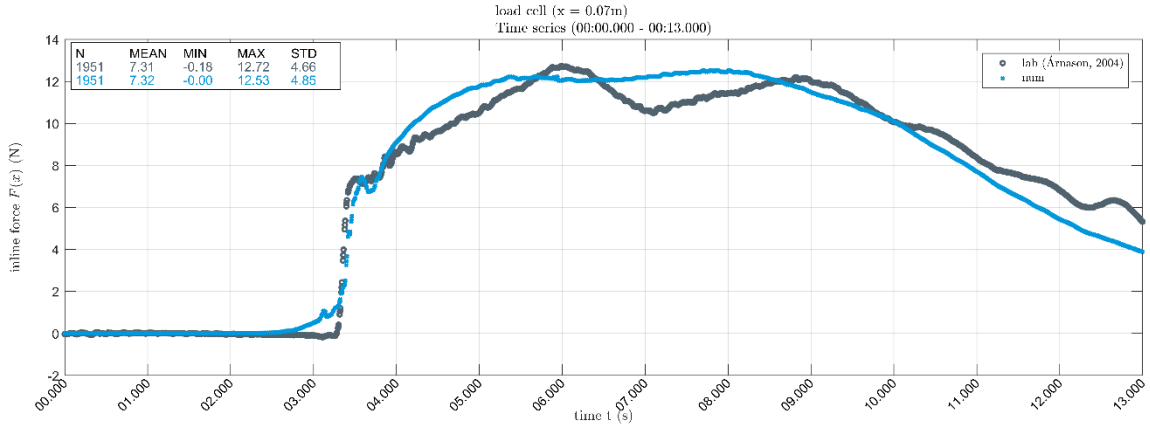

Figure A.13. Comparison of measured and simulated time series of forces.

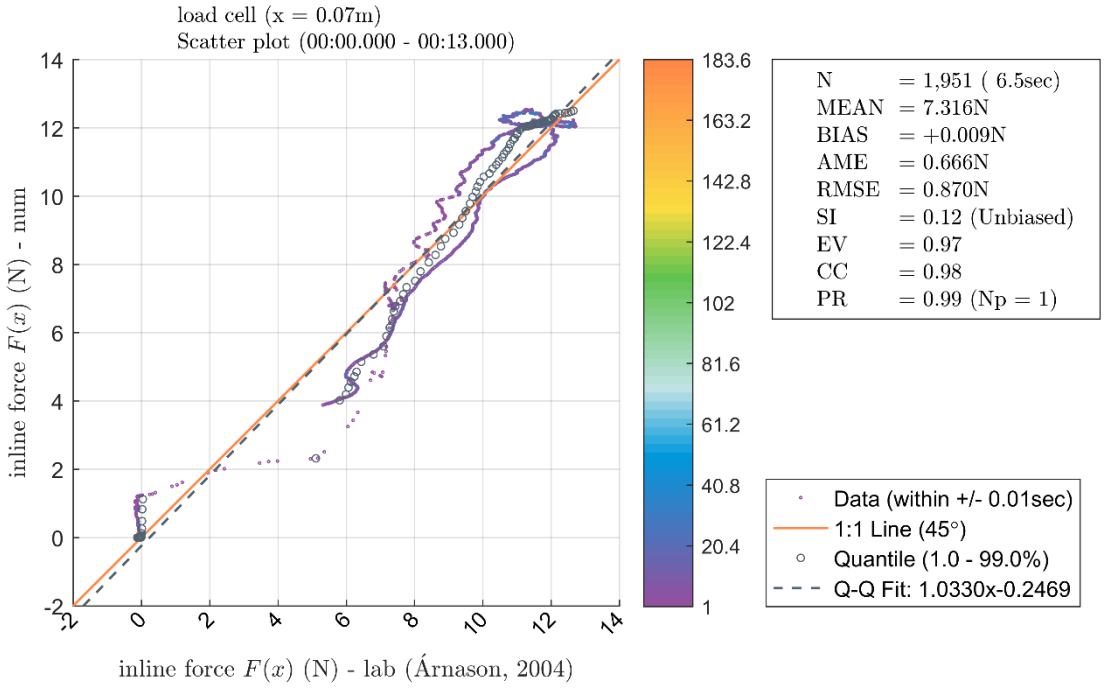

Figure A.14. Scatter plot of the comparison of measured and calculated inline forces in the load cell.

Table A.8. Peak ratios, correlation coefficient and scatter index of the comparison of measured and calculated overturning moments at the strain gauge.

Load cell	x [m]	N [-]	PR [-]	CC [-]	SI [-]
1	0.07	1951	0.99	0.98	0.12

A.6 5th order Stokes wave at two cylinders in tandem arrangement (phase v)

The propagation of 5th order Stokes waves through the large wave flume (GWK) of the FKI in Hanover, passing two cylinders in tandem configuration, is illustrated in this section. Laboratory data (see Bonakdar, 2014; case 28060404) is compared with the results of the three-dimensional numerical model. First, wave gauge data is compared, followed by a comparison of currents and the overturning moment. Each figure shows the timeseries of the surface elevation at the wave gauge, the scatter plot and resulting quality indices (see section A.1) and a frequency of occurrence diagram of several surface elevations.

A.6.1 Wave gauges

Surface elevation data obtained from laboratory and numerical wave gauges are compared in Figure A.15, comprising of the time series at the wave gauges WG 1 and 7 upstream of the cylinder, WG 9 at the same longitudinal coordinate x as the cylinder and at WG 13 located downstream of the cylinder. The corresponding scatter plots are given in Figure A.16. The statistical descriptors peak ratio PR, correlation coefficient CC and scatter index SI are summarized in

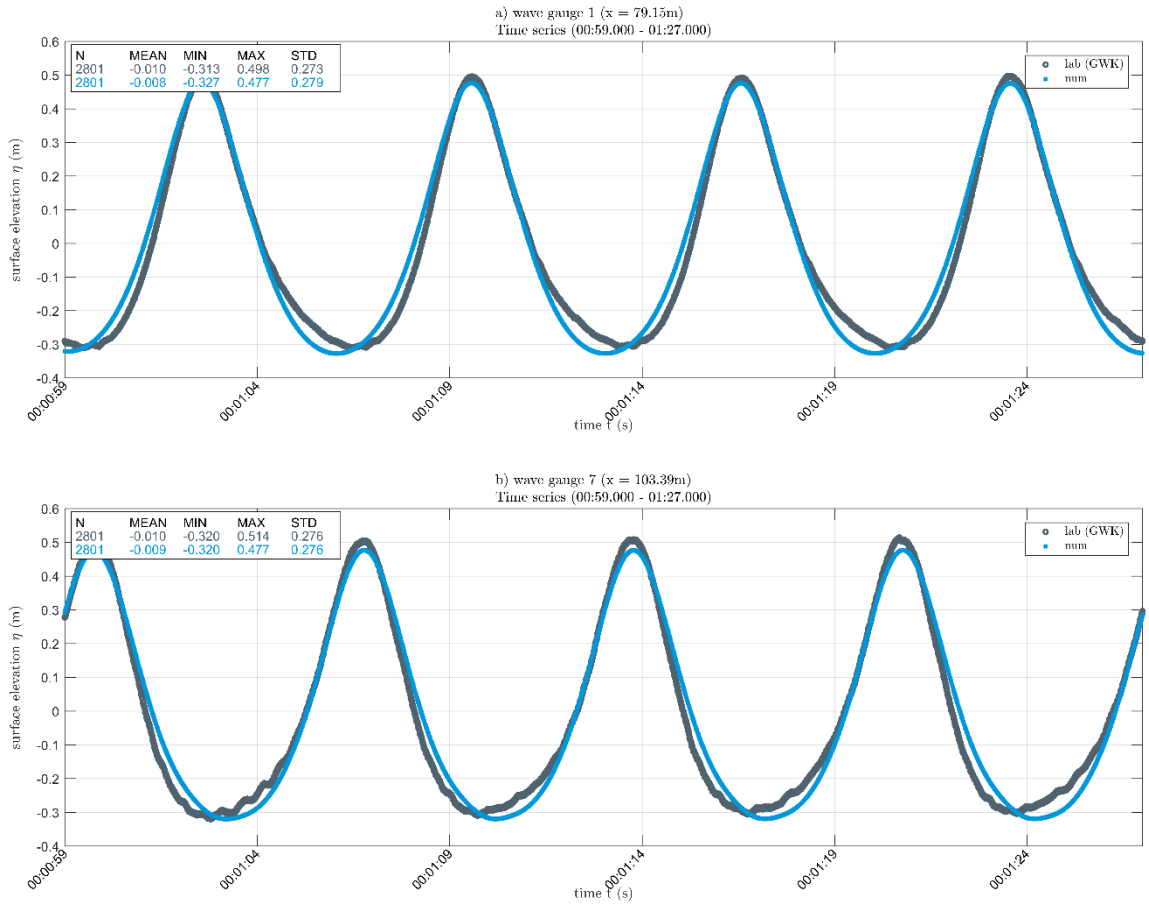

Figure A.15. Comparison of measured and simulated time series of surface elevations at a) wave gauge WG 1, b) WG 7, c) WG 9 and d) WG 13.

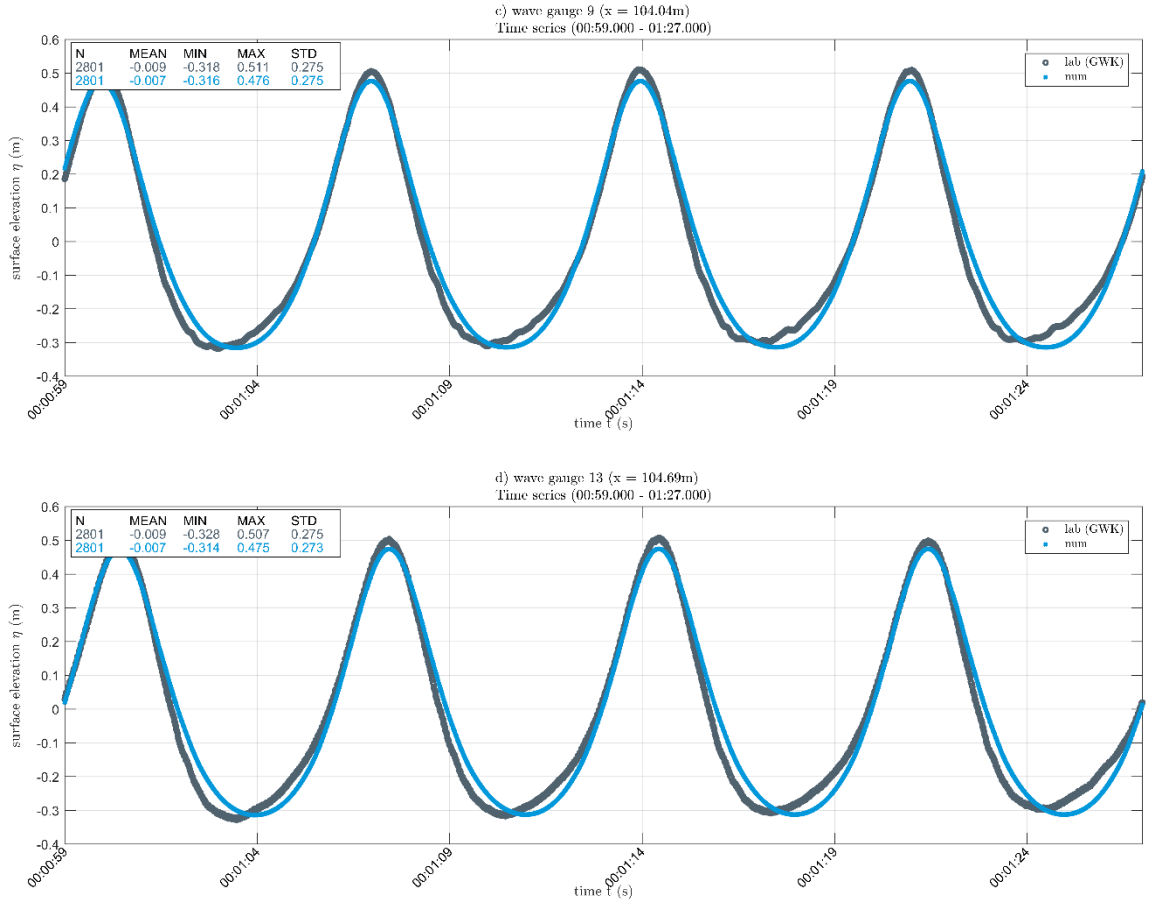

Figure A.15. (continued)

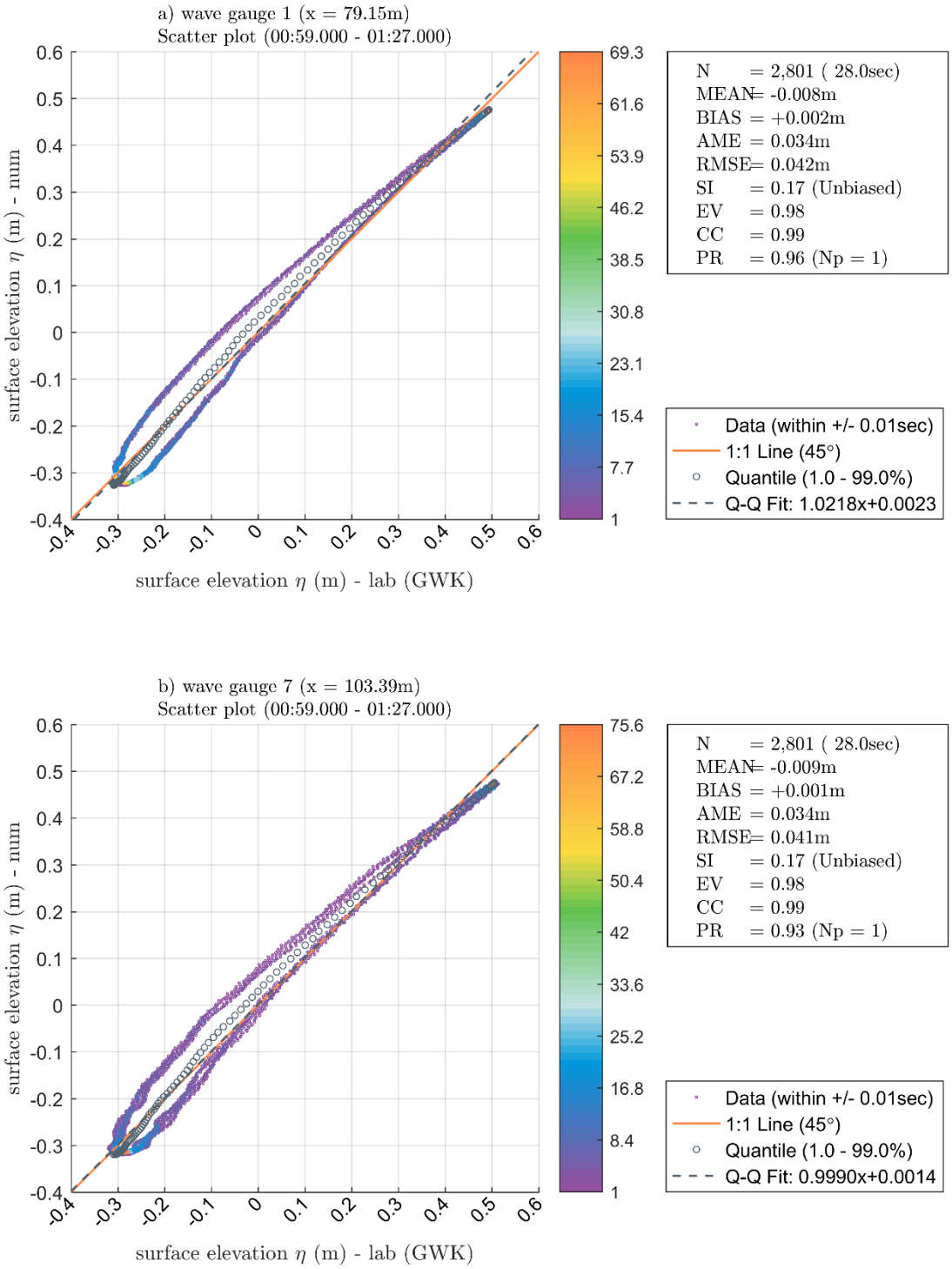

Figure A.16. Scatter plots of flow depths of measured and simulated time series of surface elevations at a) wave gauge WG 1, b) WG 7, c) WG 9 and d) WG 13.

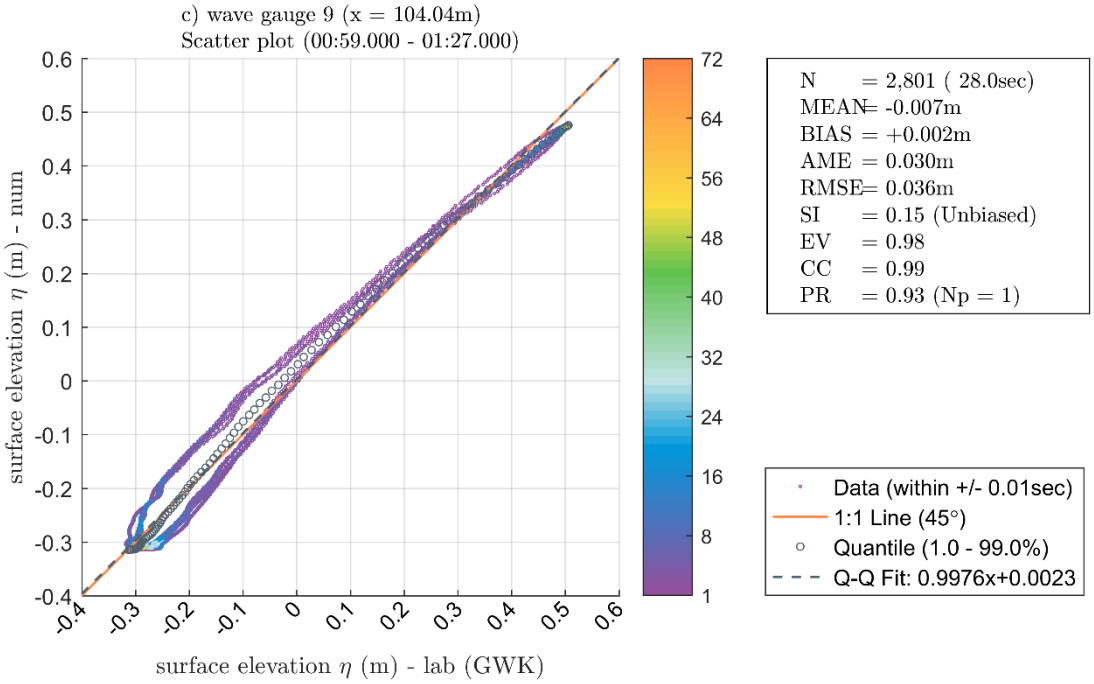

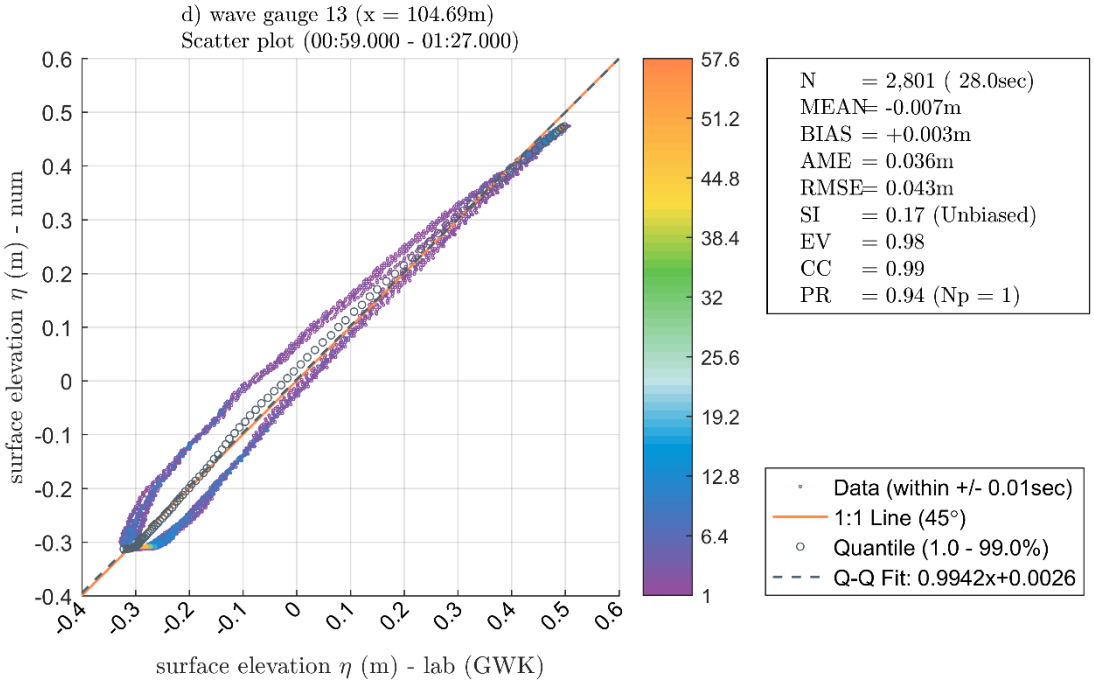

Figure A.16 (continued)

Table A.9. Peak ratios, correlation coefficient and scatter index of the comparison of measured and calculated surface elevations at the wave gauges WG 1, WG 7, WG 9 and WG 13.

gauge	x [m]	N [-]	PR [-]	CC [-]	SI [-]
1	79.15	2801	0.96	0.99	0.17
7	103.39	2801	0.93	0.99	0.17
9	104.69	2801	0.93	0.99	0.15
13	107.29	2801	0.94	0.99	0.17

A.6.2 Current meters

Current velocity data obtained from two laboratory and numerical current meters (CM) beside the cylinder are presented. The time series are shown in Figure A.17 and the scatter plots are given in Figure A.18. The statistical descriptors peak ratio PR, correlation coefficient CC and scatter index SI are provided in Table A.10.

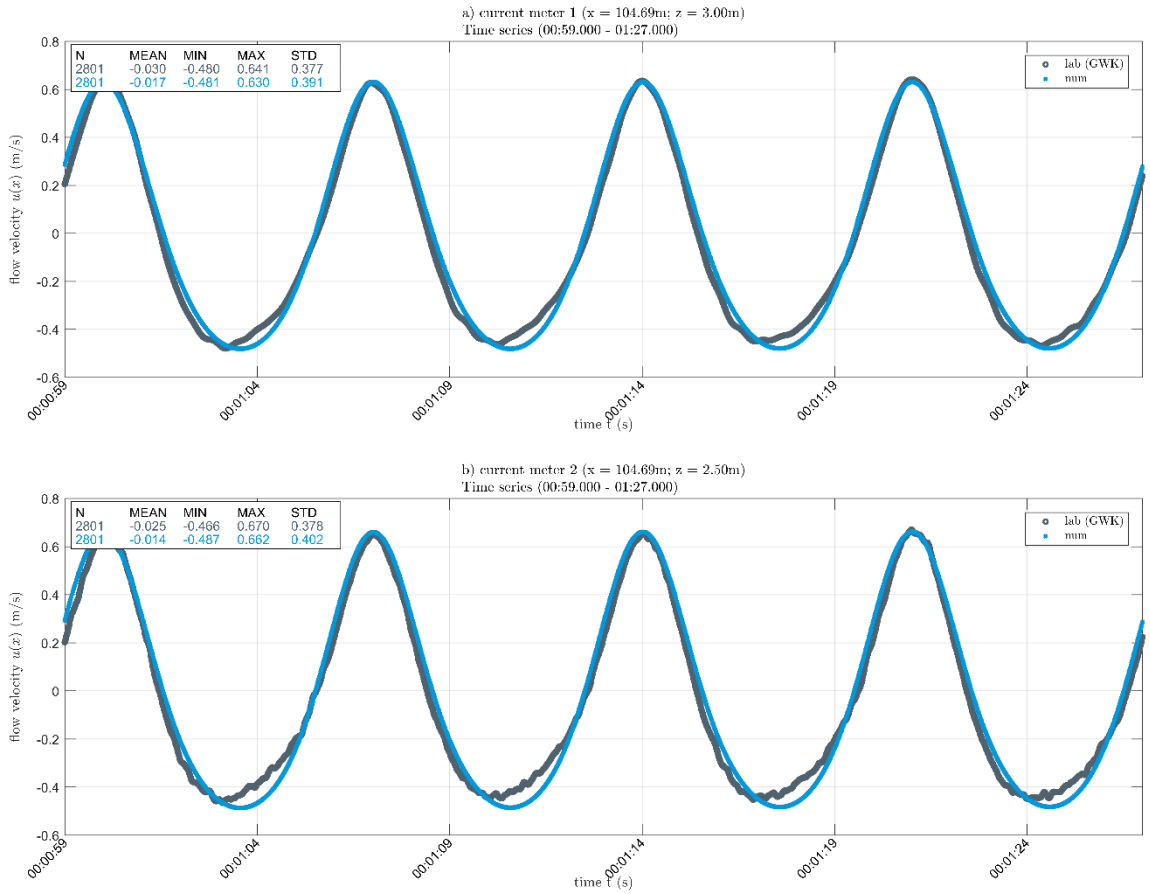

Figure A.17. Comparison of measured and simulated time series of flow velocities at a) current meter CM 1 and b) CM 2.

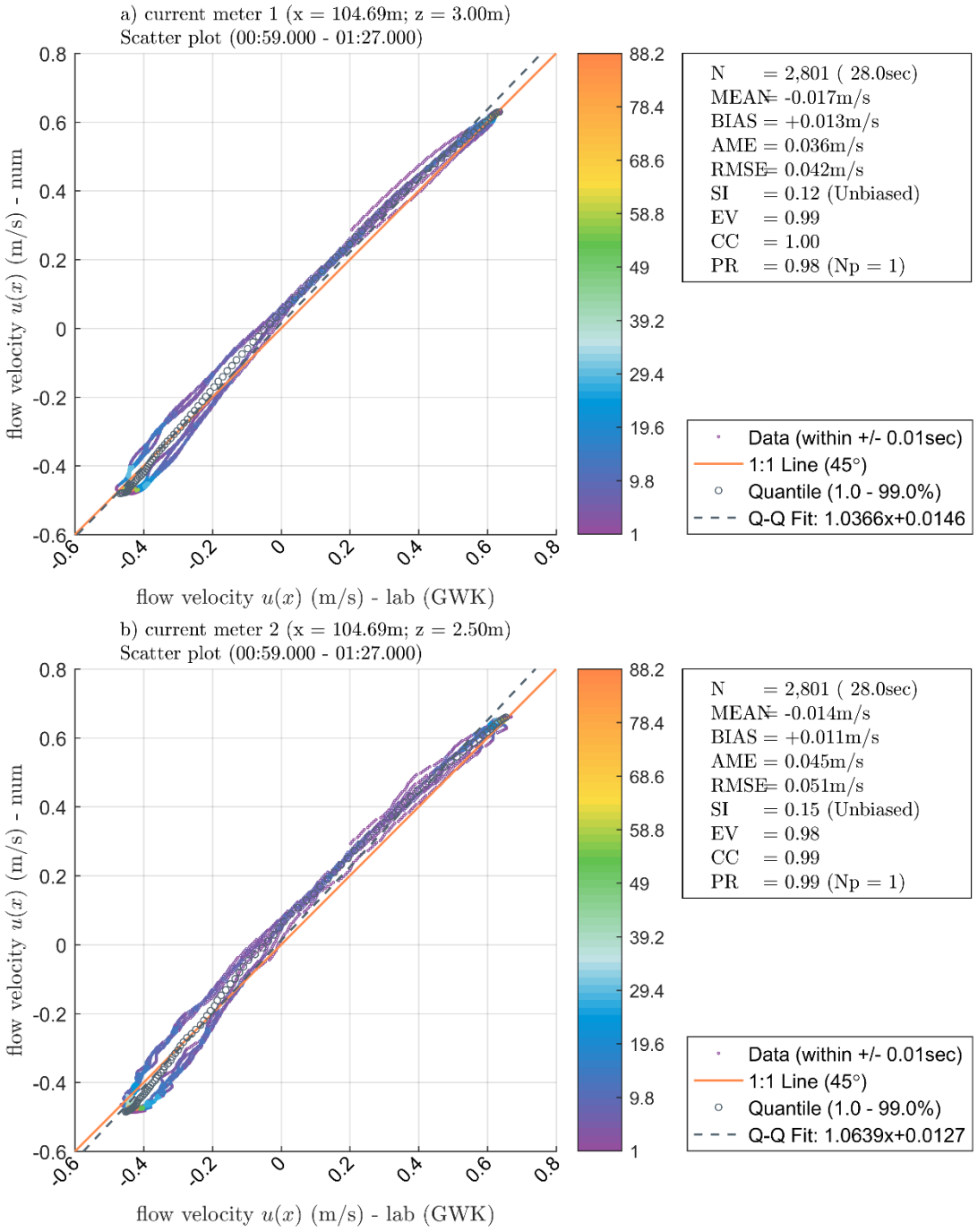

Figure A.18. Scatter plots of the comparison of measured and calculated current speeds at a) current meter CM 1 and b) CM 2.

Table A.10. Peak ratios, correlation coefficient and scatter index of the comparison of measured and calculated current speeds at the current meters CM 1 and CM 2.

Current meter	x [m]	z [m]	N [-]	PR [-]	CC [-]	SI [-]
1	104.69	2.5	2801	0.98	1.00	0.12
2	104.69	3.0	2801	0.99	0.99	0.15

A.6.3 Strain gauge

The overturning moments around the top suspension of the cylinder obtained from laboratory and numerical strain gauges are compared in this section. Figure A.20 provides the time series and Figure A.20 the corresponding scatter plot. The statistical descriptors peak ratio PR, correlation coefficient CC and scatter index SI are provided in Table A.11.

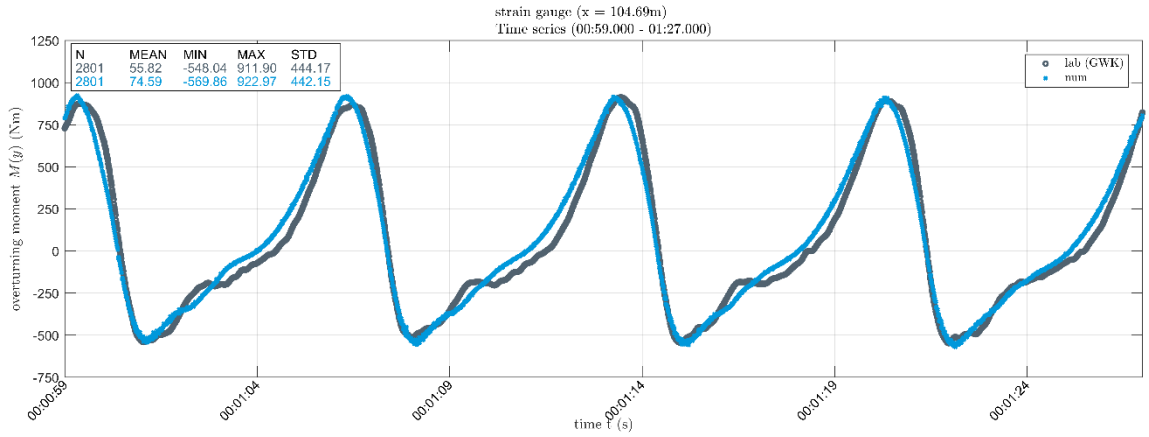

Figure A.19. Comparison of measured and simulated time series of overturning moments in the second cylinder.

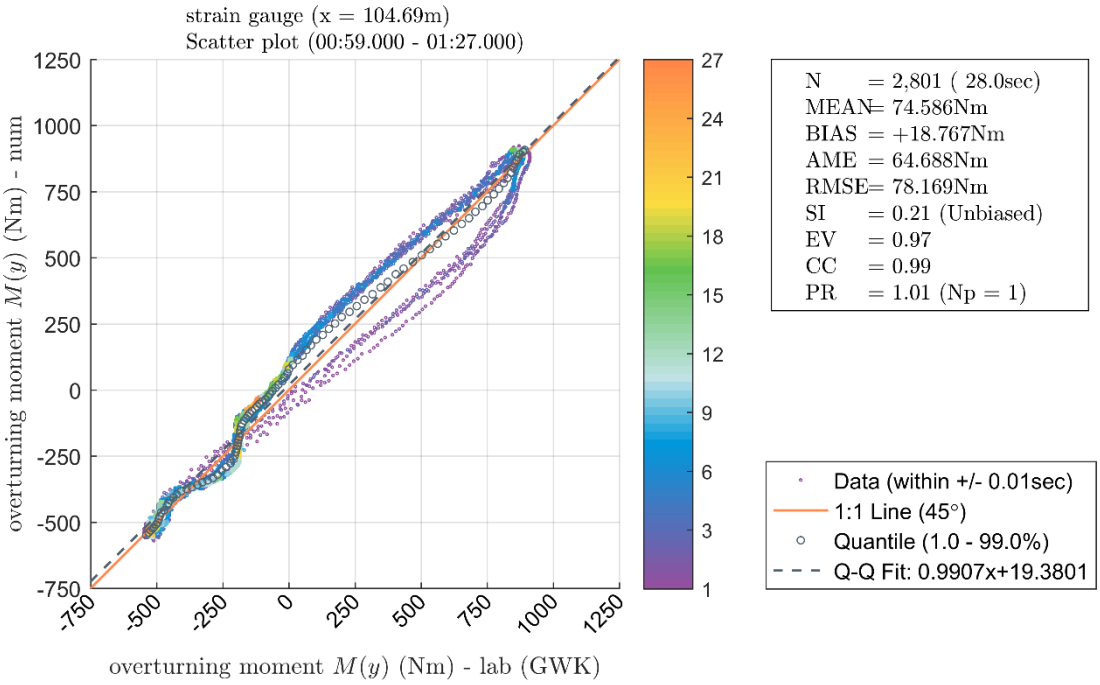

Figure A.20. Comparison of measured and simulated time series of overturning moments in the second cylinder.

Table A.11. Peak ratios, correlation coefficient and scatter index of the comparison of measured and calculated overturning moments at the strain gauge.

Strain gauge	x [m]	N [-]	PR [-]	CC [-]	SI [-]
1	104.69	2801	1.01	0.99	0.21

A.7 Effect of the symmetry boundary condition on the results of the propagation of a bore

To reduce the size of the numerical domain, symmetry boundary conditions were selected, which enable the modeller to cut one side of the domain in the case that the introduced new boundary is able to fully mirror the numerical quantities pressure, phase (water) content and velocity and thereby mimic identical conditions as simulated in the remaining part of the numerical domain.

This section shows comparisons of flux and maximum inline forces acting on a cylinder during bore propagation in a numerical domain of original width with a domain with reduced width, in which the symmetry boundary condition is applied. Each figure shows the timeseries of the surface elevation at the wave gauge, the scatter plot and resulting quality indices (see section A.1) and a frequency of occurrence diagram of several surface elevations.

A.7.1 Volume flux

The time series of horizontal flux through a cross-section in distances between x = 6.4 (x^* = 0) and x = 9.6 m (x^* = 0) from the impoundment gate is presented in Figure A.21 to Figure A.21.

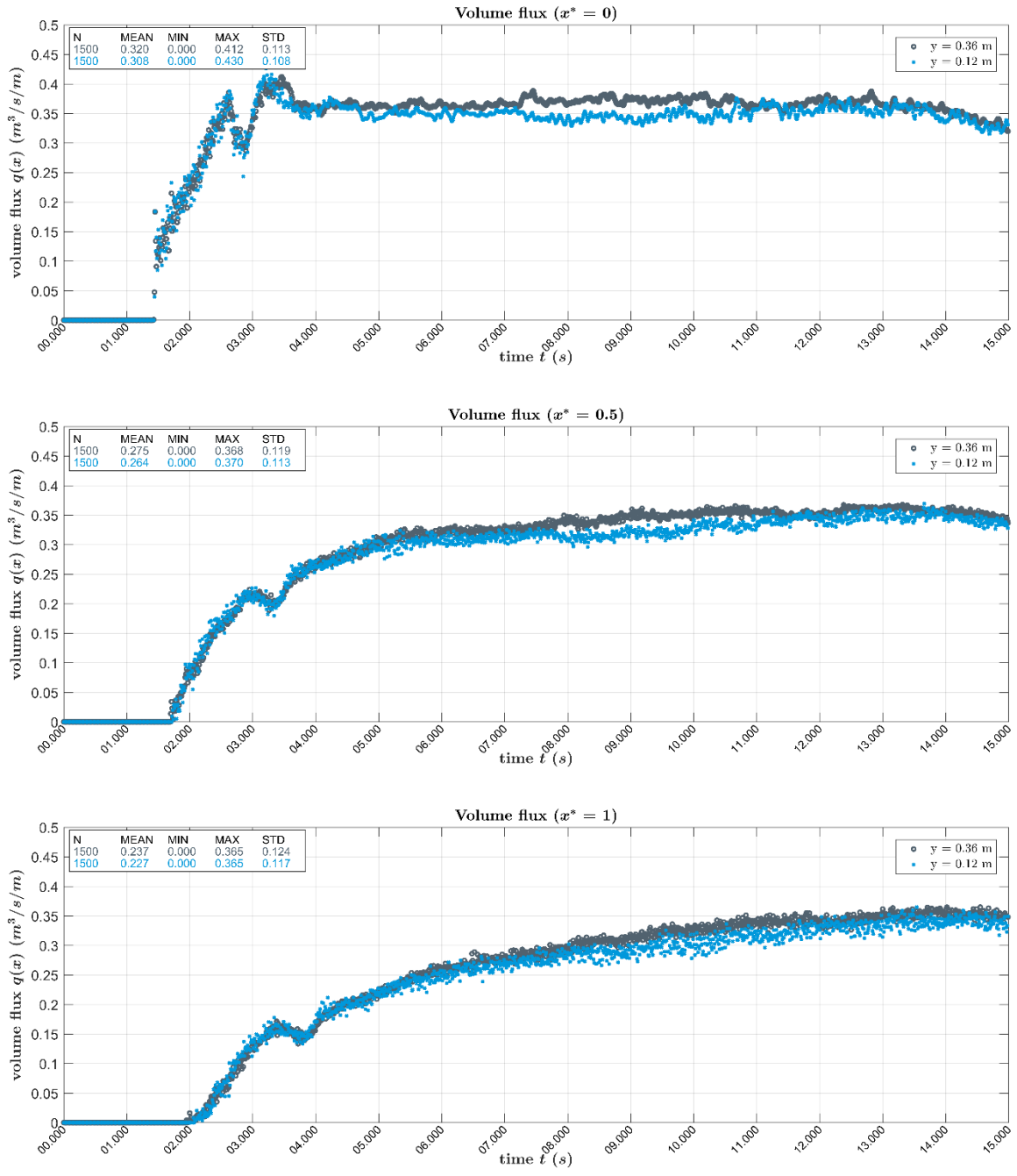

Figure A.21. Comparison simulated and measured time series of horizontal fluxes from top to bottom: at x^* = 0, 0.5 and 1.0.

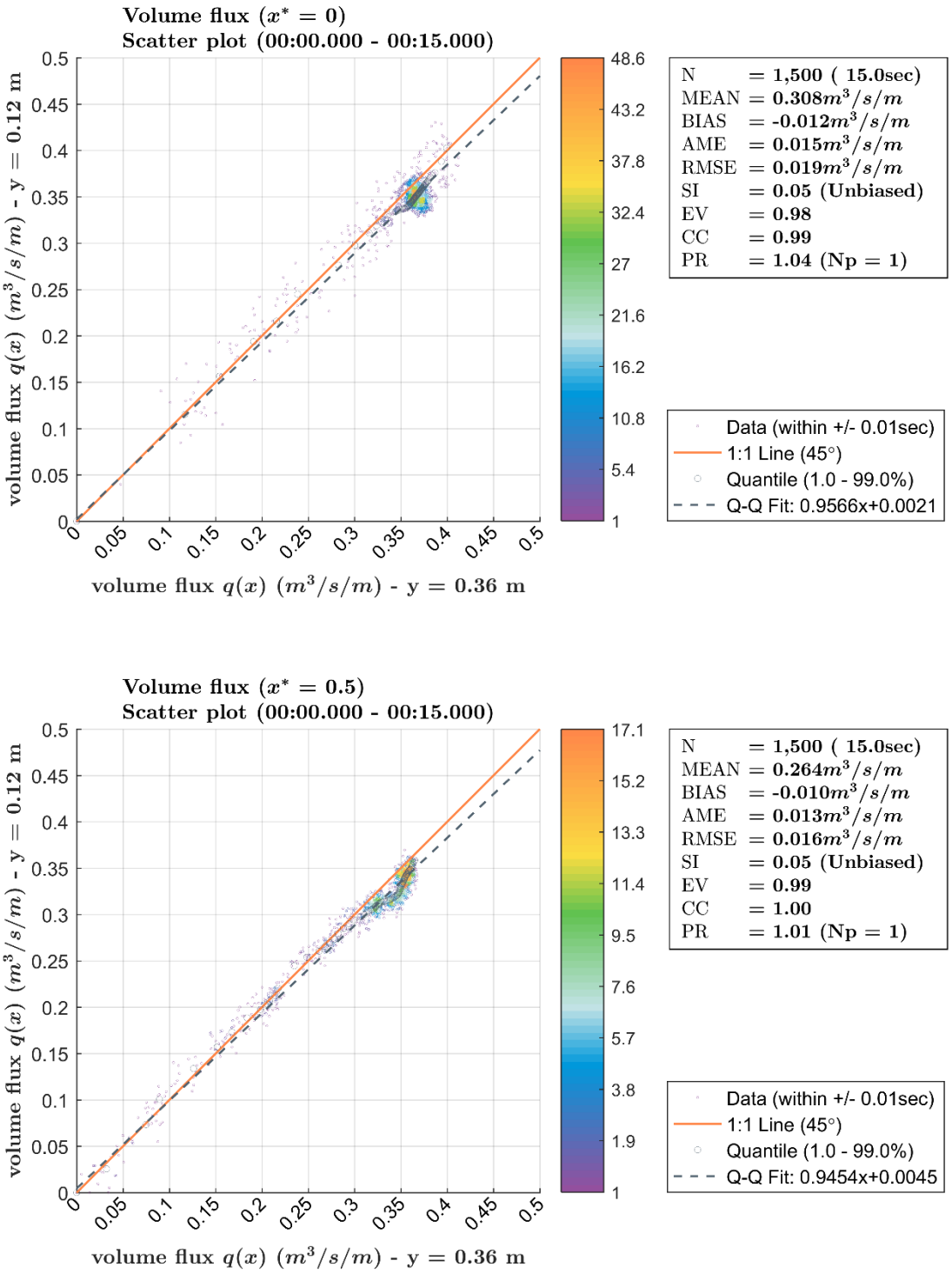

Figure A.22. Scatter plot of measured and simulated horizontal fluxes at x^* = 0, 0.5 and 1.0.

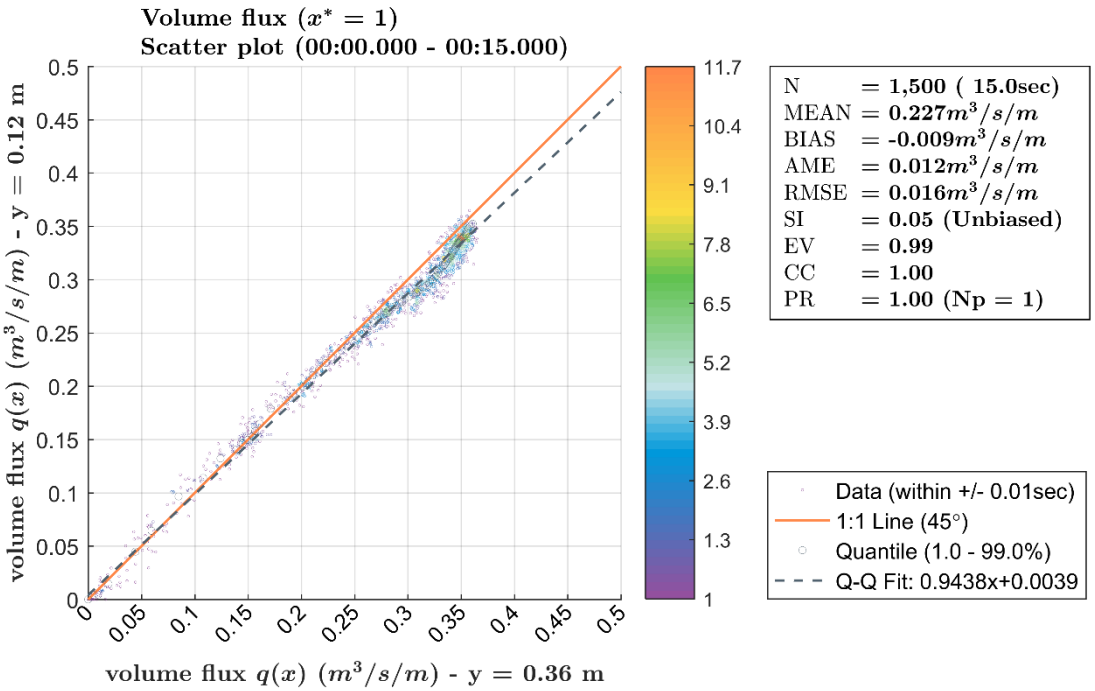

Figure A.22. (continued)

A.8 Effect of increased cell size on bore propagation and its interaction with a cylinder

The height of the numerical cells is doubled and compared with the original cell height Δz = 0.0125 m. The comparison was performed by means of flow velocity in the free flow region. Furthermore, the original width of the numerical cells of $\Delta x = 0.625 \cdot 10^{-3}$ m was doubled in the boundary layer of a cylinder. The effect is shown by means of the horizontal flux with both cell sizes. Each figure shows the timeseries of the surface elevation at the wave gauge, the scatter plot and resulting quality indices (see section A.1) and a frequency of occurrence diagram of several surface elevations.

A.8.1 Increased cell height in the free flow region

The comparison of the flow velocity in 8 m distance from the impoundment gate for both investigated cell sizes is presented in Figure A.23.

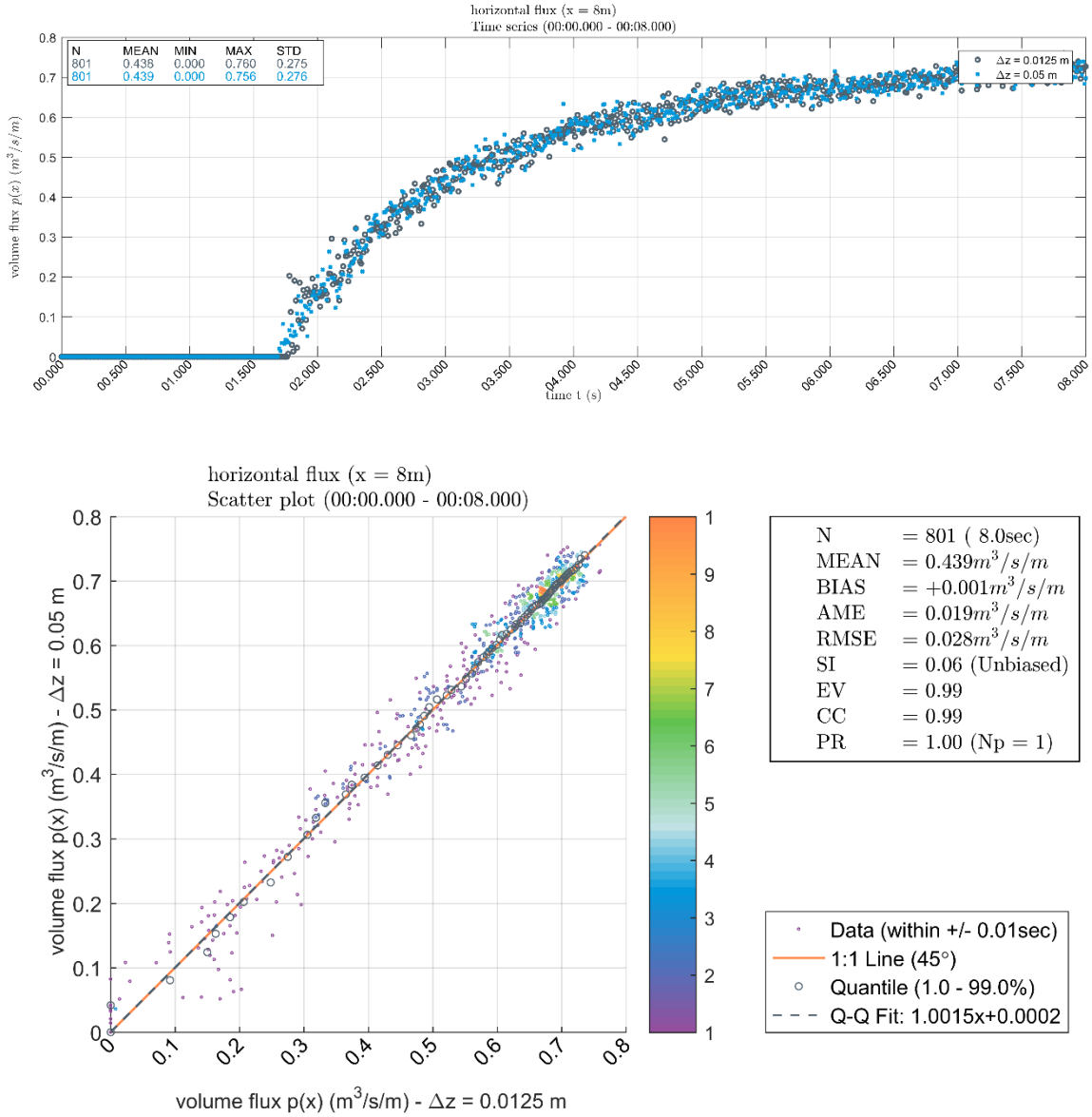

Figure A.23. Comparison of simulated time series of flow velocities with two mesh resolutions in the free flow regions: Top: time series, bottom: scatter plot.

A.8.2 Increases cell width in the boundary layer of the cylinder

The comparison of the horizontal flux through cross-sections between 6.4 m and 9.6 m distance from the impoundment gate for both investigated cell sizes is presented in Figure A.24 and Figure A.25.

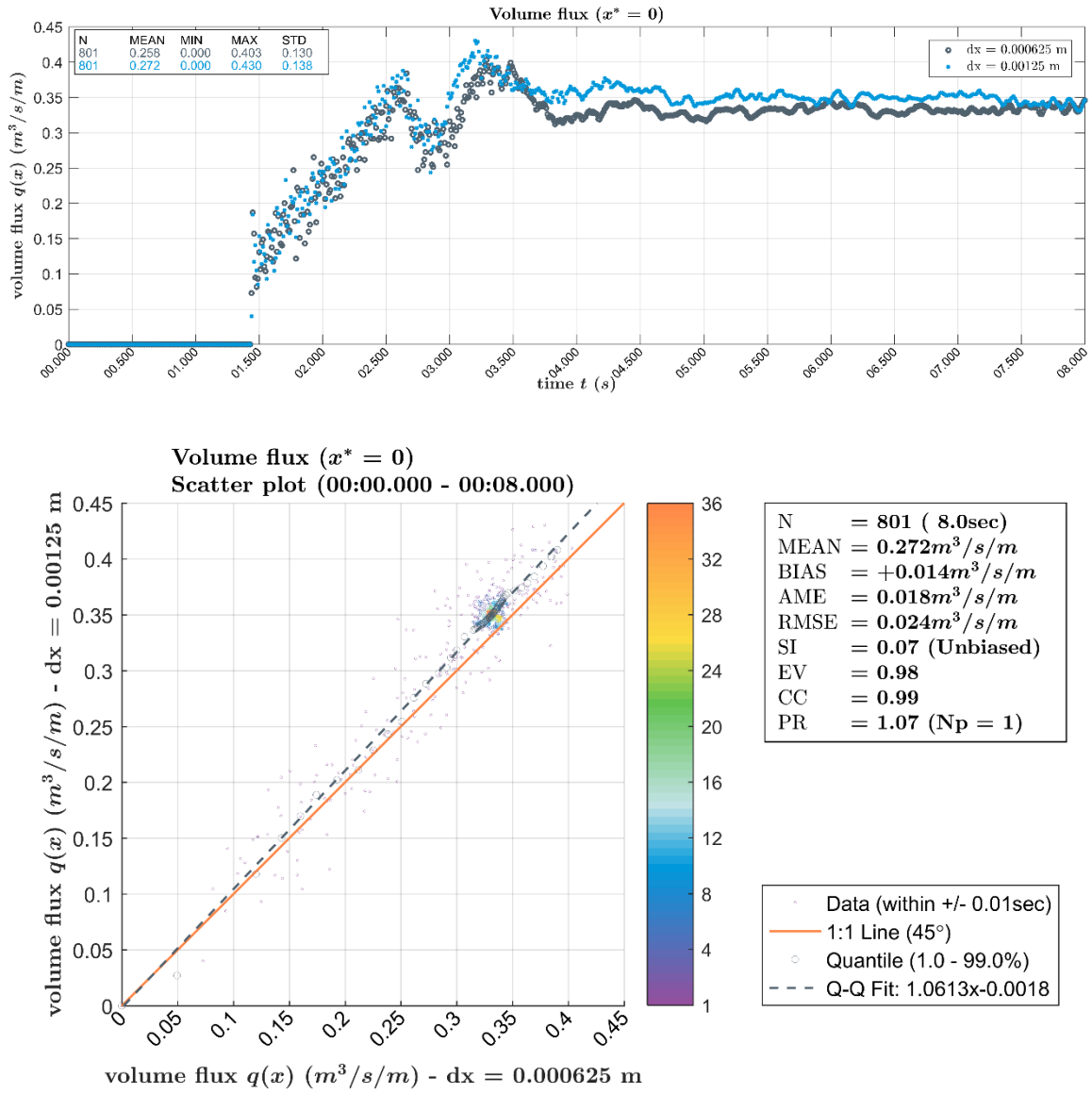

Figure A.24. Comparison of simulated time series of horizontal fluxes with two mesh resolutions in the bounded flow regions at $x^* = 0$: Top: Time series, bottom: scatter plot.

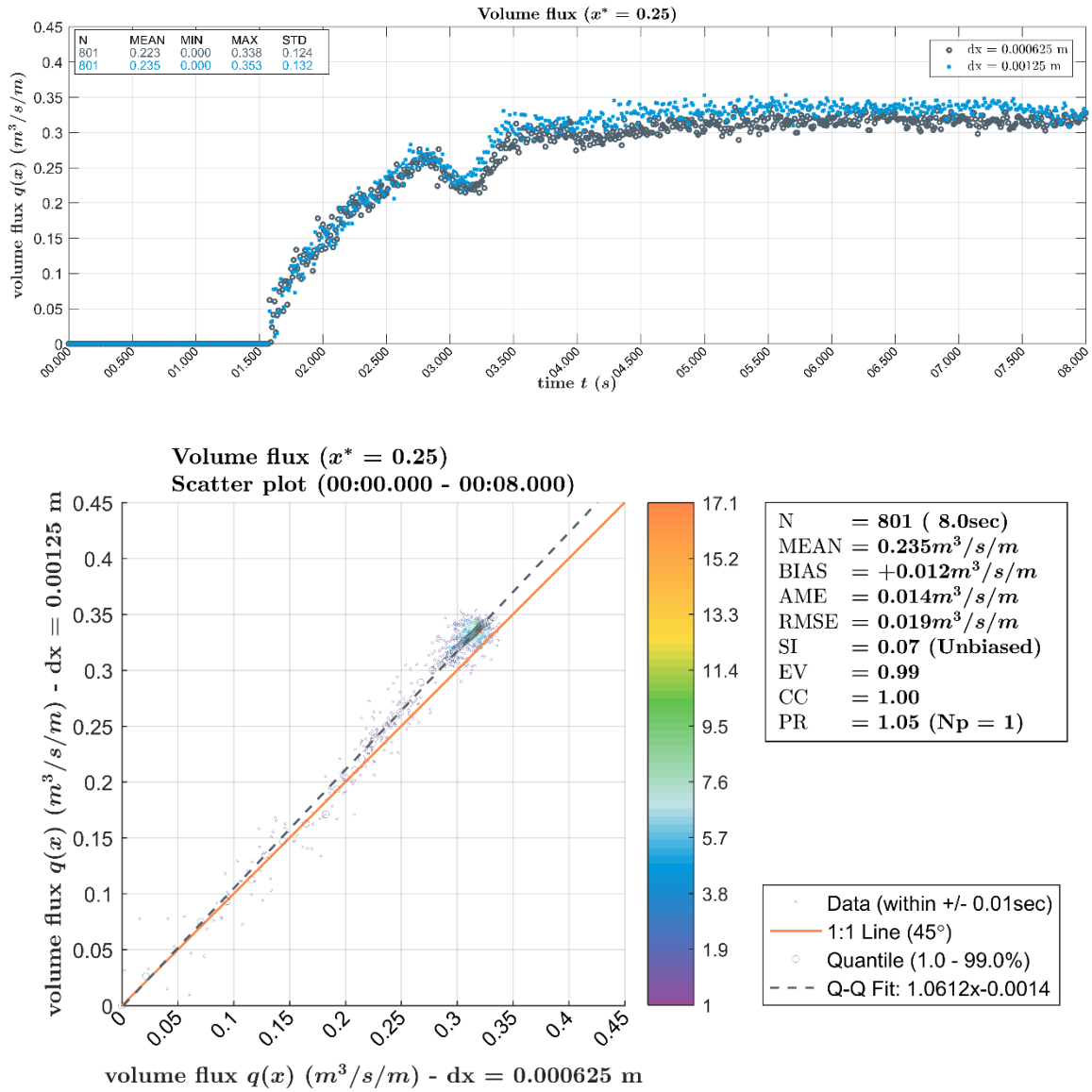

Figure A.25. Comparison of simulated time series of horizontal fluxes with two mesh resolutions in the bounded flow regions at x^* = 0.25: Top: Time series, bottom: scatter plot.

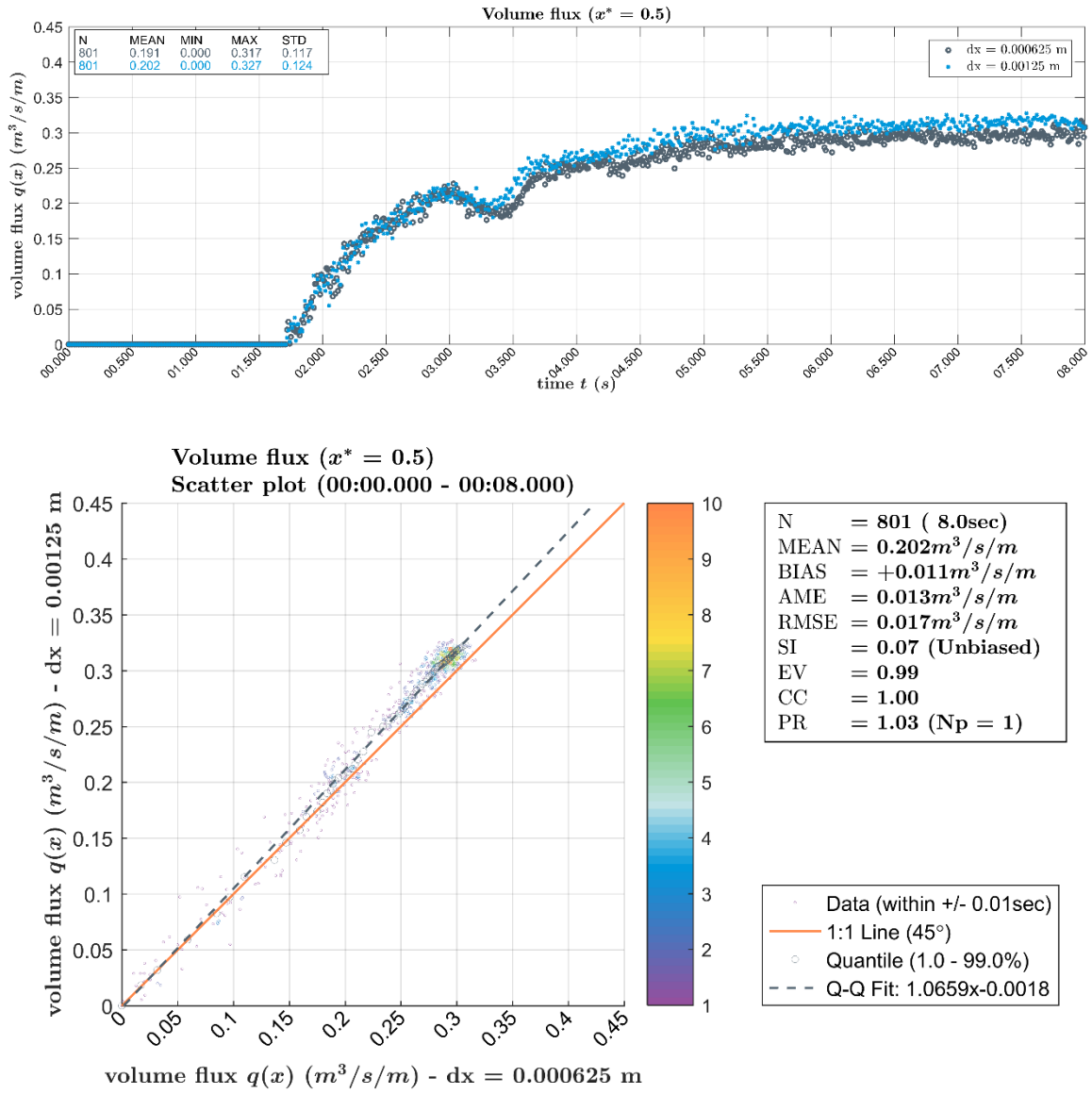

Figure A.26. Comparison of simulated time series of horizontal fluxes with two mesh resolutions in the bounded flow regions at x^* = 0.5: Top: Time series, bottom: scatter plot.

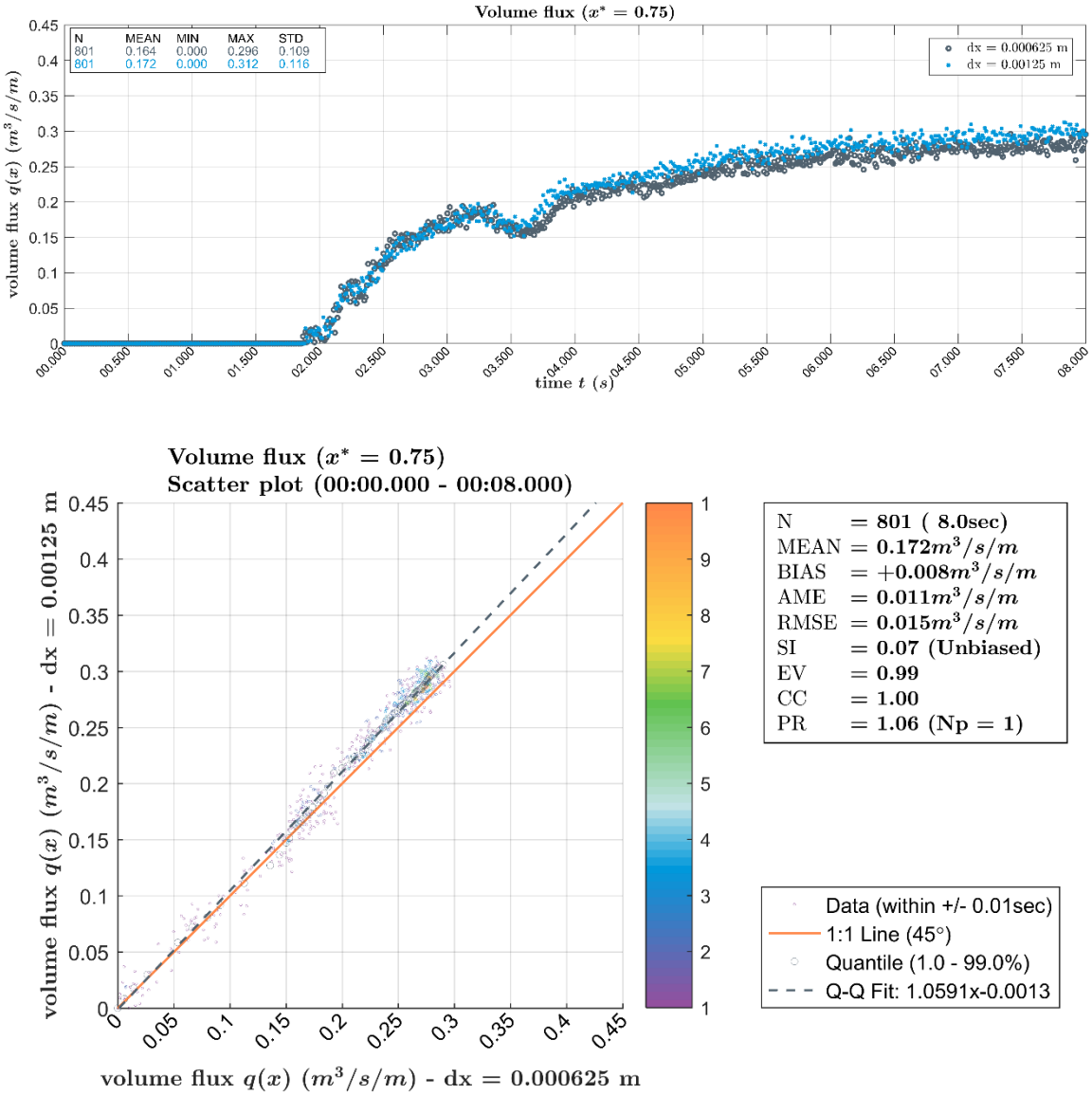

Figure A.27. Comparison of simulated time series of horizontal fluxes with two mesh resolutions in the bounded flow regions at x^* = 0.75: Top: Time series, bottom: scatter plot.

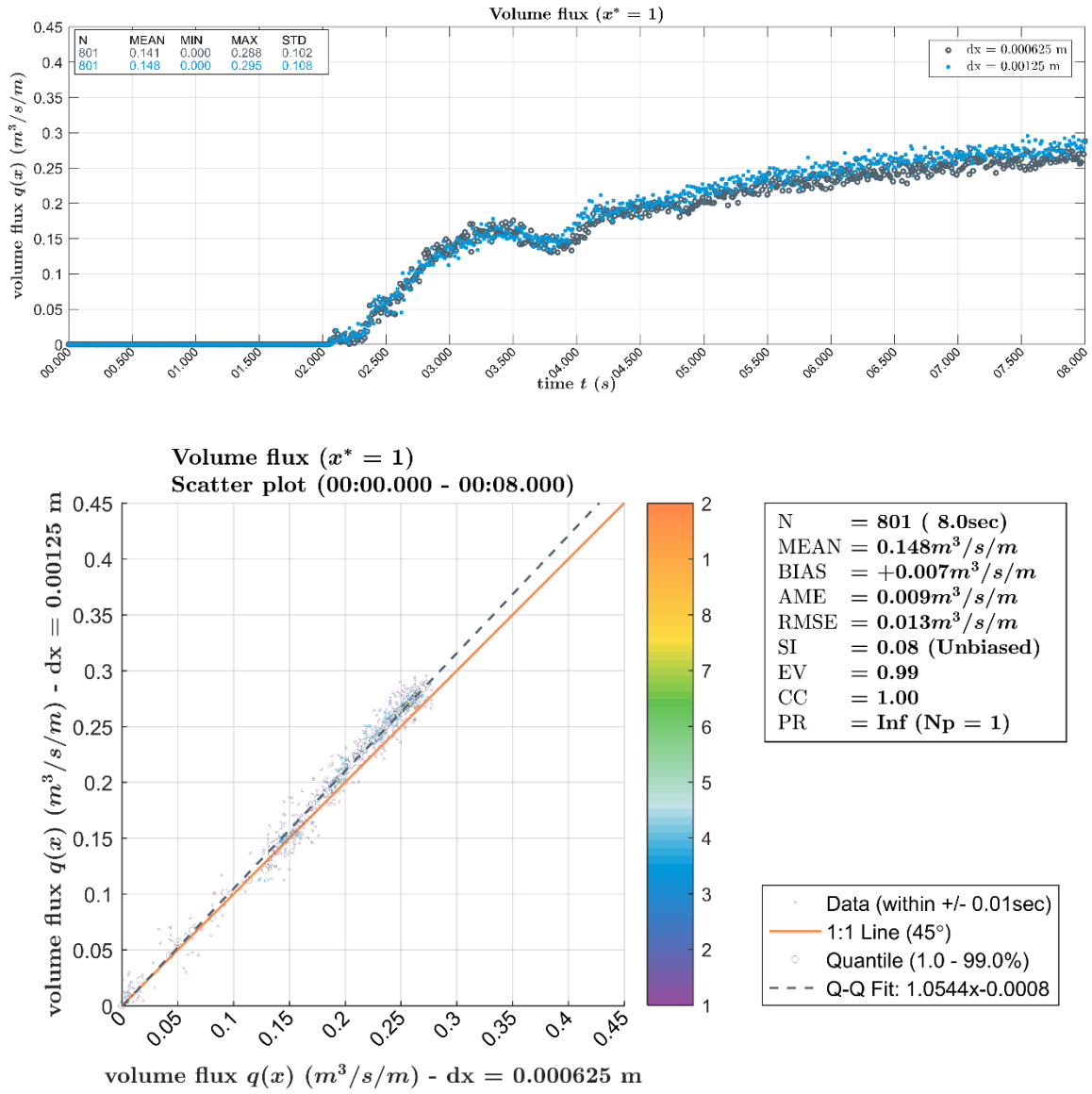

Figure A.28. Comparison of simulated time series of horizontal fluxes with two mesh resolutions in the bounded flow regions at x^* = 1: Top: Time series, bottom: scatter plot.

A.9 Inline forces in single isolated roughness elements

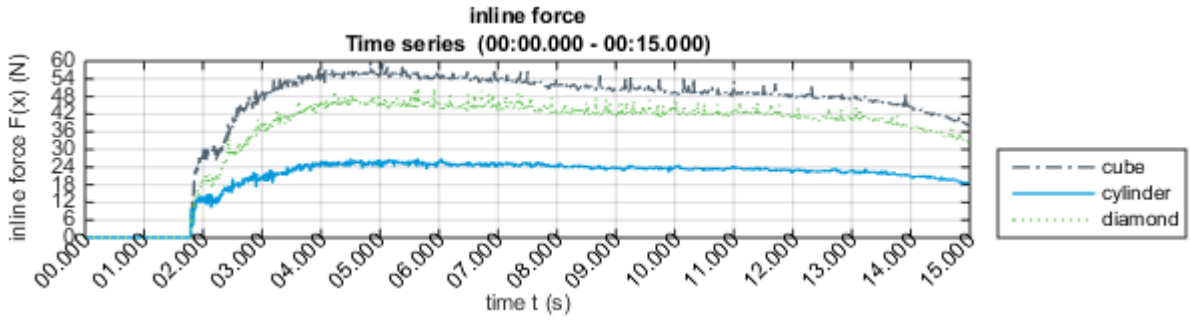

Figure A.29. Inline forces on a single isolated-standing cube, cylinder and diamond.

Appendix B Inline forces on three cylinders subject to a solitary wave and a bore

This appendix contains the timeseries of inline forces on three cylinders subject to a solitary wave and a bore in tandem, side-by-side and two staggered configurations and several spacings.

B.1 Inline forces on three cylinders in tandem arrangement (Ψ_B = 0°)

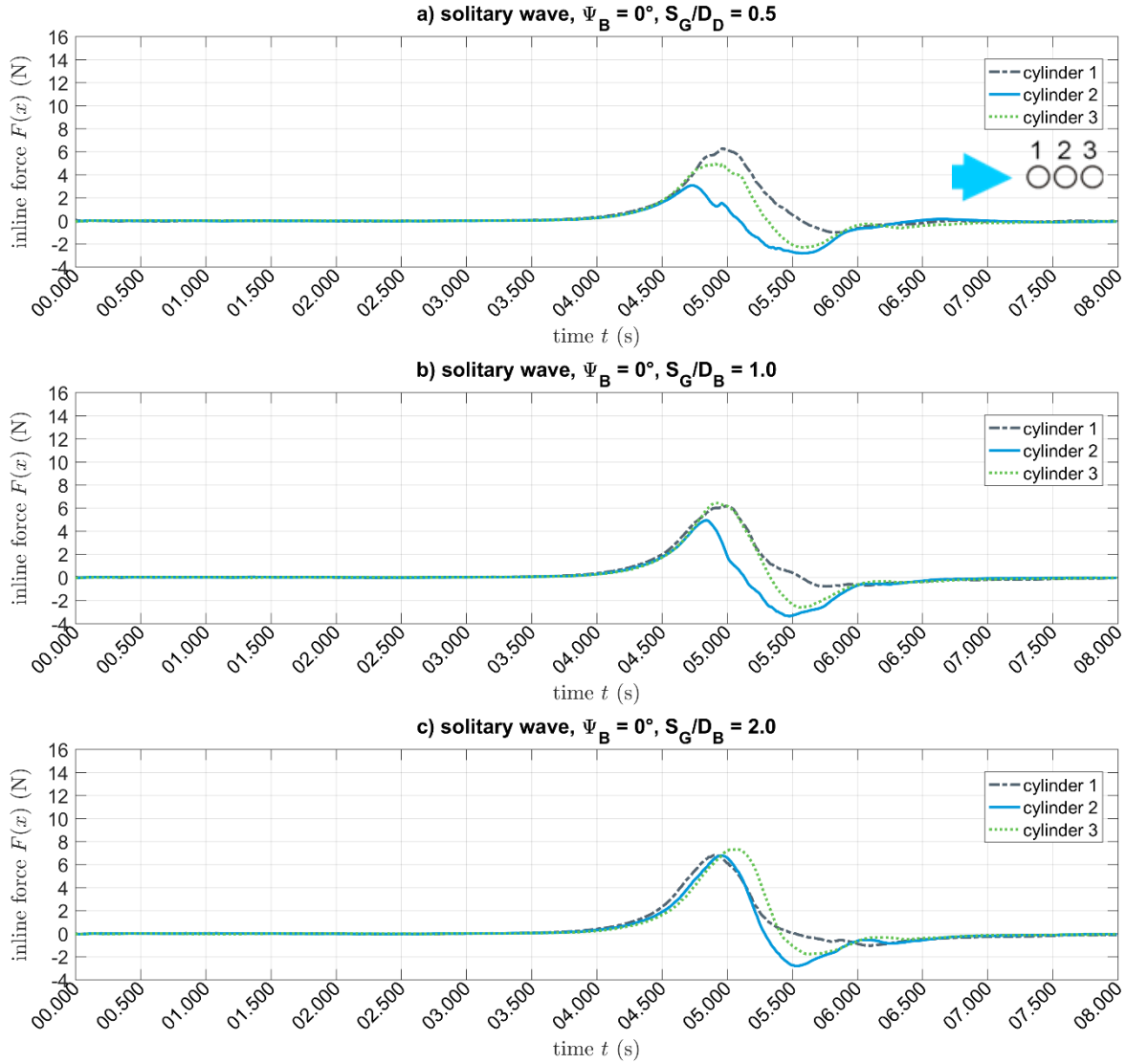

Figure B.1. Inline forces acting on three cylinders in tandem arrangement subject to a solitary wave. Spacing: a) 0.5 D_B, b) 1.0 D_B, c) 2.0 D_B, d) 3.0 D_B and e) 5.0 D_B.

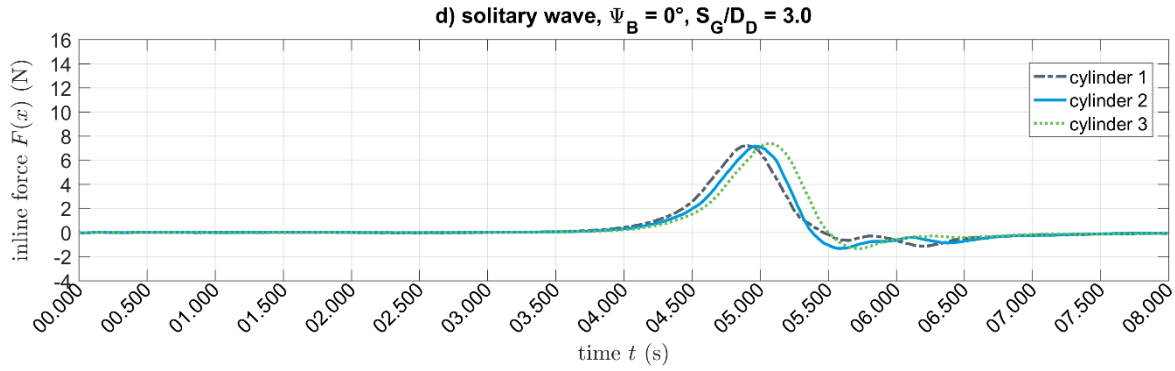

Figure B.1 (continued)

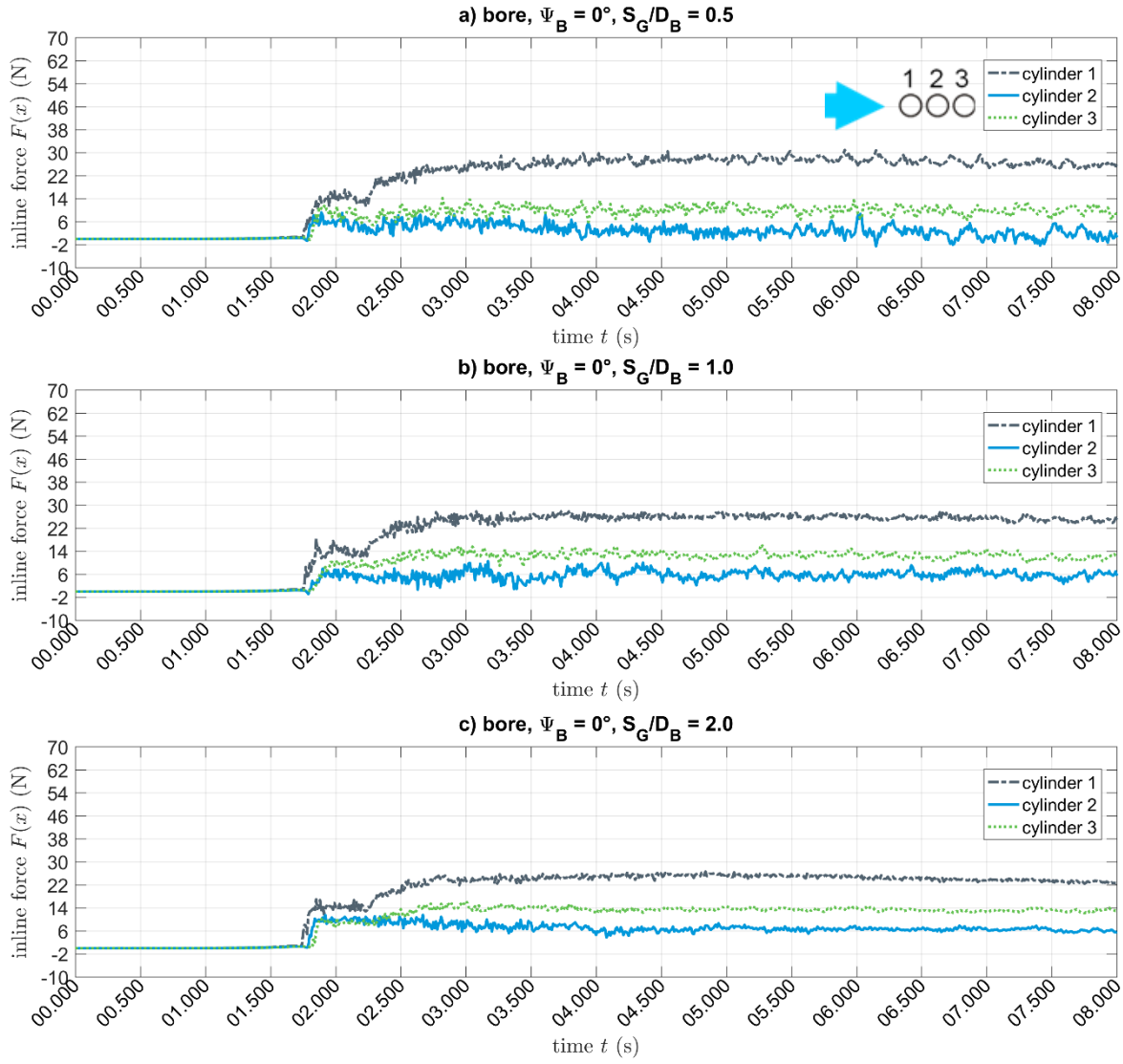

Figure B.2. Inline forces acting on three cylinders in tandem arrangement subject to a bore. Spacing: a) 0.5 D_B, b) 1.0 D_B, c) 2.0 D_B, d) 3.0 D_B and e) 5.0 D_B.

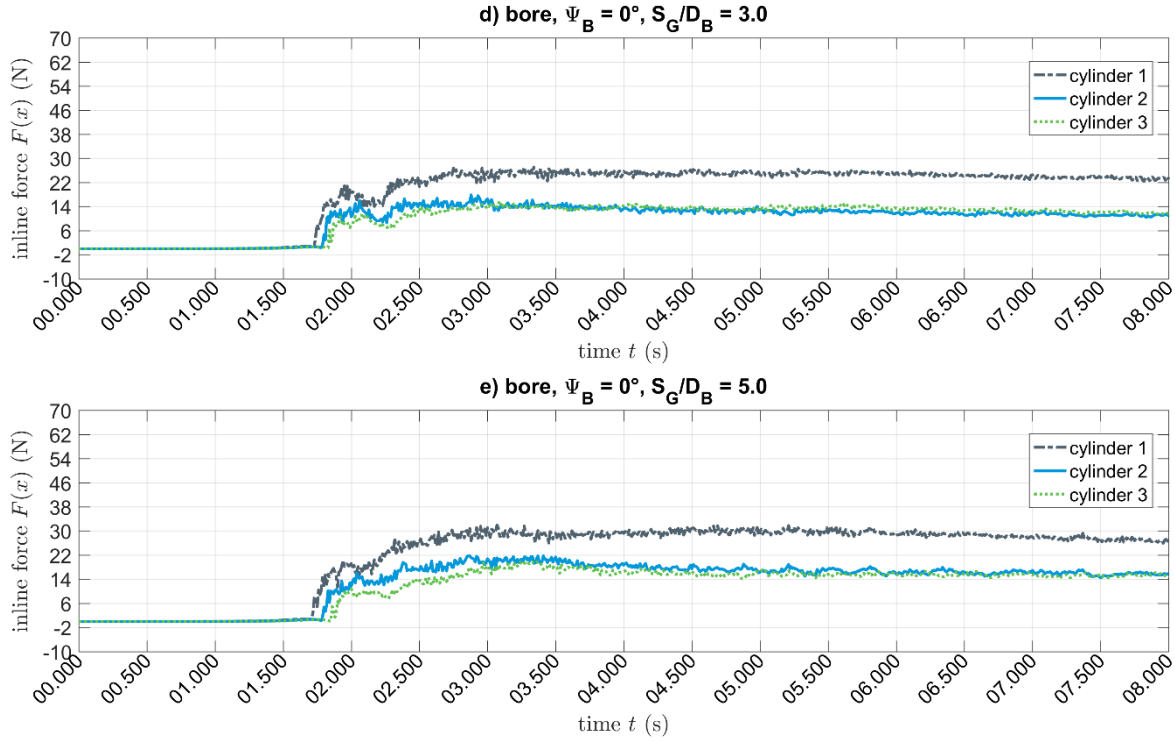

Figure B.2 (continued)

B.2 Inline forces on three cylinders in staggered1 arrangement (Ψ_B = 45°)

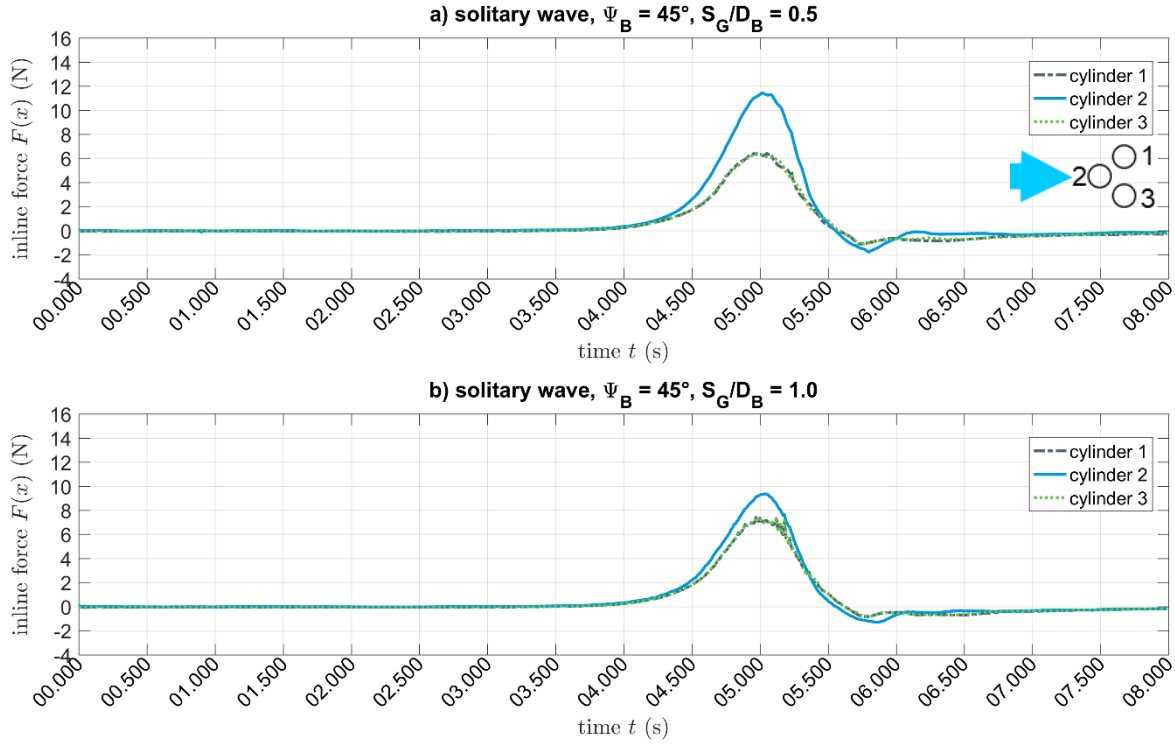

Figure B.3. Inline forces on three cylinders in staggered 1 arrangement subject to a solitary wave. Distance between the cylinders: a) 0.5 D_B, b) 1.0 D_B, c) 2.0 D_B, d) 3.0 D_B and e) 5.0 D_B.

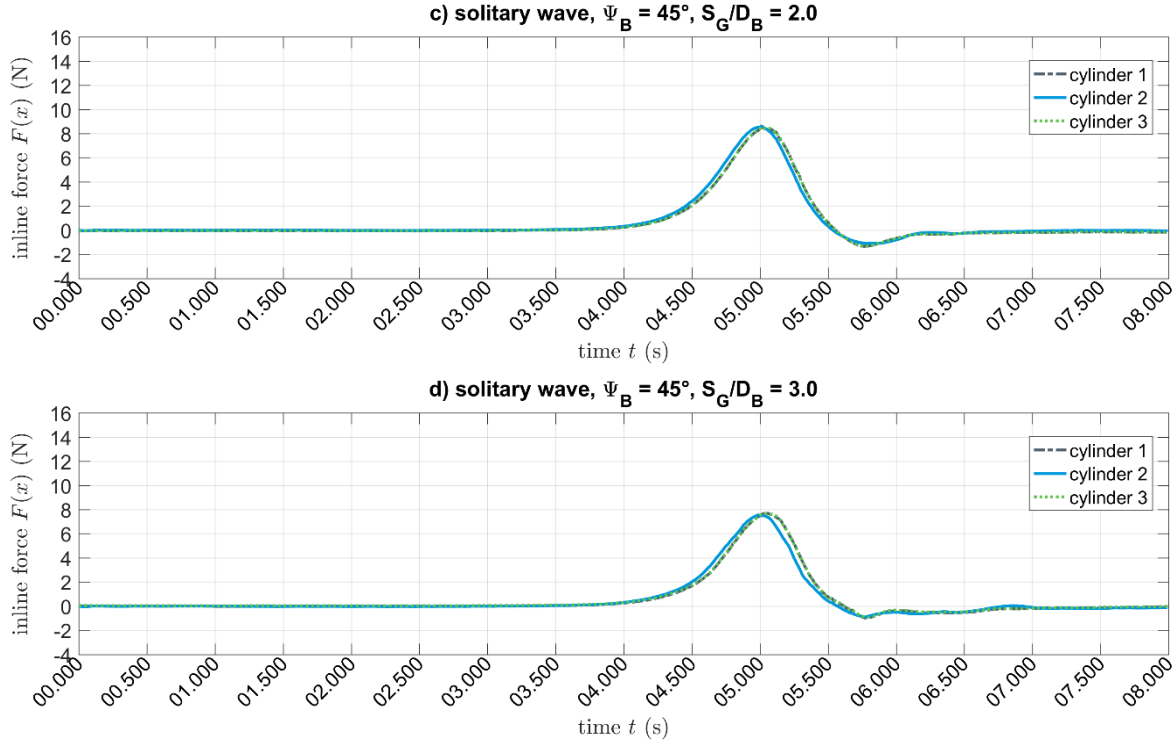

Figure B.3 (continued)

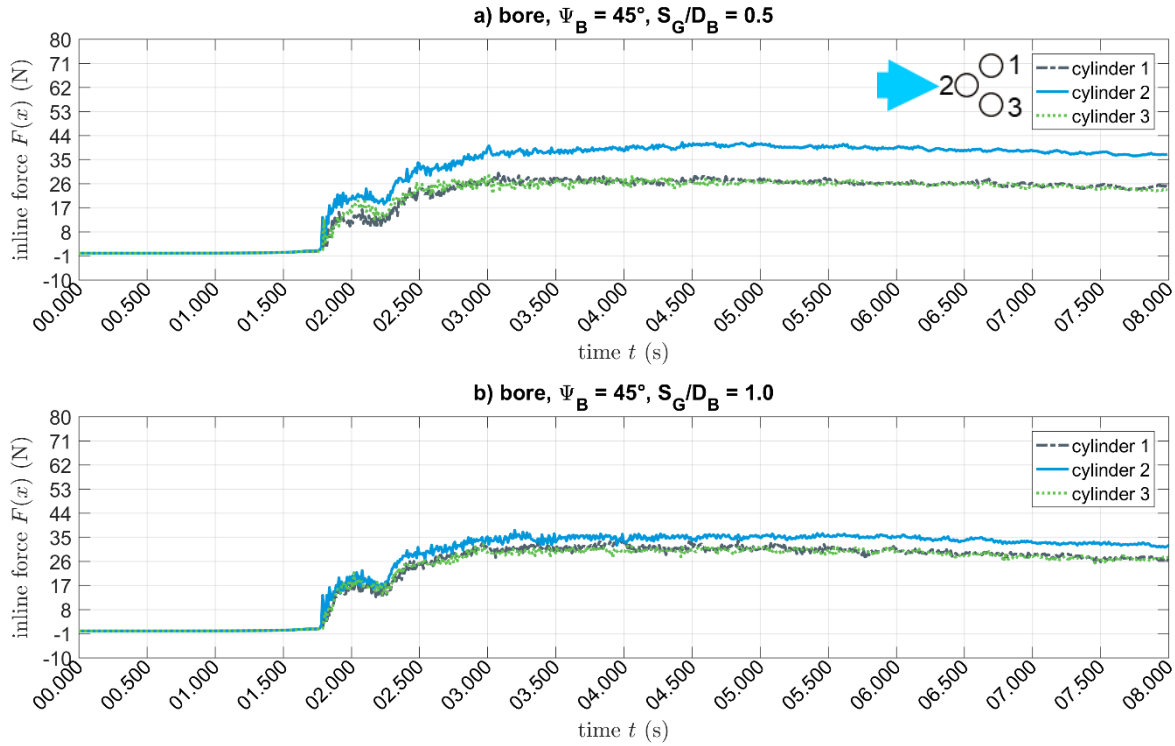

Figure B.4. Inline forces on three cylinders in staggered 1 arrangement subject to a bore. Distance between the cylinders: a) 0.5 D_B, b) 1.0 D_B, c) 2.0 D_B and d) 3.0 D_B.

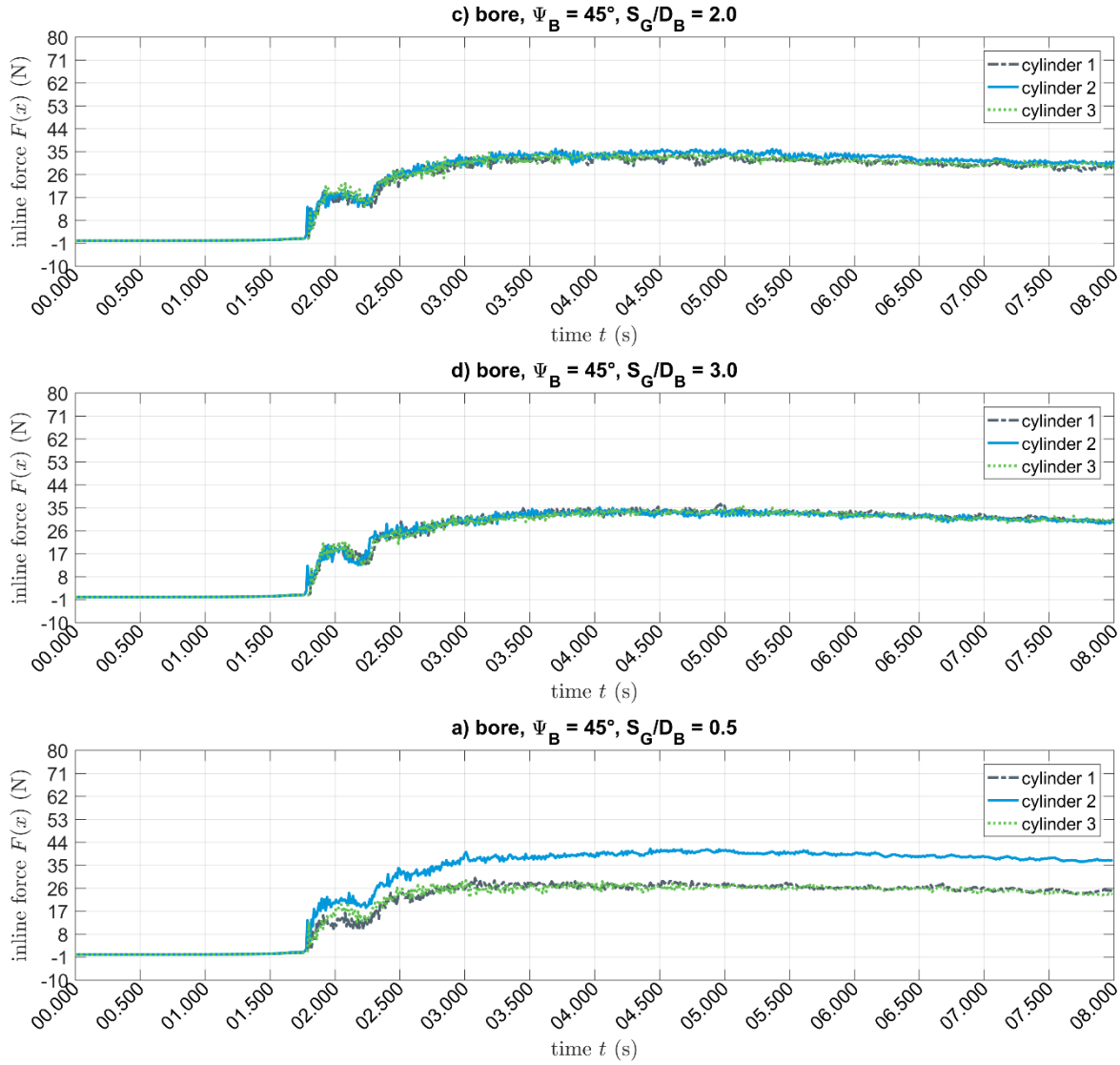

Figure B.4 (continued)

B.3 Inline forces on three cylinders in side-by-side arrangement (Ψ_B = 90°)

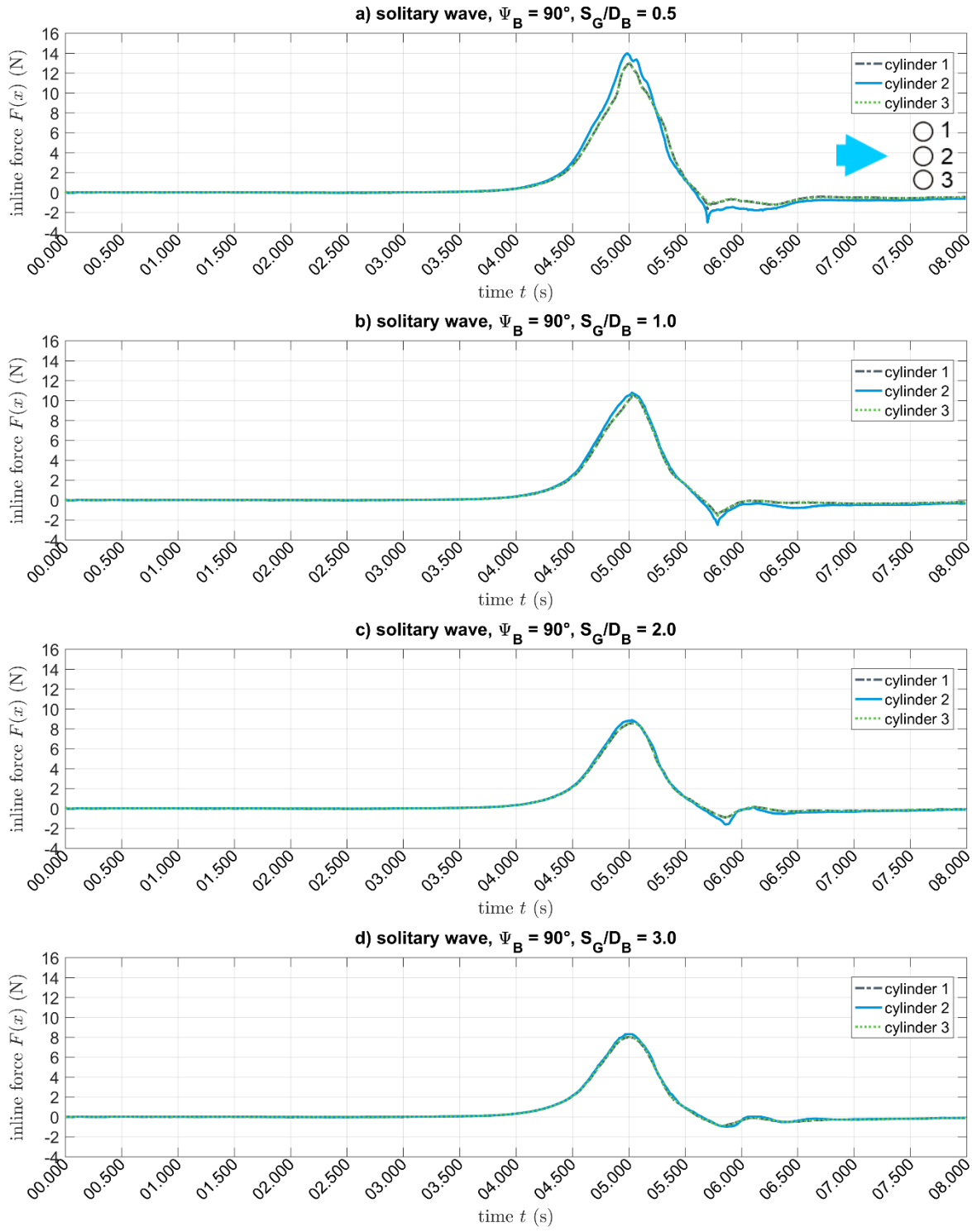

Figure B.5. Inline forces on three cylinders in side-by-side arrangement subject to a solitary wave. Distance between the cylinders: a) 0.5 D_B, b) 1.0 D_B, c) 2.0 D_B and d) 3.0 D_B.

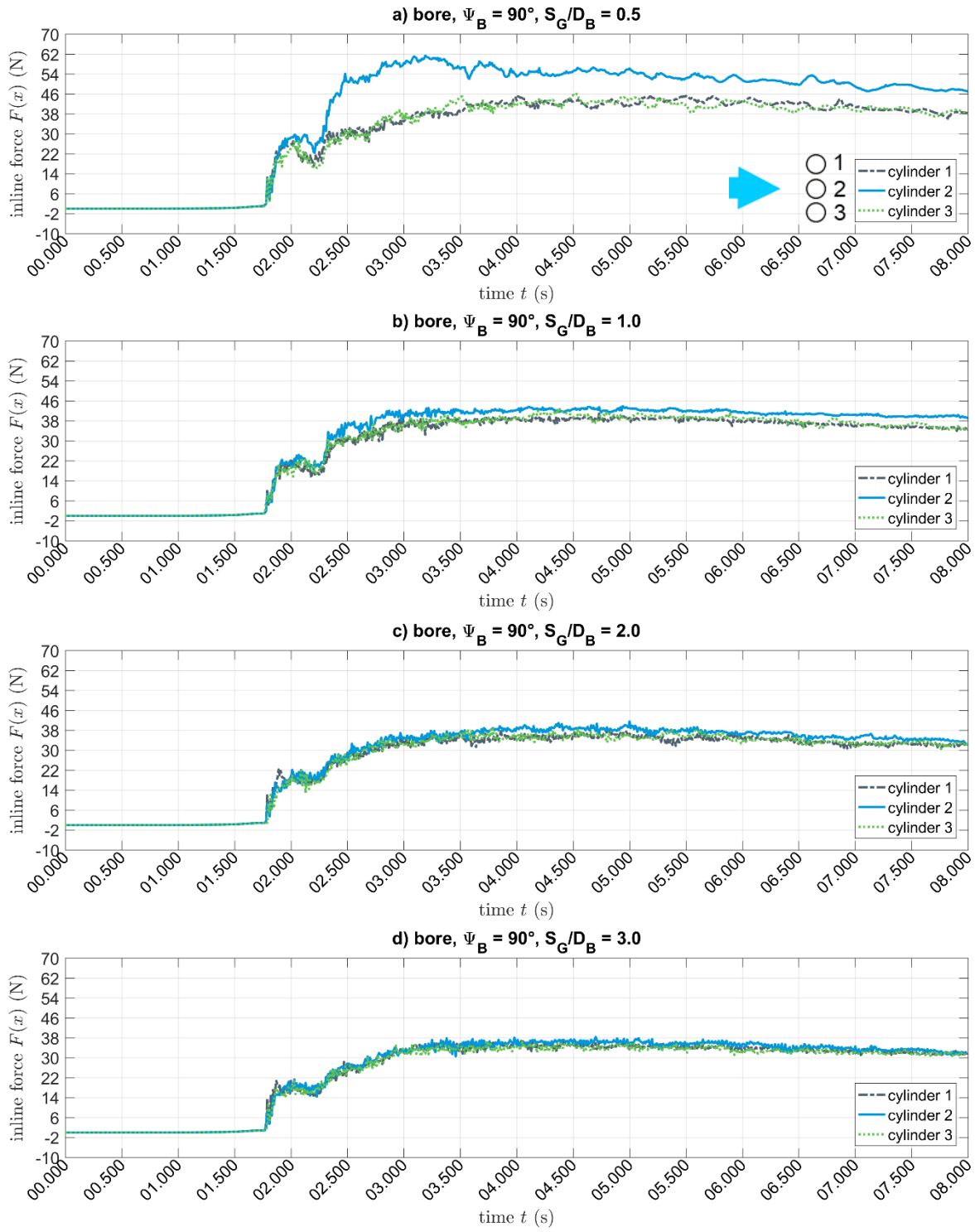

Figure B.6. Inline forces on three cylinders in side-by-side arrangement subject to a bore. Distance between the cylinders: a) 0.5 D_B, b) 1.0 D_B, c) 2.0 D_B and d) 3.0 D_B.

B.4 Inline forces on three cylinders in staggered 2 arrangement (Ψ_B = 135°)

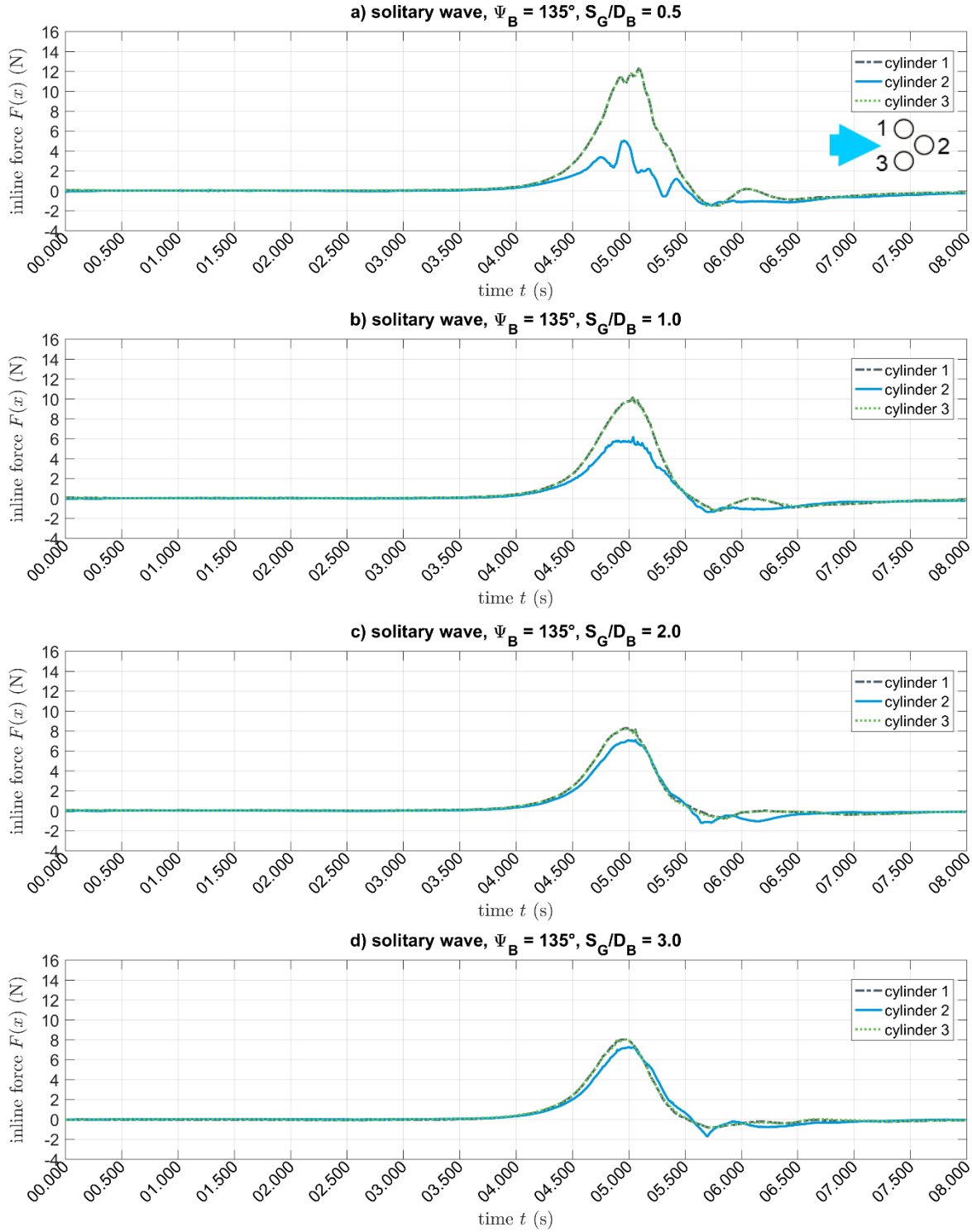

Figure B.7. Inline forces on three cylinders in staggered 2 arrangement subject to a solitary wave. Distance between the cylinders: a) 0.5 D_B, b) 1.0 D_B, c) 2.0 D_B and d) 3.0 D_B.

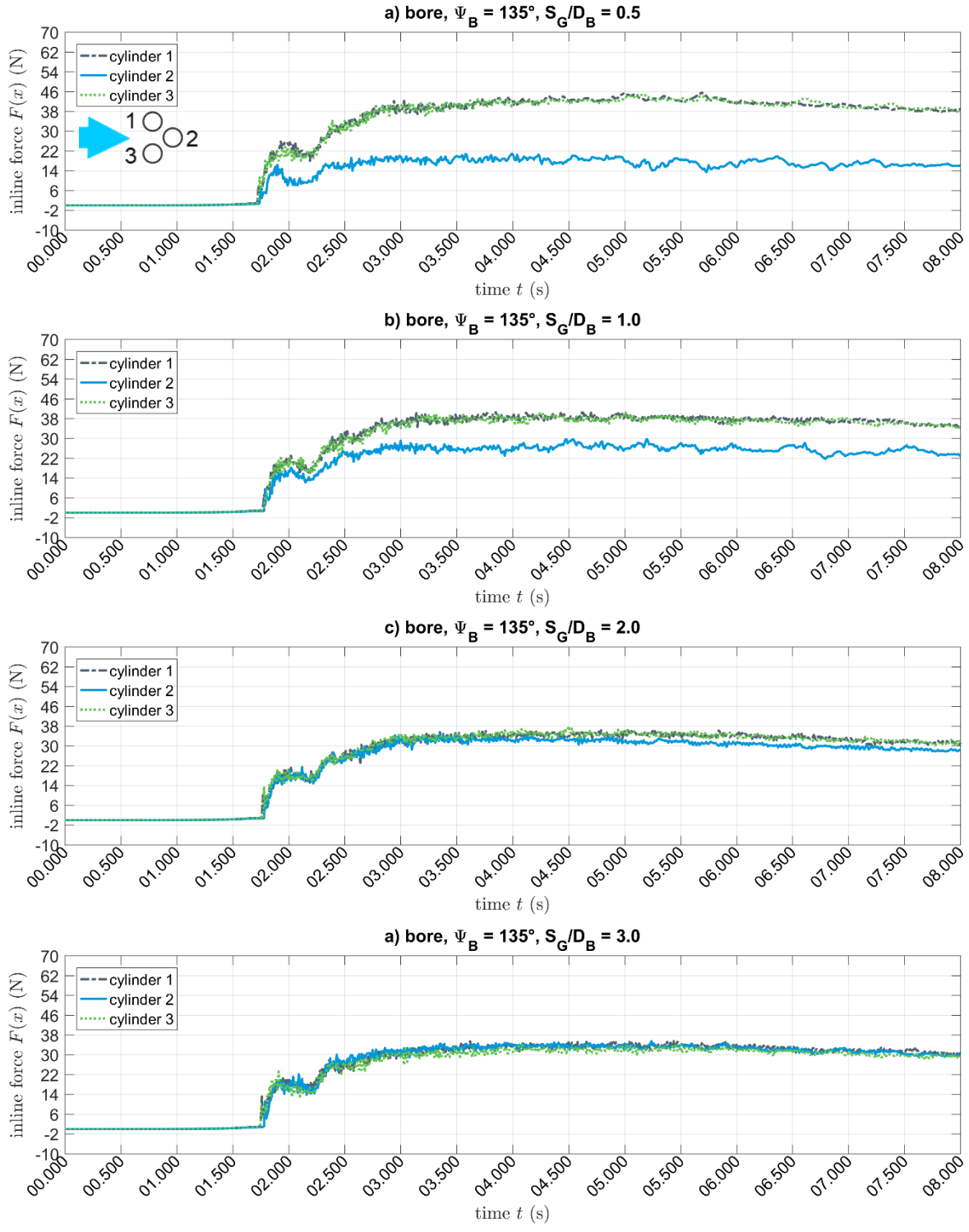

Figure B.8. Inline forces on three cylinders in staggered 2 arrangement subject to a bore. Distance between the cylinders: a) 0.5 D_B, b) 1.0 D_B, c) 2.0 D_B and d) 3.0 D_B.

Appendix C Averaged flow depths, flow velocities and volume fluxes

This appendix contains time series data and statistical parameters of the numerical testing programme. Averaged flow depth, depth-averaged flow velocities and integrated volume fluxes are presented for six cross-sections throughout the macro-roughness element (MRE) zone. Section C.1 is dedicated to the time series data. Section C.2 contains the statistical parameters.

C.1 Time series of flow depth, velocity and volume flux

This section contains time series data of flow depth, flow velocity and volume flux. In each cross-section, the flow depth is calculated from the phase fraction of the 3D model results. The flow velocities are integrated over each computational cell of the 3D model results, taking into account the phase fraction and the size of each cell. The volume flux is determined by integrating the flow velocities weighted with the phase fractions, the cell sizes. The data is then temporarily averaged based on the depth-averaged flow velocities and the distance between the cross-sections. Here, a distance of 0.6 m is considered. For details, please refer to chapter 5, sections 5.3 and 5.4.

C.1.1 Case 0.0: Reference case without any macro-roughness elements

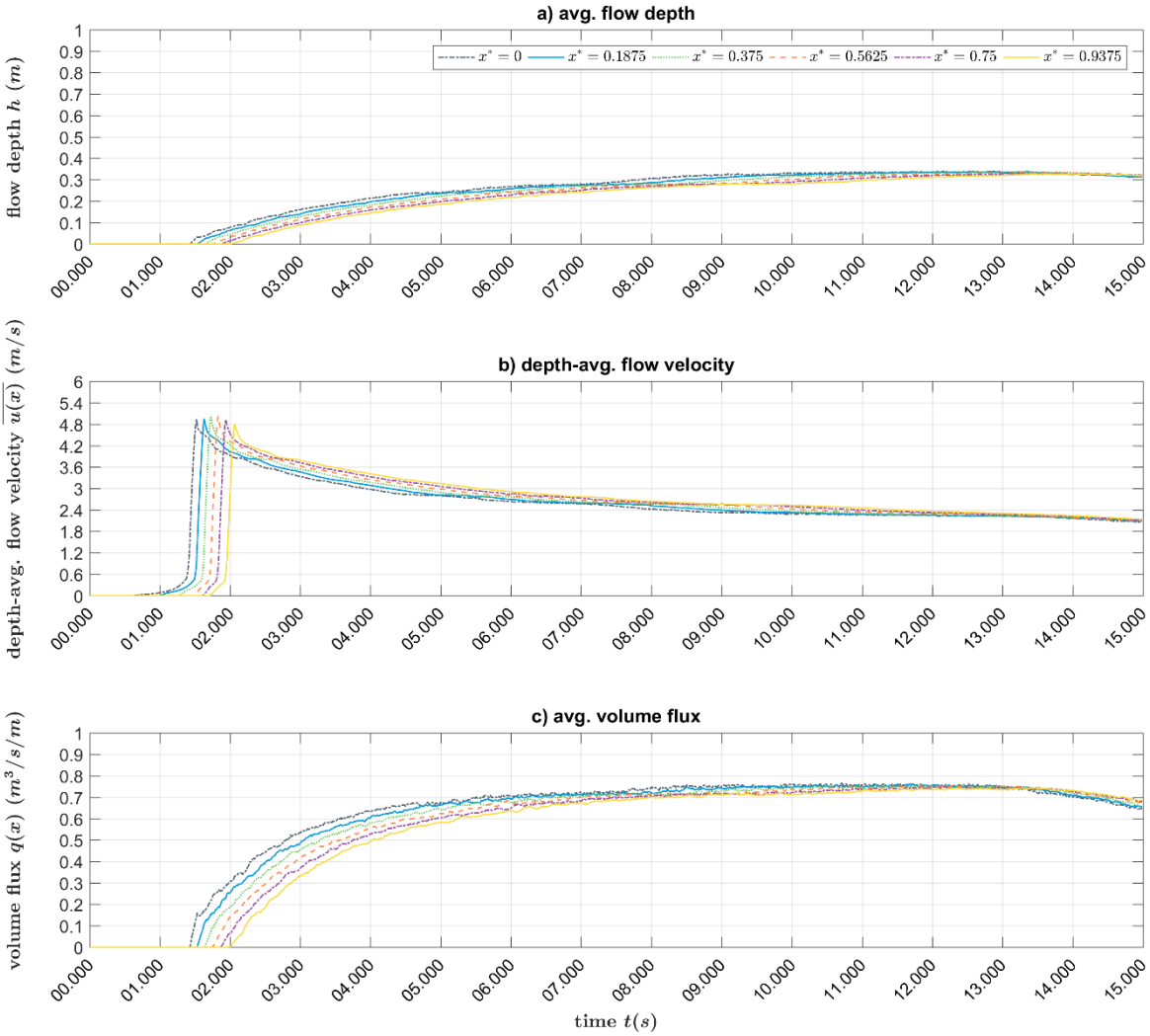

Figure C.1. Time series at cross-sections x^* = {0; 0.1875; 0.375; 0.5625; 0.75; 0.9375}, case 0.0 (reference case without any MRE): a) averaged flow depths, b) depth-averaged flow velocities, c) averaged volume fluxes.

C.1.2 Case 1.0: Basic configuration

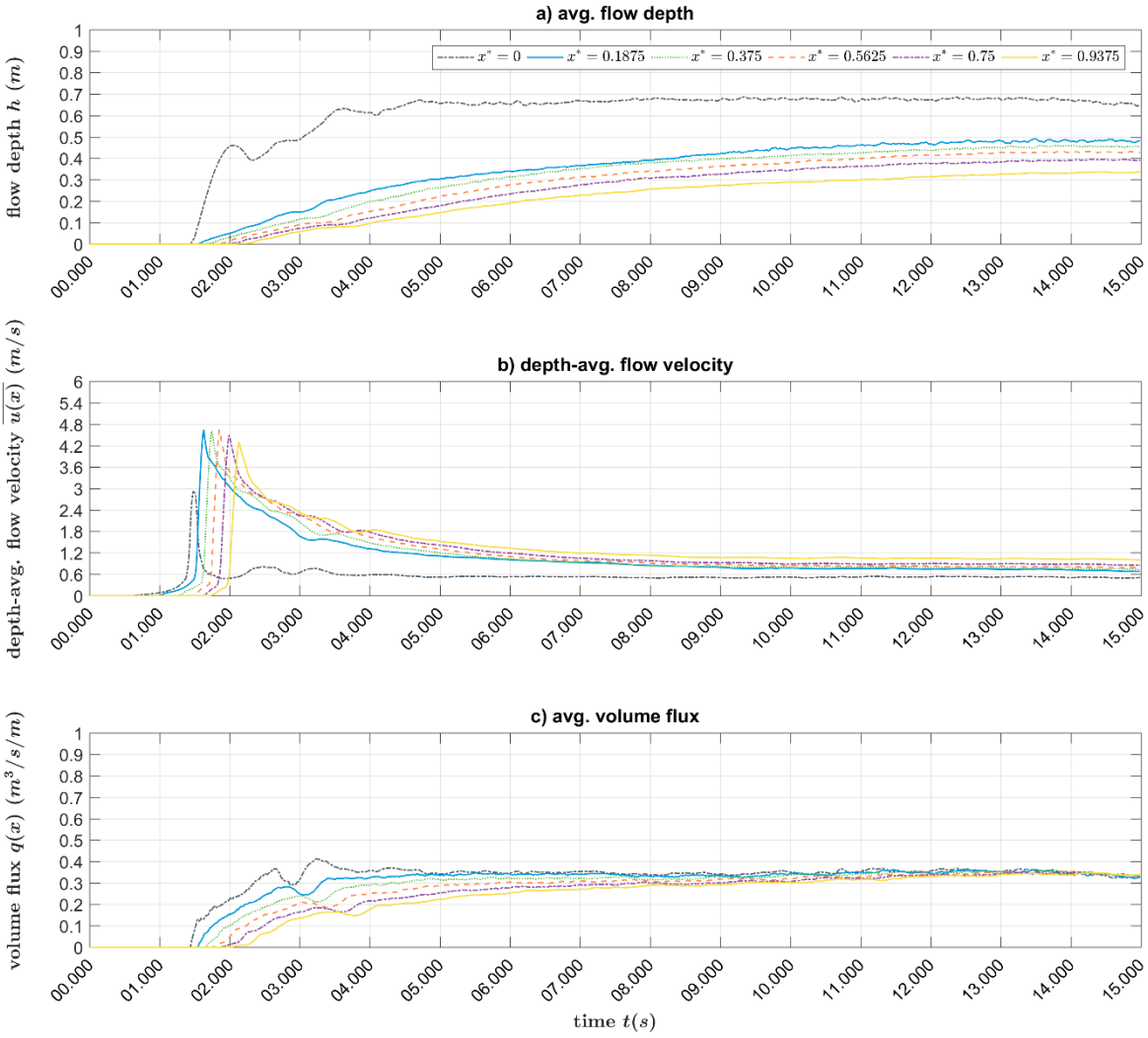

Figure C.2. Time series at cross-sections x^* = {0; 0.1875; 0.375; 0.5625; 0.75; 0.9375}, case 1.0 (basic configuration): a) averaged flow depths, b) depth-averaged flow velocities, c) averaged volume fluxes.

C.1.3 Cases 1.1 and 1.2: Variation of the shape

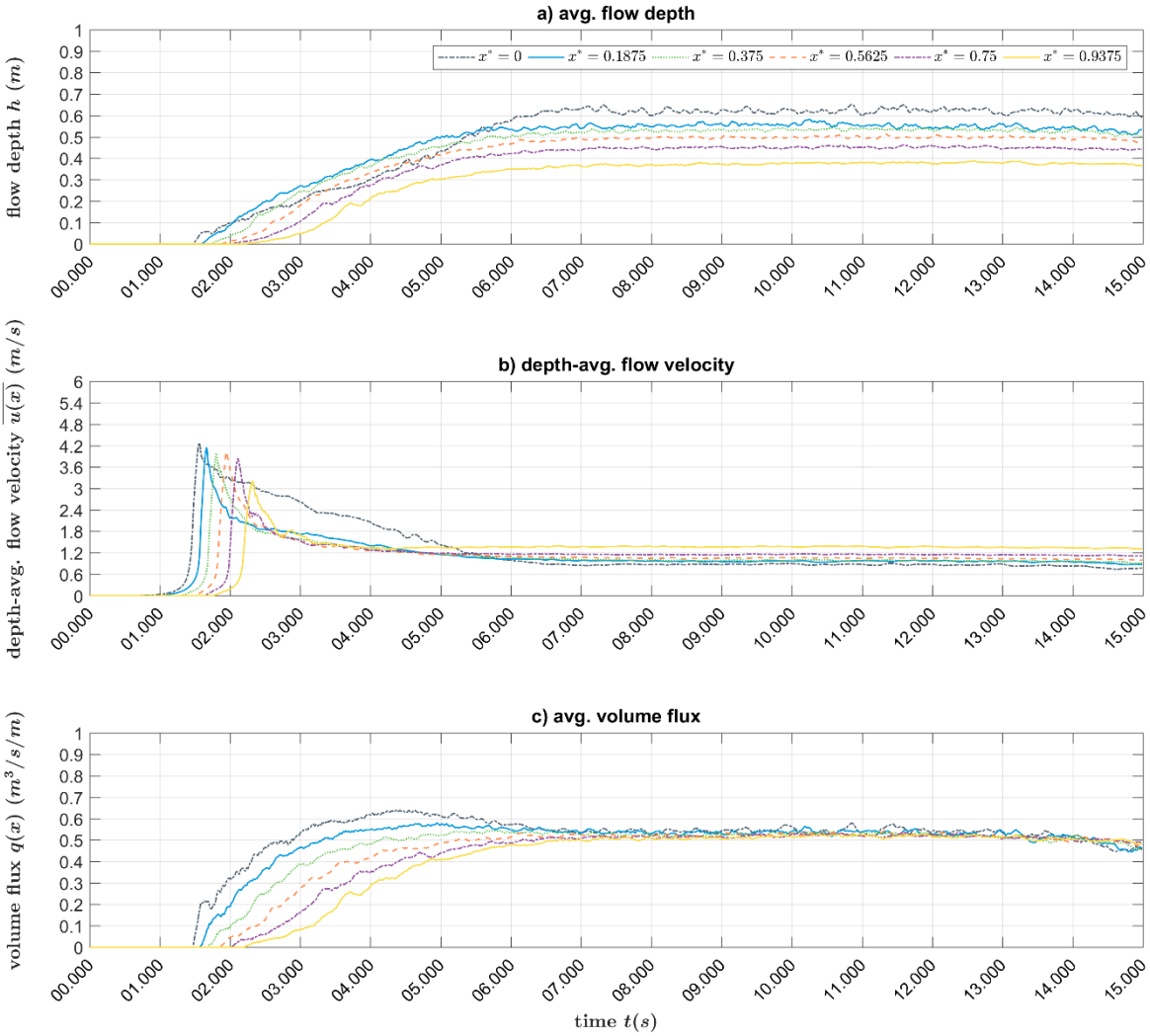

Figure C.3. Time series at cross-sections $x^* = \{0; 0.1875; 0.375; 0.5625; 0.75; 0.9375\}$, case 1.1 (cylindrical shape), a) averaged flow depths, b) depth-averaged flow velocities, c) averaged volume fluxes.

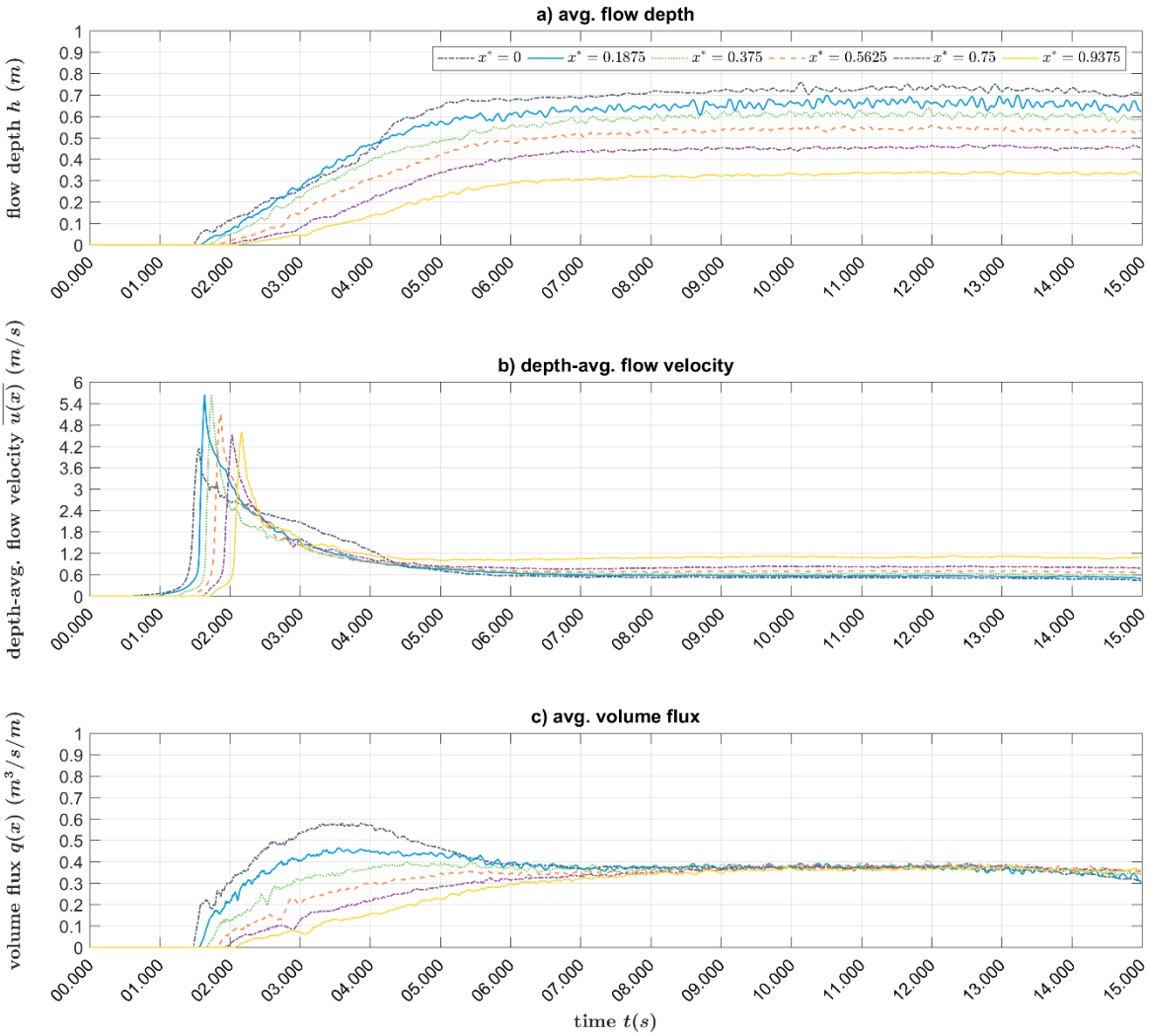

Figure C.4. Time series at cross-sections x^* = {0; 0.1875; 0.375; 0.5625; 0.75; 0.9375}, case 1.2 (diamond-shaped), a) averaged flow depths, b) depth-averaged flow velocities, c) averaged volume fluxes.

C.1.4 Cases 2.1 and 2.2: Variation of the relative width

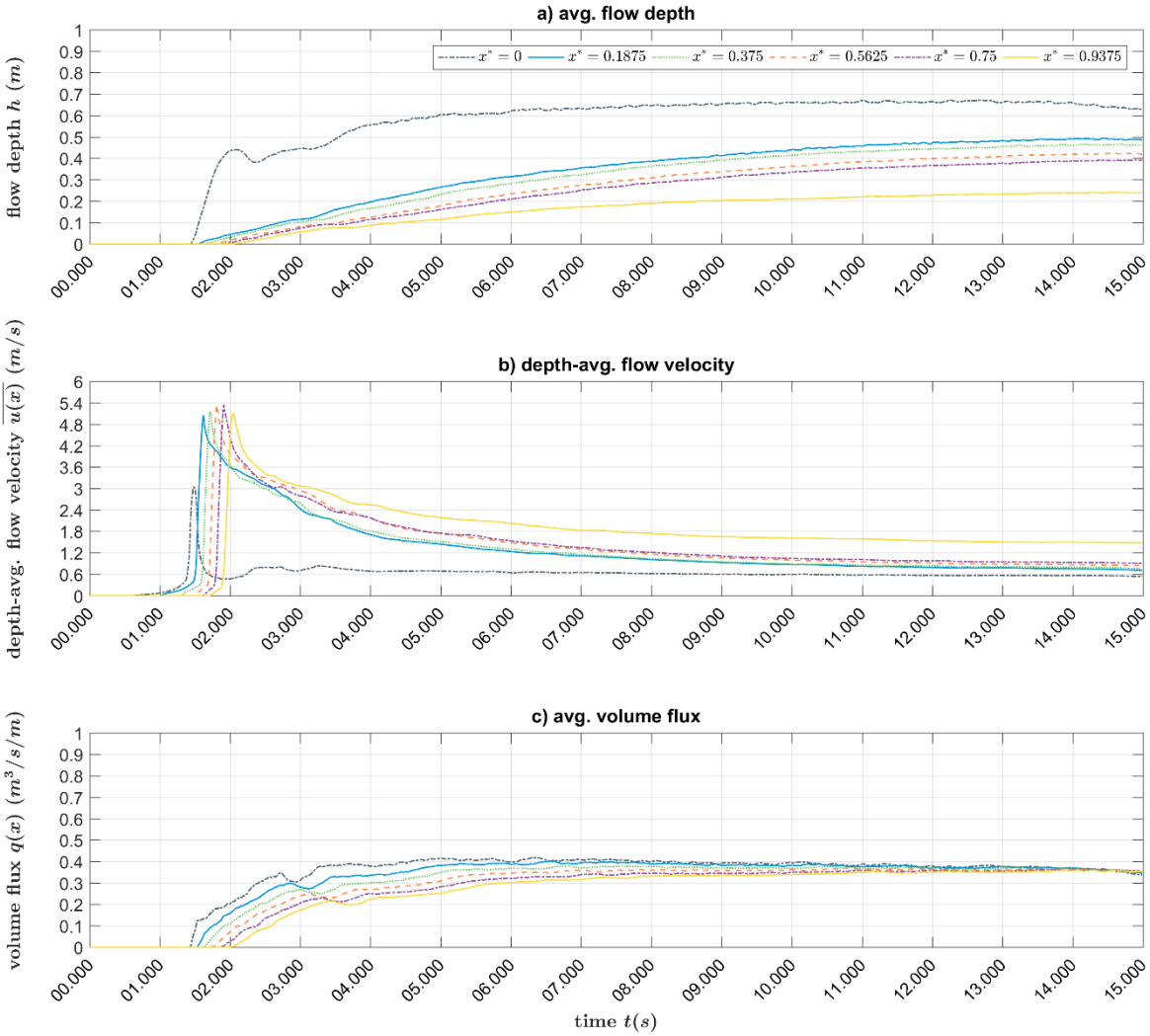

Figure C.5. Time series at cross-sections x^* = {0; 0.1875; 0.375; 0.5625; 0.75; 0.9375}, case 2.1 (D_B/h_{max} = 0.232), a) averaged flow depths, b) depth-averaged flow velocities, c) averaged volume fluxes.

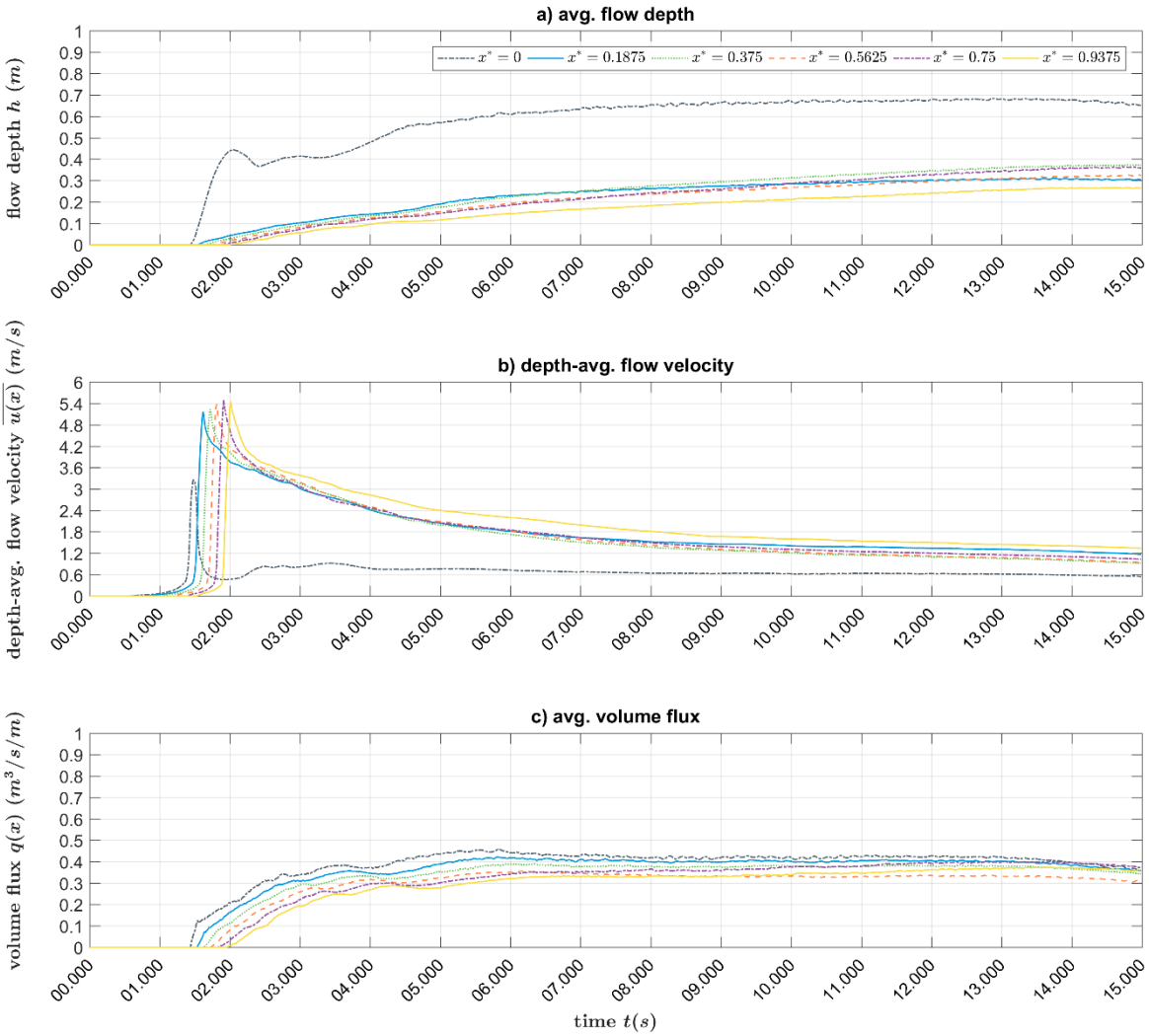

Figure C.6. Time series at cross-sections x^* = {0; 0.1875; 0.375; 0.5625; 0.75; 0.9375}, case 2.2 (D_B/h_{max} = 0.464), a) averaged flow depths, b) depth-averaged flow velocities, c) averaged volume fluxes.

C.1.5 Cases 3.1 and 3.2: Variation of the arrangement

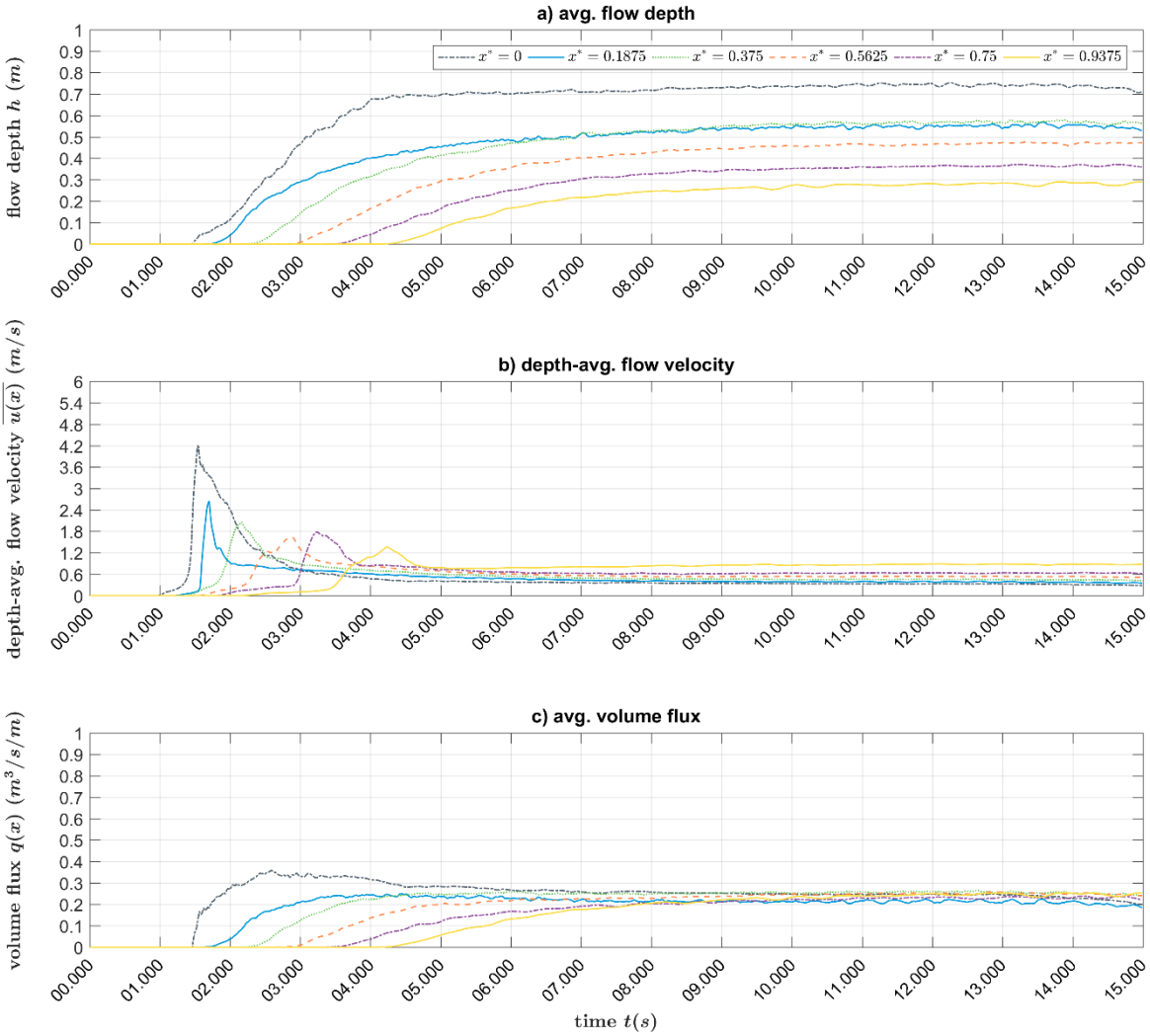

Figure C.7. Time series at cross-sections x^* = {0; 0.1875; 0.375; 0.5625; 0.75; 0.9375}, case 3.1 (arctanΨ = 0.5), a) averaged flow depths, b) depth-averaged flow velocities, c) averaged volume fluxes.

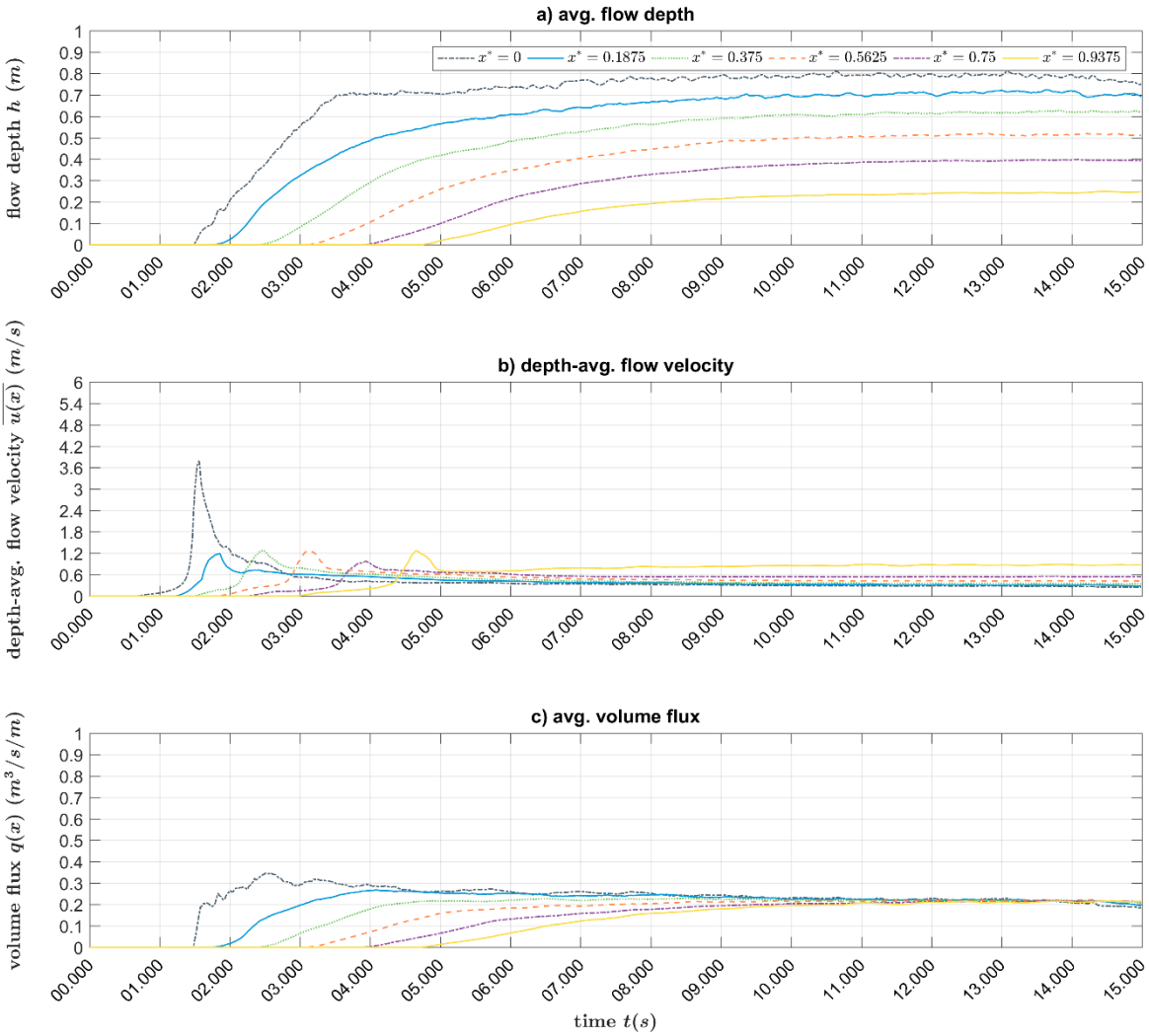

Figure C.8. Time series at cross-sections $x^* = \{0;\ 0.1875;\ 0.375;\ 0.5625;\ 0.75;\ 0.9375\}$, case 3.2 ($\arctan\Psi = 1.0$), a) averaged flow depths, b) depth-averaged flow velocities, c) averaged volume fluxes.

C.1.6 Cases 4.1 to 4.4: Variation of the relative spacing

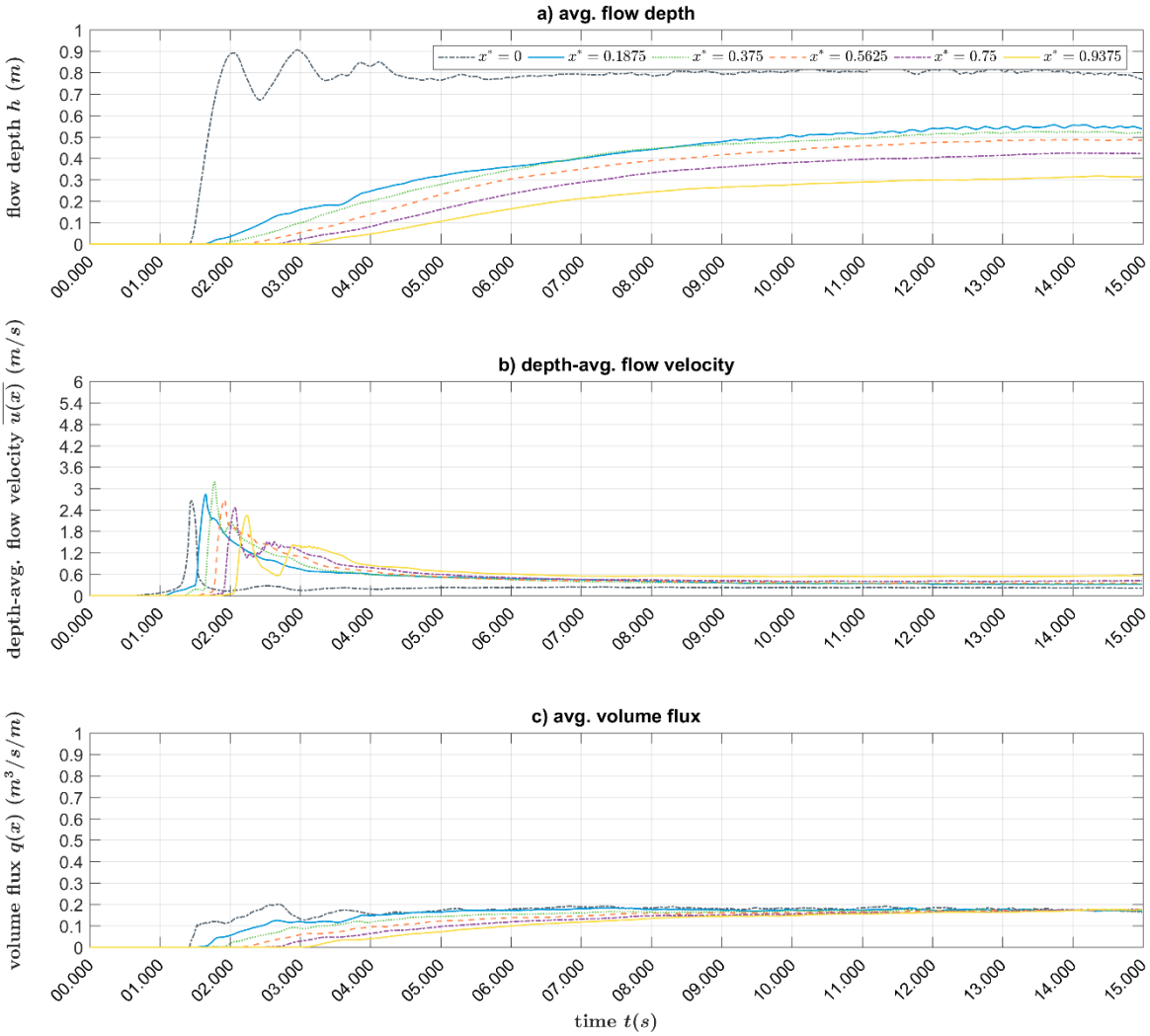

Figure C.9. Time series at cross-sections x^* = {0; 0.1875; 0.375; 0.5625; 0.75; 0.9375}, case 4.1 (S_G/D_B = 0.5), a) averaged flow depths, b) depth-averaged flow velocities, c) averaged volume fluxes.

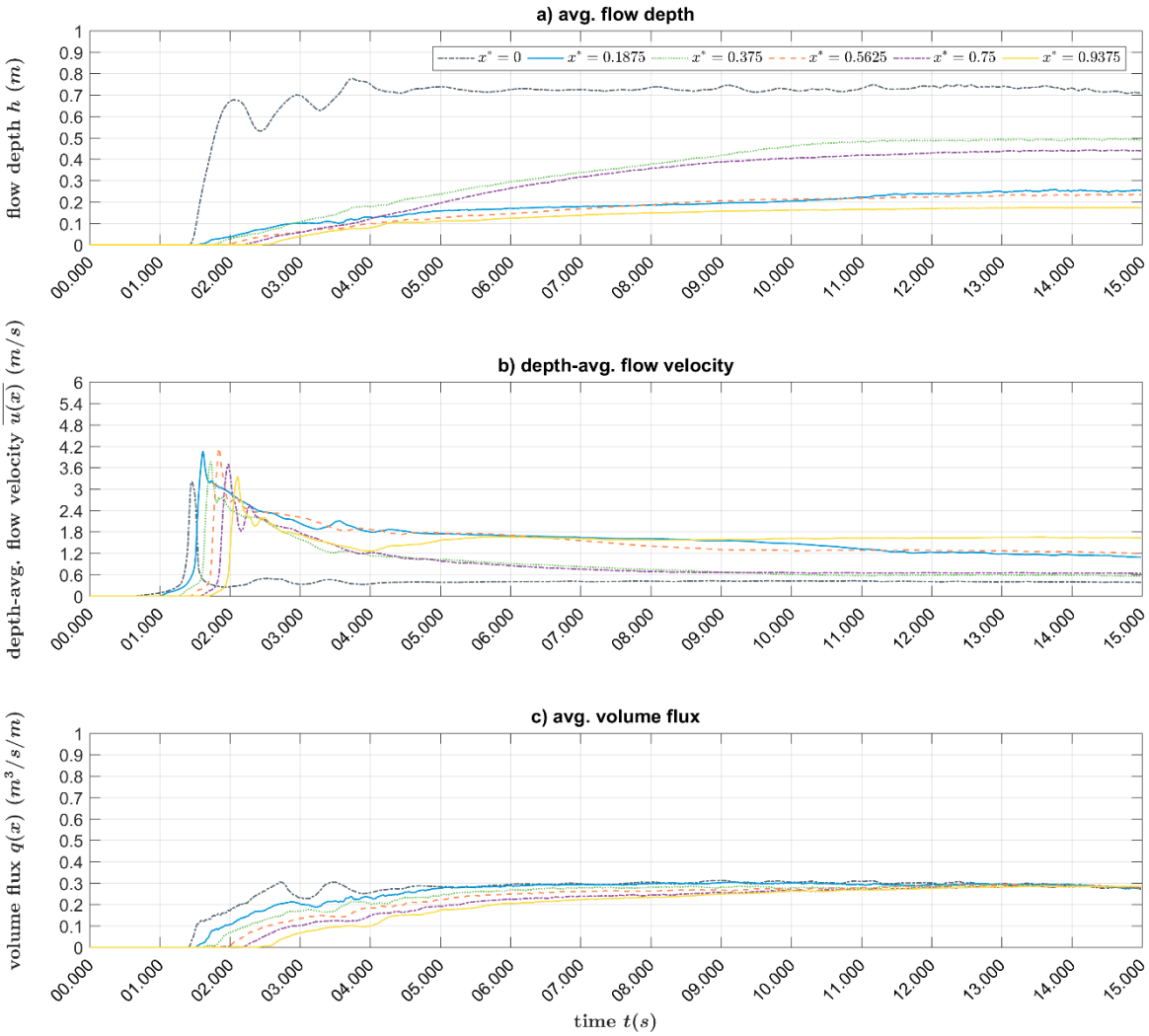

Figure C.10. Time series at cross-sections x^* = {0; 0.1875; 0.375; 0.5625; 0.75; 0.9375}, case 4.2 (S_G/D_B = 1.0), a) averaged flow depths, b) depth-averaged flow velocities, c) averaged volume fluxes.

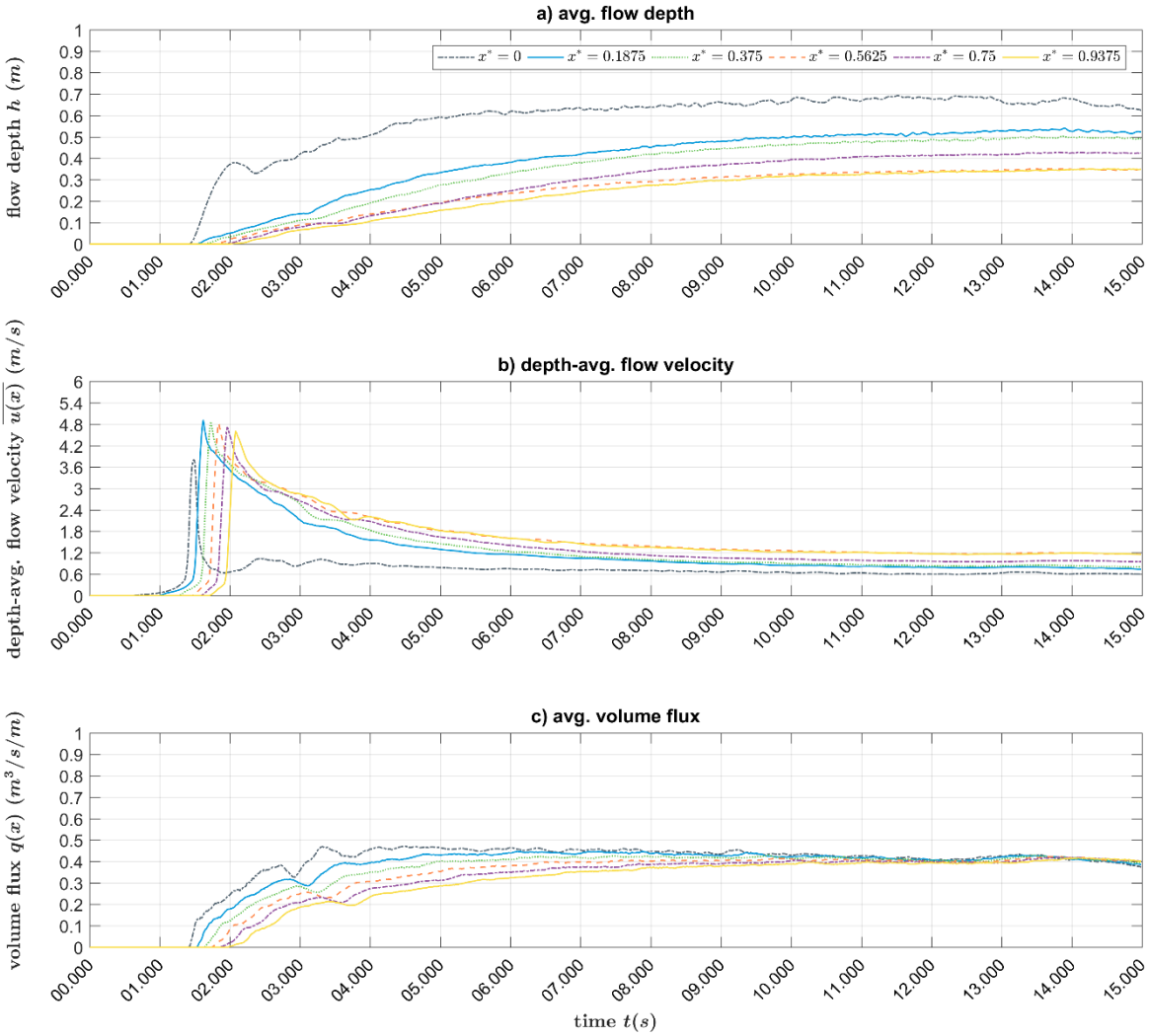

Figure C.11. Time series at cross-sections x^* = {0; 0.1875; 0.375; 0.5625; 0.75; 0.9375}, case 4.3 (S_G/D_B = 3.0), a) averaged flow depths, b) depth-averaged flow velocities, c) averaged volume fluxes.

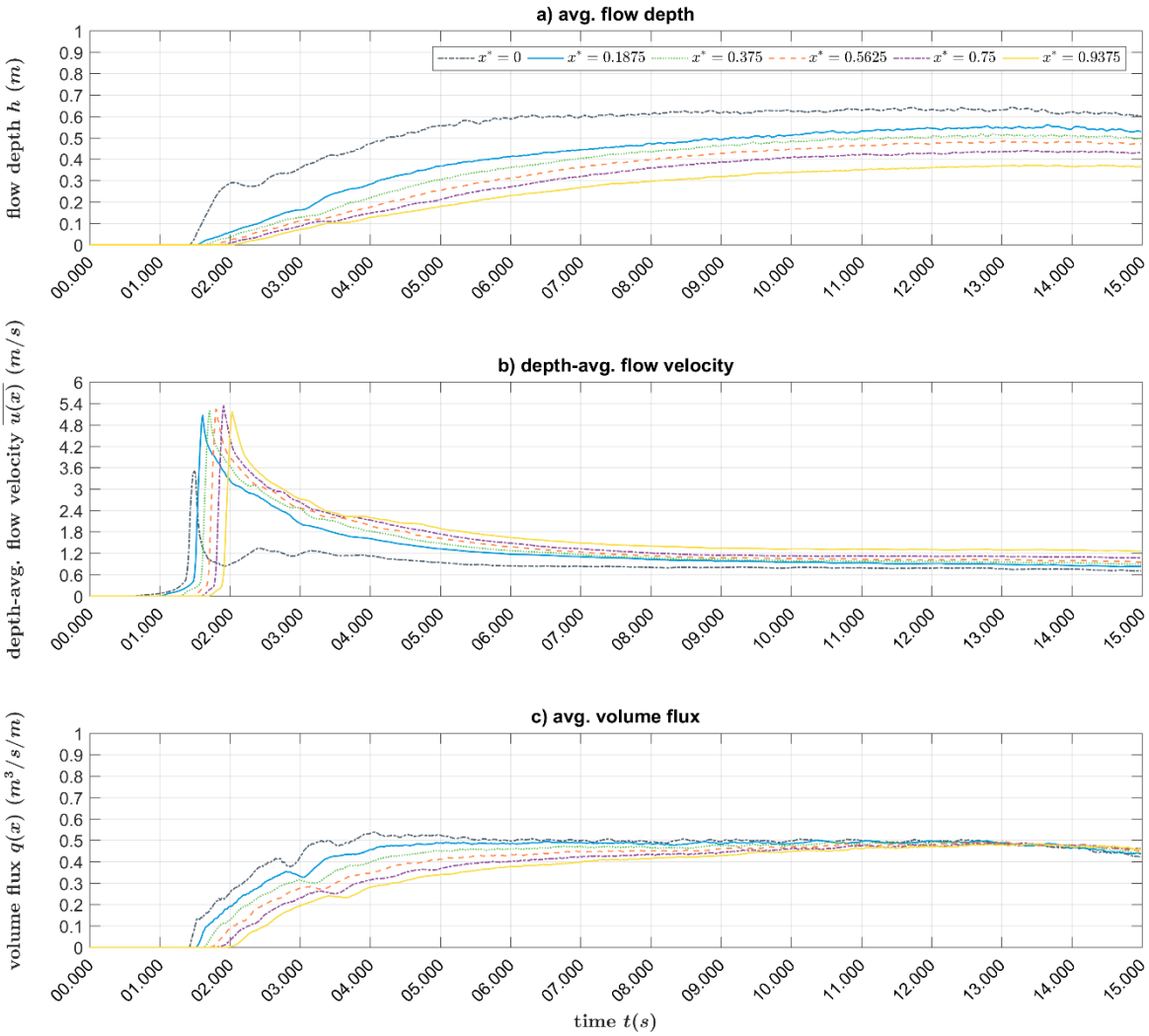

Figure C.12. Time series at cross-sections x^* = {0; 0.1875; 0.375; 0.5625; 0.75; 0.9375}, case 4.4 (S_G/D_B = 4.0), a) averaged flow depths, b) depth-averaged flow velocities, c) averaged volume fluxes.

C.1.7 Cases 5.1 to 5.4: Variation of the relative height

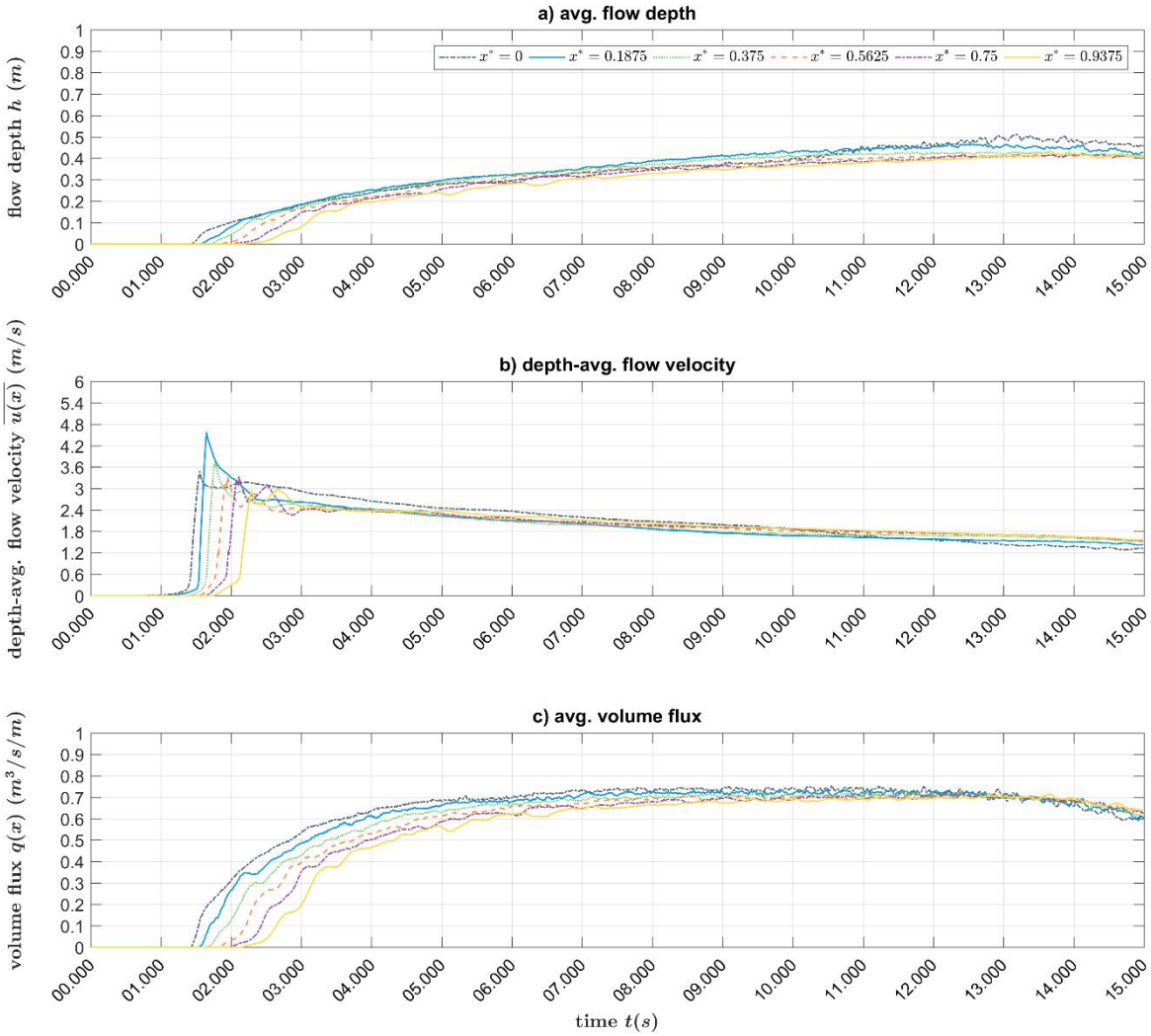

Figure C.13. Time series at cross-sections x^* = {0; 0.1875; 0.375; 0.5625; 0.75; 0.9375}, case 5.1 (h_B/h_{max} = 0.25), a) averaged flow depths, b) depth-averaged flow velocities, c) averaged volume fluxes.

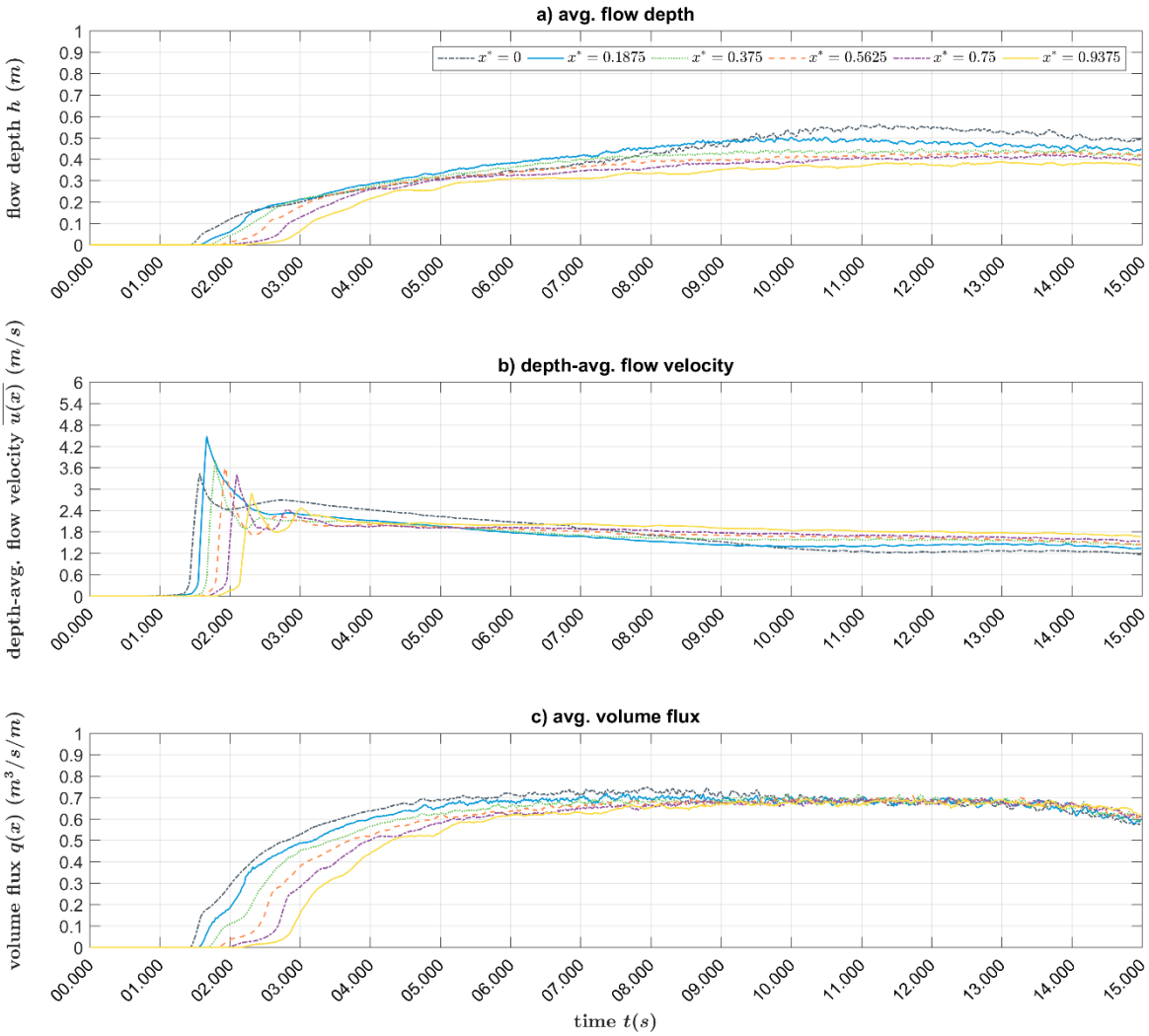

Figure C.14. Time series at cross-sections x^* = {0; 0.1875; 0.375; 0.5625; 0.75; 0.9375}, case 5.2 (h_B/h_{max} = 0.5), a) averaged flow depths, b) depth-averaged flow velocities, c) averaged volume fluxes.

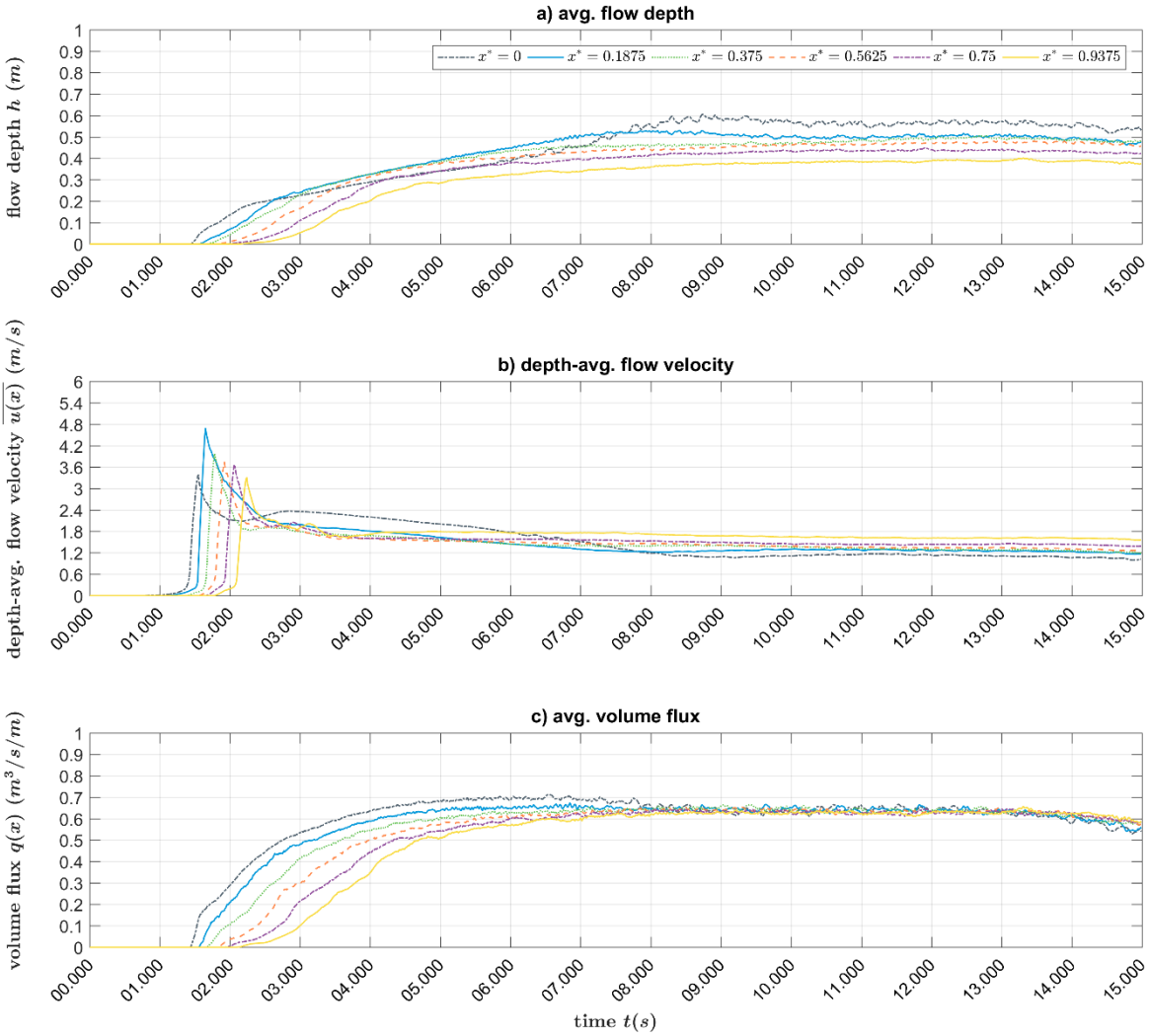

Figure C.15. Time series at cross-sections x^* = {0; 0.1875; 0.375; 0.5625; 0.75; 0.9375}, case 5.3 (h_B/h_{max} = 0.75), a) averaged flow depths, b) depth-averaged flow velocities, c) averaged volume fluxes.

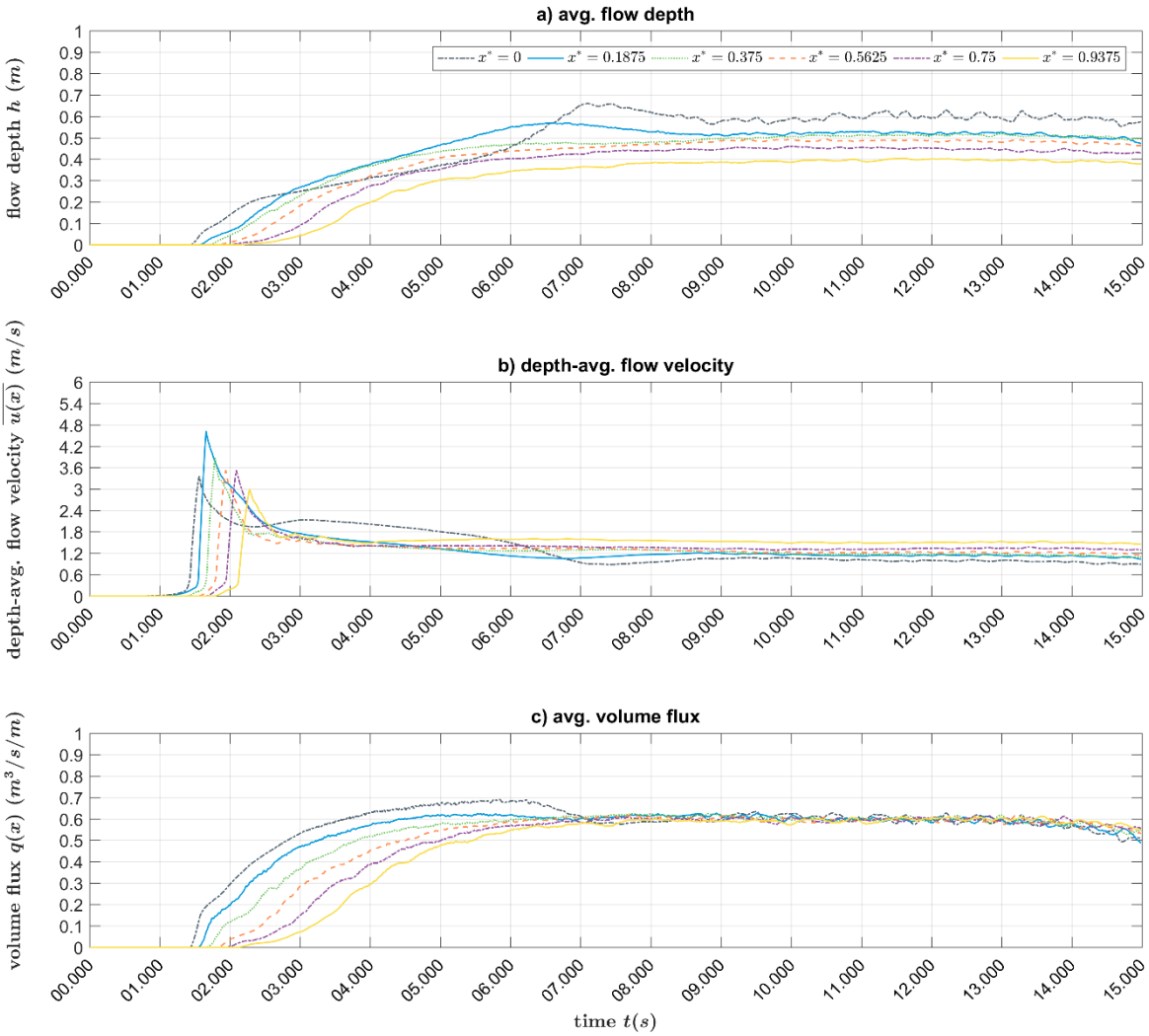

Figure C.16. Time series at cross-sections x^* = {0; 0.1875; 0.375; 0.5625; 0.75; 0.9375}, case 5.4 (h_B/h_{max} = 1.0), a) averaged flow depths, b) depth-averaged flow velocities, c) averaged volume fluxes.

C.2 Data tables

This section contains the tables of mean values and standard deviations of the change of the averaged volume flux between neighbouring cross-sections for the segments I to VI. The values are representative for time frames of Δt = 3 s during the steady and the unsteady phase of bore propagation. In order to assess the impact of the macro-roughness element (MRE) parameter variations, the mean values of the reference case without any MRE have been subtracted from each case. For details, please refer to chapter 5, section 5.4.

C.2.1 Unsteady phase of bore propagation

Table C.1. Mean values of the averaged volume flux change during the unsteady phase of bore propagation.

segment / case	I	II	III	IV	V	VI
1.0: Basic configuration [m³/s/m²]	-0.293	-0.033	-0.024	-0.015	-0.015	-0.013
1.1: Shape, cylinder [m³/s/m²]	-0.007	-0.066	-0.078	-0.067	-0.075	-0.069
1.2: Shape, diamond [m³/s/m²]	-0.052	-0.106	-0.103	-0.097	-0.092	-0.084
2.1: Relative width, D_B/h_{max} = 0.232 [m³/s/m²]	-0.292	-0.025	-0.017	-0.012	-0.011	-0.007
2.2: Relative width, D_B/h_{max} = 0.464 [m³/s/m²]	-0.296	-0.010	0.003	0.002	-0.001	0.005
3.1: Arrangement, $arctan\Psi$ = 0.5 [m³/s/m²]	-0.332	-0.120	-0.070	-0.063	0.002	-0.060
3.2: Arrangement, $arctan\Psi$ = 1.0 [m³/s/m²]	-0.355	-0.075	-0.071	-0.081	-0.085	-0.076
4.1: Relative spacing, S_G/D_B = 0.5 [m³/s/m²]	-0.553	0.003	0.0065	0.008	0.002	-0.002
4.2: Relative spacing, S_G/D_B = 1.0 [m³/s/m²]	-0.414	-0.023	-0.019	-0.002	-0.006	0.003
4.3: Relative spacing, S_G/D_B = 3.0 [m³/s/m²]	-0.21	-0.046	-0.036	-0.029	-0.026	-0.021
4.4: Relative spacing, S_G/D_B = 4.0 [m³/s/m²]	-0.143	-0.052	-0.041	-0.033	-0.033	-0.0268
5.1: Relative height, h_B/h_{max} = 0.25 [m³/s/m²]	0.004	-0.007	-0.009	-0.010	-0.022	-0.019
5.2: Relative height, h_B/h_{max} = 0.5 [m³/s/m²]	-0.003	-0.018	-0.029	-0.027	-0.037	-0.036
5.3: Relative height, h_B/h_{max} = 0.75 [m³/s/m²]	-0.003	-0.031	-0.048	-0.049	-0.057	-0.054
5.4: Relative height, h_B/h_{max} = 1.0 [m³/s/m²]	-0.013	-0.048	-0.075	-0.070	-0.071	-0.070

Table C.2. Standard deviations of the averaged volume flux change during the unsteady phase of bore propagation.

segment / case	I	II	III	IV	V	VI
1.0: Basic configuration [m³/s/m²]	0.142	0.052	0.042	0.031	0.028	0.023
1.1: Shape, cylinder [m³/s/m²]	0.032	0.028	0.026	0.027	0.030	0.033
1.2: Shape, diamond [m³/s/m²]	0.083	0.044	0.039	0.034	0.038	0.038
2.1: Relative width, D_B/h_{max} = 0.232 [m³/s/m²]	0.119	0.030	0.029	0.025	0.022	0.020
2.2: Relative width, D_B/h_{max} = 0.464 [m³/s/m²]	0.115	0.036	0.021	0.021	0.021	0.014
3.1: Arrangement, $arctan\Psi$ = 0.5 [m³/s/m²]	0.202	0.074	0.062	0.059	0.056	0.047
3.2: Arrangement, $arctan\Psi$ = 1.0 [m³/s/m²]	0.215	0.107	0.077	0.062	0.053	0.046
4.1: Relative spacing, S_G/D_B = 0.5 [m³/s/m²]	0.234	0.036	0.025	0.021	0.017	0.017
4.2: Relative spacing, S_G/D_B = 1.0 [m³/s/m²]	0.182	0.041	0.030	0.021	0.018	0.018
4.3: Relative spacing, S_G/D_B = 3.0 [m³/s/m²]	0.095	0.043	0.037	0.032	0.028	0.025
4.4: Relative spacing, S_G/D_B = 4.0 [m³/s/m²]	0.060	0.039	0.035	0.030	0.027	0.024
5.1: Relative height, h_B/h_{max} = 0.25 [m³/s/m²]	0.013	0.021	0.024	0.025	0.027	0.031
5.2: Relative height, h_B/h_{max} = 0.5 [m³/s/m²]	0.019	0.030	0.056	0.047	0.050	0.051
5.3: Relative height, h_B/h_{max} = 0.75 [m³/s/m²]	0.016	0.021	0.040	0.039	0.041	0.040
5.4: Relative height, h_B/h_{max} = 1.0 [m³/s/m²]	0.013	0.020	0.036	0.032	0.036	0.039

C.2.2 Steady phase of bore propagation

Table C.3. Mean values of the averaged volume flux change during the steady phase of bore propagation.

segment / case	I	II	III	IV	V	VI
1.0: Basic configuration [m³/s/m²]	-0.677	-0.013	-0.012	-0.010	-0.007	-0.010
1.1: Shape, cylinder [m³/s/m²]	-0.349	-0.005	-0.010	-0.004	-0.004	0.000
1.2: Shape, diamond [m³/s/m²]	-0.633	0.001	0.016	0.009	0.014	0.013
2.1: Relative width, D_B/h_{max} = 0.232 [m³/s/m²]	-0.617	-0.011	-0.010	-0.010	-0.010	-0.012
2.2: Relative width, D_B/h_{max} = 0.464 [m³/s/m²]	-0.536	-0.035	-0.001	-0.015	-0.038	0.065
3.1: Arrangement, $arctan\Psi$ = 0.5 [m³/s/m²]	-0.838	-0.052	-0.012	0.012	0.070	0.011
3.2: Arrangement, $arctan\Psi$ = 1.0 [m³/s/m²]	-0.876	-0.003	-0.003	-0.003	-0.005	-0.002
4.1: Relative spacing, S_G/D_B = 0.5 [m³/s/m²]	-0.547	-0.014	-0.005	-0.009	-0.007	-0.009
4.2: Relative spacing, S_G/D_B = 1.0 [m³/s/m²]	-0.532	-0.010	-0.017	-0.007	-0.012	-0.002
4.3: Relative spacing, S_G/D_B = 3.0 [m³/s/m²]	-0.558	-0.010	-0.009	-0.007	-0.008	-0.008
4.4: Relative spacing, S_G/D_B = 4.0 [m³/s/m²]	-0.417	-0.004	-0.006	-0.003	-0.004	-0.002
5.1: Relative height, h_B/h_{max} = 0.25 [m³/s/m²]	-0.064	-0.014	-0.011	-0.003	-0.003	-0.003
5.2: Relative height, h_B/h_{max} = 0.5 [m³/s/m²]	-0.123	-0.006	-0.004	0.010	0.014	0.004
5.3: Relative height, h_B/h_{max} = 0.75 [m³/s/m²]	-0.161	0.002	0.005	0.003	0.001	0.004
5.4: Relative height, h_B/h_{max} = 1.0 [m³/s/m²]	-0.165	-0.025	-0.023	0.005	0.007	0.005

Table C.4. Standard deviations of the averaged volume flux change during the steady phase of bore propagation.

segment / case	I	II	III	IV	V	VI
1.0: Basic configuration [m³/s/m²]	0.011	0.014	0.013	0.011	0.011	0.009
1.1: Shape, cylinder [m³/s/m²]	0.024	0.029	0.032	0.021	0.019	0.016
1.2: Shape, diamond [m³/s/m²]	0.010	0.018	0.020	0.016	0.019	0.020
2.1: Relative width, D_B/h_{max} = 0.232 [m³/s/m²]	0.017	0.010	0.011	0.011	0.009	0.009
2.2: Relative width, D_B/h_{max} = 0.464 [m³/s/m²]	0.019	0.010	0.011	0.010	0.008	0.010
3.1: Arrangement, $arctan\Psi$ = 0.5 [m³/s/m²]	0.016	0.016	0.014	0.015	0.015	0.012
3.2: Arrangement, $arctan\Psi$ = 1.0 [m³/s/m²]	0.012	0.013	0.013	0.012	0.009	0.009
4.1: Relative spacing, S_G/D_B = 0.5 [m³/s/m²]	0.237	0.012	0.010	0.011	0.010	0.010
4.2: Relative spacing, S_G/D_B = 1.0 [m³/s/m²]	0.130	0.011	0.010	0.011	0.010	0.012
4.3: Relative spacing, S_G/D_B = 3.0 [m³/s/m²]	0.016	0.011	0.011	0.010	0.009	0.009
4.4: Relative spacing, S_G/D_B = 4.0 [m³/s/m²]	0.019	0.012	0.011	0.013	0.011	0.010
5.1: Relative height, h_B/h_{max} = 0.25 [m³/s/m²]	0.021	0.023	0.024	0.026	0.020	0.021
5.2: Relative height, h_B/h_{max} = 0.5 [m³/s/m²]	0.021	0.029	0.029	0.027	0.023	0.025
5.3: Relative height, h_B/h_{max} = 0.75 [m³/s/m²]	0.050	0.038	0.039	0.023	0.020	0.019
5.4: Relative height, h_B/h_{max} = 1.0 [m³/s/m²]	0.090	0.073	0.055	0.029	0.024	0.026

Appendix D Dimensional analysis and data tables

The appendix details data and procedure to derive the source term descriptions for the macro-roughness elements (MRE) in the non-linear shallow water momentum equation.

In section D.1, the dimensional analysis is a mathematical method to comprehend the relation between physical quantities without knowing the exact equation. The dimensionless constants that arise in the result obtained help to design experiments and to judge whether the parameters are important or not.

Section D.2 contains the data, which is post-processed from the CFD simulation results provided in Chapter 5. In section D.2.1, the results for analysing the cross-sections of various unit areas is stated. The data is then averaged over the unit areas. The data tables are provided in section D.2.2. They serve as data basis for the development of the MRE source term $S_{MRE,fit}$.

D.1 Dimensional analysis

First, the fundamental system is formed. Then, the systems of equations are derived, from which the dimensionless quantities are determined.

D.1.1 Fundamental system

The fundamental system reads as follows:

			M [kg]	**L [m]**	**T [s]**	**1.**	**2.**	**3.**	**4.**
k_1	Velocity	u	0	1	-1	k_1	k_1	k_1	k_1
k_2	Length	l	0	1	0	k_2	k_2	k_2	k_2
k_3	Area	A	0	2	0	0	0	0	0
k_4	Density	ρ	1	-3	0	k_4	k_4	k_4	k_4
k_5	Dynamic viscosity	μ	1	-1	-1	1	0	0	0
k_6	Acceleration	g	0	1	-2	0	1	0	0
k_7	Pressure	p	1	-1	-2	0	0	1	0
k_8	Force	F	1	1	-2	0	0	0	1

D.1.2 Systems of equations and solutions

$(\boldsymbol{k_1} \quad \boldsymbol{k_2} \quad \boldsymbol{0} \quad \boldsymbol{k_4} \quad \boldsymbol{1} \quad \boldsymbol{0} \quad \boldsymbol{0} \quad \boldsymbol{0})$

$0 = k_4 + 1$

$0 = k_1 + k_2 - 3k_4 - 13$

$0 = -k_1 - 1$

➔ $k_1 = -1, k_2 = -1, k_4 = -1$

➔ $\Pi_1 = \frac{ul\rho}{\mu} = Re$, Reynolds no.

$(k_1 \quad k_2 \quad 0 \quad k_4 \quad 0 \quad 1 \quad 0 \quad 0)$

$0 = k_4$

$0 = k_1 + k_2 - 3k_4 + 1$

$0 = -k_1 - 2$

➔ $k_1 = -2, k_2 = 1, k_4 = 0$

➔ $\Pi_2 = \frac{u^2}{la} = Fr$, Froude no.

$(\boldsymbol{k_1} \quad \boldsymbol{k_2} \quad \boldsymbol{0} \quad \boldsymbol{k_4} \quad \boldsymbol{0} \quad \boldsymbol{0} \quad \boldsymbol{1} \quad \boldsymbol{0})$

$0 = k_4 + 1$

$0 = k_1 + k_2 - 3k_4 - 1$

$0 = -k_1 - 2$

➔ $k_1 = -2, k_2 = 0, k_4 = -1$

➔ $\Pi_3 = \frac{P}{u^2\rho} = Eu$, Euler no.

$(\boldsymbol{k_1} \quad \boldsymbol{k_2} \quad \boldsymbol{0} \quad \boldsymbol{k_4} \quad \boldsymbol{0} \quad \boldsymbol{0} \quad \boldsymbol{0} \quad \boldsymbol{1})$

$0 = k_4 + 1$

$0 = k_1 + k_2 - 3k_4 + 1$

$0 = -k_1 - 2$

➔ $k_1 = -2, k_2 = -2, k_4 = -1$

➔ $\Pi_3 = \frac{F}{u^2 l^2 \rho} = Eu$, Euler no.

D.2 Post-processed CFD data

D.2.1 Data tables for various unit area lengths

The following tables summarize the relevant CFD data including the derived source term and the fitted source term. The data tables including the MRE and flow parameters averaged over various unit area sizes for all investigated conditions, the source terms and the fitted source terms are provided in this section. Table D.1 states the data for the edge zone under steady flow conditions, Table D.2 contains the data for the edge of the MRE zone under unsteady flow conditions, and Table D.3 provides the data for the inner edge zone under unsteady flow conditions.

Table D.1. Averaged data MRE and flow conditions at the edge of the MRE zone (segments I and II) under steady flow conditions.

Case	Description	Drag coefficient C_D [-]	Width D_B [m]	Spacing S_C [m]	Height h_B [m]	Arrangement angle $tan(\Psi)$ [-]	Flow depth h [m]	Volume flux $q(x)$ [m³/s/m]	Spat. Derivative of norm. width $\frac{\partial D_B^*}{\partial x}$ [1/m]	Relative effective height $\frac{h_{B,eff}}{h}$ [-]	Reynolds number Re [-]	Froude number Fr [-]	Source term S_{MRE} [m²/s²]	Fitted source term $S_{MRE,fit}$ [m²/s²]
1.0	Basic configuration	2.05	0.04	0.08	>h	0	0.517	0.539	0.238	2	149990	0.46	-0.361	-0.205
1.1		1.20	0.04	0.08	>h	0	0.511	0.657	0.238	2	183710	0.57	-0.136	-0.179
1.2	Shape variation	1.55	0.04	0.08	>h	0	0.585	0.577	0.238	2	150942	0.41	-0.123	-0.153
3.1		2.05	0.04	0.08	>h	0.5	0.591	0.492	0.238	2	128052	0.35	-0.185	-0.129
3.2	Arrangement variation	2.05	0.04	0.08	>h	1	0.621	0.492	0.238	2	124924	0.32	-0.155	-0.113
4.1		2.05	0.04	0.02	>h	0	0.555	0.480	0.476	2	128737	0.37	-0.506	-0.303
4.2		2.05	0.04	0.04	>h	0	0.546	0.517	0.357	2	140048	0.41	-0.378	-0.269
4.3		2.05	0.04	0.12	>h	0	0.534	0.577	0.179	2	157910	0.47	-0.223	-0.169
4.4	Normalized width variation	2.05	0.04	0.16	>h	0	0.522	0.618	0.143	2	171074	0.52	-0.159	-0.159
5.1		2.05	0.04	0.08	0.054	0	0.503	0.681	0.238	0.428	125766	0.61	-0.092	-0.071
5.2		2.05	0.04	0.08	0.108	0	0.484	0.700	0.238	0.333	116228	0.66	-0.067	-0.062
5.3		2.05	0.04	0.08	0.161	0	0.451	0.712	0.238	0.238	103589	0.75	-0.077	-0.049
5.4	Relative height variation	2.05	0.04	0.08	0.215	0	0.427	0.727	0.238	0.126	79046	0.83	-0.054	-0.031

Table D.2. Averaged data MRE and flow conditions at the edge MRE zone (segments I and II) under unsteady flow conditions.

Case	Description	Drag coefficient C_D [-]	Width D_B [m]	Spacing S_G [m]	Height h_B [m]	Arrangement angle $tan(\Psi)$ [-]	Flow depth h [m]	Volume flux $q(x)$ [m³/s/m]	Spat. Derivative of norm. width $\frac{\partial D_B^*}{\partial x}$ [1/m]	Relative effective height $\frac{h_{B,eff}}{h}$ [-]	Reynolds number Re [-]	Froude number Fr [-]	Source term S_{MRE} [m²/s²]	Fitted source term $S_{MRE,fit}$ [m²/s²]
1.0	Basic configuration	2.05	0.04	0.08	>h	0	0.220	0.384	0.238	2	163361	1.18	-0.279	-0.280
1.1		1.17	0.04	0.08	>h	0	0.124	0.323	0.238	2	183429	2.36	-0.192	-0.188
1.2	Shape variation	1.55	0.04	0.08	>h	0	0.134	0.301	0.238	2	164745	1.97	-0.246	-0.199
3.1		2.05	0.04	0.08	>h	0.5	0.260	0.366	0.238	2	143744	0.88	-0.387	-0.308
3.2	Arrangement variation	2.05	0.04	0.08	>h	1	0.353	0.447	0.238	2	150431	0.68	-0.401	-0.410
4.1		2.05	0.04	0.02	>h	0	0.340	0.434	0.476	2	148644	0.70	-0.398	-0.497
4.2		2.05	0.04	0.04	>h	0	0.277	0.412	0.357	2	156588	0.90	-0.342	-0.396
4.3		2.05	0.04	0.12	>h	0	0.187	0.362	0.179	2	167052	1.42	-0.224	-0.213
4.4	Normalized width variation	2.05	0.04	0.16	>h	0	0.163	0.334	0.143	2	165800	1.63	-0.201	-0.164
5.1		2.05	0.04	0.08	0.054	0	0.139	0.324	0.238	1.548	173672	2.00	-0.193	-0.222
5.2		2.05	0.04	0.08	0.108	0	0.132	0.328	0.238	1.217	179990	2.17	-0.167	-0.187
5.3		2.05	0.04	0.08	0.161	0	0.122	0.327	0.238	0.883	176403	2.46	-0.130	-0.147
5.4	Relative height variation	2.05	0.04	0.08	0.215	0	0.110	0.326	0.238	0.489	137598	2.86	-0.093	-0.090

Table D.3. Averaged data MRE and flow conditions in the inner MRE zone (segments III to VI) under unsteady flow conditions.

Case	Description	Drag coefficient C_D [-]	Width D_B [m]	Spacing S_G [m]	Height h_B [m]	Arrangement angle $tan(\Psi)$ [-]	Flow depth h [m]	Volume flux $q(\chi)$ [m³/s/m]	Norm. width D_B^* [1/m]	Relative effective height $\frac{h_{B,eff}}{h}$ [-]	Reynolds number Re [-]	Froude number Fr [-]	Source term S_{MRE} [m²/s²]	Fitted source term $S_{MRE,fit}$ [m²/s²]
1.0	Basic configuration	2.05	0.04	0.08	>h	0	0.058	0.126	0.333	2	104709	2.89	-0.010	-0.023
1.1		1.20	0.04	0.08	>h	0	0.118	0.199	0.333	2	116043	1.57	-0.085	-0.014
1.2	Shape variation	1.55	0.04	0.08	>h	0	0.096	0.147	0.333	2	94782	1.58	-0.061	-0.032
3.1		2.05	0.04	0.08	>h	0.5	0.183	0.135	0.333	2	63228	0.55	-0.339	-0.333
3.2	Arrangement variation	2.05	0.04	0.08	>h	1	0.271	0.172	0.333	2	65969	0.39	-0.605	-0.618
4.1		2.05	0.04	0.02	>h	0	0.033	0.040	0.667	2	43846	2.13	-0.009	-0.049
4.2		2.05	0.04	0.04	>h	0	0.051	0.078	0.5	2	69597	2.20	-0.024	-0.039
4.3		2.05	0.04	0.12	>h	0	0.062	0.153	0.25	2	123099	3.15	-0.003	-0.017
4.4	Normalized width variation	2.05	0.04	0.16	>h	0	0.069	0.167	0.2	2	128567	2.97	0.008	-0.014
5.1		2.05	0.04	0.08	0.054	0	0.118	0.208	0.333	1.824	120979	1.64	-0.068	-0.008
5.2		2.05	0.04	0.08	0.108	0	0.112	0.218	0.333	1.433	130131	1.85	-0.052	-0.002
5.3		2.05	0.04	0.08	0.161	0	0.134	0.296	0.333	0.800	144189	1.91	-0.079	-0.006
5.4	Relative height variation	2.05	0.04	0.08	0.215	0	0.122	0.307	0.333	0.442	117090	2.31	-0.059	0.001

D.2.2 Data tables for various turbulence intensities

The turbulence intensity is varied between I= 0 and I= 35 %, found in literature (e.g. Wu, 2004; Árnason, 2004) to asses its impact on the source terms. Exemplarily, a unit length of dx= 1.4 m is selected. The contribution of the turbulent shear stress term to the source term S_{MRE} in the edge zone under steady flow conditions, in the edge of the MRE zone under unsteady flow conditions and in the inner edge zone under unsteady flow conditions are provided in Table D.4.

Table D.4. Contribution of the turbulent shear stress term to the source term S_{MRE} for various turbulence intenities under a) unsteady conditions in the inner MRE zone, b) steady conditions in the edge MRE zone and c) unsteady conditions in the edge MRE zone.

Case	Description	condition	Turbulence intensity			
			***I*= 5 % [%]**	***I*= 10 % [%]**	***I*= 20 % [%]**	***I*= 35 % [%]**
1.0	Basic configuration	a)	0.3	1.6	6.3	22.1
		b)	0.4	0.7	3.3	11.2
		c)	0.0	20.0	200.0	185.7
1.1	Cylinder	a)	1.1	4.4	19.2	100.0
		b)	0.5	1.0	4.7	15.1
		c)	0.0	2.1	6.1	14.8
1.2	Diamond	a)	1.6	8.3	41.3	983.3
		b)	0.4	1.2	4.2	14.2
		c)	0.0	2.1	7.8	19.0
2.1	$tan\Psi = 0.5$	a)	0.9	4.4	21.6	122.6
		b)	0.3	0.8	3.2	10.9
		c)	0.0	0.3	1.3	3.8
2.2	$tan\Psi = 1$	a)	0.3	1.6	7.3	26.9
		b)	0.2	0.7	3.1	10.4
		c)	0.0	0.3	1.4	3.8
4.1	$S_G/D_B = 0.5$	a)	0.2	0.8	3.2	10.6
		b)	0.3	0.8	3.2	10.7
		c)	0.0	12.5	50.0	70.8
4.2	$S_G/D_B = 1$	a)	0.2	0.9	3.5	11.4
		b)	0.3	0.9	3.4	10.7
		c)	0.0	2.0	5.7	13.8
4.3	$S_G/D_B = 3$	a)	0.5	1.8	8.8	32.7
		b)	0.0	0.9	3.7	11.6
		c)	0.0	100.0	75.0	90.9
4.4	$S_G/D_B = 4$	a)	0.6	2.6	11.3	45.0
		b)	0.0	1.0	3.6	12.4
		c)	0.0	20.0	100.0	300.0
5.1	$h_B/h_{max} = 0.25$	a)	0.0	2.9	10.8	44.0
		b)	0.0	1.0	4.3	15.5
		c)	0.0	0.0	0.0	0.0
5.2	$h_B/h_{max} = 0.5$	a)	0.0	3.1	13.8	57.1
		b)	0.0	1.5	4.6	16.2
		c)	0.0	0.0	33.3	55.6
5.3	$h_B/h_{max} = 0.75$	a)	2.3	7.3	33.3	340.0
		b)	0.0	1.2	4.8	16.0
		c)	0.0	4.8	8.7	25.9
5.4	$h_B/h_{max} = 1$	a)	1.6	4.8	25.0	160.0
		b)	0.5	1.0	4.8	15.8
		c)	0.0	2.5	7.1	18.8
Average			0.3	5.7	19.3	75.1

Appendix E Implementation application and evaluation of the MRE model

This appendix contains additional information of the implementation of the developed source terms (see chapter 6) into COMCOT and application of the MRE model, presented in chapter 7.

First, the discretization and implementation of the new terms are given in section E.1, including the modified and extended segments of the COMCOT code. Then, the scaling factors applied to derive at the model parameters in prototype scale are summarized. This is followed by a section describing the steps which are performed to generate the bathymetries for the COMCOT model setups. Finally, the time series of all wave gauges obtained from the numerical models are provided, together with the experimental reference data.

E.1 Implementation of the source term into COMCOT

This section presents the steps for the implementation of the new source terms due to macro-roughness element (MRE) parameters into the non-linear shallow water (NLSW) model COMCOT (Wang & Power, 2011).

First, the discretization is given, followed by the implementation in the COMCOT routines.

E.1.1 Discretization

Equation 6.17 contains two differential quotients: (i) time derivative of the volume flux $\frac{\partial q(x)}{\partial t}$ and (ii) the spatial derivative of the relative width $\frac{\partial D_B^*}{\partial x}$. The temporal derivative of the flux is already solved in COMCOT. The spatial derivative of the relative width is discretized using upwind scheme. Depending on the flow direction, it reads

Flow from left to right:
$$\frac{\partial D_B^*}{\partial x} = \frac{max\left(D_{B,i,j}^* - D_{B,i-1,j}^*, 0\right)}{dx} \tag{E-1.a}$$

Flow from right to left:
$$\frac{\partial D_B^*}{\partial x} = \frac{max\left(D_{B,i+1,j}^* - D_{B,i,j}^*, 0\right)}{dx} \tag{E-1.b}$$

Flow from bottom to top:
$$\frac{\partial D_B^*}{\partial y} = \frac{max\left(D_{B,i,j}^* - D_{B,i,j-1}^*, 0\right)}{dy} \tag{E-1.c}$$

Flow from top to bottom:

$$\frac{\partial D_B^*}{\partial y} = \frac{max\left(D_{B,i,j+1}^* - D_{B,i,j}^*, 0\right)}{dy} \quad \text{(E-1.d)}$$

in which (i,j) is the actual grid cell, for which the solution is derived, $(i-1,j)$ is the upstream edge in case of flow from left to right and $(i+1,j)$ is the upstream edge in case of flow from right to left, $(i,j-1)$ is the upstream edge in case of flow from bottom to top and $(i,j+1)$ is the upstream edge in case of flow from top to bottom. dx and dy are the length of the grid cell in x and y direction, respectively.

The entire source term

$$S_{MRE,fit,x} = S_{MRE,fit,inertia,x} + S_{MRE,fit,drag,x} \quad \text{(E-2.a)}$$

$$S_{MRE,fit,y} = S_{MRE,fit,inertia,y} + S_{MRE,fit,drag,y} \quad \text{(E-2.b)}$$

consisting of the drag $S_{MRE,fit,drag,x}$ and the inertia part $S_{MRE,fit,inertia,x}$ in x direction are formulated as follows:

Inertia:

$$S_{MRE,fit,inertia,x} = \frac{\partial q(x)}{\partial t}\frac{\sqrt{g h_{i,j}}}{\frac{q(x)_{i,j}}{h_{i,j}}}\left[1.3 - cos\left(4\Psi_{i,j}\right)\right]^{0.33} \quad \text{(E-3.a)}$$

Drag:

$$\begin{aligned} S_{MRE,fit,drag,x} &= -0.4\frac{\partial D_B^*}{\partial x}\frac{q(x)^2}{h}h_{B,eff}^* C_D[0.7 + 0.3cos(4\Psi)]^{0.1} \\ &= -0.4\frac{\partial D_B^*}{\partial x}\frac{p(x)_{i,j}^2}{h_{i,j}}\frac{min\left(2h_{i,j}, h_{B,i,j}\right)}{h_{i,j}}C_{D,i,j}\left[0.7\right. \\ &\left. + 0.3cos\left(4\Psi_{i,j}\right)\right]^{0.1} \end{aligned} \quad \text{(E-3.b)}$$

In y direction, the drag $S_{MRE,fit,drag,y}$ and the inertia part $S_{MRE,fit,inertia,y}$ are formulated as follows:

Inertia:

$$S_{MRE,fit,inertia,y} = \frac{\partial q(y)}{\partial t}\frac{\sqrt{g h_{i,j}}}{\frac{p(x)_{i,j}}{h_{i,j}}}\left[1.3 - cos\left(4\Psi_{i,j}\right)\right]^{0.33} \quad \text{(E-4.a)}$$

Drag:

$$\begin{aligned} S_{MRE,fit,drag,y} &= -0.4\frac{\partial D_B^*}{\partial y}\frac{p(y)^2}{h}h_{B,eff}^* C_D[0.7 + 0.3cos(4\Psi)]^{0.1} \\ &= -0.4\frac{\partial D_B^*}{\partial y}\frac{p(y)_{i,j}^2}{h_{i,j}}\frac{min\left(2h_{i,j}, h_{B,i,j}\right)}{h_{i,j}}C_{D,i,j}\left[0.7\right. \\ &\left. + 0.3cos\left(4\Psi_{i,j}\right)\right]^{0.1} \end{aligned} \quad \text{(E-4.b)}$$

In the equations, the index j stands for the time step, $q(x)$ is the volume flux in x direction, g is the acceleration due to gravity, h is the flow depth, D_B^* is the relative width, $h_{B,eff}^*$ is the

relative effective height of the MRE, h_B is the height of the MRE, C_D is the drag coefficient and Ψ is the arrangement angle.

The source terms are included in the non-linear shallow-water (NLSW) equation as

$$\frac{\partial p(x)}{\partial t} + \frac{\partial}{\partial x}\left[\frac{p(x)^2}{h}\right] + \frac{\partial}{\partial y}\left[\frac{p(x)p(y)}{h}\right] + gh\frac{\partial \eta}{\partial x} + F_x + S_{MRE,fit,x} = 0 \qquad \text{(E-5.a)}$$

$$\frac{\partial p(y)}{\partial t} + \frac{\partial}{\partial x}\left[\frac{p(x)p(y)}{h}\right] + \frac{\partial}{\partial y}\left[\frac{p(y)^2}{h}\right] + gh\frac{\partial \eta}{\partial y} + F_y + S_{MRE,fit,y} = 0 \qquad \text{(E-5.b)}$$

In which t is the time, η is the surface elevation, and F_x and F_y are the friction source terms in x and y direction, respectively.

The fully discretized and extended NLSW equations in x direction read

$$\begin{aligned} q(x)^{n+1}_{i+\frac{1}{2},j} = {} & \frac{1}{1 + f_{MRE,inertia,x} + v_x * dt} \\ & * \Bigg\{ q(x)^{n}_{i+\frac{1}{2},j}\left(1 + f_{MRE,inertia,x} - v_x * dt\right) - S_{MRE,fit,drag,x} * dt \\ & - \frac{dt}{dx}\Bigg[\lambda_{11} * \frac{\left(q(x)^{n}_{i+\frac{3}{2},j}\right)^2}{h^{n}_{i+\frac{3}{2},j}} + \lambda_{12} * \frac{\left(q(x)^{n}_{i+\frac{1}{2},j}\right)^2}{h^{n}_{i+\frac{1}{2},j}} + \lambda_{13} \\ & * \frac{\left(q(x)^{n}_{i-\frac{1}{2},j}\right)}{h^{n}_{i-\frac{1}{2},j}}\Bigg] \\ & - \frac{dt}{dy}\Bigg[\lambda_{21} * \frac{\left(\left(q(x)p(y)\right)^{n}_{i+\frac{1}{2},j+1}\right)}{h^{n}_{i+\frac{1}{2},j+1}} + \lambda_{22} * \frac{\left(\left(q(x)p(y)\right)^{n}_{i+\frac{1}{2},j}\right)}{h^{n}_{i+\frac{1}{2},j}} \\ & + \lambda_{23} * \frac{\left(\left(q(x)q(y)\right)^{n}_{i+\frac{1}{2},j-1}\right)}{h^{n}_{i+\frac{1}{2},j-1}}\Bigg] - \frac{dt}{dx} * g \\ & * h^{n+\frac{1}{2}}_{i+\frac{1}{2},j}\left(\eta^{n+\frac{1}{2}}_{i+1,j} - \eta^{n+\frac{1}{2}}_{i,j}\right)\Bigg\} \end{aligned} \qquad \text{(E-6.a)}$$

and in y direction

$$
\begin{aligned}
q(y)_{i,j+\frac{1}{2}}^{n+1} = {} & \frac{1}{1 + f_{MRE,inertia,y} + v_y * dt} \\
& * \Bigg\{ q(y)_{i,j+\frac{1}{2}}^{n} \left(1 + f_{MRE,inertia,y} - v_y * dt\right) - S_{MRE,fit,drag,y} * dt \\
& - \frac{dt}{dy} \Bigg[\lambda_{11} * \frac{\left(q(y)_{i,j+\frac{3}{2}}^{n}\right)^2}{h_{i,j+\frac{3}{2}}^{n}} + \lambda_{12} * \frac{\left(q(y)_{i,j+\frac{1}{2}}^{n}\right)^2}{h_{i,j+\frac{1}{2}}^{n}} + \lambda_{13} \\
& * \frac{\left(q(y)_{i,j-\frac{1}{2}}^{n}\right)}{h_{i,j-\frac{1}{2}}^{n}} \Bigg] \\
& - \frac{dt}{dx} \Bigg[\lambda_{21} * \frac{\left((q(x)p(y))_{i+1,j+\frac{1}{2}}^{n}\right)}{h_{i+1,j+\frac{1}{2}}^{n}} + \lambda_{22} * \frac{\left((q(x)p(y))_{i,j+\frac{1}{2}}^{n}\right)}{h_{i,j+\frac{1}{2}}^{n}} \\
& + \lambda_{23} * \frac{\left((q(x)q(y))_{i-1,j+\frac{1}{2}}^{n}\right)}{h_{i-1,j+\frac{1}{2}}^{n}} \Bigg] - \frac{dt}{dy} * g \\
& * h_{i,j+\frac{1}{2}}^{n+\frac{1}{2}} \left(\eta_{i,j+1}^{n+\frac{1}{2}} - \eta_{i,j}^{n+\frac{1}{2}}\right) \Bigg\}
\end{aligned}
\tag{E-6.a}
$$

The coefficient λ results from the upwind scheme in the NLSW equations in COMCOT and evaluate the flow direction to adapt the upwind scheme for positive and negative directed flow (Wang & Power, 2011).

Adding the sink terms in the momentum equations result in a different factor before the parentheses where the modified inertia-related part of the sink term is added in the denominator. Further changes can be seen within the outermost parentheses where the modified inertia-related part of the sink term is multiplied with the volume flux at time step n and the drag-related part is multiplied by the time step.

E.1.2 Implementation

The COMCOT Fortran90 code is to be modified in four files type_module.f90, initialization.f90, comcot.f90 and moment.f90.

In type_module.f90, the variables are defined. Additional variables used by the MRE source term, are included in this file. Comcot.f90 deals with memory allocation for the spatial distribution of MRE parameters over the computational domain. In initialization.f90, the MRE parameters are read by subroutines from data files, which are organized in three columns: (i) x coordinate, (ii) y coordinate, (iii) MRE parameter. The discretized equations are finally implemented in the routine using Cartesian coordinates as part of moment.f90.

Variable definition in type_module.f90

The variables are defined in the modules

- LAYER_PARAMS: definition of layer parameters
- WAVE_PARAMS: definition of the wave generation parameters
- FAULT_PARAMS: definition of the earthquake's fault parameters
- LANDSLIDE_PARAMS: definition of submarine landslide parameters
- BCI_PARAMS: definition of boundary conditions

The following code is implemented in the module LAYER_PARAMS, code lines 61 to 76:

```
    !VARIABLES RELATED TO THE EXTENDED MACRO-ROUGHNESS MODEL
    INTEGER:: MRE_SWITCH  ! 0-USE MRE MAP; 1-DON'T USE MRE MAP
    REAL   :: A_COEF      ! A COEFFICIENT (INERTIA TERM)
    REAL   :: B_COEF      ! B COEFFICIENT (ARRANGEMENT, INERTIA TERM)
    REAL   :: C_COEF      ! C COEFFICIENT (ARRANGEMENT, INERTIA TERM)
    REAL   :: D_COEF      ! D COEFFICIENT (DRAG TERM)
    REAL   :: E_COEF      ! E COEFFICIENT (ARRANGEMENT, DRAG TERM)
    REAL   :: F_COEF      ! F COEFFICIENT (ARRANGEMENT, DRAG TERM)
    REAL   :: MRE_ARRCOEF ! MR COEFFICIENT ARRANGEMENT ANGLE
    REAL, DIMENSION(:,:),POINTER :: MRE_ARRVCOEF ! MRE ARRANGEMENT ANGLE
    REAL   :: MRE_ABCOEF  ! MRE WIDTH
    REAL, DIMENSION(:,:),POINTER :: MRE_ABVCOEF  ! MRE WIDTH
    REAL   :: MRE_HBCOEF  ! MRE HEIGHT
    REAL, DIMENSION(:,:),POINTER :: MRE_HBVCOEF  ! MRE HEIGHT
    REAL   :: MRE_CDCOEF  ! MRE DRAG COEFFICIENT
    REAL, DIMENSION(:,:),POINTER :: MRE_CDVCOEF  ! MRE DRAG COEFFICIENT
```

The MRE_SWITCH is an integer parameter which should be specified in the setup file comcot.ctl. If MRE_SWITCH = 0, then the MRE source terms are applied, if MRE_SWITCH = 1, then the MRE source terms are not applied. Referring to chapter 6, the remaining variables are defined in Table E.1.

Table E.1. Definition of variables in type_module.f90.

Variable	Symbol	Description
A_COEF	A	1.0; factor in inertia source term
B_COEF	α_1	1.3; coefficient for arrangement angle in inertia term
C_COEF	α_2	0.33; exponent for arrangement angle in inertia term
D_COEF	B	0.4; factor in drag term
E_COEF	B_1	0.3; coefficient for arrangement angle in drag term
F_COEF	β_3	0.1; exponent for arrangement angle in drag term
MRE_ARRCOEF	Ψ	MRE arrangement angle in computational grid format
MRE_ARRVCOEF	Ψ	MRE arrangement angle in three column format
MRE_ABCOEF	D_B^*	Normalized MRE width in computational grid format
MRE_ABVCOEF	D_B^*	Normalized MRE width in three column format
MRE_HBCOEF	h_B	MRE height in computational grid format
MRE_HBVCOEF	h_B	MRE height in three column format
MRE_CDCOEF	C_D	MRE drag coefficient in computational grid format
MRE_CDVCOEF	C_D	MRE drag coefficient in three column format

Memory allocation in comcot.f90

The comcot.f90 contains the main program and calls the subroutines, e.g. for reading the input parameters, initial and boundary conditions, for solving the NLSW equations and writing the results. As part of it, memory is allocated for spatially distributed MRE parameters in the subroutine ALLOC (), code lines 530 to 535:

```
        IF (L%MRE_SWITCH .EQ. 0) THEN
           ALLOCATE(L%MRE_ARRVCOEF(L%NX,L%NY))
           ALLOCATE(L%MRE_ABVCOEF(L%NX,L%NY))
           ALLOCATE(L%MRE_HBVCOEF(L%NX,L%NY))
           ALLOCATE(L%MRE_CDVCOEF(L%NX,L%NY))
        ENDIF
```

The integer numbers NX and NY are the number of grid cells in x and y direction, respectively.

Reading input data in initialization.f90

In initialization.f90, the setup file comcot.ctl is read. In addition, in this version of the implementation, the empirical coefficients can be specified for each simulation. The following is implemented in the subroutine READ_CONFIG () in lines 261 to 282:

```
!*    MRE COEFFICIENTS
   IF (LO%MRE_SWITCH .EQ. 0) THEN
         WRITE (*,*) 'PLEASE INPUT A_COEF (RECOMMENDED: 1.0):'
         READ *, LO%A_COEF
         WRITE (*,*) 'PLEASE INPUT B_COEF (RECOMMENDED: 1.3):'
         READ *, LO%B_COEF
         WRITE (*,*) 'PLEASE INPUT C_COEF (RECOMMENDED: 0.33):'
         READ *, LO%C_COEF
         WRITE (*,*) 'PLEASE INPUT D_COEF (RECOMMENDED: 0.4):'
         READ *, LO%D_COEF
         WRITE (*,*) 'PLEASE INPUT E_COEF (RECOMMENDED: 0.3):'
         READ *, LO%E_COEF
```

```
         WRITE (*,*) 'PLEASE INPUT F_COEF (RECOMMENDED: 0.1):'
         READ *, LO%F_COEF
      ELSEIF (LO%MRE_SWITCH .NE. 0) THEN
            LO%A_COEF = 0.0
            LO%B_COEF = 0.0
            LO%C_COEF = 0.0
            LO%D_COEF = 0.0
            LO%E_COEF = 0.0
            LO%F_COEF = 0.0
      ENDIF
```

Reading the MRE parameters is called for in lines 388 to 395:

```
      ! READ MRE ARRANGEMENT COEF. DATA FROM FILE
      IF (LO%MRE_SWITCH .EQ. 0) CALL READ_MRE_ARRCOEF (LO)
      ! READ MRE AB COEF. DATA FROM FILE
      IF (LO%MRE_SWITCH .EQ. 0) CALL READ_MRE_ABCOEF (LO)
      ! READ MRE HB COEF. DATA FROM FILE
      IF (LO%MRE_SWITCH .EQ. 0) CALL READ_MRE_HBCOEF (LO)
      ! READ MRE CD COEF. DATA FROM FILE
      IF (LO%MRE_SWITCH .EQ. 0) CALL READ_MRE_CDCOEF (LO)
```

The routine for reading the arrangement angles are included in lines 2919 to 3117:

```
!-----------------------------------------------------------------------
      SUBROUTINE READ_MRE_ARRCOEF (LO)
!.......................................................................
!DESCRIPTION:
!     #. READ ARR MRE COEFFICIENTS
!     #. ARRANGEMENT COEFICIENTS SHOULD BE WRITTEN ROW BY ROW FROM
!        LEFT TO RIGHT (OR FROM WEST TO EAST);
!NOTES:
!     #. CREATED ON OCT22 2017 (CLEMENS KRAUTWALD, TU BRAUNSCHWEIG)
!     #. SAME APPROACH AS IN THE PREVIOUS SUBROUTINE READ_FRIC_COEF
!     #. BY XIAOMING WANG (GNS)
!-----------------------------------------------------------------------
      USE LAYER_PARAMS
      TYPE (LAYER) :: LO
      REAL,ALLOCATABLE :: HTMP(:,:),H(:,:)
      REAL,ALLOCATABLE :: XCOL(:),YCOL(:),ZCOL(:)
      REAL,ALLOCATABLE :: X(:),Y(:),XTMP(:),YTMP(:)
      INTEGER      STAT, IS, JS, I, J, NXY
      INTEGER      COUNT
      CHARACTER(LEN=40) FNAME,FNAME1
      COMMON /CONS/ ELMAX,GRAV,PI,R_EARTH,GX,EPS,ZERO,ONE,NUM_GRID, &
                    NUM_FLT,V_LIMIT,RAD_DEG,RAD_MIN
```

```
      !--------------------------------------
      !  READING PARAMETERS FOR MRE ARRCOEF.
      !--------------------------------------
      WRITE (FNAME,1) LO%ID
 1    FORMAT('mre_arrcoef_layer',I2.2,'.dat')
      WRITE (*,*) '    READING MRE ARRCOEF DATA FOR LAYER',LO%ID
      OPEN (UNIT=13,FILE=FNAME,STATUS='OLD',IOSTAT=ISTAT,FORM='FORMATTED')
      IF (ISTAT /=0) THEN
         PRINT *,"ERROR:: CAN'T OPEN MRE ARR COEF. FILE; EXITING."
         STOP
      END IF

!.....DETERMINE THE LENGTH OF MRE ARR DATA FILE
      COUNT = 0
      DO WHILE (.NOT. EOF(13))
         COUNT = COUNT + 1
         READ (13,*) TEMP1,TEMP2,TEMP3
      ENDDO
      NXY = COUNT
      ALLOCATE(XCOL(NXY))
      ALLOCATE(YCOL(NXY))
      ALLOCATE(ZCOL(NXY))
      XCOL = 0.0
      YCOL = 0.0
      ZCOL = 0.0

!*!.....READING MRE ARR DATA
      REWIND(13)
      DO I = 1,COUNT
         READ (13,*) XCOL(I), YCOL(I), ZCOL(I)
         IF (ISNAN(ZCOL(I))) ZCOL(I) = 9999.0
         IF (ABS(ZCOL(I)).GE.HUGE(ZCOL(I))) ZCOL(I) = 9999.0
         IF (ZCOL(I) .LE. 0.1) ZCOL (I) = 0.1
      END DO
      CLOSE (13)

!<<<  CHECK IF THE DATA IS WRITTEN ROW BY ROW
!.....DETERMINE GRID DIMENSION: NX,NY
      TMPX = XCOL(1)
      TMPX1 = XCOL(2)
      TMPY = YCOL(1)
      TMPY1 = YCOL(2)
      IF (ABS(TMPX1-TMPX).GT.EPS .AND. ABS(TMPY1-TMPY).LT.EPS) THEN
!*    IF (TMPX1.NE.TMPX .AND. TMPY1.EQ.TMPY) THEN
         K = 1
         DO WHILE (TMPX1.GT.TMPX)
            K=K+1
```

```
            TMPX1 = XCOL(K)
         ENDDO
         NX = K-1
         NY = NINT(DBLE(NXY/NX))
!        WRITE (*,*) '       GRID DIMENSION OF MRE ARR DATA: ', NX,NY
         ALLOCATE(X(NX))
         ALLOCATE(Y(NY))
         ALLOCATE(YTMP(NY))
         ALLOCATE(HTMP(NX,NY))
         ALLOCATE(H(NX,NY))
         X = 0.0
         Y = 0.0
         YTMP = 0.0
         HTMP = 0.0
         H = 0.0

!.....   OBTAINED X,Y COORDINATES
         X(1:NX) = XCOL(1:NX)
         DO J = 1,NY
            K = (J-1)*NX + 1
            YTMP(J) = YCOL(K)
         END DO
         !GENERATE GRID DATA
         DO J=1,NY
            KS = (J-1)*NX + 1
            KE = (J-1)*NX + NX
            HTMP(1:NX,J) = ZCOL(KS:KE)
         END DO
      ENDIF
!>>>>>
!<<<<<CHECK IF THE DATA IS WRITTEN COLUMN BY COLUMN
      TMPX = XCOL(1)
      TMPX1 = XCOL(2)
      TMPY = YCOL(1)
      TMPY1 = YCOL(2)
!     write (*,*) TMPX,TMPX1,TMPY,TMPY1,NXY
      IF (ABS(TMPX1-TMPX).LT.EPS .AND. ABS(TMPY1-TMPY).GT.EPS) THEN
!*    IF (TMPX1.EQ.TMPX .AND. TMPY1.NE.TMPY) THEN
         K = 1
         DO WHILE (TMPX1.LE.TMPX)
            K=K+1
            TMPX1 = XCOL(K)
         ENDDO
         NY = K-1
!        WRITE(*,*) NX
         NX = NINT(DBLE(NXY/NY))
```

```
!*       WRITE (*,*) '       GRID DIMENSION OF MRE ARR DATA: ', NX,NY
         ALLOCATE(X(NX))
         ALLOCATE(Y(NY))
         ALLOCATE(XTMP(NX))
         ALLOCATE(YTMP(NY))
         ALLOCATE(HTMP(NX,NY))
         ALLOCATE(H(NX,NY))
         HTMP = 0.0
         X = 0.0
         Y = 0.0
         YTMP = 0.0
         H = 0.0
!........OBTAINED X,Y COORDINATES
         YTMP(1:NY) = YCOL(1:NY)
         DO I = 1,NX
            K = (I-1)*NY + 1
            X(I) = XCOL(K)
         END DO
         !GENERATE GRID DATA
         DO I=1,NX
            KS = (I-1)*NY + 1
            KE = (I-1)*NY + NY
            HTMP(I,1:NY) = ZCOL(KS:KE)
         END DO
      ENDIF
!>>>>>

!!....DETERMINE IF THE DATA NEED FLIP
!     CHECK IF Y COORDINATE IS FROM NORTH TO SOUTH OR FROM SOUTH TO NORTH
!     IFLIP = 0: FLIP; 1: NO FLIP OPERATION
      IFLIP = 0
      IF (YTMP(NY).LT.YTMP(NY-1)) IFLIP = 1

      IF (IFLIP .EQ. 1) THEN
         ! FLIP Y COORDINATES
         DO J = 1,NY
            K = NY-J+1
            Y(K) = YTMP(J)
         END DO
         ! FLIP BATHYMETRY MATRIX
         DO I = 1,NX
            DO J = 1,NY
               K = NY - J + 1
               H(I,K) = HTMP(I,J)
            END DO
         END DO
      ELSE
```

```
         Y = YTMP
         H = HTMP
      END IF
!*      WRITE (*,*) H(1,1),H(NX,NY),ZCOL(1),ZCOL(NXY)

!.....MAP THE MRE DATA ONTO THE NUMERICAL GRIDS VIA INTERPOLATION
      CALL GRID_INTERP (LO%MRE_ARRVCOEF,LO%X,LO%Y,LO%NX,LO%NY,H,X,Y,NX,NY)

!.....OUTPUT THE MRE ARR COEF INTO A DATA FILE
      IF (LO%LEVEL.LE.1) THEN
         IS = 1
         JS = 1
         IE = LO%NX
         JE = LO%NY
      ELSE
         IS = 2
         JS = 2
         IE = LO%NX
         JE = LO%NY
      ENDIF
      WRITE (FNAME1,2) LO%ID
 2    FORMAT('mre_arrlayer',I2.2,'.dat')
      OPEN (13,FILE=FNAME1,STATUS='UNKNOWN')
      DO J = JS,JE
         WRITE (13,'(15F9.4)') (LO%MRE_ARRVCOEF(I,J),I=IS,IE)
      ENDDO
      CLOSE (13)

!.....FREE ALOOCATED VARIABLES
      DEALLOCATE(HTMP,H,STAT=ISTAT)
      DEALLOCATE(XCOL,YCOL,ZCOL,STAT=ISTAT)
      DEALLOCATE(X,Y,YTMP,STAT=ISTAT)

      RETURN
      END
```

The routine for reading the normalized width are included in lines 3119 to 3317:

```
!-----------------------------------------------------------------------
      SUBROUTINE READ_MRE_ABCOEF (LO)
!.....................................................................
!DESCRIPTION:
!     #. READ MRE AB COEFFICIENTS
!     #. BUILDING AREA COEFICIENTS SHOULD BE WRITTEN ROW BY ROW FROM
!        LEFT TO RIGHT (OR FROM WEST TO EAST);
!NOTES:
!     #. CREATED ON MAR22 2019 (STEFAN LESCHKA, DHI)
```

```
!     #. SAME APPROACH AS IN THE PREVIOUS SUBROUTINE READ_FRIC_COEF
!     #. BY XIAOMING WANG (GNS)
!     #. UPDATED ON JUL13 2019 (STEFAN LESCHKA, DHI)
!---------------------------------------------------------------------
      USE LAYER_PARAMS
      TYPE (LAYER) :: LO
      REAL,ALLOCATABLE :: HTMP(:,:),H(:,:)
      REAL,ALLOCATABLE :: XCOL(:),YCOL(:),ZCOL(:)
      REAL,ALLOCATABLE :: X(:),Y(:),XTMP(:),YTMP(:)
      INTEGER      STAT, IS, JS, I, J, NXY
      INTEGER      COUNT
      CHARACTER(LEN=40) FNAME,FNAME1
      COMMON /CONS/ ELMAX,GRAV,PI,R_EARTH,GX,EPS,ZERO,ONE,NUM_GRID, &
                    NUM_FLT,V_LIMIT,RAD_DEG,RAD_MIN

      !---------------------------------------
      !  READING PARAMETERS FOR MRE ABCOEF.
      !---------------------------------------
      WRITE (FNAME,1) LO%ID
 1    FORMAT('mre_abcoef_layer',I2.2,'.dat')
      WRITE (*,*) '    READING MRE ABCOEF DATA FOR LAYER',LO%ID
      OPEN (UNIT=15,FILE=FNAME,STATUS='OLD',IOSTAT=ISTAT,FORM='FORMATTED')
      IF (ISTAT /=0) THEN
         PRINT *,"ERROR:: CAN'T OPEN MRE AB COEF. FILE; EXITING."
         STOP
      END IF

!.....DETERMINE THE LENGTH OF MRE AB DATA FILE
      COUNT = 0
      DO WHILE (.NOT. EOF(15))
         COUNT = COUNT + 1
         READ (15,*) TEMP1,TEMP2,TEMP3
      ENDDO
      NXY = COUNT
      ALLOCATE(XCOL(NXY))
      ALLOCATE(YCOL(NXY))
      ALLOCATE(ZCOL(NXY))
      XCOL = 0.0
      YCOL = 0.0
      ZCOL = 0.0

!*!.....READING MRE AB DATA
      REWIND(15)
      DO I = 1,COUNT
         READ (15,*) XCOL(I), YCOL(I), ZCOL(I)
         IF (ISNAN(ZCOL(I))) ZCOL(I) = 9999.0
         IF (ABS(ZCOL(I)).GE.HUGE(ZCOL(I))) ZCOL(I) = 9999.0
```

```
      END DO
      CLOSE (15)

!<<<  CHECK IF THE DATA IS WRITTEN ROW BY ROW
!.....DETERMINE GRID DIMENSION: NX,NY
      TMPX = XCOL(1)
      TMPX1 = XCOL(2)
      TMPY = YCOL(1)
      TMPY1 = YCOL(2)
      IF (ABS(TMPX1-TMPX).GT.EPS .AND. ABS(TMPY1-TMPY).LT.EPS) THEN
!*    IF (TMPX1.NE.TMPX .AND. TMPY1.EQ.TMPY) THEN
         K = 1
         DO WHILE (TMPX1.GT.TMPX)
            K=K+1
            TMPX1 = XCOL(K)
         ENDDO
         NX = K-1
         NY = NINT(DBLE(NXY/NX))
!        WRITE (*,*) '       GRID DIMENSION OF MRE AB DATA: ', NX,NY
         ALLOCATE(X(NX))
         ALLOCATE(Y(NY))
         ALLOCATE(YTMP(NY))
         ALLOCATE(HTMP(NX,NY))
         ALLOCATE(H(NX,NY))
         X = 0.0
         Y = 0.0
         YTMP = 0.0
         HTMP = 0.0
         H = 0.0

!.....   OBTAINED X,Y COORDINATES
         X(1:NX) = XCOL(1:NX)
         DO J = 1,NY
            K = (J-1)*NX + 1
            YTMP(J) = YCOL(K)
         END DO
         !GENERATE GRID DATA
         DO J=1,NY
            KS = (J-1)*NX + 1
            KE = (J-1)*NX + NX
            HTMP(1:NX,J) = ZCOL(KS:KE)
         END DO
      ENDIF
!>>>>>
!<<<<<CHECK IF THE DATA IS WRITTEN COLUMN BY COLUMN
      TMPX = XCOL(1)
      TMPX1 = XCOL(2)
```

```
      TMPY = YCOL(1)
      TMPY1 = YCOL(2)
!     write (*,*) TMPX,TMPX1,TMPY,TMPY1,NXY
      IF (ABS(TMPX1-TMPX).LT.EPS .AND. ABS(TMPY1-TMPY).GT.EPS) THEN
!*    IF (TMPX1.EQ.TMPX .AND. TMPY1.NE.TMPY) THEN
         K = 1
         DO WHILE (TMPX1.LE.TMPX)
            K=K+1
            TMPX1 = XCOL(K)
         ENDDO
         NY = K-1
!        WRITE(*,*) NX
         NX = NINT(DBLE(NXY/NY))

!*       WRITE (*,*) '       GRID DIMENSION OF MRE AB DATA: ', NX,NY
         ALLOCATE(X(NX))
         ALLOCATE(Y(NY))
         ALLOCATE(XTMP(NX))
         ALLOCATE(YTMP(NY))
         ALLOCATE(HTMP(NX,NY))
         ALLOCATE(H(NX,NY))
         HTMP = 0.0
         X = 0.0
         Y = 0.0
         YTMP = 0.0
         H = 0.0
!........OBTAINED X,Y COORDINATES
         YTMP(1:NY) = YCOL(1:NY)
         DO I = 1,NX
            K = (I-1)*NY + 1
            X(I) = XCOL(K)
         END DO
         !GENERATE GRID DATA
         DO I=1,NX
            KS = (I-1)*NY + 1
            KE = (I-1)*NY + NY
            HTMP(I,1:NY) = ZCOL(KS:KE)
         END DO
      ENDIF
!>>>>>

!!....DETERMINE IF THE DATA NEED FLIP
!     CHECK IF Y COORDINATE IS FROM NORTH TO SOUTH OR FROM SOUTH TO NORTH
!     IFLIP = 0: FLIP; 1: NO FLIP OPERATION
      IFLIP = 0
      IF (YTMP(NY).LT.YTMP(NY-1)) IFLIP = 1
```

```
      IF (IFLIP .EQ. 1) THEN
         ! FLIP Y COORDINATES
         DO J = 1,NY
            K = NY-J+1
            Y(K) = YTMP(J)
         END DO
         ! FLIP BATHYMETRY MATRIX
         DO I = 1,NX
            DO J = 1,NY
               K = NY - J + 1
               H(I,K) = HTMP(I,J)
            END DO
         END DO
      ELSE
         Y = YTMP
         H = HTMP
      END IF
!*      WRITE (*,*) H(1,1),H(NX,NY),ZCOL(1),ZCOL(NXY)

!.....MAP THE MRE ABY DATA ONTO THE NUMERICAL GRIDS VIA INTERPOLATION
      CALL GRID_INTERP (LO%MRE_ABVCOEF,LO%X,LO%Y,LO%NX,LO%NY,H,X,Y,NX,NY)

!.....OUTPUT THE MRE ABYCOEF INTO A DATA FILE
      IF (LO%LEVEL.LE.1) THEN
         IS = 1
         JS = 1
         IE = LO%NX
         JE = LO%NY
      ELSE
         IS = 2
         JS = 2
         IE = LO%NX
         JE = LO%NY
      ENDIF
      WRITE (FNAME1,2) LO%ID
 2    FORMAT('mre_ab_layer',I2.2,'.dat')
      OPEN (15,FILE=FNAME1,STATUS='UNKNOWN')
      DO J = JS,JE
         WRITE (15,'(15F9.4)') (LO%MRE_ABVCOEF(I,J),I=IS,IE)
      ENDDO
      CLOSE (15)

!.....FREE ALOOCATED VARIABLES
      DEALLOCATE(HTMP,H,STAT=ISTAT)
      DEALLOCATE(XCOL,YCOL,ZCOL,STAT=ISTAT)
      DEALLOCATE(X,Y,YTMP,STAT=ISTAT)
```

```
      RETURN
      END
```

The routine for reading the MRE heights are included in lines 3319 to 3516:

```
!-----------------------------------------------------------------------
      SUBROUTINE READ_MRE_HBCOEF (LO)
!.......................................................................
!DESCRIPTION:
!     #. READ MRE HB COEFFICIENTS
!     #. BUILDING HEIGHT COEFICIENTS SHOULD BE WRITTEN ROW BY ROW FROM
!        LEFT TO RIGHT (OR FROM WEST TO EAST);
!NOTES:
!     #. CREATED ON OCT12 2017 (CLEMENS KRAUTWALD, TU BRAUNSCHWEIG)
!     #. SAME APPROACH AS IN THE PREVIOUS SUBROUTINE READ_FRIC_COEF
!     #. BY XIAOMING WANG (GNS)
!-----------------------------------------------------------------------
      USE LAYER_PARAMS
      TYPE (LAYER) :: LO
      REAL,ALLOCATABLE :: HTMP(:,:),H(:,:)
      REAL,ALLOCATABLE :: XCOL(:),YCOL(:),ZCOL(:)
      REAL,ALLOCATABLE :: X(:),Y(:),XTMP(:),YTMP(:)
      INTEGER      STAT, IS, JS, I, J, NXY
      INTEGER      COUNT
      CHARACTER(LEN=40) FNAME,FNAME1
      COMMON /CONS/ ELMAX,GRAV,PI,R_EARTH,GX,EPS,ZERO,ONE,NUM_GRID, &
                    NUM_FLT,V_LIMIT,RAD_DEG,RAD_MIN

      !---------------------------------------
      !  READING PARAMETERS FOR MRE BUILDING HEIGHT COEF.
      !---------------------------------------
      WRITE (FNAME,1) LO%ID
 1    FORMAT('mre_hbcoef_layer',I2.2,'.dat')
      WRITE (*,*) '    READING MRE HBCOEF DATA FOR LAYER',LO%ID
      OPEN (UNIT=23,FILE=FNAME,STATUS='OLD',IOSTAT=ISTAT,FORM='FORMATTED')
      IF (ISTAT /=0) THEN
         PRINT *,"ERROR:: CAN'T OPEN MRE HB COEF. FILE; EXITING."
         STOP
      END IF

!.....DETERMINE THE LENGTH OF MRE HB DATA FILE
      COUNT = 0
      DO WHILE (.NOT. EOF(23))
         COUNT = COUNT + 1
         READ (23,*) TEMP1,TEMP2,TEMP3
      ENDDO
      NXY = COUNT
```

```
      ALLOCATE(XCOL(NXY))
      ALLOCATE(YCOL(NXY))
      ALLOCATE(ZCOL(NXY))
      XCOL = 0.0
      YCOL = 0.0
      ZCOL = 0.0

!*!.....READING MRE HB DATA
      REWIND(23)
      DO I = 1,COUNT
         READ (23,*) XCOL(I), YCOL(I), ZCOL(I)
         IF (ISNAN(ZCOL(I))) ZCOL(I) = 9999.0
         IF (ABS(ZCOL(I)).GE.HUGE(ZCOL(I))) ZCOL(I) = 9999.0
      END DO
      CLOSE (23)

!<<<  CHECK IF THE DATA IS WRITTEN ROW BY ROW
!.....DETERMINE GRID DIMENSION: NX,NY
      TMPX = XCOL(1)
      TMPX1 = XCOL(2)
      TMPY = YCOL(1)
      TMPY1 = YCOL(2)
      IF (ABS(TMPX1-TMPX).GT.EPS .AND. ABS(TMPY1-TMPY).LT.EPS) THEN
!     IF (TMPX1.NE.TMPX .AND. TMPY1.EQ.TMPY) THEN
         K = 1
         DO WHILE (TMPX1.GT.TMPX)
            K=K+1
            TMPX1 = XCOL(K)
         ENDDO
         NX = K-1
         NY = NINT(DBLE(NXY/NX))
!        WRITE (*,*) '       GRID DIMENSION OF MRE HB DATA: ', NX,NY
         ALLOCATE(X(NX))
         ALLOCATE(Y(NY))
         ALLOCATE(YTMP(NY))
         ALLOCATE(HTMP(NX,NY))
         ALLOCATE(H(NX,NY))
         X = 0.0
         Y = 0.0
         YTMP = 0.0
         HTMP = 0.0
         H = 0.0

!.....   OBTAINED X,Y COORDINATES
         X(1:NX) = XCOL(1:NX)
         DO J = 1,NY
            K = (J-1)*NX + 1
```

```
            YTMP(J) = YCOL(K)
         END DO
         !GENERATE GRID DATA
         DO J=1,NY
            KS = (J-1)*NX + 1
            KE = (J-1)*NX + NX
            HTMP(1:NX,J) = ZCOL(KS:KE)
         END DO
      ENDIF
!>>>>>
!<<<<<CHECK IF THE DATA IS WRITTEN COLUMN BY COLUMN
      TMPX = XCOL(1)
      TMPX1 = XCOL(2)
      TMPY = YCOL(1)
      TMPY1 = YCOL(2)
!     write (*,*) TMPX,TMPX1,TMPY,TMPY1,NXY
      IF (ABS(TMPX1-TMPX).LT.EPS .AND. ABS(TMPY1-TMPY).GT.EPS) THEN
!*    IF (TMPX1.EQ.TMPX .AND. TMPY1.NE.TMPY) THEN
         K = 1
         DO WHILE (TMPX1.LE.TMPX)
            K=K+1
            TMPX1 = XCOL(K)
         ENDDO
         NY = K-1
!        WRITE(*,*) NX
         NX = NINT(DBLE(NXY/NY))

!*       WRITE (*,*) '       GRID DIMENSION OF MRE HB DATA: ', NX,NY
         ALLOCATE(X(NX))
         ALLOCATE(Y(NY))
         ALLOCATE(XTMP(NX))
         ALLOCATE(YTMP(NY))
         ALLOCATE(HTMP(NX,NY))
         ALLOCATE(H(NX,NY))
         HTMP = 0.0
         X = 0.0
         Y = 0.0
         YTMP = 0.0
         H = 0.0
!........OBTAINED X,Y COORDINATES
         YTMP(1:NY) = YCOL(1:NY)
         DO I = 1,NX
            K = (I-1)*NY + 1
            X(I) = XCOL(K)
         END DO
         !GENERATE GRID DATA
         DO I=1,NX
```

```
            KS = (I-1)*NY + 1
            KE = (I-1)*NY + NY
            HTMP(I,1:NY) = ZCOL(KS:KE)
         END DO
      ENDIF
!>>>>>

!!....DETERMINE IF THE DATA NEED FLIP
!     CHECK IF Y COORDINATE IS FROM NORTH TO SOUTH OR FROM SOUTH TO NORTH
!     IFLIP = 0: FLIP; 1: NO FLIP OPERATION
      IFLIP = 0
      IF (YTMP(NY).LT.YTMP(NY-1)) IFLIP = 1

      IF (IFLIP .EQ. 1) THEN
         ! FLIP Y COORDINATES
         DO J = 1,NY
            K = NY-J+1
            Y(K) = YTMP(J)
         END DO
         ! FLIP BATHYMETRY MATRIX
         DO I = 1,NX
            DO J = 1,NY
               K = NY - J + 1
               H(I,K) = HTMP(I,J)
            END DO
         END DO
      ELSE
         Y = YTMP
         H = HTMP
      END IF
!*      WRITE (*,*) H(1,1),H(NX,NY),ZCOL(1),ZCOL(NXY)

!.....MAP THE MRE HB DATA ONTO THE NUMERICAL GRIDS VIA INTERPOLATION
      CALL GRID_INTERP (LO%MRE_HBVCOEF,LO%X,LO%Y,LO%NX,LO%NY,H,X,Y,NX,NY)

!.....OUTPUT THE MRE HBCOEF INTO A DATA FILE
      IF (LO%LEVEL.LE.1) THEN
         IS = 1
         JS = 1
         IE = LO%NX
         JE = LO%NY
      ELSE
         IS = 2
         JS = 2
         IE = LO%NX
         JE = LO%NY
      ENDIF
```

```
      WRITE (FNAME1,2) LO%ID
 2    FORMAT('mre_hb_layer',I2.2,'.dat')
      OPEN (23,FILE=FNAME1,STATUS='UNKNOWN')
      DO J = JS,JE
         WRITE (23,'(15F9.4)') (LO%MRE_HBVCOEF(I,J),I=IS,IE)
      ENDDO
      CLOSE (23)

!.....FREE ALOOCATED VARIABLES
      DEALLOCATE(HTMP,H,STAT=ISTAT)
      DEALLOCATE(XCOL,YCOL,ZCOL,STAT=ISTAT)
      DEALLOCATE(X,Y,YTMP,STAT=ISTAT)

      RETURN
    END
```

The routine for reading the drag coefficients are included in lines 3518 to 3715:

```
!-----------------------------------------------------------------------
      SUBROUTINE READ_MRE_CDCOEF (LO)
!.....................................................................
!DESCRIPTION:
!     #. READ MRE CD COEFFICIENTS
!     #. DRAG COEFICIENTS SHOULD BE WRITTEN ROW BY ROW FROM
!        LEFT TO RIGHT (OR FROM WEST TO EAST);
!NOTES:
!     #. CREATED ON MAR22 2019 (STEFAN LESCHKA, DHI)
!     #. SAME APPROACH AS IN THE PREVIOUS SUBROUTINE READ_FRIC_COEF
!     #. BY XIAOMING WANG (GNS)
!-----------------------------------------------------------------------
      USE LAYER_PARAMS
      TYPE (LAYER) :: LO
      REAL,ALLOCATABLE :: HTMP(:,:),H(:,:)
      REAL,ALLOCATABLE :: XCOL(:),YCOL(:),ZCOL(:)
      REAL,ALLOCATABLE :: X(:),Y(:),XTMP(:),YTMP(:)
      INTEGER      STAT, IS, JS, I, J, NXY
      INTEGER      COUNT
      CHARACTER(LEN=40) FNAME,FNAME1
      COMMON /CONS/ ELMAX,GRAV,PI,R_EARTH,GX,EPS,ZERO,ONE,NUM_GRID, &
                    NUM_FLT,V_LIMIT,RAD_DEG,RAD_MIN

      !--------------------------------------
      !  READING PARAMETERS FOR MRE CDCOEF.
      !--------------------------------------
      WRITE (FNAME,1) LO%ID
 1    FORMAT('mre_cdcoef_layer',I2.2,'.dat')
      WRITE (*,*) '    READING MRE CDCOEF DATA FOR LAYER',LO%ID
```

```
      OPEN (UNIT=15,FILE=FNAME,STATUS='OLD',IOSTAT=ISTAT,FORM='FORMATTED')
      IF (ISTAT /=0) THEN
         PRINT *,"ERROR:: CAN'T OPEN MRE CD COEF. FILE; EXITING."
         STOP
      END IF

!.....DETERMINE THE LENGTH OF MRE ARRANGEMENT DATA FILE
      COUNT = 0
      DO WHILE (.NOT. EOF(15))
         COUNT = COUNT + 1
         READ (15,*) TEMP1,TEMP2,TEMP3
      ENDDO
      NXY = COUNT
      ALLOCATE(XCOL(NXY))
      ALLOCATE(YCOL(NXY))
      ALLOCATE(ZCOL(NXY))
      XCOL = 0.0
      YCOL = 0.0
      ZCOL = 0.0

!*!.....READING MRE CD DATA
      REWIND(15)
      DO I = 1,COUNT
         READ (15,*) XCOL(I), YCOL(I), ZCOL(I)
         IF (ISNAN(ZCOL(I))) ZCOL(I) = 9999.0
         IF (ABS(ZCOL(I)).GE.HUGE(ZCOL(I))) ZCOL(I) = 9999.0
      END DO
      CLOSE (15)

!<<<  CHECK IF THE DATA IS WRITTEN ROW BY ROW
!.....DETERMINE GRID DIMENSION: NX,NY
      TMPX = XCOL(1)
      TMPX1 = XCOL(2)
      TMPY = YCOL(1)
      TMPY1 = YCOL(2)
      IF (ABS(TMPX1-TMPX).GT.EPS .AND. ABS(TMPY1-TMPY).LT.EPS) THEN
!     IF (TMPX1.NE.TMPX .AND. TMPY1.EQ.TMPY) THEN
         K = 1
         DO WHILE (TMPX1.GT.TMPX)
            K=K+1
            TMPX1 = XCOL(K)
         ENDDO
         NX = K-1
         NY = NINT(DBLE(NXY/NX))
!        WRITE (*,*) '       GRID DIMENSION OF MRE CD DATA: ', NX,NY
         ALLOCATE(X(NX))
         ALLOCATE(Y(NY))
```

```
         ALLOCATE(YTMP(NY))
         ALLOCATE(HTMP(NX,NY))
         ALLOCATE(H(NX,NY))
         X = 0.0
         Y = 0.0
         YTMP = 0.0
         HTMP = 0.0
         H = 0.0

!.....   OBTAINED X,Y COORDINATES
         X(1:NX) = XCOL(1:NX)
         DO J = 1,NY
            K = (J-1)*NX + 1
            YTMP(J) = YCOL(K)
         END DO
         !GENERATE GRID DATA
         DO J=1,NY
            KS = (J-1)*NX + 1
            KE = (J-1)*NX + NX
            HTMP(1:NX,J) = ZCOL(KS:KE)
         END DO
      ENDIF
!>>>>>
!<<<<<CHECK IF THE DATA IS WRITTEN COLUMN BY COLUMN
      TMPX = XCOL(1)
      TMPX1 = XCOL(2)
      TMPY = YCOL(1)
      TMPY1 = YCOL(2)
!     write (*,*) TMPX,TMPX1,TMPY,TMPY1,NXY
      IF (ABS(TMPX1-TMPX).LT.EPS .AND. ABS(TMPY1-TMPY).GT.EPS) THEN
!*    IF (TMPX1.EQ.TMPX .AND. TMPY1.NE.TMPY) THEN
         K = 1
         DO WHILE (TMPX1.LE.TMPX)
            K=K+1
            TMPX1 = XCOL(K)
         ENDDO
         NY = K-1
!        WRITE(*,*) NX
         NX = NINT(DBLE(NXY/NY))

!*       WRITE (*,*) '       GRID DIMENSION OF MRE CD DATA: ', NX,NY
         ALLOCATE(X(NX))
         ALLOCATE(Y(NY))
         ALLOCATE(XTMP(NX))
         ALLOCATE(YTMP(NY))
         ALLOCATE(HTMP(NX,NY))
         ALLOCATE(H(NX,NY))
```

```
         HTMP = 0.0
         X = 0.0
         Y = 0.0
         YTMP = 0.0
         H = 0.0
!........OBTAINED X,Y COORDINATES
         YTMP(1:NY) = YCOL(1:NY)
         DO I = 1,NX
            K = (I-1)*NY + 1
            X(I) = XCOL(K)
         END DO
         !GENERATE GRID DATA
         DO I=1,NX
            KS = (I-1)*NY + 1
            KE = (I-1)*NY + NY
            HTMP(I,1:NY) = ZCOL(KS:KE)
         END DO
      ENDIF
!>>>>>

!!....DETERMINE IF THE DATA NEED FLIP
!     CHECK IF Y COORDINATE IS FROM NORTH TO SOUTH OR FROM SOUTH TO NORTH
!     IFLIP = 0: FLIP; 1: NO FLIP OPERATION
      IFLIP = 0
      IF (YTMP(NY).LT.YTMP(NY-1)) IFLIP = 1

      IF (IFLIP .EQ. 1) THEN
         ! FLIP Y COORDINATES
         DO J = 1,NY
            K = NY-J+1
            Y(K) = YTMP(J)
         END DO
         ! FLIP BATHYMETRY MATRIX
         DO I = 1,NX
            DO J = 1,NY
               K = NY - J + 1
               H(I,K) = HTMP(I,J)
            END DO
         END DO
      ELSE
         Y = YTMP
         H = HTMP
      END IF
!*      WRITE (*,*) H(1,1),H(NX,NY),ZCOL(1),ZCOL(NXY)

!.....MAP THE MRE CD DATA ONTO THE NUMERICAL GRIDS VIA INTERPOLATION
      CALL GRID_INTERP (LO%MRE_CDVCOEF,LO%X,LO%Y,LO%NX,LO%NY,H,X,Y,NX,NY)
```

```
!.....OUTPUT THE MRE CDCOEF INTO A DATA FILE
      IF (LO%LEVEL.LE.1) THEN
         IS = 1
         JS = 1
         IE = LO%NX
         JE = LO%NY
      ELSE
         IS = 2
         JS = 2
         IE = LO%NX
         JE = LO%NY
      ENDIF
      WRITE (FNAME1,2) LO%ID
 2    FORMAT('mre_cd_layer',I2.2,'.dat')
      OPEN (15,FILE=FNAME1,STATUS='UNKNOWN')
      DO J = JS,JE
         WRITE (15,'(15F9.4)') (LO%MRE_CDVCOEF(I,J),I=IS,IE)
      ENDDO
      CLOSE (15)

!.....FREE ALOOCATED VARIABLES
      DEALLOCATE(HTMP,H,STAT=ISTAT)
      DEALLOCATE(XCOL,YCOL,ZCOL,STAT=ISTAT)
      DEALLOCATE(X,Y,YTMP,STAT=ISTAT)

      RETURN
      END
```

Calculating the fluxes in moment.f90

The NLSW momentum equations are solved in moment.f90. On Cartesian coordinates, this is done in the subroutine CONMOME ().

Additional variables are defined in lines 284 to 289:

```
      REAL A_COEF, B_COEF, C_COEF, D_COEF, E_COEF, F_COEF! MRE COEFFICIENTS
      REAL DBX_1, DBY_1, DB, DBX1, DBY1, DBX2, DBY2      ! MRE COEFFICIENTS
      REAL HB, ARR, C_D                                  ! MRE COEFFICIENTS
      REAL RELSPACX, RELSPACY                            ! MRE COEFFICIENTS
      REAL COEF_MX, COEF_MY, COEF_DX, COEF_DY            ! MRE COEFFICIENTS
      INTEGER IMRE                                       ! MRE SWITCH
```

Table E.2. Definition of variables in moment.f90.

Variable	Symbol	Description
A_COEF	A	1.0; factor in inertia source term
B_COEF	α_1	1.3; coefficient for arrangement angle in inertia term
C_COEF	α_2	0.33; exponent for arrangement angle in inertia term
D_COEF	B	0.4; factor in drag term
E_COEF	B_1	0.3; coefficient for arrangement angle in drag term
F_COEF	β_3	0.1; exponent for arrangement angle in drag term
DBX_1	$D^*_{B,i-1,j}$	Normalized MRE width at the upstream cell in x direction (flow from left to right)
DBY_1	$D^*_{B,i,j-1}$	Normalized MRE width at the upstream cell in y direction (flow from bottom to top)
DB	$D^*_{B,i,j}$	Normalized MRE width in actual cell
DBX1	$D^*_{B,i+1,j}$	Normalized MRE width at the upstream cell in x direction (flow from right to left)
DBY1	$D^*_{B,i,j+1}$	Normalized MRE width at the upstream cell in y direction (flow from top to bottom)
HB	h_B	MRE height in actual cell
ARR	Ψ	MRE arrangement angle in actual cell
C_D	C_D	MRE drag coefficient in actual cell
REL-SPACX	dD^*_B	Difference in normalized width between upstream and actual cell in x direction
REL-SPACY	dD^*_B	Difference in normalized width between upstream and actual cell in y direction
COEF_MX	$f_{MRE,inertia,x}$	Factor in inertia term in x direction (see equation E-3.a)
COEF_MY	$f_{MRE,inertia,y}$	Factor in inertia term in y direction (see equation E-4.a)
COEF_DX	$S_{MRE,fit,drag,x}$	Drag source term in x direction (see equation E-3.b)
COEF_DY	$S_{MRE,fit,drag,y}$	Drag source term in y direction (see equation E-4.b)
IMRE	-	MRE switch

They are initialized in the lines 323 to 344:

```
!.....FOR MACRO-ROUGHNESS ELEMENTS
      IMRE = L%MRE_SWITCH
      A_COEF = L%A_COEF
      B_COEF = L%B_COEF
      C_COEF = L%C_COEF
      D_COEF = L%D_COEF
      E_COEF = L%E_COEF
      F_COEF = L%F_COEF
      DBX_1 = 0.0
      DBY_1 = 0.0
      DB = 0.0
      DBX1 = 0.0
      DBY1 = 0.0
      HB = 0.0
      ARR = 0.0
      C_D = 0.0
      RELSPACX = 0.0
```

```
      RELSPACY = 0.0
      COEF_MX = 0.0
      COEF_MY = 0.0
      COEF_DX = 0.0
      COEF_DY = 0.0
```

The source terms for flow from right to left (negative flux in x direction) are calculated in lines 514 to 536:

```
!.. CALCULATE SOURCE TERM IN NEGATIVE X DIRECTION
IF (IMRE.EQ.0 .AND. DP(I,J,1).NE.0.0) THEN
  DB = SQRT(L%MRE_ABVCOEF(I,J))
  IF (DB.GT.0.0) THEN
    ARR = L%MRE_ARRVCOEF(I,J)
    DBX1 = SQRT(L%MRE_ABVCOEF(IP1,J))
    HB = L%MRE_HBVCOEF(I,J)
    C_D = L%MRE_CDVCOEF(I,J)
    COEF_MX = A_COEF*SQRT(9.81*DP(I,J,1))/ABS(P(I,J,1)/DP(I,J,1))*(B_COEF-
(COS(4.0*(PI/180.0*ARR-PI/2.0-ATAN(Q(I,J,1)/P(I,J,1))))))**C_COEF
    RELSPACX=MAX(DB-DBX1,0.0)
    IF (RELSPACX.GT.0.0) THEN
      COEF_DX = -1.0*D_COEF*REL-
SPACX/DX*P(I,J,1)**2.0/DP(I,J,1)*(MIN(DP(I,J,1)*2.0,HB)/DP(I,J,1))*C_D*(1.0-
E_COEF*(1.0-COS(4.0*(PI/180.0*ARR-PI/2.0-ATAN(Q(I,J,1)/P(I,J,1))))))**F_COEF
    ELSE
      COEF_DX = 0.0
    ENDIF
  ELSE
    COEF_MX = 0.0
    COEF_DX = 0.0
  ENDIF
ELSE
  COEF_MX = 0.0
  COEF_DX = 0.0
ENDIF
```

The source term for flow from left to right (positive flux in x direction) are calculated in the lines 553 to 575:

```
!..CALCULATE SOURCE TERM IN POSITIVE X DIRECTION
IF (IMRE.EQ.0 .AND. DP(I,J,1).NE.0.0 .AND. P(I,J,1).GT.0.0) THEN
  DB = SQRT(L%MRE_ABVCOEF(I,J))
  IF (DB.GT.0.0) THEN
    ARR = L%MRE_ARRVCOEF(I,J)
    DBX_1 = SQRT(L%MRE_ABVCOEF(IM1,J))
    HB = L%MRE_HBVCOEF(I,J)
```

```
    C_D = L%MRE_CDVCOEF(I,J)
    COEF_MX    =    A_COEF*SQRT(9.81*DP(I,J,1))/ABS(P(I,J,1)/DP(I,J,1))*(B_COEF-
(COS(4.0*(PI/180.0*ARR-PI/2.0-ATAN(Q(I,J,1)/P(I,J,1))))))**C_COEF
    RELSPACX=MAX(DB-DBX_1,0.0)
    IF (RELSPACX.GT.0.0) THEN
      COEF_DX                              =                              D_COEF*REL-
SPACX/DX*P(I,J,1)**2.0/DP(I,J,1)*(MIN(DP(I,J,1)*2.0,HB)/DP(I,J,1))*C_D*(1.0-
E_COEF*(1.0-COS(4.0*(PI/180.0*ARR-PI/2.0-ATAN(Q(I,J,1)/P(I,J,1))))))**F_COEF
    ELSE
      COEF_DX = 0.0
    ENDIF
  ELSE
    COEF_MX = 0.0
    COEF_DX = 0.0
  ENDIF
ELSE
  COEF_MX = 0.0
  COEF_DX = 0.0
ENDIF
```

The source term for flow from top to bottom (negative flux in y direction) are calculated in the lines 769 to 791:

```
!..CALCULATE SOURCE TERM IN Y DIRECTION
IF (IMRE.EQ.0 .AND. DQ(I,J,1).NE.0.0) THEN
  DB = SQRT(L%MRE_ABVCOEF(I,J))
  IF (DB.GT.0.0) THEN
    ARR = L%MRE_ARRVCOEF(I,J)
    DBY1 = SQRT(L%MRE_ABVCOEF(I,JP1))
    HB = L%MRE_HBVCOEF(I,J)
    C_D = L%MRE_CDVCOEF(I,J)
    COEF_MY    =    A_COEF*SQRT(9.81*DQ(I,J,1))/ABS(Q(I,J,1)/DQ(I,J,1))*(B_COEF-
(COS(4.0*(PI/180.0*ARR-ATAN(P(I,J,1)/Q(I,J,1))))))**C_COEF
    RELSPACY=MAX(DB-DBY1,0.0)
    IF (RELSPACY .GT. 0.0) THEN
      COEF_DY                          =                          -1.0*D_COEF*REL-
SPACY/DX*Q(I,J,1)**2.0/DQ(I,J,1)*(MIN(DQ(I,J,1)*2.0,HB)/DQ(I,J,1))*C_D*(1.0-
E_COEF*(1.0-COS(4.0*(PI/180.0*ARR-ATAN(P(I,J,1)/Q(I,J,1))))))**F_COEF
    ELSE
      COEF_DY = 0.0
    ENDIF
  ELSE
    COEF_MY = 0.0
    COEF_DY = 0.0
  ENDIF
ELSE
  COEF_MY = 0.0
```

```
  COEF_DY = 0.0
ENDIF
```

The source term for flow from bottom to top (positive flux in y direction) are calculated in the lines 804 to 826:

```
!..CALCULATE SOURCE TERM IN Y-DIRECTION
IF (IMRE.EQ.0 .AND. DQ(I,J,1).NE.0.0 .AND. Q(I,J,1).GT.0.0) THEN
  DB = SQRT(L%MRE_ABVCOEF(I,J))
  IF (DB.GT.0.0) THEN
    ARR = L%MRE_ARRVCOEF(I,J)
    DBY_1 = SQRT(L%MRE_ABVCOEF(I,JM1))
    HB = L%MRE_HBVCOEF(I,J)
    C_D = L%MRE_CDVCOEF(I,J)
    COEF_MY    =    A_COEF*SQRT(9.81*DQ(I,J,1))/ABS(Q(I,J,1)/DQ(I,J,1))*(B_COEF-
(COS(4.0*(PI/180.0*ARR-ATAN(P(I,J,1)/Q(I,J,1))))))**C_COEF
    RELSPACY=MAX(DB-DBY_1,0.0)
    IF (RELSPACY .GT. 0.0) THEN
      COEF_DY                              =                                D_COEF*REL-
SPACY/DX*Q(I,J,1)**2.0/DQ(I,J,1)*(MIN(DQ(I,J,1)*2.0,HB)/DQ(I,J,1))*C_D*(1.0-
E_COEF*(1.0-COS(4.0*(PI/180.0*ARR-ATAN(P(I,J,1)/Q(I,J,1))))))**F_COEF
    ELSE
      COEF_DY = 0.0
    ENDIF
  ELSE
    COEF_MY = 0.0
    COEF_DY = 0.0
  ENDIF
ELSE
  COEF_MY = 0.0
  COEF_DY = 0.0
ENDIF
```

The flux in x direction is calculated in line 635 to 636:

```
IF (IMRE .EQ. 0) XP = XP+COEF_MX*P(I,J,1)-DT*COEF_DX
IF (IFRIC.NE.1 .AND. IMRE .EQ.0) XP = XP/(1.0+COEF_MX+FF)
```

and in y direction is calculated in line 887 to 889:

```
IF (IMRE .EQ. 0) XQ = XQ+COEF_MY*Q(I,J,1)-DT*COEF_DY
IF (IFRIC.NE.1 .AND. IMRE .EQ.0) XQ = XQ/(1.0+COEF_MY+FF)
```

E.2 Post-processing of COMCOT results

Intermediate steps of result post-processing of the simulation results of the no friction (NF), constant friction (CF), variable friction map (VF) and macro-roughness element (MRE) models using various cell sizes dx are provided in this section. Table E.3 provides the bore arrival times at wave gauge A8 of the NF models $t_{A8,NF\ model,dx}$ and the time correction factors $f_{t,dx}$.

Table E.3. Bore arrival times $t_{A8,NF\ model,dx}$ and time correction factors $f_{t,dx}$ from NF model for various cell sizes dx.

cell size dx [m]	**arrival time $t_{A8,NF\ model,dx}$ [s]**	**Time correction factor $f_{t,dx}$ [-]**
5	204	1.000
10	180	0.884
20	170	0.833
40	201	0.985